

Electrification

2023 Annual Progress Report

Vehicle Technologies Office

(This page intentionally left blank)

Disclaimer

This report was prepared as an account of work sponsored by an agency of the United States government. Neither the United States government nor any agency thereof, nor any of their employees, makes any warranty, express or implied, or assumes any legal liability or responsibility for the accuracy, completeness, or usefulness of any information, apparatus, product, or process disclosed or represents that its use would not infringe privately owned rights. Reference herein to any specific commercial product, process, or service by trade name, trademark, manufacturer, or otherwise does not necessarily constitute or imply its endorsement, recommendation, or favoring by the United States government or any agency thereof. The views and opinions of authors expressed herein do not necessarily state or reflect those of the United States government or any agency thereof.

Acronyms

A

AC	Alternating Current
ACC	Adaptive Cruise Control
accel	Acceleration
ACS	Advanced Combustion Systems
ACSforEVER	Advanced Climate Systems for EV Extended Range
AER	All-electric range
AFV	Alternative Fuel Vehicle
AMI	Advanced Metering Infrastructure
AMT	Automated Mechanical Transmission
ANL	Argonne National Laboratory
ANN	Artificial Neural Network
AOI	Areas of Interest
APEC	Asia Pacific Economic Council
APRF	Advanced Powertrain Research Facility
APT	Pressure Sensor
ASD	Aftermarket Safety Device
AVTA	Advanced Vehicle Testing Activity
AVTE	Advanced Vehicle Testing and Evaluation

B

BaSce	Baseline and Scenario
Batt	Battery
BEB	Battery Next-Generation Electric Transit Bus
BEC	Bussed Electrical Center
BEMS	Building Energy Management System
BET	Battery Electric Truck
BEV	Battery Electric Vehicle
BMW	Bayerische Motoren Werke AG
BSFC	Brake Specific Fuel Consumption
BTE	Brake Thermal Efficiency

C

CAC	Charge Air Cooler
CACC	Cooperative Adaptive Cruise Control
CAE	Computer-Aided Engineering
CAFE	Corporate Average Fuel Economy
CAN	Controller Area Network
CAV	Connected and automated vehicles
CARB	California Air Resources Board
CBD	Central Business District
CCS	Combined Charging System
CW, CCW	Clockwise, Counterclockwise

CD	Charge-Depleting
CERV	Conference on Electric Roads and Vehicles
CFD	Computational Fluid Dynamics
CFDC	Commercial Fleet Data Center
CFL	Combined Fluid Loop
CH ₄	Methane
CHTS	California Household Travel Survey
CIP	Common Integration Platform
Cm ³	Cubic
CNG	Compressed Natural Gas
CO	Carbon monoxide
CO ₂	Carbon Dioxide
COMM	Commuter
Conv	Conventional Vehicle
COP	Coefficient of Performance
CPS	Cyber-Physical Security
CPSR	Constant Power Speed Ratio
CS	Charge Sustaining
Cs	Cold start
CV	Conventional vehicle

D

D3	Downloadable Dynamometer Database
DC	Direct current
DCFC	Direct Current Fast Charge
DCT	Dual-clutch transmission
decel	Deceleration
DER	Distributed energy resource
DFGM	Digital Flux Gate Magnetometer
DFMEA	Design of Failure Modes Analysis
DGE	Diesel Gallon Equivalent
DOE	U.S. Department of Energy
DOHC	Dual overhead cam
DS	Down speeding
DSM	Distributed Security Module
DSM	Diagnostic Security Module
DSP	Digital Signal Processor
DSRC	Dedicated Short Range Communications
dt	Change in time
dv	Change in velocity
Dyno	Dynamometer

E

EAVS	Electrically Assisted Variable Speed Supercharger
EC	European Commission
EDV	Electric Drive Vehicle

EDT	Electric Drive Technologies
EDX	Energy dispersive x-ray spectroscopy
EEERE	Energy Efficiency and Renewable Energy
EGR	Exhaust Gas Recirculation
EG/W	Ethylene glycol/water
EOL	End of life
EPA	Environmental Protection Agency
ePATHS	Electrical PCM Assisted Thermal Heating System
EREV	Extended-Range Electric Vehicles
ESIF	Energy Systems Integration Facility
ESS	Energy Storage System
ETT	Electric Transportation Technologies
E-TREE	Electric Truck with Range Extending Engine
EUMD	End-Use Measurement Device
EV	Electric Vehicle
EV2G	Electric Vehicle-to-Grid
EVSE	Electric Vehicle Service Equipment
EXV	Electronic Expansion Valve

F

F	Force
FASTSim	Future Automotive Systems Technology Simulator
FC	Fuel cell
FC	Fast charge
FCons	Fuel consumption
FCTO	Fuel Cell Technologies Office
FE	Fuel Economy
FEA	Finite Element Analysis
FEX	Front-end Heat Exchanger
FHWA	Federal Highway Administration
FLNA	Frito-Lay North America
FM	Friction Modifier
FMEP	Friction Mean Effective Pressure
FOA	Funding Opportunity Announcement
FTIR	Fourier transform infrared spectroscopy
FTP	Federal Test Procedure
FWD	Four-wheel drive
FY	Fiscal year

G

g	gram
GB	Gigabyte
GCEDV	Grid Connected Electrical Drive Vehicles
GEM	Gas Emissions Model
GHG	Greenhouse Gas
GITT	Grid Interaction Tech Team

GMLC	Grid Modernization Lab Consortium
GnPs	graphene nanoplatelets
GO	Graphene Oxide
GPRA	Government Performance and Results Act
GPS	Global Positioning System
GREET	Greenhouse gases, Regulated Emissions, and Energy use in Transportation
GSF1	Generic Speed Form 1
GSU	Grid side unit
GUI	Graphic User Interface
GVW	Gross Vehicle Weight

H

h-APU	hybrid Auxiliary Power Unit
HATCI	Hyundai America Technical Center, Inc.
HC	Unburned hydrocarbons
HD	Heavy Duty
HEV	Hybrid-Electric Vehicle
H-GAC	Houston-Galveston Area Council
HHDDT	Heavy Heavy-Duty Diesel Truck
HHV	Hydraulic Hybrid Vehicle
HIL	Hardware-In-the-Loop
HP	Heat Pump
Hp	Horsepower
HTML	HyperText Markup Language
HV	High Voltage
HVAC	Heating Ventilating and Air Conditioning
HWFET	Highway Fuel Economy Test
HPMS	Highway Performance Monitoring System
HVTB	High Voltage Traction Battery
HWY	Highway Program or Highway Fuel Economy Test Cycle
HPC	High Performance Computing
HTR	Heater
Hz	Hertz

I

I	Inertia
IC	Internal Combustion
ICD	Interim Component Durability
ICDV	Internal Combustion Drive Vehicles
ICE	Internal Combustion Engine
ICTF	Intermodal Container Transfer Facility
ICU	Inverter-Charger Unit
IEB	Information Exchange Bus
IEC	International Electrotechnical Commission
IGBT	Insulated Gate Bipolar Transistors
IHX	Internal Heat Exchanger

INL	Idaho National Laboratory
INTEGRATE	Integrated Network Testbed for Energy Grid Research and Technology
IOT	Internet of Things
IR	Infrared Radiation
ISO	International Organization for Standardization
ITS	Intelligent Transportation Systems

J

JIT	Just-in-Time
-----	--------------

K

kg	Kilogram
km	Kilometer
kW	Kilowatt
kWh	Kilowatt hour

L

L	litre
L1	Level 1 benchmark
L2	Level 2 benchmark
Lbf	Pounds force
LCC	Liquid-Cooled Condenser
LD	Light duty
LH	line haul
Li	Lithium
LIB	Lithium-ion battery
LLNL	Lawrence Livermore National Laboratory
LNG	Liquified natural gas
LTC	Lockport Technical Center
LV	Leading Vehicle

M

M	Mass
MBSE	Model Based System Engineering
MD	Medium Duty
mpg	Miles per gallon
MMTCE	Million Metric Tons of Carbon Equivalent
MIIT	Ministry of Industry and Information Technology
mi	Mile
MJ	Megajoules
MOSFET	Metal-Oxide Semiconductor Field-Effect Transistor
mph	Miles per hour
MPGe,	Miles per gallon equivalent, Miles per gallon gasoline equivalent
MTDC	Medium Truck Duty Cycle
MOVES	Motor Vehicle Emission Simulator
MRF	Moving Reference Frame
MURECP	Medium-Duty Urban Range Extended Connected Powertrain

MY Model year
 M2 Meters squared

N

NACFE North American Council for Freight Efficiency
 NDA Non-Disclosure Agreement
 NETL National Energy Technology Laboratory
 NHTS National Household Travel Survey
 NHTSA National Highway Transportation Safety Administration
 NM Newton meters
 NO_x Nitrogen oxides
 NR Natural Rubber
 NRE Non-Recurring Engineering
 NREL National Renewable Energy Laboratory
 NRT National Retail Trucking
 NVH Noise, vibration, and harshness
 NVUSD Napa Valley Unified School District
 NYSERDA New York State Energy Research Development Authority

O

OBC On-board charger
 OCBC Orange County Bus Cycle
 OEM Original Equipment Manufacturer
 OneSAF One Semi-Automated Forces
 ORNL Oak Ridge National Laboratories

P

P Active Power
 PC Polycarbonate
 PCM Phase-Change Material
 PCU Power Control Unit
 PCU Powertrain Control Unit
 PEEM Power Electronics and Electric Motor
 PFC Power factor correction
 PFI Port fuel injection
 PGW Pittsburgh Glass Works
 PHEV Plug-in Hybrid Electric Vehicle
 PHEV## Plug-in hybrid electric vehicle with ## miles of all-electric range
 PI Principal Investigator
 PM Permanent Magnet
 PM Particulate Matter
 ppm Parts per Million
 PTC Positive Temperature Coefficient (Electric Heater)
 PTO Power Take-Off
 PVP Polyvinylpyrrolidone
 PWWMD Public Works and Waste Management Department

λ	Power Factor
φ	Power Angle
Q	
Q	Reactive power
QA	Quality assurance
QC	Quality control
R	
R2	Coefficient of Determination
R/D	Receiver / Dryer
REV	New York State's Reforming the Energy Vision Initiative
REx	Range Extending Engine
rGO	reduced graphene oxide
RH	Relative Humidity
RMS	Root Mean Square
ROL	Ring-On-Liner
rpm	Revolutions Per Minute
RSU	Road Side Unit
RWDC	Real-World Drive-Cycle
S	
S	Apparent power
SAE	Society of Automotive Engineers
SBR	Styrene-Butadiene Rubber
SC03	SC03 Supplemental Federal Test Procedure
SCAG	Southern California Association of Governments
SCAQMD	South Coast Air Quality Management District
SCIG	Southern California International Gateway
SCR	Silicon Controlled Rectifier
SCR	Selective Catalytic Reduction
SDO	Standards Definition Organizations
SI	<u>Système International d'Unités</u>
SI	Gasoline Spark Ignition
SNR	Sensor
SOC	State of Charge
SPL	Sound Pressure Level
SR	Speed Ratio
SS	Steady State
SPaT	Signal Phase and Timing
StAR	Storage-Assisted Recharging
T	
T	Torque
TA	Technical Area
TA	Torque Assist
TC	Thermocouple

TE	Thermoelectric
TE	Transmission Error
TES	Thermal Energy Storage
TGA	thermogravimetric analysis
THC	Total hydrocarbon emissions
TIM	Thermal Interface Materials
TLRP	Thermal Load Reduction Package
TN	Testing Network
TOU	Time-Of-Use
TSDC	Transportation Secure Data Center
TSI	Turbocharged stratified injection
TUSD	Torrance Unified School District
TXVs	Thermal Expansion Valves

U

U.S. DRIVE	U.S. Driving Research and Innovation for Vehicle Efficiency and Energy Sustainability
UA	Transfer Coefficient
UC	Ultra-capacitor
UCR	University of California, Riverside
UDDS	Urban Dynamometer Driving Schedule
UN ECE	United Nations Economic Council for Europe
UPS	United Parcel Service
URL	Uniform Resource Locator
US06	Environmental Protection Agency US06 or Supplemental Federal Test Procedure
USABC	United States Advanced Battery Consortium
USCAR	U.S. Council for Automotive Research
Util	Battery capacity utilization

V

V	Voltage
V2G	Vehicle-to-Grid
VAr	Volt-Amp-reactive
VGI	Vehicle-Grid Integration
VGT	Variable Geometry Turbocharger
VIP	Vacuum Insulated Panels
VMT	Vehicle Miles Traveled
VS	Vehicle Systems
VSATT	Vehicle Systems Analysis Technical Team
VSI	Vehicle Systems Integration
VSST	Vehicle Systems Simulation and Testing
VTCab	Vehicle Thermal Cab Simulator
VTIF	Vehicle Testing and Integration Facility
VTO	Vehicle Technologies Office

W

dw	Change in Angle W
----	-------------------

WCC	Water Cooled Condenser
WEC	World Endurance Championship
WEG	Water/Ethylene Glycol
Wh	Watt hour
WHR	Waste Heat Recovery
WPT	Wireless Power Transfer
WTW	Well-to-Wheels

X

XFC	Extreme Fast Charging
XPS	x-ray photoelectron spectroscopy

Z

ZECT	Zero-emissions cargo transport
------	--------------------------------

Executive Summary

During fiscal year 2023 (FY 2023), the U.S. Department of Energy (DOE) Vehicle Technologies Office (VTO) funded early-stage research, development, demonstration, & deployment (RDD&D) projects that address Electrification of the U.S. transportation sector. The VTO Electrification Program is composed of Electric Drive Technologies, and Grid Integration activities. The Electric Drive Technologies group conducts R&D projects that advance electric motors and power electronics technologies. The Grid and Charging Infrastructure group conducts R&D projects that advance grid modernization and electric vehicle charging technologies. This document presents a brief overview of the Electrification Program and progress reports for its R&D projects. Each of the progress reports provide a project overview and highlights of the technical results that were accomplished in fiscal year (FY) 2023.

Table of Contents

Acronyms	ii
Executive Summary	xi
Vehicle Technologies Office Overview	1
Electric Drive Technologies Program Overview	3
Grid and Infrastructure Program Overview	17
I Electric Drive Technologies	34
I.1 Electric Drive Technologies Research	34
I.1.1 Non-Heavy Rare-Earth High-Speed Motors (Oak Ridge National Laboratory)	34
I.1.2 High-Voltage, High Power Density Traction Drive Inverter (Oak Ridge National Laboratory)	42
I.1.3 Highly Integrated Power Module (Oak Ridge National Laboratory)	48
I.1.4 Integrated Electric Drive System (Oak Ridge National Laboratory)	55
I.1.5 Power Electronics Materials and Bonded Interfaces – Reliability and Lifetime (National Renewable Energy Laboratory)	62
I.1.6 Advanced Packaging Designs – Reliability and Prognostics (National Renewable Energy Laboratory)	71
I.1.7 Power Module Precursors and Prognostics (National Renewable Energy Laboratory)	79
I.1.8 Power Electronics Thermal Management (National Renewable Energy Laboratory)	88
I.1.9 Electric Motor Thermal Management (National Renewable Energy Laboratory)	96
I.1.10 Integrated Traction Drive Thermal Management (National Renewable Energy Laboratory)	100
I.1.11 Bottom-Up Soft Magnetic Composites (Sandia National Laboratories)	105
I.1.12 Power Electronics: Vertical GaN Device Development (Sandia National Laboratories)	114
I.1.13 Power Electronics: Vertical GaN Device Development (Sandia National Laboratories)	120
I.1.14 Component Modeling, Co-Optimization, and Trade-Space Evaluation (Sandia National Laboratories)	128
I.1.15 Implementation of WBG devices in circuits, circuit topology, system integration as well as SiC devices (The Ohio State University)	136
I.1.16 Device- and System-Level Thermal Packaging for Electric-Drive Technologies (Georgia Institute of Technology)	146
I.1.17 Integrated Motor and Drive for Traction Application (University of Wisconsin-Madison)	160
I.1.18 Multi-Objective Design Optimization of 100 kW Non-Rare-Earth or Reduced-Rare Earth Machines (Purdue University)	169
I.1.19 Design, Optimization, and Control of a 100 kW Electric Traction Motor Meeting or Exceeding DOE 2025 Targets (Illinois Institute of Technology)	177
I.1.20 Integration Methods for High-Density Integrated Electric Drives (University of Arkansas)	185
I.1.21 Heterogeneous Integration Technologies for High-temperature, High-density, Low-profile Power Modules of Wide Bandgap Devices in Electric Drive Applications (Virginia Tech)	194

I.2 Electric Drive Technologies Development 203

- I.2.1 Cummins High Power Density Inverter (Cummins Inc.)..... 203
- I.2.2 Scalable Ultra Power-Dense Extended Range Super Inverter (BorgWarner, Inc.)..... 211
- I.2.3 Low-Cost Rare-Earth Free Electric Drivetrain Enabled by Novel Permanent Magnets, Inverter, Integrated Design and Advanced Thermal Management (Marquette University) 219
- I.2.4 Low Cost High-Performance HRE-Free 3-in-1 Electric Drive Unit (American Axle & Manufacturing)..... 232

II Grid and Charging Infrastructure 239

II.1 Industry Awards 239

- II.1.1 High-Power Inductive Charging System Development and Integration for Mobility 239
- II.1.2 Wireless Extreme Fast Charging for Electric Trucks (WAVE) 246
- II.1.3 Long-Range, Heavy-Duty Battery-Electric Vehicle with Megawatt Wireless Charging..... 253
- II.1.4 Improving the Freight Productivity of a Heavy-Duty, Battery Electric Truck by Intelligent Energy Management..... 259
- II.1.5 High Efficiency Powertrain for Heavy Duty Trucks using Silicon Carbide (SiC) Inverter - DE-EE0008806 (Ricardo)] 265
- II.1.6 eMosaic: Electrification Mosaic Platform for Grid-Informed Smart Charging Management (ABB Inc.)..... 272
- II.1.7 Demonstration of Utility Managed Smart Charging for Multiple Benefit Streams 278
- II.1.8 Bidirectional Wireless Power Flow for Medium-Duty Vehicle-to-Grid Connectivity 285
- II.1.9 Technology & Design Innovations to Maximize the Reduction Effect on DCFC Unit Cost Economics (Max-REDUCE)..... 291
- II.1.10A Solid-State Technology Enabled Compact, Modular Design to Reduce DC Fast Charging Cost and Footprint (Eaton Corporation)..... 296
- II.1.11 Development and Demonstration of Zero-Emission Technologies for Commercial Fleets - SuperTruck 3 (PACCAR)..... 304
- II.1.12 Volvo SuperTruck 3: A Zero Emission Freight Future (Volvo Group)..... 310
- II.1.13 Intelligent, Grid-Friendly, Modular Extreme Fast Charging System with Solid-State DC Protection (North Carolina State University) 315
- II.1.14 Enabling Extreme Fast Charging with Energy Storage (Missouri S&T)..... 322

II.2 EVs at Scale - VGI and SCM 329

- II.2.1 EVs@Scale Flexible charging to Unify the grid and transportation Sectors for EVs at scale (FUSE) 329

II.3 EVs at Scale - High Power Charging..... 339

- II.3.1 High-Power Electric Vehicle Charging Hub Integration Platform (eCHIP)..... 339
- II.3.2 Assessment and Validation of Next Generation Electric Vehicles High Power Charging Profiles 348

II.4 EVs at Scale - Advanced Charging Grid Integration Technologies 354

- II.4.1 Feasibility of Dynamic Wireless Power Transfer Corridors for Heavy-Duty Battery Electric Commercial Freight Vehicles (Oak Ridge National Laboratory) 354

II.4.2 Behind-the-Meter Storage (NREL, INL, ORNL, SNL, ANL).....	359
II.5 EVs@Scale - Cyber-Physical Security	368
II.5.1 Cybersecurity Projects with Unified National Lab Collaboration (CyberPUNC)	368
II.5.2 Electric Vehicle Integrated Safety, Intelligence, Operations (eVision)	374
II.5.3 Zero Trust Approach to Electric Vehicle Charging Infrastructure Security (PNNL)	382
II.6 EVs at Scale - Codes and Standards.....	388
II.6.1 Support development and validation testing of SAE J1634 (ANL)	388
II.6.2 Wireless Charging Standard- (J2954/1-2-3) and Closeout of SWIFT Charge Consortium Support (Argonne National Laboratory, Idaho National Lab, Oakridge National Lab)	393
II.6.3 Wireless Power Transfer, DER Standards Tasks (Idaho National Laboratory).....	397
II.6.4 Wireless Power Transfer, Medium Voltage Power Converter Standards Tasks (Oak Ridge National Laboratory).....	398

List of Figures

Figure 1. Assembled substrate for thermal evaluation: the conventional direct bonded copper (DBC) substrate (left) and the modified DBC with copper substrate (right). 10

Figure 2. Experimental setup to evaluate the thermal performance of the proposed DBC with copper substrate. 10

Figure 3. Comparison of device temperature (top) and substrate thermal resistance (bottom) at various power loss injections for traditional and modified DBCs..... 11

Figure 4. Developed MACHINE concept with embedded cooling channels and non-heavy rare earth magnets 11

Figure 5. Multi-physics design optimization of MACHINE concept. 12

Figure 6. Experimentally measured winding temperature vs. model predictions at various current loading. 12

Figure 7. 50% scale version of the DHAM short stator assembly. This component consists of 55 vol.% Fe4N. 13

Figure 8. DHAM rotor assembly during removal from custom hot pressing die. 13

Figure 9. Demagnetization loops for samples without any sintering aids and their performance with increasing weight percent of the Pr-Al-Cu compound at room temperature..... 14

Figure 10. Summary of temperature effect on energy product as a function of wt.% addition of Pr-Al-Cu. 14

Figure 11. Pictures of the SiC module installed within the dielectric-fluid-based plastic heat exchanger (left). Modeling results showing the slot jet cooling design (right). 15

Figure 12. Junction-to-fluid thermal resistance versus pumping power showing modeling and experimental results with comparisons to commercially available, WEG-cooled power modules (Si-based and SiC-based modules). 16

Figure 13 Key technologies and challenges addressed by the Grid and Infrastructure Program. 17

Figure 14 Examples of EV Connector Standards, Sources:ANL, SAE,,, ORNL , CEC 21

Figure 15 Strategic areas of the Grid and Infrastructure Program. 23

Figure 16 Key elements of Smart Charge Management. 25

Figure 17 Conceptual configuration of an HPC station. 26

Figure I.1.1.1 Summary of specifications. 35

Figure I.1.1.2 The integrated motor drive shows the outer rotor, stator, heat exchangers, manifold, bearings, external mountings, and power electronics..... 36

Figure I.1.1.3 (a) Original and (b) modified rotors. The arc magnets were flattened, and locating tabs were included in the rotor core. 36

Figure I.1.1.4 (a) Temperature distribution at the rated condition and (b) at the 20,000 rpm top-speed condition. Air flow of 14 m/s is needed in the air gap to ensure heat transfer coefficients that will result in magnet temperatures within the limits..... 37

Figure I.1.1.5 Campbell diagram for the rotor. 38

Figure I.1.1.6 (a) Stator with accelerometers and (b) signal from the accelerometer after impacting the stator with a hammer and its fundamental component. The fundamental component is a 700 Hz signal. 39

Figure I.1.1.7 (a) Prototype rotor, (b) one magnet with 43 segments, and (c) 3D printed heat exchanger. 39

Figure I.1.2.1 Major components of a three-phase segmented inverter. 43

Figure I.1.2.2 Test setup for the 100 kW segmented inverter.....	43
Figure I.1.2.3 Operating waveforms of the 100 kW inverter. From top to bottom: dc bus voltage, line-to-line voltages, and three-phase currents.	44
Figure I.1.2.4 Measured efficiency of the 100 kW inverter vs. output power.	44
Figure I.1.2.5 Photos of cooling subsystem pressure test setup for the 200 kW inverter.	44
Figure I.1.2.6 Measured cooling system pressure drop vs. flow rate for the 200 kW inverter.	44
Figure I.1.2.7 Setup for functionality test of the 200 kW inverter.	45
Figure I.1.2.8 Gate signal waveforms of the 200 kW inverter: (<i>left</i>) gate signals and (<i>right</i>) zoom-in showing dead times at turn-on and turn-off.	45
Figure I.1.2.9 Photos of the 200 kW inverter prototype.	46
Figure I.1.2.10 Test setup for the 200 kW segmented inverter.	46
Figure I.1.2.11 Operating waveforms of the 200 kW inverter. From top to bottom: dc bus voltage, line-to-line voltage, phase current, line-to-line voltages, and two phase currents.	46
Figure I.1.2.12 Measured efficiency of the 200 kW inverter vs. output power.	46
Figure I.1.3.1 ODBC-based power module with integrated gate driver and heat sink	49
Figure I.1.3.2 Fabricated copper-ODBC-based integrated power module	50
Figure I.1.3.3 Test setup and waveforms of a double-pulse test.....	50
Figure I.1.3.4 Power module thermal evaluation setup and test results.....	50
Figure I.1.3.5 Novel stacked–die cap power module.....	51
Figure I.1.3.6 Fabricated stacked–die cap power module (left) and testing of the power module at 756 V/50 A (right).....	51
Figure I.1.3.7 Illustrations of single profile–extruding (left) and multiprofile-merging (right) schemes	52
Figure I.1.3.8 Generated GA-optimized heat sink designs using a multiprofile-merging method	52
Figure I.1.3.9 Simulated thermal performance of the selected new heat sink design compared with the single profile–extruding baseline	53
Figure I.1.3.10 Mechanisms of improved performance for the multiprofile-merging method.....	53
Figure I.1.4.1 Assembled substrate for thermal evaluation: the conventional direct bonded copper (DBC) substrate (left) and the modified DBC with copper substrate (right).	56
Figure I.1.4.2 Experimental setup to evaluate the thermal performance of the proposed DBC with copper substrate.	56
Figure I.1.4.3 Thermal evaluation results captured using an infrared thermal camera comparing the traditional direct bonded copper (DBC, left) and the proposed DBC with copper (right) substrates.....	57
Figure I.1.4.4 Comparison of device temperature (left) and thermal resistance (right) at various power loss injections for the direct bonded copper (DBC) and DBC with copper (DBCwCu) substrates. These data show the advantages of DBCwCu over the traditional DBC.	57
Figure I.1.4.5 Module layout showing that opposing current paths are next to each other, thus reducing the layout inductance.	58
Figure I.1.4.6 Current distribution among the parallel metal-oxide semiconductor field-effect transistors (MOSFETs, left) showing unequal current distribution (right) impedance matching by varying wire bond length showing equal current distribution.....	58

Figure I.1.4.7 Designed DBC with copper substrate with optimized layout to improve thermal and electric performances..... 59

Figure I.1.4.8 A printed circuit board (PCB) based secondary board showing decoupling capacitor and current sensor on top of the board (left) and gate driver circuitry on the bottom (right). 59

Figure I.1.4.9 Assembled prototype of the designed power block integrating power module, gate driver, capacitor, and AC current sensor. 60

Figure I.1.5.1 Synthesis profile of sintered copper 64

Figure I.1.5.2 Sintered copper stencil patterns and bonded sample..... 64

Figure I.1.5.3 SAM images of HM-3 (bottom) and HM-4 (top) samples..... 65

Figure I.1.5.4 Degradation of polymer samples under thermal cycling..... 65

Figure I.1.5.5 Temperature measured on the samples under thermal shock..... 66

Figure I.1.5.6 SAM images of sintered copper samples with a 3-mm-thick Cu baseplate, 0 cycles (left) and 500 cycles (right) 66

Figure I.1.5.7 Image denoising using spatial – frequency domain transfer 67

Figure I.1.5.8 Defect progression in sintered copper (left) and comparison of different techniques to estimate the defect percentage (right) 67

Figure I.1.5.9 Predictive performance of statistical models (top) and machine learning techniques (bottom) in estimating the defect growth in bonded samples 68

Figure I.1.5.10 Defect growth prediction of sintered silver 69

Figure I.1.6.1 Polyimide absorption analysis..... 73

Figure I.1.6.2..... 73

Figure I.1.6.3 Test pattern and HAZ before ultrasonic cleaning..... 74

Figure I.1.6.4 Test cut optimization pattern..... 74

Figure I.1.6.5 Test cutting process (left) and completed optimization pattern 75

Figure I.1.6.6 HAZ from 30-W, 10.6- μ m CO₂ desktop laser cutter 75

Figure I.1.6.7 Comparison of edge quality from 9.3- μ m CO₂ laser (left) and 10.6- μ m CO₂ laser (right)..... 76

Figure I.1.6.8 Polyimide layers for module fabrication..... 76

Figure I.1.6.9 Vacuum high-temperature press..... 76

Figure I.1.6.10 Half-bridge power module design..... 77

Figure I.1.6.11 Half-bridge power module assembly 77

Figure I.1.7.1 ALTs on various SiC MOSFET module samples: (a) power/temperature cycling on the CCS020-M12CM2 six-pack module and (b) power/temperature cycling on the FS55MR1-2W1M1H-B11 six-pack module 81

Figure I.1.7.2 ALT result on the CCS020-M12CM2 device after approximately 10,000 cycles: (a) R_{ds,on} versus I_{drain} of a new device in the CCS020-M12CM2 six-pack and (b) R_{ds,on} versus I_{drain} of an aged device in the CCS020-M12CM2 six-pack 81

Figure I.1.7.3 ALT result on the C3M0075120D device after approximately 55,000 cycles: (a) V_{th} of a new device in the C3M0075120D TO-247 single module and (b) V_{th} of an aged device in the C3M0075120D TO-247 single module..... 81

Figure I.1.7.4 Transient behavior and equivalent circuit: (a) two resonant loops and (b) circuit model. Variable-dependent and nonlinear components are highlighted in blue.	82
Figure I.1.7.5 Model for the two resonant loops during transients.	83
Figure I.1.7.6 Waveform of the first two/three resonant peaks of v_{gs} : (a) after turning on after dead time and (b) after turning off at the beginning of dead time. Note that the darker traces correspond to larger amounts of change in respective parameters. The total increase of $R_{ds,on}$, V_{th} , and R_g corresponding to the respective spans are 28 m Ω , 1.4 V, and 140 m Ω , with even intervals.....	83
Figure I.1.7.7 Principle of the level searching circuit for v_{gs} acquisition: (a) generation of pulses and (b) circuit functionality diagram.....	84
Figure I.1.7.8 Level searching circuit and test bench setup.....	84
Figure I.1.7.9 Detection results for $R_{ds,on}$ change: (a)--(d) scope measurements; (e)--(h) detection results; (a,e) turn-on, zero bus voltage; (b,f) turn-on, 30-V bus voltage; (c,g) turn-off, zero bus voltage; and (d,h) turn-off, 30-V bus voltage.....	85
Figure I.1.7.10 Detection results for V_{th} change: (a)--(d) scope measurements; (e)--(h) detection results; (a,e) turn-on, zero bus voltage; (b,f) turn-on, 30-V bus voltage; (c,g) turn-off, zero bus voltage; and (d,h) turn-off, 30-V bus voltage.....	85
Figure I.1.8.1 Computer-aided design (CAD) drawings of the SiC thermal demonstration module (left) and the dielectric fluid heat exchanger with modules (right). MOSFET: metal–oxide–semiconductor field-effect transistor.	89
Figure I.1.8.2 Pictures of the SiC module installed within the dielectric fluid heat exchanger (left) and the jet impingement manifold mounted over the module’s fin structures (right)	90
Figure I.1.8.3 Picture of the assembled dielectric heat exchanger piped into the dielectric fluid loop and electrically connected to the PowerTester	91
Figure I.1.8.4 Junction-to-fluid thermal resistance versus pumping power showing modeling and experimental results with comparisons to commercially available, WEG-cooled power modules.....	91
Figure I.1.8.5 Model-predicted junction-to-fluid thermal resistance versus pumping power for 70°C (left) and –40°C (right) inlet fluid temperatures.....	92
Figure I.1.8.6 CAD drawing of the two-phase cold plate (left) and a picture of the two-phase cold plate piped into the two-phase fluid loop (right)	93
Figure I.1.8.7 High-speed video images of boiling on the cold plate surface showing boiling incipience begins at the downstream device and then quickly propagates to the upstream device. The red squares denote the approximate locations of the SiC devices.....	93
Figure I.1.9.1 ORNL and NREL motor analysis approach.....	97
Figure I.1.9.2 Schematic of airflow through rotor-stator air gap showing flow exiting through the cavity containing the power electronics	98
Figure I.1.9.3 Left: Steady-state temperature plot of high-torque condition used as the starting point for transient analysis. Right: Steady-state temperature map of peak power condition. Center: Plot depicting maximum temperatures of key components over time in response to step loading of the peak power condition.	98
Figure I.1.10.1 ORNL’s outer-rotor motor with integrated inverter and cooling system components. <i>Illustration by Vandana Rallabandi, ORNL</i>	101
Figure I.1.10.2 Stator cooling assembly with 18 T-shape heat exchangers attached to the coolant distribution manifold. <i>Illustration by Bidzina Kekelia, NREL</i>	101

Figure I.1.10.3 Ceramic T-shape in-slot heat exchanger 3D-printed by Lithoz from alumina (left) and crack after sintering (right). *Illustration by Bidzina Kekelia, NREL* 102

Figure I.1.10.4 Experimental setup for evaluation of the T-shape heat exchanger performance. Illustration by Bidzina Kekelia, NREL 102

Figure I.1.10.5 Current design of the cylindrical inverter housing. *Illustration by Bidzina Kekelia, NREL* 103

Figure I.1.11.1 Die for pressing larger toroids and cubes. 106

Soft magnetic toroids with an Outer Diameter (O.D.) of 35 mm. 106

Figure I.1.11.2 Soft magnetic toroids with an Outer Diameter (O.D.) of 35 mm. 107

Figure I.1.11.3 PLA anti-molds for the fabrication of DHAM soft magnetic components. From left to right: stator long leg assembly, stator short leg assembly, and rotor assembly. 107

Figure I.1.11.4 Full size DHAM parts fabricated using neat epoxy. From left to right: stator long leg assembly, stator short leg assembly, and rotor assembly. 108

Figure I.1.11.5 50% scale version of the DHAM short stator assembly. This part is 55 vol.% Fe₄N. 108

Figure I.1.11.6 Composite under both pressure and heat. 109

Figure I.1.11.7 DHAM rotor assembly during demolding. 109

Figure I.1.11.8 DHAM rotor assembly after partial demolding. 110

Figure I.1.11.9 DHAM rotor after complete demolding and polishing. A hairline fracture, barely visible in the image, is the only defect in this sample. 110

Figure I.1.11.10 Average Berkovich modulus for a sample of 55 vol.% Fe₄N in epoxy. 111

Figure I.1.11.11 Average Berkovich hardness for a sample of 55 vol.% Fe₄N in epoxy. 111

Figure I.1.11.12 An SEM image of the indentations in a sample of 55 vol.% Fe₄N in epoxy. 111

Figure I.1.12.1 Schematic representation of current results showing change in frequency-dependent time to failure as a function of acceleration conditions. The differentiation between these two and the behavior at use conditions is unknown. 115

Figure I.1.12.2 Current vs time plots for all degradation conditions at DC and 0.1Hz conditions. Red lines are DC and Green lines are 0.1Hz. Average failure current (10x average initial current) is marked for each condition. Failure locations of all parts which shorted before failure current was reached are marked with black arrows. 115

Figure I.1.12.3 Weibull plots of MLCC failure as a function of bipolar AC frequency for three acceleration conditions: 45V 255°C (a), 65V 225°C (b), and 100V 210°C (c). (d) MTTF as a function of voltage stress signal frequency for each condition normalized to MTTF under DC conditions. 116

Figure I.1.12.4 Failure Current as a function of acceleration condition and switching frequency of voltage stress. Red dotted lines are the average failure criterion for slow degradation (10x the initial leakage current). 116

Figure I.1.12.5 Degradation rate as a function of switching frequency of voltage stress for different acceleration conditions. 117

Figure I.1.12.6 Examples of fits to linear portion of I(t) curves for degradation rate assessment for 45V 255°C 5mHz condition. 117

Figure I.1.12.7 Change in Time to Failure for lower acceleration conditions for high voltage (100V and 175°C) and low voltage (45V 210°C). 118

Figure I.1.13.1 (a) Schematic drawing of JBS diode, (b) schematic drawing of Trench MOSFET, and (c) schematic drawing of a Double-well MOSFET. 121

Figure I.1.13.2 Studies on these three devices, the pn diode, the Schottky Barrier diode, and the MOSCAP lends insight into improving performance for the JBS and MOSFET devices.....	122
Figure I.1.13.3 (a) Breakdown voltages of pre/post-passivation devices compared to a simulation model. Images showing electroluminescence during avalanche confirm that at $t_{JTE} = 250$ nm (b) the JTE fully depletes, and breakdown occurs near the inner edge. At $t_{JTE} = 295$ nm (c) the JTE does not fully deplete and breakdown occurs near the outer edge.....	123
Figure I.1.13.4 Etch damage recovery and Etch-and Regrowth Progress, showing (a) reverse IV curves of Schottky Barrier Diode with and without in-situ XeF_2 surface treatment before regrowth. XeF_2 is removing residual ICP etch damage yielding diodes with lesser leakage current. (b) SIMS profile of interrupted growth with no air exposure. Matches that of continuously grown diode. (c) SIMS profile of regrown interface with ICP and XeF_2 etching.....	123
Figure I.1.13.5 Generational improvements for the MOSFET continue, showing (a) the improvement of breakdown voltage from generation 1 to the current generation 3; (b) a cross-sectional schematic of the device and (c) TCAD simulation results demonstrating the importance of mitigating the peaking of the electric field at the gate dielectric-semiconductor interface. Note that our 3 rd generation device breakdown voltage is like that of the ideal TCAD breakdown.....	124
Figure I.1.13.6 Implementation of a buried field shield showing a) the electric field profile of the device, b) corresponding horizontal cut line across the dielectric, and c) the peak electric field seen by the dielectric as a function of the shield-to-channel distance. In a) and b), the shield-to-channel distance is 0.4 μ m and measured from the edge of the channel to the nearest edge of the shield.	125
Figure I.1.13.7 Method for forming a buried field shield via etch and regrowth showing a) the trench view, b) the cross-section view, and c) the metals view of this approach1. More details are available in Ref. [11]......	126
Figure I.1.14.1 (Left) Test boards built to evaluate thermal performance (right) high-resolution thermal imaging is used to establish baseline thermal performance	130
Figure I.1.14.2 Comparison of measured and modeled temperature for baseline case.....	130
Figure I.1.14.3 Illustrates design and use of simple Al_2O_3 caps	130
Figure I.1.14.4 (Left) Illustrates six design cases and the simulated temperature rise of the device junction for each, (middle and right) modeled impact of ceramic caps on EPC transistor temperature. Case 4 & 5 not shown.....	131
Figure I.1.14.5 (Left) Illustrates equivalent circuit of transmission line with distributed capacitance and inductance (center) planar 3-phase configuration and (right) spiral 3-phase configuration	131
Figure I.1.14.6 (Top) Magnetic field norm and (Bottom) Electric field norm visualized in COMSOL® for planar and spiral 3-phase configurations	132
Figure I.1.14.7 Per unit length (top) inductances and (bottom) capacitances for planar and spiral configurations	132
Figure I.1.14.8 General Optimization architecture, including US06 driving profile [9], PLECS model of Electric Vehicle Powertrain System, EV motor [7], and Python-based GA [3];	133
Figure I.1.14.9 (left) The comparison of the time domain junction temperature and efficiency performance characteristics over the entire driving cycle between the IGBT-based and SiC-based solution, operating at 5 kHz, 380 V, and 5kHz, 750V, respectively. (Right) The comparison of the weighted efficiency for each driving cycle of an optimized inverter design solution with the SiC modules and IGBT modules.....	134
Figure I.1.15.1 SiC MOSFET Reliability Issues.	136
Figure I.1.15.2 Key Partnerships.	136
Figure I.1.15.3 Measurement Sequence of V_{th} before and after Gate Oxide Screening	137

Figure I.1.15.4 Effect of 100 ms/1 s high gate-voltage pulse screening on the ΔV_{th2} of (a) vendor E devices, and (b) vendor K devices. Devices are screened at 150°C. 138

Figure I.1.15.5 $t_{63\%}$ versus E_{ox} at 150°C for (a) vendor E devices, and (b) vendor K devices with and without high gate-voltage screening 139

Figure I.1.15.6 Diagram of liquid metal cooling system. 140

Figure I.1.15.7 Vector diagram of Lorentz force. 140

Figure I.1.15.8 Separate capacitor bank design in Gen-5 inverter..... 141

Figure I.1.15.9 Detailed design of the PM-based integrated MHD pump 141

Figure I.1.15.10 Inverter-5 prototype 141

Figure I.1.15.11 Schematic of the experimental test setup 142

Figure I.1.15.12 Inverter-5 prototype experimental setup 142

Figure I.1.15.13 Inverter-5 test waveform at 20 kVA..... 143

Figure I.1.15.14 Inverter-5 efficiency and temperature curve 143

Figure I.1.15.15 Inverter-5 liquid metal cooling system flow rate and thermal resistance curve 143

Figure I.1.15.16 Water cooling system flow rate and thermal resistance curve 144

Figure I.1.16.1 Schematic representation of the Cu nanoparticles synthesis through hydrothermal reaction from precursor preparation and nucleation, to resulting growth of nanostructured copper..... 147

Figure I.1.16.2 Voltera V-One: 3D Printer used in printing conductive traces on AlN substrates [3]. 148

Figure I.1.16.3 Illustration of Ink Jetting Process: Deposition of Copper Nanoplate-Based Ink onto AlN Ceramic Substrate. 148

Figure I.1.16.4 Typical copper conductive ink printed on AlN. 148

Figure I.1.16.5 Boundary conditions of the numerical model. 149

Figure I.1.16.6 Frequency-dependent relative permittivity of AlN with and without printed CuG ink. Results indicate the Cu ink sintering process has minimal impact on the dielectric strength of the AlN substrate. 150

Figure I.1.16.7 Impact of ink layer thickness on the electrical conductivity and sheet resistance of (a) Cu NPLs and (b) CuG ink printed AlN substrates..... 151

Figure I.1.16.8 Current density measurements for copper nanoplates ink and copper graphene ink..... 151

Figure I.1.16.9 Current density measurements for conventional direct bond copper. 152

Figure I.1.16.10 (L) Baseline heat exchanger design, (R) Proposed heat exchanger design optimized for integrated end winding cooling..... 152

Figure I.1.16.11 Framework for multiscale thermal performance analysis of baseline and proposed cooling solutions. 153

Figure I.1.16.12 Variation in $heff$ with flow rate for both HX designs. 153

Figure I.1.16.13 Test sections for both HX designs with attached inlet/outlet manifold for coolant supply.... 154

Figure I.1.16.14 Actual thermal testing loop setup for component-level HX effectiveness testing, at Georgia Institute of Technology..... 154

Figure I.1.16.15 Experimental versus CFD/HT $heff$ versus flow rate for both HX designs..... 154

Figure I.1.16.16 Experimental versus CFD/HT $heff$ versus flow rate for both HX designs..... 155

Figure I.1.16.17 Theoretical enhancement in maximum allowable RMS J_{max} with respect to flow rate, resulting from the change in HX design from baseline to proposed.....	155
Figure I.1.16.18 Reduction in winding (L) and end winding (R) temperature maximum caused by the HX design change, as evaluated by both the FEA and Motor-CAD models.....	156
Figure I.1.16.19 Variation of HTC with pumping power compared to a previous study [11].....	157
Figure I.1.16.20 Streamlines and temperature contours of heat spreader, solid and fluid phases of copper foam for 1 m/s inlet velocity.....	157
Figure I.1.17.1 Baseline CSI-based motor drive system for traction application.....	161
Figure I.1.17.2 (a) Original benchtop CSI design with film capacitors; (b) New prototype CSI design with ceramic capacitors for integration into IMD.....	162
Figure I.1.17.3 Drive-end view of assembled electrical machine showing 4 air inlets.....	162
Figure I.1.17.4 Side view of assembled electrical machine with stator jacket water inlet and outlet.....	162
Figure I.1.17.5 Non-drive-end view of assembled electrical machine showing electrical and RTD leads, air outlets, and encoder.....	162
Figure I.1.17.6 Dynamometer test configuration for back-EMF measurement.....	163
Figure I.1.17.7 Measured line-to-neutral back-EMF voltage waveforms at 4000 rpm.....	163
Figure I.1.17.8 Two views of the fabricated prototype integrated motor drive.....	163
Figure I.1.17.9 Cascaded closed-loop control structure.....	164
Figure I.1.17.10 Experimental validation of closed-loop control. (a) CSI's line-to-line output voltages; and (b) CSI's motor phase currents.....	164
Figure I.1.17.11 Sensor schematics and signal conditioning circuits. (a) current sensor; (b) voltage sensor...	165
Figure I.1.17.12 Calculated map of torque/speed operating points (blue circles) for Chevrolet Spark during a UDDS drive cycle with overlaid torque/speed envelopes for prototype CSI-IMD unit showing both steady-stage (55 kW) and transient (100 kW) limits. The assumed ratio of motor shaft speed to tire speed is 13.8...	165
Figure I.1.17.13 Predicted IMD (power electronics + machine) efficiency map for 12 operating points.....	166
Figure I.1.17.14 Estimated temperature distribution (55 kW at 6,667 rpm).....	166
Figure I.1.17.15 Estimated temperature distribution (55 kW at 20,000 rpm).....	166
Figure I.1.17.16 Estimated temperature distribution after 60s operation at 100 kW peak power @ 6,667 rpm.....	167
Figure I.1.17.17 Predicted temperature increase of key machine components vs. time during 100 kW peak power application.....	167
Figure I.1.18.1 Performance requirements.....	171
Figure I.1.18.2 DHAM and PMAC comparisons.....	171
Figure I.1.18.3 Prototype DHAM FEA results.....	172
Figure I.1.18.4 Prototype DHAM (upper) and inverter (lower).....	173
Figure I.1.18.5 Prototype DHAM experimental results.....	174
Figure I.1.18.6 DHAM speed control.....	174
Figure I.1.18.7 Simulation of DHAM startup.....	175
Figure I.1.18.8 Inert-core machine (left) and new notched-pipe cooling topology (right).....	175

Figure I.1.19.1 Cast copper concentrated windings with seven half turns and square heat distribution blocks connecting the turns. There are three variants of the end turn surfaces, (a) no pins in the end turns (traditional end turns), (b) medium pins in the end turns, and (c) large pins in the end turns..... 178

Figure I.1.19.2 Heat flux to the coils provided by (a) cartridge heaters embedded in heater blocks which surround the heat distribution blocks. Thermocouples are embedded in the heater blocks and (b) base of the turns where they interface to the heat distribution blocks..... 178

Figure I.1.19.3 Enclosure and spray apparatus for testing temperature rise of cast half coils, (a) overhead view with single concentrated jet of ATF, (b) view of cast half coil without end turn pins mounted in the enclosure, and (c) flow pattern of single concentrated jet of ATF striking cast half coil with large end turn pins..... 179

Figure I.1.19.4 Thermal step responses (a) with and without spray cooling for a power input of 20.4 (W) and ATF flow rate of 0.57 (l/m), and (b) three cast copper half coils with and without pins for a power input of 40 (W) and ATF flow rate of ~0.58 (l/m). 179

Figure I.1.19.5 Comparison of the estimated thermal resistance to the (a) mean turn bases and (b) mean heater block for the cast copper coils with no pins, medium pins, and large pins. The points are the design of experiments responses and the surfaces the fitted 2nd order polynomial surfaces. 180

Figure I.1.19.6 Comparison of the estimated thermal permeance to fluid power for the (a) mean turn bases and (b) mean heater block for the cast copper coils with no pins, medium pins, and large pins. The points are the design of experiments responses and the surfaces the fitted 2nd order polynomial surfaces. 181

Figure I.1.19.7 Trial insertion of one pole of a continuous wave winding. 181

Figure I.1.19.8 Example simple radial heat flux path in the stator of an electric machine, (a) thermal equivalent circuit overlaid on a slot pitch, and (b) equivalent Cauer network model. 182

Figure I.1.19.9 Cauer thermal models of electric machine stators capturing, (a) radial and circumferential heat flux paths, and (b) radial, circumferential, and axial heat flux paths..... 182

Figure I.1.19.10 Input power loss into the motor winding and output housing temperature used in ARX least squares regression model to estimate coefficients of radial heat flux path transfer function..... 183

Figure I.1.19.11 Comparison of average winding temperature estimated by reference model and model with ARX identified coefficients..... 183

Figure I.1.20.1. Integration methods for high-density inverter..... 186

Figure I.1.20.2 Fabrication flow and fabricated Gen 2 power module 187

Figure I.1.20.3 DPT setup and resulting waveforms of Gen 2 power module at 800 V, 164 A. 187

Figure I.1.20.4 (a) Gate driver die size comparison, (b) Close view of the wirebonded die 188

Figure I.1.20.5 Module-integrable gate driver PCB along with the power supply board 189

Figure I.1.20.6 Integration method of the gate driver inside the SiC power module..... 189

Figure I.1.20.7 TGS solution with the proposed configuration 190

Figure I.1.20.8 (a) Design 1 prototype, (b) Test result 190

Figure I.1.20.9 (a) Design 2 prototype, (b) Test results for investigating impact of thin current carrying trace underneath sensor on coupling effect, 30A..... 191

Figure I.1.20.10 (a) Design 3 prototype board for slitted current carrying trace, (b) Test results to validate the TGS method integrated into the power module, 70 A 191

Figure I.1.20.11 Signal conditioning overview..... 192

Figure I.1.20.12 Signal conditioning PCB..... 192

Figure I.1.20.13 Output of IA1. 192

Figure I.1.20.14 Output of IA2	192
Figure I.1.20.15 Final output (IA3)	192
Figure I.1.21.1 Schematic of the hardware to be developed in this project.	195
Figure I.1.21.2 Layout 3.5 for the double-side cooled SiC MOSFET phase-leg module.....	196
Figure I.1.21.3 An improved aluminum soldering fixture that aligns signal pins and high-voltage leads during solder-reflow.....	196
Figure I.1.21.4 EP-2000 encapsulated double-side cooled SiC phase-leg module capable of operating at 200°C junction	196
Figure I.1.21.5 Cross-section of the generic DSC module for which FEA simulations were run to analyze the thermo-mechanical reliability of the three sintered-silver interfaces.....	197
Figure I.1.21.6 Plot of the simulated plastic strain at the sintered-silver (a) chip bond, (b) spacer-chip bond, (c) spacer-substrate bond per temperature cycle versus the encapsulants' elastic modulus and coefficient of thermal expansion.	197
Figure I.1.21.7 The schematic of the integrator circuit with a dynamic compensator for parasitic resistance (a) Circuit diagram (b) Timing diagram.....	198
Figure I.1.21.8 The experiments of the current sensor (a) The set-up of the Buck converter (b) The waveforms (c) The waveforms in the turn-on transient.....	198
Figure I.1.21.9 The diagram of the phase-leg.....	199
Figure I.1.21.10 The gate driver board.	199
Figure I.1.21.11 The hardware of the current sensor based on parasitic inductance.	199
Figure I.1.21.12 The hardware of the high-temperature phase-leg.....	199
Figure I.1.21.13 The schematics and hardware of the two-output Class-E gate power supply.	200
Figure I.1.21.14 Testing waveforms at 10 W output power.	200
Figure I.1.21.15 Efficiency at different power conditions.....	201
Figure I.1.21.16 Thermal performance at 10 W.	201
Figure I.2.1.1 (left) Fabrication Steps of Power Module Leading up to Encapsulation & (right) Challenges Faced During the Fabrication Process Due to Contamination in the Processing Facility.....	205
Figure I.2.1.2 (top left) Primary Circuit of the Gate-Drive Power Supply, (top center) Secondary Circuit of the Current Transformer of Gate-Drive Power Supply, (top right) 24V Output From the Gate-Drive Power Supply, (bottom left) Coupling Capacitance Measurement of the Gate-Drive Power Supply Between Primary and Secondary Circuits & (bottom right) Discharge Data to Show Isolation between Primary and Secondary Circuits.....	206
Figure I.2.1.3 (left) Main Gate-Drive board, (center) Daughter Board Interface Between the Gate-Drive Board and the Power Module & (right) Output Gate Pulses Generated During Bench-Testing of the Board	206
Figure I.2.1.4 Bus-Bar Board Design With AC traces, DC traces, Current Sensors and Power Modules attached.....	207
Figure I.2.1.5 (left) Inverter Package Design with Ceramic Capacitors and Bus-Bar Board Attached to the Heat Sink-Power Module Structures on Both Sides with Two-Inlet-Two-Outlet Manifold Design & (right) Dimensions of the Latest Packaging Design Showing a Volume of 2.9 L	208
Figure I.2.1.6 Layout Process of Control Board With Top and Bottom Sides Populated and (right) 3D Model of First Steps in the Layout Process	208

Figure I.2.1.7 (left) Graph Showing Aggregated Temperature Cycles on the Power Module as an Effect of the Drive Cycle & (right) Strain-Energy Density Plots of Different Layers of the Power Module..... 209

Figure I.2.1.8 (left) Temperature Profile of the Entire Bus-Bar, Capacitors and Power Module – Heat Sink Structure & (right) Temperature Distribution on the Film Capacitors Showing a max. Temperature up to 110°C..... 209

Figure I.2.2.1 Released Single Switch Design..... 213

Figure I.2.2.2 Al and Cu Heatsink Assembly 213

Figure I.2.2.3 Lower and Upper Cu Heatsink Prototype 213

Figure I.2.2.4 Thermal Interface Material (TIM) Area on the Heatsink Assembly 214

Figure I.2.2.5 Thermal Simulation of Heatsink and Cooling Channel Design 214

Figure I.2.2.6 Segmented Capacitor with NanoLam™ Blocks..... 215

Figure I.2.2.7 DC Bulk Capacitor Prototype (Top view)..... 215

Figure I.2.2.8 Main (Single) w/ Controller, Gate Driver, and INSSA 216

Figure I.2.2.9 AC Current Sensing Subassembly 216

Figure I.2.2.10 Inverter Design and Assembly 217

Figure I.2.2.11 Stress Plot of Power Leads..... 218

Figure I.2.3.1 Baseline Designs for higher speed and higher DC bus voltage..... 220

Figure I.2.3.2 2-layer and 3-layer U-shaped PMASynRM designs with side bridges. 220

Figure I.2.3.3 B-H curves of various magnet materials at (a) -20oC, (b) 70oC, and (c) 150oC..... 220

Figure I.2.3.4 36 MGOe vs 24 MGOe B-H curves for FeN magnets. 221

Figure I.2.3.5 Optimized Rotor Designs for 2-Layer and 3-Layer PMASynRMs with C1 – C4 magnet combinations..... 222

Figure I.2.3.6 Mechanical Stress at 16000 rpm in the Optimized Rotor Designs..... 222

Figure I.2.3.7 Localized demagnetization in the Optimized Rotor Designs of 2-Layer PMASynRMs with C1 – C4 magnet combinations. 223

Figure I.2.3.8 Localized demagnetization in the Optimized Rotor Designs of 3-Layer PMASynRMs..... 223

Figure I.2.3.9 Temperature studies: temperature vs. powder packing %..... 224

Figure I.2.3.10 Addition of a lubricant compared to packing density (%). 224

Figure I.2.3.11 Densities of magnets made from different batches of coated powder..... 224

Figure I.2.3.12 Topology Comparison in terms of number of devices needed..... 225

Figure I.2.3.13 Four state-of-art 1.2 kV SiC MOSFETs static evaluation and comparison. 225

Figure I.2.3.14 Summary of the 1.2 kV discrete SiC MOSFET 226

Figure I.2.3.15 HC-PCB Prototype..... 226

Figure I.2.3.16 Low-cost 200 kW SiC Traction Inverter design..... 226

Figure I.2.3.17 1.2 kV SiC MOSFET PCB-embedding phase-legs..... 227

Figure I.2.3.18 Switching speed demonstration of PCB-embedded phase-leg..... 227

Figure I.2.3.19 PCB-embedded Rogowski current sensor. 227

Figure I.2.3.20 PCB-embedded Rogowski current sensor measurement results.	228
Figure I.2.3.21 Left: Plot of critical temperatures over time for peak loading condition. Right: temperature plot of continuous loading condition at steady-state	228
Figure I.2.3.22 SiC discrete power device temperatures at different configurations and cooling intensity.....	229
Figure I.2.4.1 Modified MOSFET heat sink design	233
Figure I.2.4.2 Thermal FEA analysis of new heat sink.....	233
Figure I.2.4.3 Copper sintered MOSFET assemblies	233
Figure I.2.4.4 Stator core with completed winding.....	234
Figure I.2.4.5 Stator cores with M15 material (left) and Arnon7 material (right)	234
Figure I.2.4.6 Assembled induction rotor with non-insulated copper bars (left) and insulated copper bars (right)	234
Figure I.2.4.7 Rotor shaft assembly with oil cooled heat sink inserts.....	234
Figure I.2.4.8 Potted stator assembly using EP-3500 material	235
Figure I.2.4.9 Injection over molded stator assembly using CoolPoly D5110	235
Figure I.2.4.10 Machined motor housing.....	236
Figure I.2.4.11 Output housing for motor only.....	236
Figure I.2.4.12 Assembled power stage with 24 MOSFETs.....	236
Figure I.2.4.13 Assembled power stage with gate drive PCB	236
Figure I.2.4.14 Motor only unit on high speed dyno	237
Figure I.2.4.15 Motor only dyno test setup.....	237
Figure II.1.1.1 System level diagram of the proposed XFC inductive charging system with open-ended winding inverter and rectifier designs and LCC-LCC resonant tuning components.	241
Figure II.1.1.2 The LCC-LCC tuning circuit designed for primary and secondary side in the hardware design.....	241
Figure II.1.1.3 Transmitter and receiver coil diameters, geometric designs, and surface power density.	241
Figure II.1.1.4 Experimental test setup with the hardware and instrumentation.....	242
Figure II.1.1.5 Power analyzer results for 100-kW power transfer for resistive load (a) and battery load (b) test conditions.....	243
Figure II.1.1.6 Primary-side waveforms and RMS measurements including the inverter input voltage and current and the inverter output Phase-A, B, and C voltage and current measurements.	243
Figure II.1.2.1 WXFC project activities.	247
Figure II.1.2.2 Project design and implementation approach.	247
Figure II.1.2.3 System block diagram.....	248
Figure II.1.2.4 Marked the charger location at the site	249
Figure II.1.2.5 Cummins Truck	250
Figure II.1.2.6 All DC-DC Modules	250
Figure II.1.2.7 DC-DC Module and Unfolder after assembly	250
Figure II.1.2.8 Integrated MV Off-vehicle Testing	251

Figure II.1.3.1 System block diagram..... 254

Figure II.1.3.2 Site location of the Union Pacific Railyard located within the Utah Inland Port (UIPA) of northern Utah. 255

Figure II.1.3.3 Location of Construction at the Utah State University Electric Vehicle Center (EVR) and proposed 1MW charger location..... 255

Figure II.1.4.1. Current eco-routing result on the test route (a) and the fastest route (b)..... 261

Figure II.1.4.2. Go-No-Go analysis for long-route testing (250+ miles), utilizing a single on-route charge. In this case, the charger was assumed to be placed in Waseca, Minnesota. The total trip time was estimated to be 6.5 hours, including a roughly 2-hour charge to recuperate 44% of the battery SOC (250 kWh out of the total 564 kWh capacity). 262

Figure II.1.4.3: OsmAnd will be used on a separate device to help drivers navigate eco-routes, as it provides visual and audio turn-by-turn directions for custom routes. Directions can also be printed for further review by fleet partners. 263

Figure II.1.5.1 Inverter Assembly 267

Figure II.1.5.2 Inverter Power Efficiency Test (A vs B-Sample) & Inverter Power Max Efficiency 268

Figure II.1.5.3 Flux Linkage as a Function of Current 269

Figure II.1.5.4 Torque vs, speed map 269

Figure II.1.5.5 Inverter Motor Performance Tests on Dyno 270

Figure II.1.6.1 Key Components of a Synthetic Environment to Train an RL Agent 273

Figure II.1.6.2 High-Level Solution Architecture..... 275

Figure II.1.6.3 LiteOn Gateway Charger Integration Test..... 276

Figure II.1.7.1 (Shift in load from counterfactuals. Source: WeaveGrid PJM Integration Impact Report)..... 281

Figure II.1.7.2 (Daily home charging load for 3 of 4 SCM scenarios using real-world TOU demonstration. Source: Argonne National Lab ATEAM model)..... 283

Figure II.1.7.3 Exelon’s Managed Charging Program Phase 1 Review report. Source: SEPA <https://sepapower.org/resource/managed-charging-incentive-design>)..... 284

Figure II.1.8.1 System level diagram of the proposed architecture for the bidirectional wireless charging system. 287

Figure II.1.8.2 Final look of the primary and secondary side hardware enclosures. 287

Figure II.1.8.3 UPS truck with bidirectional wireless charging with full operation at the ORNL’s GRIDC facility. 288

Figure II.1.8.4 UPS truck at the loading dock with the wireless charging equipment installed underneath the dock..... 289

Figure II.1.8.5 Temperature profiles of the primary-side and vehicle-side coolant for a three-hour charge duration. 289

Figure II.1.8.6 The operation of the wireless charging system with low voltage ride through capability. 290

Figure II.1.9.1 Energy transfer topology..... 292

Figure II.1.9.2 Charger and dispensers rendering 293

Figure II.1.9.3 60kW A sample power module prototype functional electronics hardware 293

Figure II.1.9.4 Successful modulation generation on AC-AC convertor..... 294

Figure II.1.9.5 Auburn Hills lab implementation.....	294
Figure II.1.10.1 Single Phase Rendering a Multilevel Cascaded H-Bridge Based Solid State Transformer Topology.....	301
Figure II.1.10.2 Overall MV-SST System Architecture based on Cascaded H-Bridge Topology	301
Figure II.1.10.3 Figures of Merit: Top Left: Total Mass vs. Coil Space; Top Right: Temperature Rise vs. Coil Space; Bottom: Flux Density vs. Coil Space	302
Figure II.1.10.4 Thermal Management Design with Thermo-Syphon (MV section)	303
Figure II.1.11.1 Overview of PACCAR SuperTruck3 Goals to Support the Transition to a Zero Emissions Transport System.....	305
Figure II.1.11.2 PACCAR SuperTruck 3 Program Overview	305
Figure II.1.11.3 Micro-grid including chargers, solar panels, and battery energy storage system.	306
Figure II.1.11.4 First Gen1 BEV (Peterbilt 579EV) Deployed at Knight Swift	307
Figure II.1.11.5 Gen3 BEV Development Scope.....	308
Figure II.1.11.6 Connectivity Feature Development Overview.....	309
Figure II.1.12.1 Updated Project Schedule & Phasing (Volvo).....	311
Figure II.1.13.1 Key components of the proposed XFC Station: MV SST, DC distribution network, and dispenser (DC node) that contains the dc/dc converter and vehicle interface.....	316
Figure II.1.13.2 Prototype of one phase of the SST assembled in the lab with the front panels in place.	317
Figure II.1.13.3 (Left) AFE+DAB module implementation. (Right) Module efficiency measurements, showing the efficiency of the AFE stage, the DAB stage and the overall efficiency.....	317
Figure II.1.13.4 ABB switchgear after testing at ABB and prior to shipping to NCSU.	318
Figure II.1.13.5 CAD drawing of interconnected system within the shipping container.....	318
Figure II.1.13.6 One line diagram of the planned installation. The installation includes a (1) dedicated disconnect switch to the 13.2kV utility feed; (2) A shipping container that houses the MV filters, breakers, the SST and the SS DCCB inside a shipping container; (3) an auxiliary 208V power feed; and (4) four charging ports.	319
Figure II.1.13.7 Charger deployment at NYPA site. (Left) View of system installation with three DC/DC nodes, shipping container and Trenwa trench housing the DC cables. (Right) View inside the container showing DC connection.....	319
Figure II.1.14.1. Block-diagram schematic of the XFC station.	323
Figure II.1.14.2. Coupled power and transportation networks.	324
Figure II.1.14.3. Coordinated planning results with different EV driving ranges.	324
Figure II.1.14.4. Modified Four-Port FTF Architecture with VAR Injection.....	324
Figure II.1.14.5. XFC CAN Communication Layer.	325
Figure II.1.14.6. Single low-voltage prototype module.....	325
Figure II.1.14.7. Low-voltage prototype cabinet showing the six modules integrated and ready for testing. ..	325
Figure II.1.14.8. Anode of cells cycled with CQtCV (a) and CCCV (b) after 130 cycles using Hirox KH-8700 microscope.....	326
Figure II.1.14.9. XFC Project Testbed at Bitrode Corporation. Battery packs are in the foreground (white). Charge station is centered in the background (dark blue).....	326

Figure II.1.14.10. Battery Charge + ESS Discharge Results: State-of-Charge..... 327

Figure II.1.14.11. Battery Charge + ESS Discharge Results: Pack Voltages 327

Figure II.2.1.1 Charging hardware testbed at NREL. 332

Figure II.2.1.2 Boxplots of voltage difference for 19 feeders..... 333

Figure II.2.1.3 Distribution feeder voltage comparison - sample voltage distance plots..... 333

Figure II.2.1.4 Commercial Mk II Prototype OptiQ EVSE. 334

Figure II.2.1.5 Changing current set-point limits through OCPP (left). Histogram of charging current error and response time (right). 334

Figure II.2.1.6 Long-dwell MD/HD vehicle charging loads over one week (left) and across a subregion of the analysis area (right)..... 335

Figure II.2.1.7 Feeder network topology; (a) EV hosting capacity heat map, (b) High power charging capable nodes. marked. 336

Figure II.2.1.8 density of charging need based on EV charging at the end of each trip 337

Figure II.3.1.1 Charging site architectures available today. 339

Figure II.3.1.2 (a) Proposed taps to select between 400 V class and 800 V class vehicles. (b) Proposed zero state modulation (ZSM) technique to improve optimal DAB control range..... 341

Figure II.3.1.3 SpEC module Gen I (left) and Gen II (right). 342

Figure II.3.1.4 MW-Level DC charging hub demonstration. 343

Figure II.3.1.5: DC charging hub demonstration tested at 150 kW: (a) Overview of the setup, (b) SEMS platform implementation on hardware..... 343

Figure II.3.1.6 UPER: (a) 1000 V, 175 kW, 20 kHz DC/DC charger, (b) Charger test results at 950 V and 150 A. 344

Figure II.3.1.7 (a) UPER-Spec Integration setup, (b) UPER-SPEC interface testing Results at 600 V and 10 A. 344

Figure II.3.1.8 Demonstrating a V2G session with the Lion Electric Bus at ANL..... 345

Figure II.3.1.9. Experimental results for DC charging hub operation with rule-based SEMS. 346

Figure II.3.2.1 Seven NGP EVs, Nominal Temperature 10-100% DCFC Power Analysis 350

Figure II.3.2.2 EV Profile Capture Boost Converter Physical Setup..... 352

Figure II.3.2.3 Efficiency characterization of the 100-kW WPT system under four different battery voltages at different power levels. 352

Figure II.3.2.4 Off-nominal condition definitions with respect to coil positions..... 353

Figure II.4.1.1 Use cases selected for exploration in techno-economic analysis..... 355

Figure II.4.1.2 Overall workflow based on OR-AGENT..... 356

Figure II.4.1.3 Parameters considered for the techno-economic analysis..... 357

Figure II.4.1.4 Outcome of use-case analysis study. 357

Figure II.4.2.1 Decrease in specific and volumetric energy density of ESS from the cell to the rack. Source: NREL..... 361

Figure II.4.2.2 Modular DC-coupled battery pack for BTMS. Source: NREL..... 362

Figure II.4.2.3 Overview of the BMS for a modular battery. Source: NREL..... 362

Figure II.4.2.4 Experimental setup for the three modular DAB converters. Source: NREL	363
Figure II.4.2.5 DAB converters following a reference current to verify the controller. Source: NREL.....	363
Figure II.4.2.6 Experimental results for SOC equalization. Source: NREL	363
Figure II.4.2.7 DAB converter current and voltage satisfying SOC equalization. Source: NREL.....	363
Figure II.4.2.8 Temperature contour and profiles of the maximum temperature in the failure cell, the impinged cell and neighbor cells predicted by the ejection model when SHR is 1000°C/min.....	365
Figure II.4.2.9 Flowchart of the multi-objective thermal design and optimization.	365
Figure II.4.2.10 Three different thermal control strategies were used for three 20 Ahr lithium iron phosphate cells connected in parallel.	366
Figure II.4.2.11 Nail penetration of the insulation only module.....	366
Figure II.4.2.12 Average temperature of each cell (left, center, right) for the three thermal strategies during nail penetration.	367
Figure II.5.1.1 EVSE PKI Virtual Testing Platform Enables Scaled Testing of Security and Resilience (credit: Craig Rodine, SNL)	370
Figure II.5.1.2 Cerberus Cybersecurity Solution for High-Power EV Charging Infrastructure	371
Figure II.5.1.3 Representative Schematic of a DC Charger’s Communications Networks	372
Figure II.5.2.1 Areas for resiliency improvement.....	375
Figure II.5.2.2 Typhoon HIL controller hardware-in-the-loop with integrated automation and testing system.	376
Figure II.5.2.3 Automated test platform results plotted from fault use case.....	377
Figure II.5.2.4 CHIL RT simulation results (stored in the station controller historian): DFRT strategy conducted in the multi-layer control framework. Changes of converter ratings, EV charging setpoints, and measurements according to the system limitations and the station controller optimization.	379
Figure II.5.2.5 MD/HD Charging Depot Point of Interconnection (POI) Power for Different System Events	379
Figure II.5.2.6 EVSE Charging Emulator Components and Layout.....	380
Figure II.5.3.1 The security services edge networks the chargers	384
Figure II.5.3.2 Request rate limiting and shaping reduce electric supply impacts.....	385
Figure II.6.1.1 Test sequence diagrams for the MCT (from older version of J1634) and the SMCT+ (from latest version of J1634)	390
Figure II.6.1.2 Looking for bias in two different test procedures (J1634 MCT and SMCT+) with results from two EVs	390
Figure II.6.1.3 Comparing regen operation in two different tests of the same EV. Slight changes in initial battery temperatures yielded substantially different operation and cycle consumption results.	391
Figure II.6.1.4 Comparing the effect of changes in usable battery energy (UBE) across varying test temperatures.....	392
Figure II.6.2.1 Vision of SWIFTCHARGE consortium on industry led wireless power transfer methodology not constrained by decisions set in SAE J2954/IEC61980, facilitating technical innovation with fewer boundaries.....	394
Figure II.6.2.2 Vision of SWIFTCharge range of interoperable arrays of ground assemblies in a distributed network	396

List of Tables

Table 1. Technical Targets for Electric Traction Drive System	6
Table 2. Technical Targets for High-Voltage Power Electronics	7
Table 3. Technical Targets for Electric Traction Motor	7
Table 4. Technical Targets for DC/DC Converter	8
Table 5. Technical Targets for On-Board Charger	8
Table 6. Comparison of Current Status with 2025 Technical Targets for ETDS	9
Table 7. Current Status and 2025 Technical Targets for Power Electronics and Electric Motors.....	9
Table 8. Comparison of magnetic properties	15
Table 9. Light Duty Conventional and Electric Vehicle Refueling Characteristics	20
Table I.1.1.1. Electromagnetic Performance with the Rotor Modified for Prototyping	37
Table I.1.1.2 Rotor Natural Frequencies for Different Modes at Different Speeds	37
Table I.1.1.3 Stator Natural Frequencies	38
Table I.1.2.1 Inverter Specifications.....	43
Table I.1.4.1 Current distribution among SiC metal-oxide semiconductor field-effect transistors (MOSFETs) with and without impedance matching	58
Table I.1.5.1 Thermal Cycling Plan for the Polymeric Bonded Materials.....	63
Table I.1.6.1 Laser Optimization Pattern Power and Speed Levels.....	74
Table I.1.16.1 Properties of investigated copper foams.....	150
Table I.1.16.2 Properties of coolant used in simulations.	150
Table I.1.17.1 Power Electronics and Motor Requirements	160
Table I.1.17.2 Summary of Measured Back-EMF Waveforms (Fund. Component Peak)	163
Table I.1.17.3 Predicted Max. Machine Temperatures From Thermal FEA with 20°C Coolant.....	167
Table I.1.19.1 EDT Consortium Motor Targets.....	177
Table I.1.20.1. Power Electronics Requirements.....	185
Table I.1.20.2 Power Loss per Device from Simulation and Experiment	188
Table I.1.21.1 Material properties of the three encapsulants used in the experiment.	197
Table I.1.21.2 Inductance measurement results.	200
Table I.1.21.3 Summary of the output voltages and efficiency.	200
Table I.2.2.1 Heatsink verification at 10LPM, 65°C coolant, and WEG 50/50.....	214
Table I.2.2.2 Power Density of Inverter Assembly Variants	217
Table I.2.3.1 Matrix of thermal FEA modeling results for Infineon and Wolfspeed/Cree devices.	229
Table II.1.1.1 Primary and Secondary Side Coupler Specifications.....	242
Table II.1.3.1 Project Milestones.....	258
Table II.1.6.1 L2 Charger Deployment Summary Plan	275

Table II.1.7.1 (Wholesale Cost Savings from PJM Demonstration. Source: WeaveGrid PJM Integration Impact Report)	281
Table II.1.9.1 Next Gen Unit Performance vs BorgWarner Baseline	291
Table II.1.9.2 60kW power module metrics comparison.....	295
Table II.1.10.1. Primary Program Objectives in BP1	297
Table II.1.10.2. Target Data Matrix	298
Table II.3.2.1 Impact of AC Input Voltage Deviation on DC Output Current	351
Table II.4.1.1 TCOs for diesel vehicles, FCEVs, BEVs, and BEVs with DWPT for drayage application.....	358
Table II.4.2.1 Design standards certifications to be used for the rack design. Source: NREL	360
Table II.4.2.2 Important design parameters for the advanced rack design. Source:NREL	361
Table II.5.2.1 Energy and Completed Sessions for Different Scenarios.....	380

Vehicle Technologies Office Overview

Vehicles move our national economy. Each year in the United States, vehicles transport 18 billion tons of freight—about \$55 billion worth of goods each day¹—and move people more than 3 trillion vehicle-miles.² Growing our economy requires transportation, and transportation requires energy. The transportation sector accounts for approximately 27% of total U.S. energy needs³ and the average U.S. household spends over 15% of its total family expenditures on transportation,⁴ making it, as a percentage of spending, the most costly personal expenditure after housing. Transportation is critical to the overall economy, from the movement of goods to providing access to jobs, education, and healthcare.

The transportation sector has historically relied heavily on petroleum, which supports over 90% of the sector's energy needs today,⁵ and, as a result, surpassed electricity generation to become the largest source of CO₂ emissions in the country.⁶ The Vehicle Technologies Office (VTO) will play a leading role in decarbonizing the transportation sector and address the climate crisis by driving innovation and deploying clean transportation technologies, all while maintaining transportation service quality and safety.

VTO funds research, development, demonstration, and deployment (RDD&D) of new, efficient, and clean mobility options that are affordable for all Americans. VTO leverages the unique capabilities and world-class expertise of the National Laboratory system to develop new innovations in vehicle technologies, including: advanced battery technologies; advanced materials for lighter-weight vehicle structures and better powertrains; energy-efficient mobility technologies (including automated and connected vehicles as well as innovations in efficiency-enhancing connected infrastructure); innovative powertrains to reduce greenhouse gas (GHG) and criteria emissions from hard to decarbonize off-road, maritime, rail, and aviation sectors; and technology integration that helps demonstrate and deploy new technology at the community level. Across these technology areas and in partnership with industry, VTO has established aggressive technology targets to focus RDD&D efforts and ensure there are pathways for technology transfer of federally supported innovations into commercial applications.

VTO is uniquely positioned to accelerate sustainable transportation technologies due to strategic public-private research partnerships with industry (e.g., U.S. DRIVE, 21st Century Truck Partnership) that leverage relevant expertise. These partnerships prevent duplication of effort, focus DOE research on critical RDD&D barriers, and accelerate progress. Working closely and in collaboration with the Office of Energy Efficiency and Renewable Energy's Bioenergy Technologies and Hydrogen and Fuel Cell Technologies Offices, VTO advances technologies that assure affordable, reliable mobility solutions for people and goods across all economic and social groups; enable and support competitiveness for industry and the economy/workforce; and address local air quality and use of water, land, and domestic resources.

Annual Progress Report

As shown in the organization chart (below), VTO is organized by technology area: Batteries R&D; Electrification R&D; Materials Technology R&D; Decarbonization of Off-Road, Rail, Marine, and Aviation; Energy Efficient Mobility Systems; Technology Integration; and Analysis. Each year, VTO's technology areas prepare an Annual Progress Report (APR) that details progress and accomplishments during the fiscal year. VTO is pleased to submit this APR for Fiscal Year (FY) 2023. The APR presents descriptions of each active project in FY 2023, including funding, objectives, approach, results, and conclusions.

¹ Bureau of Transportation Statistics, DOT, Transportation Statistics Annual Report 2020, Table 4-1, <https://www.bts.gov/tsar>.

² Davis, Stacy C, and Robert G Boundy. Transportation Energy Data Book: Edition 40. Oak Ridge, TN: Oak Ridge National Laboratory 2022. <https://doi.org/10.2172/1878695>. . Table 3.09 Shares of Highway Vehicle-Miles Traveled by Vehicle Type, 1970-2019.

³ [Ibid. Table 2.02 U.S. Consumption of Total Energy by End-use Sector, 1950-2021.](#)

⁴ [Ibid. Table 11.1 Average Annual Expenditures of Households by Income, 2020.](#)

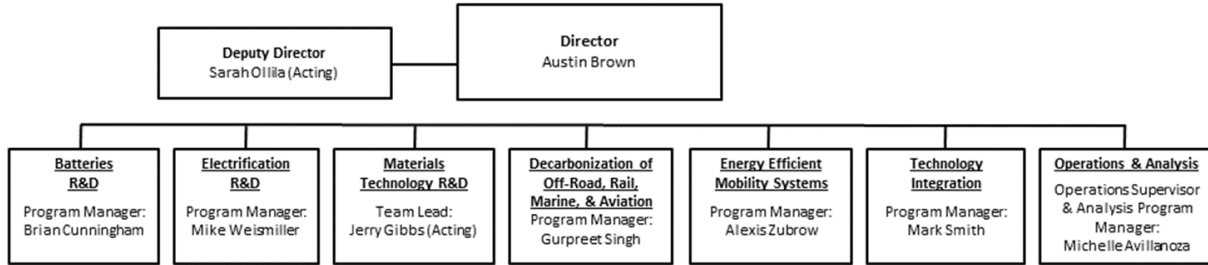
⁵ [Ibid. Table 2.03 Distribution of Energy Consumption by Source and Sector, 1973 and 2021.](#)

⁶ Environmental Protection Agency, Draft U.S. Inventory of Greenhouse Gas Emissions and Sinks, 1990-2019, Table 2-11. Electric Power-Related Greenhouse Gas Emissions and Table 2-13. Transportation-Related Greenhouse Gas Emissions.

Organization Chart

Vehicle Technologies Office Federal Staff

September 2023



Electric Drive Technologies Program Overview

Introduction

The Electric Drive Technologies (EDT) program's mission is to conduct early-stage research and development on transportation electrification technologies that accelerate the development of cost-effective and compact electric traction drive systems that meet or exceed performance and reliability requirements of internal combustion engine (ICE)-based vehicles, thereby enabling electrification across all vehicle types.

Goals and Objectives

The goal of the EDT program is to develop an electric traction drive system at a cost of \$4/kW for a 150-kW system by 2025, \$3/kW for a 200 kW system by 2030, and \$2.67/kW for a 22k kW system in 2035.

Targets are based on the following assumptions:

- Power levels are peak power for 30 seconds
- System voltage level is 600V for 2025, moving to 800V by 2030
- Reliability requirement of 15 years/300,000 miles
- Targets based on annual production volume of a million units
- Gearbox is not included.

Program Design and Execution

The EDT program provides support and guidance for many cutting-edge automotive technologies now under development. Researchers focus on developing revolutionary new power electronics (PE), electric motor (EM), and traction drive system (TDS) technologies that will leapfrog current on-the-road technologies. This will lead to lower cost and better efficiency in transforming battery energy to useful work. Research and development (R&D) is also aimed at achieving greater understanding of, and improvements in how the various components of tomorrow's automobiles will function as a unified system.

In supporting the development of advanced vehicle propulsion systems, the EDT program fosters the development of technologies that will significantly improve efficiency, costs, and fuel economy.

The EDT program directs early-stage research through a three-phase approach intended to

- Identify overall propulsion- and vehicle-related needs by analyzing programmatic goals and reviewing industry recommendations and requirements, and then develop and deliver the appropriate technical targets for systems, subsystems, and component R&D activities.
- Develop, test, and validate individual subsystems and components, including EMs and PE
- Estimate how well the components and subsystems work together in a vehicle environment or as a complete propulsion system and whether the efficiency and performance targets at the vehicle level have been achieved.

The research performed under this program addresses the technical and cost barriers that currently inhibit the introduction of advanced propulsion technologies into hybrid electric vehicles (HEVs), plug-in HEVs, battery electric vehicles (BEVs), and fuel cell powered automobiles that meet the DOE goals.

A key element in making these advanced vehicles practical is providing an affordable electric TDS. This will require attaining weight, volume, efficiency, and cost targets for the PE and EM subsystems of the TDS. Areas of development include:

- Novel traction motor designs that result in increased power density and lower cost
- Inverter technologies that incorporate advanced wide bandgap (WBG) semiconductor devices to achieve higher efficiency while accommodating higher-temperature environments and delivering higher reliability.
- Converter concepts that leverage higher-switching-frequency semiconductors, nanocomposite magnetics, higher-temperature capacitors, and novel packaging techniques that integrate more functionality into applications offering reduced size, weight, and cost.
- New onboard battery charging electronics that build from advances in converter architectures for decreased cost and size
- More compact and higher-performing thermal controls achieved through novel thermal materials and innovative packaging technologies
- Integrated motor-inverter TDS architectures that optimize the technical strengths of the underlying PE and electric machine subsystems.

VTO competitively awards funding through funding opportunity announcement (FOA) selections, and projects are fully funded through the duration of the project in the year that the funding is awarded. The future direction for direct-funded work at the National Laboratories is subject to change based on annual appropriations.

Electric Drive Technologies Lab Consortium

The multi-lab EDT Consortium will leverage U.S. research expertise and facilities at the national labs and universities to improve the power density of electric drives by 10X compared with the 2015 numbers while reducing the cost by 50% and doubling the lifetime miles within the next 5 years.

The EDT Consortium's research consists of a multi-disciplinary team that will plan, establish, conduct, and manage a portfolio of multi-lab and multi-university research efforts to advance the state-of-the-art in electric drive technologies.

The consortium is organized around three Keystone projects: (1) Power Electronics; (2) Electric Motors; and (3) Traction Drive System. The consortium will focus on early-stage research projects on advanced materials, high-density integration of dissimilar layers/materials, multifunctional subcomponents, and optimized and new thermal/electrical/magnetic architectures. New materials such as WBG semiconductors, soft magnetic materials, and ceramic dielectrics, merged using multi-objective co-optimization design techniques, will be utilized to achieve the program goals. Moreover, integration of components and subcomponents will further propel the research toward the goals of the consortium.

Consortium National Laboratory members include Ames National Laboratory, The National Renewable Energy Laboratory (NREL), Oak Ridge National Laboratory (ORNL), and Sandia National Laboratories (SNL). University consortium partners include North Carolina State University, The University of Arkansas, Virginia Polytechnic Institute, University of Wisconsin-Madison, Georgia Institute of Technology, University of California-Berkeley, Illinois Institute of Technology (IIT), Purdue University, The State University of New York (SUNY), and The Ohio State University.

Technical Targets & Status

Target Definition

The technical targets for the ETDS are based upon what is needed for EDVs to be competitive in performance and economics with ICE vehicles. The targets recognize the need to provide solutions that enable all vehicle segments to be addressed by providing a better value proposition to consumers. Providing consumers with a better value proposition will ensure market adoption. Achieving these aggressive targets will require major technological breakthroughs through early-stage research. In order to establish U.S. industry as a leader in electrification, it is critical that this early-stage research can be translated into competitive advantages for industry in the U.S. The technical breakthroughs need to focus on those technologies that can be best taken advantage of by a highly skilled and capitalized industrial base. Consumers want to see vehicles that are more usable, functional, and cost effective to operate. This translates into high-density packaging of power electronics and electric motors, high drive cycle efficiency, reliability, and cost effectiveness. Accomplishing this will come from creating new materials and enabling higher orders of integration to occur from in-situ fabrication. The EDTT metrics focus on key issues related to component cost and size to enable widespread acceptance of these vehicles. The metrics are normalized based on a component or system peak power rating into cost per kilowatt (\$/kW) and power density (kW/liter).

Cost

Ultimately, the purchase price of EDVs should be comparable ICE vehicles, but also be able to provide greater value to the consumer. The cost targets in this roadmap allow for a small initial price premium, but the cost difference should be no greater than 3 years of fuel cost savings. As part of the US DRIVE 2025 target-setting process, vehicle-level modeling and simulation in Autonomie was carried out by ISATT (Integrated Systems Analysis Tech Team), and the collection of inputs from SMEs (Subject Matter Expert) in Power Electronics and Electronic Machines. The result was a target of \$4/kW for a 150kW peak power ETDS being set.

Power Density

Power density is a very important target because of limited space “under the hood” and on the vehicle in general. Packaging constraints vary with the different vehicle types: for PHEV architectures, the ETDS must be added to a conventional ICE vehicle (i.e., a secondary drive train) as well as a high-voltage battery, DC/DC converter and on-board charger; for BEV applications, the space constraints are different, primarily driven by the large battery size and a small vehicle footprint to achieve acceptable driving range (200 miles for 2020 and more than 300 for 2025). For BEV applications, the design freedom enabled by the lack of requirements for the ICE compartment and driveline tunnel, which manufacturers typically use to expand the passenger and cargo space, further limit ETDS component packaging to around the battery, in the chassis alongside steering and suspension, and distant from vehicle crash zones. Increased power density is required to address these packaging constraints and to enable a skateboard-like chassis design that allows widespread electrification across all vehicle platforms.

Reliability

Previous EDTT’s reliability targets were set to the traditional automotive life of 15 years or 150,000 miles. Longer range EVs (200+ miles) are starting to be tested in MaaS/fleet applications due to lower operating costs compared to ICE vehicles. HEVs and PHEVs are also gaining popularity in MaaS applications because they can run power accessories at “idle” without running the ICE, thereby saving on fuel costs. Some of the taxi-like MaaS applications (up to 20 hours per day of operation) can accumulate between 50,000 to 80,000 miles per year. Several automotive OEMs, including Ford, Stellantis, General Motors, Tesla and Volkswagen and a number of startups have indicated significant interest in EDV use for MaaS/Delivery, and recent literature and analysis reports see synergy between electrification and automation.

Meeting the future EDTT targets by reducing the costs and size of ETDS components would accelerate market penetration of EDVs in MaaS/Delivery applications and thereby significantly increasing energy efficiency and reducing emissions (greenhouse gas and criteria pollutants) per vehicle mile traveled. Mileage accumulation,

and therefore vehicle turnover is a lot faster for MaaS/Fleet; hence, it presents an opportunity for much faster and greater impact of reducing petroleum use in the transportation sector. This is the primary reason for the EDV EDTT reliability requirement of 300,000 miles or 15 years being adopted.

Future of Targets

Targets have been the basis of metrics to guide research and component development and establish the basic tipping point for electric propulsion to be viable. These metrics have been in existence for over 25 years and helped guide electric vehicles to where they are today. Given the progression of the EV market, the U.S. generally has high operating cost and must lead through innovation to be competitive in electrification. Innovation must provide differentiators that consumers find of value, such as safety, Miles per Gas Gallon Equivalent (MPGe), driving enjoyment, portable power, and end-of-vehicle-life value. For example, significant opportunity for improvement of MPGe exist when accounting for the traction system performance over the whole drive cycle. This can be illustrated by reviewing Tesla's MPGe rating from 97.1 MPGe in 2015 to over 119.1 in 2020. While multiple factors contribute to this improvement, drive cycle efficiency is a key contributor. The EDTT assessed on-the-road drive cycle efficiency (e.g., US06) for electric vehicles moved from the MPGe of 70's to the 80's over those same years. Additionally, if a drive cycle efficiency improvement of 5% can be obtained, it would have a meaningful impact on reducing battery needs and the overall vehicle cost and range.

Value Proposition

Improving the value proposition provided to the consumer and fleet operator is at the heart of driving the adoption of EVs. Electrification of the propulsion system - besides providing clean transportation - can provide greater control yielding greater performance, efficiency, and safety than incumbent technology. This leads the EDTT to identify and evaluate new functions or capabilities that have the potential to create value and what new performance metrics need to be established.

Recyclability

The ETDS contains materials that are rare or come from areas of the world that may or may not continue to be available to the United States. Therefore, recapturing those elements and ensuring the appropriate disposal of other materials is critical for wide market adoption of the technology.

Electric Traction Drive System Targets

The technical targets for 2025 shown in Table 1 are appropriate for all EDV applications. The targets are progressively increased starting at 100kW in 2025 and increasing until the year 2035. This is to accommodate the addition of new vehicle types and their associated requirements. The target includes high-voltage power electronics (one inverter and if needed a boost converter) and a single traction-drive electric motor.

Table 1. Technical Targets for Electric Traction Drive System

ETDS Targets			
Year	2025	2030	2035
Power Level kW (Peak)	150	200	225
Voltage	600	800	800
Cost (\$/kW)	4	3	2.67
Power Density (kW/L)	50	66	75

High-Voltage Power Electronics Technical Targets

An approximate allocation of the targets for the high-voltage power electronics is shown in Table 2. The values estimate how much can be achieved with improvements to the high-voltage power electronics and are consistent with the system-level targets. The targets in Table 1 refer to a single power inverter and a boost converter if applicable; the DC/DC converter for powering the auxiliary loads and the on-board charger have their own targets and are not included in the table.

Table 2. Technical Targets for High-Voltage Power Electronics

Power Electronics Targets			
Year	2025	2030	2035
Power Level kW	150	200	225
Voltage	600	800	800
Cost (\$/kW)	1.80	1.35	1.20
Power Density (kW/L)	150	200	225

The 2025 power electronics cost, and volume targets are driven by the opportunity to replace silicon switches with WBG devices which can significantly reduce the size of the power modules while enabling operation at higher temperatures and frequencies. WBG devices are significantly costlier than silicon equivalents but enable overall power electronics cost to decrease due to the system cost reductions.

Electric Traction Motor Technical Targets

The technical targets have been established for the electric traction motor. The values in Table 3 estimate how much can be achieved with improvements to the motor and, along with comparable numbers for the power electronics, are consistent with the system-level targets.

Table 3. Technical Targets for Electric Traction Motor

Electric Motor Targets			
Year	2025	2030	2035
Power Level kW	150	200	225
Voltage	600	800	800
Cost (\$/kW)	2.20	1.65	1.47
Power Density (kW/L) ⁷	75	100	112.5

Certain motor designs may have an impact on the weight, volume, and cost of other parts of the vehicle. Many hybrid vehicle architectures require two electrical machines to optimize for vehicle efficiency, one as a motor and another as a generator. Some of the architectures make use of a single machine for both purposes for cost and packaging reasons. The targets in Table 2 and Table 3 refer to a single electric machine used for traction

⁷ 2020 power density target was based on 55 kW peak power at a 325 V nominal DC and resulted in 9.6 L motor volume; 2025 target is based on 100 kW peak power at a 650 V nominal DC resulting in a 2L motor volume.

drive, specifically its rotor, rotor shaft, stator with end windings, housing and cooling, but not the reduction gearing.

The 2025 electric motor cost and volume targets are driven by the opportunity to reduce material use with better application of existing or use of new materials to improve motor performance and efficiency. Additional consideration is needed to account for extreme expansion (10X) of materials usage in the scenario of near-full adoption of EV vehicles.

DC/DC Converter Technical Targets

In addition to running accessories from the high-voltage bus, current PEVs require up to 5 kW at 14 V DC; the power level depends on the vehicle architecture and feature content. At a minimum, a buck DC/DC converter is required to reduce the nominal 325 V battery voltage to 14 V to power most of the accessories. The DC/DC converter is not part of the propulsion system but is an important part of electrification and increasing vehicle efficiency; therefore, it is included in the scope of EDTT. In addition, some of the technical developments for DC/DC converters may be transferable to inverter designs. Table 4 shows technical targets for a 7.5 kW DC/DC converter to reduce the battery voltage from a nominal input voltage of the vehicle to 14 V. The 2025 cost target is such that it will cost no more than the alternator that it replaces.

Table 4. Technical Targets for DC/DC Converter

DC/DC Converter Targets	2025	2030	2035
Cost, \$/kW	30	20	16.67
Specific power, kW/kg	4	6	6.25
Power density, kW/L	4.6	6.8	7.5
Efficiency	>98%	98.5%	98.5%

Future long-range PEVs (300+ miles of all-electric range) will be capable of extreme fast charging at power levels higher than 350 kW resulting in much higher battery voltages (i.e., 800 VDC) and thus placing additional requirements on the DC/DC converter.

On-Board Charger Technical Targets

All PEVs require an OBC, which converts AC input power from the EVSE (part of off-board charging infrastructure, not located on the vehicle) into DC power for the on-board battery. Table 5 shows technical targets for the OBC.

Table 5. Technical Targets for On-Board Charger

On-Board Charger Targets	2025	2030	2035
Power Level	6.6	19.2	19.2
Voltage	600	800	800
Cost, \$/kW	30	20	16.67
Specific power, kW/kg	4	12	12.8
Power density, kW/L	4.6	13.7	14.8
Efficiency	98%	98.5%	98.5%

Wireless charging will likely become a more widespread option on future PEVs for consumer convenience (i.e., not having to plug in the cord to charge the vehicle) and as an enabling technology for CAVs in fleet use (i.e., automated charging). The vehicle receiver coil of the WPT system and the supporting power electronics components will be integrated into the OBC; however, none of these WPT system components are included in the targets presented in Table 5 since the technology is still in the R&D stage.

Many R&D gaps are currently being addressed to enable XFC beyond 350 kW to meet consumer expectations of an 80% charge within 15 minutes or less. While EDTT members are actively engaged in closing the early-stage research gaps associated with XFC power transfer (i.e., 800 V WBG electrical vehicle architecture), no specific targets exist since the technology is still in the R&D stage.

Current Technical Target Status

The 2022 manufacturing cost of a commercial on-road 100 kW ETDS, consisting of a single electric traction motor and inverter is currently estimated to be \$1,140 based on the publicly available data and scaling it for 150kW system.⁸ Of this cost, the electric motor accounts for approximately \$756 and inverter about \$384.

The 2020 EDTT R&D target for the ETDS was \$8/kW which was met for a 100 kW peak power ETDS based on the U.S. Department of Energy (DOE) Vehicle Technology Office co-sponsored industry and national laboratory R&D efforts. Table 6 shows comparison of 2025 ETDS technical targets with current on-road technology status. A significant size reduction is required to increase the ETDS power density by 733%, while achieving the necessary cost reduction. The complexity of achieving the power density while reducing cost by 47% when compared to on-road technology is daunting.

Table 6. Comparison of Current Status with 2025 Technical Targets for ETDS

ETDS Targets	On-road Status	2025 R&D Target	2025 versus On-road
Cost, \$/kW	7.6	4	-47%
Power density, kW/L	6	50	+733%

Table 7 presents the same comparison as above for power electronics and electric motors.

Table 7. Current Status and 2025 Technical Targets for Power Electronics and Electric Motors

*On-road cost doesn't represent a SiC-based system, that will have significantly higher cost.

	On-road Status	2025 R&D Target	2025 versus On-road
Power Electronics			
Cost, \$/kW	2.6	1.8	-30%*
Power density, kW/L	30	150	+400%
Electric Motor			
Cost, \$/kW	5.0	2.2	-56%
Power density, kW/L	9	75	+733%

⁸ UBS, "UBS evidence lab electric car teardown: Disruption ahead?" (2017), <https://neo.ubs.com/shared/d1ZTxnvF2k> icct The International Council of Clean Transportation, Working Paper 2019-06

The on-road inverter and electric motor cost assessment is based on information from the International Council on Clean Transportation (ICCT) Working Paper 2019-06. Cost information was presented from the working paper for 2017 along with projected cost in 2025 that was then extrapolated for 2023. Additionally, information presented at the Vehicle Technology Office annual merit reviews from industry projects were used along with other public source information to check reasonableness. It is important to note that current on-road inverter uses silicon insulated-gate bipolar transistors (IGBTs). The introduction of SiC to achieve higher efficiency over the drive cycle and higher power density will significantly increase the cost being reported as On-road.

Electric Drive Technologies Research Highlights

Modified DBC Substrate for Space Restricted Application

Designed and evaluated low thermal resistance modified DBC substrate

Oak Ridge National Laboratory (ORNL)

The traditional direct bonded copper (DBC) substrates do not utilize heat spreading because of the thinner copper layer, thus using a much smaller active surface area for cooling. To improve heat transfer, a modified DBC substrate has been proposed, named DBCwCu. The modification includes a thick copper block/tile in between the semiconductor device and the DBC substrate. This simple modification improves heat spreading underneath the die, thus using a much larger substrate area for heat transfer. Traditional and modified DBC substrates are shown in Figure 1.

The modified DBC substrate's performance has been experimentally evaluated and compared with a traditional DBC substrate. Two half-bridge modules were made: one traditional DBC (Figure 1, left) and one DBCwCu (Figure 1, right) for comparison. A single wolfspeed MOSFET was soldered in each switching position and was wire bonded to the substrate for gate, drain, and source terminations. The substrate was then attached to a heat sink using a thermal interface material and was clamped using a 3D-printed structure. Two holes were made in the heat sink to place thermocouples underneath the substrate to capture the substrate's bottom surface temperature. The device surface was painted with matte black paint to increase emissivity, and the device temperature was captured using a thermal camera. The thermal evaluation experimental setup is shown in Figure 2. In this experiment, MOSFET body diodes were conducted to generate losses. A DC source was used to inject current through body diodes, and the top and bottom diodes were connected in series.

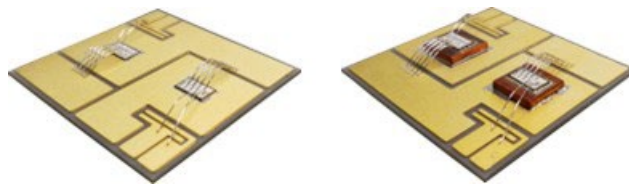


Figure 1. Assembled substrate for thermal evaluation: the conventional direct bonded copper (DBC) substrate (left) and the modified DBC with copper substrate (right).

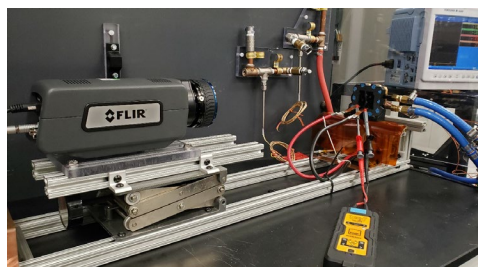


Figure 2. Experimental setup to evaluate the thermal performance of the proposed DBC with copper substrate.

The gate and source pins were shorted to keep the MOSFETs shut for the evaluation. Injection current was varied to introduce losses within the device, and the power loss was varied from 25 W up to 250 W. The device temperature and thermal resistance improvement results are plotted in Figure 3 for both the traditional and modified DBC substrates.

The traditional DBC substrate temperature reaches 160°C with 180W Power Loss whereas the DBCwCu device temperature reaches the same value when the injected loss was 250W. Results (Figure 3, top) show that the modified DBCwCu substrate can handle 30% higher losses than the traditional DBC which implies the improved thermal resistance shown in Figure 3 (bottom).

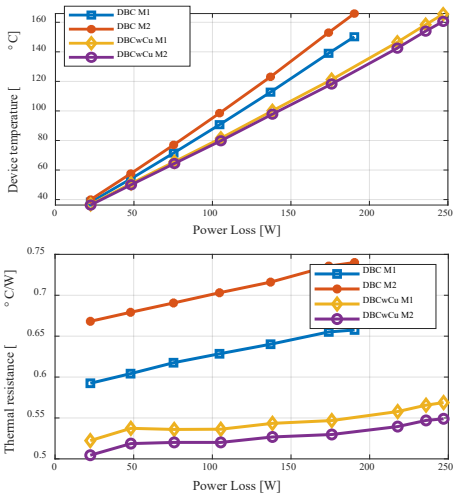


Figure 3. Comparison of device temperature (top) and substrate thermal resistance (bottom) at various power loss injections for traditional and modified DBCs.

Motor with Advanced Concepts for High power density and INtegrated cooling for Efficiency (MACHINE)
In-slot embedded cooling reduces winding temperature by 50% by reducing thermal resistance from source to sink by 65%.

RTX Technology Research Center (RTRC)

Electric motor power density and efficiency are limited by design trade-offs between material options, electromagnetics, thermal management, and structural design considerations. The RTRC team has developed a Motor with Advanced Concepts for High power density and INtegrated cooling for Efficiency (MACHINE), demonstrating an 8X improvement in power density by leveraging three key technology elements: (a) use of non-heavy rare earth hard magnets, (b) high Silicon soft magnetic steel, and (c) embedded in-slot cooling, shown in Figure 4. To achieve better performance, the team has utilized multi-physics design optimization methods to maximize the optimal magnetic loading, electric loading, and airgap shear stress while efficiently removing the generated heat.

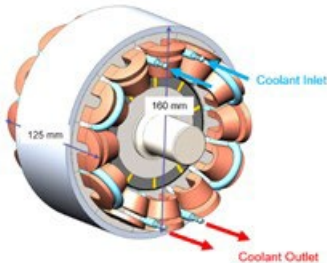


Figure 4. Developed MACHINE concept with embedded cooling channels and non-heavy rare earth magnets.

The developed MACHINE concept considers surface permanent magnet rotor architecture with fractional slot concentrated windings along with embedded in-slot cooling. With optimization, it is designed to handle ~17-20 Arms/mm² for a select duty cycle. The team has developed a multi-physics analysis and design framework as shown in Figure 5 to verify the design operation and performance including electromagnetics, thermal, structural and flow distribution into the cooling channels. The motor winding design was optimized for overall performance while considering manufacturability.

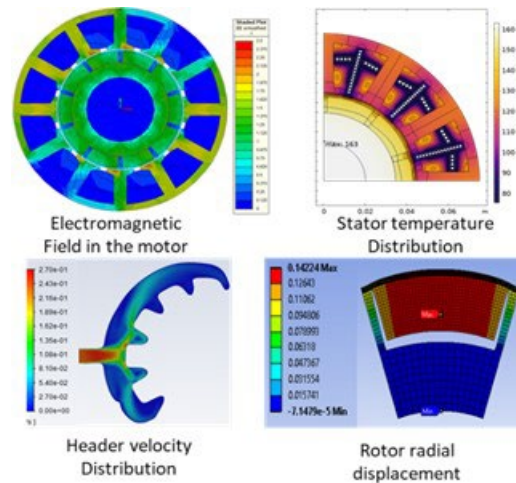


Figure 5. Multi-physics design optimization of MACHINE concept.

The RTRC team has successfully completed building, testing and validation of a sectional stator with embedded cooling channels with ethylene glycol water (EGW) 50:50 coolant. Experimental results were then compared with high fidelity model predictions, and the team updated finite element models to reflect experimental conditions. A series of experimental tests and model analysis at various conditions are shown in Figure 6. The model predicted temperature matches well with the experimental temperature measurements.

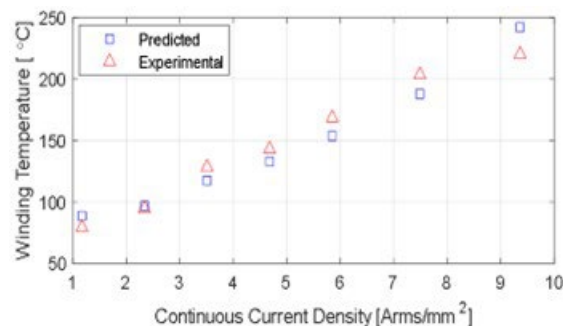


Figure 6. Experimentally measured winding temperature vs. model predictions at various current loading.

Fabrication of Soft Magnetic Components with High Volume Loading of Fe₄N

Earth-Abundant Soft Magnetic Composites for Electric Machines and Power Electronics

Sandia National Laboratories

Sandia National Laboratories has developed high-magnetization, low-loss, earth-abundant, iron-nitride-based (Fe₄N) soft magnetic composites (SMCs) and has successfully formed them into components for electric machines and motor drives. These new magnetic components will enable low eddy current losses and highly efficient motor operation at rotational speeds up to 20,000 rpm at temperatures up to 150°C. As our capability to produce Fe₄N/epoxy samples has improved, we have progressed to the fabrication of larger parts, which is key to the utilization of these materials in automotive systems.

This year, our team devoted significant effort to the fabrication of soft magnetic parts for a dual rotor homopolar AC machine (DHAM) designed by our collaborators at Purdue University. A benefit to fabricating soft magnetic motor parts using SMCs is that a monolithic Fe₄N composite can replace a stack of many electrical steel laminations, and moreover this machine design does not require permanent magnets. The first parts fabricated used a molding process, where CAD drawings of the soft magnetic parts were shared by Purdue and were used to 3D print anti-molds at Sandia using polylactic acid. Using this method, a 50% scaled version of the short stator assembly was fabricated using 55 vol.% Fe₄N in epoxy (Figure 7).



Figure 7. 50% scale version of the DHAM short stator assembly. This component consists of 55 vol.% Fe₄N.

A die for a DHAM rotor was evaluated in Sandia's current hot pressing setup. This die is significantly larger than any others used previously in our lab, so a new heating band and approach to heating was required. The temperature of the die was closely monitored at several physical points until a method for consistent heating was established. Once the uncured composite is in the die, the preheated anvil is inserted and the composite is pressed at 37 MPa. This is significantly lower than the pressure used for smaller pressed parts due to the size and shape of the DHAM rotor assembly and die.

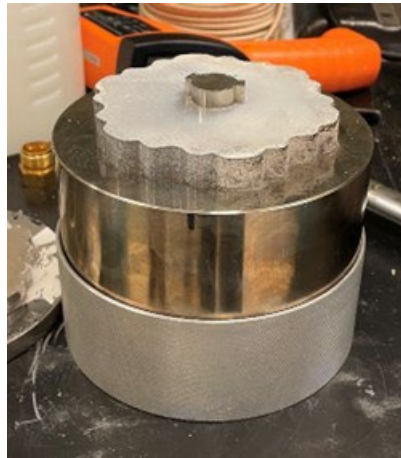


Figure 8. DHAM rotor assembly during removal from custom hot pressing die.

Carbon paper was utilized between the base and the outer die to ensure that the base and sample could be demolded. This worked well, and the demolding process was performed effectively. Currently, samples have been demolded with very few or negligible defects such as hairline fractures or chipping along the inner or outer edges (Figure 8). Components such as this will greatly facilitate rare-earth-free motor components that can be readily fabricated, as well as magnetic components (e.g. inductor cores) for motor drives.

Development of Sustainable High Performance Magnets for Exceptional Power Density Electric Drive Motors

Grain boundary engineering to replace heavy rare earth elements

Ames National Laboratory

Ames National Laboratory (AMES) researchers have developed a grain boundary additive to improve the magnetic performance of fine-grained Nd-based sintered magnets. Minimizing the loss in coercivity at elevated temperatures in traction motors typically requires the addition of heavy rare-earths (HREs). Ames has been developing processing methods to produce fine grain feed stock powders and their handling without HREs (e.g., Dy). An additional challenge when sintering ultrafine grain powders is to get a fully dense magnet without growing the grains since very high temperatures are required. The sintering temperature can be lowered if a suitable sintering aid can be added. However, these sintering aids must be tailored to the overall chemistry of the alloy since they must not degrade the magnetic properties of the matrix phase nor take up too much volume and dilute the effective work the magnet performs in a motor.

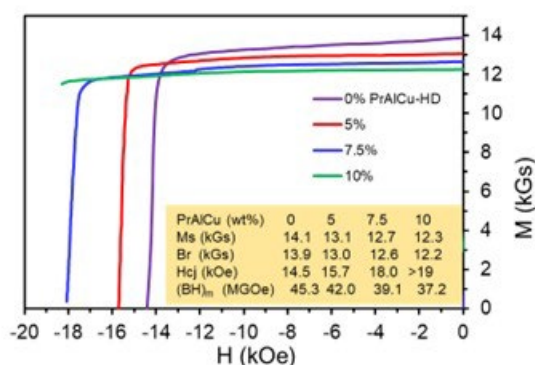


Figure 9. Demagnetization loops for samples without any sintering aids and their performance with increasing weight percent of the Pr-Al-Cu compound at room temperature.

Ames researchers tested two promising compounds, Pr-Cu and Pr-Cu-Al, both with melting points more than 250°C lower than the lowest peritectic reaction temperature in Nd-Fe-B alloy compositions used in typical traction motors. As shown in Figure 9, the sintering aid increases coercivity and slightly decreases remanence.

More importantly, is how the grain boundary phase also affects the higher temperature performance of the magnet. Note (Figure 10), the magnet with 3 wt.% of sintering aid has the best performance.

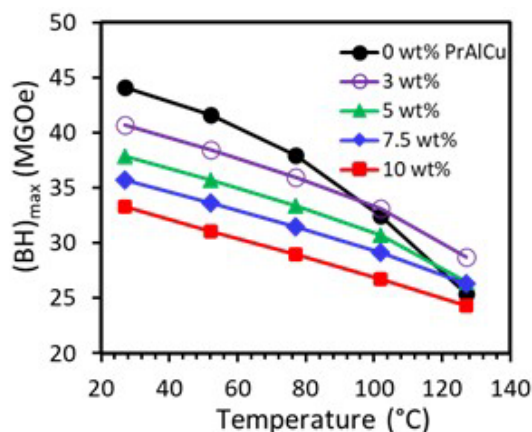


Figure 10. Summary of temperature effect on energy product as a function of wt.% addition of Pr-Al-Cu.

Compared to a commercial alloy with 4.5wt.%Dy, the Ames alloy is only slightly lower in coercivity and has very similar thermal coefficients for remanence and coercivity as the commercial alloy.

Table 8. Comparison of magnetic properties.

Sample ID	no PrAlCu	3 wt% PrAlCu	7.5 wt% PrAlCu	Arnold N45H
Dy wt%	0	0	0	4
Br (kGs)	13.8	13.4	12.1	13.5
Hc (kOe)	13.5	15.6	17.6	17
(BH) _{max} (MGOe)	44.1	40.7	35.7	44
-α _{25-125°C} , %/°C	0.12	0.12	0.14	0.12
-β _{25-125°C} , %/°C	0.7	0.64	0.64	0.61

Dielectric Fluid (Liquid) Cooling Demonstration Using a Silicon Carbide (SiC) Module

Demonstrated reduced thermal resistance (20%) and pumping power (80%) using a dielectric fluid cooling solution.

National Renewable Energy Laboratory (NREL)

NREL designed a new, dielectric fluid (liquid) cooling concept for power electronics. The concept uses dielectric fluids to simplify the package configuration and eliminate the thermally resistive ceramic component used in metalized ceramic substrates. The new concept incorporates dielectric fluid jets impinging on finned copper heat spreaders to cool silicon carbide (SiC) devices. The use of dielectric fluids enables reducing the junction-to-fluid thermal resistance by eliminating the ceramic component, allows for cooling other inverter components (e.g., capacitors, bus bars), and enables integrating the power electronics with the electric motor.

A thermal demonstration module was fabricated using two 650 V SiC metal-oxide-semiconductor field-effect transistor (MOSFET) devices. The two devices were connected in parallel and represented one electrical switch. The SiC devices were soldered to copper heat spreader substrates and installed within the dielectric fluid heat exchanger (Figure 11). The heat exchanger was made from polyphenylene sulfide and polyetheretherketone materials which are high-temperature plastics, compatible with dielectric fluids, used in automotive applications, and are lightweight.

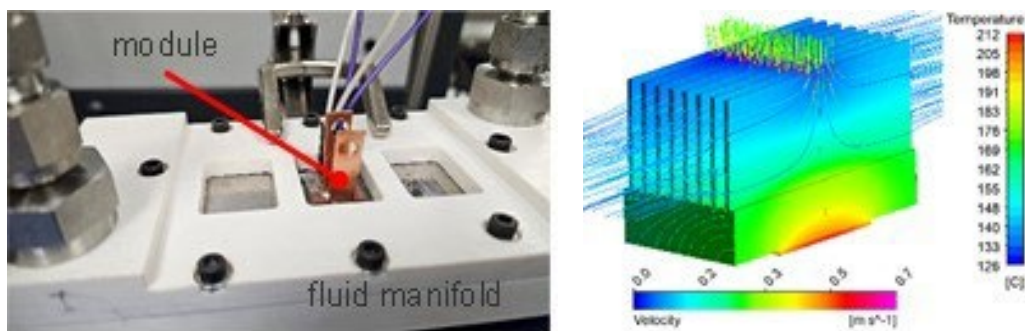


Figure 11. Pictures of the SiC module installed within the dielectric-fluid-based plastic heat exchanger (left). Modeling results showing the slot jet cooling design (right).

The assembled module and heat exchanger were piped into the dielectric fluid loop to circulate AmpCool-110 dielectric fluid. AmpCool-110 (from Engineered Fluids) is designed to cool the battery packs and electric machines in electric-drive vehicles (EV), and hence is an appropriate fluid for this application. We are also

collaborating with Infineum fluids to evaluate new driveline fluids that are being developed specifically for EVs.

The experimentally measured results show that the dielectric fluid concept can outperform water-ethylene glycol (WEG) cooling systems (Figure 12). The dielectric fluid concept was found to reduce the junction-to-fluid thermal resistance and pumping power by 20% and 80%, respectively, compared to a WEG-cooled CREE SiC module. Additionally, the model predictions were found to be in good agreement with experimentally measured values.

A preliminary analysis was conducted to size an air-cooled heat rejection system for the dielectric fluid which indicates that a 218-cm² folded-fin heat exchanger is required to dissipate 2.5 kW of heat assuming 50°C air temperature. This is about 8% smaller than a WEG-based heat exchanger. The size decrease is enabled by the dielectric's fluid's higher temperature compared with WEG. Long-term reliability for this flow configuration will also be investigated in the near future.

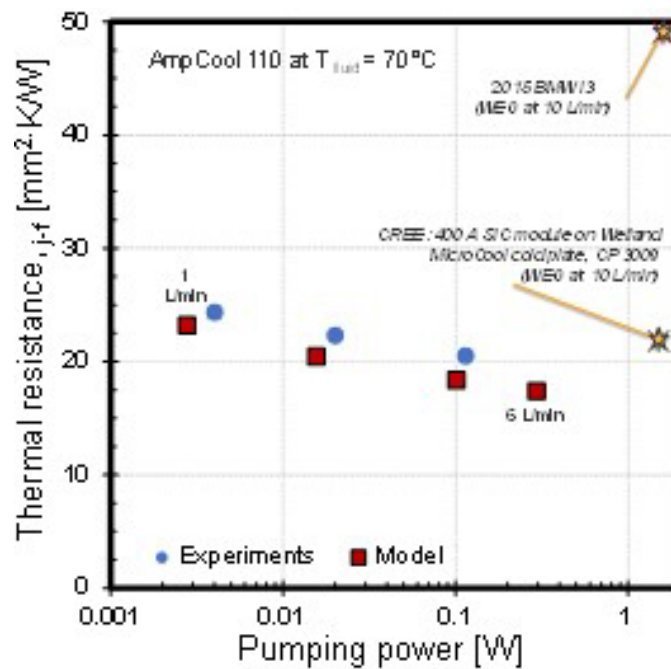


Figure 12. Junction-to-fluid thermal resistance versus pumping power showing modeling and experimental results with comparisons to commercially available, WEG-cooled power modules (Si-based and SiC-based modules).

Grid and Infrastructure Program Overview

Introduction

The Grid and Charging Infrastructure (G&I) program's mission is to conduct early-stage research and development on transportation electrification technologies that enable reduced petroleum consumption by light, medium, and heavy-duty vehicles. The program identifies and enables the role of vehicles in the future electrical grid.

Charging of EVs at scale creates an unpredictable and stochastic load demand on the electric grid. Newer EVs being introduced in the market can charge at low and high rates based on the need and availability of charging infrastructure. Additionally, charging profiles for EVs manufactured by different Original Equipment Manufacturers (OEMs) vary significantly which complicates meeting the aggregated charging loads. This creates difficulty in the prediction of magnitude, location, and timing of charging loads and could potentially have a detrimental grid impact.

To enable successful deployment of EVs at scale, a holistic approach is required across the vehicle, charging infrastructure, and electric grid. Figure 13 presents the key components of charging ecosystems that create challenges to be addressed. This includes controls, high voltage power electronics, interoperability, wireless and other advanced high power charging (HPC) technologies, and integration and optimization with the grid and Distributed Energy Resources (DERs) such as stationary storage and photovoltaics.

Hence, the effective control and optimization of the charging ecosystem is essential and is otherwise known as Smart Charge Management (SCM). SCM emphasizes the identification of pathways to reduce the potential grid impacts of EVs at scale, while providing enhanced value for EV/charging/grid systems including reduced costs and increased opportunities for grid services. If unmanaged, EVs at scale connecting to the grid would create numerous challenges for utilities, particularly at the distribution level, such as feeder voltage violations, system imbalances, flickers, equipment overloading, and large increases in daily peak loads. Interoperability and scalability, and high-speed communications and control are critical challenges facing SCM. Effective SCM will enable response to inappropriate energy management, malfunctioning equipment, and Cyber-Physical Security (CPS) breaches. SCM can also facilitate the provision of grid services from EV charging, including, but not limited to, peak load shaving, demand charge mitigation, voltage support, frequency regulation, and integration of renewable energy generation.

HPC of up to 400 kW for light-duty (LD) EVs, and 1+ MW for medium-duty (MD) and heavy-duty (HD) EVs, can enable greater vehicle utilization, extended range, and reduce recharging times. Technical advances are steadily being made with regards to HPC, but further progress is needed to facilitate the mass market adoption

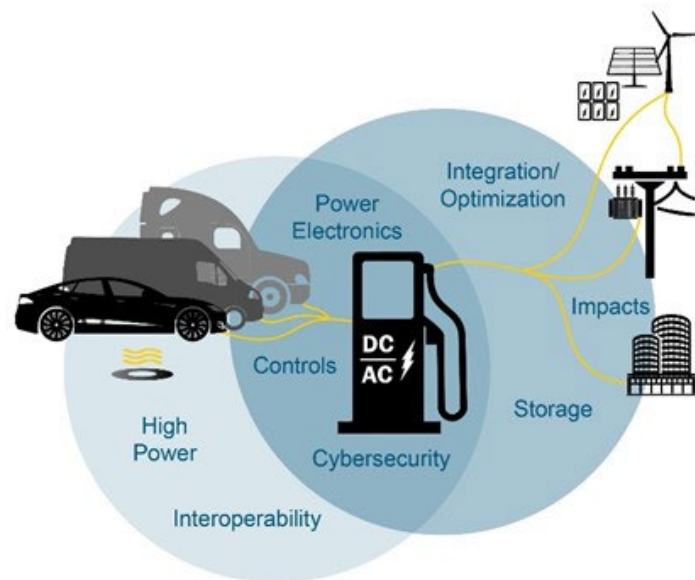


Figure 13 Key technologies and challenges addressed by the Grid and Infrastructure Program.

of EVs. Specific technical challenges include the requirement for intelligent design and integration with the grid and DERs, to mitigate ramp rates and surge power demands, lower system cost of ownership, and interoperability of HPC infrastructure with MD and HD EVs. Additionally, as the charging power levels steadily increase, new challenges are manifested in ensuring HPC is effectively integrated with the grid in an efficient, flexible, and secure manner. High voltage power electronics and materials with better thermal and electrical properties are key enabling technologies for advancing HPC. Furthermore, improvements in wireless charging are required including the development of novel coils, advanced field shaping techniques, and control strategies.

Rapidly increasing numbers of EVs with advanced communication functionalities and networked chargers, as well as the trend towards HPC, dramatically increase cyber related risks and consequences. Coordinated cyber-attacks on chargers/charging stations can lead to serious local and potentially broader grid disruptions such as wide-scale blackouts and/or brownouts. A comprehensive understanding of the threat environment, including risks and consequences therein, is needed to identify, minimize, and/or eliminate critical cyber-physical vulnerabilities. Advances are required in strategies, systems, and tools, including hardware/software for intrusion detection, threat mitigation and isolation, and charging system recovery.

Addressing the barriers above can only be done by conducting high risk projects that are beyond the suitable scope and developmental timeframes of industry. Furthermore, the transportation and utility sectors historically have not worked together, which complicates collaboration. A significant level of pre-competitive and vendor-neutral Research and Development (R&D) effort is needed to address the challenges associated with a safe and secure charging ecosystem for EVs at scale.

State of the Art

Electric Vehicle Charging

It is desirable to reduce EV refueling times to be competitive with conventional vehicle refueling times (e.g., 5-10 minutes for 400 miles of LD vehicle driving range). The table below lists the refueling characteristics of several types of installed commercial chargers and a conventional gasoline fueling pump. The technologies employed in the EV charging stations are shown in the figure below. It is important to note that the rate of energy transfer peaks early in the charging cycle and decreases as the battery pack approaches 100% state of charge (SOC). While the energy transfer rate is not constant during charging, given two chargers with different peak power ratings the charger with the higher peak power rating is potentially capable of minimizing EV charging times when compared to the EVSE with a lower maximum power rating. It is notable that the EV must be capable of accepting the higher power provided by the EVSE with the higher maximum power rating. To accomplish this capability some vehicle OEMs are increasing the operating voltage of the on-board battery pack and the maximum C-rate for charging battery cells. Currently Electrify America offers commercial charger solutions with peak power rating of 350 kW DC.⁹ However, currently the maximum charge rate that is accepted by a LD vehicle is 300 kW DC (Lucid Air, 900V+ electrical architecture). This LD vehicle can add 20 miles of range per minute when charging at this maximum charge rate using a 350 kW DC Fast Charger (CCS Charging Standard).¹⁰

Charging Standards

In the U.S. there are two existing open fast charging standards and a third charging standard is “in-development” and listed as a “Work in Progress” by SAE. The two open fast charging standards on the market today CCS and CHAdeMO were both originally designed to work at 400V and have evolved to increase their peak charging power ratings. As of August 2023, The “North American Charging Standard” (NACS) has been widely deployed at Tesla Superstations in North America and is currently being developed by SAE’s Hybrid-

⁹ <https://electrify-commercial.com/> 1/25/2021

¹⁰ Source: <https://www.lucidmotors.com/media-room/lucid-air-fastest-charging-ev/>. August 2020

EV J3400 NACS Electric Vehicle coupler Task Force.¹¹ The development of the SAE J3400 NACS has significance and urgency in the context of NACS adoption announcements by nine automakers, four charging networks, four charger manufacturers, and one EV developer during 2023¹². In 2023, several EV manufacturers announced agreements with Tesla to allow their EV customers to start accessing the Tesla charging network^{13, 14}. The EV manufacturers will start integrating NACS charging into their future EVs builds¹⁵. An adapter can be used to enable EVs with CCS connectors to charge using the Tesla charging stations.

The Combined Charging System (CCS) is an open, universal, and international charging system for electric vehicles based on international standards. It provides the solution for all charging requirements. The Combined Charging System is therefore ONE system for ALL. The CCS combines single-phase with fast 3-phase AC charging using alternating current of maximum of 43 kW. It also provides very fast high-power DC charging (up to 450 kW) within a single system. Members are presently also working on a High-Power charging connector for commercial vehicles that can take multiple MW charging power. This extended High-Power charging will be used for specialty EV like busses, truck, etc. The CCS system includes the connector, the managing of control functions and the charging communication between electric vehicle and infrastructure.¹⁶ The standard is backed by major European and U.S. OEMs.

CHAdeMO was an initiative of Japanese car companies and was originally designed to charge at up to 50 kW at 400V.

The mid-term objective of XFC is to reduce LD charging time to approximately 10 minutes via a charge rate of approximately 350 to 400 kW. The long-term objective is to achieve charge rates of greater than 1 MW that will enable fast charging of both LD and Heavy Duty (HD) vehicles. The CHARIN SAE J3271 Megawatt Charging Standard (MCS) connector standard is dedicated to achieving charge rates of up to 4 MW.

In addition to the conductive charging standards discussed above the wireless power transfer standard J2954 addresses charging of LD vehicles at peak rates of 22 kW and MD/HD vehicle charge rates of approximately 500 kW.

Currently Installed Charging Systems in the U.S

The characteristics of charging stations that are currently installed in the U.S. are provided in Table 9 and are included in Figure 14.

¹¹ <https://standardsworks.sae.org/standards-committees/hybrid-ev-j3400-nacs-electric-vehicle-coupler-task-force>. Accessed 9/21/2023.

¹² “More automakers plug into Tesla’s EV charging network”, Reuters., September 21, 2023. <https://www.reuters.com/business/autos-transportation/more-automakers-plug-into-teslas-ev-charging-network-2023-09-21/>

¹³ <https://media.ford.com/content/fordmedia/fna/us/en/news/2023/05/25/ford-ev-customers-to-gain-access-to-12-000-tesla-superchargers--.html>. 5/25/2023.

¹⁴ <https://www.media.volvocars.com/global/en-gb/media/pressreleases/316416/electric-volvo-car-drivers-will-get-access-to-12000-tesla-superchargers-across>

¹⁵ <https://www.caranddriver.com/news/a44133661/gm-electric-vehicles-tesla-charging-2024/>

¹⁶ <https://www.charinev.org/faq/> 1/25/2021.

Table 9. Light Duty Conventional and Electric Vehicle Refueling Characteristics

Type of Refueling	Gasoline	Level 1 110V (~1.4 kW)	Level 2 220V (~7.2 kW)	DC Fast Charger (50 kW, 150 kW, 350 kW)	Tesla V2 & V3 SuperChargers (145 kW, 250 kW)
Range per Charge Time	400 miles /5 mins	3–5 miles /60 mins	25 miles /60 mins	50 kW: 150 miles /90 mins	250 kW: ~360 miles ¹⁷ /60 mins
Time to Charge for 200 miles	<5 mins	37 hours	8 hours	50 kW: 2 hours	250 kW: 24 mins
Number of U.S. stations/connectors circa 2023 ¹⁸	153,000	676/3130	54,038/129,184	8,255/34,281	1,911/21,039

The summary of charge connector standards provided in the figure below includes the connector diagram, maximum output power, applications, and development status for each of the connector standards. It is notable that several of these charging standards are evolving as evidenced by the frequency of the “in development” and “updating” status of the charge connector standards in Figure 14.

¹⁷ Source: Tesla Model 3 range, battery & charging, June 2021. <https://www.drivingelectric.com/tesla/model-3/range>

¹⁸ Source: Alternative Fuels Data Center, National Renewable Energy Laboratory, June 2021. <https://afdc.energy.gov>








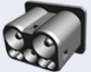

Diagram	Main Standard/ System	Maximum Output Power, Volts, Amps	Standard Status as of August 2023	Application Notes
	SAE J1772 / AC Level 1, AC Level 2	19.2 kW AC, 208/240VAC., 80A	Released	Used for Level 1 and Level 2 in North America. Commonly found on home, workplace, and public chargers.
	SAE J1772+ IEC 61851 / CCS1	450 kW DC, 1000VDC, 500A	Updating	Used for DC fast charging most vehicles in North America. Generally installed at public chargers.
	IEC 61851 IEEE 2030.1/ CHAdeMO	400 kW DC, 1000VDC, 400A	Released	Used for DC fast charging select vehicles in North America. Generally installed at public chargers.
	SAE J3400 / NACS	250 kW DC, 410VDC, 610A	In-development	Used for both AC and DC fast charging. Standard is under development and is based on Tesla's design.
	SAE J3068	166 kW AC, 600VAC, 160A 450 kW DC, 1000VDC, 450A	Updating	Standard for both AC and DC charging using the IEC 61851 'type 2' connector for North America three-phase charging.
	SAE J2954	22 kW AC light duty, 480VAC, 30A 500 kW AC heavy duty, 480VAC, 670A	Released	Wireless power transfer standard for MD/HD vehicles is J2954/2. In U.S. the maximum power for light-duty is 11KW (WPT3).
	SAE J3105	1.2 MW DC, 1000VDC, 1200A	Released	Automated connection device to charge MD/HD vehicles. Variants include pantograph up or down and pin-and-socket.
	IEC 61851 IEEE 2030.1 / Chaoji	900 kW DC, 1500VDC, 600A	In-development	Sub-MW conductive charging for LD/MD/HD vehicles in Asia
	SAE J3271 IEC 63379 / MCS	3.75 MW DC, 1500VDC, 3000A	In-development	Conductive MW level charging for MD/HD vehicles.

Figure 14 Examples of EV Connector Standards, Sources:ANL¹⁹, SAE^{20, 21, 22}, ORNL²³, CEC^{24, 25, 26, 27, 28, 29, 30}

¹⁹ ANL T. Bohn, “Global DC Charging Systems” SAE Committee Presentation Slide (draft) August 2023.

²⁰ SAE 2022 “Wireless Power Transfer for Heavy-Duty Electric Vehicles J2954/2_202212”,

https://www.sae.org/standards/content/j2954/2_202212/.

²¹ “SAE PUBLISHES TIR J2954, WIRELESS POWER TRANSFER EV/PHEV”, 31 May 2016 | Jesse Schneider, David Law,

<https://www.standardsuniversity.org/e-magazine/june-2016/sae-publishes-tir-j2954-wireless-power-transfer-evphev/>

²² SAE 2023 “WIP 2023-7-11 SAE J3400: NACS Electric Vehicle Coupler J3400”, <https://www.sae.org/standards/content/j3400/>

²³ ORNL Veda Prakash Galigekere and Omer Onar, Interview by author, September 26, 2023.

²⁴ U.S. Department of Energy Alternative Fuels Data Center. “Developing Infrastructure to Charge Plug-In Electric Vehicles.”

https://afdc.energy.gov/fuels/electricity_infrastructure.html

²⁵ CharIn. 2020 “Mapping Standards for Low- and Zero-Emission Electric Heavy-Duty Vehicles,” presentation. International Transportation Forum February 18-20, 2020 Workshop. <https://www.itf-oecd.org/sites/default/files/docs/charging-infrastructure-standardisation-developments-bracklo.pdf>.

²⁶ ChAdeMO. “Technology Overview.” <https://www.chademo.com/technology/technology-overview/>.

Prototype Charging Systems

The research community has developed prototypes that charge at rates greater than 400 kW.

Light Duty Charging Station Prototype

Initiated in July 2016, the “Fast Charge” research project has received €7.8 million in funding from the German Federal Ministry of Transport and Digital Infrastructure. The implementation of the funding guidelines is being coordinated by the German National Organization Hydrogen and Fuel Cell Technology (NOW). The industrial consortium includes automotive manufacturers the BMW Group and Dr. Ing. h. c. F. Porsche AG, as well as operators Allego GmbH, Phoenix Contact E-Mobility GmbH (charging technology) and Siemens AG (electrical engineering)

The research consortium presented a prototype for a charging station with an output of up to 450 kW in Jettingen-Scheppach, located near the A8 motorway between Ulm and Augsburg. The new charging station is suitable for electric models of all brands with the European standard Type 2 variant of the widely used Combined Charging System (CCS) and is now available for use free of charge. A Porsche research vehicle with a net battery capacity of approximately 90 kWh achieved a charging capacity of over 400 kW on the new charging station, allowing for charging times of less than 3 minutes for the first 100 km range

Medium and Heavy-Duty Charging Station Prototype

Portland General Electric and Daimler Trucks North America are co-developing “Electric Island,” a large public charging site for medium- and heavy-duty electric commercial vehicles expected to be the first of its kind in the United States. It is designed to support up to nine vehicle charging stations with charging levels of up to greater than one megawatt.³¹

Charging at Scale

The largest EV fast charging station in the U.S. in 2023 boasts 98 Tesla Supercharging spots at Tesla’s Harris Ranch station located in Southern California³²

There are several charging networks that have been initiated in the U.S.

- The Electrify America charging network currently has 843 installed charging stations and 118 charging stations that are ‘coming soon’. The network currently has 3702 Fast chargers, and 116 Level 2 chargers.³³
- The FordPass network will include more than 12,000 charging stations with a total of 35,000 plugs in the United States and some parts of Canada.³⁴
- The Tesla charging network has 1911 public charging stations with about 21,039 plugs in the United States, according to the Alternative Fuels Data Center.
- General Motors Co. is working with electric-vehicle charging operator EVgo Services to build a nationwide fast-charging infrastructure as the automaker prepares a major push into battery-powered

²⁷ Tesla Motors. 2015. Form 10-K. Edgar Online. <http://large.stanford.edu/courses/2015/ph240/romanowicz2/docs/tesla-annual.pdf>

²⁸ Tesla Motors. 2019. “Introducing V3 Supercharging.” <https://www.tesla.com/blog/introducing-v3-supercharging>.

²⁹ SAE. 2013. “Wireless Power Transfer of Heavy-Duty Plug-In Electric Vehicles and Positioning Communication J2954/2 Standard”. <https://www.sae.org/standards/content/j2954/2/>.

³⁰ CharIn. 2020. “Mapping Standards for Low- and Zero-Emission Electric Heavy-Duty Vehicles.” presentation. International Transportation Forum February 18-20, 2020 Workshop. <https://www/itf-oecd.org/sites/default/files/docs/charging-infrastructure-standardisation-developments-bracklo.pdf>.

³¹ https://www.greenfleetmagazine.com/10131365/daimler-announces-electric-island-commercial-vehicle-charging-showcase?utm_source=feedburner&utm_medium=feed&utm_campaign=Feed%3A+GreenFleetMagazine-All+%28Green+Fleet+Magazine%29. December 1, 2020.

³² “Tesla’s Mega 98-Supercharger Location Runs In Part On A Diesel Generator: Report”, Jalopnik, Sept. 6,2023. <https://jalopnik.com/tesla-supercharger-location-diesel-generator-report-1850804146>

³³ Source: <https://www.electrifyamerica.com/locate-charger/>

³⁴ <https://www.cnn.com/2019/10/17/cars/ford-electric-vehicle-charging-network/index.html>

models. The two companies will jointly invest in 2,750 fast chargers in cities and suburbs across the U.S. as GM moves to solve a chicken-and-egg problem that comes with selling EVs: A sparse network of chargers has turned off some potential buyers, but utilities and charging companies have been loath to expand the infrastructure until more plug-ins are on the road.³⁵ As of August 2023, the GM-EVgo network has established nearly 230 public charging locations with a network total of 1000 DC Fast Charging stalls.³⁶

Goals and Objectives

Program Goal

The goal of the Grid and Infrastructure Program is to identify system pathways and conduct research to facilitate the development and harmonization of robust, interoperable, and cyber-secure electric vehicle charging and grid infrastructure that supports EVs at scale and incorporates advanced charging technologies, Distributed Energy Resources (DER), and grid services

The G&I Program is focused on EVs, Electric Vehicle Supply Equipment (EVSE or chargers), and integration with the grid. The emphasis is upon foundational systems analyses; exploratory Research, Development, and Deployment (RD&D); and Cyber-Physical Security (CPS); especially in critical areas that other stakeholders are not able to address. The three strategic areas addressed by the program are SCM, HPC, and CPS of charging infrastructure, as shown in Figure 15.

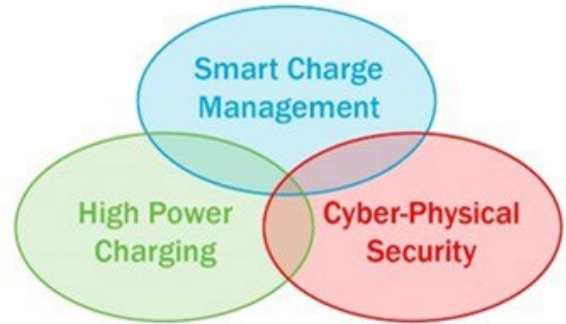


Figure 15 Strategic areas of the Grid and Infrastructure Program.

Each strategic area informs the others, providing a feedback mechanism to continuously refine and adjust program direction and focus. R&D activities span electrification of the LD, MD, and HD sectors of transportation. Additionally, given the cross-sectoral nature (vehicle, charging infrastructure, and the electric grid) of these activities, the program emphasizes close communication and coordination with other governmental and industry stakeholders, including Federal agencies, charger and vehicle OEMs, utilities, and charging network providers.

The G&I Program has established two targets for each of these strategic areas (SCM, HPC, and CPS) for the years 2023 and 2026. The strategic area targets directly support the long-term 2030 G&I Program targets, which are focused on resolving barriers and operationalizing solutions, in concert with transportation electrification stakeholders. All targets for 2023, 2026, and 2030 are listed below.

Year 2023

- SCM: Develop at least two viable smart charge management strategies and relevant tools to reduce the potential grid impacts of EVs at scale and enhance the value of EV charging systems by enabling grid services.

³⁵ <https://www.ttnews.com/articles/gm-build-nationwide-ev-charging-network>, July 31, 2020.

³⁶ “EVgo and General Motors Open 1,000th DC Fast Charging Stall as Part of Metropolitan Charging Collaboration”, Aug. 1, 2023. <https://www.evgo.com/press-release/evgo-and-general-motors-open-1-000th-dc-fast-charging-stall-as-part-of-metropolitan-charging-collaboration/>.

- HPC: Develop strategies and technologies for high power dynamic wireless charging and multi-port 1+ MW charging stations that enable vehicle charging through direct connection to medium voltage (\geq 12.47 kV) distribution.
- CPS: Develop a comprehensive threat model, prioritize high consequence events, and identify appropriate defense, detection, and mitigation strategies and tools for the EV charging ecosystem.

Year 2026

- SCM: Demonstrate and validate smart charge management strategies and relevant tools capable of controlling wide-scale utilization of high-power charging at 400 kW and above, while incorporating robust cyber-physical security methodologies.
- HPC: Demonstrate and validate viable high power dynamic wireless charging, and multi-port 1+ MW charging stations with direct connection to medium voltage distribution.
- CPS: Conduct wide-scale demonstrations to validate viable and robust cyber-physical security for the charging ecosystem in support of EVs at scale.

Year 2030

- Address technical barriers to the development and harmonization of a grid-integrated, robust, interoperable, and cyber-secure electric vehicle charging ecosystem that supports EVs at scale.
- Operationalize two technologies, tools or platforms that will enable interoperable, secure charging solutions that reduce costs for EV owners and fleets.

Program Design and Execution

The G&I Program carries out its mission by focusing its R&D investments on early stage, medium and long-term technology projects that are unlikely to be pursued by industry alone but have significant potential public benefit.

G&I R&D Functions

Smart Charge Management (SCM)

Importance

The focus of SCM is to identify pathways to reduce the potential grid impacts of EVs at scale, while providing enhanced value for EV/charging/grid systems, including reduced costs and increased opportunities for grid services. If unmanaged, EVs at scale connecting to the grid would create numerous challenges for utilities, particularly at the distribution level. SCM techniques can be employed to intelligently control, and shift charging loads to mitigate this problem and facilitate the provision of advanced grid services from EV charging.

Specific challenges and barriers to SCM include determining the impact of controlled charging versus uncontrolled charging, identifying critical strategies, and enabling technologies, developing, and demonstrating

SCM in integrated networks of building systems and DERs including stationary storage, and facilitating bi-directional power flow. Interoperability and scalability of SCM systems are needed to allow EVs from all OEMs to charge at EVSEs from multiple vendors to enable EVs at scale. High speed communication and controls with compatible device protocols and test tools for verification are required. SCM research is also needed to develop strategies and technologies for charging all EVs to enhance station resilience and mitigate potentially negative grid impacts. Finally, costs should be factored into the design of SCM hardware and grid upgrades so that they are minimized, while still providing the necessary charging service.

VTO's current SCM R&D efforts

The G&I Program's SCM activities include systems analyses; research, development, and validation of critical enabling strategies and technologies; and demonstrations. Current projects have created tools and methodologies that form the building blocks for effective SCM. The DOE National Laboratories are focused on quantifying the effects of uncontrolled charging versus controlled charging, developing and evaluating the effectiveness of smart charge control strategies, and identifying required constraints and mechanisms to implement high-value charge control strategies.

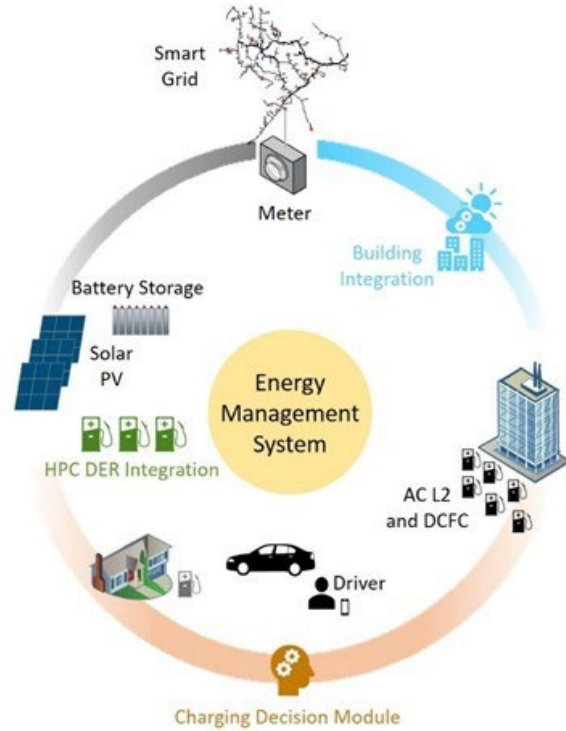


Figure 16 Key elements of Smart Charge Management.

In the fall of 2020, VTO launched utility-managed SCM projects that include research, development, and execution of a wide-scale demonstration that enables grid services from EVs and provides benefits to electricity grid operators, energy services providers, charging network operators, and EV owners. Figure 16 illustrates key elements of SCM including predictive charge decision making, controls, and integration of vehicle charging and distributed energy resources with buildings and the grid.

VTO R&D Outlook for Key Focus Areas

Building on the advances from current R&D efforts, future SCM activities target LD, MD, and HD EVs and fleets at charging stations, fleet depots, and travel centers. R&D is needed for real time detection and implementation of mitigation procedures when an EV charging station is acting out of the norm or has suffered a cyber breach. Likewise, for MD/HD EV fleet charging at depots and travel centers, the focus is to develop and demonstrate SCM strategies, systems, and tools to provide benefit to MD/HD fleets and owners, and to reduce potential grid impacts. To achieve effective SCM, a thorough understanding of HPC charge profiles, both conductive and inductive, is required for optimal integration of charging stations and the utility distribution grid. Another future thrust is to identify viable vehicle-to-everything (V2X) applications and requirements, and to subsequently develop and demonstrate technologies (on and off board) for low cost, interoperable, controllable, and bi-directional power flow. The following identifies specific targets for SCM for the years 2023 and 2026.

YEAR 2023

- Develop at least two viable smart charge management strategies and relevant tools to reduce the potential grid impacts of EVs at scale and enhance the value of EV charging systems by enabling grid services.

YEAR 2026

- Demonstrate and validate smart charge management strategies and relevant tools capable of controlling wide-scale utilization of high-power charging at 400 kW and above, while incorporating robust cyber-physical security methodologies.

High Power Charging

Importance

Successful deployment of HPC for LD (up to 400 kW) and MD/HD (1+ MW) EVs offers numerous benefits, including greater vehicle utilization, extended range, and recharging times comparable to refueling for conventional vehicles. However, HPC systems face multiple technical challenges and must be intelligently designed and integrated with the grid and DERs to mitigate ramp rates and surge power demands, lower system total cost of ownership, maximize the potential for grid services, and enable interoperability of HPC infrastructure with MD and HD EVs.

HPC exploratory R&D and analyses are needed to address issues associated with materials, power electronics, thermal management, and overall costs. Specific barriers exist with thermal loading of equipment and cables that enable service from the medium voltage grid and power transfer to the vehicle. Investigations are also needed into automated EVSE for HPC, especially above 400 kW charging levels. Advances in wireless charging are required, including the development of novel coils, advanced field shaping technologies, and mitigation of stray electric and magnetic fields.

Likewise, assessment and research are needed to understand the impacts of HPC on the grid, and unexpected grid events on HPC-enabled vehicles, and to help determine the appropriate response from EVs and EVSE. Clear understanding of both the impact of large numbers of HPC systems on distribution feeders and of methods to integrate and control stationary storage and other DERs, in support of HPC, are needed. Furthermore, identification and development of control strategies will be required to enable HPC stations to provide grid and building services.

VTO's current HPC R&D efforts

The G&I Program supports RD&D of HPC in three areas: charging stations with multiple 400 kW EVSE for LD EVs, multi-MW charging stations for MD/HD EVs, and high-power static and dynamic wireless charging. For LD EVs, the focus

is on developing and demonstrating charging stations with charging ports rated up to 400 kW and a total combined power rating that exceeds 1 MW. These stations will connect directly to medium voltage distribution networks and utilize stationary storage systems to minimize negative impacts on the grid. For MD/HD EVs, efforts are focused on developing strategies and technologies for 1+ MW multi-port chargers at fast charging travel plazas/truck stops and/or fleet depots. The G&I Program will conduct charging station utilization and load analysis, grid impacts and interconnection analysis, detailed power electronics component design, site and battery charge control, and charging connector design. Figure 17 provides a conceptual configuration of an HPC station for MD/HD EVs. High power

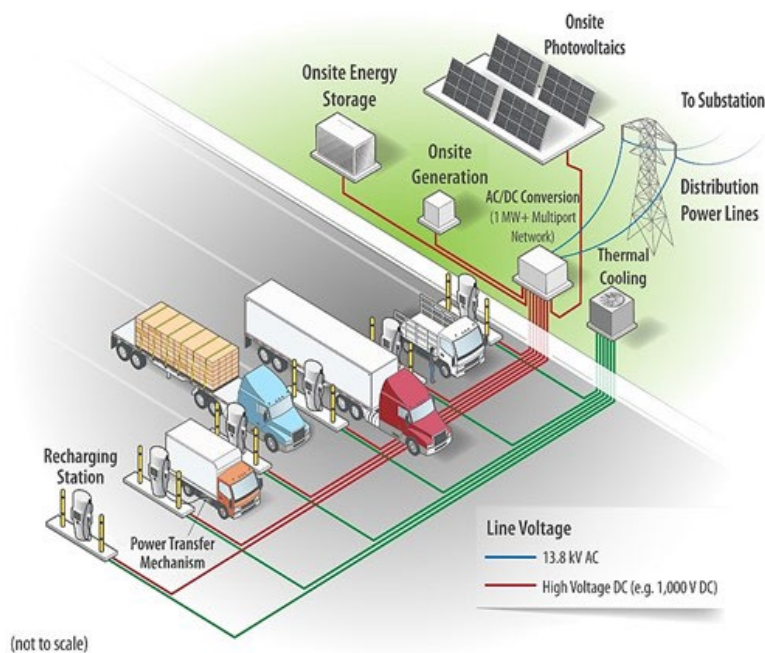


Figure 17 Conceptual configuration of an HPC station.

static and dynamic wireless charging activities target establishing feasibility, overcoming technology gaps, and validating high power wireless charging with vehicle-level demonstrations. Efforts will analyze, design, build, and validate integrated high-power static and dynamic wireless charging systems that are viable for real world traffic conditions in the U.S.

VTO R&D Outlook for Key HPC Focus Areas

Future HPC activities target several areas including integration of dynamic wireless power transfer (dWPT) into roadways and development of innovative means to provide service to charging facilities. Deployment of dWPT into the roadway will require researching performance, field emissions, and power and control requirements, and addressing integration of the charging system. DC-as-a-Service (DCaaS) is an approach to provide direct current (DC) to charging stations that seamlessly integrates facility and EVSE loads, and DER. Research is needed to address DC isolation, metering, measurement, and protection. The following identifies specific HPC targets for 2023 and 2026.

YEAR 2023

- Develop strategies and technologies for high power dynamic wireless charging and multi-port 1+ MW charging stations that enable vehicle charging through direct connection to medium voltage (≥ 12.47 kV) distribution.

YEAR 2026

- Demonstrate and validate viable high power dynamic wireless charging, and multi-port 1+ MW charging stations with direct connection to medium voltage distribution.

Cyber-Physical Security

Importance

EVs and their connectivity with external systems have become increasingly complex. Apart from AC Level 1 chargers, EVSE have evolved rapidly to be networked and maintain a wide variety of communication functions. As communication networks for EVs, EVSE, and external systems increase, attack vectors and cyber-physical risks also increase for the charging infrastructure. Since EVSE at workplaces and public charging stations connect with many different EVs to provide charging services, it makes assuring CPS extremely difficult.

A major challenge posed by compromised charging infrastructure is the threat it poses to the electric grid. A localized cyber-physical attack on a set of EVSE/charging stations can lead to a sudden addition or reduction of loads that can cause local disruptions, brownouts, voltage imbalances, and undesirable power quality impacts. Large-scale, coordinated cyber-physical attacks on charging infrastructure supporting EVs at scale can also lead to wider grid disruptions, such as blackouts over large geographical areas. The lack of a comprehensive understanding of threats; disjointed implementation approaches; and limited best practices are major barriers to ensuring overall security of EVs, charging infrastructure, and the grid.

VTO's current CPS R&D efforts

Current CPS activities include research, development, and validation of technologies for real-time threat detection, mitigation, isolation, and restoration of charging infrastructure based on its physical signatures and performance. Activities at the National Laboratories include developing a comprehensive threat model, attack graphs, and technical risk assessment of the EV charging ecosystem, and prioritizing charging infrastructure high consequence events and mitigation strategies. Additional activities include penetration testing of 50 kW DC fast chargers and 400 kW HPC and developing recommendations for secure communications. VTO-funded projects led by industry, academia, and non-profit organizations are developing real-time detection, defense, and mitigation systems to protect EVs, charging infrastructure, and the grid. This includes hardened

controllers, converters, and monitoring systems; a retrofittable and scalable open-source cybersecurity architecture; and game theory-based hardware and software to provide secure charging.

VTO R&D Outlook for Key CPS Focus Areas

Based on the assessments of risk and high consequence events, future activities will implement the best approaches to mitigate vulnerabilities and threats associated with the EV charging ecosystem. This effort will incorporate strategies, systems, and tools for secure charging, including hardware/software for cyber-physical intrusion detection, threat mitigation and isolation, and recovery. The most promising CPS countermeasures will be identified based on risk formulation (e.g., public key infrastructure, blockchain, moving target defense, and redundancy). Identified countermeasures that address the highest consequence events will be demonstrated and validated. The following identifies specific CPS targets for 2023 and 2026.

YEAR 2023

- Develop a comprehensive threat model, prioritize high consequence events, and identify appropriate defense, detection, and mitigation strategies and tools for the EV charging ecosystem.

YEAR 2026

- Conduct wide-scale demonstrations to validate viable and robust cyber-physical security for the charging ecosystem in support of EVs at scale.

EA2020 Vehicle Grid Integration

In FY21, the Energy Act of 2020 (Division Z of the Consolidate Appropriations Act, 2021 Public Law No. 116-260) directed the DOE Secretary to (a) Establish a research development, and demonstration program to advance the integration of electric vehicles, including plug-in hybrid electric vehicles, onto the electric grid, and (b) produce a ‘Vehicles-To-Grid Integration Assessment Report’ that presents the results of a study that examines the research, development, and demonstration opportunities, challenges, and standards needed for integrating electric vehicles onto the electric grid. The results and knowledge gained from all of the projects in the G&I portfolio were used in preparing the study requested by Congress and the report.

Bipartisan Infrastructure Law

The Bipartisan Infrastructure Law (BIL) was passed in 2021. The legislation will invest \$7.5 billion to build out a national network of EV chargers in the United States. This is a critical step in the President’s strategy to fight the climate crisis and it will create good U.S. manufacturing jobs. The legislation will provide funding for deployment of EV chargers along highway corridors to facilitate long-distance travel and within communities to provide convenient charging where people live, work, and shop. This investment will support the President’s goal of building a nationwide network of 500,000 EV chargers to accelerate the adoption of EVs, reduce emissions, improve air quality, and create good-paying jobs across the country.

A Joint Office of Energy and Transportation has been established to support the implementation of the EV charging objectives of the BIL.

Information from the G&I projects is being fed to the Joint Office of Energy and Transportation and is being used to create requirements for the infrastructure funding established in the BIL.

EVs@Scale Consortium

In FY21 the Grid and Infrastructure program established the EVs@Scale Consortium to accelerate progress of EV Charging Infrastructure RD&D and engage stakeholders. It is an effort to streamline and coordinate Vehicle-Grid Integration activities across the national lab complex and increase the agility of the program to address rapidly evolving challenges and barriers to Vehicle-Grid Integration. The EVs@Scale Consortium includes the following national laboratories:

- Argonne National Laboratory (ANL)
- Idaho National Laboratory (INL)
- National Renewable Energy Laboratory (NREL)
- Oak Ridge National Laboratory (ORNL)
- Pacific Northwest National Laboratory (PNNL)
- Sandia National Laboratories (SNL)
- Lawrence Berkeley National Laboratory (LBNL)³⁷

The EVs@Scale organizes its activities within the following pillars:

1. Vehicle-Grid Integration and Smart Charge Management
2. High Power Charging
3. Advanced Charging & Grid Interface Technologies
4. Cyber-Physical Security
5. Codes and Standards
6. Consortium Management.

Specific activities identified in the pillars above will be covered in future Annual Progress Reports.

Grid and Infrastructure Research Highlights

Accomplishments	Organization	Focus Area	Project Title
<u>Made progress on developing and demonstrating a megawatt plus wireless charging system for a HD truck capable of a complete charge in 30 minutes. The team completed vehicle design and procurement. The team made significant progress on designing the charge equipment.</u>	Kenworth Truck Company	Industry Awards	Long-Range, Heavy-Duty Battery-Electric Vehicle with Megawatt Wireless Charging
<u>Developed and began process of demonstrating an electric Innovation Fleet eCascadia 2.0 to improve cost, reliability, and performance over DTNA's completed heavy-duty electric truck. The project team has completed Phase 1a: Research, Design, Building, and Commissioning and Phase 1b: Commercial Scale Production Model including production tests, commercial series production, and has finalized the design elements. The infrastructure installation and evaluations were completed. The team delivered their first vehicle to their demonstration customer.</u>	Daimler Trucks North America LLC	Industry Awards	Development and Commercialization of Heavy-Duty Battery Electric Trucks Under Diverse Climate Conditions

³⁷ LBNL became a member of the EVs@Scale Consortium in September 2023.

Accomplishments	Organization	Focus Area	Project Title
<u>The objective of the project is to use vehicle and operations data to increase the vehicle range and lower the operating cost of battery electric class 8 trucks that operate more than 250 miles per day using physics-aware machine learning algorithms.</u> The second electric truck, NME-8 was prepared for delivery to Minnesota for winter testing. Final testing planning began to validate the developed models and test the eco-routing algorithm and driver-vehicle interface in operation.	Volvo Technology of America, LLC	Industry Awards	Improving the Freight Productivity of a Heavy-Duty, Battery Electric Truck by Intelligent Energy Management
<u>The B-Sample inverters have been built and successfully tested on the bench through the EOL testing and functional testing, as well as mechanical environmental tests.</u> The bench tests with RL load confirmed the inverter power efficiency of 98.5%+ efficiency. The Ricardo team commenced the inverter/motor dyno testing, with inverter closed loop speed and torque controller tuning completed.	Ricardo Inc.	Industry Awards	High Efficiency Powertrain for Heavy Duty Trucks using Silicon Carbide (SiC) Inverter - DE-EE0008806
<u>There is a critical need to develop solutions for intelligent EV charging that supports, rather than strains, grid operations.</u> The eMosaic team demonstrated a preliminary platform to meet these needs, validating it in a lab setting using various hardware-in-the-loop modeling tools. Based on these efforts, several price-based approaches to managing EV load show promise.	ABB Inc.	Industry Awards	eMosaic: Electrification Mosaic Platform for Grid-Informed Smart Charging Management
<u>Exelon's Maryland Utilities and its program partners performed work to prepare for year one launch of the smart charge demonstration in 2023</u> with all three of its target customer groups: residential, commercial fleet and public charging.	Exelon - BGE	Industry Awards-	Demonstration of Utility Managed Smart Charging for Multiple Benefit Streams
The team validated the vision of the EVs-at-RISC program to enable interoperable metering, telemetry, and command-and-control capabilities across diverse, heterogeneous, and highly distributed EV charging/DER infrastructure assets and stakeholders within a zero-trust architecture leveraging free and open-source software technologies and minimal COTS components.	Liberas (formerly Dream Team)	Industry Awards	Development and Demonstration of EVs-at-RISC: A Secure and Resilient Interoperable Smart Charge Management Control System Architecture for EVs-at-ScaleMedium-Heavy Duty PHEV Work Trucks
<u>The WAVE team has completed the procurement of all the parts and systems needed to run the wireless chargers.</u> The validation of these systems was completed in a lab setting. Cummins completed the validation of the two trucks and got the motor and inverter combination certified.	WAVE, Inc	Industry Awards	Wireless Extreme Fast Charging for Electric Trucks
<u>The project completed the test of the hybrid drive strategies and completed the system integration, layout and design to be utilized for the demonstration vehicles</u>	Odyne Systems	Industry Awards-	Development and Demonstration of

Accomplishments	Organization	Focus Area	Project Title
<p><u>as well as future Odyne production.</u> The drive testing demonstrated that the system is capable of delivering up to 75% fuel economy improvement, depending on duty cycle, although a lesser driving strategy was ultimately be utilized when considering battery cost and size, stationary energy needs, and the real-world duty cycle of the Medium/Heavy Duty work truck.</p>			<p>Medium-Heavy Duty PHEV Work Trucks</p>
<p><u>A research effort was conducted to capture the DC charging behavior and efficiencies of four modern electric vehicles</u> including a 2020 Tesla Model 3, 2020 Nissan Leaf E-plus, and a 2017 and 2020 Chevrolet Bolt. The experimental study provided data for analysis of over 120 charge sessions, from a wide variety of ambient conditions and public DCFC networks.</p>	<p>ANL</p>	<p>High-Power Charging Enabling Technologies</p>	<p>Assessment and Validation of Next Generation EV High Power Charging Profiles</p>
<p><u>The project group has successfully executed device characterizations that provide the key data required to deliver an initial industry charging performance report at the end of the next fiscal year.</u> The aim of the analysis is to build a knowledge base and glean industry insights to intelligently integrate HPC systems within the grid and among co-located loads and sources. The characterization and dissemination work in the project is critical for understanding the emerging charge performance industry</p>	<p>ANL, NREL, INL, ORNL</p>	<p>High-Power Charging Enabling Technologies</p>	<p>Assessment and Validation of Next Generation Electric Vehicles High Power Charging Profiles</p>
<p><u>The first year of the project focused on scoping the work to determine the fundamental components of the system to develop a high-power, DC distribution-based, interoperable, grid-integrated charging hub platform that can scale to MW+ charging hardware development and testing.</u></p>	<p>EVs@Scale Consortium – NREL, ANL, ORNL</p>	<p>High Power Charging Enabling Technologies</p>	<p>High-Power Electric Vehicle Charging Hub Integration Platform (eCHIP)</p>
<p><u>Laboratory characterization of the 200 kW DWPT system was carried out in stationary and dynamic power transfer modes</u> using the DICE. The rated power (200 kW input) tests indicated successful operation in both stationary and dynamic modes, thereby indicating viability of vehicle-integrated dynamic charging tests with couplers embedded in the roadway.</p>	<p>ORNL, INL, and NREL</p>	<p>Wireless Power Transfer Enabling Technologies</p>	<p>High-Power and Dynamic Wireless Charging of Electric Vehicles</p>
<p><u>Completed project year one to develop a prototype system and reference design for the DC-to-DC power conversion stages for a 50kW WEVC system including ground-side inverter, ground and vehicle electromagnetic couplers and resonant networks, and vehicle side to rectifier.</u> This work featured a comparative study of of LCC-LCC and LCCP resonant networks.</p>	<p>ORNL, Stellantis</p>	<p>Wireless Power Transfer Enabling Technologies</p>	<p>Misalignment Tolerant Three-phase Wireless Fast Charging System for EVs</p>
<p><u>A concretized coil was designed, and four ground-side units were built and tested.</u> The electrical behavior was characterized before and after the concretization process, and it remained unchanged, suggesting that</p>	<p>EVs@Scale Consortium – ORNL, INL, NREL</p>	<p>Wireless Power Transfer Enabling Technologies</p>	<p>Integrating Dynamic Wireless Power Transfer Systems in Roadways</p>

Accomplishments	Organization	Focus Area	Project Title
the coil is suitable for deployment from the perspective of power transfer capability.			
<u>The benefits of smart charging versus controlled and uncontrolled charging were assessed.</u> From a technical standpoint, optimized smart charging via charge scheduling, although the most technically involved, has the greatest benefit to all actors in the SCM ecosystem.	ANL	Vehicle-Grid Integration and Smart Charge Management	Charging Infrastructure Technologies: Smart Vehicle-Grid Integration
<u>The project made progress to commercialize a smart charge adapter that enables metering, monitoring and management control of charge sessions in response to local supply/demand levels.</u> The development of the hardware and software under this project helped garner a new industry partner. There still remains additional testing and debugging but the technology is very close to becoming a commercialized product.	ANL	Vehicle-Grid Integration and Smart Charge Management	Electric Vehicle Smart Charge Adapter
The first year of this project has expanded capabilities in transportation analysis, SCM assessments, and EVSE technologies to support EVs@Scale. EV charging loads have been developed across Virginia to represent electrification of 52% of the passenger vehicle stock. These loads represent the vehicle energy needs and charge flexibility, which will be critical in assessing grid impacts and SCM effectiveness throughout the utility partner grid models.	EVs@Scale Consortium – NREL, ANL, INL, SNL	Vehicle-Grid Integration and Smart Charge Management	Flexible charging to Unify the grid and transportation Sectors for EVs at scale (FUSE)
<u>This project helped identify EV charger vulnerabilities and quantify the risk to critical infrastructure when vehicle chargers are maliciously controlled.</u> This risk assessment is only an initial step in a continuous process of hardening charging infrastructure against cyber-attacks.	EVs@Scale Consortium - ORNL, PNNL, INL	Cyber-Physical Security	Electric Vehicle Integrated Safety, Intelligence, Operations (eVision)
<u>This project helped identify EV charger vulnerabilities and quantify the risk to critical infrastructure when vehicle chargers are maliciously controlled.</u>	SNL, PNNL, ANL	Cyber-Physical Security	Securing Vehicle Charging Infrastructure
<u>The multi-lab team within the cybersecurity pillar have initiated a portfolio of work to address key challenges including:</u> <ul style="list-style-type: none"> • <u>Industry implementation and utilization of latest security methods is not consistent</u> • <u>Lack of methods to identify, protect, detect, respond, and recover from cyber events</u> • <u>Unknown vulnerabilities in new, emerging features and standards</u> • <u>Existing training for the EV charging infrastructure cybersecurity workforce</u> 	EVs@Scale Consortium - INL, SNL, NREL, PNNL, ORNL, ANL	Cyber-Physical Security	Cyber-physical Security Pillar for Unified National Lab Collaboration (CyberPUNC)
<u>In this two-year program, two important documents were successfully revised and well-received by the testing community.</u> Testing burden was reduced, and accuracy improved for HEV and PHEV testing. With	ANL	Codes and Standards	Electrified Vehicles Test Procedure Development

Accomplishments	Organization	Focus Area	Project Title
these changes, HEVs, and especially PHEVs can be designed with more control flexibility and opportunities for optimization. The expectation is small but noticeable increases in efficiency for future HEVs and PHEVs.			
INL leveraged previous SAE standards testing and procedure development as well as grid modernization lab consortium (GMLC) work to support the IEEE P2030.13 to review definitions and block diagrams.	EVs@Scale Consortium - INL	Codes and Standards	Wireless Power Transfer, DER Standards Tasks
NREL leveraged previous DOE funded activities under the CharIN MCS work group on previous MCS coupler designs for the latest pre-production prototype couplers. Likewise NREL leveraged grid modernization lab consortium (GMLC) work to support the IEEE P2030.13 to create definitions and block diagrams.	EVs@Scale Consortium - NREL	Codes and Standards	SAE J3271 MCS Coupler Testing, DER Standards Tasks
ORNL staff created industry and academia engagement for direct distribution level medium-voltage (MV) connected charging infrastructures with solid-state transformers or modular multilevel converters (MMC) for high-power charging plazas.	EVs@Scale Consortium - ORNL	Codes and Standards	Wireless Power Transfer, Medium Voltage Power Converter Standards Tasks
PNNL staff have participated in CharIN MCS work group meetings and EV Charging standards. Knowledge of cyber security, smart charging and other standards was utilized to draft wording in the EVSP standards roadmap augmenting the input from industry participants. I.e. perform the actual writing of the roadmap documents as well as SAE J3271 MCS standard first draft	EVs@Scale Consortium - PNNL	Codes and Standards	Wireless Power Transfer, Medium Voltage Power Converter Standards Tasks
To determine DC fast charger technologies compliance and calculation methods that help check the compliance with NIST's HB44-3.40, ANL conducted benchmark research on DC meters and cables. A conclusion from this benchmarking research is that manufacturers of EVSE DC fast charging equipment do not need to have a revenue grade meter in the coupler at the end of the cable to comply with HB44-3.40 specifications for measurement.	ANL	Codes and Standards	DC Meters for Commercial Charging Benchmark Study

In this report the Grid and Infrastructure project reports that follow have been grouped into the chapter categories of Industry Awards (IA), High Power Charging (HPC) Enabling Technologies, Vehicle-Grid Integration (VGI) & Smart Charge Management (SCM), and Cyber-Physical Security (CPS), and Wireless Power Transfer (WPT) Enabling Technologies. Many of the projects address multiple programs objectives. The Industry section describes projects that were awarded to commercial industry performers via DOE’s Funding Opportunities Announcement (FOA) solicitation process. The HPC, VGI & SCM, CPS, and WPT projects were awarded to National Laboratories via direct funding agreements.

Questions regarding the Grid and Infrastructure Program can be directed to the Technology Manager, Lee Slezak via email: lee.slezak@ee.doe.gov or telephone: (202) 586-2335

I Electric Drive Technologies

I.1 Electric Drive Technologies Research

I.1.1 Non-Heavy Rare-Earth High-Speed Motors (Oak Ridge National Laboratory)

Vandana Rallabandi, Principal Investigator

Oak Ridge National Laboratory
1 Bethel Valley Road
Oak Ridge, TN 37831
E-mail: mohammadm@ornl.gov

Susan Rogers, DOE Technology Development Manager

U.S. Department of Energy
E-mail: susan.rogers@ee.doe.gov

Start Date: October 1, 2022

End Date: September 30, 2023

Project Funding: \$1,009,587

DOE share: \$1,009,587

Non-DOE share: \$0

Project Introduction

Because of their high torque, power density, and excellent efficiency, most electric traction motors currently in production are permanent magnet (PM) synchronous motors, which use costly, heavy rare-earth magnet materials such as dysprosium. However, the price and supply of dysprosium have historically shown volatilities. To deal with these risks, substantial progress has been made in PM material technologies to significantly reduce or eliminate dysprosium from the material composition. Dysprosium-free PM materials, now commercialized by major suppliers, can help lower the cost of traction motors and accelerate the market penetration of electric vehicles. However, dysprosium-free PM materials have lower coercivity; thus, they are more prone to demagnetization compared with conventional heavy rare-earth counterparts. Therefore, special attention should be paid to demagnetization when designing dysprosium-free PM motors.

This report presents an outer-rotor dysprosium-free PM motor design, enabling the integration of the drive and a shared cooling system between the power electronics and motor.

Objectives

The overall objectives of this project are to enable the adoption of high-speed and high-power density, nonheavy, rare-earth traction motors and analyze the effect of new advanced materials for nonheavy, rare-earth electric motors. More specifically, the objectives for FY 2023 were to complete the following:

- Analysis of rotor-dynamics of the outer rotor motor
- Analysis of stator modal
- Initiation of motor prototyping
- Updating of motor geometry and simulation models as required

Approach

The overall objective of this project is to develop a 100 kW, high-speed and high-power density, nonheavy, rare-earth traction motor to target the U.S. DRIVE specifications presented in Figure I.1.1.1. A dysprosium-free PM motor with an outer rotor configuration is designed to enable the integration of the drive and a shared cooling system between the power electronics and motor. The electromagnetic, thermal, and mechanical feasibility of the design is verified. Because low-coercivity, dysprosium-free PMs are used, the robustness of

the design against demagnetization is also confirmed. The current rating and direct current (DC)-link voltage are selected in accordance with the power devices used in the drive. The design uses a dual three-phase winding configuration powered by a dual three-phase segmented drive featuring interleaved switching to reduce the current ripple and, therefore, the DC link capacitor [2].

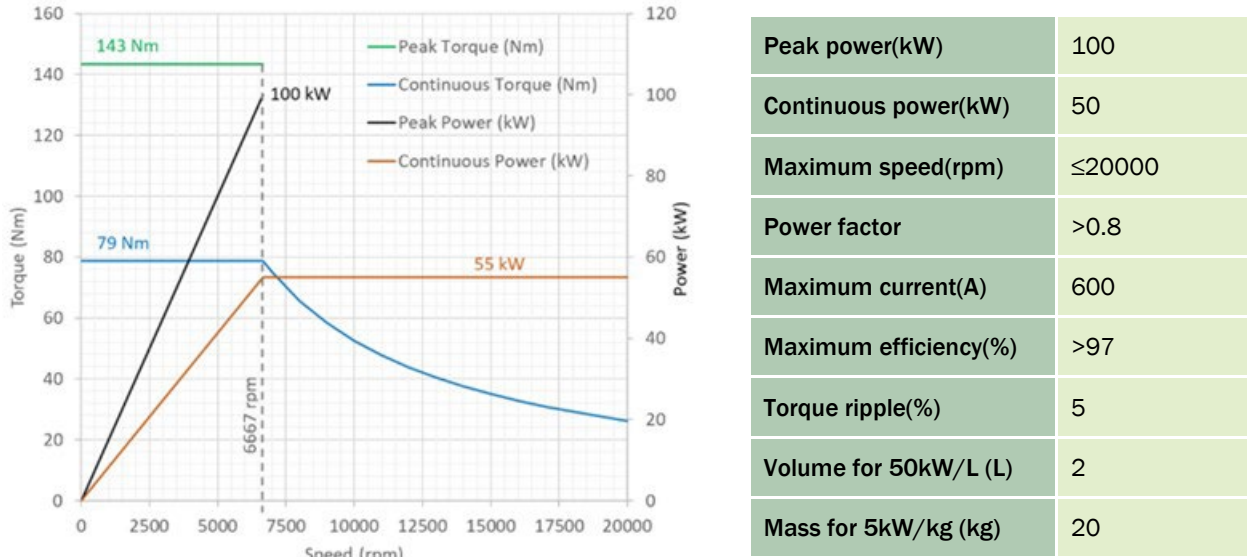


Figure I.1.1.1 Summary of specifications.

Results

A 18 slot/16 pole PM motor was designed in FY 2020–2021. Because the design uses low-coercivity, nonheavy, rare-earth PMs, a Halbach magnetization arrangement was selected to maximize the air-gap flux density and reinforce the resistance to demagnetization. The operating frequency ranges from 888 Hz at the base speed to about 2.67 kHz at the top speed of 20,000 rpm, and the slot passing frequency at the maximum speed is 6 kHz. To minimize the PM eddy current loss, the PMs are axially laminated with a segment thickness of 1 mm. Litz wire, with 150 strands of 33 American wire gauge, and two wires in hand are used for the coils to minimize high frequency losses [3]. The materials used for the stator and rotor laminations are Cogent NO 18 with a thickness of 0.18 mm. The magnets are N50. The rotor casing uses 17-4 PH steel. Carbon fiber will be filament-wound on the rotor casing to maintain the magnets under compression throughout the operating region. 3D printed in-slot ceramic heat exchangers are used for motor cooling [4]. The mechanical drawing for the integrated motor drive is shown in Figure I.1.1.2.

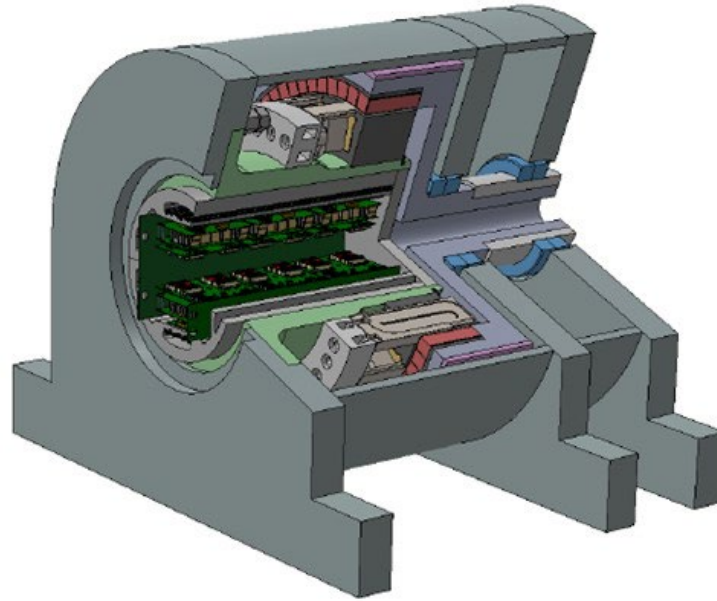


Figure I.1.1.2 The integrated motor drive shows the outer rotor, stator, heat exchangers, manifold, bearings, external mountings, and power electronics.

The rotor geometry was modified to facilitate easier prototyping. To ensure contact between the magnets and rotor back iron, the magnet shapes, originally arcs, were modified to be rectangular, so that the contact area between the magnets and back iron is a flat plane. This modification also allows easier manufacturing and avoids the tolerance stack-up, which can arise if the magnet arcs are all not exactly spanning the specified angle. One potential concern with rectangular magnets is that the airgap is not uniform, however, this was determined to have little impact on the performance as the magnets have a high energy product. The rotor back iron was also modified accordingly. Additionally, tabs are added in the rotor back iron to locate the PMs. This addition avoids tolerance stack-up. The designed and modified rotors are shown in Figure I.1.1.3. The electromagnetic finite element analysis (FEA) for the new rotor geometry was conducted. The electromagnetic performance is shown in Table I.1.1.1 The modified rotor meets the target performance.



Figure I.1.1.3 (a) Original and (b) modified rotors. The arc magnets were flattened, and locating tabs were included in the rotor core.

Table I.1.1.1. Electromagnetic Performance with the Rotor Modified for Prototyping

Rotor	Speed (rpm)	Root mean square current (total, A)	Gamma (degrees)	Torque (N·m)	Line-line fundamental (V)	Copper loss (W)	Core loss (W)	Magnet loss (W)
Rated, 50kW	6,666.667	193.75	0	85.94	184.16	700.8	615.5	25.8
Peak, 100kW	6,666.667	387.5	0	164.2	189.3	2,803.3	653.2	30.2
Top speed, 50 kW	20,000	193.75	73	30.42	466.2	700.8	2,595.5	190.8

Following the electromagnetic analysis, thermal analysis was conducted on the modified geometry. The temperature distribution at different operating points is shown in Figure I.1.1.4. Researchers observed that the magnet temperatures at the top-speed operating condition far exceed the recommended limits. The solution proposed is to flow air along the motor air gap. Computational fluid dynamics simulations showed that the air velocity needs to be 14 m/s to ensure that the operating magnet temperatures are within the limits.

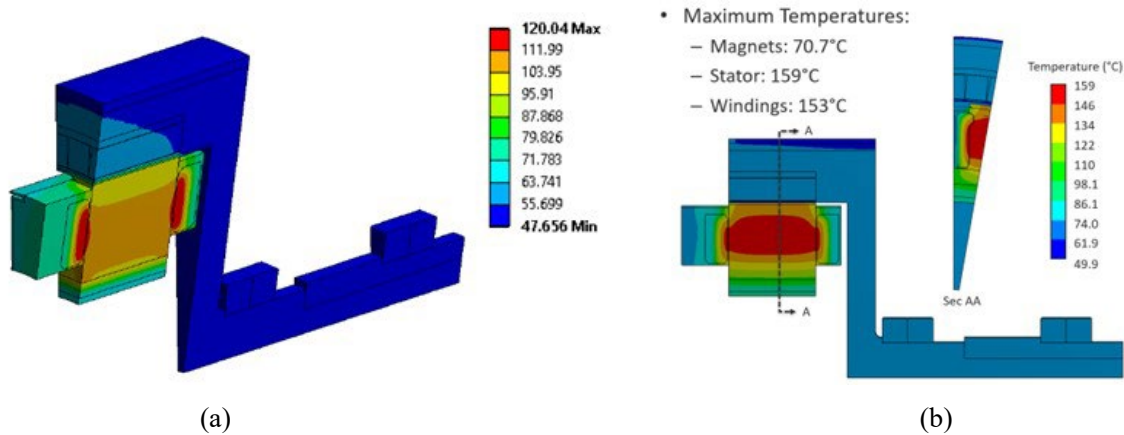


Figure I.1.1.4 (a) Temperature distribution at the rated condition and (b) at the 20,000 rpm top-speed condition. Air flow of 14 m/s is needed in the air gap to ensure heat transfer coefficients that will result in magnet temperatures within the limits.

Rotordynamics analysis was conducted on the rotor structure using COMSOL, as well as a 2D lumped parameter tool, Dyrobes. The natural frequencies are listed in Table I.1.1.2. The torque ripple frequency of the motor is 48 times the fundamental mechanical frequency, which is around 5.3 kHz at the rated condition. The rotor modes are thus expected to not be excited by torque ripple.

Table I.1.1.2 Rotor Natural Frequencies for Different Modes at Different Speeds

Modes	Frequencies (Hz)		
	0 rpm	Rated speed	Peak speed
Mode 1	400	415.83	483.33
Mode 2	401	416.46	483.92
Mode 3	836	834.35	845
Mode 4	1,743	1,706.3	1,761

The Campbell diagram (Figure I.1.1.5) for the rotor identifies the first critical speed at 10,000 rpm, which is within the operating speed range of the motor. This speed is in line with expectations for a cantilever rotor design [5]. This research found that moving to a structure supported on both sides can increase the critical speed by 5,000 rpm. Furthermore, an increase in the bearing stiffness can push the critical speed further to the

right. Moving back to a structure supported on both sides is not an option because it does not leave enough room for the electrical and coolant connections and increases the weight and volume.

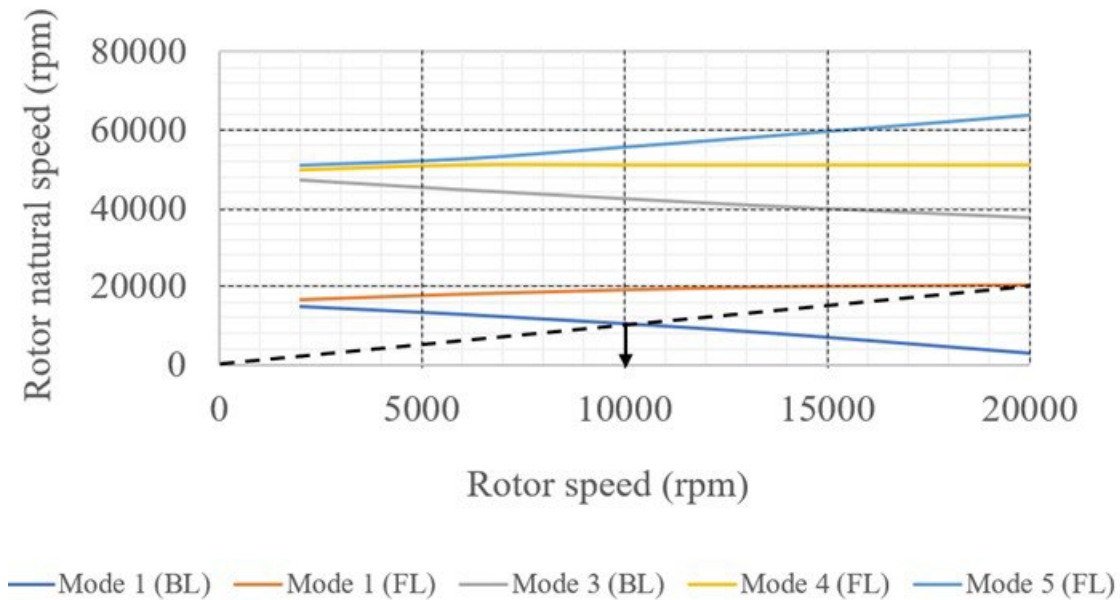


Figure I.1.1.5 Campbell diagram for the rotor.

Stator modal analysis for the free-free condition was conducted using 3D FEA, and the natural frequencies were determined for different conditions: the stator core alone and the stator core with windings and heat exchangers (Table I.1.1.3). For the stator core alone, the natural frequencies are close to the electromagnetic force frequency at normal operation and may be excited. However, with the windings and heat exchangers included, the natural frequencies increase significantly owing to higher stiffness of the structure. This increase moves the frequencies outside of the operating range, and the stator modes are expected to not be excited during motor operation.

Table I.1.1.3 Stator Natural Frequencies

Mode	Frequencies (Hz)					
	1	2	3	4	5	6
Stator alone	698	700	1,036	1,040	1,714	1,719
Stator with windings and heat exchangers	1,993	2,018	2,295	2,320	4,143	4,910

The natural frequencies were verified in the lab by conducting hammer tests on the stator. In these tests, the stator was impacted with a hammer, and the response was measured from accelerometers placed on the stator surface. The first mode was identified to be at 700 Hz, which is close to the prediction from FEA (Figure I.1.1.6).

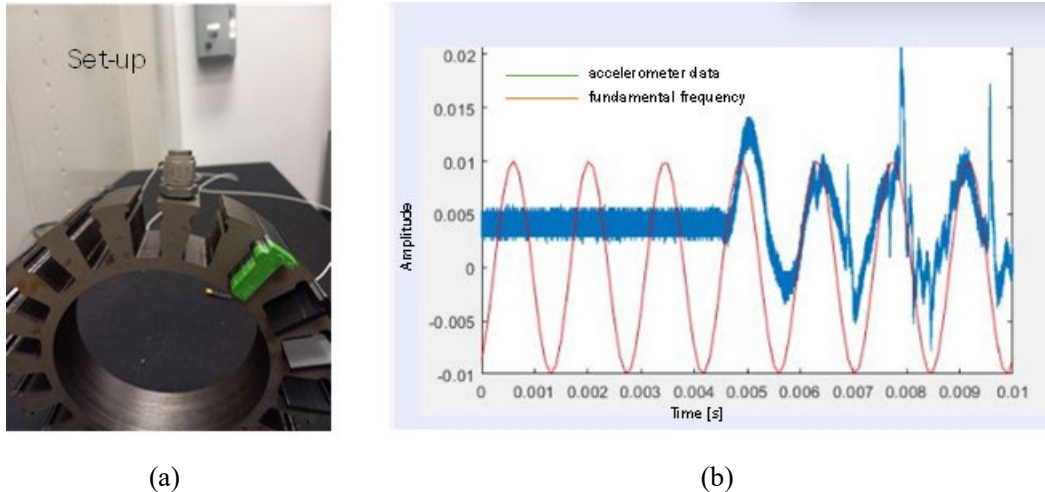


Figure I.1.1.6 (a) Stator with accelerometers and (b) signal from the accelerometer after impacting the stator with a hammer and its fundamental component. The fundamental component is a 700 Hz signal.

In this motor, the desired torque speed curve of Figure I.1.1.1 is obtained by oversizing the inverter. The motor is designed with a high air gap flux density to achieve the highest motor power density. Another approach would be to design the motor so that the desired torque speed curve is achieved through field weakening. A motor design variation, which achieved field weakening, was evaluated, and it was found that the inverter rating could be reduced by 40%. However, the motor stack length needed to increase by 65%.

Studying the volume breakup of the inverter, it was revealed that a 40% reduction in its rating would only lead to a 10% reduction in its volume. Thus, it was concluded that oversizing the inverter to achieve the desired torque–speed characteristics and designing the motor to maximize its air gap flux density would result in the minimum motor drive volume.

The prototype rotor core is shown in Figure I.1.1.7, as well as one of the segmented magnets and the 3D printed ceramic slot heat exchanger. The carbon fiber sleeve will be wound on the rotor using the filament winding approach [6].

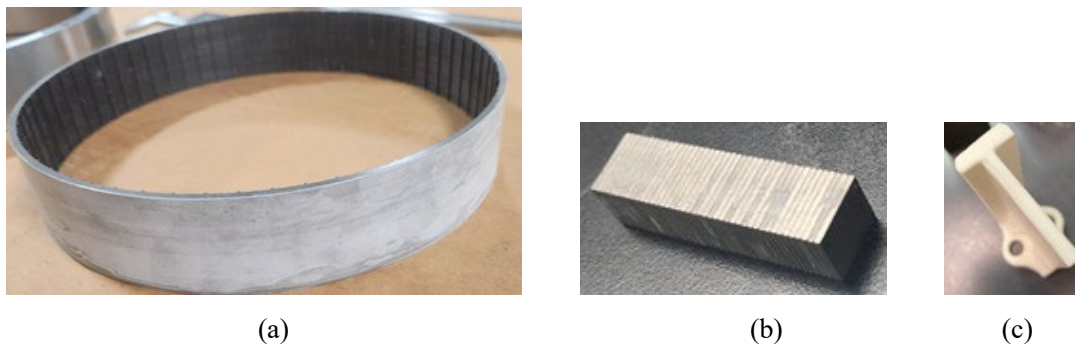


Figure I.1.1.7 (a) Prototype rotor, (b) one magnet with 43 segments, and (c) 3D printed heat exchanger.

Conclusions

A high-speed and high-power density, nonheavy, rare-earth, PM traction motor was designed to enable the integration of the drive and a shared cooling system between the motor and the power electronics. This work found that to minimize the volume of the motor drive system, it may be advantageous to design the motor with a high magnetic loading and to oversize the inverter to achieve the desired torque–speed characteristics. Stator cooling using in-slot ceramic heat exchangers keeps the winding temperatures below the limits; however, air

gap cooling is required to maintain the magnets under the recommended operating temperature at the high-speed point. Based on the results of the modal analysis conducted for the stator, it is expected that none of the modes are likely to be excited during normal operation of the motor. Although a cantilever rotor design is used to simplify the assembly and to allow the use of off-the-shelf bearings, it will lead to a critical speed within the motor operating range.

Key Publications

1. Rallabandi, V., S. Chowdhury, H. Barua, P. Paranthaman, M. Mohammad, S. Bullock, and E. Cousineau. 2023. "Traction Motor Design Trade-Offs with Additively Manufactured Anisotropic Bonded Magnets." IEEE Conference on Transportation Electrification, Detroit, Michigan, June 2023.
2. Ananthanpillai, A., P. Masson, V. Rallabandi, and M. Senti. 2023. "Analysis of a Continuous Halbach Array Permanent Magnet Motor for Electric Vehicles." IEEE International Electric Machines and Drives Conference, San Francisco, California, May 2023.
3. Rallabandi, V., O. A. Badewa, B. Ozpineci, and D. M. Ionel. "A Comparison of Outer Rotor Radial and Axial Flux Machines for Application in Electric Vehicles." IEEE International Electric Machines and Drives Conference, San Francisco, California, May 2023.
4. Rallabandi, V., M. Mohammad, V. Prakash Nagabhushana Galigekeere, and V. Molina. "An Integrated Electric Vehicle Drive Motor and Wireless Charger." IEEE Wireless Power Technology Conference and Expo, San Diego, California, 2023.
5. Rallabandi, V., M. Mohammad, H. Barua, S. Chowdhury, B. Ozpineci, J. Wilkins, L. Lin, B. Kekelia, and E. Cousineau. "A High-Speed Surface Permanent Magnet External Rotor Motor and Integrated Drive for Electric Vehicles." IEEE Energy Conversion Congress and Expo, Nashville, Tennessee, October 2023.
6. Lin, L., H. Barua, and V. Rallabandi. "Mechanical Analysis of Carbon Fiber Retaining Sleeve for A High-speed Outer Rotor SPM Electric Motor Design." IEEE Energy Conversion Congress and Expo, Nashville, Tennessee, October 2023.

References

1. U.S. DRIVE. 2017. Electrical and Electronics Technical Team Roadmap. U.S. DRIVE. <https://www.energy.gov/sites/prod/files/2017/11/f39/EETT%20Roadmap%2010-27-17.pdf>.
2. Su, G., and L. Tang. 2012. "A Segmented Traction Drive System with a Small dc Bus Capacitor." Proceedings of the 2012 IEEE Energy Conversion Congress and Exposition (ECCE), Raleigh, North Carolina: 2847–2853. DOI: 10.1109/ECCE.2012.6342375.
3. New England Wire Technologies. 2003. Litz Wire Technical Information.
4. Sixel, W., M. Liu, G. Nellis, and B. Sarlioglu. 2018. "Cooling of Windings in Electric Machines via 3D Printed Heat Exchanger." Proceedings of the 2018 IEEE Energy Conversion Congress and Exposition (ECCE), Portland, Oregon: 229–235. DOI: 10.1109/ECCE.2018.8557845.
5. Yu, Y. et al.. 2020. "Rotordynamic Assessment for an Inside Out, High Speed Permanent Magnet Synchronous Motor." Proceedings of the 2020 International Conference on Electrical Machines 529–535.
6. Zu, L., H. Xu, B. Zhang, D. Li, H. Wang, and B. Zi. 2018. "Filament-Wound Composite Sleeves of Permanent Magnet Motor Rotors with Ultra-High Fiber Tension." Composite Structures 204: 525–535.

Acknowledgements

The principal investigator would like to thank Oak Ridge National Laboratory's (ORNL's) Shajjad Chowdhury and Jon Wilkins for the design of the integrated drive (refer to project elt221, "Integrated Electric Drive System," by Shajjad Chowdhury [ORNL]) and the overall mechanical assembly, and the National Renewable Energy Laboratory's (NREL's) Emily Cousineau and Bidzina Kekelia for the thermal analysis and the design of the cooling system (refer to project elt214, "Electric Motor Thermal Management," by Emily Cousineau [NREL]).

I.1.2 High-Voltage, High Power Density Traction Drive Inverter (Oak Ridge National Laboratory)

Gui-Jia Su, Principal Investigator

Oak Ridge National Laboratory
1 Bethel Valley Road
Oak Ridge, TN 37831
E-mail: sugj@ornl.gov

Susan Rogers, DOE Technology Development Manager

U.S. Department of Energy
E-mail: Susan.Rogers@ee.doe.gov

Start Date: October 1, 2022

End Date: September 30, 2023

Project Funding: \$919,633

DOE share: \$919,633

Non-DOE share: \$0

Project Introduction

Growing demand for significantly faster acceleration and larger, more versatile electric vehicles with performance matching or even exceeding internal combustion engine-based vehicles are driving the need for higher-power traction drive systems at lower cost, weight, and volume. The U.S. Department of Energy (DOE) and its industrial partners have set aggressive 2025 targets for the Electrification Program (ELT) to meet these demands [1]. Among these goals is an inverter power density target of 100 kW/L, which is increased more than eight times from the 2015 targets. All the major components of an inverter design must be minimized to meet the aggressive target.

The direct current (dc) bus capacitor in the inverter is one of the barriers to meeting these DOE power electronics targets. Using pulse width modulation schemes in the voltage source inverter in a traction drive to produce a desired set of alternating current voltages generates large ripple components in the dc-link current with root mean square values greater than 60% of the motor root mean square currents. The dc bus filter capacitor must absorb the ripple currents and suppress transient voltage spikes, both of which are detrimental to the battery life and the reliability of the semiconductor switches in the inverter. Film capacitors that can meet these requirements are costly and bulky: they make up one-fifth of the volume and cost of the inverter. Inverter topologies are needed that can minimize this bulky component by significantly reducing the inverter dc ripple current.

The goal for this project is to increase the power density of the traction drive power electronics system to meet DOE ELT 2025 targets (100 kW/L, \$2.70/kW, and 300,000 mi lifetime) by focusing on power inverter architecture research, bus bar designs, and cooling system optimization to reduce the need for passive components.

Objectives

The overall objective of this project is to develop technologies for next-generation traction drive power electronics systems with an 8× increase in power density. This objective will achieve the DOE ELT 2025 power density target of 100 kW/L using novel traction drive inverter architecture, optimizing the bus bar design, and minimizing passive components. The objectives for fiscal year (FY) 2023 were to (1) test and characterize the 100 kW segmented inverter prototype built in FY 2022 [2] and (2) build and test a 200 kW segmented inverter using technologies developed in the Electric Drive Technologies (EDT) Consortium.

Approach

Three technical approaches were considered in this project [2]. The first approach selected inverter architectures that can reduce the dc bus capacitor requirements. Multiphase inverters, segmented inverters [3], and open stator winding inverter drive configurations were evaluated. The second approach increased the

inverter dc bus voltage to 800 V or higher. This increase took advantage of the inherently higher voltage ratings of SiC switching devices, reduced the size of SiC dies (thus lowering the cost), and reduced phase and dc bus currents. The third approach optimized the designs for the inverter dc bus bars by employing embedded and distributed capacitors and direct cooling of the bus bars.

Results

The segmented inverter topology was selected because of its significantly (over 50%) reduced dc bus capacitance requirement [3]. Figure I.1.2.1 shows a block diagram for the major components of a three-phase segmented inverter, and Table I.1.2.1 lists the specifications of two inverter designs. The inverter design optimized the SiC metal-oxide semiconductor field-effect transistor (MOSFET) power module packaging with double-side cooled heat sinks, a gate drive, and current sensing. Wolfspeed SiC MOSFET dies (CPM3-1200-0013A) were selected for the power modules. A 100 kW design and a 200 kW design for segmented inverters were completed using the power modules developed by EDT Consortium members Virginia Tech and the University of Arkansas. A 100 kW inverter prototype based on the first design using the Virginia Tech-designed power modules was fabricated in FY 2021, and it was refined and tested initially in FY 2022.

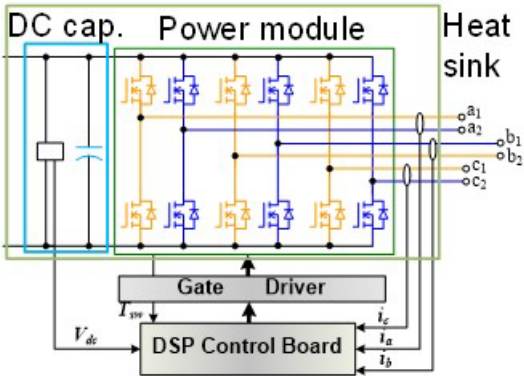


Figure I.1.2.1 Major components of a three-phase segmented inverter.

Table I.1.2.1 Inverter Specifications

Designs	#1	#2	Notes
Dc bus voltage, Vdc (V)	800	800	—
Power (kW)	100	200	#1: 143 kVA, #2: 286 kVA at power factor of 0.7
Efficiency (%)	98	98	—
Coolant flow rate (L/min)	10	10	Ethylene glycol/water 50/50 mixture

Test and Characterization of the 100 kW Segmented Inverter Prototype

After the successful test of the cooling subsystem, functional verification tests were conducted first for the 100 kW segmented inverter, and the results verified (1) the gate signals’ propagation delay time and dead band, which are within the design limits, and (2) the proper functionality of the power modules and control logics. The inverter was tested with a resistive load bank, and the test setup is shown in Figure I.1.2.2. Figure I.1.2.3 shows typical operating waveforms for (from top to bottom) dc bus voltage, line-to-line voltages, and three-phase currents. Figure I.1.2.4 plots measure inverter efficiency vs. output power; the measured inverter efficiency is more than 98% over the tested load conditions.

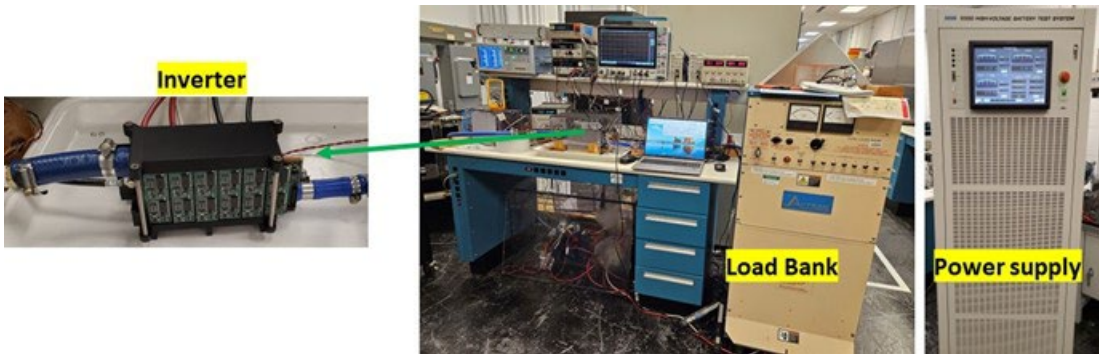


Figure I.1.2.2 Test setup for the 100 kW segmented inverter.

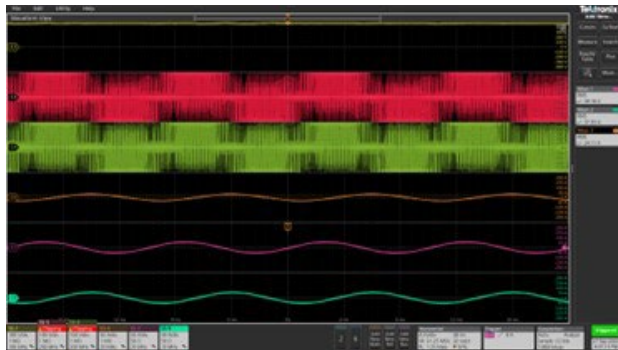


Figure I.1.2.3 Operating waveforms of the 100 kW inverter.
From top to bottom: dc bus voltage, line-to-line voltages,
and three-phase currents.

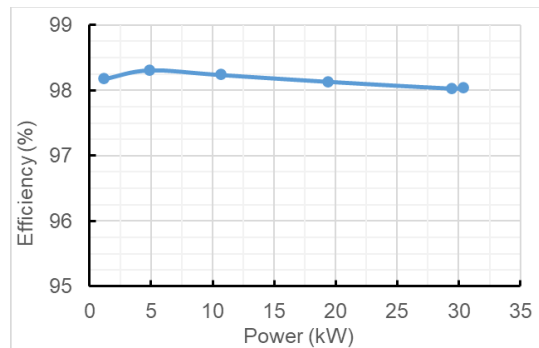


Figure I.1.2.4 Measured efficiency of the 100 kW inverter
vs. output power.

Test and Characterization of the 200 kW Segmented Inverter Prototype

A 200 kW inverter prototype based on the second design was fabricated and tested in FY 2023. The inlet and outlet manifolds were modified to fit the variations in the thickness of the fabricated power modules. The power modules and heat sinks were then assembled with the new manifolds. Before adding the gate drive and dc bus capacitor boards, the cooling subsystem was tested for leaks, and a pressure drop measurement was taken. Figure I.1.2.5 shows photos of the cooling subsystem test setup. Figure I.1.2.6 plots measured cooling subsystem pressure drops at various flow rates. At the rated flow rate of 10 L/min, the measured pressure drop was 0.97 psi, which is 54.8% lower than the maximum specification of 2 psi.

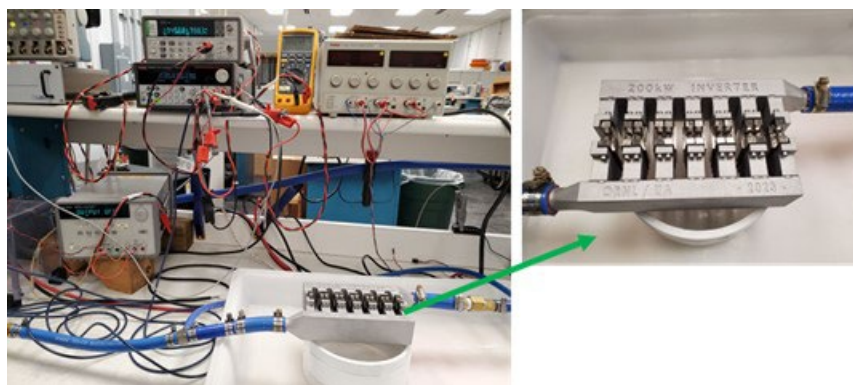


Figure I.1.2.5 Photos of cooling subsystem pressure test setup for the 200 kW inverter.

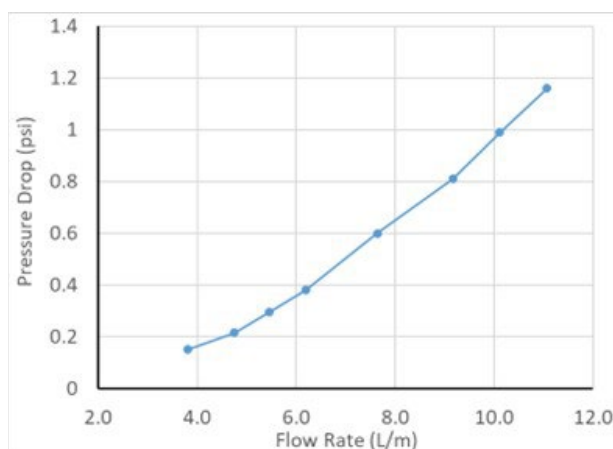


Figure I.1.2.6 Measured cooling system pressure drop vs. flow rate for the 200 kW inverter.

Functional verification tests were conducted first. Figure I.1.2.7 shows a photo of the test setup, and Figure I.1.2.8 shows operating waveforms for gate signals. The results verified that the gate signals' propagation delay time and dead band are within the design limits.

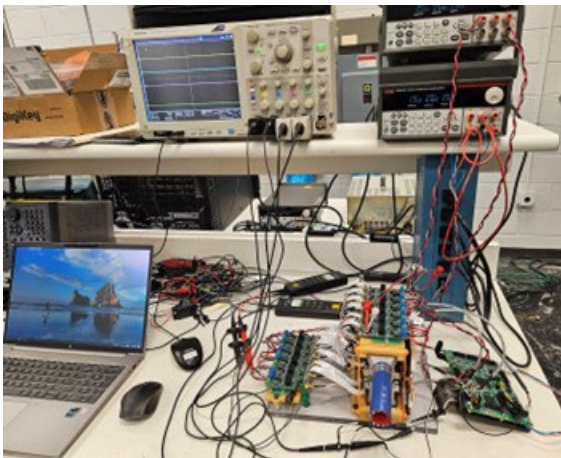


Figure I.1.2.7 Setup for functionality test of the 200 kW inverter.

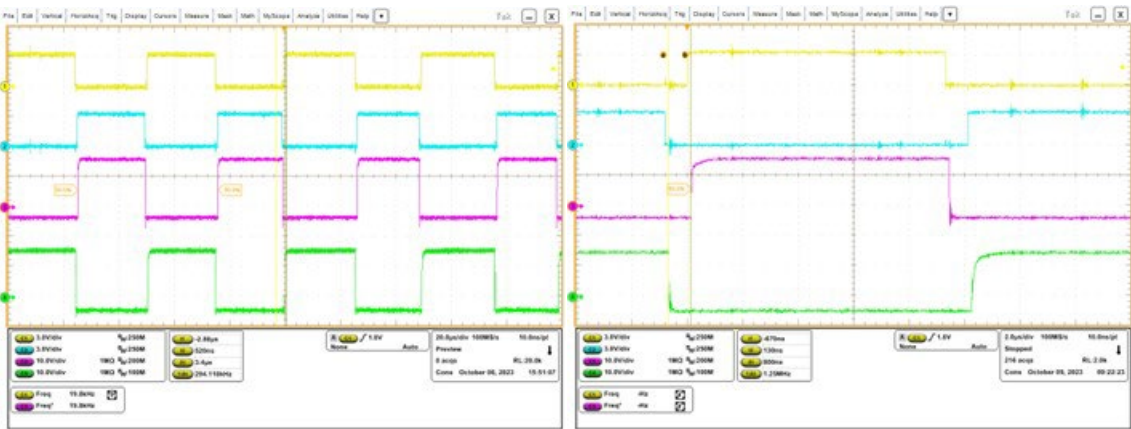


Figure I.1.2.8 Gate signal waveforms of the 200 kW inverter: (left) gate signals and (right) zoom-in showing dead times at turn-on and turn-off.

After the successful test of the cooling subsystem, the gate drive and dc bus capacitor boards were installed into the power modules to complete the 200 kW inverter assembly. Figure I.1.2.9 shows photos of the reassembled inverter prototype. The inverter was tested with a resistive load bank, and the test setup is shown in Figure I.1.2.10. Figure I.1.2.11 shows typical operating waveforms for the (from top to bottom) dc bus voltage, line-to-line voltage, phase current, line-to-line voltages, and two-phase currents. Figure I.1.2.12 plots measure inverter efficiency vs. output power; the measured inverter efficiency is more than 97.5% overload conditions greater than 0.6 kW.

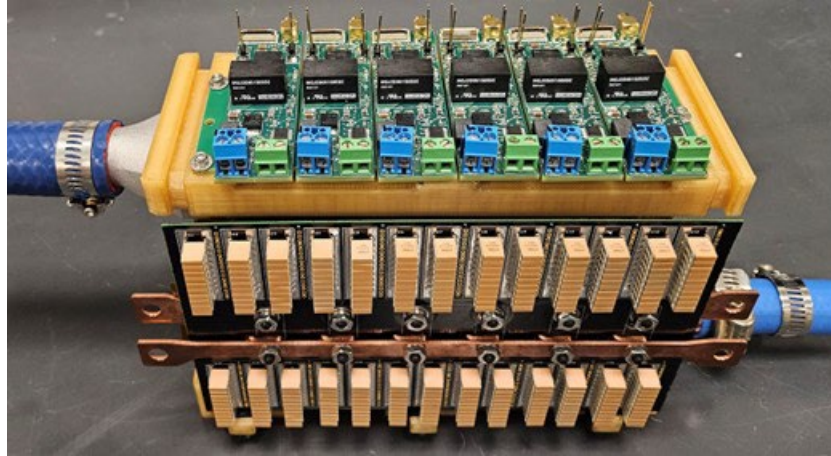


Figure I.1.2.9 Photos of the 200 kW inverter prototype.

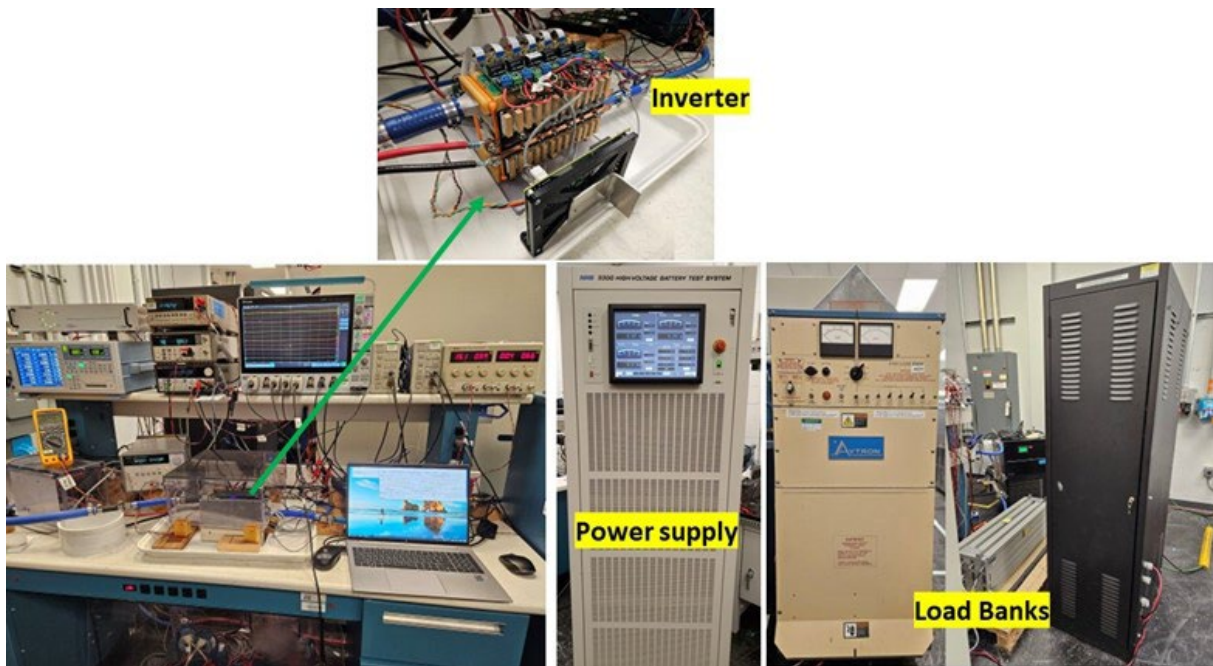


Figure I.1.2.10 Test setup for the 200 kW segmented inverter.

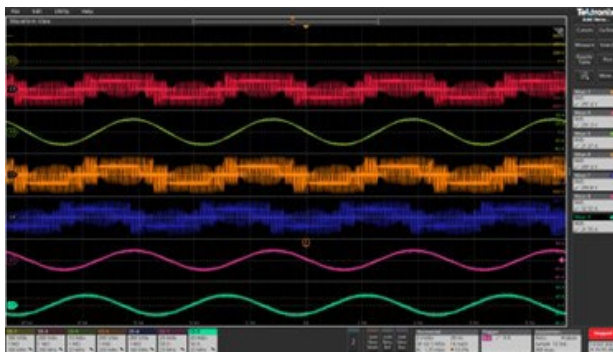


Figure I.1.2.11 Operating waveforms of the 200 kW inverter. From top to bottom: dc bus voltage, line-to-line voltage, phase current, line-to-line voltages, and two phase currents.

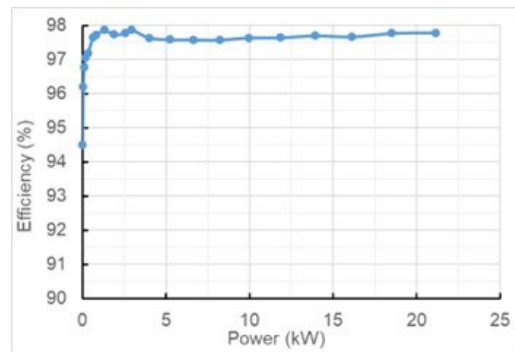


Figure I.1.2.12 Measured efficiency of the 200 kW inverter vs. output power.

Conclusions

The combination of the segmented inverter topology, low-profile, planar, double side-cooled SiC MOSFET power modules, optimized mini channel heat sinks, and high-ripple current capacitor led to a compact 100 kW traction inverter design with power density greater than 100 kW/L (143 kVA/L at a power factor of 0.7). This report summarizes the load test results for the 100 kW segmented inverter (up to 30.3 kW) with a resistive load bank. Test results show high inverter efficiency above 98% over the tested load conditions.

This report also summarizes the fabrication of a 200 kW segmented inverter prototype, as well as test results from the cooling subsystem, gate drive, and control logic functionality to load tests. Test results for up to 21.1 kW show high inverter efficiency above 97.5% when the output power is greater than 0.6 kW.

Future work will pursue further optimizing the power module packaging and integrating gate drive and current sensing capabilities into the power modules.

Key Publications

1. G. -J. Su, J. Wilkins, L. Xue, B. Ozpineci, R. Sahu, and E. Gurpinar, “A High-Power Density Segmented Traction Drive Inverter.” *Proceedings of the 2023 IEEE Energy Conversion Congress and Exposition (ECCE)*, Nashville, Tennessee, October 29–November 2, 2023, pp. 1825–1830.

References

1. U.S. DRIVE Partnership *Electrical and Electronics Technical Team Roadmap*. Washington, DC: US Department of Energy. <https://www.energy.gov/sites/prod/files/2017/11/f39/EETT%20Roadmap%2010-27-17.pdf>.
2. VTO. 2023. *Electrification: 2022 Annual Progress Report*. Washington, DC: US Department of Energy. https://www.energy.gov/sites/default/files/2023-10/VTO_2022_APR_ELECTRIFICATION_DRAFT%20REPORT_compliant_min.pdf.
3. G. Su and L. Tang, “A Segmented Traction Drive System with a Small DC Bus Capacitor.” *Proceedings of the 2012 IEEE Energy Conversion Congress and Exposition (ECCE)*, Raleigh, North Carolina: IEEE, 2012, pp. 2847–2853. DOI: 10.1109/ECCE.2012.6342375.

Acknowledgements

The principal investigator wishes to thank the Oak Ridge National Laboratory team members: Lincoln Xue, Jon Wilkins, Cliff White, and Clayton Hickey. The principal investigator also thanks the Virginia Tech team led by Prof. G. Q. Lu and the University of Arkansas team led by Prof. Alan Mantoath.

I.1.3 Highly Integrated Power Module (Oak Ridge National Laboratory)

Lincoln Xue, Principal Investigator (former)

Oak Ridge National Laboratory
1 Bethel Valley Road
Oak Ridge, TN 37830
E-mail: xuel@ornl.gov

Veda Galigekere, Principal Investigator

Oak Ridge National Laboratory
1 Bethel Valley Road
Oak Ridge, Tennessee, 37830
E-mail: galigekerevn@ornl.gov

Susan Rogers, DOE Technology Development Manager

U.S. Department of Energy
E-mail: susan.rogers@ee.doe.gov

Start Date: October 1, 2022
Project Funding: \$1,181,000

End Date: September 30, 2023
DOE share: \$1,181,000

Non-DOE share: \$0

Project Introduction

This project covers the design and development of next-generation wide-bandgap (WBG) power modules and the associated components within the system. Various component challenges were addressed to reduce the footprint of the system and increase the level of integration. Challenges included substrates, integrated heat sinks, and automated design tools for power electronics to increase the power density.

Objectives

The overall objective of the project is to develop technologies for next-generation advanced integrated power electronic systems. These systems have high power density and reliability to achieve the U.S. Department of Energy (DOE) Electrification Program's 2025 technical targets: 100 kW/L power density, \$2.70/kW cost, and 300,000-mi. lifetime. Under the overall objective, two main lines of inquiry were identified: power module design and automated design of power electronics.

Approach

The main approach of the project is to increase the power density and reliability of power electronics to meet the DOE Electrification Program's 2025 targets (100 kW/L, \$2.70/kW, and 300,000 mi. lifetime) by focusing on power module design and the automated design of power electronics.

Under the power module design line of inquiry, substrates were investigated to find power electronic modules that result in increased power density and high reliability for WBG device-based power modules. The project considered better matching of coefficients of thermal expansion matching between WBG devices and power module materials, improved heat extraction, and enhanced thermal and power-cycling capabilities. Additionally, multilayer substrates for enhanced electrical and thermal performance were evaluated. These solutions enabled reduced parasitic inductance in the system for optimum switching performance, reduced power module size, and the direct attachment of high-performance heat sinks.

In fiscal year 2023, two main tasks were carried out: the design, fabrication, and evaluation of the integrated silicon carbide (SiC) power module and the simulation investigation of a multiprofile-merging heat sink design.

Results

Task 1: Design, Fabrication, and Evaluation of the Integrated Silicon Carbide Power Module

In previous years, the team designed the thermal pyrolytic graphite–embedded organic direct bonded copper (ODBC)–based power module, which integrated the gate driver and artificial intelligence–optimized heat sink. The concept is shown in Figure I.1.3.1. The power module consisted of the ODBC-based substrate, gate-driver circuits, and the silicon carbide chips. In the three-layer substrate (shown as the bottom part of the structure in the figure), the top layer was used for placing the dies and terminations, the middle layer was used for common mode shielding, and the bottom layer was used for the integrated heat sink. Additional layers above the top layer could be included for the gate driver and additional termination requirements. The design was optimized by finite element analysis simulations for thermal and electrical performance that meet the requirement of 2025 DOE Electrification Program. The substrate and cooling manifold have been fabricated.

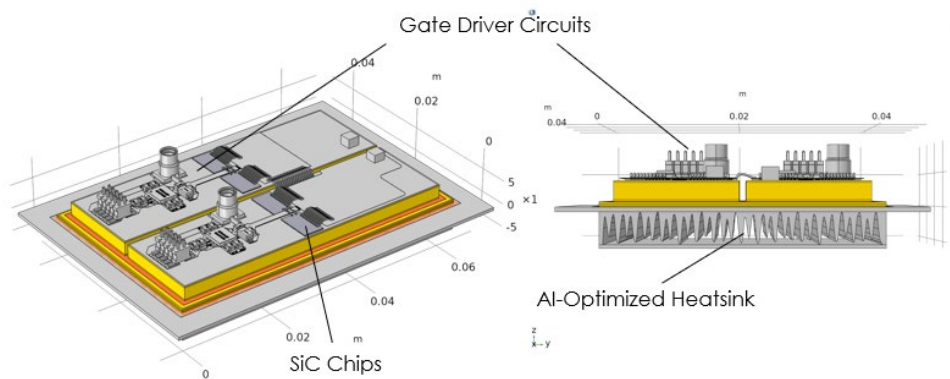


Figure I.1.3.1 ODBC-based power module with integrated gate driver and heat sink

In fiscal year 2023, the team fabricated the integrated power module with the copper-ODBC-based substrates by integrating four silicon carbide MOSFET (metal–oxide–semiconductor field-effect transistor) chips, a gate-driver printed circuit board, and a heat sink [1]. The completed power module is shown in Figure I.1.3.2. The electrical performance of the power module was evaluated in a double-pulse-test configuration. The test setup and tested waveforms at 460 V/26 A are shown in Figure I.1.3.3. The current measurement, I_L , and the voltage between the modules, V_{sw} , are shown. A breakdown occurred during the stage of voltage ramping up without driving signal been provided. It is therefore suspected that either the substrate or the dice structures were unable to sustain higher voltage. The breakdown voltage of the substrate could have been degraded during the heat sink–machining process, so more substrates were fabricated with the breakdown voltage tested before and after each step of the heat sink–machining process. Another possible explanation for the breakdown is the insufficient encapsulating of the module. Encapsulants leaked in liquid form during the initial curing process, which may have created air voids in the module, thus compromising the voltage standing capability. An improved enclosure will be designed to contain the encapsulant to minimize the leakage.

The power module’s thermal performance was evaluated by the following method. The power module was assembled with the cooling manifold and connected to a liquid cooling system with a flow meter and pressure-drop meter. A current source was set to flow through the body diodes of the silicon carbide chips, and the current level and voltage level were measured to determine the power loss on each chip. A power loss of 38 W was applied to each chip. The coolant temperature was set as 21°C, and the flow rate was varied from 4 to 8 L/min. The chip temperature was measured using a high-precision thermal camera. Figure I.1.3.4 shows the measured thermal resistance from coolant to chip against the flow rate. A thermal resistance of 0.56 K/W was achieved at a 4 L/min flow rate. The thermal resistance value matches well with the finite element simulation, within 5% error. Note that this thermal performance was achieved by the copper-based ODBC (Cu-ODBC) module; with embedded TPG, thermal performance is expected to improve further for FY 2024.

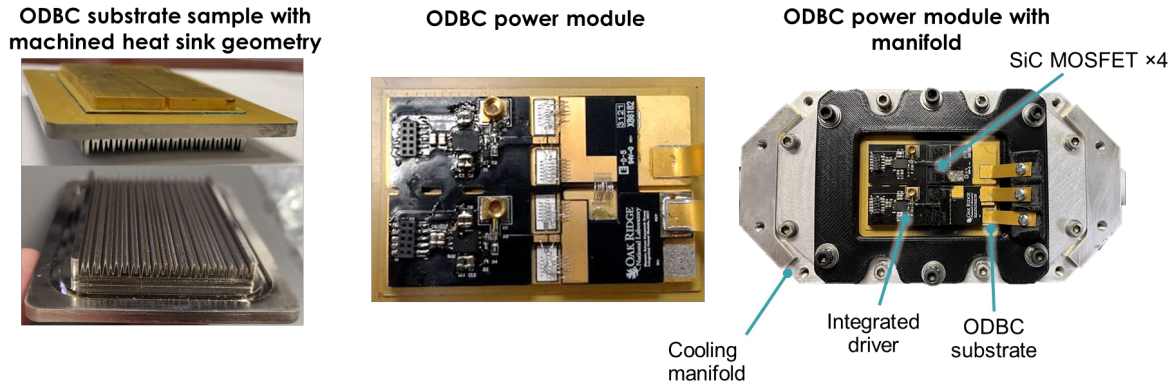


Figure I.1.3.2 Fabricated copper-ODBC-based integrated power module

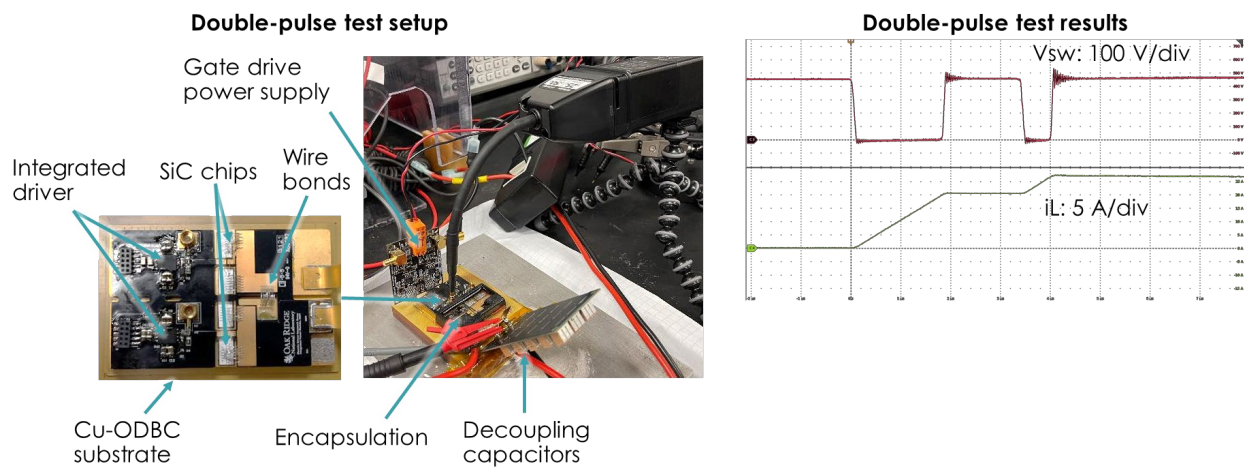


Figure I.1.3.3 Test setup and waveforms of a double-pulse test

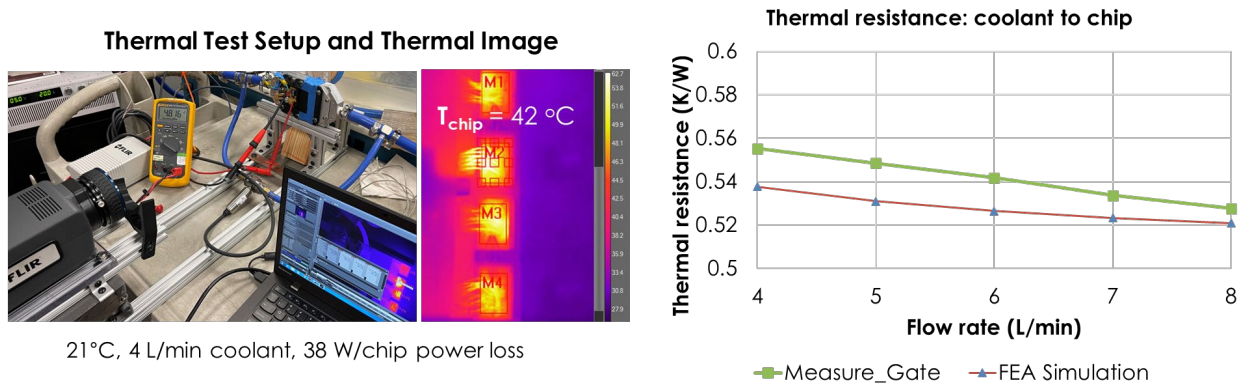


Figure I.1.3.4 Power module thermal evaluation setup and test results

In fiscal year 2023, to improve the power density and electrical performance of the power module, the team invented a stacked-die cap technology to minimize the footprint and parasitic inductances of the power module. Figure I.1.3.5 shows the structure of the proposed power module structure. In the figure, Vdc- and Vdc+ are the connection terminals that connects the half-bridge structure to the direct current voltage source (Vdc), Vsw is the switch node connection between low-side die drain and high-side die source and Vgs is the point of measurement for the gate voltage signal. It is an integrated half-bridge power module design in which

two vertical-conducting power device bare chips, a conductive spacer, and multiple high-density capacitors are stacked, which creates the shortest conducting path and loop to minimize parasitic inductance and resistance. As a result, the voltage overshoot and switching losses can be minimized. Figure I.1.3.6 shows the fabricated power module and the tested waveforms. No external gate resistor was used to maximize the switching speed and to reduce switching loss. It was demonstrated that the module can switch off 50 A at 756 V with only 5% overshoot. The estimated loop inductance is less than 0.5 nH.

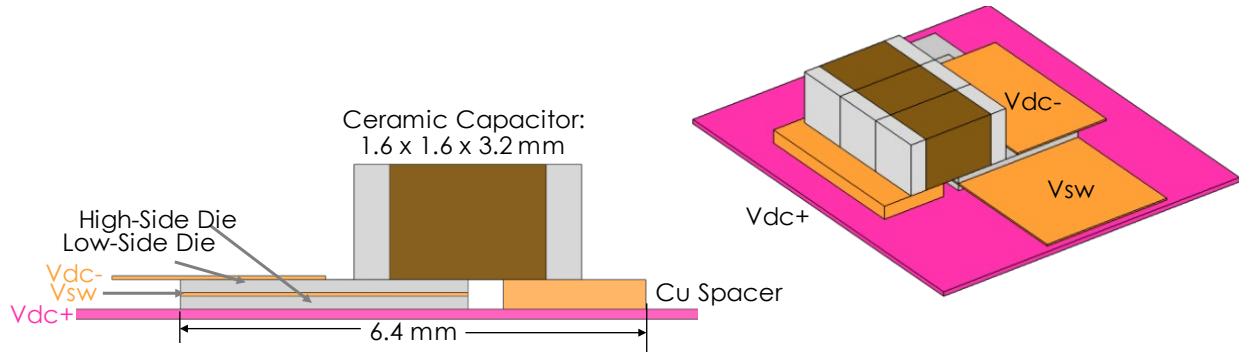


Figure I.1.3.5 Novel stacked-die cap power module

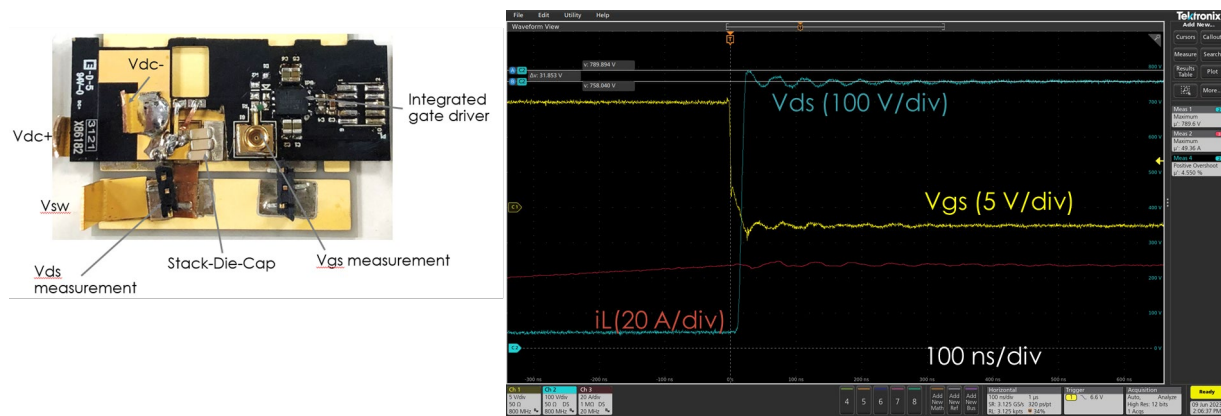


Figure I.1.3.6 Fabricated stacked-die cap power module (left) and testing of the power module at 756 V/50 A (right)

Task 2: Simulation Investigation of Multiprofile-Merging Heat Sink Design

In fiscal year 2023, the team evaluated and compared a multiprofile heat sink design scheme [2] with Oak Ridge National Laboratory’s (ORNL’s) existing single profile–extruding design scheme [3]. Those two schemes are illustrated in Figure I.1.3.7. The single profile–extruding design resembles ORNL’s existing Fourier series–based scheme [4], whereas the multiprofile-merging method is newly proposed as an extension. In Figure I.1.3.7, the working planes are considered in three positions: one at the inlet, one at the outlet, and another one somewhere between the inlet and outlet. From each plane, a heat sink with a certain length was generated using extrusion. The number of heat sinks was equal to the number of planes. For easy manufacturability, a 3-mm gap was placed between the heat sinks. Each heat sink had variable length, which was fed to an optimization algorithm to find the optimum length.

For the surface-merging method of heat sink design, genetic algorithm (GA)–optimization was done for 10 generations each consisting of 20 populations. To compare with the single profile–extruding design, the height of the heat sink was kept 5 mm. The design variables were the frequencies of fins at different planes, the amplitudes of fins at those corresponding planes, and the distances between the planes. The GA-optimized heat sink designs using the multiprofile-merging method results are shown in Figure I.1.3.8 in comparison with the single profile–extruding design, which has been verified and served as a baseline. The selected design point is compared with

the baseline in Figure I.1.3.9. The new method achieved 11% lower temperature rise and 21% lower pressure drop. Figure I.1.3.10 explains the mechanism of the improved performance for the multiprofile-merging method.

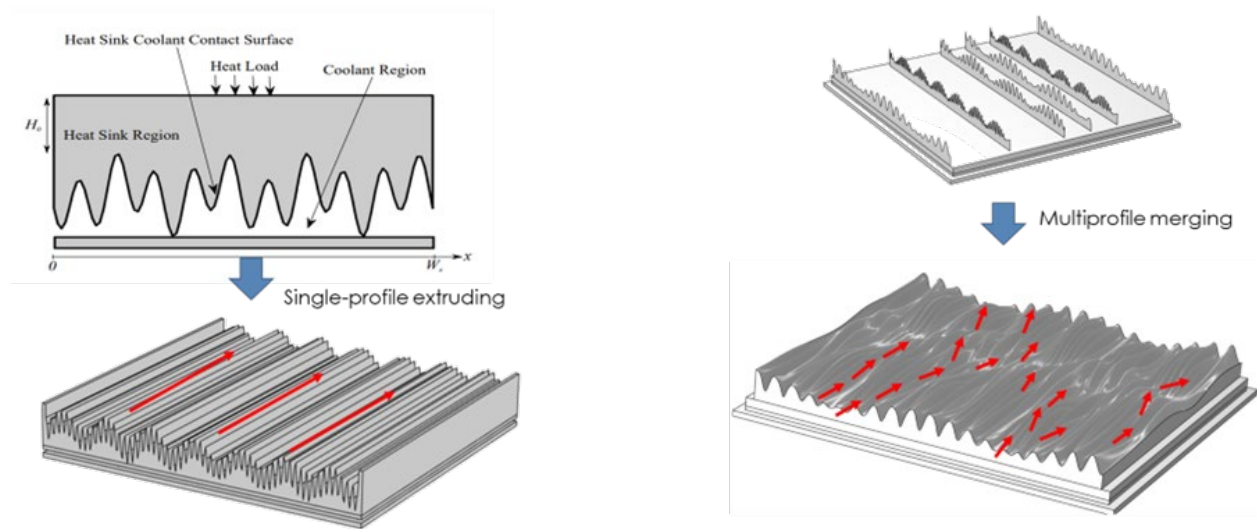


Figure I.1.3.7 Illustrations of single profile-extruding (left) and multiprofile-merging (right) schemes

In the dashed-line triangle in Figure I.1.3.10, there are a high-speed zone and low-speed zone for the coolant. The high-coolant speed zone close to the baseplate helps extract heat, and the low-coolant speed zone far from the baseplate helps reduce pressure drop. By optimizing the shape of the heat sink structure and taking advantage of this mechanism, excellent heat extraction and low-pressure drop can be achieved. This beneficial mechanism occurs only perpendicular to the flow direction for single profile-extruding but occurs both along and perpendicular to the flow direction for multiprofile merging. That is the reason the multiprofile-merging scheme can achieve better performance.

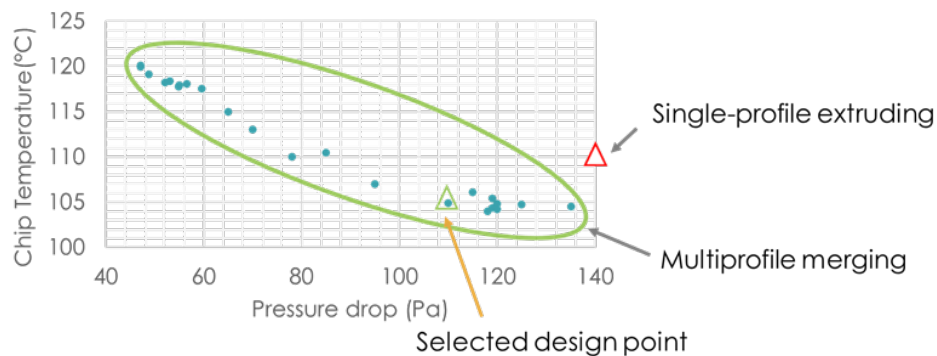


Figure I.1.3.8 Generated GA-optimized heat sink designs using a multiprofile-merging method

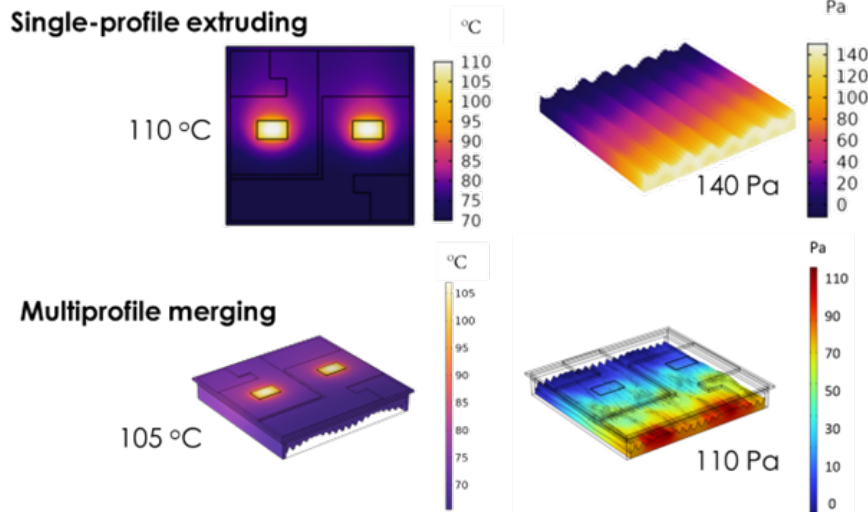


Figure I.1.3.9 Simulated thermal performance of the selected new heat sink design compared with the single profile-extruding baseline

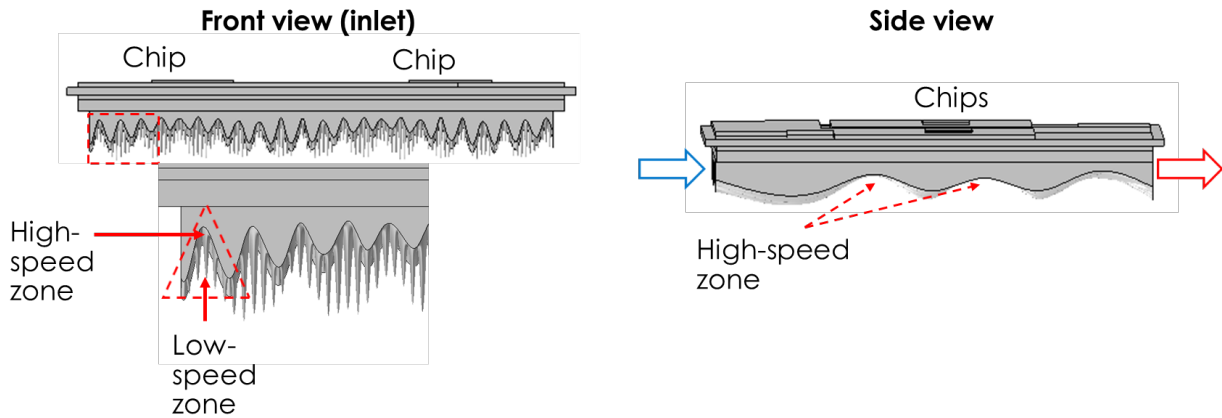


Figure I.1.3.10 Mechanisms of improved performance for the multiprofile-merging method

Conclusions

The designed copper-ODBC power module was fabricated and evaluated thermally and electrically. A thermal resistance of 0.56 K/W was achieved between the coolant and chip, and the result aligned well with the simulation. The power module switched at 460 V/26 A but failed at higher voltage because of breakdown. The module-fabrication process was carefully reviewed and repeated to understand and address this issue. A new stacked-die cap power module structure was designed to improve the electrical performance and increase power density. The module can achieve a loop inductance of less than 0.5 nH with over 5% overshoot and with no gate resistor. A new heat sink design method was invented to further reduce the thermal resistance, shrink the heat sink volume, and reduce the coolant pressure drop. ORNL’s existing single profile-extruding scheme can shrink the heat sink volume by 50% compared with a traditional pin-fin design; the new multiprofile-merging scheme achieves a further 11%-lower temperature and 21%-lower pressure drop than the single profile-extruding design, according to the simulation modeling.

Key Publications

1. Barua, Himel, Emre Gurpinar, Lingxiao Xue, and Burak Ozpineci. 2022. “Comparative Analysis of Direct and Indirect Cooling of Wide-Bandgap Power Modules and Performance Enhancement of Jet Impingement-Based Direct Cooling.” Presented at ASME 2022 International Technical Conference

and Exhibition on Packaging and Integration of Electronic and Photonic Microsystems (InterPACK), Garden Grove, CA.

2. Barua, Himel, Lingxiao Xue, and Burak Ozpineci. 2023. “Surface Merging Technique to Design GA-Optimized Heat Sinks.” Presented at IEEE Energy Conversion Conference and Expo (ECCE) 2023, Nashville, TN.
3. Xue, Lincoln. 2023. “Power Modules with Electrical and Thermal Integration.” Presented at Industry Session IS07 of the Applied Power Electronics Conference (APEC) 2023, Orlando, FL.

References

1. Lingxiao Xue. 2023. “Highly Integrated Power Module.” *2023 Vehicle Technologies Annual Merit Review*. Vehicle Technologies Office, US Department of Energy.
2. Barua, Himel, Lingxiao Xue, and Burak Ozpineci. 2023. “Surface Merging Technique to Design GA-Optimized Heat Sinks.” Presented at IEEE Energy Conversion Conference and Expo (ECCE) 2023, Nashville, TN.
3. Sahu, Raj, Gurpinar, Emre, and Ozpineci, Burak. 2021. "Liquid-Cooled Heat Sink Optimization for Thermal Imbalance Mitigation in Wide-Bandgap Power Modules". United States. <https://doi.org/10.1115/1.4052068>. <https://www.osti.gov/servlets/purl/1822070>.
4. Gurpinar, Emre, Raj Sahu, and Burak Ozpineci. 2021. “Heat Sink Design for WBG Power Modules Based on Fourier Series and Evolutionary Multi-Objective Multi-Physics Optimization.” *IEEE Open Journal of Power Electronics* 2: 559–569. <https://doi.org/10.1109/OJPEL.2021.3119518>.

Acknowledgements

The authors wish to thank the following project team members: Jon Wilkins for mechanical design support, Himel Barua for thermal analysis, and Pedro Ribeiro for assisting in power module fabrication and testing.

I.1.4 Integrated Electric Drive System (Oak Ridge National Laboratory)

Shajjad Chowdhury, Principal Investigator

Oak Ridge National Laboratory
1 Bethel Valley Road
Oak Ridge, TN. 37932
E-mail: chowdhurys@ornl.gov

Susan Rogers, DOE Technology Development Manager

U.S. Department of Energy
E-mail: susan.rogers@ee.doe.gov

Start Date: October 1, 2022

End Date: September 30, 2023

Project Funding: \$500,000

DOE share: \$500,000

Non-DOE share: \$0

Project Introduction

The US Department of Energy (DOE) in 2017 announced technical targets for light-duty electric vehicles. DOE targets a power density of 33 kW/L for a 100 kW traction drive system by 2025 [1] to increase the state-of-the-art power density by more than eight times compared to 2015 targets. This project focuses on the tight integration of motor and inverter components to improve power density and thus achieve the target. Furthermore, this project optimizes the bulky direct current (DC)-link capacitor's volume and identifies optimal substrate technology for space-restricted applications to improve performance and lifetime.

Objectives

This project aims to research technologies that enable tight integration of the inverter with the motor and that, as a result, enable a high-power-density, integrated traction drive. FY 2023 objectives were the following:

- Build and evaluate the modified direct bonded copper (DBC) substrate.
- Develop an inverter phase leg that integrates bus bars, gate drivers, capacitors, and current sensors.

Approach

The approaches to achieving the project objectives were the following:

- Compare state-of-the-art substrate technologies to find the best solution for thermal performance.
- Design a single-phase-leg module that integrates the power module, gate drivers, capacitors, current sensors, and bus bars that fit inside the motor.
- Evaluate the designed module's electrical performance.

Results

Substrate Technologies for Space-Restricted Application

The modified DBC substrate's performance has been experimentally evaluated and compared with a traditional DBC substrate. Although the substrates used in the simulation accommodated four switches, the designed substrate was not ready for evaluation. Thus, a different DBC substrate layout that was available was used for the evaluation. Two half-bridge modules were made: one traditional DBC and one DBC with copper (DBCwCu) (Figure I.1.4.1) for comparison. A single SiC metal-oxide semiconductor field-effect transistor (MOSFET) [2] was soldered in each switching position and was wire bonded to the substrate for gate, drain, and source terminations. The substrate was then attached to a heat sink using a thermal interface material [3] and was clamped using a 3D printed structure. Two holes were made in the heat sink to place thermocouples underneath the substrate to capture the substrate's bottom surface temperature. The device surface was painted

with matte black paint to increase emissivity, and the device temperature was captured using a thermal camera. The experimental setup to evaluate thermal performance is shown in Figure I.1.4.2.

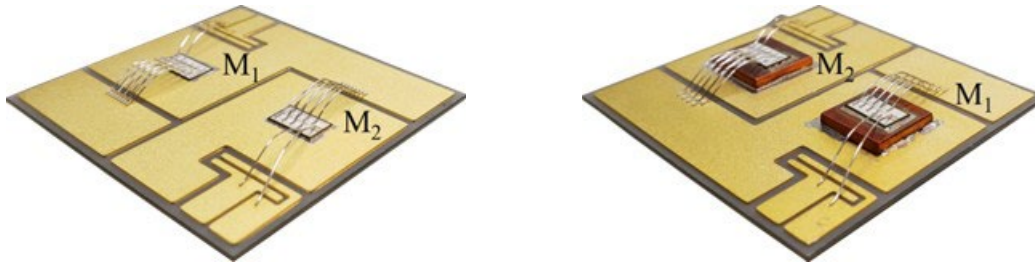


Figure I.1.4.1 Assembled substrate for thermal evaluation: the conventional direct bonded copper (DBC) substrate (left) and the modified DBC with copper substrate (right).

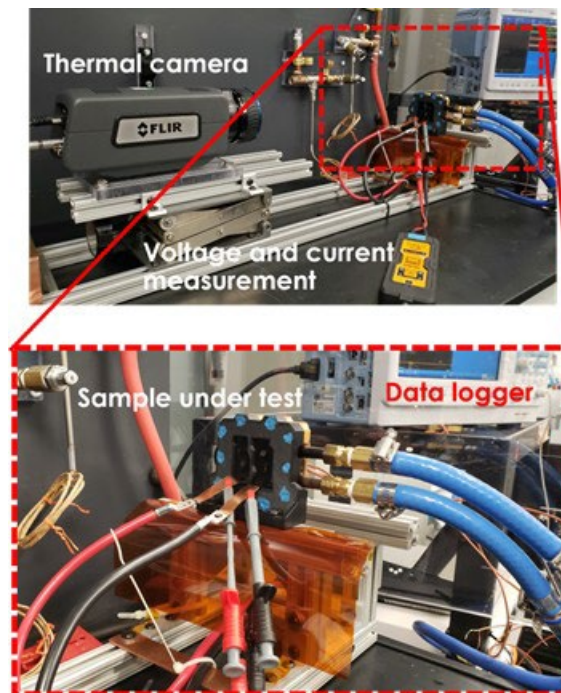


Figure I.1.4.2 Experimental setup to evaluate the thermal performance of the proposed DBC with copper substrate.

In this experiment, MOSFET body diodes were used for conducting the current to generate maximum losses for minimum current injection. A DC source was used to inject current through body diodes, and the top and bottom diodes were connected in series. The gate and source pins were shorted to keep the MOSFETs off during the evaluation. Injection current was varied to introduce losses within the device where the power loss was varied from 25 to 250 W. A thermal camera result for both substrate technologies is shown in Figure I.1.4.3, where the temperature spreading and lower device temperature can be distinguished. The results captured for each data point were then plotted in Figure I.1.4.4. Not much difference was shown in device temperatures at lower power losses, but the device temperature difference increases with higher power loss. Also, the traditional DBC substrate temperature reaches 150°C–160°C at 190 W losses, whereas the modified DBC substrate can handle 32% more losses (250 W) for the same device temperature. Furthermore, the thermal resistance of each device to the substrate's bottom surface was calculated based on the injected losses and measured thermal values, which are plotted in Figure I.1.4.4. The results show that the DBCwCu has 35% lower thermal resistance than that of the traditional DBC substrate.

The experimental results show that the proposed DBCwCu substrate will use more area for cooling and thus will improve thermal performance compared with a traditional DBC substrate. The proposed substrate can be a viable solution for space-restricted applications such as integrated electric drives and electric aircraft applications.

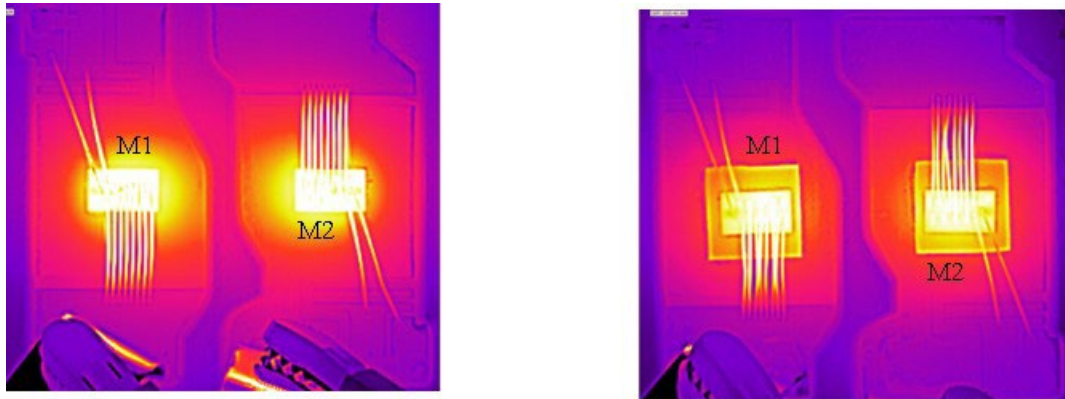


Figure I.1.4.3 Thermal evaluation results captured using an infrared thermal camera comparing the traditional direct bonded copper (DBC, left) and the proposed DBC with copper (right) substrates.

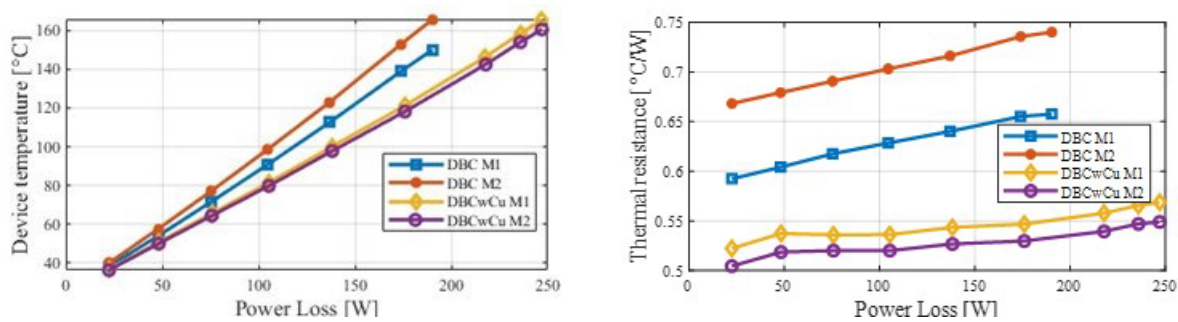


Figure I.1.4.4 Comparison of device temperature (left) and thermal resistance (right) at various power loss injections for the direct bonded copper (DBC) and DBC with copper (DBCwCu) substrates. These data show the advantages of DBCwCu over the traditional DBC.

Power Block for an Integrated Electric Drive

A power electronic system requires a power module, gate driver, capacitors, bus bars, sensors, and heat sink. Traditionally, these subcomponents are designed separately and integrated to form an inverter/converter system. This approach sometimes leads to high-voltage overshoot due to large power-loop inductance and gate-voltage oscillation, especially at high-voltage and high-current operations. Thus, power electronic components must be co-optimized and co-designed to achieve better performance. The core idea was to use multiple power blocks to develop an inverter/converter with little or no compromise on performance.

The first component of the power block is the substrate that houses the semiconductor die and electrically insulates it. Placement of the devices and layout of the substrate traces play critical roles in ensuring lower power loop inductance. The designed module contains one phase leg of an inverter and has two dies in parallel to handle 200 A phase current (Figure I.1.4.5). The DC+, DC-, and output planes were strategically placed to oppose the current direction so that the layout inductance is minimal. Furthermore, each parallel device has a different commutation loop length, which will ensure unequal current distribution during transient conditions (switching); therefore, unbalanced temperature will be seen among the parallel branches. To balance the current, an impedance balancing approach has been taken whereby the device close to termination will have a longer wire bond length to have an impedance similar to that of the other device. The designed substrate has been simulated using finite element analysis software to evaluate current crowding in the wire bonds; the

simulation clearly shows the unbalanced current in the wire bonds (Figure I.1.4.6, left). The transient current can be balanced by increasing the wire bond length by 3 mm, and the analysis results show almost equal current distribution through the wire bonds (Figure I.1.4.6, right). Current distribution results for low-frequency (steady state) and high-frequency (transient) conditions are shown in Table I.1.4.1. Finally, to improve heat extraction, the DBCwCu substrate was used because of its better loss handling capacity. The designed DBCwCu substrate is shown in Figure I.1.4.7.

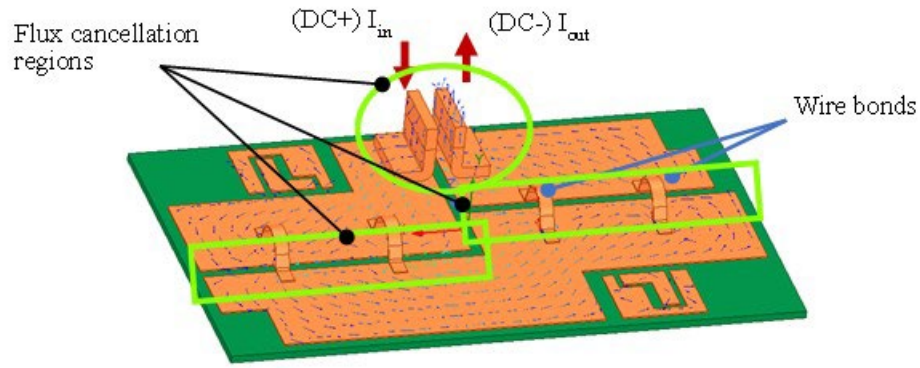


Figure I.1.4.5 Module layout showing that opposing current paths are next to each other, thus reducing the layout inductance.

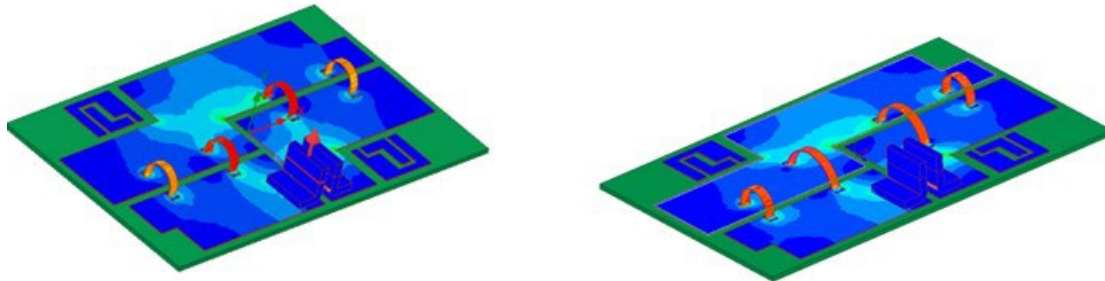


Figure I.1.4.6 Current distribution among the parallel metal-oxide semiconductor field-effect transistors (MOSFETs, left) showing unequal current distribution (right) impedance matching by varying wire bond length showing equal current distribution.

Table I.1.4.1 Current distribution among SiC metal-oxide semiconductor field-effect transistors (MOSFETs) with and without impedance matching.

	Frequency	D1	D2	D3	D4
Traditional	1 Hz	2.07	2.52	2.51	2.08
	30 MHz	2.36	3.26	3.23	2.42
Modified	1 Hz	2.33	2.31	2.29	2.35
	30 MHz	2.90	2.77	2.77	3

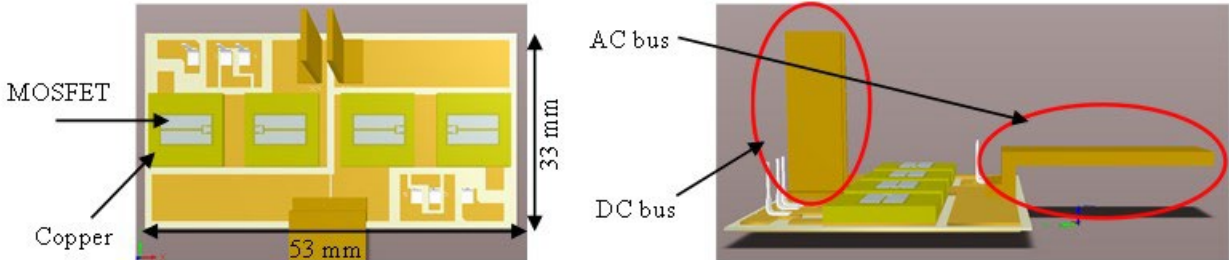


Figure I.1.4.7 Designed DBC with copper substrate with optimized layout to improve thermal and electric performances.

The second layer of the power board contains the main gate driving circuit, a few decoupling capacitors, and a current sensor, shown in Figure I.1.4.8. The gate driver and decoupling capacitors were placed on the same board to minimize gate and power loop inductances. A hall-effect, surface-mounted, IC-based AC sensor was placed on top of the AC bus bar to capture the magnetic field and then translate it to current for the control algorithm. The third layer of the board was then added to increase the capacitance to keep the overall DC voltage swing at 40 V, which is 5% of the overall DC bus voltage. The total capacitance of each board was 4.5 μF , yielding a total of 27 μF for the six-phase inverter, enough for a triangular modulation technique [4]. Finally, a gate driver board that contains an isolated power supply, signal isolator, dead time generation, and shoot-through protection circuitry was added on top. The designed circuit was then prototyped and assembled, as shown in Figure I.1.4.9. The designed single-phase leg module has dimensions of 52 \times 52 \times 35 mm, which translates to 0.1 L volume. The six-phase inverter will occupy a 0.6 L volume, and the rest will be occupied by the heat sink, manifold, and motor winding connectors.

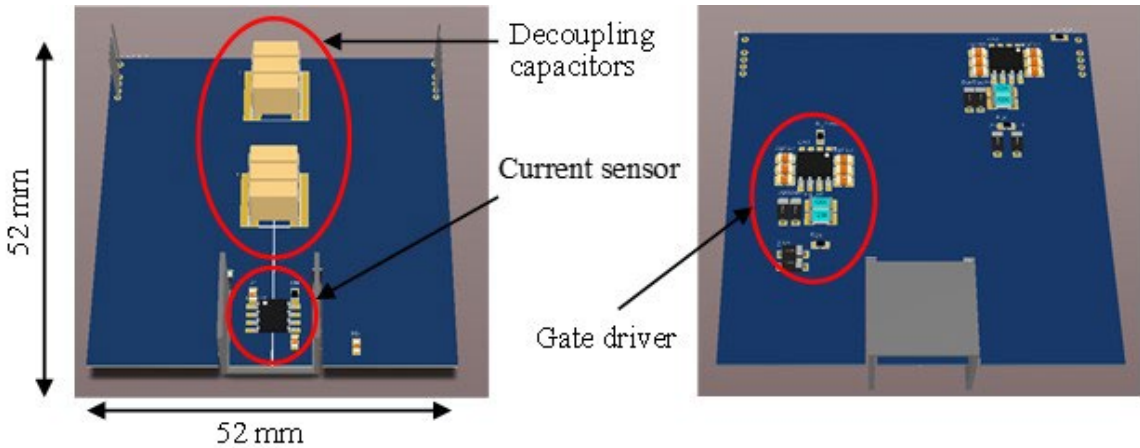


Figure I.1.4.8 A printed circuit board (PCB) based secondary board showing decoupling capacitor and current sensor on top of the board (left) and gate driver circuitry on the bottom (right).

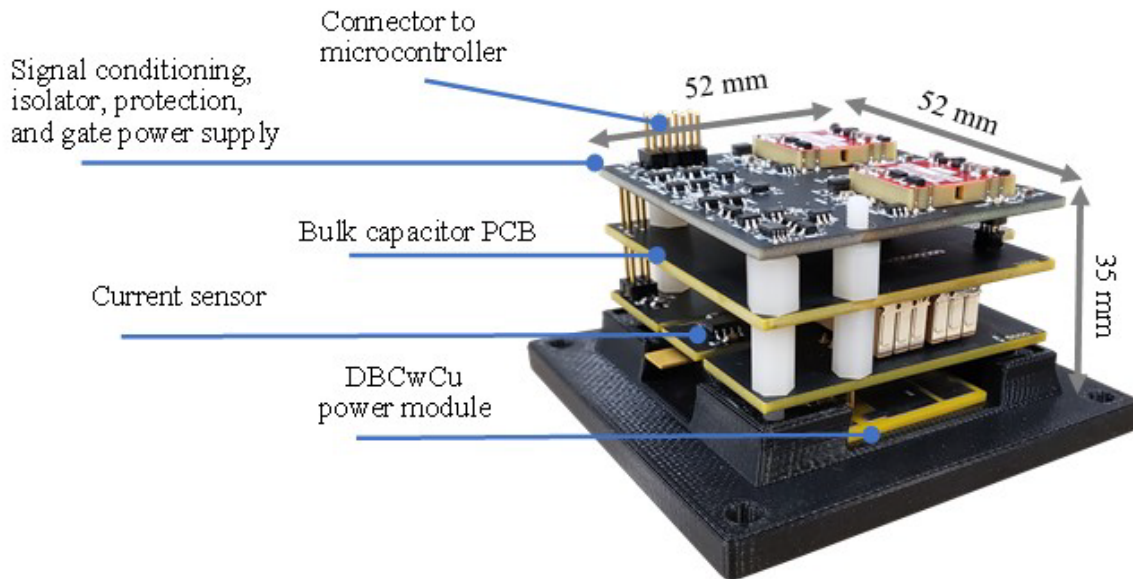


Figure I.1.4.9 Assembled prototype of the designed power block integrating power module, gate driver, capacitor, and AC current sensor.

Conclusions

In FY 2022, various substrates were analyzed to identify the best solution. The DBC substrate showed much better thermal performance than the insulated metal substrate (IMS) and IMS with thermally pyrolytic graphite (IMSwTPG) substrates for space-restricted applications; thus, the DBC substrate was selected for this project. Additionally, a modified DBC substrate was proposed to improve thermal performance, and it was compared with various available substrates. This year the substrates were prototyped and experimentally evaluated. Results show the DBCwCu has an additional 32% loss handling capacity and 35% lower thermal resistance than those of the traditional DBC substrate.

In FY 2023, a single-phase-leg power module was also designed that complied with the available form factor inside the motor. The power board integrates the substrate, capacitor board, bus bars, current sensor, and gate-driver circuitry. The board—designed to operate at 800 V and 200 A currents—shows lower power loop inductance with better transient current distribution among the parallel branches.

Key Publications

1. S. Chowdhury, E. Gurpinar, and B. Ozpineci. 2022. "Capacitor Technologies: Characterization, Selection, and Packaging for Next-Generation Power Electronics Applications." *IEEE Transactions on Transportation Electrification* 8 (2): 2710–20. <https://doi.org/10.1109/TTE.2021.3139806>.
2. V. Rallabandi, S. Chowdhury *et al.*, "Traction motor design trade-offs with additively manufactured anisotropic bonded magnets," *2023 IEEE Transportation Electrification Conference & Expo (ITEC)*, Detroit, MI, USA, 2023, pp. 1-5, doi: 10.1109/ITEC55900.2023.10187005.

References

1. U.S. DRIVE. 2017. *Electrical and Electronics Technical Team Roadmap*. US Department of Energy, Vehicle Technologies Office. <https://www.energy.gov/sites/prod/files/2017/11/f39/EETT%20Roadmap%2010-27-17.pdf>.
2. Cree Inc. 2021. "CCPM2-1200-0025A, Silicon Carbide Power MOSFET C2M™ MOSFET Technology." <https://assets.wolfspeed.com/uploads/2021/05/CPM2-1200-0025A.pdf>.

3. Laird Technologies Inc. 2022. “Tflex™ HD700 Series Thermal Gap Filler.” Accessed July 24, 2023. https://www.laird.com/sites/default/files/2022-03/A17758-00%20Tflex%20HD700_03-15-22.pdf.
4. Chowdhury, S., E. Gurpinar, and B. Ozpineci. 2022. “Capacitor Technologies: Characterization, Selection, and Packaging for Next-Generation Power Electronics Applications.” *IEEE Transactions on Transportation Electrification* 8 (2): 2710–20. <https://doi.org/10.1109/TTE.2021.3139806>.

Acknowledgments

The principal investigator thanks the project team members—Mostak Mohammad, Himel Barua, Vandana Rallabandi, Gui-Jia Su, and Jon Wilkins of the US Department of Energy’s Oak Ridge National Laboratory—for their contributions and thanks Bidzina Kekelia of the National Renewable Energy Laboratory for collaborating with the team.

I.1.5 Power Electronics Materials and Bonded Interfaces – Reliability and Lifetime (National Renewable Energy Laboratory)

Paul Paret, Principal Investigator

National Renewable Energy Laboratory (NREL)
15013 Denver West Parkway
Golden, CO 80401
E-mail: paul.paret@nrel.gov

Susan Rogers, DOE Technology Development Manager

U.S. Department of Energy
E-mail: susan.rogers@ee.doe.gov

Start Date: October 1, 2018

End Date: September 30, 2024

Project Funding: \$150,000

DOE Share: \$150,000

Non-DOE Share: \$0

Project Introduction

Increased electrification of various technologies across renewable energy and energy efficiency sectors has brought a great deal of attention to power electronics components and systems that can achieve cleaner and efficient modes of energy storage, conversion, and transmission. The efficiency of power conversion processes depends heavily on the semiconductor die material, device topology, and related properties. Equally important as the device structure is the power electronics package, which can be defined as the integrated system of components surrounding the device that enables the transfer of electrical signals to and from external connections in addition to providing thermal pathways and mechanical support.

Robust and reliable power electronics packaging technologies are critical for the safe operation of wide-bandgap devices such as silicon carbide and gallium nitride, particularly at high temperatures. The cost and power density targets for these packages or modules only increase the challenges associated with their design and development. A careful and meticulous design of the package, including material selection, geometric layout, and integration of components—from an electrical, thermal, and mechanical standpoint—is critical to bridge the gap between theoretical and measured performance and efficiency of the devices.

From a thermomechanical perspective, the high-temperature operation of wide-bandgap devices presents a strong materials challenge for other component layers within the package. Materials typically used in packages with Si devices such as solders cannot withstand the operating temperature range (200°C and beyond) with wide-bandgap devices, and as a result, new material formulations need to be considered. It is widely documented that the failure mechanisms within conventional power electronics packages involve crack formations at the bonded interfaces (die-attach and substrate-attach), along with electrical interconnect (wire bonds and ribbon bonds) failures. As most of these failures are temperature-dependent, the high-temperature environment only serves to exacerbate the thermomechanical performance of these components, and it thus deserves a great deal of attention in the context of wide-bandgap devices.

This report describes research at NREL on the thermomechanical performance and reliability evaluation of bonded interfaces: near-vertical carbon fibers embedded in polymers and sintered copper. We purchased two types of polymeric bonded materials (one with a thermoplastic and the other with a thermoset polymer) and fabricated samples at NREL for reliability evaluation. We also collaborated with CuNex GmbH in Germany to study the degradation mechanics of sintered copper—a promising alternative to sintered silver—under thermal shock accelerated experiments. In addition to evaluating the reliability of different materials, we worked on creating novel frameworks to develop lifetime prediction models. To this end, we compared the prediction accuracies of statistical models and machine learning models to estimate the crack growth behavior of solders using scanning acoustic microscope (SAM) images.

Objectives

The major objectives of this project are to:

- Evaluate the reliability of high-temperature bonded interfaces by subjecting coefficient of thermal expansion-mismatched coupons to accelerated thermal cycling. Crack propagation and any other failure mechanisms that originate and evolve under thermal cycling will be periodically monitored through SAM imaging.
- Develop thermomechanical models to obtain theoretical parameters such as strain energy density and formulate a lifetime prediction model based on these modeling outputs and experimental data.
- Investigate the performance of statistical and machine learning models in predicting the crack growth of bonded interfaces under thermal cycling.

Approach

Polymeric Bonded Materials

In the past, experiments were conducted at NREL on a material named HM-2 (manufactured by *btechcorp*). HM-2 is a composite structure consisting of 8- to 10- μm -diameter near-vertical carbon fibers embedded in a polyamide adhesive at approximately 40% fill factor by volume. HM-2 exhibited excellent reliability under a thermal cycling profile of -40°C to 150°C ; however, the maximum operating temperature of approximately 165°C prevented its application in wide-bandgap-device-based packages (maximum operating temperature of 175°C and above). Newer versions of HM-2, known as HM-3 and HM-4 (manufactured by ADA Technologies), are compatible with high temperatures and have a thermoplastic and thermoset polymer, respectively.

To study the thermomechanical behavior of HM-3 and HM-4 under thermal cycling, we fabricated samples in which the material was bonded between aluminum nitride (AlN - 0.63-mm-thick) and copper (Cu - 3-mm-thick) coupons. The footprint of the samples was 25.4 mm \times 25.4 mm. Table I.1.5.1 shows the thermal cycling plan for the HM-3 and HM-4 samples.

Table I.1.5.1 Thermal Cycling Plan for the Polymeric Bonded Materials

Material	Thermal Cycling Profile		
	Temperature	Ramp Rate	Dwell Time
HM-3	Case 1: -40°C - 150°C	5 $^{\circ}\text{C}/\text{min}$	10 min
	Case 2: -40°C - 175°C	5 $^{\circ}\text{C}/\text{min}$	10 min
	Case 3: -40°C - 200°C	>10 $^{\circ}\text{C}/\text{min}$	10 min
HM-4	Case 1: -40°C - 150°C	5 $^{\circ}\text{C}/\text{min}$	10 min
	Case 2: -40°C - 175°C	5 $^{\circ}\text{C}/\text{min}$	10 min
	Case 3: -40°C - 200°C	>10 $^{\circ}\text{C}/\text{min}$	10 min

Sintered Copper

Sintered copper is considered to be a promising alternative to sintered silver for high-temperature power electronics packaging due to its low cost and reliable performance under low-temperature thermal cycling profiles [1]. The performance of this material under high-temperature accelerated conditions has not yet been reported in the literature; hence, we included it in our research study. The sample configuration consists of Cu baseplates (50 mm \times 50 mm) bonded to active-metal-bonded substrates with silicon nitride as the ceramic layer. These substrates were supplied by Rogers Corporation, and the Cu baseplates were purchased from Evek, GmbH, in Germany.

The bonding of the samples was conducted using a Budatec SP300 sinter press by CuNex. The synthesis profile, as shown in Figure I.1.5.1, included a pre-drying stage where the samples were held at 100°C for 15

minutes, followed by ramping the temperature up to 275°C. A sintering pressure of 20 MPa was applied for 5 minutes at this high temperature to form the sintered copper bond. The whole fabrication process was conducted in a nitrogen atmosphere to prevent the oxidation of copper.

For the bond pattern, two different stencil prints—a grid type and a stripe type—were used. These patterns were used instead of a full area print to allow an easy path for the additive agents such as the dispersant and binder to evaporate completely during the drying stage in the synthesis process. A total of 24 samples were fabricated, out of which 8 samples each had a Cu baseplate thickness of 3 mm, 4 mm, and 5 mm, respectively. Figure I.1.5.2 shows the stencil patterns imprinted on the sintered copper bond and the bonded sample.

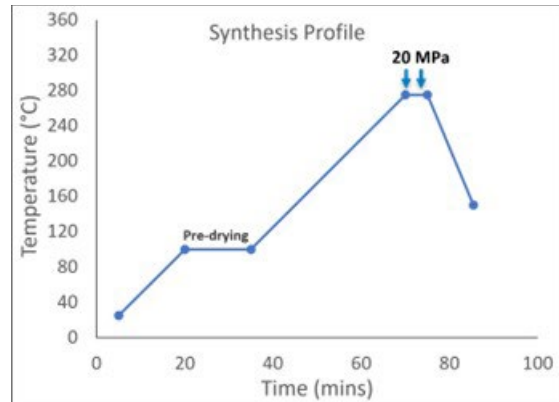


Figure I.1.5.1 Synthesis profile of sintered copper

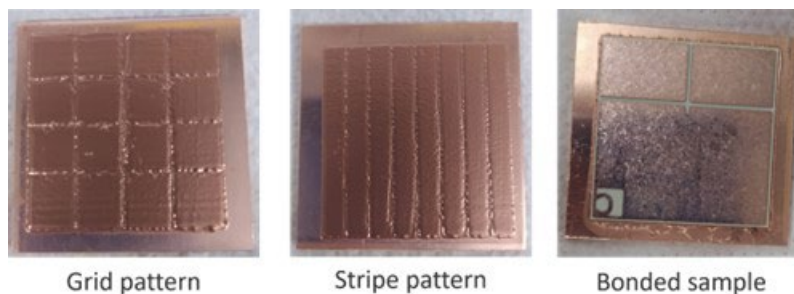


Figure I.1.5.2 Sintered copper stencil patterns and bonded sample

Image-Based Lifetime Prediction

In this task, we compared the performance of statistical models such as Holt linear, simple exponential smoothing, and autoregressive models against machine learning models such as regression, random forest, xgboost, and a multilayer perceptron (MLP) model. A time series of SAM images of eutectic solder under accelerated thermal cycling was used as the training and validation dataset for these models. Additionally, the predictive performance of Holt linear and MLP models were investigated using sintered silver SAM images.

Results

Polymeric Bonded Materials

Among the different thermal profiles listed in Table I.1.5.1, we conducted the -40°C – 175°C thermal cycling profile on both HM-3 and HM-4 samples. The samples were taken out of the cycling chambers at every 100-cycle interval for SAM imaging. Figure I.1.5.3 shows the SAM images of HM-3 and HM-4 at different stages of thermal cycling. The emergence of certain patterns after 100 cycles is clearly evident in the images of both HM-3 and HM-4, which can be most likely attributed to the degradation of the polymer base. Despite the promise of thermoset polymers for high-temperature operation, HM-4 samples exhibited a higher degradation than HM-3 samples. To quantify the defect percentage in these samples, we converted the grayscale images into binary format and used the *OpenCV* library in Python to compute the ratio of white pixels to the total pixel count. It should be noted that the defect percentages estimated through the aforementioned technique are highly sensitive to the threshold value used for the grayscale binary conversion. Figure I.1.5.4 shows the calculated defect percentages as a function of thermal cycles. Based on these calculations, HM-4 samples reached the failure criterion (20% of defect growth over the bond area) in just 100 cycles, whereas the defect percentage in HM-3 samples is around 16% after 600 cycles. Overall, it can be concluded that the HM-4 samples are not reliable for operation at temperatures above 175°C .

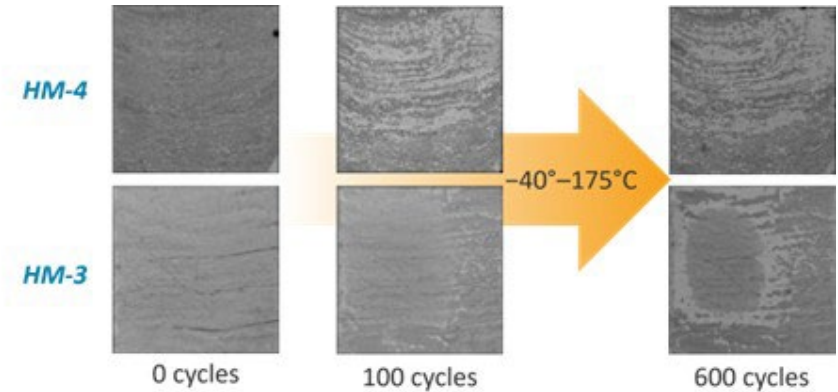


Figure I.1.5.3 SAM images of HM-3 (bottom) and HM-4 (top) samples

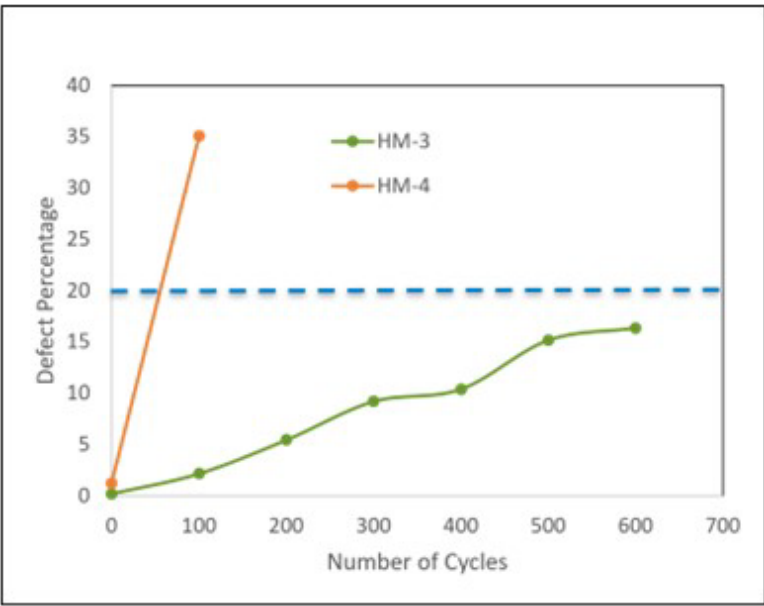


Figure I.1.5.4 Degradation of polymer samples under thermal cycling

Sintered Copper

As mentioned in the Approach section, there were two design variables among the sintered copper samples—stencil print (grid and stripe) and Cu baseplate thickness (3 mm, 4 mm, and 5 mm). Each design type (e.g., grid bond pattern with 3-mm-thick baseplate) had four samples for the thermal shock experiments. Figure I.1.5.5 shows the temperature measured from the samples while under thermal shock. It can be seen that despite the quick variation in temperatures for a major part of the ramping phases, the ramp rate slows down as the temperature approaches 200°C, which is mainly due to a chamber limitation and thermal mass of the samples. Similar to the polymer materials, we obtained the SAM images of the sintered copper samples periodically at every 100 cycles, as shown in Figure I.1.5.6.

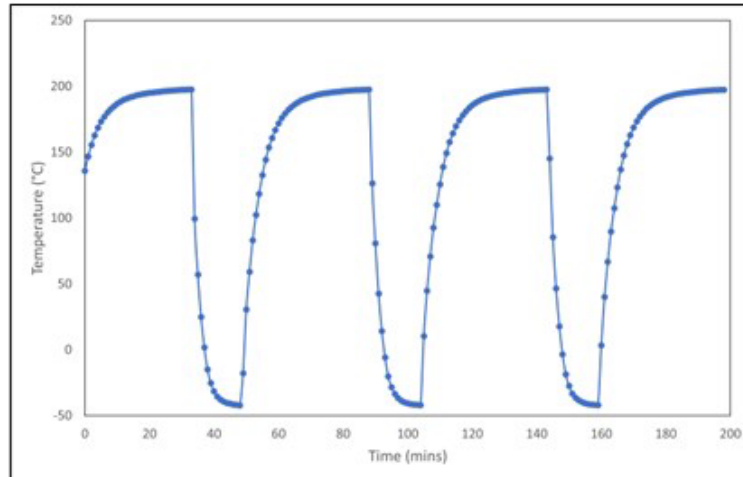


Figure I.1.5.5 Temperature measured on the samples under thermal shock

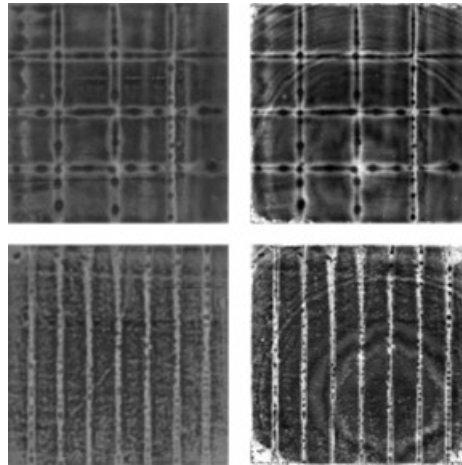


Figure I.1.5.6 SAM images of sintered copper samples with a 3-mm-thick Cu baseplate, 0 cycles (left) and 500 cycles (right)

Due to the presence of grid and stripe patterns in the SAM images, measuring the defect percentage in these samples proved to be a challenge, as these patterns appeared as white regions similar to an actual void or a crack. To overcome this issue, we manually edited the images by masking the patterns with black rectangles, leaving out the regions where the crack formations were observed. We also employed a domain transfer technique to denoise the images [2], which can possibly exclude the patterns from the defect calculations. In this approach, we first converted the SAM image from its spatial domain to frequency domain using Fourier transform. In the frequency domain, most of the information pertinent to the bond region is represented as a bright spot in the center of the graph, and the higher frequency components, which is typically the noise in the form of patterns, appear toward the edges. Hence, a low-pass filter can then be applied to the image data in the frequency domain to cancel out the higher frequency components. The low-pass filter can take any form, but we used rectangular masks in this project. Finally, the filtered image is transferred back to the spatial domain and converted to binary format for the defect calculation. Figure I.1.5.7 shows the sequential process of image denoising. It can be seen that the domain transfer method resulted in eliminating most of the grid patterns, although traces of white spots still remain in the final image. Further adjustments can be made by changing the filter mask size or even using a different type of filter to remove these small traces of spots, and this task will be explored in FY24. It should also be noted that the domain transfer technique to denoise the image does not work for all SAM images and is highly dependent on the type of noise present in the raw image; however, the major advantage is that this technique avoids the laborious manual editing of the images and results in a faster calculation of the defect percentages.

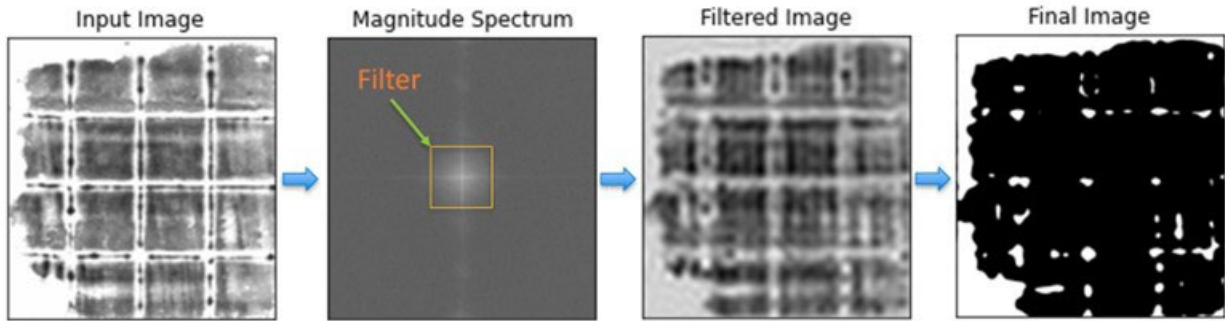


Figure I.1.5.7 Image denoising using spatial – frequency domain transfer

Figure I.1.5.8 shows the defect percentages (calculated through manual editing of the SAM images) of the different sintered copper samples as a function of baseplate thickness, as well as a comparison of the two techniques. As expected, the defect percentage is higher for samples with thicker baseplates, but not much difference can be observed between the 4-mm-thick and 5-mm-thick samples, even at 500 cycles. As the thermal shock experiments continue, the rates of defect propagation could widen between these samples and remains to be observed. Also, the domain transfer technique resulted in a defect percentage (5-mm-thick Cu baseplate) that is only about 2.5% higher than the manual process, and with further improvements, this difference can be decreased to a negligible amount.

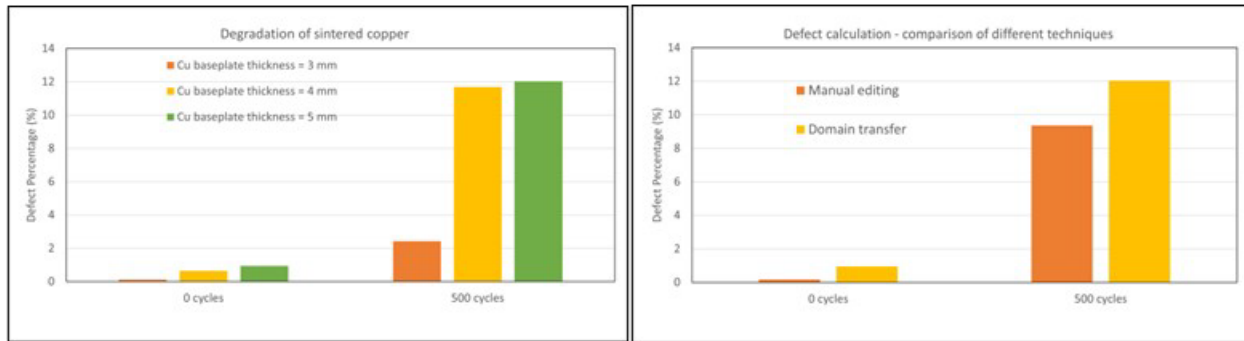


Figure I.1.5.8 Defect progression in sintered copper (left) and comparison of different techniques to estimate the defect percentage (right)

Image-Based Lifetime Prediction

In FY22, we investigated the time-series forecasting performance of statistical models by leveraging the defect percentages, obtained from eutectic lead solder-bonded samples under accelerated thermal cycling conditions, as the training and validation datasets. The dataset consisted of defect percentages at every 100 cycles up to 1,200 cycles. In FY23, we expanded the time-series models to include machine learning techniques and compared their performance with statistical models. Also, we increased the dataset size by interpolating between the defect values at 100-cycle intervals to include data points at every 10 cycles. Figure I.1.5.9 shows the predictive performance of statistical and machine learning models based on this new dataset. In this figure, the predictive accuracy of different models is estimated by calculating the root mean square (RMS) difference between the predicted values and the actual dataset. We obtained the statistical models from the statsmodels package in Python and used other libraries for the machine learning models.

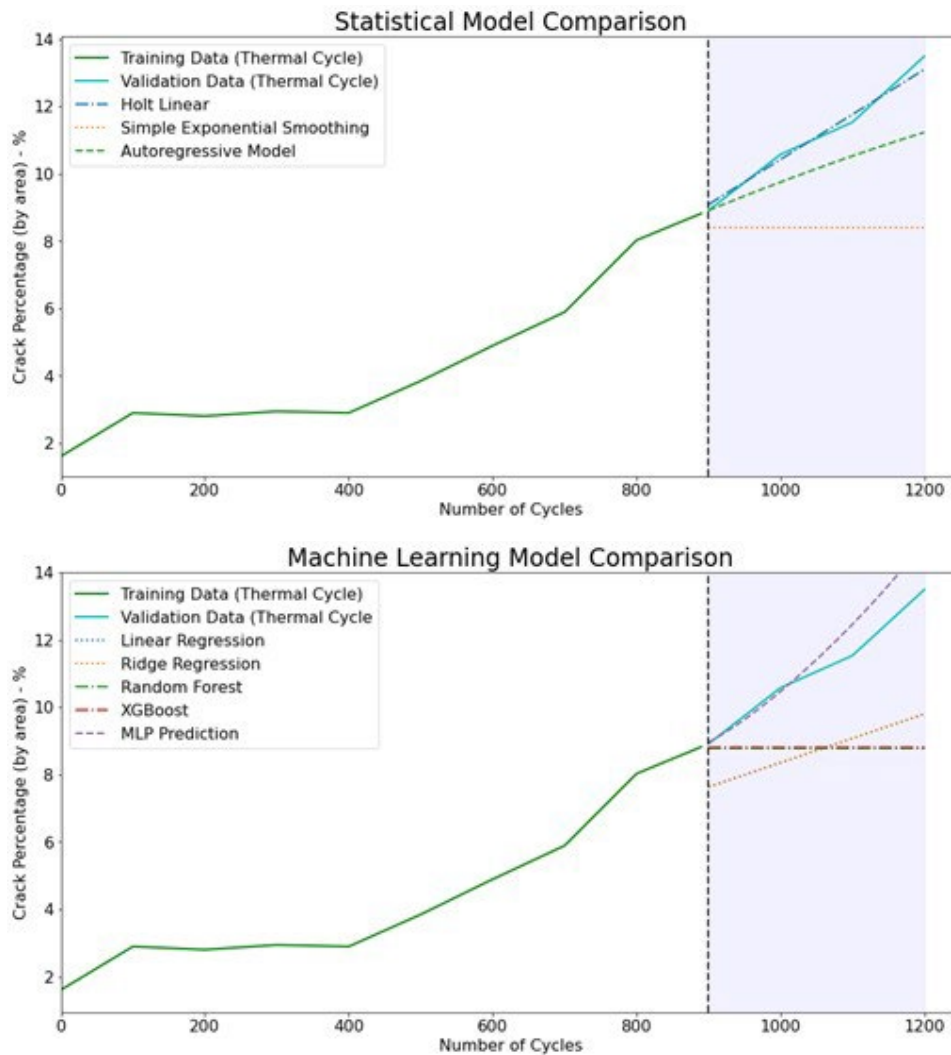


Figure I.1.5.9 Predictive performance of statistical models (top) and machine learning techniques (bottom) in estimating the defect growth in bonded samples

Among the statistical models, Holt linear resulted in the highest accuracy with an RMS error of 0.15, whereas in the machine learning model category, the MLP-based approach (RMS error ≈ 2) slightly outperformed the supervised techniques. Although not shown in the figure, we noticed that both random forest and xgboost captured the trend in the training data but did not result in accurate predictions. These results confirm the superior time-series prediction capability of statistical models over machine-learning techniques.

As Holt linear and the MLP technique resulted in the most accurate predictions among the models included in this study, we investigated its predictive performance on a similar dataset obtained from sintered silver samples subjected to thermal cycling, shown in Figure I.1.5.10. Even with this dataset, Holt linear resulted in closer predictions to the actual data than the MLP model. It should be noted that MLP is a neural network-based model and is sensitive to the number of layers in the network. Further investigations to improve the accuracy of MLP will be performed in FY24.

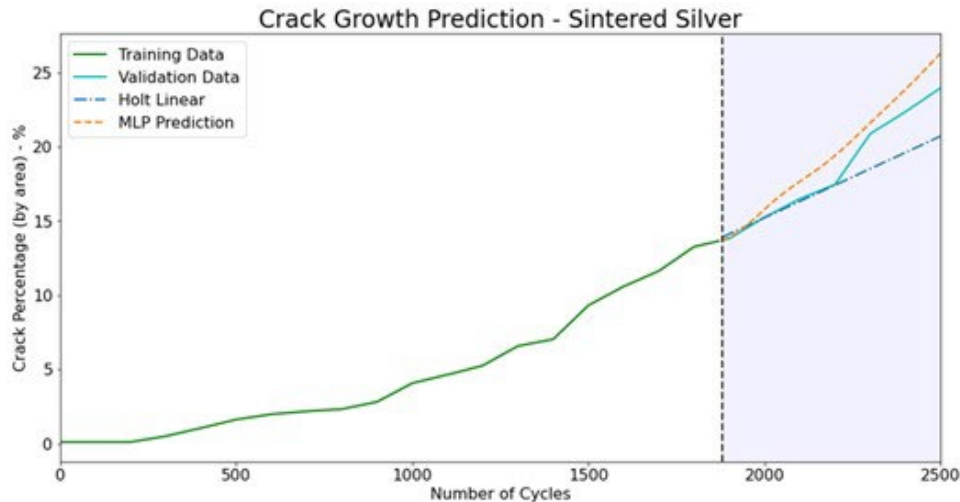


Figure I.1.5.10 Defect growth prediction of sintered silver

Conclusions

Power electronics packaging for the safe and reliable operation of wide-bandgap devices at high temperatures is a challenging research goal. This project focuses on reliability evaluation and lifetime prediction of bonded materials to determine their applicability in high-temperature packaging. The bonded materials of interest are polymeric materials and sintered copper.

Although initial SAM images of polymeric bonded materials indicated good bonding quality, it performed poorly under thermal cycling conditions with the thermoset polymer samples failing in just 100 cycles. These results indicate that thermoset polymer is not reliable for operation at temperatures above 175°C. Compared to the thermoset polymer, the rate of degradation in thermoplastic polymer samples was found to be slower, and the total defect percentage was estimated to be around 16% after 600 thermal cycles.

Sintered copper, a promising low-cost alternative to sintered silver, is currently undergoing thermal shock experiments at NREL. These samples include two different bond patterns and baseplates with different thicknesses. After 500 cycles, the defect percentages in samples with thicker baseplates were found to be around 12%. The cycling of these samples will continue until the defect amount reaches 20% or up to 2,000 cycles. In FY24, we plan to conduct power cycling experiments on sintered copper and compare its reliability against sintered silver and SAC305 solder.

Finally, we compared the lifetime or defect percentage prediction performance of statistical and machine learning models by leveraging the SAM images of eutectic lead solder under thermal cycling. Among the different models that we investigated, Holt linear and MLP models resulted in the most accurate predictions of defect growth. Overall, statistical models outperformed the machine learning models in this time-series forecasting study.

Key Publications

1. P. Paret, D. Finegan, and S. Narumanchi. 2023. "Artificial Intelligence for Power Electronics in Electric Vehicles: Challenges and Opportunities." *ASME J. Electron. Packag.* 145 (3): 034501. <https://doi.org/10.1115/1.4056306>.
2. P. Paret, J. Major, D. DeVoto, S. Narumanchi, C. Ding, and G.-Q. Lu. 2022. "Reliability and Lifetime Prediction Model of Sintered Silver Under High-Temperature Cycling." *IEEE Journal of Emerging and Selected Topics in Power Electronics* 10 (5): 5181–5191. doi: 10.1109/JESTPE.2021.3121195.

3. C. Imediegwu, S. Graham, D. G. Pahinkar, S. Narumanchi, P. Paret, and J. Major. 2022. “Interdiffusion and formation of intermetallic compounds in high-temperature power electronics substrate joints fabricated by transient liquid phase bonding.” *Microelectron. Reliab.* 137: 114788. doi: 10.1016/j.microrel.2022.114788.

References

1. M. Wang, Y. Shan, Y. Mei, X. Li, and G. Lu. 2020. “Sintered-copper Die-attach: Processing, Properties, and Reliability.” Presented at CIPS 2020; 11th International Conference on Integrated Power Electronics Systems, 24–26 March 2020, 1–6.
2. L. Fan, F. Zhang, H. Fan, and C. Zhang. 2019. “Brief review of image denoising techniques.” *Visual Computing for Industry, Biomedicine, and Art* 2 (1): 7. doi: 10.1186/s42492-019-0016-7.

Acknowledgements

The author acknowledges the contributions of Sri Krishna Bhogaraju in fabricating the sintered copper samples at CuNex GmbH, Germany, and obtaining the initial SAM images. The author would also like to thank Joshua Major at NREL for bonding the polymer material-based samples for thermal cycling.

I.1.6 Advanced Packaging Designs – Reliability and Prognostics (National Renewable Energy Laboratory)

Douglas DeVoto, Principal Investigator

National Renewable Energy Laboratory (NREL)
15013 Denver West Parkway
Golden, CO 80401
E-mail: douglas.devoto@nrel.gov

Susan Rogers, DOE Technology Development Manager

U.S. Department of Energy
E-mail: susan.rogers@ee.doe.gov

Start Date: October 1, 2018
Project Funding: \$150,000

End Date: September 30, 2024
DOE share: \$150,000

Non-DOE share: \$0

Project Introduction

The U.S. Department of Energy’s Office of Energy Efficiency and Renewable Energy Vehicle Technologies Office and the Electrical and Electronics Technical Team have proposed aggressive research and development targets [1] aimed at improving power electronics technology to enable the mass-market penetration of electric-drive vehicles. Achieving these aggressive power electronics targets will require a decrease in cost (year 2025 cost target: \$2.70/kW) and an increase in power density (year 2025 power density target: 100 kW/L) as compared with current, on-road technology. Replacing traditional silicon device-based components with more efficient and higher-temperature wide-bandgap semiconductor device-based components will enable increasing the power density. However, meeting the power density target will also require innovative packaging and thermal management solutions to increase the heat fluxes dissipated and allow for compact electronics packaging.

Decreasing the thermal resistance pathway in power electronics packages is a primary objective for maximizing the performance of wide-bandgap devices. This can be accomplished by either replacing package layers with new materials that enable greater thermal, electrical, and reliability performance or eliminating layers and components through new packaging designs. Safe and robust operation of the power electronics requires electrical isolation of the high-voltage circuitry within the power electronics module. For example, typical power electronics modules use a ceramic material within the package for electrical isolation.

Objectives

The primary deliverable for this project will be to construct a power electronics package utilizing an organic, electrically insulating substrate material and demonstrate superior thermal performance and greater reliability under thermal cycling, thermal aging, vibration, power cycling, and electrical high-potential evaluation over traditional packages. This will be accomplished through the following tasks:

- *Design optimization of a power electronics package.* A multiphysics optimization process will incorporate the electrically insulating substrate alternative into a novel power electronics package. Electrical, thermal, and mechanical constraints will be balanced through this optimization.
- *Prototype construction and evaluation.* Example power electronics packages based on an electrically insulating substrate alternative will be developed. A multiphysics modeling evaluation of the sample geometries will determine thermal and thermomechanical performance, while a reliability assessment will measure performance during accelerated tests.

Approach

The project aim is to develop a power-dense, reliable, and cost-effective 3D power electronics package enabled by an alternative electrical isolation material: an organic direct-bond copper (ODBC) substrate. This material

provides equivalent electrical isolation to current technologies while providing high thermomechanical reliability at high device junction temperatures, as well as enabling higher power densities. In addition, eliminating design constraints associated with traditional ceramic substrates reduces device-to-coolant thermal resistance, simplifies package design, and offers more design flexibility. This package design will eliminate component layers in a new, low-cost, simplified manufacturing process for a packaging design that will allow for higher power densities and reliability. Additionally, the new circuit board structure will transport heat out of encapsulated component areas within a 3D structure. This work is being performed in collaboration with Oak Ridge National Laboratory and DuPont.

Traditional ceramic substrates perform three functions in a power module assembly: a thermal management path from the switching devices to the heatsink or cold plate, electrical connections between the devices and external busbars, and electrical isolation of the thermal management components. Direct-bond-copper (DBC) substrates with an aluminum oxide (Al_2O_3) ceramic were conventionally selected for power modules due to their adequate performance in electrical isolation, thermal management, and reliability. A thin copper-oxide layer on the Cu foils is used to bond the metallization layers to the ceramic in an oxygen-rich environment at a eutectic point of $1,066^\circ\text{C}$. The process temperature must be carefully controlled, as the melting point of Cu is $1,085^\circ\text{C}$. Foils are symmetrically bonded to both sides of the ceramic to prevent cracking or warping during cooling to room temperature [2]. Alternative ceramic materials have aimed to improve performance over Al_2O_3 substrates by increasing bending strength, fracture toughness, thermal conductivity, or dielectric strength, or more closely matching their coefficient of thermal expansion (CTE) to Si or wide-bandgap devices. Zirconia-toughened alumina (ZTA) substrates add a percentage of zirconium oxide (ZrO_2) to Al_2O_3 prior to sintering to improve the ceramic's bending strength. ZTA substrates typically have a lower thermal conductivity than Al_2O_3 substrates but can compensate for this by using a thinner ceramic layer due to their enhanced mechanical properties [3]. Aluminum nitride (AlN) ceramics have been selected for their higher thermal conductivity and low CTE that is closely aligned with semiconductor devices. AlN is bonded to Al metallization layers through a direct-bond-aluminum (DBA) brazing process using an Al-Si alloy film that exhibits a eutectic phase at 577°C [4]. Further package CTE alignment with DBA substrates can be obtained by selecting aluminum silicon carbide (AlSiC) baseplates. AlN substrates can also be bonded with Cu metallization layers through the DBC process or by active metal brazing, which commonly bonds AlN or silicon nitride (Si_3N_4) to Cu with a brazing material under an inert gas or vacuum environment. The higher fracture toughness of Si_3N_4 and ZTA ceramics has allowed for thicker Cu metallization layers and higher device operating temperatures, but metallization layers have typically not exceeded thicknesses of 1.0 mm. Substrate reliability studies have shown that the lifetime of substrates significantly decreases as metallization layer thickness increases from modeling [5] and experimental [6] results. Previous work has outlined the thermal performance and reliability of the ODBC substrate [7], [8] and has shown that the thermal resistance of an ODBC substrate is comparable to ceramic-based substrates. Reliability experiments have shown no concerns with thicker (>1.0 mm) Cu metallization layers under thermal cycling conditions. Recent efforts have focused on synthesizing ODBC substrates into prototype half-bridge power module designs [9], [10].

Results

Polyimide Material Analysis

The polyimide material from DuPont (Temprion electrically insulating film) was evaluated for its ability to be patterned and bonded through several experimental analysis techniques. Previous work mechanically cut the polyimide to shape with a sharp blade, but this manual process limited the complexity of shapes that could be patterned. Instead, patterning the polyimide with a carbon dioxide (CO_2) laser was assessed. Two common commercial laser wavelengths are $9.3\ \mu\text{m}$ and $10.6\ \mu\text{m}$, both within the range of infrared light. To aid in the decision process between the laser wavelengths, Fourier-transform infrared spectroscopy was completed to obtain the infrared spectrum of absorption of the polyimide, shown in Figure I.1.6.1.

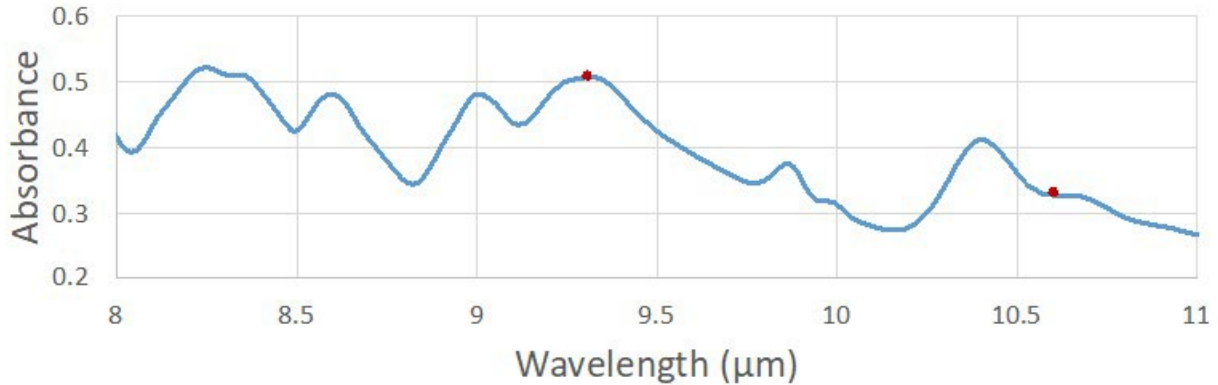


Figure I.1.6.1 Polyimide absorption analysis

Results indicate that the polyimide has a higher absorption response at the 9.3- μm wavelength than at 10.6 μm , allowing for a more efficient cutting process. Next, thermogravimetric analysis was completed to evaluate the polyimide's thermal stability.

Figure I.1.6.2 shows that the material is stable past 500°C, with an onset temperature of thermal decomposition of 594°C under air. The analysis was repeated under a nitrogen environment, and a similar onset temperature of thermal decomposition of 596°C was measured. This confirms the large, stable processing window that has previously been observed during bonding.

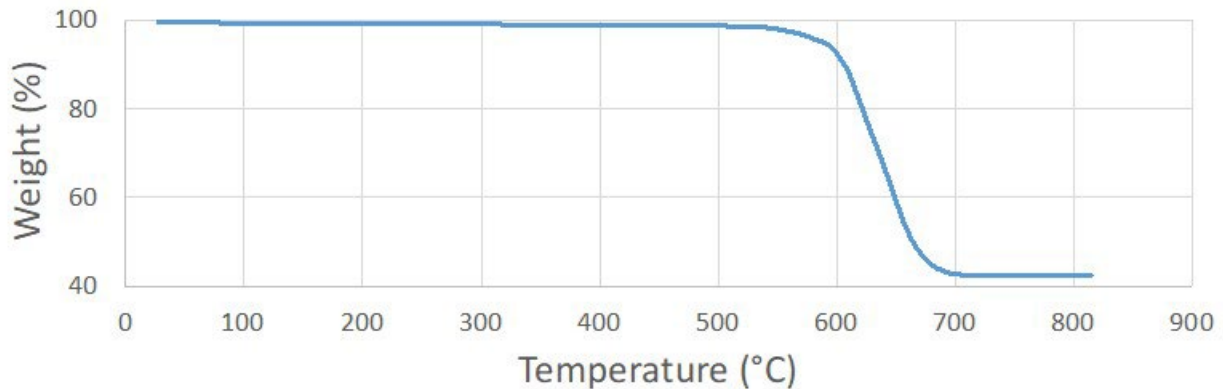


Figure I.1.6.2

Next, the polyimide was patterned in two different laser cutters. A test pattern was first created and patterned on a Universal Laser Systems VLS3.60DT laser platform. The system used a 30-W, 9.3- μm CO₂ laser with a high-power, density-focusing optics option that helps collimate and focus the laser to a smaller focal spot size, which then creates a smaller heat-affected zone (HAZ). The laser power was optimized, and a power level of 19.5 W was found to create a clean cut. Charred material in the HAZ, measured to be approximately 85 μm wide, was present along the cut path but was removed by placing the polyimide sample in an ultrasonic bath. The test pattern and cut performance are shown in Figure I.1.6.3.



Figure I.1.6.3 Test pattern and HAZ before ultrasonic cleaning

This analysis was repeated on a FLUX beamo 30-W, 10.6- μm CO₂ desktop laser cutter. The less optimal laser wavelength and basic focusing optics meant that the quality of the laser cut would be lower, but testing was needed to determine if the tolerances would still be acceptable for substrate patterning. A standard test pattern was first used to cut the polyimide at a variety of power levels and cutting speeds. The test pattern is shown in Figure I.1.6.4.



Figure I.1.6.4 Test cut optimization pattern

Each rectangle corresponds to a different power level and cutting speed. For clarity, Table I.1.6.1 quantifies the test pattern labels to exact power and speed values.

Table I.1.6.1 Laser Optimization Pattern Power and Speed Levels

Power (W)	P10	P15	P20	P25	P30	P35	P40	P45	P50	P55	P60
	3	4.5	6	7.5	9	10.5	12	13.5	15	16.5	18
Speed (mm/s)	S003	S004	S005	S006	S007	S008	S009	S010	S012	S014	
	3	4	5	6	7	8	9	10	12	14	

The test cut pattern process took approximately 10 minutes to complete on the desktop laser cutter. Afterwards, the pattern was inspected for cut quality. For settings at higher power levels and lower speeds, the polyimide was severely burned and no longer had a linear cut path. Lower power levels, between 3 and 4.5 W, at first appeared to not completely cut through the polyimide. However, on closer inspection, only a small amount of polyimide material remained in the desired cut path. This accidental creation of perforations had the benefit of securely holding samples within the larger polyimide sheet during the cutting process. Small samples that were completely freed during cutting tended to circulate around in the work area due to the need for exhaust extraction of smoke and fumes. The cutting process and the completed optimization pattern are shown in Figure I.1.6.5.

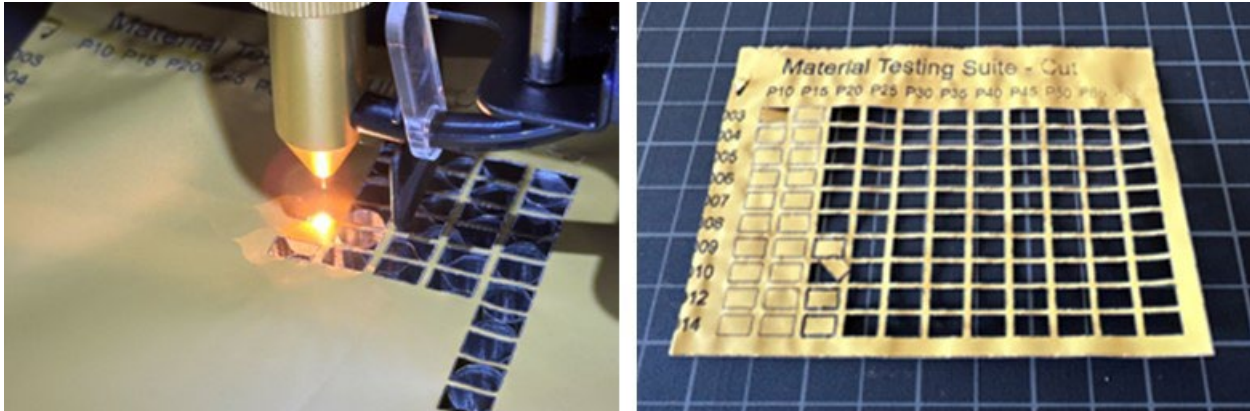


Figure I.1.6.5 Test cutting process (left) and completed optimization pattern

After inspection, a power level of 3 W at a speed of 10 mm/s were selected as the optimal parameters for cutting polyimide with the desktop laser cutter. These values are emphasized in bold in Table I.1.6.1. The HAZ, seen in Figure I.1.6.6, was found to be larger at approximately 200 μm in width, an increase over the commercial laser by 115 μm . Due to the change in both laser wavelength and focusing optics, it is not possible to quantify the impact of each parameter individually on the size of the HAZ.



Figure I.1.6.6 HAZ from 30-W, 10.6- μm CO₂ desktop laser cutter

Samples cut from both laser machines were sonicated in an ultrasonic bath for 5 minutes. The cleaned samples were again inspected under an optical microscope and are shown in Figure I.1.6.7. The overall quality of both samples after sonication is similar. The cut from the 10.6- μm laser is observed to be rougher, but in context of required tolerances for power module fabrication, it is negligible. The widths of the HAZs from either laser can be compensated for by adding an offset to the desired dimensioned drawings, allowing for similar final sample sizes from either laser system.

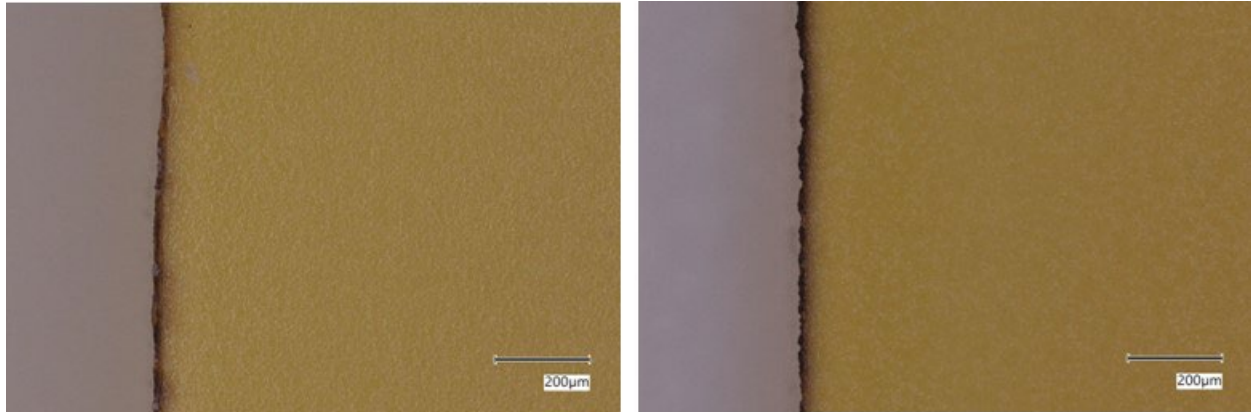


Figure I.1.6.7 Comparison of edge quality from 9.3- μm CO₂ laser (left) and 10.6- μm CO₂ laser (right)

Power Electronics Module Fabrication

With the lessons learned on optimized laser patterning of polyimide, substrate patterns for a power module design utilizing the organic insulating substrate were cut. Three polyimide layers were cut using the optimized settings of the 30-W, 10.6- μm CO₂ desktop laser cutter, shown in Figure I.1.6.8.

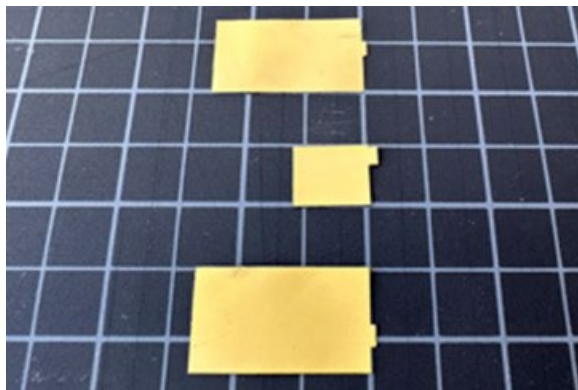


Figure I.1.6.8 Polyimide layers for module fabrication

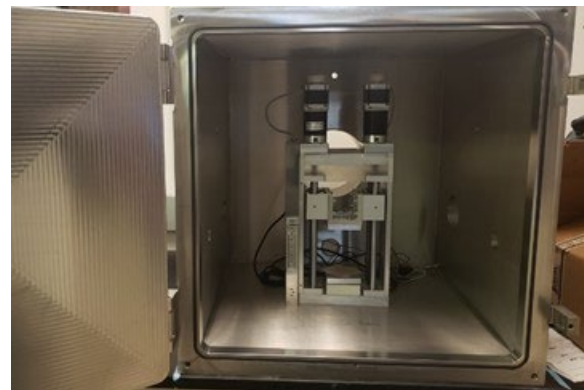


Figure I.1.6.9 Vacuum high-temperature press

The design and fabrication steps for this module were detailed in the previous year's annual progress report [\[10\]](#) and will not be repeated here for brevity. One significant improvement in the bonding process has been made by installing the high-temperature press into a vacuum chamber. Bonding in a vacuum or an inert environment eliminates detrimental oxidation on Cu surfaces during the bonding process. The vacuum high-temperature press is shown in Figure I.1.6.9.

The power module design from FY 2022 is shown in Figure I.1.6.10. This year has focused on bonding the Cu busbars and polyimide insulation layers together.

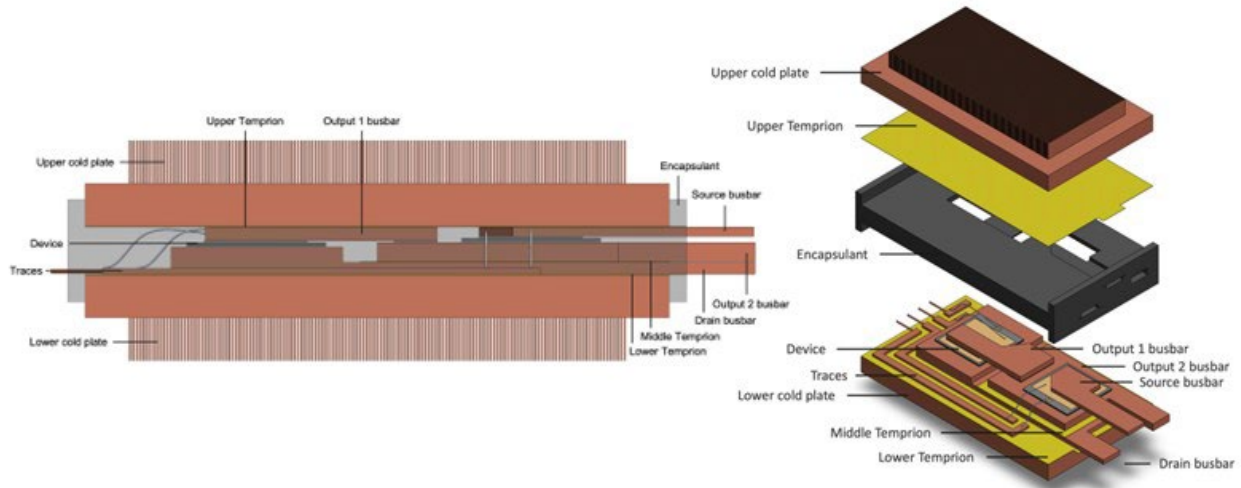


Figure I.1.6.10 Half-bridge power module design

A partial subassembly of this power module design is shown in Figure I.1.6.11 with the lower cold plate, polyimide layers, busbar layers, and devices shown. Cu busbars and cold plates were machined on a computer numerical control router. The fabrication steps were modified to not machine any Cu parts after they have been bonded to the polyimide layer. While the bond between both materials is strong, the machining process imparts shear stresses into the interface that can weaken smaller interfaces. Manually aligning Cu and polyimide layers has also proven to be difficult. In the future, additional fixtures will be machined to keep components aligned during the bonding process.

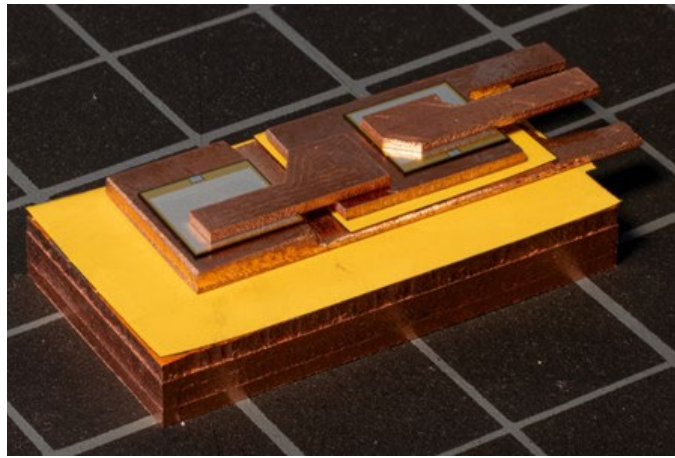


Figure I.1.6.11 Half-bridge power module assembly

Due to supply chain constraints, SiC metal–oxide–semiconductor field-effect transistors (MOSFETs) with topside metallization layers compatible with Ag sintering were not available to integrate into the module, so SiC junction-gate field-effect transistors (JFETs) with topside Al metallization were used instead. The output 1 busbar and source busbar were placed on top of the JFETs for illustrative purposes but are not bonded with Ag sinter at this time. The package will also require traces and wire bonds for gate and Kelvin source connections. These additional steps for a fully functional package will be completed in FY 2024.

Conclusions

The project aim is to develop a power-dense, reliable, and cost-effective 3D power electronics package enabled by an alternative electrical isolation material. The project accomplishments for FY 2023 are summarized below:

- Polyimide material was characterized for compatibility with laser patterning. Laser cutting parameters of power and speed were optimized for the polyimide material.
- Bonding ODBC substrates was improved with the integration of a high-temperature press into a vacuum chamber. A simplified packaging process was developed and tested with ODBC substrates in a double-side-cooled module, with a functional power module prototype to be completed in FY 2024.

Key Publications

1. D. DeVoto. 2023. “Advanced Packaging Designs – Reliability and Prognostics (NREL).” In *Electrification: 2022 Annual Progress Report*, Washington, D.C.: U.S. DOE EERE VTO, 68–76.
2. E. Gurpinar, R. Sahu, B. Ozpineci, and D. DeVoto. 2020. “Analysis and Optimization of a Multi-Layer Integrated Organic Substrate for High Current GaN HEMT-Based Power Module.” 2020 IEEE Workshop on Wide Bandgap Power Devices and Applications in Asia (WiPDA Asia), Japan, September 2020.

References

1. U.S. DRIVE. 2017. *Electrical and Electronics Technical Team Roadmap*. Washington, D.C.: USDRIIVE. <https://www.energy.gov/eere/vehicles/downloads/us-drive-electrical-and-electronics-technical-team-roadmap>.
2. A. Miric and P. Dietrich. 2015. “Inorganic Substrates for Power Electronics Applications.” *Heraeus Deutschland*.
3. J. Park, M. Kim, and A. Roth. 2014. “Improved thermal cycling reliability of ZTA (Zirconia Toughened Alumina) DBC substrates by manipulating metallization properties.” CIPS 2014; 8th International Conference on Integrated Power Electronics Systems, 2014, 1–9.
4. H. T. Lin, A. A. Wereszczak, and S. Waters. 2013. “Low-Cost Direct Bonded Aluminum (DBA) Substrates.” 2013 DOE VTO Annual Merit Review, Washington, D.C., May 2013.
5. L. Xu, Y. Zhou, and S. Liu. 2013. “DBC substrate in Si- and SiC-based power electronics modules: Design, fabrication and failure analysis.” 2013 IEEE 63rd Electronic Components and Technology Conference, 2013, 1341–1345. doi: 10.1109/ECTC.2013.6575747.
6. L. Dupont, Z. Khatir, S. Lefebvre, and S. Bontemps. 2006. “Effects of metallization thickness of ceramic substrates on the reliability of power assemblies under high temperature cycling.” *Microelectronics Reliability*, 46 (9–11): 1766–1771. <https://doi.org/10.1016/J.MICROREL.2006.07.057>.
7. D. DeVoto. 2020. “Advanced Packaging Designs – Reliability and Prognostics (NREL).” In *Electrification: 2019 Annual Progress Report*, Washington, D.C.: U.S. DOE EERE VTO, 95–101. doi:10.2172/1637435.
8. D. DeVoto. 2021. “Advanced Packaging Designs – Reliability and Prognostics (NREL).” In *Electrification: 2020 Annual Progress Report*, Washington, D.C.: U.S. DOE EERE VTO, 57–64.
9. D. DeVoto. 2022. “Advanced Packaging Designs – Reliability and Prognostics (NREL).” In *Electrification: 2021 Annual Progress Report*, Washington, D.C.: U.S. DOE EERE VTO, 70–77.
10. D. DeVoto. 2023. “Advanced Packaging Designs – Reliability and Prognostics (NREL).” In *Electrification: 2022 Annual Progress Report*, Washington, D.C.: U.S. DOE EERE VTO, 68–76.

Acknowledgements

We acknowledge the significant contributions of Joshua Major, Bob Allen, and Joel Miscall.

I.1.7 Power Module Precursors and Prognostics (National Renewable Energy Laboratory)

Faisal Khan, Principal Investigator

National Renewable Energy Laboratory (NREL)
15013 Denver West Parkway
Golden, CO 80401
Email: faisal.khan@nrel.gov

Susan Rogers, DOE Technology Development Manager

U.S. Department of Energy
Email: susan.rogers@ee.doe.gov

Start Date: October 1, 2022

End Date: September 30, 2024

Project Funding: \$150,000

DOE share: \$150,000

Non-DOE share: \$0

Project Introduction

The 2017 *Electrical and Electronics Technical Team Roadmap* [1], aiming at improving power electronics technologies to promote the market penetration of electric vehicles, highlights aggressive R&D targets that include increasing module-level power density to >100 kW/L and decreasing system-level costs to <\$2.70/kW USD—huge leaps compared to current state-of-the-art technologies. These requirements point to two directions for power module R&D: pushing existing state-of-the-art semiconductor and power module technologies further toward the boundaries of the safe operating area for higher utilization and creating new generations of wide-bandgap semiconductor components based on silicon carbide (SiC) and gallium nitride (GaN). Both SiC- and GaN-based power modules require close monitoring of the state of health and early identification of failure scenarios. Prolonged operation near the safe operating area boundaries results in statistically higher probability of degradation and failures. The causes of failures are certain material and geometrical properties of the new semiconductors (such as the much thinner gate oxide layer of SiC metal-oxide-semiconductor field-effect transistors [MOSFETs] compared to their silicon-based counterparts) and higher failure rates due to less maturity in fabrication techniques. In order to maintain the operational safety of electric vehicles, degradation and failure detection and prognostics are of particular importance.

In this project, research is being conducted to identify precursors to power module aging, degradation, and failure, and correspondingly develop prognostics techniques that will be able to utilize the identified precursors to evaluate the state of health and detect the onset of failures for the information of users to achieve higher vehicle safety and reliability. The challenges in this project mainly include the effort required to build the necessary infrastructure for creating power module samples with different modes and levels of aging, degradation, and faults for analysis and testing; the effort needed to upgrade and configure the testing workbench to handle signals with very high frequency and subtle changes; and conceiving strategies for implementing detection in practical and nonintrusive ways with low cost.

Objectives

The key objective of this project is to develop and validate complete solutions for aging, degradation, and failure detection and evaluation with simplified and low-cost hardware implementation. Two sub-objectives are the following:

Applying accelerated life tests (ALT) to multiple power module samples to create a collection of aged modules with known aging levels; categorizing these samples to form a database and correlating specific phenomena to degradation mechanisms and conditions; identifying most promising precursors for detection and evaluation.

Developing and validating low-cost hardware solutions to measure device degradation capable of implementing inside a gate driver.

Approach

The approach to achieving the milestones can be summarized in three steps: review, identification, and development.

The review process is necessary for several reasons. First, power device/module aging mechanism analysis, precursor identification, and detection techniques are not entirely new areas for research. Extensive research exists with many accounts of promising results. Second, these mainly come from academia and are highly device-specific. Therefore, a review has significance in identifying the most advanced hardware configurations and methodologies for ALT of power module samples for the most relevant types of devices and modules to the wide-bandgap device-based next-generation modules currently under development in our lab. In the future, silicon-based devices will also be included for the completeness of the project.

Different aging mechanisms and their indicators have been extensively studied and summarized [2], [3], [4]. Generally, there are two types of aging: device aging and packaging aging. For SiC MOSFETs, the indicators for device aging mainly include increases of gate threshold voltage (V_{th}), gate leakage current (I_{gss}), and drain-source leakage current (I_{dss}). The indicator for packaging aging mainly includes increases of on-state resistance ($R_{DS,ON}$). These are the most prominent and consistent indicators. Other reported indicators include increases of body diode forward voltage drop (V_{bdf}) and turn-on delay time (t_{on}). The aging mechanisms are also reported in the literature, with a detailed theoretical foundation available from [5].

The methodologies for various types of ALTs that may trigger different modes of aging and degradation, as well as the design of their corresponding hardware and cycling procedures, are described in [3]. Generally, for SiC MOSFETs, there are two main groups of ALTs: gate cycles to induce gate area degradations and thermal cycles to induce packaging-level failures. For each group, specific power stage configurations for the ALTs can be applied to emulate the real-world operation of the respective power converters to better reflect actual aging scenarios.

For precursor detection, gate-driver-integrated detection mechanisms are of great interest both because of the susceptibility to degradation of gate area in SiC [5], [6] which makes the gate circuit elements preferable since they are close to the degradation source, and its convenience in usage. Gate-driver-integrated detectors utilizing Miller voltage [7], gate leakage current [8], junction temperature [9], ON-state resistance [10], input capacitance curve [11], and spectrum analysis [12] have been proposed. All the previous work reported effective results, although some studies reported issues such as cost, complexity in connection, and being target-specific.

There are no reported online aging detection solutions from industry. Reliability and lifetime estimations based on extensive module tests and field data logs are typically used in industry for service purposes.

Based on the results from the aging mechanism and precursor review, aging stations were constructed considering the best results from available resources. ALTs on multiple SiC MOSFET samples from different manufacturers and models were conducted. The results are given in the next section.

Based on the results from the integrated precursor detection review and the precursor types featured in the corresponding literature, V_{th} and $R_{DS,ON}$ are **identified** as aging precursors to be detected in the current phase of the project.

Based on all the findings described above, a gate-driver-integrated detection system is **developed** with the capability of detecting both V_{th} and $R_{DS,ON}$ without interfering with the normal operation of the power stage. Experimental validation for the current phase is given in the next section.

Results

For this phase of the project, a significant amount of effort has been put into building the foundations for subsequent research and testing, including the procurement and preparation of SiC MOSFET samples of

different makes and models, configuration and testing of the in-house aging station, and training for designing and testing high-speed and high-accuracy circuit boards. The end results built on these foundations is described below.

ALTs on Various SiC MOSFET Samples and Aging Results

The in-house aging station has four channels. The gate voltage for all channels is 20 V. The amperage for each channel can be independently adjusted within a range of 0–23 A. All channels work in temperature-feedback mode—i.e., a temperature probe for each channel is located in the vicinity of the device under test (DUT), whose temperature reading is used as feedback to control the ON and OFF state of the current flowing through the DUT. When ON, the DUT is heated up from the ON-state resistive loss, and when OFF, the DUT is cooled down by forced convective flow of air provided by the fan beneath the DUT. At this point, seven samples of SiC MOSFETs from four models (WolfSpeed CCS020M12CM2, C2M0080120D, C3M0075120D, and Infineon FS55MR12W1M1H-B11) have been prepared as DUTs as shown in Figure I.1.7.1.

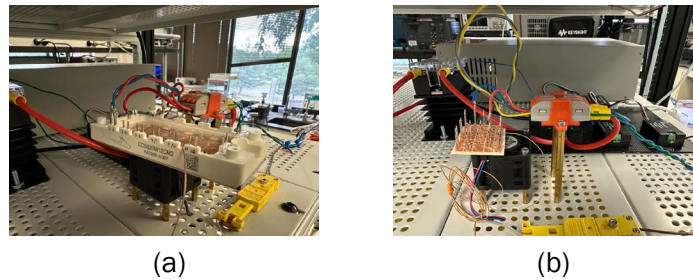


Figure I.1.7.1 ALTs on various SiC MOSFET module samples: (a) power/temperature cycling on the CCS020-M12CM2 six-pack module and (b) power/temperature cycling on the FS55MR1-2W1M1H-B11 six-pack module

For the two six-pack power modules, the rated gate voltage is 20 V in continuous operation, the temperature range is controlled to 50°C to 90°C, and the current is fixed at 20 A. Given the rated gate voltage and relatively high thermal capacitance of the packaging, thermal cycles induced by power cycles are effectively applied on the DUT. For the two TO-247 single modules, the rated gate voltage is 15 V in continuous operation, the temperature range is controlled from 50°C to 55°C, and the current is fixed at 18 A. Given the low-rated gate voltage versus the 20 V the aging station can apply, the relatively low thermal capacitance of the packaging, and the low temperature and narrow temperature range, the gate switching cycles are effectively applied on the DUTs.

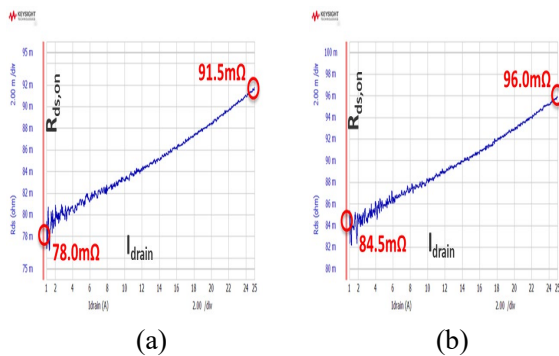


Figure I.1.7.2 ALT result on the CCS020-M12CM2 device after approximately 10,000 cycles: (a) $R_{ds,on}$ versus I_{drain} of a new device in the CCS020-M12CM2 six-pack and (b) $R_{ds,on}$ versus I_{drain} of an aged device in the CCS020-M12CM2 six-pack

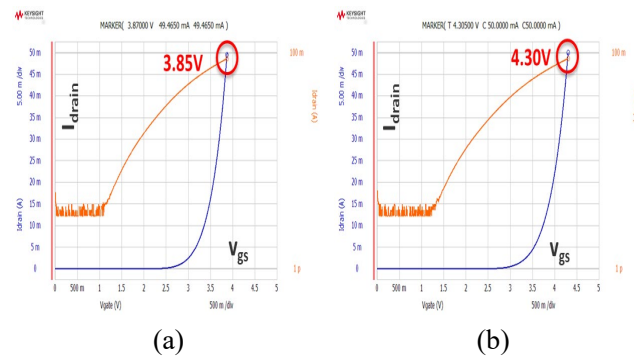


Figure I.1.7.3 ALT result on the C3M0075120D device after approximately 55,000 cycles: (a) V_{th} of a new device in the C3M0075120D TO-247 single module and (b) V_{th} of an aged device in the C3M0075120D TO-247 single module

After approximately 10,000 cycles on one device (Phase V upper switch) of the CCS020M12CM2 six-pack, the $R_{DS,ON}$ increased by approximately 7 m Ω , as shown in Figure I.1.7.2. After approximately 55,000 cycles on one of the C3M0075120D TO-247 single modules, there was an approximately 0.45 V increase in V_{th} , as shown in Figure I.1.7.3. These results are generally consistent with the underlying idea for the respective channels—the former to induce thermal-related aging and the latter to induce gate-related aging. These two sets of samples will be used for the subsequent precursor detector testing and validation. For the other two channels and their corresponding DUTs, the aging results showed no clear patterns for any change in precursor values. Therefore, the ALT conditions for these two will be further adjusted to create aging effects with more observable patterns.

Detection Principle: Using Change of Gate-Source Voltage Peaks to Detect the Changes in V_{th} and $R_{ds,on}$

In order to utilize the correlation between an easy-to-detect electrical signal with V_{th} and $R_{DS,ON}$, the change of resonant peak values of gate-source voltage (v_{gs}) at turn-ON and turn-OFF switching transients have been identified to be the signal of interest after several theoretical reasoning and simulations, and the corresponding circuit hardware and implementations are designed to extract the change of v_{gs} peaks. The reasoning and design process are described as follows.

A half-bridge module, one of the most commonly used fundamental structures for power electronic converters, is taken as the subject of study. In this subsection, the behavior and corresponding equivalent circuit during the commutation transients (from ON to OFF or vice versa) are modeled and analyzed to reveal the pattern of v_{gs} change. The two resonant loops in Figure I.1.7.4 are delimited by the conduction state of the channel, which is controlled by the gate voltage. Generally, when $v_{gs} < V_{th}$, the channel is in the OFF state, and the second resonant loop is engaged. When $v_{gs} > V_{th}$, the channel is in conduction state, and the gate transient is generally restrained within the first resonant loop. Using simplified models for the nonlinear components yields the following model for the equivalent circuit for a specific leg in the form of a system of ordinary differential equations, as shown in Figure I.1.7.5, where R_{g1} and R_{g2} are gate driving loop resistances, C_{gs} , C_{gd} , and C_{ds} are gate-source capacitance, gate-drain capacitance, and drain-source capacitance, respectively. R_{ds1} and R_{ds2} are V_{gs} -dependent and temperature-dependent channel resistances, respectively. R_{dd1} and R_{dd2} are V_{ds} -dependent equivalent body diode resistances for the respective MOSFETs. C_{CT} is the equivalent total capacitance of the complementary MOSFET when the channel is in the OFF state. L_p and R_p are the power loop parasitic inductance and resistance, respectively. V_B and I_L are the steady-state DC bus voltage and quasi-steady-state load current at the beginning of transients, respectively. i_g , v_{gs} , v_{gd} , v_{ds} , i_p , and V_{ct} are gate driving current, gate-source voltage, gate-drain voltage, drain-source voltage, power loop current, and complementary switch voltage, respectively. K_{subs} are the various coefficients.

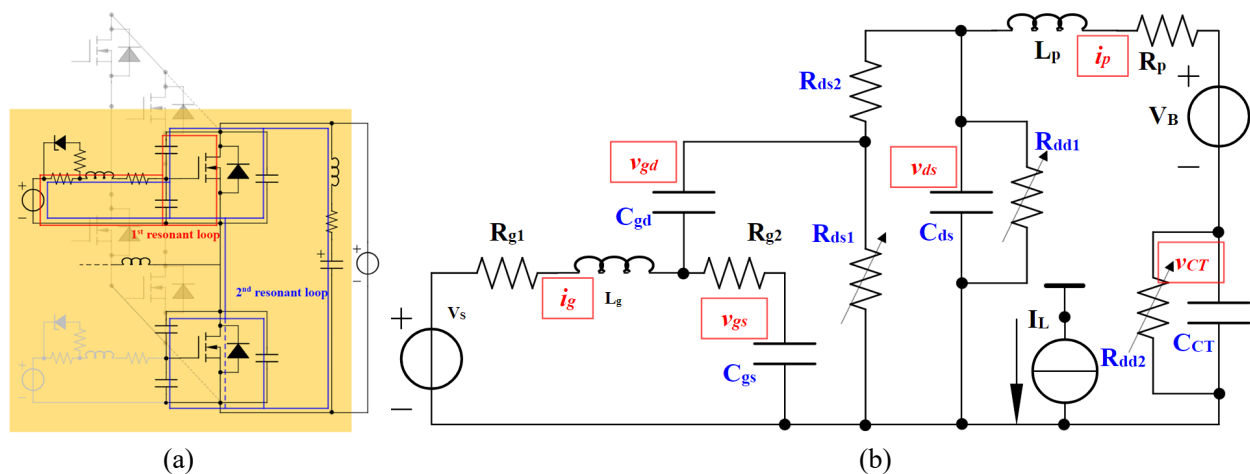


Figure I.1.7.4 Transient behavior and equivalent circuit: (a) two resonant loops and (b) circuit model. Variable-dependent and nonlinear components are highlighted in blue.

$$\begin{aligned}
 TA &= \left(-\frac{v_{ds}(t)}{R_{ds1}(v_{ds}(t)) + R_{ds2}} + \frac{v_{gs}(t) - v_{gd}(t) + R_{g2} \cdot i_g(t)}{R_{ds1}(v_{ds}(t))} \right) \\
 &\quad / \left(1 + \frac{R_{g2}}{R_{ds1}(v_{ds}(t))} + \frac{R_{ds1}(v_{ds}(t))}{R_{ds1}(v_{ds}(t)) + R_{ds2}} \right) \quad (1) \\
 \frac{dv_{gs}(t)}{dt} &= \frac{1}{C_{gs}(v_{gs}(t))} (i_g(t) - TA) \quad (2) \\
 \frac{dv_{gd}(t)}{dt} &= \frac{TA}{C_{gd}(v_{gd}(t))} \quad (3) \\
 \frac{dv_{ds}(t)}{dt} &= \frac{1}{C_{ds}(v_{ds}(t))} \left(-\frac{v_{ds}(t)}{R_{ds1}(v_{ds}(t)) + R_{ds2}} - i_p(t) - \frac{v_{ds}(t)}{R_{dd1}(v_{ds}(t))} \right. \\
 &\quad \left. + \frac{R_{ds1}(v_{ds}(t))}{R_{ds1}(v_{ds}(t)) + R_{ds2}} TA \right) \quad (4) \\
 \frac{dv_{cr}(t)}{dt} &= \frac{1}{C_{cr}(v_{cr}(t))} \left(i_p(t) - \frac{v_{cr}(t)}{R_{dd2}(v_{cr}(t))} \right) \quad (5) \\
 \frac{di_g(t)}{dt} &= \frac{1}{L_g} (V_S - (R_{g1} + R_{g2}) i_g(t) - v_{gs}(t) + R_{g2} \cdot TA) \quad (6) \\
 \frac{di_p(t)}{dt} &= \frac{1}{L_p} (v_{ds}(t) - R_p \cdot i_p(t) - v_{cr}(t) - V_B) \quad (7) \\
 R_{ds1}(v_{ds}(t)) &= 1 / \left(2K_{Rds1} \cdot \ln \left(1 + K_{Rds1} \cdot e^{v_{gs}(t) - V_{th}} \right)^{K_{Rds3}} \right) \quad (8) \\
 C_{gs}(v_{gs}(t)) &= C_{GS} \left(1 - K_{dCgs} \frac{1}{2} (\tanh(K_{Cgs} (v_{gs}(t) - V_{Cgs} (t)) + \right. \\
 &\quad \left. \tanh(K_{Cgs} (v_{gs}(t) - V_{Cgs} (t)))) \right) \quad (9) \\
 C_{gd}(v_{gd}(t)) &= C_{GD} \left(\left(1 - \frac{1}{2} (1 - \tanh(v_{gd}(t))) v_{gd}(t) \right) \right. \\
 &\quad \left. \cdot \left(1 + K_{Cgd1} \frac{1}{2} (1 + \tanh(-K_{Cgd2} v_{gd}(t) - K_{Cgd3})) \right) \right) \quad (10) \\
 C_{ds}(v_{ds}(t)) &= C_{DS} \cdot K_{Cds1} \left(1 + \frac{1}{2} (1 + \tanh(K_{Cds3} \cdot v_{ds}(t))) \right. \\
 &\quad \left. v_{ds}(t) K_{Cds3} \cdot v_{ds}(t) \right)^{-0.5} \quad (11) \\
 C_{cr}(v_{cr}(t)) &= C_{ds}(-v_{cr}(t)) + 1 / \left(\frac{1}{C_{gd}(v_{cr}(t))} + \frac{1}{C_{GS}} \right) \quad (12) \\
 R_{dd}(v_{dd}) &= R_{dd,on} \cdot \frac{1}{2} (1 - \tanh(K_{dd}(v_{dd} + V_{ddh}))) \\
 &\quad + R_{dd,off} \cdot \frac{1}{2} (1 + \tanh(K_{dd}(v_{dd} + V_{ddh}))) \quad (13) \\
 R_{dd1}(v_{ds}(t)) &= R_{dd}(v_{ds}(t)) \cdot R_{dd2}(v_{cr}(t)) = R_{dd}(-v_{cr}(t)) \quad (14)
 \end{aligned}$$

Figure I.1.7.5 Model for the two resonant loops during transients.

Using numerical solvers for this model and taking parameter values based on any real-world module, we can obtain the full knowledge of the behavior of the subject switch leg for the time shortly after the switching.

The implications of the changes in $R_{ds,on}$ and V_{th} , two of the most reliable and commonly referred aging indicators of SiC power MOSFETs, on the v_{gs} waveform are investigated. Particularly, the corresponding change in the resonant peak values are of interest for the sake of practical reasons introduced in the next section. Change in any parameter differently impacts v_{gs} , as shown in Figure I.1.7.6. Therefore, a database of these changes can be created for any power module with known parameters. Subsequently, by combining the v_{gs} peaks at different instants (turning ON/OFF) in different conditions (power stage ON/OFF), a multidimensional dataset can be formed with which one can pinpoint and quantify the change in a particular parameter using the database.

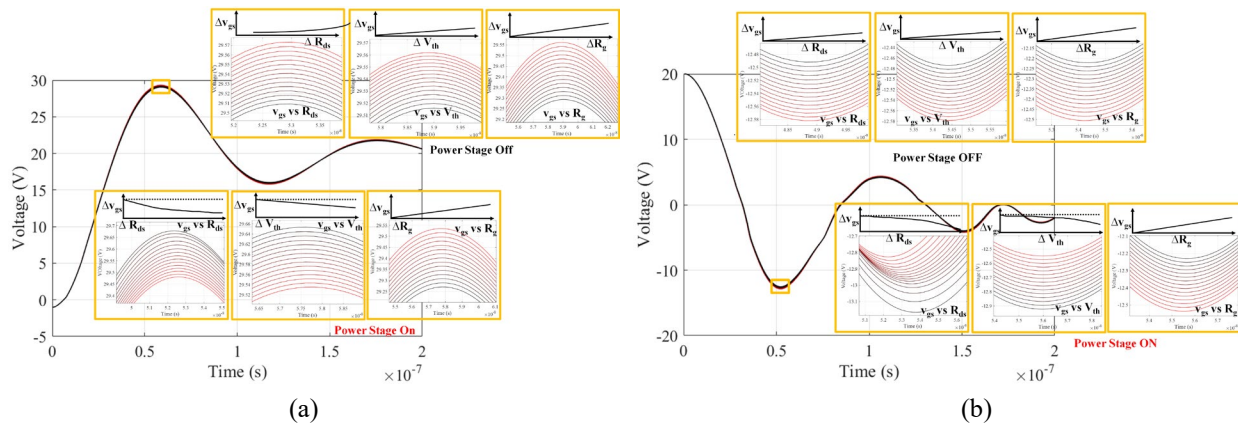


Figure I.1.7.6 Waveform of the first two/three resonant peaks of v_{gs} : (a) after turning on after dead time and (b) after turning off at the beginning of dead time. Note that the darker traces correspond to larger amounts of change in respective parameters. The total increase of $R_{ds,on}$, V_{th} , and R_g corresponding to the respective spans are 28 mΩ, 1.4 V, and 140 mΩ, with even intervals.

Detection Principle: Detection System Design and Validation

Although the combination of v_{gs} peak values is highly informative as described in the previous section, the changes caused by any degradation are delicate, and the time window to acquire the information is short. An ultra-high-bandwidth and high-resolution A/D might work but will defeat the purpose of cost-effective and easy integration into the gate driver. Instead, a simple level-searching circuit has been developed to quantify v_{gs} peak values. The principle is shown in Figure I.1.7.7.

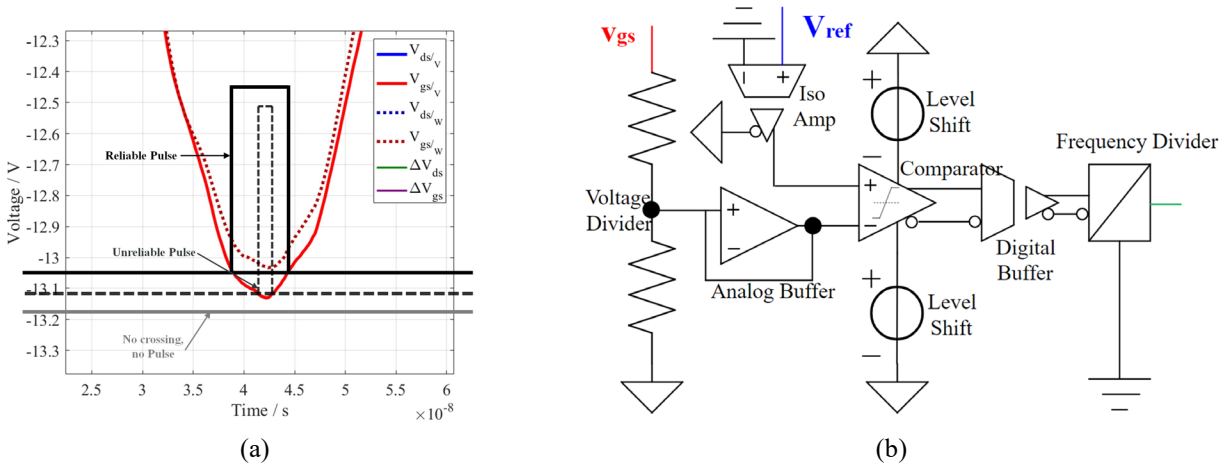


Figure I.1.7.7 Principle of the level searching circuit for v_{gs} acquisition: (a) generation of pulses and (b) circuit functionality diagram

An adjustable voltage reference is generated externally, and the controller gradually sets the reference value from an initial low value while maintaining high resolution. The voltage reference and conditioned v_{gs} values are handled by a comparator such that when the reference reaches the negative v_{gs} peak, a pulse is generated. The pulse can finally be picked up by the controller to quantify the v_{gs} peak value. For positive peaks during turning ON, the approach is similar but with reverse direction. The level searching circuit and the test setup are shown in Figure I.1.7.8.

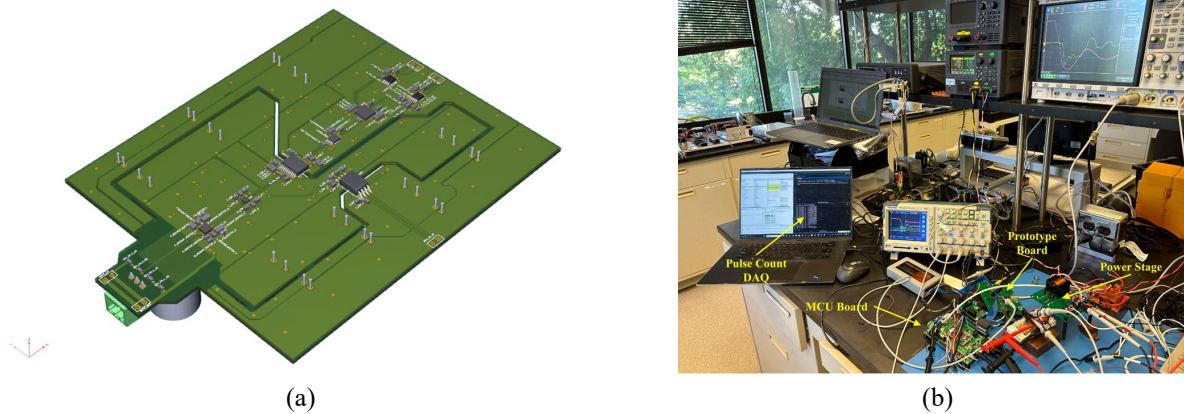


Figure I.1.7.8 Level searching circuit and test bench setup

The test results for $R_{DS,ON}$ and V_{th} are shown in Figure I.1.7.9 and Figure I.1.7.10, respectively. The v_{gs} peak value differences indicated by the difference in pulse emerging/vanishing indices in the figures for all groups of results show patterns that generally match those from the numerical analysis and circuit simulations. This suggests the validity of the prototype and the proposed detection method.

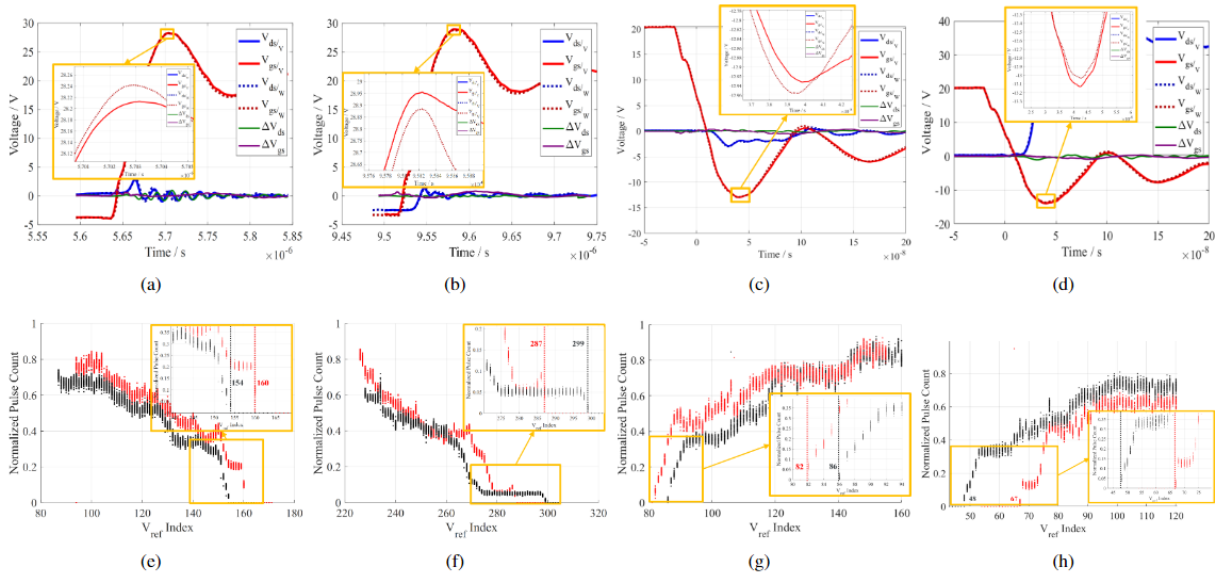


Figure I.1.7.9 Detection results for $R_{ds,on}$ change: (a)–(d) scope measurements; (e)–(h) detection results; (a,e) turn-on, zero bus voltage; (b,f) turn-on, 30-V bus voltage; (c,g) turn-off, zero bus voltage; and (d,h) turn-off, 30-V bus voltage

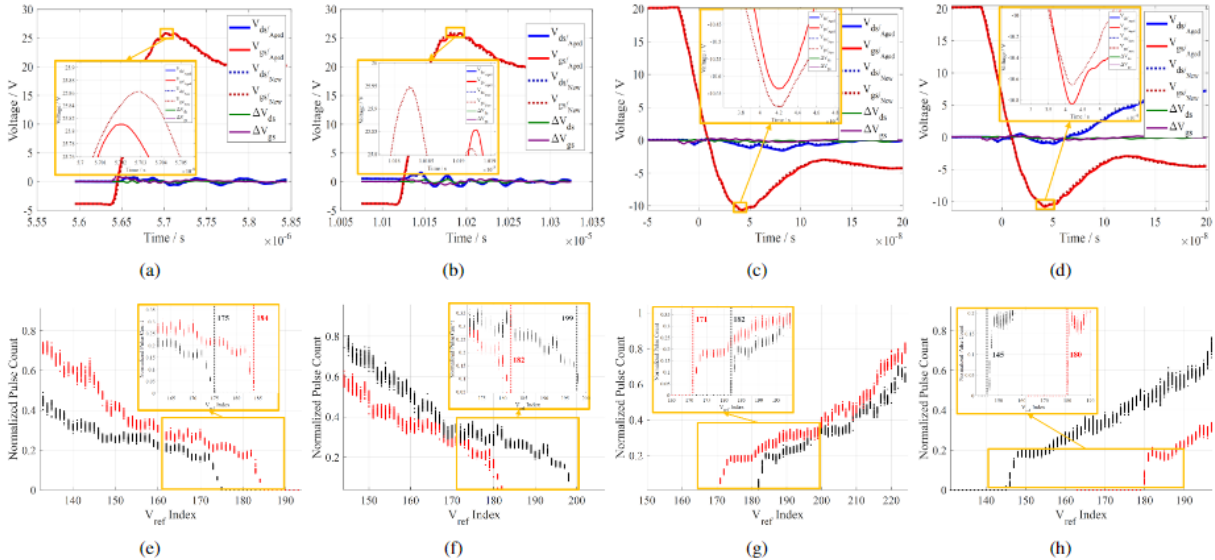


Figure I.1.7.10 Detection results for V_{th} change: (a)–(d) scope measurements; (e)–(h) detection results; (a,e) turn-on, zero bus voltage; (b,f) turn-on, 30-V bus voltage; (c,g) turn-off, zero bus voltage; and (d,h) turn-off, 30-V bus voltage

Conclusions

For the present phase of the project, a review was conducted to obtain knowledge of the latest findings regarding SiC power module aging mechanisms and corresponding precursors and techniques of ALTs to create various aging modes and levels. Based on these conclusions, the review has been conducted to obtain knowledge of existing gate-integrated precursor detection methods. Subsequently, a novel detection system for detecting the precursors of interest is developed and tested. The main results for the current phase are listed below:

- Using the in-house aging station, the ALTs on seven samples of SiC MOSFETs from four models (WolfSpeed CCS020M12CM2, C2M0080120D, C3M0075120D, and Infineon FS55MR12W1M1H-B11) with controlled amperage and temperature range are ongoing and have so far rendered

approximately 30 detailed datasets with observable aging evolutions. So far, the elevated ON-state resistance observed in one device inside the CCS020M12CM2 six-pack has been induced after approximately 10,000 thermal cycles, and V_{th} in one C3M0075120D single module has increased after approximately 55,000 gate overvoltage cycles. Other samples show no clear pattern in precursor values at this moment.

- A detection system with the capability of being fully integrated into the gate driver circuit of power modules has been developed. It is based on detecting the changes in V_{th} and $R_{ds,on}$ by analyzing the peak values of v_{gs} at various time instants during switching transients. This detection architecture uses a comparator-based circuit to extract the nuanced changes in the v_{gs} peak to correlate the changes in V_{th} and $R_{ds,on}$. Early-stage experimental results showed that the detection system can successfully extract the changes in V_{th} and ON-state resistance independently for two separate modules.

References

1. U.S. DRIVE. 2017. *Electrical and Electronics Technical Team Roadmap: October 2017*. Washington, D.C.: U.S. Department of Energy Office of Energy Efficiency and Renewable Energy Vehicle Technologies Office.
2. A. Hanif, Y. Yu, D. DeVoto and F. Khan. 2019. “A Comprehensive Review Toward the State-of-the-Art in Failure and Lifetime Predictions of Power Electronic Devices.” *IEEE Transactions on Power Electronics* 34 (5): 4729–4746. doi: 10.1109/TPEL.2018.2860587.
3. S. Pu, F. Yang, B. T. Vankayalapati, and B. Akin. 2022. “Aging Mechanisms and Accelerated Lifetime Tests for SiC MOSFETs: An Overview.” *IEEE Journal of Emerging and Selected Topics in Power Electronics* 10 (1): 1232–1254. doi: 10.1109/JESTPE.2021.3110476.
4. Z. Ni, X. Lyu, O. P. Yadav, B. N. Singh, S. Zheng, and D. Cao. 2020. “Overview of Real-Time Lifetime Prediction and Extension for SiC Power Converters.” *IEEE Transactions on Power Electronics* 35 (8): 7765–7794. doi: 10.1109/TPEL.2019.2962503.
5. B. Jayant Baliga. 2019. “Power MOSFETs.” In *Fundamentals of Power Semiconductor Devices*, 283–520.
6. Kimoto, Tsunenobu, and James A. Cooper. 2014. *Fundamentals of silicon carbide technology: growth, characterization, devices and applications*. John Wiley & Sons.
7. X. Ye, C. Chen, Y. Wang, G. Zhai, and G. J. Vachtsevanos. 2017. “Online Condition Monitoring of Power MOSFET Gate Oxide Degradation Based on Miller Platform Voltage.” *IEEE Transactions on Power Electronics* 32 (6): 4776–4784. doi: 10.1109/TPEL.2016.2602323.
8. F. Erturk, E. Ugur, J. Olson, and B. Akin. 2019. “Real-Time Aging Detection of SiC MOSFETs.” *IEEE Transactions on Industry Applications* 55 (1): 600–609. doi: 10.1109/TIA.2018.2867820.
9. F. Yang, S. Pu, C. Xu, and B. Akin. 2021. “Turn-on Delay Based Real-Time Junction Temperature Measurement for SiC MOSFETs With Aging Compensation.” *IEEE Transactions on Power Electronics* 36 (2): 1280–1294. doi: 10.1109/TPEL.2020.3009202.
10. Z. Chen, C. Chen, and A. Q. Huang. 2022. “Driver Integrated Online Rds-on Monitoring Method for SiC Power Converters.” 2022 IEEE Energy Conversion Congress and Exposition (ECCE), Detroit, MI, 01–07. doi: 10.1109/ECCE50734.2022.9947617.
11. S.-I. Hayashi and K. Wada. 2022. “Gate Drive Circuit with In situ Condition Monitoring System for Detecting Gate Oxide Degradation of SiC MOSFETs.” 2022 IEEE Applied Power Electronics

Conference and Exposition (APEC), Houston, TX, 1838–1845. doi: 10.1109/APEC43599.2022.9773501.

12. S. Roy, A. Hanif, and F. Khan. 2021. “Aging Detection and State of Health Estimation of Live Power Semiconductor Devices Using SSTDR Embedded PWM Sequence.” *IEEE Transactions on Power Electronics* 36 (5): 4991–5005. doi: 10.1109/TPEL.2020.3032996.

Acknowledgments

The author would also like to thank Susan Rogers, Technology Development Manager for the U.S. Department of Energy Vehicle Technologies Office Electric Drive Technologies Program, for supporting the work. The author would like to thank Shuofeng Zhao (email: shuofeng.zhao@nrel.gov) for his major contribution to this work and EDT Task Leader Sreekant Narumanchi (sreekant.narumanchi@nrel.gov).

I.1.8 Power Electronics Thermal Management (National Renewable Energy Laboratory)

Gilbert Moreno, Principal Investigator

National Renewable Energy Laboratory (NREL)
15013 Denver West Parkway
Golden, CO 80401
Email: gilbert.moreno@nrel.gov

Susan Rogers, DOE Technology Development Manager

U.S. Department of Energy
Email: susan.rogers@ee.doe.gov

Start Date: October 1, 2018

End Date: September 30, 2024

Project Funding: \$250,000

DOE share: \$250,000

Non-DOE share: \$0

Project Introduction

The 2017 *Electrical and Electronics Technical Team Roadmap* [1] proposes aggressive research and development targets aimed at improving power electronics technology to enable the mass-market penetration of electric-drive vehicles. Achieving these aggressive targets will require a decrease in cost (year 2025 cost target: \$2.70/kW) and an increase in power density (year 2025 power density target: 100 kW/L) as compared with current on-road technology. Replacing traditional silicon device-based components with more efficient and higher-temperature wide-bandgap (WBG) semiconductor device-based components will enable increased power density. However, meeting the power density target will also require innovative thermal management solutions to increase the heat fluxes dissipated and allow for compact electronics packaging.

This project conducts research to develop new power electronics thermal management technologies to increase power density, enable high-temperature WBG device operation, and decrease cost. The performance (e.g., thermal resistance, pumping power) of the power electronics cooling technologies developed in this project are compared to the performance of current on-road technology. One of the main challenges to achieving high power densities is associated with packaging high-temperature (up to 250°C) WBG devices near lower-temperature-rated components (e.g., electrical boards and capacitors).

Objectives

The primary project objective is to develop novel thermal management technologies to enable achieving the 100-kW/L power density target. Additional project objectives are to:

- Develop cooling solutions that enable high-heat-flux, high-temperature WBG operation and low-temperature, low-cost capacitors.
- Decrease cost by proposing low-cost cooling technologies that enable decreasing the number of semiconductor devices and use automotive-qualified fluids (e.g., water-ethylene glycol [WEG], driveline fluids).

Approach

This project designs and evaluates dielectric fluid, single-phase heat-transfer cooling systems for automotive power electronics modules. Dielectric fluids have poor thermal properties compared with WEG, but they enable a redesign of the power module to eliminate thermal bottlenecks (i.e., dielectric ceramic) within the package. Jet impingement configurations are used to augment the fluid's convective cooling and offset the fluid's poor properties. The single-phase dielectric fluids proposed are synthetic hydrocarbons (oils), have properties similar to automatic transmission fluid (ATF), are relatively inexpensive, and are environmentally friendly (e.g., global warming potential <1). This proposed cooling concept may enable the use of new driveline fluids (ATF-like fluids) that are tailored for these power electronics cooling applications. Single- and

double-side-cooled dielectric fluid concepts were designed via modeling, and their performance was predicted and compared to current on-road technology. Experiments were conducted and used to validate model predictions under different operating conditions (e.g., different fluid flow rates, types, and temperatures). NREL is also collaborating with Georgia Tech to evaluate two-phase-based, dielectric fluid cooling strategies for power modules.

Results

The work conducted in Fiscal Year 2023 was a continuation of past efforts to develop and demonstrate dielectric fluid concepts for cooling automotive power electronics. This year we fabricated a silicon-carbide (SiC) power module and used it for a thermal demonstration of the dielectric fluid cooling concept. We also modeled the thermohydraulic performance of new driveline fluids that are being developed specifically for direct cooling of power electronics in electric-drive vehicles. Finally, we collaborated with Georgia Tech to demonstrate dielectric, two-phase cooling of power electronic modules. The results from each topic are discussed below.

Dielectric Fluid Cooling Demonstration Using a SiC Module

A SiC thermal demonstration module was fabricated and used to experimentally demonstrate the dielectric fluid (single-phase heat transfer) cooling concept. Two 650 V SiC devices (approximately 5×5 mm in footprint) were soldered to a finned copper heat spreader as shown in Figure I.1.8.1. Electrical connections were provided to enable the passing of current and heating the devices. Wire bonds were used to connect to the source pad on the devices and for the gate and Kelvin source connections. The two devices were connected in parallel and represented one electrical switch.

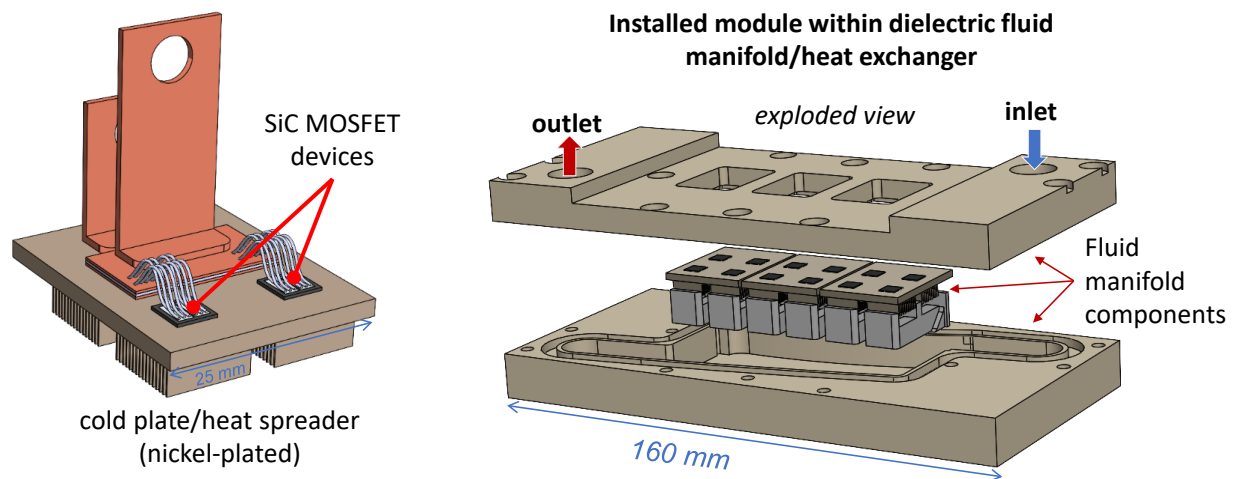


Figure I.1.8.1 Computer-aided design (CAD) drawings of the SiC thermal demonstration module (left) and the dielectric fluid heat exchanger with modules (right). MOSFET: metal-oxide-semiconductor field-effect transistor.

The SiC module was then installed within a dielectric fluid heat exchanger. The heat exchanger consists of three parts as shown in Figure I.1.8.1. The top and bottom components were machined out of polyphenylene sulfide (PPS) and are used to contain and distribute the fluid to multiple devices. The middle component is the jet distribution manifold that was 3D-printed out of polyetheretherketone (PEEK) plastic and used to generate the slot jets that impinged onto finned structures directly below the devices. PPS and PEEK were used because they are high-temperature plastics, are compatible with dielectric fluids, and are used in automotive applications. Pictures of the heat exchanger and module assembly are provided in Figure I.1.8.2. Details of the dielectric fluid concept are provided in past progress reports [2], [3], publications [4], and a patent [5].

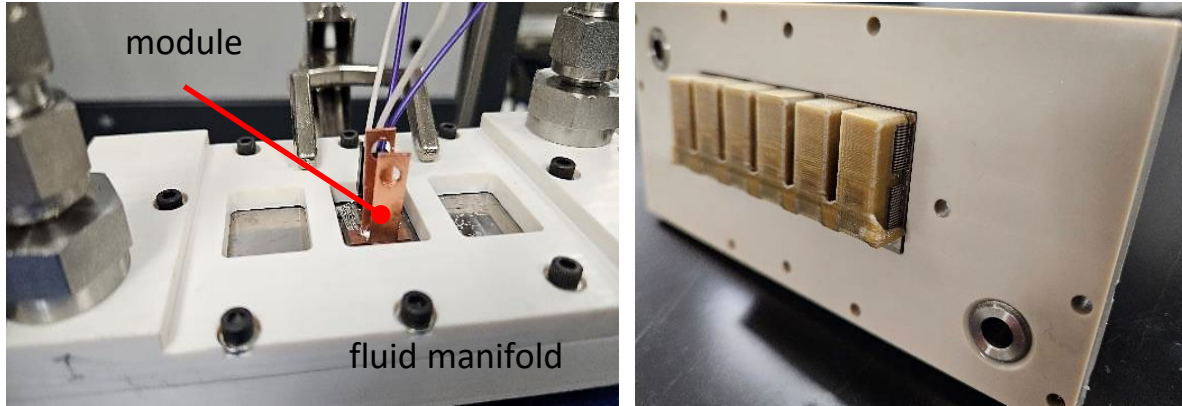


Figure I.1.8.2 Pictures of the SiC module installed within the dielectric fluid heat exchanger (left) and the jet impingement manifold mounted over the module's fin structures (right)

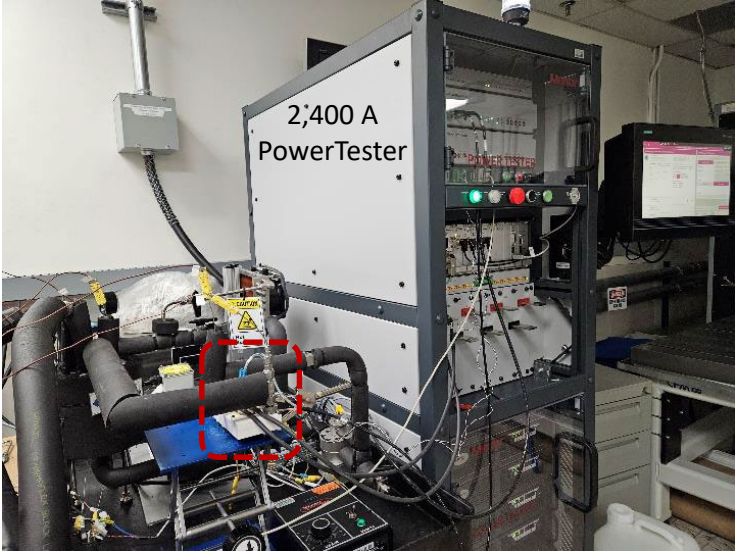
The heat exchanger and module assembly were piped into the dielectric fluid loop and electrically connected to the PowerTester (Figure I.1.8.3). Experiments were performed to measure the junction-to-fluid thermal resistance and pumping power of the dielectric fluid heat exchanger using 70°C inlet fluid temperature at various flow rates (1 L/min to 4 L/min). AmpCool 110 was the coolant used for these experiments. AmpCool 110 is a dielectric fluid intended for cooling battery packs and electric machines in electric vehicle applications. The PowerTester was used to provide high current to heat the devices and to measure the junction temperature. The junction temperature was measured via a temperature-sensitive parameter (i.e., body diode voltage drop). Calibration of the diode voltage drop to the temperature was performed initially.

Figure I.1.8.4 shows the junction-to-fluid specific thermal resistance versus the pumping power. The specific thermal resistance was defined per Eq. 1:

$$R''_{th} = Area \cdot (T_j - T_f) / Heat \quad (1)$$

where *Area* is the area of one SiC device, T_j is the junction temperature, T_f is the inlet fluid temperature, and *Heat* is the heat per device. The pumping power is the total flow rate times the pressure drop (inlet to outlet).

The experimentally measured results are found to be in good agreement with computational fluid dynamics (CFD) model predictions (within ~10%). The simulations were performed at a higher flow rate case of 6 L/min to evaluate the effect of a higher flow rate on performance. The dielectric fluid cooling system results were compared with the performance of the 2015 BMW i3 and a Cree SiC module. Both the BMW i3 and Cree modules were cooled with WEG at a 10-L/min flow rate and 65°C inlet fluid temperature and used metalized copper substrates. The 2015 BMW i3 uses silicon insulated-gate bipolar transistor technology and a copper, pin-fin cold plate for cooling [6]. The Cree SiC module (WAB400M12BM3) was cooled using a Weiland cold plate (CP3009) with thermal grease at the interface. The dielectric fluid cooling system (at 6 L/min) is found to reduce thermal resistance and pumping power by 65% and 80%, respectively, compared with the 2015 BMW i3. Compared to the Cree module, the dielectric fluid concept reduces the thermal resistance and pumping power by 20% and 80%, respectively. A low thermal resistance of 17.4 mm²·K/W was predicted at 6 L/min.



Dielectric fluid loop circulating AmpCool 110

Figure I.1.8.3 Picture of the assembled dielectric heat exchanger piped into the dielectric fluid loop and electrically connected to the PowerTester

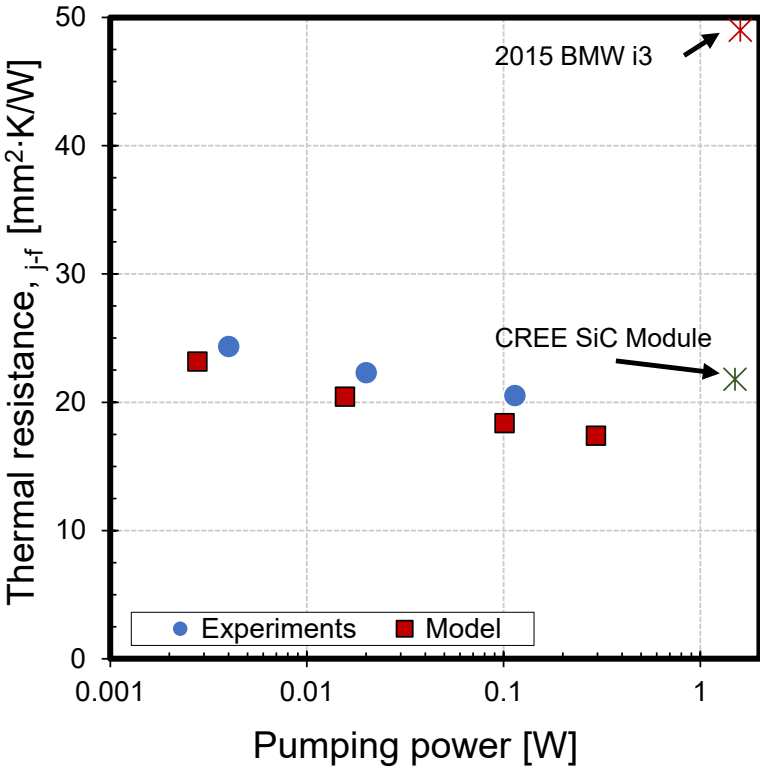


Figure I.1.8.4 Junction-to-fluid thermal resistance versus pumping power showing modeling and experimental results with comparisons to commercially available, WEG-cooled power modules

New Driveline Fluids Evaluated

NREL is collaborating with Infineum to evaluate new driveline fluids that are under development for electric vehicle, power electronics cooling applications. Infineum provided fluid properties for four driveline fluids, and NREL modeled their performance within NREL's dielectric fluid heat exchanger concept (Figure I.1.8.1). The effect of fluid flow rate (1 L/min to 6 L/min) and fluid inlet temperature (-40°C and 70°C) on junction-to-fluid thermal resistance and pumping power were evaluated using CFD models. The objective for this modeling work was to identify the best-performing fluid and to compare the performance of the Infineum fluids to the performance of other dielectric fluids (AmpCool 100 [Engineered Fluids] and Alpha 6 [DSI Ventures]).

Model-predicted junction-to-fluid thermal resistance versus pumping power values are provided in Figure I.1.8.5. The four new driveline fluids are labeled Fluids 1–4 in the figure legend. The performance of dielectric fluids AmpCool 100 and Alpha 6 are provided for comparison and obtained from [4]. At 70°C , the four Infineum fluids are predicted to produce similar performance in terms of thermal resistance and pumping power. At -40°C , Fluid 2 provides the lowest thermal resistance and pumping power—lower than the other Infineum fluids, AmpCool 100, and Alpha 6. The pumping power of Fluid 2 is $\sim 82\%$ lower compared to Fluid 4 due to its lower viscosity. Additionally, Fluid 2 is predicted to provide the lowest thermal resistance at the -40°C temperature condition, even lower than Alpha 6 and AmpCool 100 fluids.

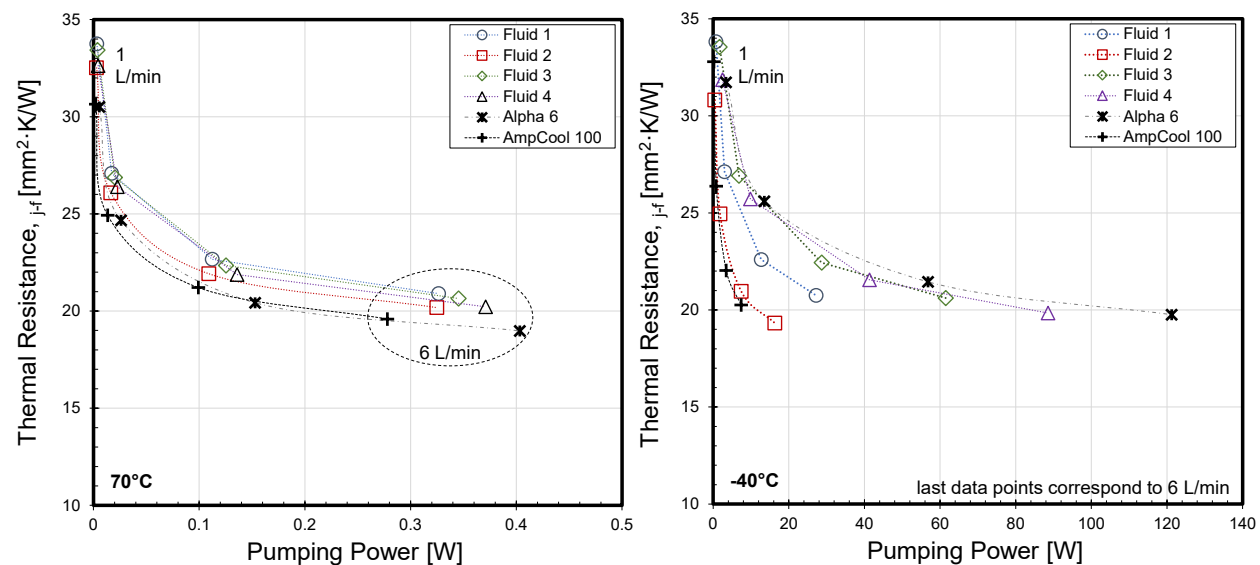


Figure I.1.8.5 Model-predicted junction-to-fluid thermal resistance versus pumping power for 70°C (left) and -40°C (right) inlet fluid temperatures

Collaborating with Georgia Tech to Evaluate Two-Phase Cooling Strategies

Dielectric fluid power electronics cooling concepts that use two-phase (boiling) heat transfer were also evaluated in collaboration with Georgia Tech. Georgia Tech designed and fabricated a copper pin-fin cold plate that uses flow boiling heat transfer as the cooling mechanism (Figure I.1.8.6). The cold plate used a PEEK fluid manifold to distribute the fluid and was designed to cool several semiconductor devices. A clear polycarbonate plate was used to provide a fluid seal and enable visualization of the boiling phenomena. HFE-7200 was the working fluid used for the two-phase cooling experiments.

Two sets of experiments were conducted at NREL to characterize the thermal performance of the flow boiling cold plate. Cartridge heaters embedded within copper blocks were used as the heat sources for the first set of experiments. These tests allowed for higher heat dissipation and were used to measure the cold plate thermal resistance. The second set of experiments used SiC devices provided by SUNY Polytechnic Institute. The SiC devices were soldered to the copper cold plate to create a module that was used to measure the junction-to-fluid thermal resistance of the two-phase cooling system. NREL's PowerTester was used to provide heating for

the SiC devices and to measure junction temperatures. The SiC devices and copper blocks with embedded heaters had a footprint of approximately 3.1×3.1 mm. The two-phase cold plate was piped into a two-phase fluid loop to circulate near saturated HFE-7200 through the cold plate (Figure I.1.8.7) at a 1-L/min flow rate. A Georgia Tech graduate intern (Akshith Narayanan) spent 3 months at NREL and conducted the experiments.

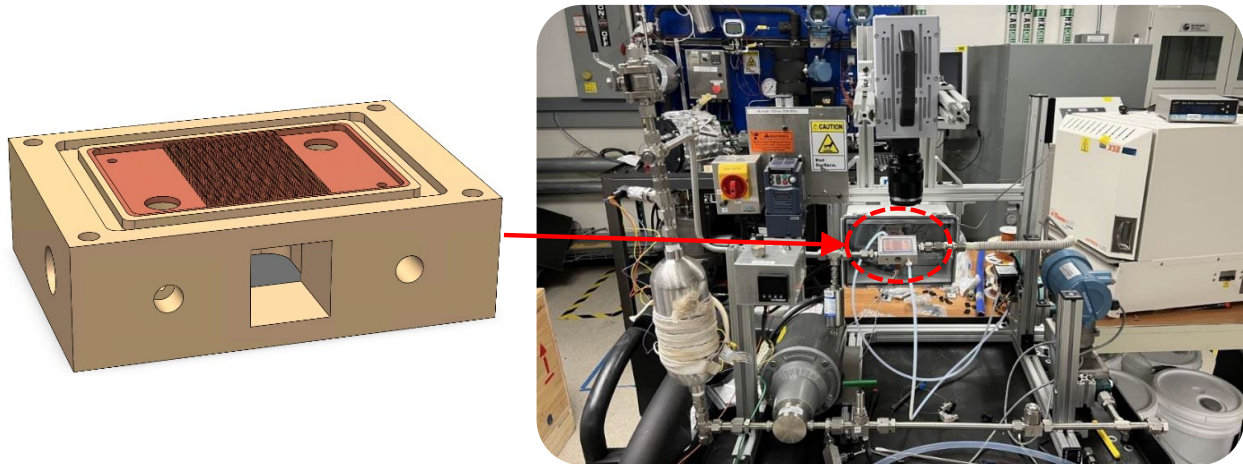


Figure I.1.8.6 CAD drawing of the two-phase cold plate (left) and a picture of the two-phase cold plate piped into the two-phase fluid loop (right)

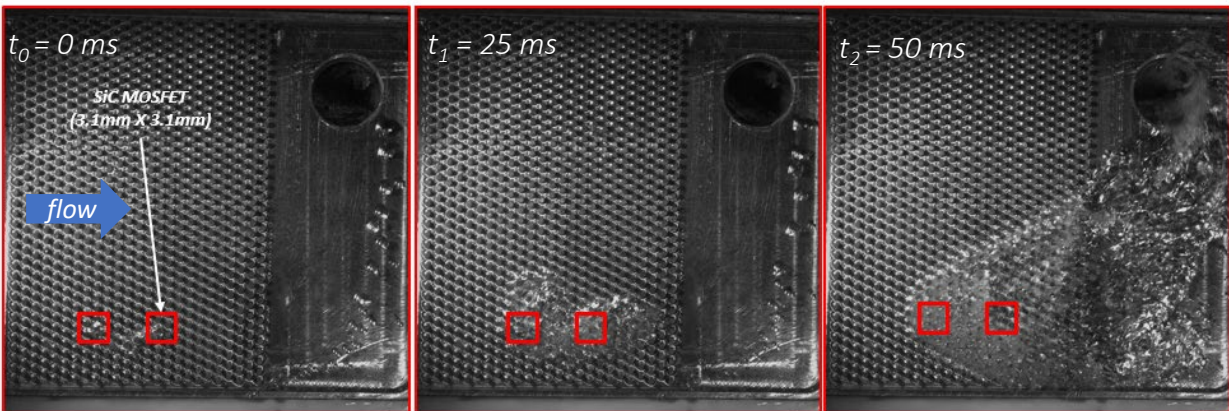


Figure I.1.8.7 High-speed video images of boiling on the cold plate surface showing boiling incipience begins at the downstream device and then quickly propagates to the upstream device. The red squares denote the approximate locations of the SiC devices.

Figure shows images of boiling on the cold plate surface that were obtained from high-speed video. The sequence of images shows the approximate location of the two SiC devices denoted by red squares. Boiling incipience first occurs at the downstream device and then quickly propagates to the upstream device within about 50 milliseconds. Highlights from these experiments include achieving heat fluxes at high as 934 W/cm^2 , specific thermal resistance values as low as $12.8 \text{ mm}^2\text{-K/W}$, and low pumping power requirements ($\sim 0.08 \text{ W}$).

Conclusions

This project evaluates dielectric fluid cooling technologies for power electronics. Single- and two-phase dielectric fluid technologies were experimentally evaluated and compared with conventional WEG-based cooling solutions. Additionally, new driveline fluids that are being developed specifically for electric-drive vehicles were evaluated through modeling. The project's major conclusions are summarized below:

- We designed and fabricated a SiC module and used it for an experimental demonstration of the dielectric-fluid-cooled (single-phase heat transfer) concept. Experiments were conducted using AmpCool

110 dielectric fluid at various flow rates and a 70°C inlet temperature. We demonstrated that dielectric fluid concepts provide both lower thermal resistance and pumping power values compared to WEG-based cooling systems. Junction-to-fluid thermal resistance values as low as 17.4 mm²·K/W were predicted through validated models.

- We collaborated with Infineum to evaluate new driveline fluids that are being developed specifically for electric-drive vehicle applications. The performance of four developmental driveline fluids was modeled within NREL’s dielectric fluid cooling concept to predict junction-to-fluid thermal resistance and pumping power values. We identified the best-performing fluid (Fluid 2) and compared the performance of the Infineum fluids to the performance of other dielectric fluids (AmpCool 100 and Alpha 6).
- We collaborated with Georgia Tech to experimentally evaluate two-phase dielectric fluid cooling concepts. A SiC module was fabricated and used for an experimental demonstration of Georgia Tech’s flow boiling thermal management concept. The experiment demonstrated high heat flux (934 W/cm²), low thermal resistance (12.8 mm²·K/W), and low pumping power values (~0.08 W) for the two-phase cooling concept using HFE-7200 coolant.

Key Publications

1. F. Xuhui, G. Moreno, P. Paret, and S. Narumanchi. 2022. “Multiphysics Co-Optimization Design and Analysis of a Double-Side-Cooled Silicon Carbide-Based Power Module.” Presented at the ASME 2022 International Technical Conference and Exhibition on Packaging and Integration of Electronic and Photonic Microsystems (InterPACK), 25–27 Oct. 2022, Garden Grove, CA. <https://doi.org/10.1115/IPACK2022-97355>.
2. G. Moreno, S. Narumanchi, J. Tomerlin, and J. Major. 2022. “Single-Phase Dielectric Fluid Thermal Management for Power-Dense Automotive Power Electronics.” *IEEE Transactions on Power Electronics* 37 (10): 12474–12485.
3. G. Moreno, S. Narumanchi, X. Feng, P. Anschel, S. Myers, and P. Keller. 2022. “Electric-Drive Vehicle Power Electronics Thermal Management: Current Status, Challenges, and Future Directions.” *ASME Journal of Electronic Packaging* 144 (1): 011004.
4. E. Cousineau, G. Moreno, K. S. Bennion, T. J. Roan, and B. N. Singh. 2022. “Condensers and Electronic Assemblies.” U.S. Patent 11,388,840 B2, issued July 12, 2022.
5. G. Moreno, S. V. J. Narumanchi, K. S. Bennion, R. M. Kotecha, P. P. Paret, and F. Xuhui. 2023. “Jet Impingement Manifolds for Cooling Power Electronics Modules.” U.S. Patent 11,751,365 B2, issued Sept. 5, 2023.
6. T. J. Roan, B. N. Singh, G. Moreno, and K. S. Bennion. 2023. “Evaporator stacks and electronic assemblies.” U.S. Patent 11,594,468 B2, issued Feb. 8, 2023.
7. E. Cousineau, G. Moreno, K. Bennion, T. J. Roan, and B. N. Singh. 2023. “Condensers and Electronic Assemblies.” U.S. Patent 11,778,782 B2, issued Oct. 3, 2023.

References

1. U.S. DRIVE. 2017. *Electrical and Electronics Technical Team Roadmap: October 2017*. Washington, D.C.: U.S. Department of Energy Office of Energy Efficiency and Renewable Energy Vehicle Technologies Office.
2. G. Moreno. 2021. “Power Electronics Thermal Management.” In *Electrification: 2021 Annual Progress Report*, Washington, D.C.: U.S. Department of Energy Office of Energy Efficiency and Renewable Energy Vehicle Technologies Office.

3. G. Moreno. 2022. “Power Electronics Thermal Management.” In *Electrification: 2022 Annual Progress Report*, Washington, D.C.: U.S. Department of Energy Office of Energy Efficiency and Renewable Energy Vehicle Technologies Office.
4. G. Moreno, S. Narumanchi, J. Tomerlin, and J. Major. 2022. “Single-Phase Dielectric Fluid Thermal Management for Power-Dense Automotive Power Electronics.” *IEEE Transactions on Power Electronics* 37 (10): 12474–12485.
5. G. Moreno, S. V. J. Narumanchi, K. S. Bennion, R. M. Kotecha, P. P. Paret, and F. Xuhui. 2023. “Jet Impingement Manifolds for Cooling Power Electronics Modules.” U.S. Patent 11,751,365 B2, issued Sept. 5, 2023.
6. G. Moreno, S. Narumanchi, X. Feng, P. Anshel, S. Myers, and P. Keller. 2022. “Electric-Drive Vehicle Power Electronics Thermal Management: Current Status, Challenges, and Future Directions.” *Journal of Electronic Packaging* 144 (1).

Acknowledgments

We acknowledge the significant contributions of Xuhui Feng (NREL), Dr. Yogendra Joshi (Georgia Tech), Joshua Major (NREL), Akshith Narayanan (Georgia Tech), Sreekant Narumanchi (NREL), and Jeff Tomerlin (NREL). We would like to thank Ryan Rieth and Sonia Oberoi (Infineum) for their collaboration and for providing information on Infineum’s new developmental driveline fluids. Finally, we would also like to thank Woongje Sung (SUNY Polytechnic Institute) for providing the SiC devices used for the two-phase demonstration work. A portion of the research was performed using computational resources sponsored by the U.S. Department of Energy’s Office of Energy Efficiency and Renewable Energy and located at NREL.

I.1.9 Electric Motor Thermal Management (National Renewable Energy Laboratory)

Emily Cousineau, Principal Investigator

National Renewable Energy Laboratory
15013 Denver West Parkway
Golden, CO 80401
E-mail: emily.cousineau@nrel.gov

Susan Rogers, DOE Technology Development Manager

U.S. Department of Energy
E-mail: susan.rogers@ee.doe.gov

Start Date: October 1, 2018

End Date: September 30, 2024

Project Funding: \$250,000

DOE share: \$250,000

Non-DOE share: \$0

Project Introduction

This project is part of a multi-lab consortium that includes multiple universities, the National Renewable Energy Laboratory (NREL), Oak Ridge National Laboratory (ORNL), Sandia National Laboratories, and Ames Laboratory. The project and consortium leverage research expertise and facilities at national labs, universities, and industry to significantly increase electric-drive power density and reliability while reducing cost. The consortium is organized around three keystone projects: (1) Power Electronics, (2) Electric Motors, and (3) Traction Drive System. The Electric Motors keystone project at NREL focuses primarily on improvements (reductions) in the passive thermal resistance of components and interfaces in electric motors and improved active fluid-based cooling technologies to increase power density, in line with the research priorities outlined in the U.S. DRIVE *Electrical and Electronics Technical Team Roadmap* [1].

In the area of electric-drive motors, the roadmap highlights the importance of reducing the thermal resistance of the motor packaging stack-up to increase power density. It also mentions that the thermal conductivities of the materials within the motor influence the amount of material necessary to generate the required mechanical power. The roadmap emphasizes research areas with a focus on material-physics-based models, improved materials, and thermally conductive epoxy and fillers.

Heat transfer and thermal management are critical to electric motors because—as mentioned in the roadmap—thermal constraints place limitations on how electric motors ultimately perform. The thermal management of electric motors for vehicles is complex because of the multiple heat transfer paths within the motor, the variations in heat arising from motor operating conditions, and the multiple material interfaces through which heat must pass to be removed. For these reasons, “heat transfer is as important as electromagnetic and mechanical design” [2] for improving the power density, cost, and reliability of electric motors, as outlined by the roadmap.

Objectives

Research under this project is performed within the framework of a research consortium consisting of a multidisciplinary team that plans, establishes, conducts, and manages a portfolio of multi-lab and multi-university research efforts to advance the state of the art in electric-drive technologies. The objective of the consortium is to develop a 100-kW traction drive system that achieves a power density of 33 kW/L, has an operational life of 300,000 miles, and costs \$6/kW. The system will be composed of a 100-kW/L inverter and a >20,000-rpm, 50-kW/L electric motor. Building on the research experience and capabilities within each laboratory, the multi-lab consortium focuses on achieving research objectives within three keystone projects: (1) Power Electronics, (2) Electric Motors, and (3) Traction Drive System.

For the Electric Motors keystone project, the consortium focuses on investigating motor technology gaps to enable increased power density and reliability, supporting research pathways in power electronics

technologies. As power electronics technologies develop to enable higher operating temperatures, higher system voltages, and higher switching frequencies, motor technologies will also be necessary to realize the electric-drive system benefits. Key consortium motor research pathways include motor material improvements (electrical, magnetic, and thermal), higher motor operating speeds, and higher system voltages. NREL research will provide motor researchers—within and outside the consortium—with the data and models necessary to enable motor innovations and the use of novel materials and designs. This work supports the broad demand for data, analytical methods, and experimental techniques to improve and better understand motor thermal management. It also incorporates unique capabilities, facilities, and expertise in addition to the data, analysis methods, and experimental techniques to improve and better understand heat transfer within electric motors to meet the demands of electric-drive vehicles. NREL’s focus in Fiscal Year (FY) 2023 included developing models, simulation tools, and experimental prototypes in support of consortium team members to quantify thermal performance and heat transfer technologies and support motor development efforts.

Approach

The collaboration with ORNL supported motor thermal analysis and thermal design of advanced machine designs led by ORNL. This collaboration is summarized in Figure I.1.9.1. ORNL led the overall iterative electric machine design process with an emphasis on the electromagnetic and mechanical assembly design. NREL, in collaboration with ORNL, performed the thermal analysis and cooling design. A summary of the initial work is provided in an ORNL-led paper presented at the 2020 IEEE Energy Conversion Congress and Exposition [3]. In FY 2023, NREL focused on approaches to reduce magnet temperature by flowing air through the rotor-stator gap, updating the thermal model to match the final design including three key operating points: continuous high torque, continuous high speed, and peak power. Peak power was analyzed using a transient thermal analysis.

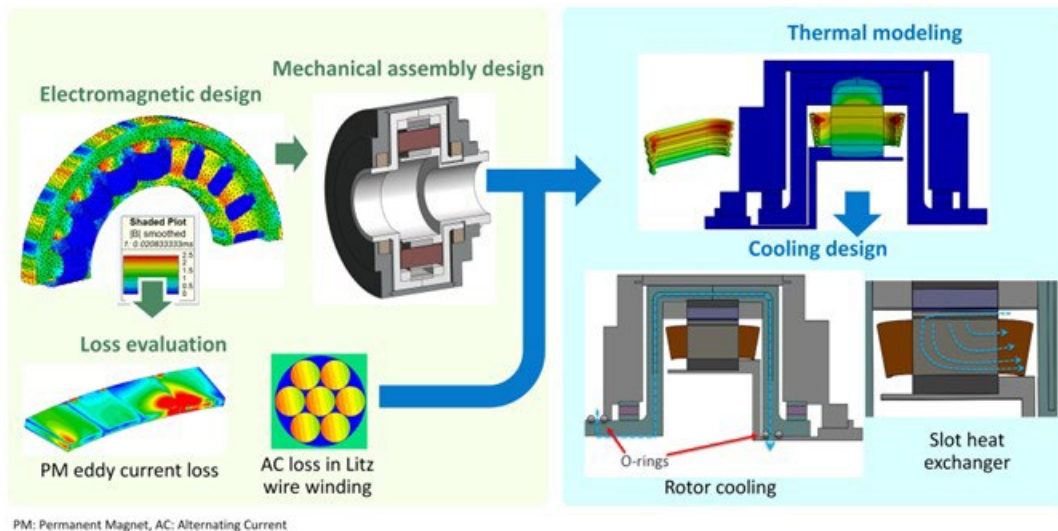


Figure I.1.9.1 ORNL and NREL motor analysis approach

Results

The work supporting the ORNL-led motor research efforts focused on an outer-rotor motor configuration, as shown in Figure I.1.9.1. The motor went through several more design iterations in FY 2023 before the final design was reached. This iterative design approach investigated design configurations to facilitate integration with the inverter that was designed in parallel. NREL led the thermal analysis aspects of the motor design to reduce steady-state rotor magnet temperatures to 80°C to meet ORNL temperature requirements. The design changes in FY 2023 resulted in the need for improved cooling for the rotor to ensure rotor magnets did not exceed 80°C. It was determined using computational fluid dynamics and finite element analysis (FEA) that flowing air through the rotor-stator air gap as shown in Figure I.1.9.2 was sufficient to isolate the rotor

thermally from the stator and maintain the magnet temperatures at or below the maximum magnet temperature. It was found that the airflow provided by a small computer server fan would meet the requirements of all three key operating conditions.

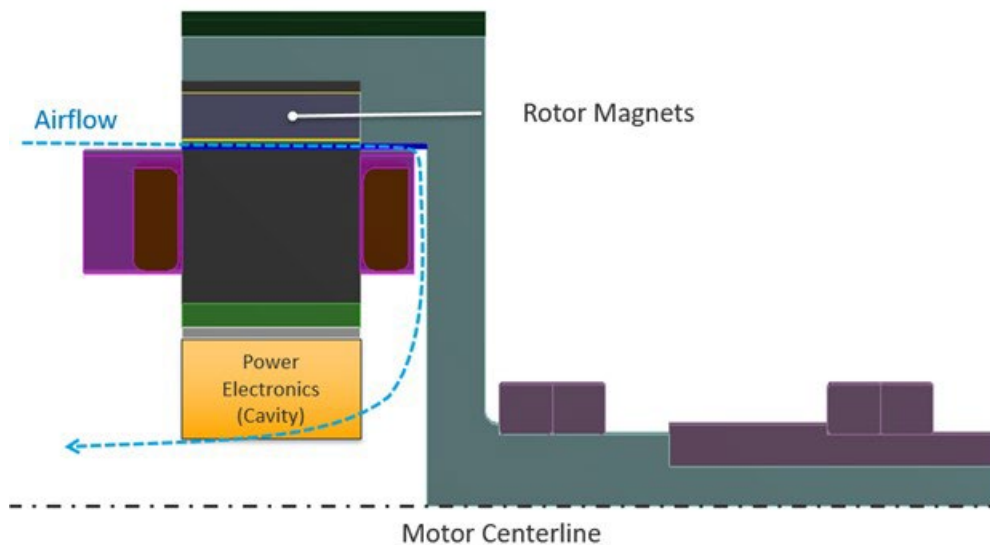


Figure I.1.9.2 Schematic of airflow through rotor-stator air gap showing flow exiting through the cavity containing the power electronics

Three key operating conditions were analyzed in FEA: a high-torque continuous condition (58 kW, 6,666 rpm), a high-speed continuous condition (50 kW, 20,000 rpm), and a high-power peak condition (100 kW, 6,666 rpm) that is intended to run for 30 s. NREL analyzed all three conditions, including evaluating three candidate potting compounds to determine the best candidate and incorporating the final as-built (prototype) rotor design. Figure I.1.9.3 shows the transient analysis performed on the peak-power condition, using the high-torque, steady-state condition as the starting point, and then at time 0 imposing peak loading to determine the temperature of each component over time. The windings reach their maximum continuous operating temperature of 200°C after 58 seconds in the model, exceeding the peak loading target of 30 seconds. The windings at no point exceed their peak temperature limit of 230°C.

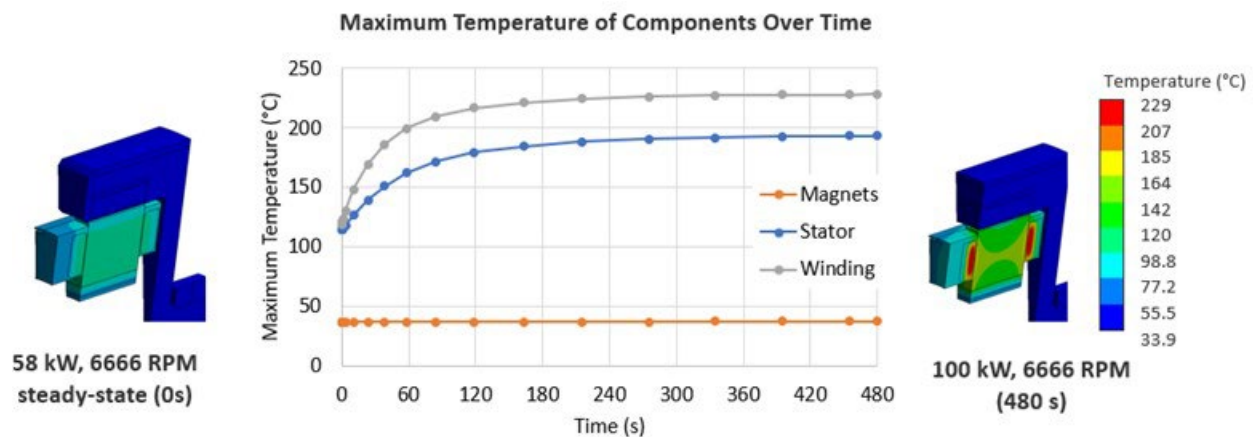


Figure I.1.9.3 Left: Steady-state temperature plot of high-torque condition used as the starting point for transient analysis. Right: Steady-state temperature map of peak power condition. Center: Plot depicting maximum temperatures of key components over time in response to step loading of the peak power condition.

Conclusions

During FY 2023, NREL efforts focused on supporting collaborations with external research partners within the Electric Drive Technologies research consortium. The collaboration with ORNL supported efforts to finalize the design of a high-speed, non-heavy-rare-earth outer-rotor motor. NREL supported the effort by leading the thermal analysis and design of advanced machines.

Key Publications

1. Cousineau, J. E. 2023. "Electric Motor Thermal Management." 2023 DOE VTO Annual Merit Review, Washington, D.C., June 2023.
2. Vandana Rallabandi, Shajjad Chowdhury, Himel Barua, M. Parans Paranthaman, Mostak Mohammad, Steve Bullock, and Emily Cousineau, 2023. "Traction motor design trade-offs with additively manufactured anisotropic bonded magnets." 2023 IEEE Transportation Electrification Conference & Expo (ITEC), 21–23 June 2023, Detroit, MI, 1–5. doi: 10.1109/ITEC55900.2023.10187005.

References

1. U.S. DRIVE. 2017. *Electrical and Electronics Technical Team Roadmap*. Washington, D.C.: U.S. Department of Energy Office of Energy Efficiency and Renewable Energy Vehicle Technologies Office. <https://www.energy.gov/sites/prod/files/2017/11/f39/EETT%20Roadmap%2010-27-17.pdf>.
2. J.R. Hendershot and T.J.E. Miller. 1994. *Design of Brushless Permanent-Magnet Motors*. Oxford, UK: Magna Physics Publishing.
3. T. Raminosa, R. Wiles, J. E. Cousineau, K. Bennion and J. Wilkins, "A High-Speed High-Power-Density Non-Heavy Rare-Earth Permanent Magnet Traction Motor," 2020 IEEE Energy Conversion Congress and Exposition (ECCE), Detroit, MI, USA, 2020, pp. 61-67, doi: 10.1109/ECCE44975.2020.9235704.

Acknowledgements

We acknowledge the significant contributions to the project from Doug DeVoto, Xuhui Feng, Bidzina Kekelia, Joshua Major, Sreekant Narumanchi (NREL EDT Task Leader), and Jeff Tomerlin (NREL). We also acknowledge the support and collaborations from Mostak Mohammad and Vandana Rallabandi (ORNL).

I.1.10 Integrated Traction Drive Thermal Management (National Renewable Energy Laboratory)

Bidzina Kekelia, Principal Investigator

National Renewable Energy Laboratory (NREL)
15013 Denver West Parkway
Golden, CO 80401
E-mail: bidzina.kekelia@nrel.gov

Susan Rogers, DOE Technology Development Manager

U.S. Department of Energy
E-mail: susan.rogers@ee.doe.gov

Start Date: October 1, 2018

End Date: September 30, 2024

Project Funding: \$250,000

DOE share: \$250,000

Non-DOE share: \$0

Project Introduction

To enable the mass-market penetration of electric-drive vehicles and meet consumer electric vehicle performance expectations, the U.S. DRIVE 2017 *Electrical and Electronics Technical Team Roadmap* [1] proposes aggressive research and development targets aimed at reducing costs and increasing electric traction-drive system power density to 33 kW/L by 2025. This target includes high-voltage power electronics and a single traction-drive electric motor. Achieving this level of system power density requires integration of the inverter and electric motor into a single traction module. However, this approach also requires innovative thermal management solutions to provide adequate cooling to more densely packed electrical components and keep their operating temperatures within optimal range.

Objectives

The main objectives of this project are to:

- Research and evaluate motor-integrated power electronics topologies and thermal management solutions for electric traction drives.
- Identify candidate driveline fluids suitable for direct cooling of traction-drive components and high-voltage power electronics.
- Characterize selected driveline fluids by measuring convective cooling and, if appropriate and feasible, electrical properties.
- Provide support to other collaborating researcher teams in the Electric Drive Technologies (EDT) Consortium in thermal management aspects for their integrated drive concepts.

Approach

We will consider previous research into the most efficient heat removal techniques from power electronics and electric machine components, as well as best integration practices, when evaluating the thermal management approaches of EDT Consortium teams' integrated drive concepts.

We are continuing to collaborate with Oak Ridge National Laboratory (ORNL) on thermal management component design and thermal simulations for their integrated traction drive. Support activities for the University of Wisconsin's integrated drive team are also ongoing.

Results

The focus of our FY23 research was finalizing design and manufacturing thermal management system components for ORNL's outer-rotor integrated drive and helping the University of Wisconsin's team evaluate

modeling and experimental testing results of their integrated traction drive. As the electromagnetic and mechanical design of ORNL's drive evolves, there is a constant need for thermal management component adjustments to accommodate the design modifications.

Supporting ORNL's Outer-Rotor Integrated Motor Design

The current design of ORNL's integrated drive is presented in Figure I.1.10-1. The design illustrates substitution of the large bearings in the original design with a set of smaller bearings (capable of over 20,000-rpm speeds) and cantilever suspension of the rotor. In addition to reducing bearing dimensions, this change allowed separate feed of coolant to the stator and inverter heat exchangers. Shifting from series (passing the inverter and then to the stator) to parallel fluid paths to the inverter and the stator should result in better cooling performance of the thermal management system. In this configuration, the coolant temperature at the stator manifold inlet will be lower, as coolant is not heated by passing through the inverter first. The overall fluid pressure drop through the thermal management system should also be lower.

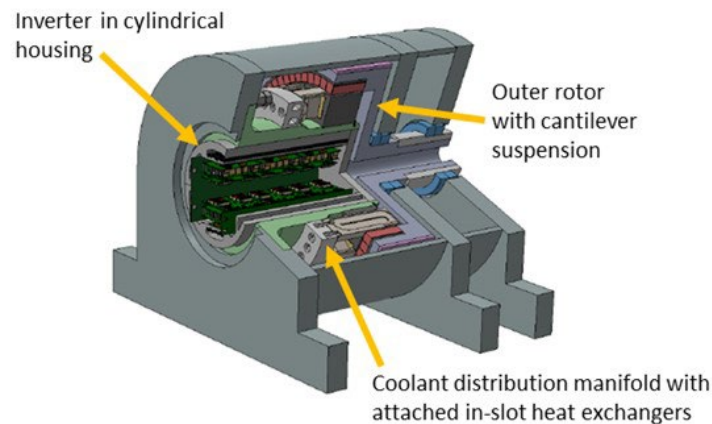


Figure I.1.10.1 ORNL's outer-rotor motor with integrated inverter and cooling system components. *Illustration by Vandana Rallabandi, ORNL*

The assembled stator cooling system is shown in Figure I.1.10.2. Ceramic (alumina) heat exchangers providing cooling to the stator windings are attached to the fluid distribution manifold using stainless steel bolts, and fluid passage is sealed with O-rings. This type of fastening solution was selected over adhesive attachment of heat exchangers to the manifold to reduce the risk of detachment and cracking of joints due to vibration.

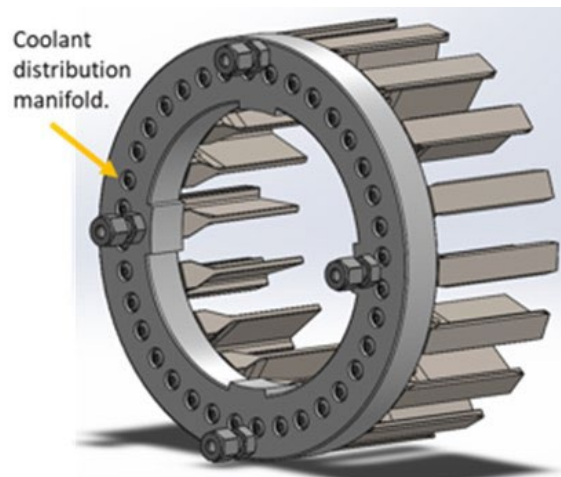


Figure I.1.10.2 Stator cooling assembly with 18 T-shape heat exchangers attached to the coolant distribution manifold. *Illustration by Bidzina Kekelia, NREL*

Due to the complex geometry of internal fluid channels in the stator T-shape heat exchangers, the first samples were 3D-printed from aluminum oxide by two different vendors (Robocasting and Lithoz). It proved very difficult to achieve the required dimensional tolerances for both manufacturers. The difficulties showed up during the sintering stage as well; uneven shrinkage of areas with different thickness of material caused cracking (Figure I.1.10.3).



Figure I.1.10.3 Ceramic T-shape in-slot heat exchanger 3D-printed by Lithoz from alumina (left) and crack after sintering (right). Illustration by Bidzina Kekelia, NREL

The performance of the successfully manufactured by Lithoz sample of the ceramic heat exchanger is currently being evaluated. The experimental setup is illustrated in Figure I.1.10.4. Water-ethylene-glycol coolant is circulated in the internal channels, removing heat provided by the cartridge heaters embedded in copper blocks, which are attached to the side surfaces of the heat exchanger. Copper blocks provide heat input to the same area as stator windings in the motor.

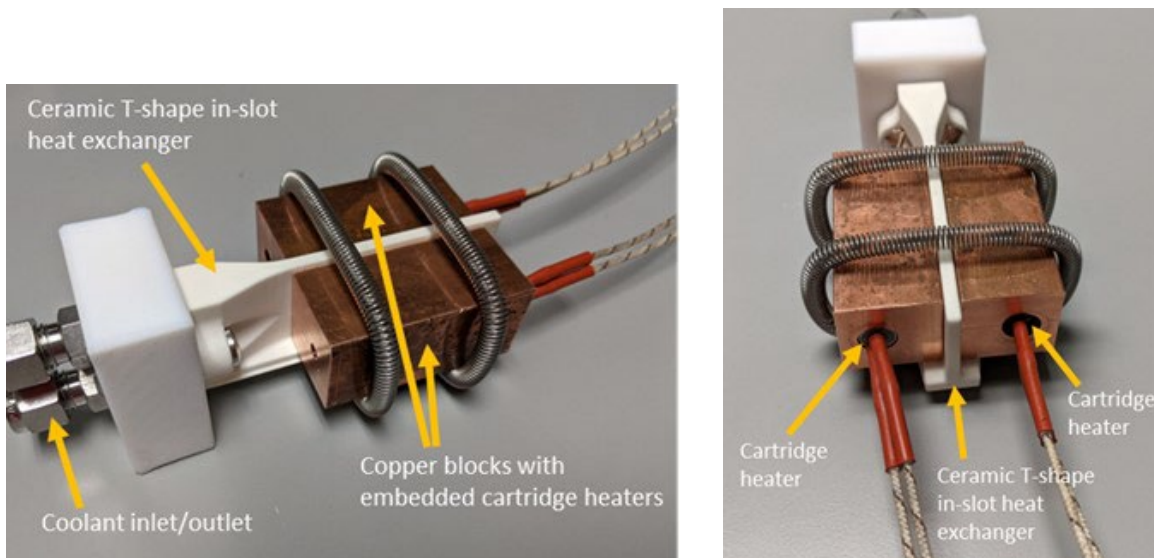


Figure I.1.10.4 Experimental setup for evaluation of the T-shape heat exchanger performance. Illustration by Bidzina Kekelia, NREL

The cylindrical inverter housing design was also updated; Figure I.1.10.5 presents the current evolution of the design. The work on accommodating the six-phase inverter assembly in the cylindrical housing is continuing, and further modifications are expected during FY24.

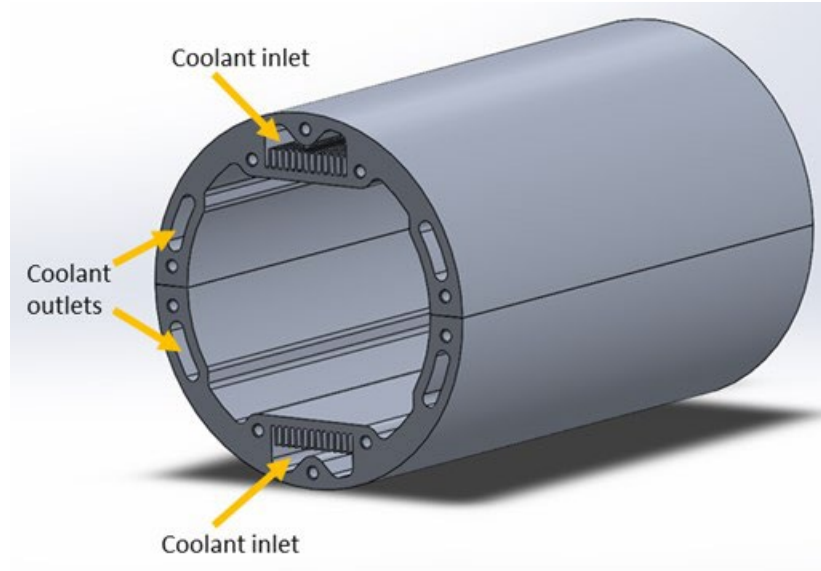


Figure I.1.10.5 Current design of the cylindrical inverter housing. *Illustration by Bidzina Kekelia, NREL*

Supporting the University of Wisconsin's Integrated Motor Design Team

The NREL team continues regular biweekly meetings with the University of Wisconsin team. In FY23, the University of Wisconsin manufactured and assembled their integrated traction drive. NREL helped evaluate the drive's thermal management system performance and review the team's conference publication materials.

Conclusions

The project accomplishments and conclusions for FY23 are summarized as follows:

- Collaboration with the integrated drive teams at ORNL and the University of Wisconsin is continuing successfully.
- We have completed several design revisions of thermal management system components (T-shape in-slot heat exchangers, coolant distribution manifold-disk, and cylindrical inverter housing) for ORNL's outer-rotor integrated drive due to changes in the drive's evolving mechanical design.
- We have manufactured (3D-printed) first samples of ceramic heat exchangers but encountered difficulties with quality and cracking during sintering. We are currently working on solutions with multiple vendors.
- Experimental evaluation of ceramic heat exchanger performance for ORNL's integrated drive is underway.
- Work continues with the ORNL team to accommodate power electronics in the cylindrical inverter housing, and further design changes are expected.
- NREL provided advisory assistance to the University of Wisconsin team in finalizing and evaluating experimental results of their integrated traction drive's demonstration unit.

Key Publications

1. Vandana Rallabandi, Mostak Mohammad, Himel Barua, Shajjad Chowdhury, Burak Ozpineci, Jonathan Wilkins, Lianshan Lin, Bidzina Kekelia, and Emily Cousineau. 2023. "A High-speed Surface Permanent Magnet External Rotor Motor and Integrated Drive for Electric Vehicles." *IEEE Energy Conversion Congress and Expo*, Nashville, TN, Oct. 29–Nov. 2, 2023.

References

1. U.S. DRIVE. 2017. *Electrical and Electronics Technical Team Roadmap*. Washington, D.C.: U.S. Department of Energy Office of Energy Efficiency and Renewable Energy Vehicle Technologies Office. <https://www.energy.gov/sites/prod/files/2017/11/f39/EETT%20Roadmap%2010-27-17.pdf>.

Acknowledgments

The author would like to acknowledge the significant contributions of Emily Cousineau and Jeff Tomerlin (NREL), as well as valuable technical input and discussions with Vandana Rallabandi, Jon Wilkins, Shajjad Chowdhury, Himel Barua, Mostak Mohammad, and Steve Bullock (ORNL). Discussions with Bulent Sarlioglu, Thomas Jahns, Ken Chen, Wenda Feng, Feida Chen, and Sanghwee Lee from the University of Wisconsin are also appreciated.

I.1.11 Bottom-Up Soft Magnetic Composites (Sandia National Laboratories)

Todd Monson, Principal Investigator

Sandia National Laboratories
P.O. Box 5800, MS 1415
Albuquerque, NM 87185
E-mail: tmonson@sandia.gov

Susan Rogers, DOE Technology Development Manager

U.S. Department of Energy
E-mail: susan.rogers@ee.doe.gov

Start Date: October 1, 2018
Project Funding: \$125,000

End Date: September 30, 2024
DOE share: \$125,000

Non-DOE share: \$0

Project Introduction

In order to meet 2025 goals for enhanced peak power (100 kW), specific power (50 kW/L), and reduced cost (3.3 \$/kW) in a motor that can operate at $\geq 20,000$ rpm, improved soft magnetic materials must be developed. Better performing soft magnetic materials will also enable rare earth free electric motors. In fact, replacement of permanent magnets with soft magnetic materials was highlighted in the Electrical and Electronics Technical Team (EETT) Roadmap [1] as a R&D pathway for meeting 2025 targets. Eddy current losses in conventional soft magnetic materials, such as silicon steel, begin to significantly impact motor efficiency as rotational speeds increase. Soft magnetic composites (SMCs), which combine magnetic particles with an insulating matrix to boost electrical resistivity (ρ) and decrease eddy current losses, even at higher operating frequencies (or rotational speeds), are an attractive solution. Today, SMCs are being fabricated with values of ρ ranging between 10^{-3} to 10^{-1} $\mu\text{ohm}\cdot\text{m}$ [2], which is significantly higher than 3% silicon steel (~ 0.5 $\mu\text{ohm}\cdot\text{m}$) [3]. The isotropic nature of SMCs is ideally suited for motors with 3D flux paths, such as axial flux motors. Additionally, the manufacturing cost of SMCs is low and they are highly amenable to advanced manufacturing and near net-shaping into complex geometries, which further reduces manufacturing costs. There is still significant room for advancement in SMCs, and therefore additional improvements in electrical machine performance. For example, despite the inclusion of a non-magnetic insulating material, the electrical resistivities of SMCs are still far below that of soft ferrites ($10 - 10^8$ $\mu\text{ohm}\cdot\text{m}$).

We are developing SMCs from the bottom up, with a final objective of creating composites with high magnetic material loading (and therefore high magnetization) while increasing the value of ρ several orders of magnitude over current state-of-the-art SMCs. To accomplish our goals, we are starting with particles of γ -Fe₄N, which have a saturation magnetic polarization (J_s) of 1.89 T, or roughly equivalent to most Si steels [4] and a ρ of ~ 2 $\mu\text{ohm}\cdot\text{m}$ [5]. In our bottom-up approach we begin by coating the magnetic particles with a diamine, which chemically reacts directly with epoxide terminated monomers to form a cross-linked epoxy composite. This “matrix-free” approach to composite formation will not suffer from the same nanoparticle aggregation and phase separation effects commonly observed in most nanocomposites [6]. Furthermore, it should ensure better separation between magnetic particles and significantly reduce or eliminate inter-particle eddy currents. A precedent already exists for the use of epoxies in electrical machine construction [7], [8]. Additionally, it is possible to design epoxy systems with glass transition temperatures (T_g) well in excess of the target maximum motor operating temperature of 150°C [9], as was documented in 2020’s annual progress report. Furthermore, composites have been successfully demonstrated in high-speed motors [10] and even flywheels rotating at speeds up to 60,000 rpm [11].

Objectives

The project objective is to develop high-magnetization, low-loss iron nitride based soft magnetic composites for electrical machines. These new SMCs will enable low eddy current losses and therefore highly efficient

motor operation at rotational speeds up to 20,000 rpm. Additionally, iron nitride and epoxy composites will be capable of operating at temperatures of 150°C or greater over a lifetime of 300,000 miles or 15 years.

Approach

A high-level overview of our methodology is:

1. Convert commercially available mixed-phase iron nitride powder to nearly phase-pure γ' -Fe₄N
2. Coat iron nitride particles with diamine molecules (part A of epoxy chemistry)
3. Combine surface functionalized particles with epoxide terminated monomers (part B of epoxy chemistry)
4. Fabricate SMC parts by adding mixture from #3 into a hot-pressing die or silicone mold
5. Evaluate and test fabricated SMC parts
6. Optimize SMC magnetic volume loading, magnetic properties, and physical properties

Results

1. Fabrication of Larger SMCs

As our capability to produce Fe₄N/epoxy samples improves we are progressing to the fabrication of larger parts. This is a key step towards producing inductor cores for motor drives and soft magnetic parts for electric motors. We recently acquired die that enables hot press toroids with an outer diameter (O.D.) of 35 mm and squares of 2 cm x 2 cm. A photograph of newly acquired die for fabricating larger toroids and cubes is displayed in Figure I.1.11.1.



Figure I.1.11.1 Die for pressing larger toroids and cubes.

Toroids with an O.D. of 35 mm were successfully fabricated using some of these new die and our in house hot pressing setup. An image of several manufactured toroids with a O.D. of 35 mm is shown in Figure I.1.11.2. These larger toroids are a significant step towards the fabrication of parts relevant for electric motors and drives. Additionally, these larger toroids can be shared with electric drive technologies research collaborators for both characterization and test bed demonstrations.

Soft magnetic toroids with an Outer Diameter (O.D.) of 35 mm.



Figure I.1.11.2 Soft magnetic toroids with an Outer Diameter (O.D.) of 35 mm.

2. Fabrication of DHAM Soft Magnetic Parts

A significant portion of the past fiscal year (FY) was devoted to the fabrication of soft magnetic parts for a dual rotor homopolar AC machine (DHAM) designed by our collaborators at Purdue University. These parts included a stator long leg assembly, stator short leg assembly, and rotor assembly. One benefit to fabricating soft magnetic motor parts using SMCs is that a monolithic Fe₄N composite would replace a stack of many electrical steel laminations. The first parts we fabricated used a molding process and therefore contained vol.% loadings of Fe₄N at 65% or less. CAD drawings of the soft magnetic parts were shared by Scott Sudhoff at Purdue and used to 3D print full size anti-molds using polylactic acid (PLA). An image of the anti-molds is displayed in Figure I.1.11.3.



Figure I.1.11.3 PLA anti-molds for the fabrication of DHAM soft magnetic components. From left to right: stator long leg assembly, stator short leg assembly, and rotor assembly.

The next step was to fabricate full size DHAM soft magnetic parts using neat epoxy. We fabricated silicone molds from the 3D printed anti-molds discussed above. Then, clear epoxy (CaldoFix-2, Struers) casts of the soft magnetic components were fabricated. An image of the clear epoxy parts are shown in Figure I.1.11.4.

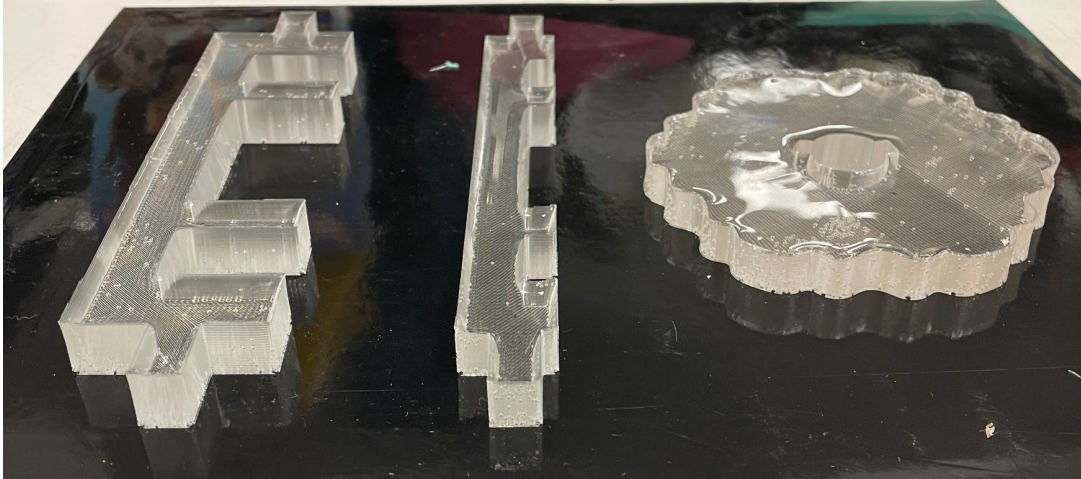


Figure I.1.11.4 Full size DHAM parts fabricated using neat epoxy. From left to right: stator long leg assembly, stator short leg assembly, and rotor assembly.

Finally, a 50% scaled version of the short stator assembly was fabricated using 55 vol.% Fe₄N in epoxy. An image of this part, after polishing, is displayed in Figure I.1.11.5.

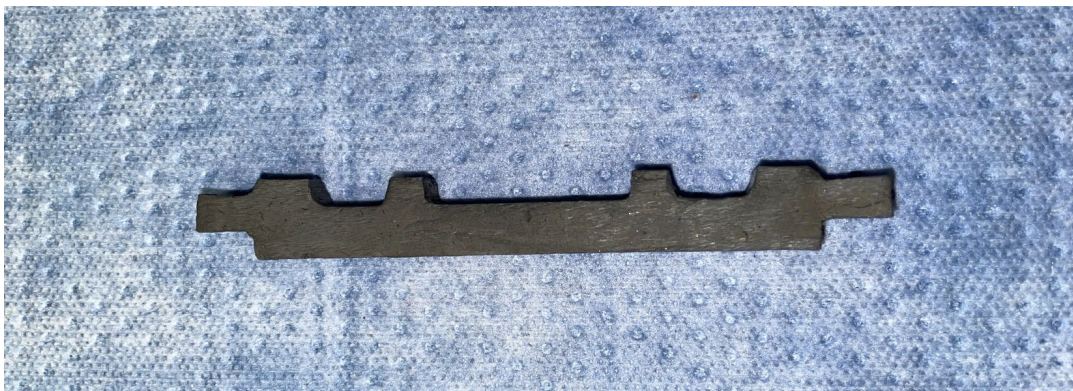


Figure I.1.11.5 50% scale version of the DHAM short stator assembly. This part is 55 vol.% Fe₄N.

After receiving a custom stainless steel die set for the rotor assembly, the next steps were to evaluate it in the current hot pressing set up in our lab. This die is significantly larger than any of the others used previously under this effort so a new heating band and approach to heating was required. The temperature of the die was closely monitored in several places on the die until a method for consistent heating was found. The procedure requires the die to be preheated to 180°C for several hours before the uncured composite is added into the die. Once the uncured composite is in the die, the preheated anvil is inserted and the composite is pressed at 37 MPa. This is significantly lower than smaller pressed parts due to the size and shape of the rotor assembly and die. The die is left under pressure overnight at a temperature of 180°C.

There were concerns with the die seizing during the press so carbon paper was used in between the base and the outer die to ensure the base and sample could be demolded. This worked well and the demolding process was able to be performed. During the very first demolding process, the sample broke into 3 pieces upon demolding. Other approaches for demolding pressed and cured rotor assemblies were then applied to ensure they came out of the die nearly defect free. Currently, samples have been demolded with very few or negligible defects including hairline fractures or chipping along the inner or outer edges. During the next FY, additional improvements will be made to ensure defect free rotor assemblies after hot pressing and demolding.

Pictures of the hot pressing setup (Figure I.1.11.6), the part during demolding (Figure I.1.11.7 and Figure I.1.11.8), and the rotor assembly after demolding and polishing (Figure I.1.11.9) are displayed below.



Figure I.1.11.6 Composite under both pressure and heat.

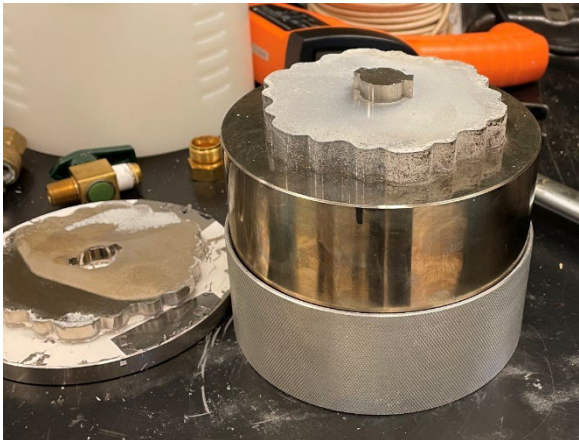


Figure I.1.11.7 DHAM rotor assembly during demolding.

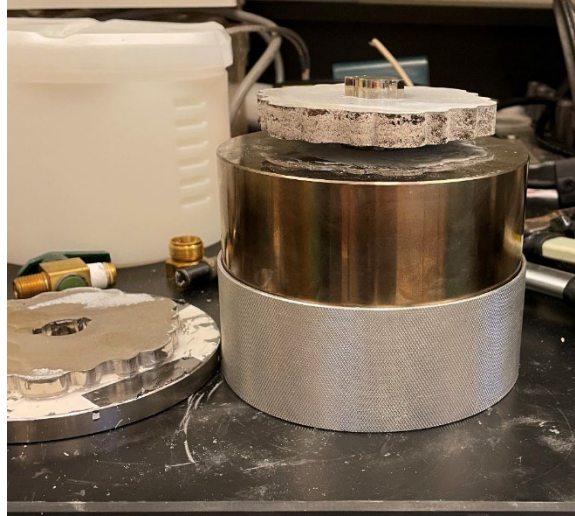


Figure I.1.11.8 DHAM rotor assembly after partial demolding.



Figure I.1.11.9 DHAM rotor after complete demolding and polishing. A hairline fracture, barely visible in the image, is the only defect in this sample.

3. Nanoindentation of Iron Nitride Based SMCs

Nanoindentation measurements of several iron nitride based epoxy composites were performed by consortium members and collaborators at Ames Lab. These data complement tensile testing performed on similar samples at NREL and were documented in the 2022 annual report. The nanoindentation experiments measured the Berkovich modulus and hardness of SMC samples at depths ranging from 1 to 5 μm . In the case of these iron nitride/epoxy composites, the modulus and hardness values across this range of depths are in agreement. As the indentation depth increased, the values do comprise a more averaged response from both Fe_4N and epoxy phases and therefore less spread in measured values. This explains the reduction in error bar height as indentation depth increases. The average Berkovich modulus for a sample of 55 vol.% Fe_4N in epoxy was measured to be 26.1 ± 0.4 GPa. A plot of this data as a function of indentation depth is shown in Figure I.1.11.10. The average Berkovich hardness for the same sample was measured to be 1.22 ± 0.03 GPa. A plot of this data as a function of indentation depth is shown in Figure I.1.11.11. Finally, a scanning electron microscope (SEM) image of the indentations in the SMC sample is displayed in Figure I.1.11.12.

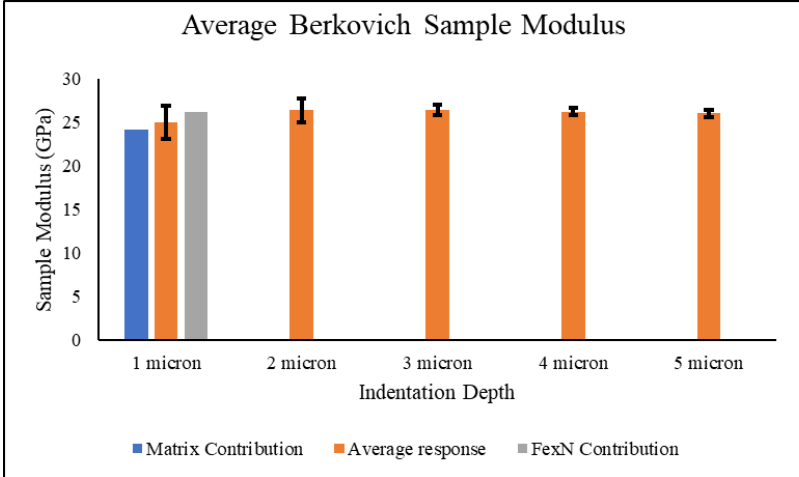


Figure I.1.11.10 Average Berkovich modulus for a sample of 55 vol.% Fe₄N in epoxy.

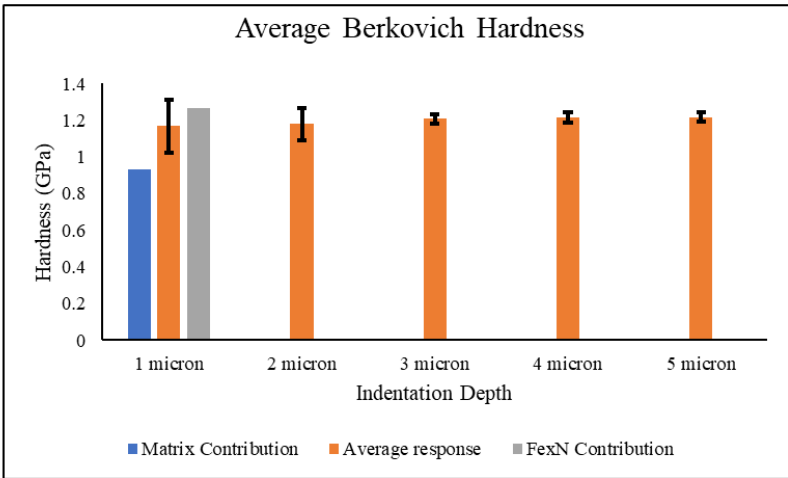


Figure I.1.11.11 Average Berkovich hardness for a sample of 55 vol.% Fe₄N in epoxy.

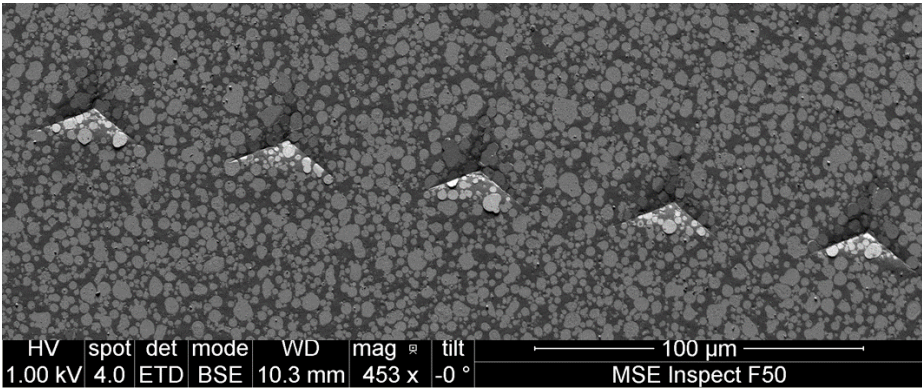


Figure I.1.11.12 An SEM image of the indentations in a sample of 55 vol.% Fe₄N in epoxy.

Conclusions

During FY23, important progress was made in the fabrication and characterization of iron nitride (γ' -Fe₄N) based soft magnetic composites and parts for electric motors. It is important to keep in mind that these materials also show substantial promise as inductor cores for motor drives. A lab based hot pressing setup was

used to produce Fe₄N based rotor assemblies for a DHAM designed at Purdue University. By the end of the FY, rotor assemblies with only minor defects were fabricated. It is anticipated that the demolding process can be improved further to produce defect free parts in FY24. Additionally, a 50% scaled version of a short stator assembly for the DHAM was fabricated using silicone mold. Samples were fabricated for nanoindentation testing by consortium partner Ames lab. The modulus and hardness of our composites are similar to other SMCs. Please keep in mind that in order to adopt Fe₄N based SMCs in electric machine rotor construction it may be necessary to utilize carbon fiber sleeves for added mechanical strength. However, there is considerable precedence already for the use of carbon fiber sleeves in electric motor construction [12]. Future work will focus on continuing to increase magnetic material volume loading and enhancing performance in both electric motor and drive applications. Finally, during FY 2024 we will continue to collaborate with EDTC consortium members NREL, Oak Ridge National Lab (ORNL), and Ames Lab to model and evaluate Fe₄N based SMCs in axial flux motor designs.

Key Publications

1. M.R. Hoyt, G.I. Falcon, C.J. Pearce, R.E. Delaney, T.E. Stevens, E.M. Johnson, T.M. Szenderski, N.R. Sorenson, S.F. Fultz-Waters, M.A. Rodriguez, L.J. Whalen, T.C. Monson, "Fabrication and characterization of net-shaped iron nitride-amine-epoxy soft magnetic composites," *Frontiers in Materials*, **10**, 1-14 (2023). DOI: [10.3389/fmats.2023.1258382](https://doi.org/10.3389/fmats.2023.1258382).
2. Iron Nitride Soft Magnetics was a 2022 R&D 100 Award winner in the Process/Prototyping category

References

1. U.S. DRIVE, "Electrical and Electronics Technical Team Roadmap," Partnership Plan, Roadmaps, and Other Documents 2017.
2. H. Shokrollahi and K. Janghorban, "Soft magnetic composite materials (SMCs)," *Journal of Materials Processing Technology*, vol. 189, no. 1-3, pp. 1-12, 2007, doi: 10.1016/j.jmatprotec.2007.02.034.
3. J. S. Corporation. Super Core™ Electrical steel sheets for high-frequency application. (2017). JFE Steel Corporation. [Online]. Available: <http://www.jfe-steel.co.jp/en/products/electrical/catalog/flc-002.pdf>
4. J. M. D. Coey, *Magnetism and Magnetic Materials*. New York: Cambridge University Press, 2010.
5. T. C. Monson et al., "Soft Magnetic Multilayered FeSiCrB–Fe₄N Metallic Glass Composites Fabricated by Spark Plasma Sintering," *IEEE Magnetics Letters*, vol. 10, pp. 1-5, 2019, doi: 10.1109/LMAG.2019.2906832.
6. M. Qu et al., "Magneto-photo-acoustic imaging," *Biomedical Optics Express*, vol. 2, no. 2, pp. 385-396, 2011/02/01 2011, doi: 10.1364/BOE.2.000385.
7. M. Magazine. <https://magneticmag.com/new-structural-adhesive-from-delo-for-magnet-bonding-has-high-temperature-stability/> (accessed).
8. Crosslinktech. <http://www.crosslinktech.com/products-by-application/featured-electric-motor-products.html> (accessed).
9. M. Bond. <https://www.masterbond.com/techtips/how-optimizing-glass-transition-temperature-tg> (accessed).
10. A. Schoppa and P. Delarbre, "Soft Magnetic Powder Composites and Potential Applications in Modern Electric Machines and Devices," *IEEE Transactions on Magnetics*, vol. 50, no. 4, pp. 1-4, 2014, doi: 10.1109/TMAG.2013.2290135.

11. P. Mason, K. Atallah, and D. Howe, Hard and soft magnetic composites in high speed flywheels. 1999.
12. V. C. d. Nascimento and S. D. Sudhoff, "Non-Axisymmetric Structural Analysis of High Speed Rotor Orthotropic Retention Sleeve," in 2019 IEEE International Electric Machines & Drives Conference (IEMDC), 12-15 May 2019 2019, pp. 797-804, doi: 10.1109/IEMDC.2019.8785324.

Acknowledgements

This work is supported by the DOE Office of Energy Efficiency and Renewable Energy, Vehicle Technologies Office. Sandia National Laboratories is a multi-mission laboratory managed and operated by National Technology and Engineering Solutions of Sandia, LLC., a wholly owned subsidiary of Honeywell International, Inc., for the U.S. Department of Energy's National Nuclear Security Administration under contract DE-NA0003525. The views expressed in the article do not necessarily represent the views of the U.S. Department of Energy or the United States Government. We wish to thank Melinda Hoyt, Charles Pearce, Jacob Krynock, and Sydney Fultz-Waters for their fabrication of magnetic composites; Robert Delaney and Charles Pearce for their assistance with magnetic characterization; and Mark Rodriguez for his help with X-ray diffraction data collection and analysis. We would also like to acknowledge key collaborators within the electric drive systems consortium: Emily Cousineau (NREL), Iver Anderson (Ames Lab), Jun Cui (Ames Lab), Matt Kramer (Ames Lab), and Scott Sudhoff (Purdue University).

I.1.12 Power Electronics: Vertical GaN Device Development (Sandia National Laboratories)

Jack Flicker, Principal Investigator

Sandia National Laboratories
P.O. Box 5800, MS 1033
Albuquerque, NM 87185
E-mail: jdflick@sandia.gov

Susan Rogers, DOE Technology Development Manager

U.S. Department of Energy
E-mail: susan.rogers@ee.doe.gov

Start Date October 1, 2018:

End Date: September 30, 2024

Project Funding: \$70,000

DOE share: \$70,000

Non-DOE share: \$0

Project Introduction

A detailed Genetic Algorithm (GA) topology optimization [1] for the vehicle Electric Traction Drive (EDT) synchronous boost converter and inverter is being carried out. Candidate designs from pareto frontiers have been identified for SiC and GaN based semiconductor switches that achieve large power densities. However, these optimal designs are enabled only through the use of high energy density of multilayer ceramic capacitors (MLCCs) in a distributed architecture of many (~250) small value MLCCs. Use of these distributed small MLCC capacitors on a DC bus enables significant gains in system power density, but, due to the increased component count, has a detrimental effect on system-level mean time to failure (MTTF). To achieve system-level power density and cost requirements while still meeting reliability targets, it will be necessary to significantly increase MTTF of base-metal electrode MLCCs. For these devices, the primary failure mechanism at high voltage and high temperature is low insulation resistance and shorting caused by electromigration of defects in the dielectric layer. Oxygen vacancies, a natural defect which occurs during firing of the capacitors in reducing atmospheres to enable base-metal electrodes (Ni), migrate under the applied electric field and gather at the cathode. This decreases the Schottky barrier at the metal-dielectric interface causing leakage and, eventually, shorting. Minimization of this failure mechanism is paramount for increasing MTTF.

Objectives

The objective of this research is to investigate ways to extend MTTF through system level control instead of from a material science approach. Decades of R&D have gone into minimizing oxygen vacancies, preventing their diffusion via the addition of migration barriers (*i.e.*, grain boundaries), binding dopants to pin them in place, etc. This vast amount of research and development has resulted in the current state of base-metal electrode MLCC's with significantly increased lifetimes. However, further increases in lifetime are difficult to achieve compositionally/microstructurally, and other solutions may be necessary on a device level. This work investigates that approach.

Approach

Instead of addressing performance/reliability through material composition and microstructure, we take an innovative approach to prevent oxygen vacancies from reaching the cathode by applying a reverse bias periodically (*i.e.*, an AC waveform) to push the oxygen vacancies back to their original positions. This approach may be difficult to implement on a circuit level, but, if successful, may allow for unique circuit designs based on much longer lifetime, high density MLCC capacitors.

A system to simultaneously evaluate 40 capacitors under AC conditions with temperature control was fabricated using a custom heating stage, multiple relays, and a H-bridge. This scale-up allows for much quicker measurements than previously, as well as for Weibull statistics to be performed. This is important due to the propensity for X7R MLCC capacitors to contain infant mortality (Weibull $\beta < 1$) and early-wear-out (Weibull $\beta \sim 1.5$) failures in conjunction with wear-out (Weibull $\beta \sim 5-10$). The unit contains a power/voltage bus that delivers the high voltage for accelerated degradation, and a low-voltage measurement bus to which capacitors

can be switched to allow for any 2-terminal device measurement - most importantly insulation resistance. The capacitor can then be returned to the high voltage bus to continue degradation.

Initial test results in FY21 using the 40-capacitor test setup showed a distinctly different trend than the initial test results. Namely, the increased frequency of voltage application resulted in *lower* lifetimes instead of *longer* lifetimes. Work during FY22 focused on expanding the capacitor study to multiple other acceleration conditions on similar parts and understanding the lifetime dependence and failure mechanism under AC conditions in different regimes. FY23 focused on re-evaluating the 100V, 200°C stress condition at a higher failure criterion (10Hz, 1Hz, 0.1Hz, etc. down to 0.001Hz) as well as completing the 60V, 225°C stress condition measurements (0.1Hz, 0.001Hz, 10Hz). Finally, MTTF of the capacitor was evaluated under low acceleration conditions (e.g., 200V, 150°C, which represent more ‘typical’ usage values) with the goal to eliminate catastrophic failure entirely and determine true MTTF vs. frequency.

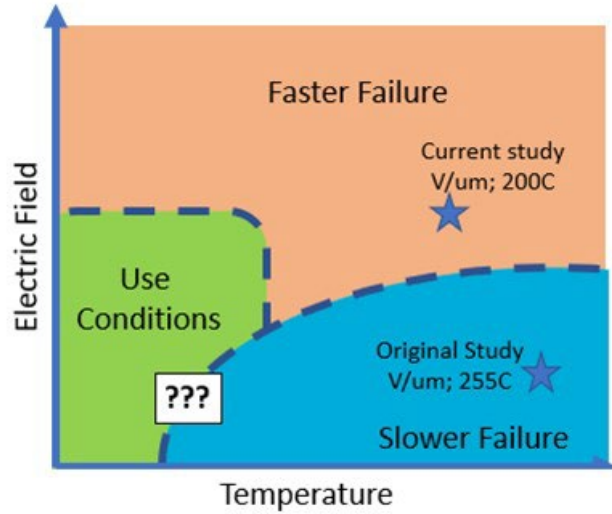


Figure I.1.12.1 Schematic representation of current results showing change in frequency-dependent time to failure as a function of acceleration conditions. The differentiation between these two and the behavior at use conditions is unknown.

Results

Leakage current vs time results are shown for both DC and 0.1Hz switching frequency conditions are shown in Figure I.1.12.2. A clear increase in leakage current over time is seen. MTTF for the 45V/255°C condition is slightly lower than the other two conditions; however, it is still roughly the same acceleration given the combined power law and exponential nature of Eq (1). Many capacitors failed and shorted before the insulation resistance degraded to the prescribed 10x failure condition. The failure time was taken as the time of shorting, and for clarity the location of these shorts on I(t) curves for all parts that shorted before the 10x current failure criterion was reached are marked with arrows.

Two clear results are seen in Figure I.1.12.2. First, alternating polarity voltage application affects lifetime significantly differently for the different combinations of voltage and temperature driven acceleration. The switch to alternating polarity stress causes an increase in lifetime under the low voltage-high temperature (45V/255°C) condition while the same stress causes a decrease in lifetime in the high voltage-low temperature (100V/200°C) condition. The medium voltage/temperature (60V/225°C) condition shows little change in median time to failure, though the

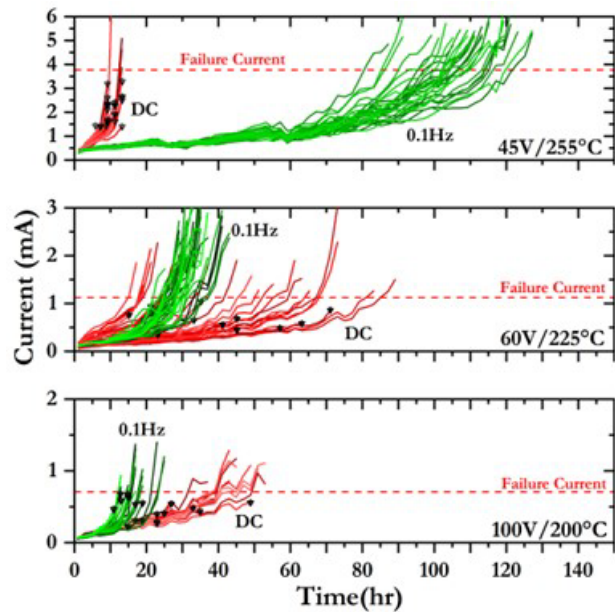


Figure I.1.12.2 Current vs time plots for all degradation conditions at DC and 0.1Hz conditions. Red lines are DC and Green lines are 0.1Hz. Average failure current (10x average initial current) is marked for each condition. Failure locations of all parts which shorted before failure current was reached are marked with black arrows.

distribution does seem to narrow. Secondly, the number of parts that failed to a short before the 10x failure criterion was reached decreases significantly with bipolar voltage application in comparison to unipolar DC voltage application. The effect of bipolar voltage bias to the lifetime to MLCC's is therefore not straightforward.

To explore the lifetime behavior further, voltage of alternating polarity at different switching frequencies were applied to capacitors. This was done for all three different acceleration conditions. The data is summarized in Figure I.1.12.3 in the form of Weibull Plots alongside a summary plot of MTTF as a function of the voltage stress signal frequency normalized to the MTTF under unipolar DC conditions.

Trends in MTTF vs voltage signal frequency are confirmed to be heavily dependent on voltage/temperature acceleration condition. The largest change is in the 45V/225°C condition with a $\sim 9x$ increase in lifetime in comparison to DC conditions, showing that lifetime extension is possible albeit in a voltage range that is less than half the rated voltage. As temperature acceleration is traded for voltage acceleration in the 60V/225°C condition, a more modest increase in MTTF of $\sim 2.6x$ at 0.5mHz is obtained. However, this is followed by a decrease in MTTF for increased frequencies, plateauing at a $MTTF/MTTF_{DC}$ of ~ 0.7 above 0.1Hz. A similar trend in MTTF is seen for the 100V/200°C condition resulting in a lower $MTTF/MTTF_{DC}$ of $\sim 0.4x$.

The increase in MTTF in the 45V/255°C condition is similar to previous results [2] and may be due to the periodic redistribution of oxygen vacancies as hypothesized; however, an infinite lifetime increase is not seen here as parts still fail eventually and therefore a limitation to this mechanism of lifetime extension seems to exist. One potential reason for this may be the mechanism proposed by Schulze et al. where oxygen vacancies under sinusoidal AC stress may still migrate, but instead of accumulating at the cathode will simply accumulate at areas such as grain boundaries instead due to chemical potential differences inside of the dielectric grain. [3] While outside of the scope of current work, impedance spectroscopy and Thermally Stimulated Depolarization Current measurements in future endeavors may help clarify the degradation physics.

The mechanism of decreasing MTTF with frequency is less clear. It may be due to cracking of the dielectric due to large bipolar stresses as is seen in multilayer piezoelectric actuators, but at 200+ °C the X7R dielectric is well above the Curie Temperature and is therefore not piezoelectric, significantly reducing this likelihood. [4], [5] Interestingly, the voltage stress magnitude which crosses over from lifetime-extension to lifetime-degradation is around the recommended AC stress maximum recommended by

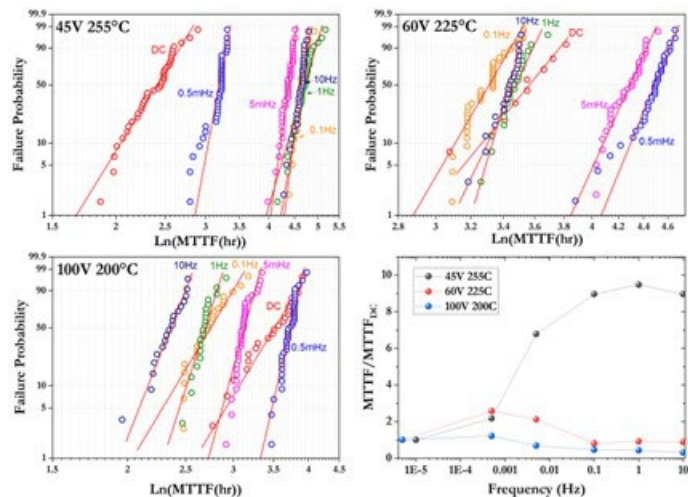


Figure I.1.12.3 Weibull plots of MLCC failure as a function of bipolar AC frequency for three acceleration conditions: 45V 255°C (a), 65V 225°C (b), and 100V 210°C (c). (d) MTTF as a function of voltage stress signal frequency for each condition normalized to MTTF under DC conditions.

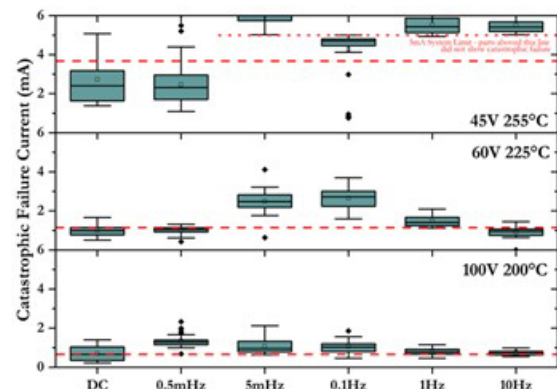


Figure I.1.12.4 Failure Current as a function of acceleration condition and switching frequency of voltage stress. Red dotted lines are the average failure criterion for slow degradation (10x the initial leakage current).

manufacturers of half the DC rated voltage. While little/no evidence in literature was found by the author to underpin these ratings, this work seems to be in line with these ratings and may add weight to them beyond simply internal knowledge of MLCC manufacturers.

As mentioned in the discussion of Figure I.1.12.2, the added complexity of catastrophic failure vs slow degradation of IR exists. It's well known that voltage acceleration increases the probability of catastrophic failure due to short in comparison to temperature acceleration. Questions in literature have been raised as to the validity of lumping catastrophic failures due to a short and failures via slow degradation of insulation resistance together as a similar failure mechanism. Studies from Keyocera showed that in X7S MLCCs the failure due to a short was the result of an anomalously thin dielectric layer while propensity for slow degradation is related to changes in dielectric grain size. [6], [7] Others have separated these out into 'catastrophic' or 'slow-degradation' failures showing slightly different acceleration constants, though it is difficult to determine if this is simply survivorship bias reflected in fitting. [8]

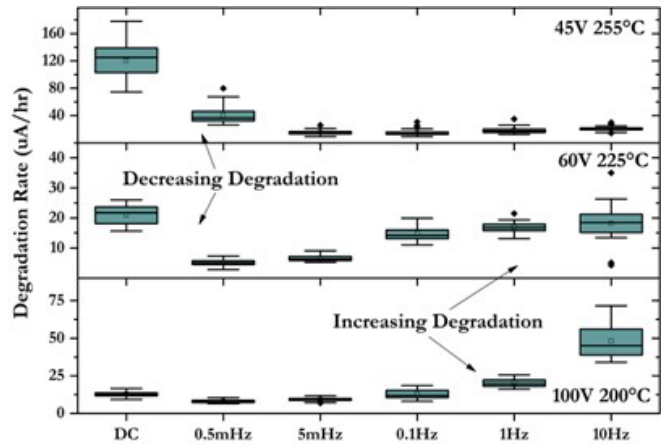


Figure I.1.12.5 Degradation rate as a function of switching frequency of voltage stress for different acceleration conditions.

Due to the difference in prevalence of these different failure modes in bipolar and unipolar conditions, data for all samples was investigated to determine the rough share of these two mechanisms. To achieve this, the final measured current before catastrophic failure occurred was pulled from data and plotted for all parts. This data is shown in Figure I.1.12.4 in the form of box plots and compared to the average 10x initial current failure criterion.

Figure I.1.12.4 shows the expected behavior in the DC case. Namely, that catastrophic failure current decreases with increasing voltage stress. All parts show an increase in catastrophic failure current for a subset of switching frequencies; however, for the 60V/225°C and 100V/200°C conditions, this trend is reversed with an increasing failure current with increasing frequency. The degree that the catastrophic failure current distributions straddle the 10x failure current condition represents the amount of mixing of catastrophic and slow degradation failures, and this seems to change drastically with frequency condition. This shows that under many conditions the increase in catastrophic failure current may be skewing total MTF results. Given this result, a different metric was used to gain additional assurance of trends.

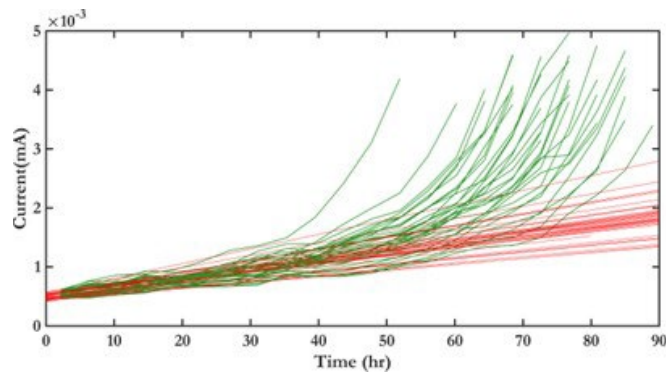


Figure I.1.12.6 Examples of fits to linear portion of I(t) curves for degradation rate assessment for 45V 255°C 5mHz condition.

The complex trend of catastrophic failure current as a function of switching frequency was removed by investigating degradation rate directly. Degradation rate was assessed using via fitting to the linear portion of I(t) curves. Example data is shown for the 45V 255C 5mHz condition in Figure I.1.12.5 and degradation rates for all measured DUT's are summarized as box plots in Figure I.1.12.6

The low voltage condition shows the expected trend of decreasing degradation rate with increasing frequency. The medium and high voltage conditions show an initial decrease in degradation rate followed by an increase in degradation rate as frequency increases. This matches the trends in MTTF and suggests that the change in MTTF is not primarily driven by changes in failure mechanism from shorting to slow degradation.

Despite the agreement of MTTF and degradation rate data, it was decided to confirm this result on lower acceleration conditions to minimize over-test risk. The results are shown in Figure I.1.12.7

As can be seen, the low voltage condition (45V 210°C) shows an increase in lifetime while a high voltage condition (100V 175°C) shows a decrease in lifetime, confirming previous trends.

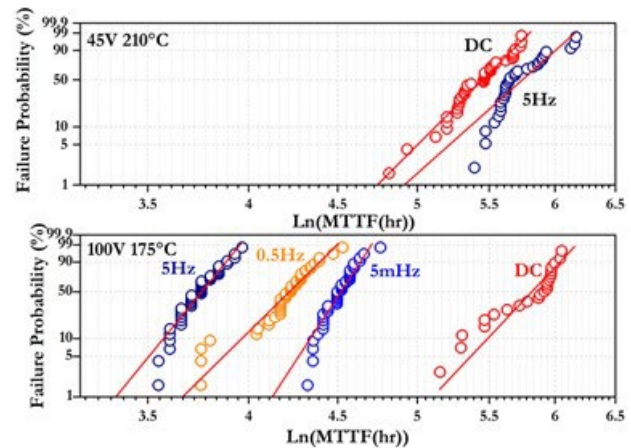


Figure I.1.12.7 Change in Time to Failure for lower acceleration conditions for high voltage (100V and 175 °C) and low voltage (45V 210 °C).

Conclusions

The data taken here shows that the effect of alternating polarity voltage stress on MLCC lifetime is heavily affected by the choice between voltage or temperature acceleration during Highly Accelerated Lifetime Testing (HALT). Lifetime extension under increasing switching frequency occurs under lower voltage stress while increasing voltage acceleration switches behavior to a lifetime degradation with increasing switching frequency. While the lower voltage lifetime extension suggests that oxygen vacancies can be redistributed by reversing the field polarity, further work via impedance spectroscopy, thermally stimulated depolarization currents, and destructive physical analysis including Transmission Electron Microscopy Electron Energy Loss Spectroscopy (TEM EELS) is suggested for proving this supposition.

Key Publications

- Jonathan Bock, Will Bachman, Scott Ehlers, and Jack Flicker. "Reliability of X7R MLCCs Under Alternating Polarity Highly Accelerated Lifetime Testing". *Transactions on Components, Packaging and Manufacturing Technology*. (Submitted, 2023).

References

- L. Gill, J. Neely, L. Rashkin, J. Flicker and R. Kaplar, "Co-Optimization of Boost Converter Reliability and Volumetric Power Density Using Genetic Algorithm," in 2020 IEEE Energy Conversion Congress and Exposition (ECCE), Detroit, MI, October 2020.
- L. M. Garten, J. A. Bock, E. A. Patterson, I. Graham, M. A. Blea and H. J. Brown-Shaklee, "Increasing Capacitor Lifetime with AC Electric Field Cycling," in Proceedings of the 2022 US-Japan Seminar on Dielectris and Piezoelectrics, Charleston, South Carolina, 2022.
- W. A. Schulze, L. E. Cross and W. R. Buessem, "Degradation of BaTiO₃ Ceramic Under High AC Electric Fields," *Journal of the American Ceramic Society*, vol. 63, no. 1-2, pp. 83-87, 1980.
- J. Thongrueng, T. Tsuchiya and K. Nagata, "Lifetime and Degradation Mechanism of Multilayer Ceramic Actuator," *Japanese Journal of Applied Physics*, vol. 37, no. 9B, pp. 5306-5310, 1998.
- P. Pertsch, S. Richter, D. Kopsch, N. Kramer, J. Pogodzick and E. Henning, "Reliability of Piezoelectric Multilayer Actuators," in ACTUATOR 2006 Conference, Bremen, Germany, 2006.

6. T. Sada and N. Fujikawa, "Analysis of Insulation Resistance Degradation in Ni-BaTiO₃ multilayer ceramic capacitors under highly accelerated life test," Japanese Journal of Applied Physics, vol. 56, pp. 10PB04-1-4, 2017.
7. M. Nagayoshi, K. Matsubara and N. Fujikawa, "Analyses of microstructure at degraded local area in Ni-Multilayer Ceramic capacitors under highly accelerated life test," Japanese Journal of Applied Physics, vol. 59, p. SPPC01, 2020.
8. D. Liu, "A General Reliability Model for Ni-BaTiO₃-Based Multilayer Ceramic Capacitors," in Capacitors and Resistors Technology Symposium, Santa Clara, CA, 2014.

Acknowledgements

This work is supported by the DOE Office of Energy Efficiency and Renewable Energy, Vehicle Technologies Office. Sandia National Laboratories is a multi-mission laboratory managed and operated by National Technology and Engineering Solutions of Sandia, LLC., a wholly owned subsidiary of Honeywell International, Inc., for the U.S. Department of Energy's National Nuclear Security Administration under contract DE-NA0003525. The views expressed in the article do not necessarily represent the views of the U.S. Department of Energy or the United States Government.

I.1.13 Power Electronics: Vertical GaN Device Development (Sandia National Laboratories)

Andrew Binder, Principal Investigator

Sandia National Laboratories
P.O. Box 5800, MS 1086
Albuquerque, NM 87185
E-mail: abinder@sandia.gov

Susan Rogers, DOE Technology Development Manager

U.S. Department of Energy
E-mail: susan.rogers@ee.doe.gov

Start Date: October 1, 2018

End Date: September 30, 2024

Project Funding: \$750,000

DOE share: \$750,000

Non-DOE share: \$0

Project Introduction

This project is part of a multi-lab consortium that leverages U.S. research expertise and facilities at national labs and universities to significantly advance electric drive power density and reliability, while simultaneously reducing cost. The final objective of the consortium is to develop a 100 kW traction drive system that achieves 33 kW/L, has an operational life of 300,000 miles, and a cost of less than \$6/kW. One element of the system is a 100 kW inverter with a power density of 100 kW/L and a cost of \$2.7/kW. New materials such as wide-bandgap semiconductors, soft magnetic materials, and ceramic dielectrics, integrated using multi-objective co-optimization design techniques, will be utilized to achieve these program goals. This project focuses on a subset of the power electronics work within the consortium, specifically the design, fabrication, and evaluation of vertical GaN power devices suitable for automotive applications.

Objectives

Gallium Nitride (GaN) is a promising wide-bandgap (WBG) semiconductor material that could enable higher-performance power electronic devices than traditional Silicon (Si) or even its WBG counterpart, Silicon Carbide (SiC). This is based on the increased critical electric field of GaN, which would enable lower-resistance devices with the same hold-off voltage as devices fabricated from the other materials. This is a key performance metric for power devices. Laterally-oriented, High Electron Mobility Transistors (HEMTs) based on AlGaN and GaN materials are common in high-frequency applications and are being established in lower-voltage power switching applications (approximately 600 V and below). However, with the emerging commercial maturation of GaN substrates, traditional vertically-oriented device structures (such as are common in Si and SiC) can now be realized in GaN, with several promising demonstrations of high-voltage pn diodes and vertical transistors appearing in the literature [1], [2], [3]. While GaN pn diodes may be of interest, the ~3 V turn-on voltage, determined mainly by the bandgap of the material, discourages their use in some power-switching circuits due to the loss of power conversion efficiency resulting from this high turn-on voltage. Instead, more promising candidates for these power conversion systems, including automotive inverters, are GaN Schottky barrier diodes (SBDs) and Junction Barrier Schottky (JBS) diodes, shown in Figure I.1.13.1(a), which have turn on voltages of ~1 V as determined by the Schottky barrier height of the metal to the semiconductor material, rather than the semiconductor bandgap.

Similarly, vertically-oriented GaN transistors promise high-performance as power electronic devices if several key growth and fabrication challenges are overcome for the GaN material system. Interestingly, several different types of vertical GaN transistors have been demonstrated including Metal Oxide Semiconductor Field-Effect Transistors (MOSFETs) in the trench configuration (T-MOSFET, shown in Figure I.1.13.1b), the double-well (D-MOSFET) configuration (shown in Figure I.1.13.1c), and the Current Aperture Vertical Electron Transistor (CAVET) configuration [4], [5], [6]. Each of these device topologies has benefits and challenges associated with fabrication and performance, but the MOSFET designs show the most promise for power switching applications and are being investigated during this effort. With the MOSFET device designs, challenges exist in making the semiconductor/insulator (or oxide) interface due to the lack of a good native

oxide for GaN (Si and SiC both have native oxides). In addition, selective-area doping control, which is needed to form lateral pn junctions, cannot be easily achieved in GaN. Current state-of-the-art GaN devices use techniques such as ion implantation with special anneal processes (high-pressure and high-temperature) [7] or epitaxial regrowth [8] to realize selective-area doping control. Both techniques are relatively immature in GaN, and their behavior needs to be studied and techniques need to be developed to control these processes for eventual use in power systems for electric vehicles.

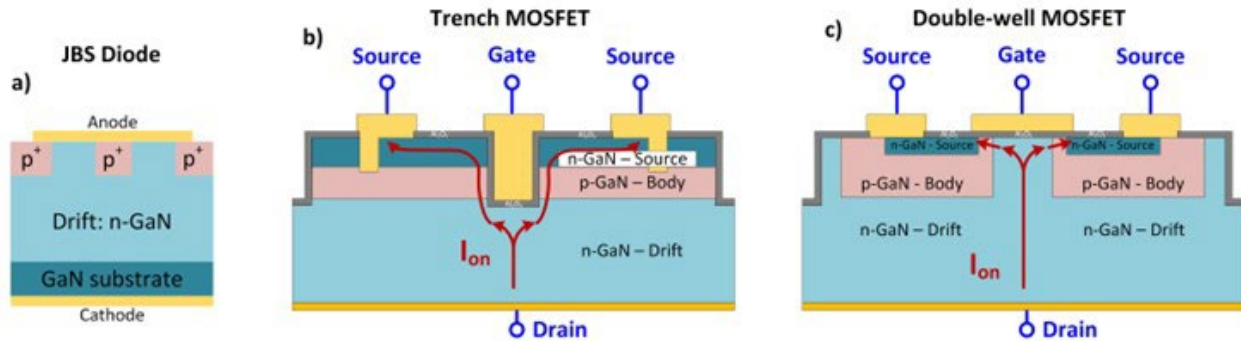


Figure I.1.13.1 (a) Schematic drawing of JBS diode, (b) schematic drawing of Trench MOSFET, and (c) schematic drawing of a Double-well MOSFET.

The first year of this effort focused on the development of simulation and modeling capabilities to help drive the designs of future GaN diodes and transistors. In parallel, epitaxial growth and fabrication processes were initiated toward realizing and demonstrating these devices. The second year of this effort has focused on fabrication and a first-generation demonstration of these devices. With demonstrators for both the JBS and trench MOSFET complete, the third year of the program focused on improving the baseline performance by improving passivation quality, tackling challenges related to etch-and-regrowth, and improving off-state characteristics for both the JBS and MOSFET devices. This year's effort is focused again on improving baseline performance. These efforts resulted in reaching the goal of 1200-V MOSFETs, further improvements in etch-and-regrowth processes, and an optimization for the edge termination process. In the future, once devices of sufficient performance are achieved, they will be further characterized in a performance and reliability testbed (created under a different project within the consortium) to evaluate their suitability for electric drive applications, especially regarding their ability to meet the DOE consortium targets. Also, with increasing maturity, the devices can be shared with the consortium partners, who will evaluate them in electric drive systems and provide feedback to us for further improvement in their performance for power electronics.

Approach

The focus of this past year has been on improving baseline performance for both the JBS and MOSFET device. In many cases, challenges faced by both devices can more easily be addressed through cycles of learning on a simpler device. For instance, the pn diode platform can be used to benchmark passivation quality and to evaluate edge termination effectiveness, a simple Schottky Barrier diode can be used to understand the influence of etch damage and etch-damage recovery procedures on n-type GaN, and the MOSCAP can be used to evaluate gate dielectric performance on m-plane GaN. Experiments on these three devices were heavily leveraged in the past year to improve device performance for the JBS and MOSFET platforms. Examples of the three devices are shown in Figure I.1.13.2.

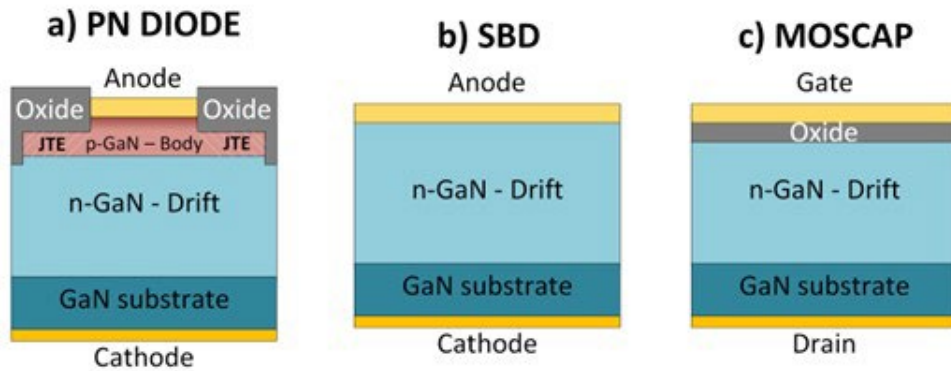


Figure I.1.13.2 Studies on these three devices, the pn diode, the Schottky Barrier diode, and the MOSCAP lends insight into improving performance for the JBS and MOSFET devices.

Results

Vertical GaN Edge Termination

In FY21 we established a new passivation process for GaN pn diodes using a bilayer film consisting of 100 nm of atomic layer deposited (ALD) alumina (Al_2O_3) and 2 μm of silicon nitride (SiN) by plasma enhanced chemical vapor deposition (PECVD). Compared to early attempts to establish a passivation process, this new film resulted in low leakage diodes and the ALD- Al_2O_3 film appears robust to the addition of PECVD- SiN as a subsequent layer. This bilayer passivation has been robust across multiple device lots and has even been successfully deployed to other diode projects at Sandia. As was discussed last year, while a new and robust passivation process was established, the addition of a passivation film causes a reduction in breakdown where three varieties of passivation all established a nominal reduction in breakdown voltage of 300V compared to an unpassivated sample. According to theory, a 300 V drop in breakdown voltage corresponds with a reduction of charge of 4×10^{12} in the step-etched JTE (junction termination extension) which is a reasonable amount of charge to expect at the interface between the passivation and semiconductor and is consistent with some preliminary models and data from the GaN MOSFET and MOSCAP work.

The results from the passivation work highlights a need to optimize the design of the edge termination to account for non-idealities such as the charge from the passivation, epitaxy and doping variations, and other factors that impact the effectiveness of the edge termination. An edge termination is designed to minimize and distribute the peak electric field at the edge of the device where the junction has been terminated. In the case of a step-etched JTE, proper management of the surface electric field requires precise control of the charge in the JTE. This charge is set primarily by the product of doping and thickness for the JTE but many factors can alter the charge in the JTE including charge from the passivation layer. According to theoretical calculations the breakdown voltage can be quite sensitive to the dose in the JTE, and when considering the unknowns, it is near impossible to know the optimal etch depth to achieve the required dose. Therefore, we ran a multivariable JTE experiment to pinpoint the optimal JTE thickness target. These results presented are the first multipoint step-etched JTE study reported in GaN. The diode and single-zone step-etched JTE are presented in Figure I.1.13.3. Three experiments were carried out on three separate quarters of the same wafer, each with a different JTE etch depth target. Average breakdown from the three quarters, taken both pre- and post-passivation is shown and compared to a simulation model in Figure I.1.13.3a. The experimental results align well to the model that predicts a fully depleted edge termination for JTE thicknesses of 140 and 250 nm and a partially depleted edge termination for a JTE thickness of 295 nm. The accuracy of this model is further confirmed by electroluminescence imaging. It is shown that for $t_{\text{JTE}} = 250$ nm the location of the breakdown is at the inner edge of the JTE (Figure I.1.13.3b) which corresponds to a fully depleted JTE. For $t_{\text{JTE}} = 295$ nm, the breakdown location shifts to the outer edge of the JTE (Figure I.1.13.3c) corresponding to a partially depleted JTE.

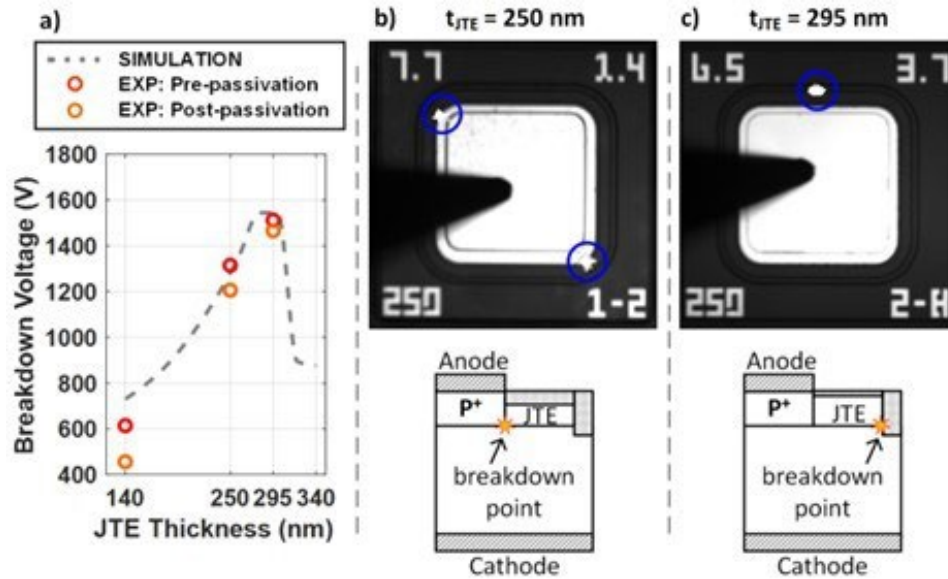


Figure I.1.13.3 (a) Breakdown voltages of pre/post-passivation devices compared to a simulation model. Images showing electroluminescence during avalanche confirm that at $t_{JTE} = 250$ nm (b) the JTE fully depletes, and breakdown occurs near the inner edge. At $t_{JTE} = 295$ nm (c) the JTE does not fully deplete and breakdown occurs near the outer edge.

Etch and Regrowth

The vertical GaN Junction Barrier Schottky (JBS) process that we are developing utilizes an etch-and-regrowth process to form the selective-area doped regions. Similarly, advanced trench-MOSFET and double-well MOSFETs require one or more selective-area doped regions. This selective-area doping process by etch-and-regrowth generally results in a junction with considerably more leakage than a continuously grown sample. To tackle this challenge, we have been developing a process that can reduce the etch damage that contributes to leakage. Two primary issues are responsible for high reverse current leakage in regrown diodes: 1) Residual etch damage and 2) impurities at the regrowth interface. In the past year we were able to demonstrate a novel solution for regrown diodes using in-situ XeF₂ etching that removes residual etch damage preceding regrowth (Figure I.1.13.4). The result is low leakage diodes with no impurities at the regrowth interface aside from silicon (due to short exposure to air).

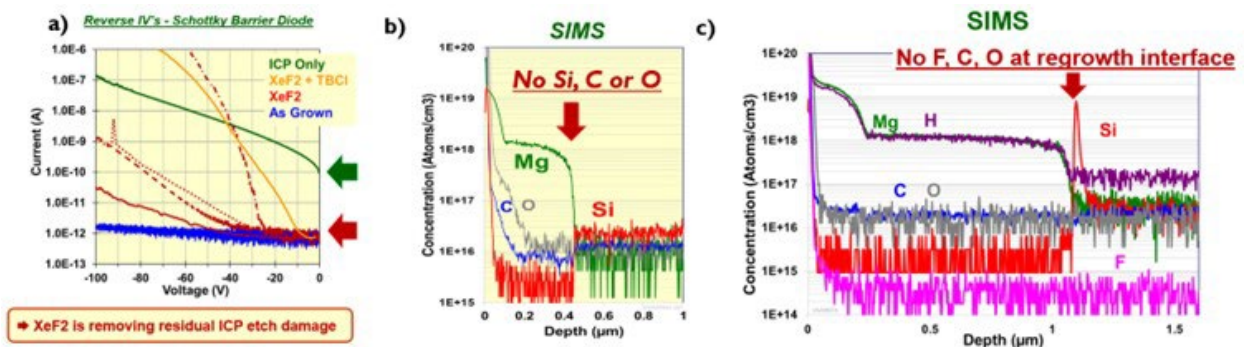


Figure I.1.13.4 Etch damage recovery and Etch-and Regrowth Progress, showing (a) reverse IV curves of Schottky Barrier Diode with and without in-situ XeF₂ surface treatment before regrowth. XeF₂ is removing residual ICP etch damage yielding diodes with lesser leakage current. (b) SIMS profile of interrupted growth with no air exposure. Matches that of continuously grown diode. (c) SIMS profile of regrown interface with ICP and XeF₂ etching.

Generational MOSFET Improvements

In the previous years we demonstrated a 1st generation process for the vertical GaN trench MOSFET, then identified several key challenges [10] to address based on that result. We also demonstrated a 2nd generation

gate dielectric process that improved on the leakage and breakdown strength for ALD-SiO₂ gate dielectrics. Then, we incorporated those revisions into the 2nd generation MOSFET process resulting in doubling the MOSFET blocking voltage. Most recently, our 3rd generation devices had a shallower etch for the trench recessing to reduce the electric field at the gate oxide resulting in a nearly 4-fold improvement in the device breakdown. The first generation MOSFETs suffered from surface and channel leakage that dominated the off-state characteristics and resulted in a 250V breakdown with high leakage current. Revisions to that design and incorporation of new processes developed in this program resulted in a 500V breakdown with nearly six orders of magnitude reduction in leakage current for the 2nd generation devices (Figure I.1.13.5a). Premature failure at 500V was found to be due to a rupture of the gate dielectric at the bottom of the trench arising from high electric-fields during the blocking state as depicted in Figure I.1.13.5b. This agrees with our TCAD modeling which predicts that for a device with an avalanche voltage of 1400V, an early failure will occur in the 450-550V range due to high fields in the gate dielectric (Figure I.1.13.5c). The agreement between TCAD and experimental results is a positive outcome which highlights that many early failure points for the MOSFET have been solved and the device behavior is as expected. In our most recent year, the blocking voltage was further improved by applying conventional rules of scaling. Since the magnitude of electric-field strength in the gate dielectric below the trench is proportional to the depth that the trench protrudes below the body/drift pn junction, we reduced the etch-depth to lessen the peak electric field seen by the gate-oxide. In addition, reducing the thickness of the p-GaN body layer reduces the channel length, which is a significant portion of the total device resistance. Despite the breakdown voltages of the device, device reliability will remain problematic if the gate dielectric is not shielded, resulting in low market uptake of the design. In Si and SiC technology, shielding the gate dielectric is typically done by the insertion of a p-type layer beneath the dielectric / semiconductor interface. However, due to difficulty of selective-area doping and ion implantation in GaN, conventional techniques for forming a structure to protect the gate dielectric are not viable. Thus, we developed a new process to form a buried field shield by an etch-and-regrowth process. This field shield serves to protect the gate dielectric during the blocking state from high electric fields. The method devised is outlined in the provisional patent [11].

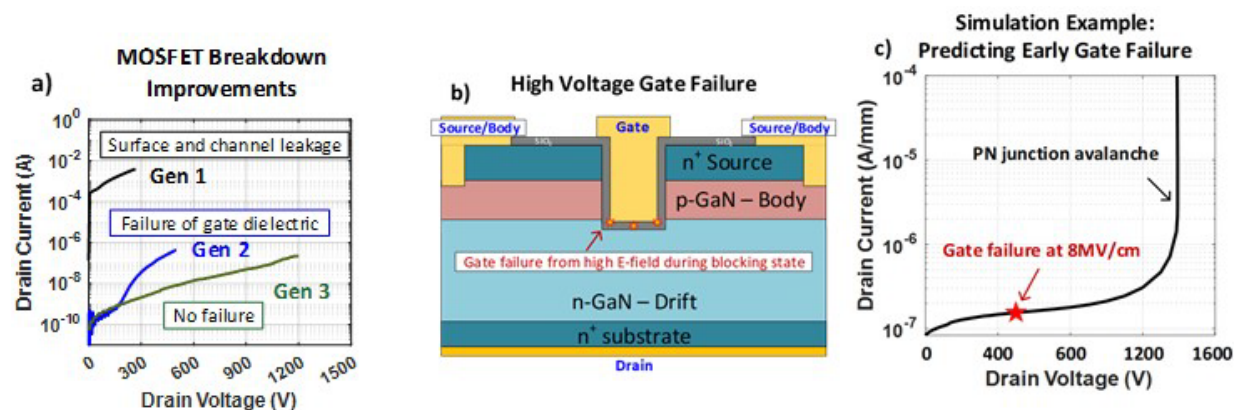


Figure I.1.13.5 Generational improvements for the MOSFET continue, showing (a) the improvement of breakdown voltage from generation 1 to the current generation 3; (b) a cross-sectional schematic of the device and (c) TCAD simulation results demonstrating the importance of mitigating the peaking of the electric field at the gate dielectric-semiconductor interface.

Note that our 3rd generation device breakdown voltage is like that of the ideal TCAD breakdown.

Next Generation MOSFET Design

To assess the efficacy of our approach, 2-D simulations of the structure were performed. Like in our other simulations, the devices were pushed to avalanche breakdown, and the electric field profiles are extracted. A cutline of the electric field profile through the dielectric illustrates the peak electric field within the dielectric. The cutline plot and electric field intensities reported in Figure I.1.13.6 show that the implementation of the buried field shield reduces the electric field within the dielectric and terminates the field lines within the PN-junction of the buried field shield. The reduction of the electric field magnitude within the gate dielectric is

proportional to the shield-to-channel distance, where a smaller distance results in more protection for the gate dielectric. To determine the feasibility of the etched-and-regrown buried field shield approach for typical commercial processes, we investigated the effect of the shield-to-channel distance on the peak electric field seen by the gate dielectric. We define the shield-to-channel distance as the distance between the active channel edge and the nearest edge of the buried shield. Simulated field intensity is plotted against shield-to-channel distance in Figure I.1.13.6c. From that data, the peak electric field seen by the dielectric remains below 6 MV/cm until the shield is approximately 0.6 μm from the gate edge, and approaches 5 MV/cm at a distance of 0.4 μm . Considering that an i-line stepper has a typical resolution of $< 0.35 \mu\text{m}$ with alignment tolerances of $< 0.1 \mu\text{m}$, the peak electric field seen by the dielectric can be reliably reduced by at least 1.5-fold in a typical manufacturing setting if the shield-to-channel distance is kept below 0.4 μm . In principle, this reduction in the peak electric field intensity should enable the device to reach the expected breakdown voltage without premature dielectric failure.

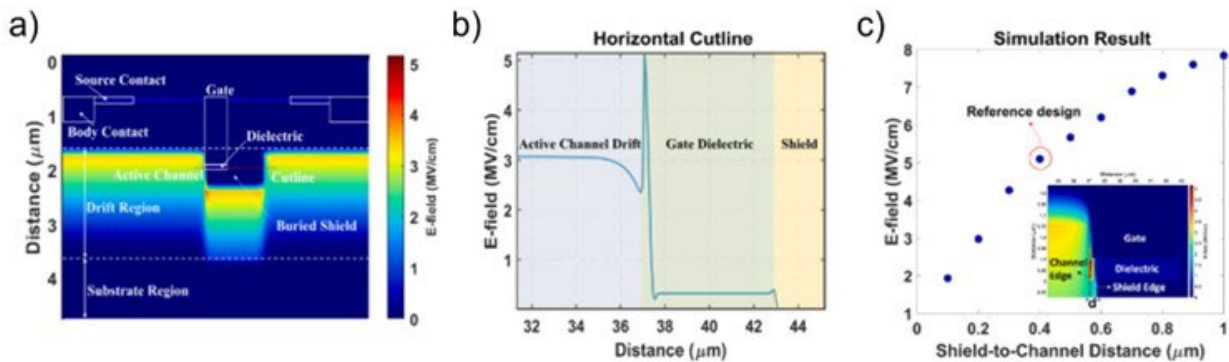


Figure I.1.13.6 Implementation of a buried field shield showing a) the electric field profile of the device, b) corresponding horizontal cut line across the dielectric, and c) the peak electric field seen by the dielectric as a function of the shield-to-channel distance. In a) and b), the shield-to-channel distance is 0.4 μm and measured from the edge of the channel to the nearest edge of the shield.

Considering the positive results of our TCAD simulations on the buried field shield approach, we next endeavored to design a commercially compatible device architecture. Due to the difficulties associated with ion implantation, this device architecture relies on our improved etch and regrowth process. The following discussion summarizes this architecture and fabrication methodology. The buried field shield should be comprised of a region doped opposite the conductivity of the drift region and should be electrically tied to the body. For this proposed process, the shield is formed by etch and regrowth and is located underneath the gate dielectric but otherwise can take many forms. One such method for forming a buried field shield via etch and regrowth is detailed in Figure I.1.13.7. The process begins with a masked etch to form trenches in the drift epilayer, followed by a maskless, blanket regrowth and planarization of the p-body layer and subsequent growth of the n⁺ source epilayer. Following the planarization growth, another etch is performed to form the gate trench. This etch is offset from the shield etch so that the shield only covers a portion of the gate trench and wraps around one side. In this way, a double channel MOSFET only has one active sidewall channel, and the other sidewall is an inactive channel. With this method, the top metal contacts for the gate, source, and body can be laid out with no need to have a source/body/source metal configuration as is common for double-channel devices. Instead, the body contact is laid out on the side of the inactive sidewall and the source contact is on the side of the active channel. After contact metallization, they are subsequently interconnected via the device bond pads. This is one such method to form a buried field shield via etch and regrowth. This approach allows the buried field shield to electrically connect with the body region through the epilayer without the need for an additional metal layer to form the connection.

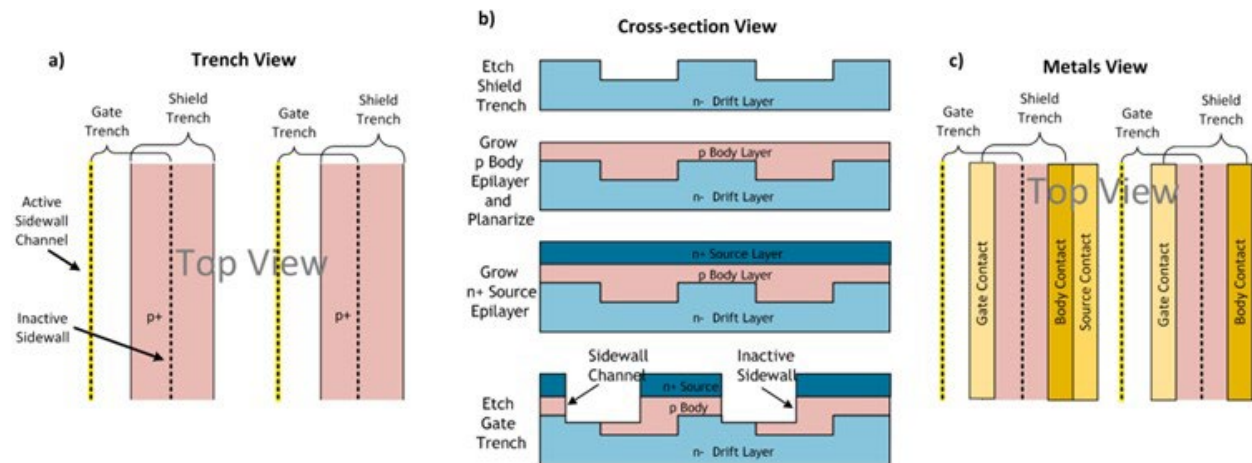


Figure I.1.13.7 Method for forming a buried field shield via etch and regrowth showing a) the trench view, b) the cross-section view, and c) the metals view of this approach¹. More details are available in Ref. [11].

Conclusions

GaN offers the promise of power electronic devices with performance that exceeds conventional Si and even SiC-based devices. This is due to its advantageous material properties, chiefly its higher breakdown electric field. Due to the increased maturity of GaN substrates, vertical GaN devices showing promising performance are being demonstrated and are being considered for insertion into power conversion applications. This project has focused on the design, simulation, and fabrication processes needed to build vertical GaN diodes and transistors for use in electric drive traction systems. This year we developed a process for edge termination in vertical GaN power devices and our group is the first to report a multipoint fit from theory to experiment, which serves to mark a milestone of maturity for these devices. For the GaN MOSFET the second-generation device demonstrated double the blocking voltage (500 V) compared to the previous generation and a reduction of leakage current by six orders of magnitude. The blocking voltage was further increased to 1200V utilizing an optimized epilayer structure enabling a reduced gate trench depth as well as improved fabrication procedures for our etch and regrowth process. Using 2-D TCAD simulations, we demonstrated the efficacy of a buried field shield approach with aim to improve the device reliability via a reduction of the gate oxide peak electric field at dimensions which are commercially viable. Finally, we devised a device architecture for future fabrications of such MOSFETs equipped with the buried field shield.

Key Publications

1. A. T. Binder *et al.*, "Gate protection for vertical gallium nitride trench MOSFETs: The buried field shield," *e-Prime - Adv. Electr. Eng. Electron. Energy*, vol. 5, p. 100218, Sep. 2023.
2. A. Binder and J.A. Cooper, "Buried Field Shield in GaN Trench MOSFETs via Etch and Regrowth," US Provisional Patent 63/208,119.
3. A. T. Binder *et al.*, "Etched and Regrown Vertical GaN Junction Barrier Schottky Diodes," in *The 8th Workshop on Wide Bandgap Power Devices and Applications (WiPDA 2021)*, 2021.
4. C. E. Glaser, A. T. Binder, L. Yates, A. A. Allerman, D. F. Feezell, and R. J. Kaplar, "Analysis of ALD Dielectric Leakage in Bulk GaN MOS Devices," in *The 8th Workshop on Wide Bandgap Power Devices and Applications (WiPDA 2021)*, 2021.
5. L. Yates, A. Binder, J. Dickerson, G. Pickrell, and R. Kaplar, "Electro-thermal Simulation and Performance Comparison of 1.2 kV, 10 A Vertical GaN MOSFETs," Rio Grande Symposium on Advanced Materials, Albuquerque, NM (September 2019).

References

1. I. C. Kizilyalli, A. P. Edwards, O. Aktas, T. Prunty, and D. Bour, “Vertical power p-n diodes based on bulk GaN,” *IEEE Trans. Electron Devices*, vol. 62, no. 2, pp. 414–422, Feb. 2015.
2. A. Armstrong et al., “High voltage and high current density vertical GaN power diodes,” 2016.
3. H. Ohta, K. Hayashi, F. Horikiri, M. Yoshino, T. Nakamura, and T. Mishima, “5.0kV breakdown-voltage vertical GaN p-n junction diodes,” *Jpn. J. Appl. Phys.*, vol. 57, no. 4, pp. 4–09, 2018.
4. T. Oka, Y. Ueno, T. Ina, and K. Hasegawa, “Vertical GaN-based trench metal oxide semiconductor field-effect transistors on a free-standing GaN substrate with blocking voltage of 1.6 kV,” *Appl. Phys. Express*, vol. 7, no. 2, p. 021002, Feb. 2014.
5. H. Otake, S. Egami, H. Ohta, Y. Nanishi, and H. Takasu, “GaN-based trench gate metal oxide semiconductor field effect transistors with over 100cm²/(Vs) channel mobility,” *Japanese J. Appl. Physics, Part 2 Lett.*, vol. 46, no. 25–28, p. L599, Jul. 2007.
6. S. Chowdhury, M. H. Wong, B. L. Swenson, and U. K. Mishra, “CAVET on bulk GaN substrates achieved with MBE-regrown AlGaIn/GaN layers to suppress dispersion,” *IEEE Electron Device Lett.*, vol. 33, no. 1, pp. 41–43, Jan. 2012.
7. T. J. Anderson et al., “Activation of Mg implanted in GaN by multicycle rapid thermal annealing,” *Electron. Lett.*, vol. 50, no. 3, pp. 197–198, Jan. 2014.
8. G. W. Pickrell et al., “Regrown Vertical GaN p–n Diodes with Low Reverse Leakage Current,” *J. Electron. Mater.* 2019 485, vol. 48, no. 5, pp. 3311–3316, Mar. 2019.
9. A. T. Binder et al., “Etched and Regrown Vertical GaN Junction Barrier Schottky Diodes,” in 2021 IEEE 8th Workshop on Wide Bandgap Power Devices and Applications (WiPDA), 2021, pp. 288–292.
10. C. E. Glaser, A. T. Binder, L. Yates, A. A. Allerman, D. F. Feezell, and R. J. Kaplar, “Analysis of ALD Dielectric Leakage in Bulk GaN MOS Devices,” in 2021 IEEE 8th Workshop on Wide Bandgap Power Devices and Applications (WiPDA), 2021, pp. 268–272.
11. A. Binder and J.A. Cooper, “Buried Field Shield in GaN Trench MOSFETs via Etch and Regrowth,” US Provisional Patent 63/208,119.

Acknowledgements

This work is supported by the DOE Office of Energy Efficiency and Renewable Energy, Vehicle Technologies Office. Sandia National Laboratories is a multi-mission laboratory managed and operated by National Technology and Engineering Solutions of Sandia, LLC., a wholly owned subsidiary of Honeywell International, Inc., for the U.S. Department of Energy’s National Nuclear Security Administration under contract DE-NA0003525. The views expressed in the article do not necessarily represent the views of the U.S. Department of Energy or the United States Government.

I.1.14 Component Modeling, Co-Optimization, and Trade-Space Evaluation (Sandia National Laboratories)

Jason Neely, Principal Investigator

Sandia National Laboratories
P.O. Box 5800, MS 1152
Albuquerque, NM 87185
E-mail: jneely@sandia.gov

Susan Rogers, DOE Technology Development Manager

U.S. Department of Energy
E-mail: susan.rogers@ee.doe.gov

Start Date: October 1, 2018
Project Funding: \$350,000

End Date: September 30, 2024
DOE share: \$350,000

Non-DOE share: 0

Project Introduction

This project is intended to support the development of new traction drive systems that meet the targets of 100 kW/L for power electronics and 50 kW/L for electric machines with reliable operation to 300,000 miles. To meet these goals, new designs must be identified that make use of state-of-the-art and next-generation electronic materials and design methods. Designs must exploit synergies between components, for example converters designed for high-frequency switching using wide band gap (WBG) devices and ceramic capacitors. This project includes: (1) a survey of available technologies; (2) investigating new technologies, that for example, reduce volume of thermal management or magnetic components; (3) the development of design tools that consider the converter volume, reliability, and electrical performance; (4) exercising the design software to evaluate performance gaps and predict the impact of certain technologies and design approaches, i.e. GaN semiconductors, ceramic capacitors, ceramic thermal management components, and select topologies; (5) building and testing hardware prototypes to validate models and concepts. The design tools enable co-optimization of the power module and passive elements and provide some design guidance; later instantiations will enable the co-optimization of inverter and machine.

Objectives

For FY23, objectives included:

- Evaluate options for reducing size of filter and thermal management components
- Generate high-fidelity dimensional and electrical models for principal power electronic components within a novel inverter design
- Co-Optimize inverter and machine designs for power density, reliability, and efficiency
- Demonstrate and evaluate representative converter prototypes.

Approach

The R&D approach employed by the team includes four strategies for generating design guidance and optimal designs, listed in order of increased fidelity and resources:

1. **Empirical and First-Principles Analysis:** This uses first-principles knowledge, such as physical models, as well as comparative designs to inform the design.
2. **High-Fidelity Modeling and Analysis:** This uses higher-order models that consider the component equivalent circuits, dimensions, reliability calculations, etc.

3. **Global Co-Optimization:** With the definition of one or more performance metrics, components are simulated together and their performance is measured and compared.
4. **Hardware Iteration:** Using optimal designs identified in software, hardware exemplars are built and evaluated; 3 and 4 are iterated to create the best results.

In FY23, the project included elements of strategies 1, 2 and 3, applied with different weight to the four objectives. Empirical analysis and modeling (strategies 1 and 2) were applied to evaluate the potential performance improvement of using 3D printed ceramic surround cooling components (i.e. for heat spreading) to cool bare-die or passivated die power devices. Strategies 1 and 2 were also applied to evaluate the potential for a distributed filter, based on embedding bus bars into a nanocomposite material, to replace bulky filter inductors. The team also continued work to develop a new simulation + optimization platform with greater capability and flexibility than the highly customized Matlab-based code developed through FY21 (strategies 2 and 3). This has allowed the team to start conducting optimizations that consider the vehicle operation and vehicle lifetime in miles (strategy 3). Hardware experimentation was limited in FY23.

Based on previous optimization results attained for an inverter drive, the principal contributors to inverter volume remained to be the thermal management components (i.e. the cold plate) and the AC EMI filter that connected the inverter drive to the motor. To address the filter size, the feasibility of using nano-composite materials to realize a distributed EMI filter was investigated. To address the thermal management component size, the team investigated the use of 3D printed ceramic components that could be used to realize a “surround cooling” capability. Some experimentation was done in FY23 that was an extension of work begun in FY22.

For the optimization work, the team had previously used the Genetic Optimization System Engineering Tool (GOSET) developed by Purdue University [1] in concert with a highly customized simulation of the power electronics. In FY22, the team began development of a new platform with optimization and parameter evaluation workflow process between power electronics simulation platform, PLECS [2] and Python [3]. The team continued development of this platform in FY23 and published a paper describing the new platform and comparing the predicted reliability of inverter drives using Si IGBT vs SiC devices [4]

Results

Investigation of 3D printed ceramics to improve thermal management

To improve thermal management, either to reduce the volume of thermal management components, or to reduce junction temperatures for a given volume, a new approach is being investigated for the removing heat from the semiconductor devices. Specifically, 3D printed Al₂O₃ ceramic components can be used to surround and even encase electronic components with significant thermal loads. With this approach, a cold plate would still be used, but the ceramic components would also route heat away from the top of devices down to the cold plate. This accomplishes double-sided cooling but avoids the complexity of contemporary assemblies. These components can have high resolution features ~100 μm and thus tightly fit around components and potentially include additional features, such as fins.

In FY22, test boards were built to enable precise heating of passivated die power devices with enough board real estate to try different ceramic surround cooling designs. The boards included commercial eGaN high electron mobility transistors (HEMTs) from Efficient Power Conversion (EPC). The team had just begun DC testing to determine a steady state temperature as a baseline to compare 3D printed ceramic heatsinks. Baseline temperatures were determined using a high-resolution thermal camera. See Figure I.1.14.1

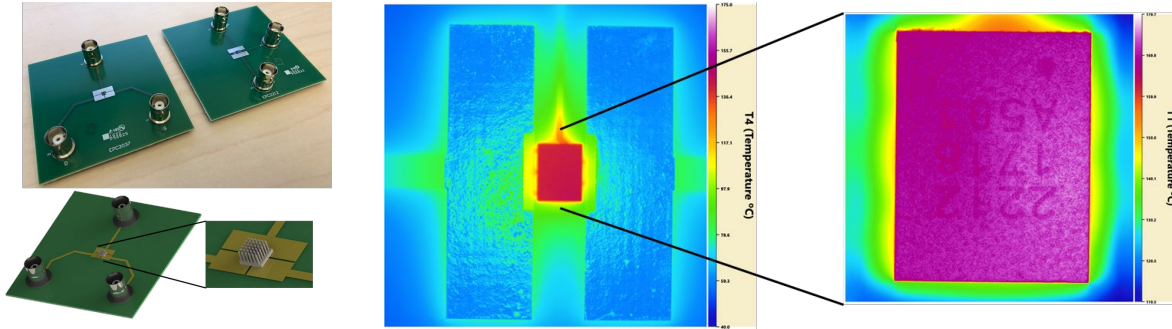


Figure I.1.14.1 (Left) Test boards built to evaluate thermal performance (right) high-resolution thermal imaging is used to establish baseline thermal performance

In FY23, testing continued and the baseline performance was evaluated to validate the thermal model; see Figure I.1.14.2. Simple Al_2O_3 cap structures with pin fins were designed and printed (by Lithoz) to evaluate a passive cooling solution; see Figure I.1.14.3.

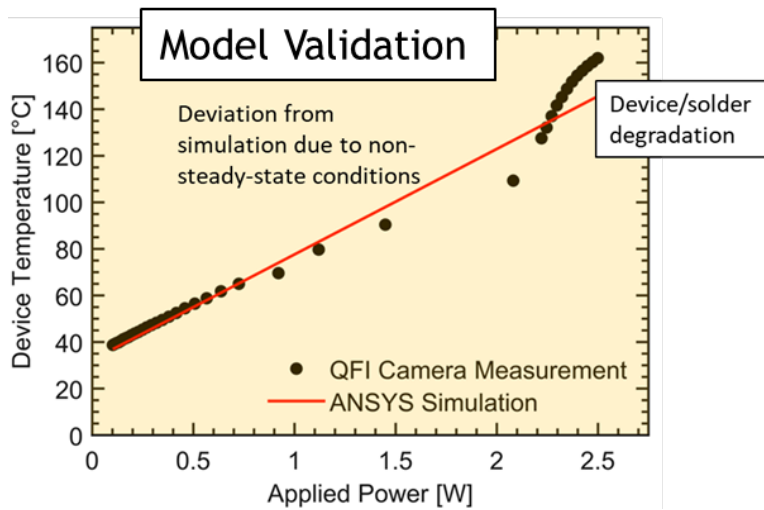


Figure I.1.14.2 Comparison of measured and modeled temperature for baseline case

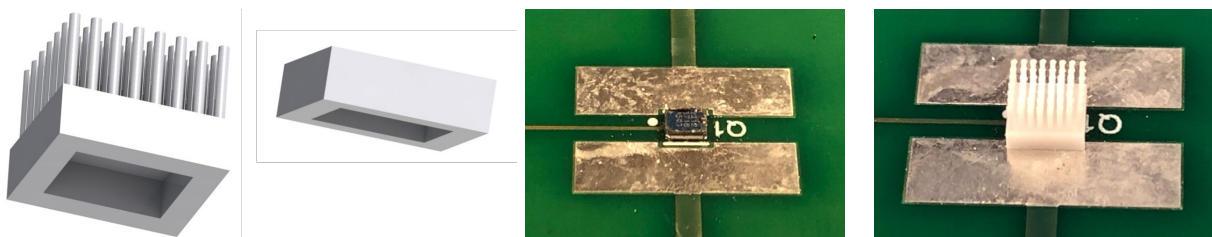


Figure I.1.14.3 Illustrates design and use of simple Al_2O_3 caps

The thermal simulation model was used to predict the performance of passive cooling using ceramic caps with and without fins; see Figure I.1.14.4.

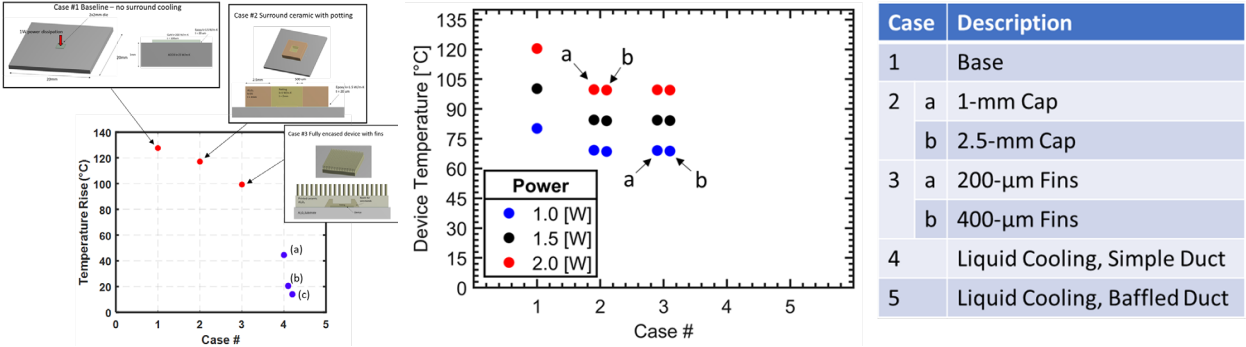


Figure I.1.1.14.4 (Left) Illustrates six design cases and the simulated temperature rise of the device junction for each, (middle and right) modeled impact of ceramic caps on EPC transistor temperature. Case 4 & 5 not shown.

Investigation of Distributed Bus Filter design to reduce EMI Filter Size

Results of several genetic optimization runs have identified the filter inductors located between inverter and machine to be among the largest components in the electric drive. To potentially reduce the size of these filter components, a method to create a “distributed filter” was investigated using nanocomposite magnetic material. In particular, since the material has both a large permittivity (due to the epoxy substrate) and high permeability from the magnetic nanoparticles, the material may enable a high combined distributed inductance and capacitance. Thus, it may be possible to accomplish sufficient filtering by replacing the cabling with a rigid transmission line containing this material and appropriate conductor geometries. The nanocomposite medium was assumed to have $\epsilon_r = 10$; $\mu_r = 10$, and two geometries were considered: 3-phase planar conductors, and 3-phase spiral conductors. Figure I.1.14.5 illustrates the transmission line equivalent circuit and the two geometries.

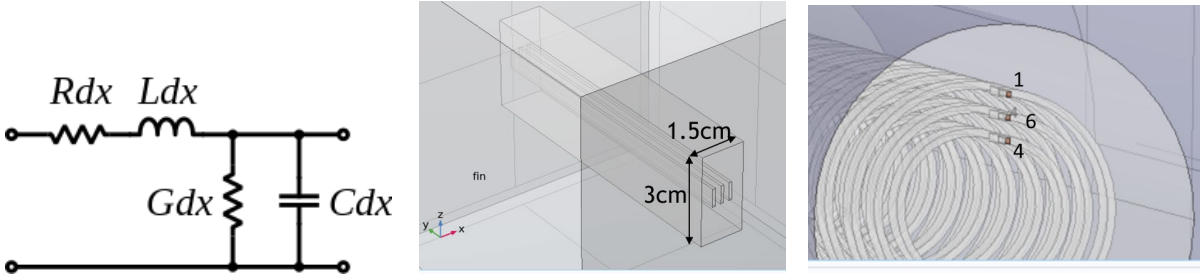


Figure I.1.14.5 (Left) Illustrates equivalent circuit of transmission line with distributed capacitance and inductance (center) planar 3-phase configuration and (right) spiral 3-phase configuration

The objective is to accomplish a low enough cut-off frequency with the transmission line to eliminate the need for filter inductors. The electric field and magnetic field profiles for the candidate assemblies were modeled using COMSOL®; see Figure I.1.14.6. Computed per unit length inductances and capacitances for candidate designs are shown in Figure I.1.14.7.

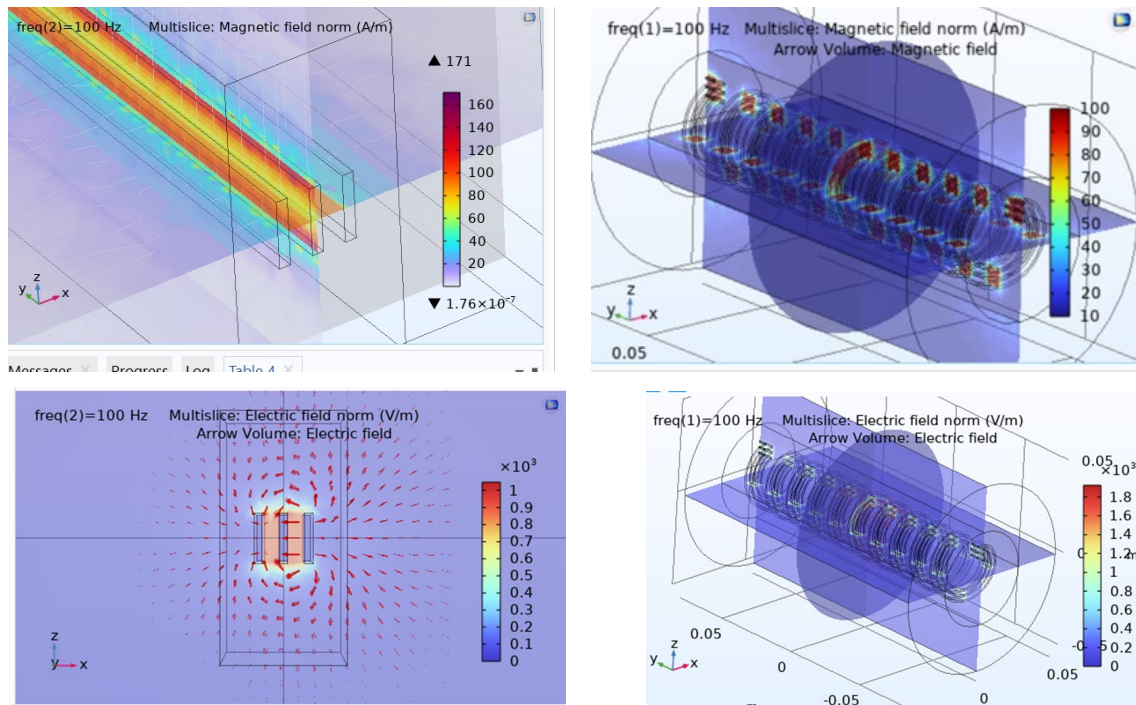


Figure I.1.14.6 (Top) Magnetic field norm and (Bottom) Electric field norm visualized in COMSOL® for planar and spiral 3-phase configurations

Line-line inductance	Inductance Term 1-6 (uH/m)	Inductance Term 6-4 (uH/m)	Inductance Term 4-1 (uH/m)
Planar	1.2	1.2	1.8
Spiral	8.5	7	13.5
Line-line Capacitance	Capacitance Term 1-2 (pF/m)	Capacitance Term 2-3 (pF/m)	Capacitance Term 3-1 (pF/m)
Planar	950	950	490
Spiral	4480	3830	2070

Figure I.1.14.7 Per unit length (top) inductances and (bottom) capacitances for planar and spiral configurations

Unfortunately, these per unit values are, according to this analysis, too small to enable a compact filter design that filters primary current ripple. For a 100 cm transmission line, a lumped parameter approximation of the LC filter cut-off frequencies would be between 4.7-5.6 MHz for a planar configuration and 815-975 kHz for the spiral configuration. The spiral configuration has more per unit capacitance and inductance, but the geometry is also more complex, likely heavier and the resistance would be larger; though, it wasn't computed here. Neither configuration would be effective in filtering the current ripple that results from 10-200 kHz switching; however, these filters may potentially act as electromagnetic interference (EMI) filters to mitigate noise from the switching edge rates, typically >10 MHz for WBG devices.

the modules and hence, lowest efficiency whereas the cruising results in the lowest stress and highest average efficiency during the driving cycle. This and other study details were published in [4].

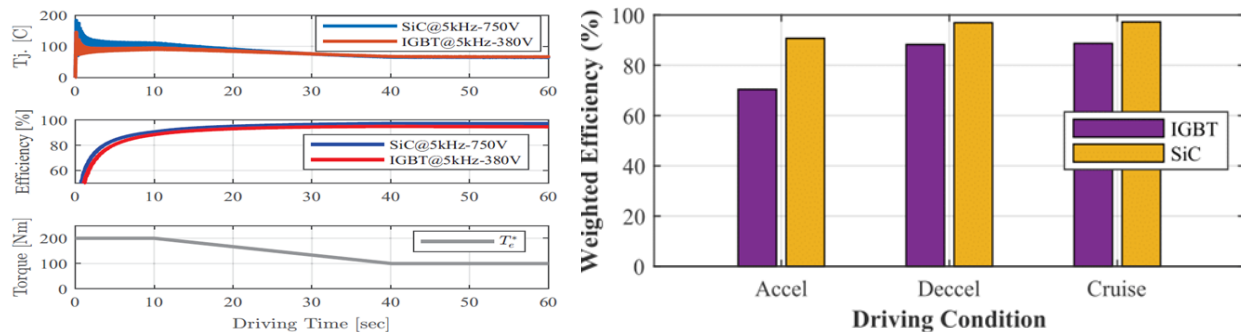


Figure I.1.14.9 (left) The comparison of the time domain junction temperature and efficiency performance characteristics over the entire driving cycle between the IGBT-based and SiC-based solution, operating at 5 kHz, 380 V, and 5kHz, 750V, respectively. (Right) The comparison of the weighted efficiency for each driving cycle of an optimized inverter design solution with the SiC modules and IGBT modules.

Conclusions

This project is focused on developing improved designs for future traction drive systems through the combined use of WBG devices, ceramic capacitors, high-frequency switching, advanced component development (i.e. for thermal management) and advanced designs that enable considerable improvements in power density. Designs are developed with the help of tools developed to perform multi-objective optimizations on electric drive designs. Unlike previous work, these include optimizations that consider component and inverter reliability.

In FY23, the team continued to investigate the use of 3D printed Al_2O_3 ceramic components to aid in thermal management. Initial results indicate validity of the thermal model and potential value of using the ceramic components to reduce device temperatures. The team also investigated, through simulation and analysis, the concept of a distributed filter, to replace bulky filter inductors; unfortunately, this concept is not predicted to be effective for filtering ripple current but may be useful for EMI filtering. In particular, the project team continued development of the new optimization \leftrightarrow simulation platform using PLECS for simulation and the NSGA-II genetic optimization tool using Python. New optimization study results were attained and published using the more comprehensive simulations, which included representations of the vehicle, drive profiles, and power electronics.

Key Publications / Presentations

1. J. Neely, G. Pickrell, J. Flicker, L. Rashkin, R. Kaplar; "The Case for Vertical Gallium Nitride Devices in Electric Vehicle Drives," *2020 IEEE Applied Power Electronics Conference (APEC2020)*, Industry Session: Vehicle Electrification II.
2. L. Gill, J. C. Neely, L. J. Rashkin, J. D. Flicker and R. J. Kaplar; "Co-Optimization of Boost Converter Reliability and Volumetric Power Density Using Genetic Algorithm," *2020 IEEE Energy Conversion Congress and Exposition (ECCE)*, Detroit, MI, USA, 2020, pp. 5302-5309, doi: 10.1109/ECCE44975.2020.9235716.
3. L. Rashkin, J. Neely, L. Gill, J. Flicker and R. Darbali-Zamora; "Optimal Power Module Design for High Power Density Traction Drive System," *2020 IEEE Transportation Electrification Conference & Expo (ITEC)*, Chicago, IL, USA, 2020, pp. 134-138, doi: 10.1109/ITEC48692.2020.9161703.
4. L. Gill, L. Rashkin, L. Yates, J. Neely and R. Kaplar, "Multi-Objective Parametric Analysis of EV Traction Inverter between Reliability and Efficiency," *2023 IEEE Applied Power Electronics Conference and Exposition (APEC)*, Orlando, FL, USA, 2023, pp. 3174-3181, doi: 10.1109/APEC43580.2023.10131644.

References

1. S. D. Sudhoff, GOSET: Genetic Optimization System Engineering Tool: For Use with MATLAB®, ver 2.6, Jan 1, 2014.
2. J. Allmeling and W. Hammer, “PLECS-piece-wise linear electrical circuit simulation for Simulink,” in Proceedings of the IEEE 1999 International Conference on Power Electronics and Drive Systems. PEDS’99 (Cat. No.99TH8475), vol. 1, 1999, pp. 355–360 vol.1.
3. J. Blank and K. Deb, “pymoo: Multi-objective optimization in python,” IEEE Access, vol. 8, pp. 89 497–89 509, 2020.
4. L. Gill, L. Rashkin, L. Yates, J. Neely and R. Kaplar, "Multi-Objective Parametric Analysis of EV Traction Inverter between Reliability and Efficiency," 2023 IEEE Applied Power Electronics Conference and Exposition (APEC), Orlando, FL, USA, 2023, pp. 3174-3181, doi: 10.1109/APEC43580.2023.10131644.
5. L. Gill, J. C. Neely, L. J. Rashkin, J. D. Flicker and R. J. Kaplar, "Co-Optimization of Boost Converter Reliability and Volumetric Power Density Using Genetic Algorithm," 2020 IEEE Energy Conversion Congress and Exposition (ECCE), Detroit, MI, USA, 2020, pp. 5302-5309, doi: 10.1109/ECCE44975.2020.9235716.
6. L. Rashkin, J. Neely, L. Gill, J. Flicker and R. Darbali-Zamora, "Optimal Power Module Design for High Power Density Traction Drive System," 2020 IEEE Transportation Electrification Conference & Expo (ITEC), Chicago, IL, USA, 2020, pp. 134-138, doi: 10.1109/ITEC48692.2020.9161703.
7. S. Oki, S. Ishikawa, and T. Ikemi, “Development of High-Power and High-Efficiency Motor for a Newly Developed Electric Vehicle,” SAE International Journal of Alternative Powertrains, vol. 1, no. 1, pp. 104–111, 2012.
8. K. Deb, A. Pratap, S. Agarwal, and T. Meyarivan, “A fast and elitist multiobjective genetic algorithm: NSGA-II,” IEEE Transactions on Evolutionary Computation, vol. 6, no. 2, pp. 182–197, 2002.
9. US Environmental Protection Agency (EPA). Dynamometer Drive Schedules. [Online]. Available: <https://www.epa.gov/vehicle-and-fuelemissions-testing/dynamometer-drive-schedules>

Acknowledgements

This work is supported by the DOE Office of Energy Efficiency and Renewable Energy, Vehicle Technologies Office. Sandia National Laboratories is a multi-mission laboratory managed and operated by National Technology and Engineering Solutions of Sandia, LLC., a wholly owned subsidiary of Honeywell International, Inc., for the U.S. Department of Energy’s National Nuclear Security Administration under contract DE-NA0003525. The views expressed in the article do not necessarily represent the views of the U.S. Department of Energy or the United States Government.



I.1.15 Implementation of WBG devices in circuits, circuit topology, system integration as well as SiC devices (The Ohio State University)

Dr. Anant Agarwal, Principal Investigator

The Ohio State University
2015 Neil Avenue
Columbus, OH, 43210
E-mail: agarwal.334@osu.edu

Dr. Jin Wang, CO-Principal Investigator

The Ohio State University
2015 Neil Avenue
Columbus, OH, 43210
E-mail: wang.1248@osu.edu

Susan Rogers, DOE Technology Development Manager

U.S. Department of Energy
E-mail: susan.rogers@ee.doe.gov

Start Date: April 1, 2023
Project Funding: \$300,000

End Date: March 31, 2024
DOE share: \$300,000

Non-DOE share: \$0

Project Introduction

All device vendors have compromised reliability/ruggedness of SiC MOSFETs to reduce cost. Short channel length is a good example that reduces device size and cost at the expense of reduced short-circuit time of 2 - 3 μs . Another example is the gate oxide thickness which has been thinned to 30 - 40 nm without reducing the gate voltage in order to reduce device size and cost. This leads to gate oxide leakage issues and susceptibility to rupture during extreme events such as short-circuit and exposure to static electricity. Hence, commercial devices, available to-date, are not suitable for insertion into a vehicle powertrain for long operational life. A comprehensive reliability study is warranted for commercially available devices both as discrete devices and in an inverter to uncover failures such as threshold voltage instability, inadequate short circuit time, gate oxide failures due to gate voltage overshoot and high junction temperature, as well as body diode instability (Figure I.1.15.1). OSU is working collaboratively with Sandia National Lab and Suny Poly on this project (Figure I.1.15.2).

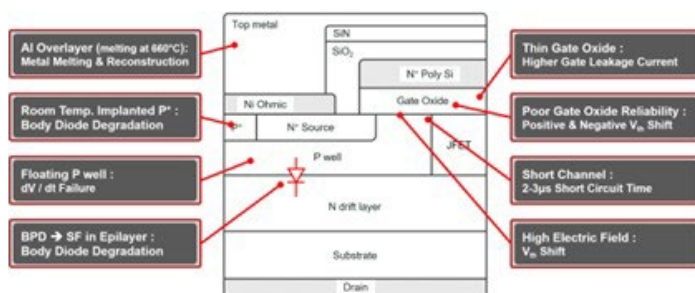


Figure I.1.15.1 SiC MOSFET Reliability Issues.

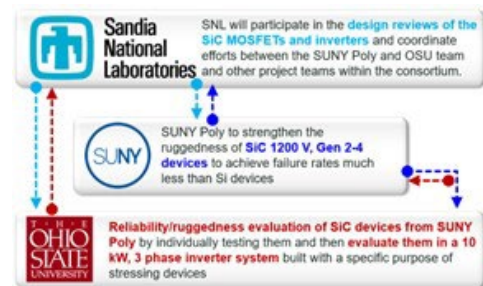


Figure I.1.15.2 Key Partnerships.

Objectives

The overall objective of the project is to ensure that SiC devices are reliable and rugged as required in automotive applications for the operational life of 300,000 hrs and create new device designs to address various weaknesses in currently available commercial devices. OSU work will focus on reliability/ruggedness evaluation of SiC devices by individually testing them and then evaluating them in a 10 kW, 3-phase inverter system built with a specific purpose of stressing devices using realistic drive cycles such as a 10-minute hill

climb. It should be noted that the primary purpose of the 10 kW inverter is to provide a platform for stressing the SiC devices under accelerated but realistic drive conditions and NOT to meet the 100 kW power and power density goals. The 100 kW inverter will be built by other team members. OSU will share the findings with SUNY Poly and collaborate with them to strengthen the existing device designs to overcome the specific weaknesses in the device. These devices will be fabricated in a state-of-the-art commercial SiC Foundry. The new designs will be improved every year through extensive testing by OSU, re-design (in collaboration between OSU and SUNY Poly) and subsequent fabrication.

Objectives (FY2023)

- Enhancing the reliability of SiC MOSFETs through the study of screening techniques.
- An improved three-phase Inverter (Inverter-5) is built using Gen-3 MOSFETs to test the devices under realistic drive cycles

Approach

Collaboration with National Laboratory

OSU will coordinate and collaboratively conduct work with the Sandia National Laboratory (SNL) on selected tasks integral to the completion of the project. The results of this collaborative effort with the national laboratory will be included in all the reports. SNL will participate in the design reviews of the SiC MOSFETs and inverters and coordinate efforts between the SUNY Poly and OSU team and other project teams within the consortium.

Results

Task 1 - Reliability evaluation of commercial SiC MOSFETs

Gen-4 devices from SUNY POLY have not been received yet. Reliability measurements on commercial SiC MOSFETs are reported on the following pages.

The effects of different screening methods for non-infant extrinsic defects on the gate oxide reliability of commercial 1.2 kV 4H-SiC power MOSFETs with planar and trench gate structure have been investigated. The behavior of V_{th} during the screening process are recorded and analyzed. In addition, constant-voltage time-dependent dielectric breakdown (TDDDB) measurements are conducted on screened and unscreened SiC MOSFETs to explore the impact of screening techniques on the intrinsic lifetime of gate oxide.

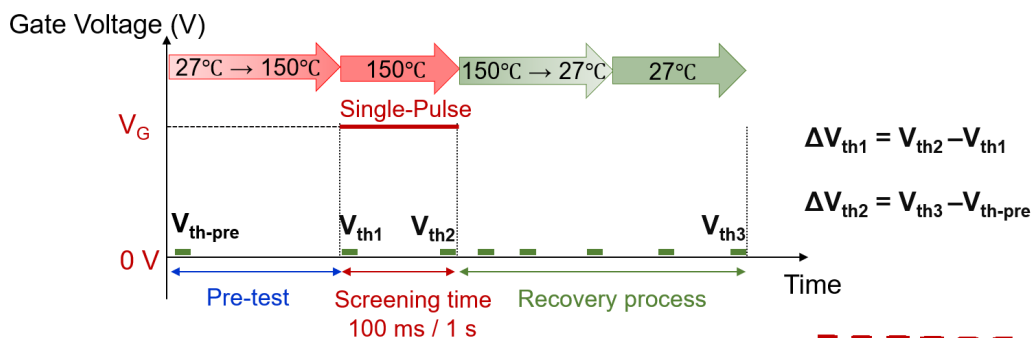


Figure I.1.15.3 Measurement Sequence of V_{th} before and after Gate Oxide Screening

To monitor the shifts of V_{th} before and after gate oxide screening treatment, a schematic of the V_{th} test sequence used in this study is shown in Figure I.1.15.3. V_{th} is read out during the stress and recovery process by using the constant current method. An initial threshold voltage (V_{th-pre}) at RT is measured to establish a reference for comparison. The screening temperature is set at 150°C to screen early failures. During the screening, gate voltage stress is applied with source and drain grounded. The V_{th} before and after gate oxide screening at 150°C are measured as V_{th1} and V_{th2} , respectively. ΔV_{th1} is equal to the difference between V_{th1}

and V_{th2} which represents the V_{th} shift after the screening process. After stress, the device is cooled back to room temperature without the gate voltage stress. The recovery in V_{th} occurs when the stress is removed from the device. V_{th} is recorded during the recovery process until the value of V_{th} stabilizes (V_{th3}). ΔV_{th2} is defined as the difference between V_{th-pre} and V_{th3} which represents the V_{th} shift after the recovery phase.

The V_{th} shifts after the screening process influence the subsequent recovery of V_{th} . Figure I.1.15.4 plots ΔV_{th2} of vendor E and vendor K devices subjected to various E_{ox} stress levels with a duration of 100 ms and 1 s. The left Y-axis shows ΔV_{th2} , the residual shift after the recovery process. The right Y-axis is the ratio of ΔV_{th2} to initial V_{th} . For vendor E devices, ΔV_{th2} is positive due to the electron trapping when E_{ox} of less than 9 MV/cm is applied for 100 ms [Figure I.1.15.4 (a)]. And ΔV_{th2} is approximately less than 5% of the initial value. It should be noted that V_{th3} shows a negative shift compared to the initial value after high E_{ox} (> 9 MV/cm) stress for 100 ms due to the dominance of hole trapping. This phenomenon needs to be taken seriously in the industry because a pronounced reduction in threshold voltage can lead to an increase in the leakage current of SiC MOSFETs in the OFF state and has the potential to turn the device to normally-on. To prevent negative V_{th} shift of vendor E devices, the recommended screening voltage should be kept below ~ 41 V for 100 ms. The V_{th} recovery of vendor E devices is susceptible to the impact of screening time. From the test results, it can be found that electron trapping still dominates even at high E_{ox} (> 9 MV/cm) when the screening time is 1 s. Despite the increased screening time of 1 s, the V_{th} shift does not exceed 5% of the initial value after the recovery process. Due to the thicker oxide, negative ΔV_{th2} appears only when the screening voltage exceeds ~ 54 V for vendor K devices. A large screening voltage can be applied to vendor K devices without causing ΔV_{th2} to exceed 10% of its initial value [Figure I.1.15.4 (b)]. Previous studies have shown that the higher the ratio of screening voltage to gate use-voltage, the higher the efficiency of the screening technology [1]. Thus, a lower field failure probability after screening treatment for vendor K devices can be acquired.

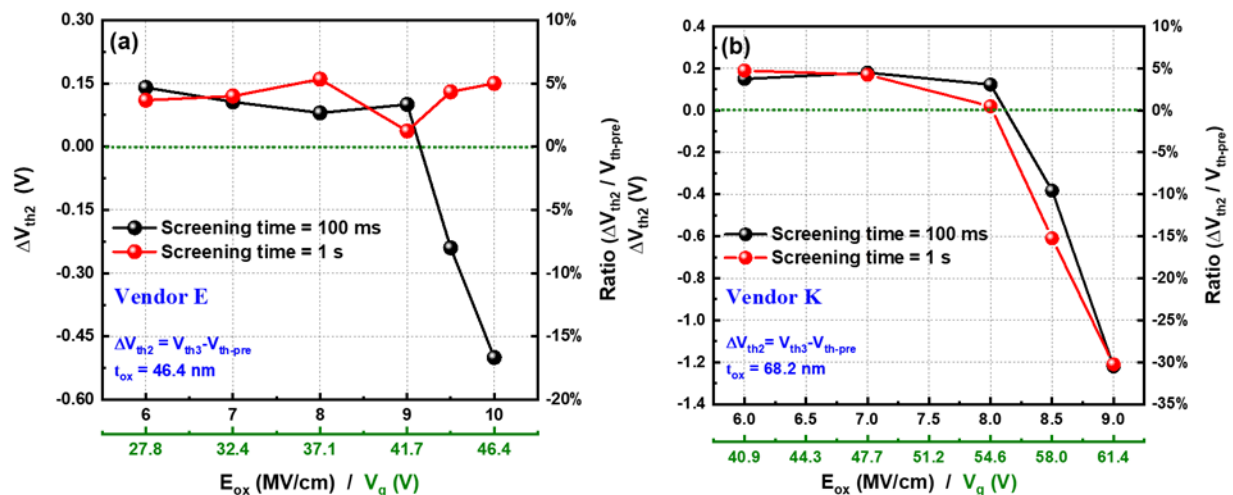


Figure I.1.15.4 Effect of 100 ms/1 s high gate-voltage pulse screening on the ΔV_{th2} of (a) vendor E devices, and (b) vendor K devices. Devices are screened at 150°C .

Comparison of gate oxide lifetimes of the screened and unscreened vendor E and vendor K devices at 150°C are depicted in Figure I.1.15.5. For vendor E devices, an abrupt change in field acceleration factors (slopes of the fitted lines) is observed at E_{ox} of ~ 9.4 MV/cm [Figure I.1.15.5 (a)]. In previous studies, it has been found that the Fowler-Nordheim (F-N) tunneling current rises continuously during high E_{ox} stress periods (> 9.4 MV/cm) due to hole generation in the gate oxide, which degrades the gate oxide lifetime, making $t_{63\%}$ decrease more rapidly as E_{ox} increases. The result indicates that high screening voltage is an important factor affecting the oxide intrinsic lifetimes of SiC MOSFETs. Two types of screening conditions are selected for vendor E devices: E_{ox} of 9.9 MV/cm for 100 ms and E_{ox} of 9.9 MV/cm for 3 min. The $t_{63\%}$ of vendor E devices screened by E_{ox} of 9.9 MV/cm for 100 ms and 3 min are extracted and plotted in Figure I.1.15.5 (a). Less variation of gate oxide lifetimes can be observed for vendor E devices with 100 ms of screening and

without screening. Therefore, it can be concluded that applying an oxide electric field of 9.9 MV/cm or less for 100 ms has no obvious damage to the gate oxide lifetimes of vendor E devices. However, TDDB measurement results on vendor E after screening E_{ox} of 9.9 MV/cm for 3 min demonstrate a notable degradation of oxide lifetimes. In addition, the predicted oxide lifetime at an operational condition ($E_{ox} = 4$ MV/cm) decreases by two orders of magnitude compared to the result on SiC MOSFETs without screening. These observations suggest that high gate voltage stress with long duration has the risk of damaging the intrinsic lifetime of the gate oxide because the hole generation is triggered and produces an enhanced F-N tunneling current, so it is not advisable to apply a high screening voltage for a long time.

TDDB results for vendor K devices at 150°C with three gate voltages are shown in Figure I.1.15.5 (b). Compared with the results for vendor E devices, vendor K devices with a trench gate structure maintain considerably longer oxide lifetimes at the same applied gate voltage. This result clearly demonstrates the advantage of the thicker gate oxide. The stress of 10.15 MV/cm for 1 s is selected as the screening condition for vendor K devices. Consequently, no noticeable degradation of gate oxide lifetimes for vendor K devices after the screening process is observed. To summarize, in terms of gate oxide lifetime, vendor K devices with thicker gate oxide can accept higher screening voltages and thereby achieve higher screening efficiency.

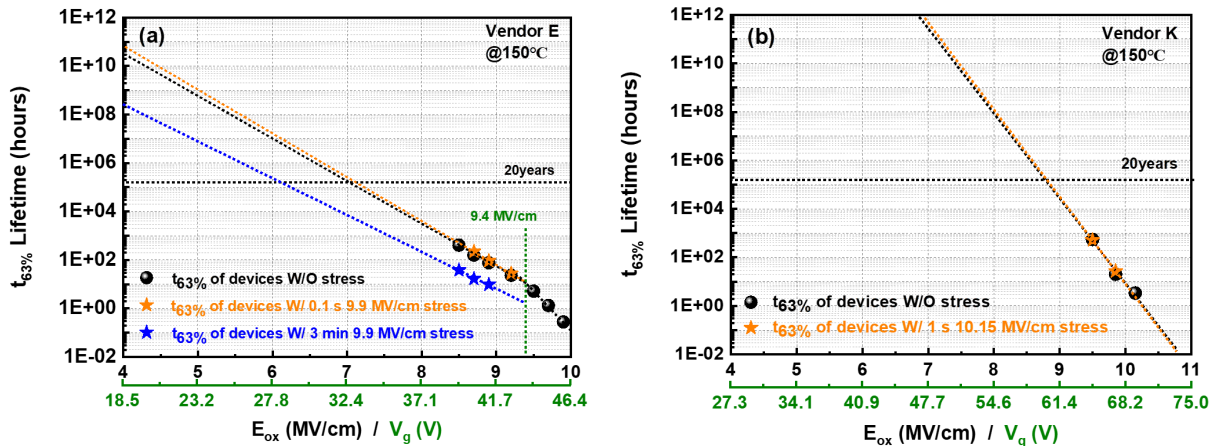


Figure I.1.15.5 $t_{63\%}$ versus E_{ox} at 150°C for (a) vendor E devices, and (b) vendor K devices with and without high gate-voltage screening

Task 2 - Inverter-5 build with Gen-3 MOSFETs

A. Inverter-5 with liquid metal cooling system

The liquid metal cooling system, as depicted in Figure I.1.15.6, consists primarily of three components:

- a cold plate with the object to be cooled;
- a coolant pump, which is the MHD pump based on electromagnetic force;
- a radiator with cooling fans.

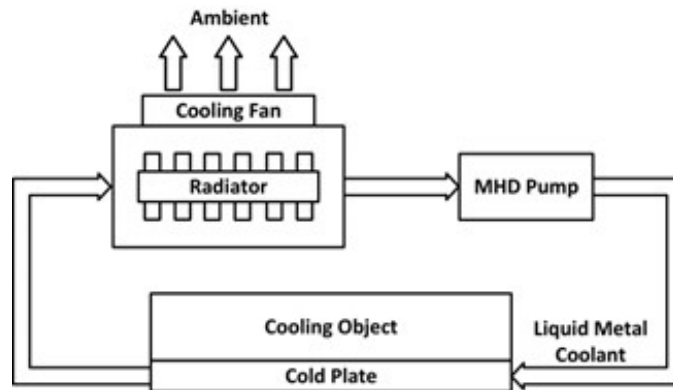


Figure I.1.15.6 Diagram of liquid metal cooling system.

In contrast to conventional mechanical coolant pumps designed for water or glycol-based coolants, the MHD pump employs Lorentz force instead of centrifugal force to drive liquid metal coolant. Lorentz force is generated inside the pump when the current is applied across the pump channel filled with conductive liquid metal in the presence of a perpendicular magnetic field. As illustrated in Figure I.1.15.7, the Lorentz force F can be expressed as

$$F = BIw.$$

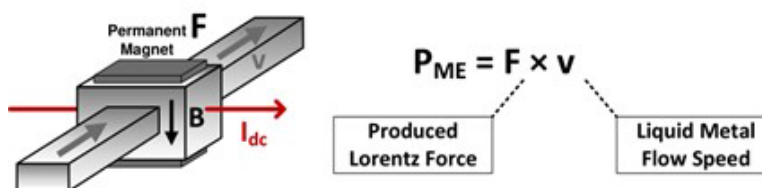


Figure I.1.15.7 Vector diagram of Lorentz force.

Pushed by the MHD pump, the liquid metal coolant will effectively carry heat from the power electronics converter to the ambient. In the cooling loop, liquid flow rate Q is determined by the head pressure P_{Head} generated by the pump and the total pressure drop P_{Drop} caused by flow resistance. Based on Poiseuille's law, under laminar flow conditions, the coolant flow rate Q can be derived as

$$Q = \frac{BIw^3h^2}{8\eta L(w+h)^2},$$

where w , h and L are the dimensions of the channel, η is the dynamic viscosity of liquid metal.

To reduce the thermal resistance of the cold plate and radiator, a higher flow rate is desirable, which can be achieved by using stronger magnets, injecting more current, or optimizing cooling loop geometry. The optimal point between thermal performance and overall cooling system size can be determined based on the calculations and FEA simulation tools.

In the inverter-5, as shown in Figure I.1.15.8, the PM-based integrated MHD pump is inserted in the input dc bus. To eliminate the need of external auxiliary power source to inject current into the channel, the dc bus current of the power converter will pass through the liquid metal coolant channel before flowing into the inverter. Generally, the dc bus current can be calculated as

$$I_{Dc} = \frac{P_{Out}}{V_{In}},$$

thus, the higher the output power, the higher the input dc current and the larger the flow rate.

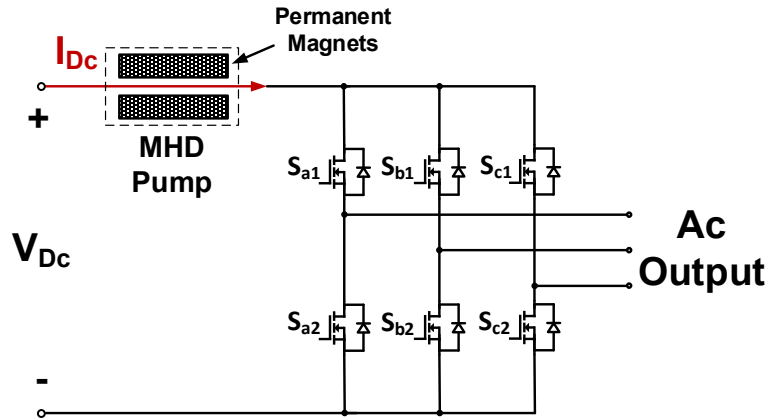


Figure I.1.15.8 Separate capacitor bank design in Gen-5 inverter

Figure I.1.15.9 illustrates the details of the dc bus-integrated PM MHD pump design. The pump body is 3D printed with SLA resin material. The electrode pair is made of pure copper for better electrical conductivity and compatibility with the Galinstan alloy. Since conventional mechanical flow rate meters will no longer be suitable for the liquid metal cooling loop due to the size restriction, the EMF introduced by the liquid metal flow is utilized to calculate the flow rate. An additional pair of permanent magnets and electrodes are added to the cooling loop to function as the flow rate measurement unit. The induced voltage potential $E = Bwv$ is measured for flow rate calculation, where v is the velocity of the liquid metal.

Figure I.1.15.10 presents the implemented 20 kW inverter with an impressively compact form factor and a high power density exceeding 120 kW/L.

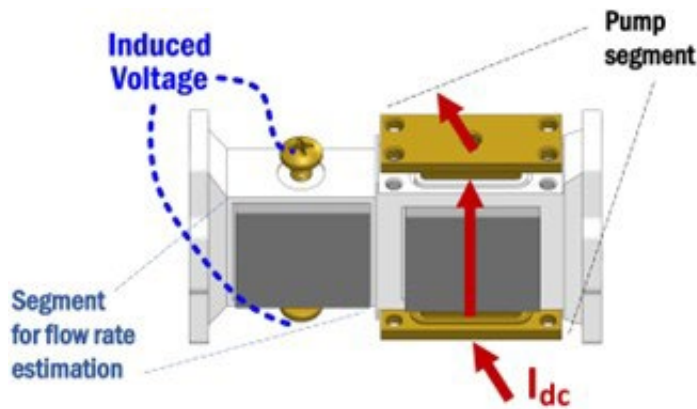


Figure I.1.15.9 Detailed design of the PM-based integrated MHD pump

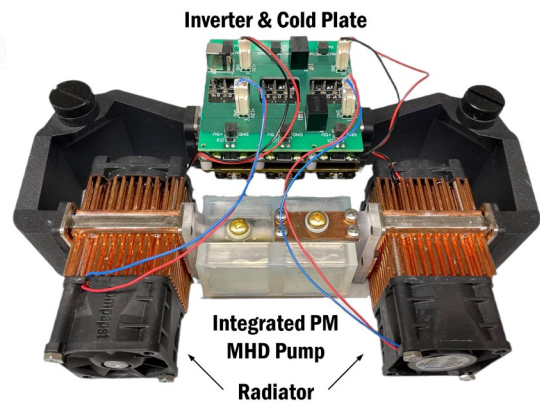


Figure I.1.15.10 Inverter-5 prototype

B. Experimental results of Inverter-5

As the cooling system is entirely self-contained, the experimental setup is more straightforward, and the number of peripheral equipment is significantly reduced. The schematic of the experimental test setup is shown in Figure I.1.15.11. The images of the setup in Figure I.1.15.12 illustrate the electrical connections of the inverter and peripheral equipment using the experimental tests. To monitor the electrical performance of switching poles, two pairs of Tektronix differential probes are connected to the circuit's test points: one for the device gate and the other for the device drain. The gate-to-source voltage (V_{GS}) and drain-to-source voltage (V_{DS}) are used to ensure that cross-talk and overshoot remain within tolerable limits.

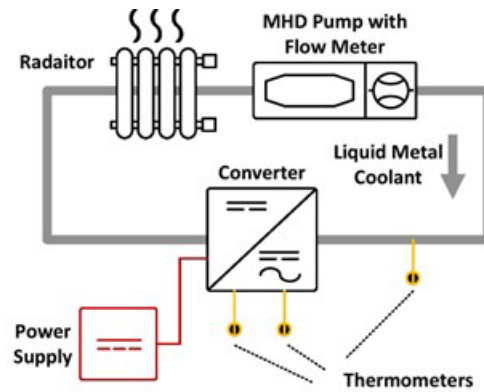


Figure I.1.15.11 Schematic of the experimental test setup

Three sets of temperature sensors are placed in different locations within the system. As shown in the zoomed in view in Figure I.1.15.12, two fiber optic temperature sensors (Opsenc OTG-F) are directly attached to the device's metal plate to monitor the case temperature. The device on the left side is close to the coolant inlet and the device on the right side is close to the outlet, thus, higher device temperature is expected on the right side. These fiber optic sensors are well-suited for environments with high voltage and severe electromagnetic disturbances (EMI), resulting in more fidelity measurement. The liquid metal coolant temperature is monitored by a thermocouple immersed in the cooling loop. Since the junction temperature of the switching devices can not be directly measured, it can be estimated based on the measured case temperature and device power loss, which relies on the measurement from a precision power analyzer (ZES Zimmer LMG670).

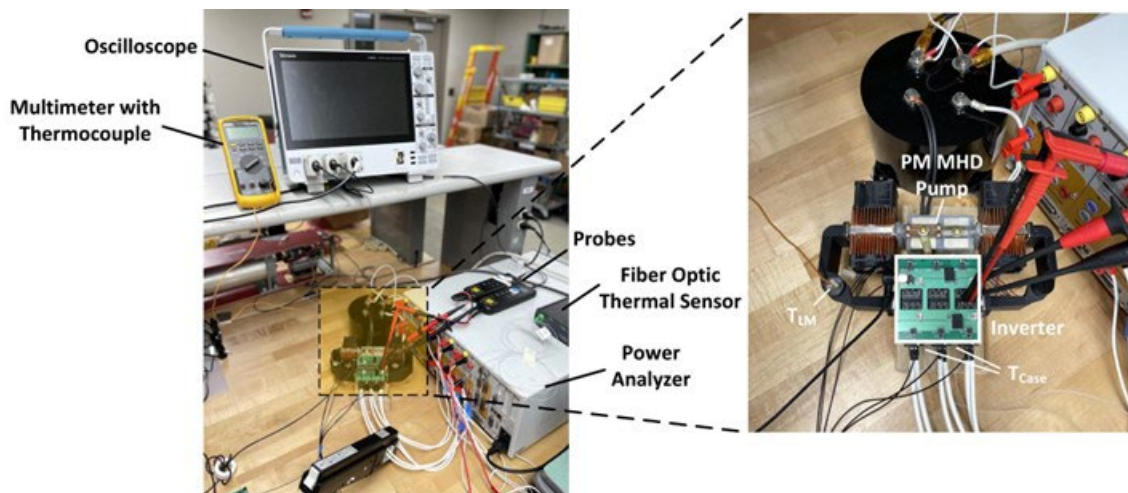


Figure I.1.15.12 Inverter-5 prototype experimental setup

The To-247 SiC switching devices have 80 mohms on-resistance. At 20 kVA output, the waveform is shown in Figure I.1.15.13. The power loss on the switching devices, which manifests as heat dissipated by the liquid metal cooling system, is 244 W (40.7 W on each device). The maximum device junction temperature rise is around 80 K. At a flow rate of 0.52 L/min, the measured thermal resistance from the device case to the coolant is only 0.55 K/W (1.25 K/W for junction-to-coolant with 0.7 K/W junction-to-case given by the datasheet), which includes the thermal resistance of the thermal interface material (TIM). The system efficiency, calculated device junction temperature and measured liquid metal coolant temperature are plotted in Figure I.1.15.14. It can be seen that the device junction temperature of inverter-5 only reaches 115 degree C at 22 kVA output power, leaving enough margin for possible higher power operation. And the system efficiency peaks at 98.8 % when the output power is around 16 kVA.

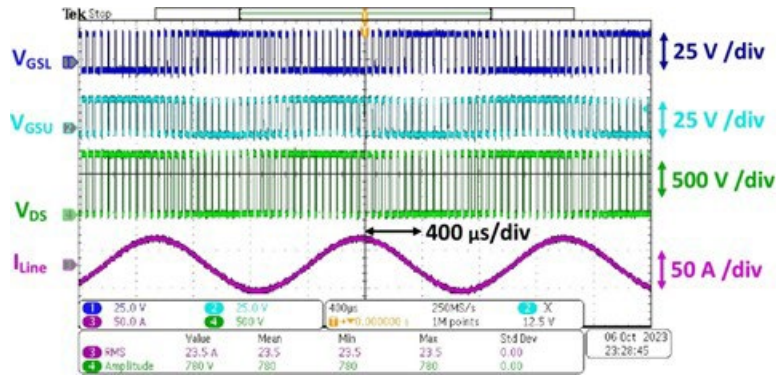


Figure I.1.15.13 Inverter-5 test waveform at 20 kVA

During the operation, the liquid metal coolant flow rate is also traced along with the inverter output power. With an output power ranges from 3.67 kVA to 21.95 kVA, the input current goes up from 0.76 A to 8.77 A, the flow rate increases from 0.11 L/min to 0.45 L/min, and the measured junction-to-coolant thermal resistance decreases from 2.85 K/W to 1.25 K/W, validating the self-adaptive cooling capability of the system. The traced coolant flow rate and corresponding junction-to-coolant thermal resistance are plotted in Figure I.1.15.15. Furthermore, the power consumption of the integrated PM MHD pump is negligible; even when considering the additional resistance due to the liquid metal channel, the total power consumption remains under 0.1 W.

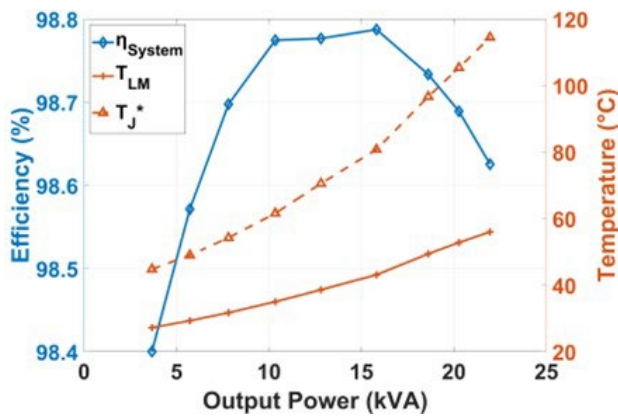


Figure I.1.15.14 Inverter-5 efficiency and temperature curve

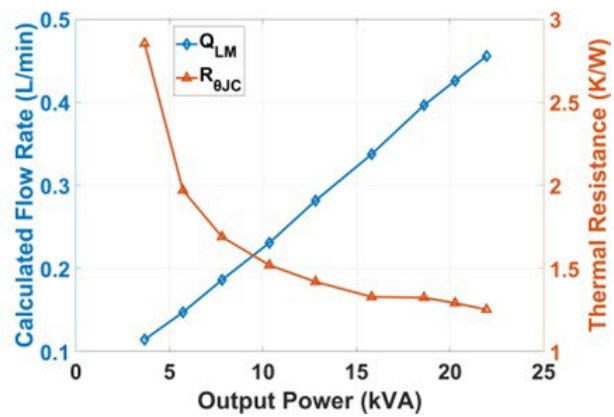


Figure I.1.15.15 Inverter-5 liquid metal cooling system flow rate and thermal resistance curve

For the same cold plate in a water cooling setup, the coolant flow rate increased from 2.5 L/min to 5.7 L/min. This change resulted in a reduced junction-to-coolant thermal resistance from 1.39 K/W to 1.27 K/W. Data shows that the thermal resistance with water coolant at 5.7 L/min is comparable to that of a liquid metal cooling system. However, there is a notable difference in power consumption. The water pump consumes over 17 W at 5.7 L/min, which is more than 100 times the power consumption of the integrated liquid metal MHD pump.

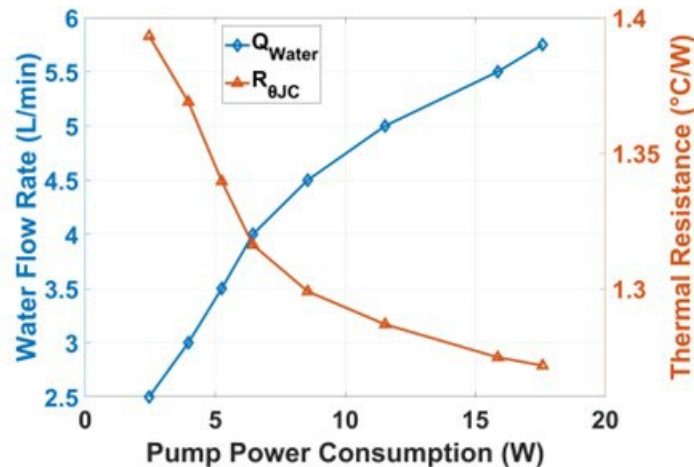


Figure I.1.15.16 Water cooling system flow rate and thermal resistance curve

Conclusions

In this work, both threshold voltage and time-dependent dielectric breakdown measurements are performed on commercial 1.2 kV SiC MOSFETs with planar and trench gate structures to investigate the effects of high gate-voltage screening. **The high gate voltage screening is necessary to reduce the failure rate from 2-3% to 2-3 ppm.** The V_{th} shift and recovery under different screening conditions for SiC MOSFETs are evaluated. For both structures, V_{th} shifts depend on the hole and electron trapping in the oxide. To avoid negative V_{th} shifts of SiC MOSFETs under high screening voltage conditions, it is recommended to keep screening voltage less than ~ 41 V (9 MV/cm) and ~ 54 V (8 MV/cm) for vendor E and K devices, respectively. In addition, the fast high gate-voltage screening technology (100 ms, 9.9 MV/cm for vendor E and 1 s, 10.15 MV/cm for vendor K at 150°C) does not significantly degrade the gate oxide intrinsic lifetime during the screening process. The major advantage of SiC trench structure is that it allows higher screening voltages to reduce non-infant extrinsic failure probability as well as fulfil the long-term reliability requirements of the automotive market.

Inverter-5 reached a power density of more than 120 kVA/liter and an efficiency of more than 98% at 800 V input and 480 V output voltage. The liquid metal cooling system with integrated PM MHD pump shows great heat dissipation capability and cooling efficiency. This inverter is being used to test Gen-3 devices under realistic drive conditions and will be used to test Gen-4 devices as well.

Key Publications

1. Limeng Shi, Shengnan Zhu, Jiashu Qian, Michael Jin, Marvin H. White, and Anant K. Agarwal, "Investigation of different screening methods on threshold voltage and gate oxide lifetime of SiC Power MOSFETs," 2023 IRPS.
2. Limeng Shi, Tianshi Liu, Shengnan Zhu, Jiashu Qian, Michael Jin, Hema Lata Rao Maddi, Marvin H. White, and Anant K. Agarwal, "Effects of Oxide Electric Field Stress on the Gate Oxide Reliability of Commercial SiC Power MOSFETs," 2022 IEEE 9th WiPDA.
3. Junchong Fan, Yue Zhang, Jin Wang, Madhu S. Chinthavali and Radha K. Moorthy, "Liquid Metal based Cooling for Power Electronics Systems with Inductor Integrated Magnetohydrodynamic Pump (MHD Pump)," 2021 IEEE 8th WiPDA.
4. Junchong Fan, Zhining Zhang, Siddhant Shah, Jin Wang and Anant K. Agarwal. "Development of Ultra High Power Density Liquid Metal Cooled Inverter," AIAA 2023-4543. AIAA AVIATION 2023 Forum. June 2023.

5. Junchong Fan, Zhining Zhang, Siddhant Shah, Jin Wang and Anant K. Agarwal. "A High Performance Liquid Metal-based Cooling System for an Ultra High Power Density Inverter," 2023 IEEE Energy Conversion Congress and Exposition (ECCE) , Nashville, TN, USA, 2023

References

1. T. Aichinger and M. Schmidt, "Gate-oxide reliability and failure-rate reduction of industrial SiC MOSFETs," 2020 IEEE International Reliability Physics Symposium (IRPS), Dallas, TX, USA, 2020, pp. 1-6.

I.1.16 Device- and System-Level Thermal Packaging for Electric-Drive Technologies (Georgia Institute of Technology)

Yogendra Joshi, Principal Investigator

Georgia Institute of Technology
771 Ferst Drive,
Atlanta, GA, 30332
E-mail: yogendra.joshi@me.gatech.edu

Samuel Graham, Co-PI

Georgia Institute of Technology
801 Ferst Drive,
Atlanta, GA, 30332
E-mail: sgraham@gatech.edu

Satish Kumar, Co-PI

Georgia Institute of Technology
771 Ferst Drive,
Atlanta, GA, 30332
E-mail: satish.kumar@me.gatech.edu

Susan Rogers, DOE Technology Development Manager

U.S. Department of Energy
E-mail: susan.rogers@ee.doe.gov

Start Date: April 1, 2019
Project Funding: \$300,000

End Date: September 30, 2024
DOE share: \$300,000

Non-DOE share: \$0

Project Introduction

This project aims to research, develop, and test Electric Traction Drive System Technology for use in vehicle applications capable of meeting the targets set by the Department of Energy Vehicle Technologies Office. The project is categorized into three major thrusts: bonding interfaces for packaging, thermal management of electric vehicles (EVs) power inverters, and electric motor thermal management.

A transient liquid phase bonding technique has been developed to directly bond dielectric substrates with AlSiC heatsinks for use in power electronic packages. To realize a comprehensive package design, the metallization of the bonded AlN substrate-AlSiC heat sink structure is fundamental to not only facilitate the robust attachment of electronic components, but also establish efficient pathways for uninterrupted flow of electrical current. This is achieved through the development of an additive manufacturing process to print conductive Cu nanoplatelets ink on AlN dielectric substrates. Dielectric measurements affirmed that the AlN properties remained intact during the fabrication process, maintaining a relative permittivity of 8.5 ± 0.05 . The conductor's ampacity significantly surpassed conventional counterparts, peaking at $390 \times 10^6 \text{ A/m}^2$ —two orders higher than direct bond copper substrates. Reliability assessments provided insights into the conductors' endurance; in particular, the copper-graphene conductor exhibited remarkable thermal stability, enduring temperatures up to 400°C , and sustaining low resistance at 250°C for 140 hours, validating its suitability for demanding environments. The integration of printed conductors in power electronics packaging can yield more compact, reliable, and efficient power modules, laying the groundwork for advancements in industries ranging from electronics to renewable energy. Moreover, the adoption of additive manufacturing presents a promising and viable alternative to the multi-step procedures inherent in the direct bond copper (DBC) manufacturing process.

In-slot liquid cooling heat exchangers (HX) with integrated microchannels, that reduce the thermal resistance between the windings and the ambient, have been explored and optimized as a thermal management solution.

Specifically, enhancements have been made to integrate end-winding cooling with in-slot cooling for these heat exchangers. Additionally, a validated, multi-pronged thermal modeling approach for analyzing the impact of proposed motor cooling solutions at a multiscale level has been implemented. Such improvements in cooling efficiency and insights will improve performance, efficiency, and longevity of EV motors.

Using metal foams for jet impingement cooling of power electronics has been numerically investigated. Some preliminary results have been obtained by using porous media equations to reveal if potential heat transfer enhancement is possible.

Objectives

- Evaluate techniques for metalizing the top surface of an AlN substrate bonded to AlSiC heat sink using additive manufacturing.
- Develop a copper ink conductor suitable for 3D printing on AlN ceramic.
- Assess the electrical performance of the printed conductor.
- Investigate a direct liquid-cooling in-slot heat exchanger (HX) integrating in-slot winding and end-winding cooling for electric vehicle applications
- Investigate the development of an optimized multiscale thermal modeling framework in order to rapidly and accurately predict the motor-level impact of proposed cooling solutions, such as the proposed heat exchanger design.
- Reveal the potential heat transfer enhancement by introducing metal foams in jet impingement cooling.

Approach

Diffusion Modeling Bonded Packaging Interface

A large batch of copper nanoplates (CuNPLs) precursor is made by mixing copper chloride dihydrate ($\text{CuCl}_2 \cdot 2\text{H}_2\text{O}$, 38.4 g), D-glucose ($\text{C}_6\text{H}_{12}\text{O}_6$, 62.4 g), Hexadecyl-amine (HDA, $\text{CH}_3(\text{CH}_2)_{15}\text{NH}_2$, $\geq 90\%$, 232.8 g), and sodium iodide (NaI, 1.44 g) with 3600 mL deionized water [1]. This mixture is placed in an oil bath with a mechanical stirrer for 16 hours at 100 °C. During heating, the HDA acts as a coordinating ligand and forms a Cu^{2+} - HDA complex. As time passes, the Cu^{2+} gradually reduces to Cu^0 due to glucose, thus forming Cu seeds in the precursor solution. Once the seeds start to grow, iodide forces Cu growth parallel to the basal plane by preferentially absorbing onto the facets. Once the precursor feedstock is synthesized, it is filtered via a 160 μm mesh, followed by centrifuging at 6,000 rpm for 5 minutes. The solids are collected, re-dispersed in DI water and ethanol in a 1:1 ratio, and again centrifuged to obtain the CuNPLs feedstock. Once the CuNPLs feedstock is obtained, hydroxypropyl methylcellulose (HPMC) solution (2 wt. % in deionized water) and deionized water are mixed with the feedstock to make conductive, printable ink. Dopamine hydrochloride is added to this conductive ink (0.3 wt.%), and the solution is mixed in a Thinky ARE-310 Mixer for 30 seconds to obtain a homogenous ink mixture.

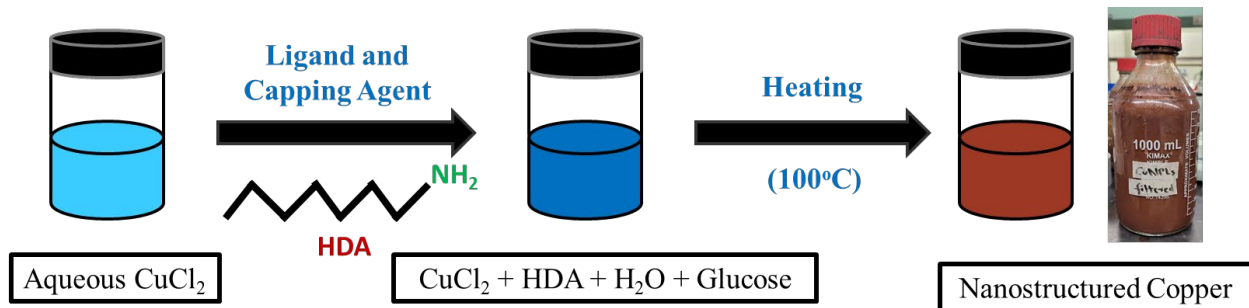


Figure I.1.16.1 Schematic representation of the Cu nanoparticles synthesis through hydrothermal reaction from precursor preparation and nucleation, to resulting growth of nanostructured copper.

To prevent undesired coupling of signals between channels during electrical testing, 9in² bare AlN substrates (Accuratus, US) [2] – each 630 μm thick – were cut into 25 mm x 5 mm pieces using a high-precision laser before printing. This ensured that each sample was subjected to an isolated testing environment, thereby mitigating the potential for crosstalk or spurious effects induced by neighboring samples. The bare AlN substrates were submerged in a 25% hydrochloric acid (HCl) solution at room temperature, sonicated in deionized (DI) water for 10 mins, and then cleansed with an organic solvent to eliminate residual oils or greases.

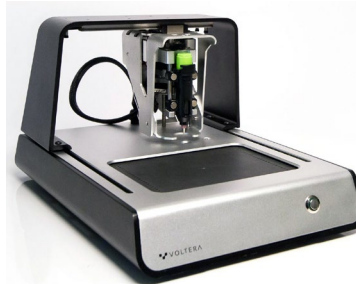


Figure I.1.16.2 Voltera V-One: 3D Printer used in printing conductive traces on AlN substrates [3].

The conductive inks were printed onto the AlN substrates using a direct-write approach with a Voltera V-One printer depicted in Figure I.1.16.2. The printed conductor was allowed to dry under ambient conditions for one hour, after which the substrates were transferred into a three-inch diameter alumina tube and fired in a forming gas atmosphere composed of 5% hydrogen (H) and 95% argon (Ar). The temperature was ramped up at a rate of 1°C/min until it reached 350 °C, where it was held for 1 hour to ensure furnace equilibrium. The temperature was then further increased at a rate of 1°C per minute until it reached 800°C, at which point it was held for 1 hour. After the hold, the furnace gradually cooled down at 2 °C per minute until the samples reached room temperature. Once at room temperature, the flowing forming gas was turned off, and the end cap of the furnace was removed to allow retrieval of the sintered samples.

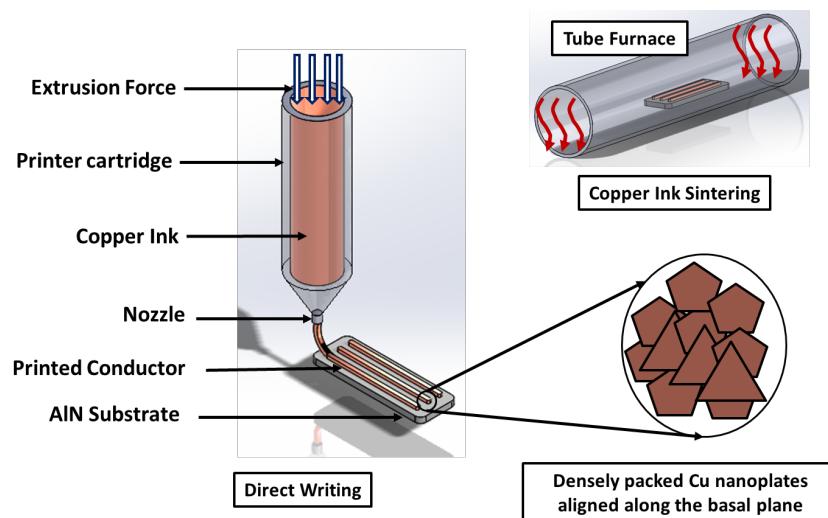


Figure I.1.16.3 Illustration of Ink Jetting Process: Deposition of Copper Nanoplate-Based Ink onto AlN Ceramic Substrate.



Figure I.1.16.4 Typical copper conductive ink printed on AlN.

Electrical conductivity and sheet resistance measurements were performed using an Ossila four-point probe system connected to a Keithley 2450 source meter. The system employed four equidistant and co-linear probes with rounded tips to establish electrical contact with the ink material. The probes were spring-loaded, ensuring a consistent 60 grams of force was applied on each sample during contact. Consequently, the resistance of the material was measured in a direction perpendicular to the thickness of the ink layer.

Electric Motor Thermal Management

Direct in-slot liquid-cooling heat exchangers (HX) was investigated as the thermal management solution, with the focus of the work being the thermal performance evaluation of a new proposed heat exchanger design that integrates end winding cooling with in-slot cooling. A combination of experimentation and multiscale computational methodology were used to evaluate and compare the performance of the baseline and proposed heat exchanger designs. First, the designs were computationally evaluated at component-level in Ansys Fluent (CFD/HT), yielding component-level metrics such as the effective heat transfer coefficient. The CFD/HT results were experimentally validated on alumina HX prototypes via a subscale test with polyamide patch heaters. Subsequently, various motor-level analysis approaches yield insights regarding the thermal impact of the proposed and baseline designs at motor-level. Firstly, a universal, condition-agnostic metric “winding-to-coolant thermal resistance” calculated using a thermal resistance network revealed the possible motor current density enhancement with the proposed design. Subsequently, two motor-level models were developed and run at a single operating point for contextual insights – one, a sub-motor level FEA model (half-slot) for steady-state thermal performance insights at a system level, and the other, a reduced-order full motor-level model in Ansys Motor-CAD for rapid insights at full scale level. The various metrics for cooling enhancement with the proposed design were analyzed across all motor-level approaches and used to draw conclusions regarding the HX design change. Hence, prior work done on end-winding cooling channels designed for an existing industrial motor was expanded and optimized for the concept motor design being explored by NREL, ORNL and Georgia Tech under the EDT objectives.

Use of Metal Foams in Jet Impingement Cooling

A porous media model was developed to simulate the flow and heat transfer of metal foams. The Local Thermal Non-Equilibrium (LTNE) model was used to solve the energy equation in the porous region for solid and fluid phases. A model developed by Calmidi and Mahajan [4] was used to assess the heat transfer between the solid and fluid, and was embedded in the CFD/HT solver. The boundary conditions are shown in Figure I.1.16.5. AmpCool 110 dielectric fluid was assumed as the coolant.

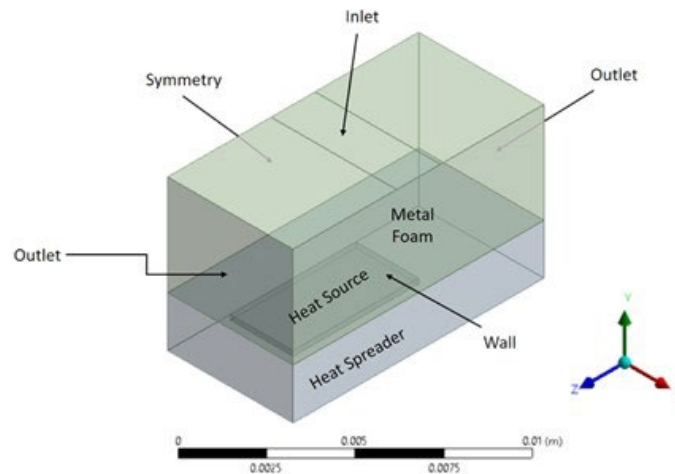


Figure I.1.16.5 Boundary conditions of the numerical model.

The heat transfer performance of two different copper foams having 10 and 100 pores per inch (PPI) was assessed by using a preliminary CFD/HT simulation. The properties of the simulated metal foams are shown in Table I.1.16.1. Also, the coolant properties can be found in Table I.1.16.2.

Table I.1.16.1 Properties of investigated copper foams.

	10 PPI	100 PPI
Porosity	0.897	0.9
Permeability (m ²)	0.87	0.0267
Form Coefficient	0.0786	0.108
Specific Surf. Area (m ⁻¹)	732	10160

Table I.1.16.2 Properties of coolant used in simulations.

Fluid	AmpCool 110
Inlet Temperature	70 °C
Density	783 kg/m ³
Thermal Conductivity	0.134 W/mK
Specific Heat	2326 J/kgK
Dynamic Viscosity	0.0034 Pa s
Prandtl Number	59.53

Results

Diffusion Modeling Bonded Packaging Interface

The relative permittivity, ϵ_r , of the AlN substrate with Cu printed conductor was determined from measured values of the sample's thicknesses, capacitance, and electrode area [5], [6]. The investigation encompassed an analysis of both pristine AlN substrates and substrates printed with Cu-ink conductor to analyze the potential impact of the printing and sintering procedures on the dielectric strength of the ceramic material. The results for the unmodified AlN samples maintained at room temperature, demonstrated that the permittivity remained consistent across frequencies, yielding a value of $\epsilon' = 8.6 \pm 0.04$ as illustrated in Figure I.1.16.6. This outcome aligns with previously reported values in the literature [7], [8]. Comparatively, AlN substrates subjected to the CuG ink printing process demonstrated a frequency-independent relative permittivity value of 8.5 ± 0.05 . This observation indicates that the entire process involving the printing and subsequent sintering of the copper-graphene ink does not adversely impact or alter the dielectric strength of the AlN substrate.

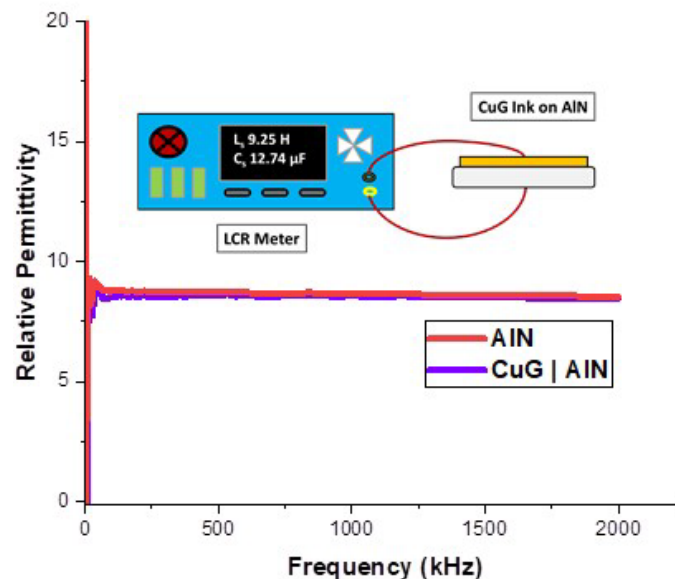


Figure I.1.16.6 Frequency-dependent relative permittivity of AlN with and without printed CuG ink. Results indicate the Cu ink sintering process has minimal impact on the dielectric strength of the AlN substrate.

The results presented in Figure I.1.16.7 demonstrate the relationship between the electric conductivity and sheet resistance of Cu nanoplates and Cu graphene conductors with respect to the printed ink thickness. The electrical conductivity of the pure copper nanoplates ink on AlN ranged from 2.2 MS/m to 7.17 MS/m, while that of the copper graphene ink ranged from 4.77 to 10.87 MS/m.

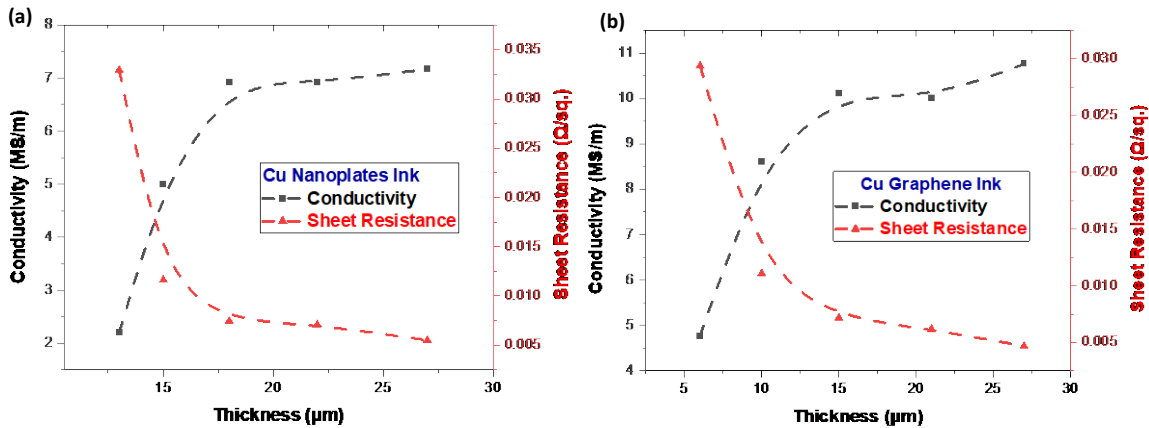


Figure I.1.16.7 Impact of ink layer thickness on the electrical conductivity and sheet resistance of (a) Cu NPLs and (b) CuG ink printed AlN substrates.

The current carrying capacity of the printed inks was evaluated by subjecting a series of Cu nanoparticle layers (Cu NPLs) and Cu-graphene (CuG) samples to steadily increasing voltage while recording the corresponding current. The obtained results, illustrating the performance of the samples, are presented in Figure I.1.16.8. As seen in Figure I.1.16.8 (a), at current densities up to $220 \times 10^6 \text{ A/m}^2$, the resistivity of the Cu-NPL ink printed on AlN substrates remained relatively unchanged. Beyond this limit, the thin ink traces experienced failure in the central region of the samples leading to an exponential increase in resistivity. However, the CuG ink samples sustained their current carrying ability well beyond the Cu-NPL limit and went as high as $390 \times 10^6 \text{ A/m}^2$, almost doubling the maximum ampacity results for pure Cu-NPLs.

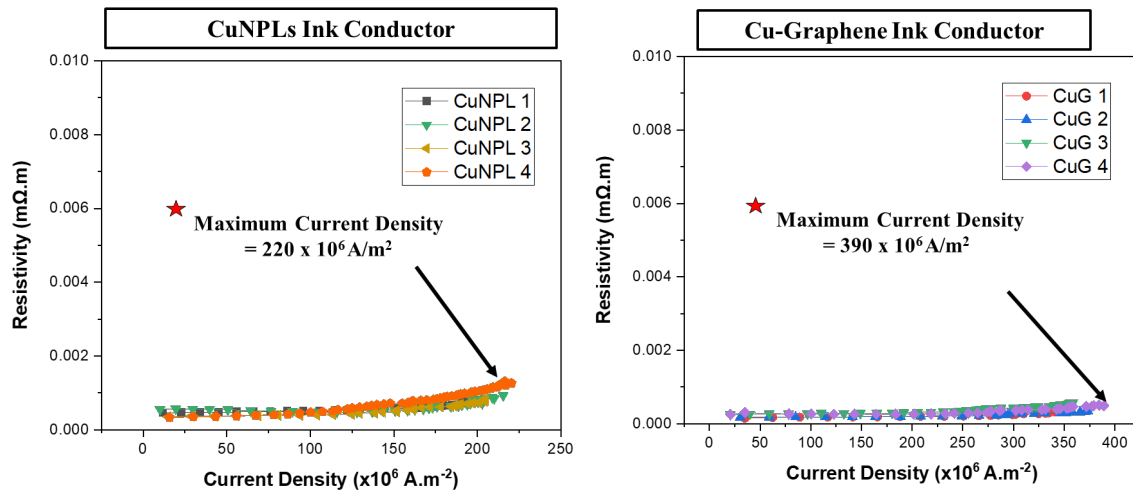


Figure I.1.16.8 Current density measurements for copper nanoplates ink and copper graphene ink

In contrast, direct bonded copper substrate samples tested in a similar setup displayed ampacities in the $4.1 - 5.6 \times 10^6 \text{ A/m}^2$ range, a hundred times lower than the for both the copper nanoplates and copper graphene ink as shown in Figure I.1.16.9. The significantly higher current density values observed in this study may be attributed to the inherent ability of nanoplates to sustain elevated ampacities due to their 2-D geometry, which facilitates plate stacking, consequently bolstering their current-carrying capacity [9], [10].

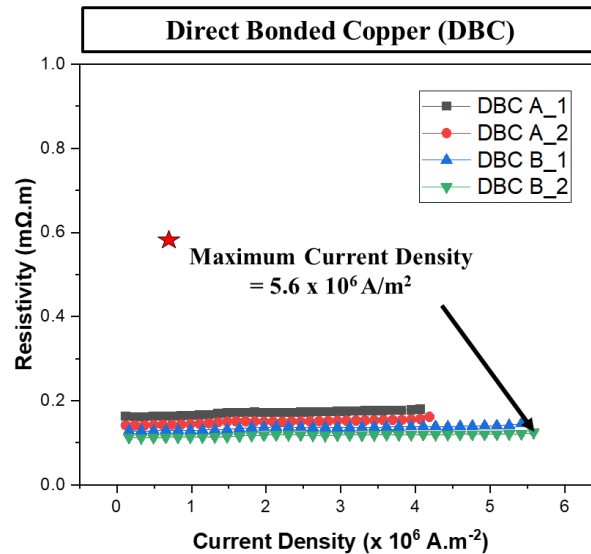


Figure I.1.16.9 Current density measurements for conventional direct bond copper.

To determine how much electrical current a typical power electronics circuit layer carries in operation, an estimation was made using the EETT roadmap for the 2025 Wide Bandgap Advanced Power Module [78]. The technical guidelines for future advanced integrated power modules (AIPM) outline anticipated voltage ratings of near 1 kV and maximum device currents of 200 A. Considering the typical surface footprint of SiC devices varies in area, with a maximum assumed area of approximately 5mm x 5mm, the ideal maximum current density of a power module can be approximated by dividing the maximum current by the known area, resulting in $8 \times 10^6 \text{ A/m}^2$. Comparatively, the ampacity of CuG ink significantly surpasses this requirement, making it a promising option for advancing power electronics packaging.

Electric Motor Thermal Management

The recent work involved the further optimization of in-slot heat exchangers identified as direct liquid-cooling solutions for the 100 kW high-power density outer rotor motor being developed under the EDT program objectives. The baseline design for these heat exchangers does not specifically address the cooling of end windings which extend out of the stator lamination stack. Hence, a new design is developed that addresses end winding cooling with two major advantages – (1) minimal alterations in motor critical design parameters, and (2) no additional provision required for coolant delivery to end windings (see Figure I.1.16.10).

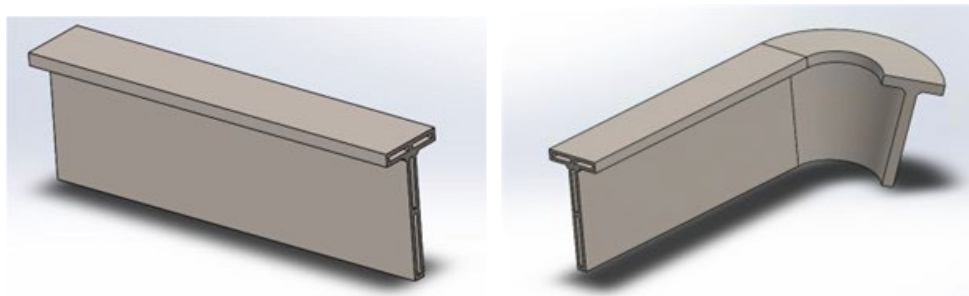


Figure I.1.16.10 (L) Baseline heat exchanger design, (R) Proposed heat exchanger design optimized for integrated end winding cooling.

It is desired to evaluate and compare the thermal performance of the two HX designs both at component-level and in terms of their impact on motor-level cooling. A multiscale framework that uses experimentally validated component-level insights and target motor parameters to drive various motor-level analyses is

proposed as shown in Figure I.1.16.11. First, a component-level CFD/HT model is developed using Ansys Fluent for both HX geometries with coolant (deionized water) flooding the internal channels, and with heat fluxes on the HX outer walls simulating heat dissipation from motor components. The tetrahedrally meshed $k-\epsilon$ SST model is run for various heat flux magnitudes and at various coolant flow rates, and then post-processed to calculate the average effective heat transfer coefficient h_{eff} . The h_{eff} shows negligible dependence on heat flux magnitude for a given heating configuration, but shows logarithmic growth with flow rate for both HX designs. Comparing between the two designs, the proposed design h_{eff} is higher than that of the baseline design past a threshold flow rate of 0.4 lpm (see Figure I.1.16.12). The component-level results are experimentally validated using a subscale test with polyamide patch heaters as the heat source, on LithaLox 350 HP alumina prototypes. The two HX test sections are shown in Figure I.1.16.13, while the experimental setup is shown in Figure I.1.16.14. The experimental results successfully validate the simulation results for h_{eff} , and show that the proposed design has enhanced thermal performance relative to the baseline past 0.4 lpm (see Figure I.1.16.15).

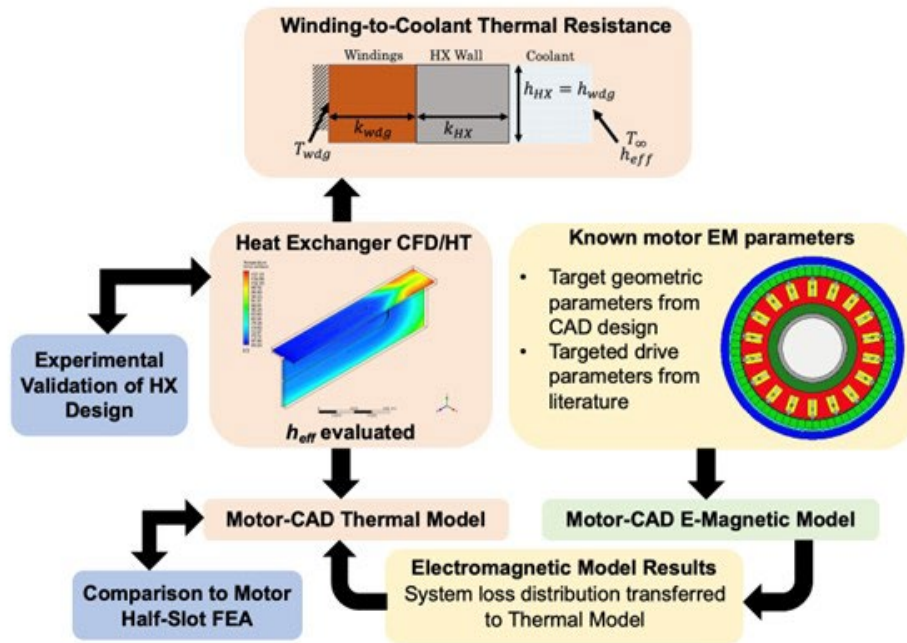


Figure I.1.16.11 Framework for multiscale thermal performance analysis of baseline and proposed cooling solutions.

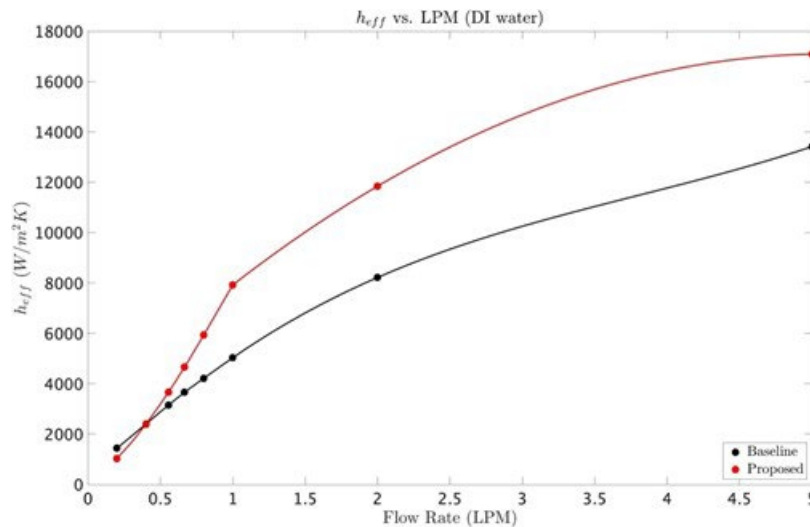


Figure I.1.16.12 Variation in h_{eff} with flow rate for both HX designs.

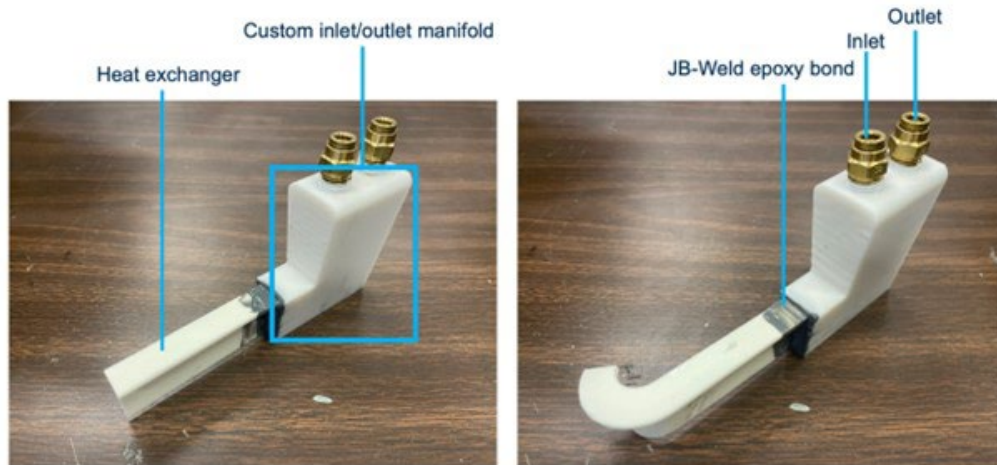


Figure I.1.16.13 Test sections for both HX designs with attached inlet/outlet manifold for coolant supply.

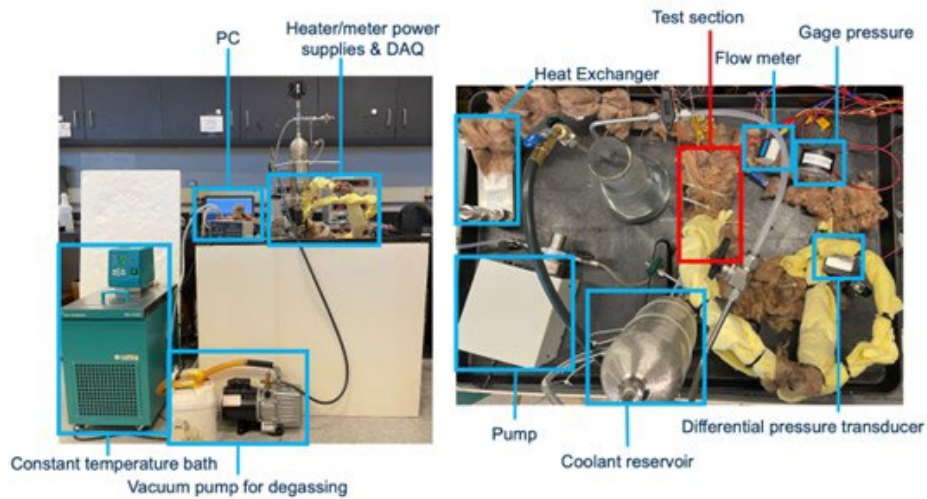


Figure I.1.16.14 Actual thermal testing loop setup for component-level HX effectiveness testing, at Georgia Institute of Technology.

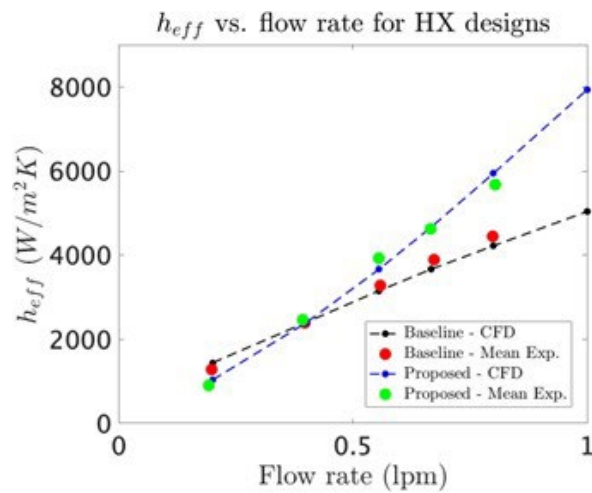


Figure I.1.16.15 Experimental versus CFD/HT h_{eff} versus flow rate for both HX designs.

The component-level results are used to drive various motor-level analyses. First, the ‘winding-to-coolant thermal resistance’ ($R_{th,wtc}$) for both designs is evaluated. This is based on a thermal resistance network simplified to ignore contact resistances and air gaps in the path between the windings and the coolant flow in the HX (see Figure I.1.16.16). The increase in coolant axial flow length and contact length between HX and windings in the proposed HX design led to a 30.5% reduction in the total conduction resistance. This, combined with reduced convective resistance (as seen in the component-level CFD/HT results) led to a $R_{th,wtc}$ that was up to 33% lower with the proposed design relative to the baseline. Subsequent calculations showed that the use of the proposed design would enable the motor to be run at a higher winding RMS current density per slot (up to $\approx 24\%$), and consequently deliver a greater power density, without breaching the NEMA Class F insulation temperature limit of 155 °C (see Figure I.1.16.17).

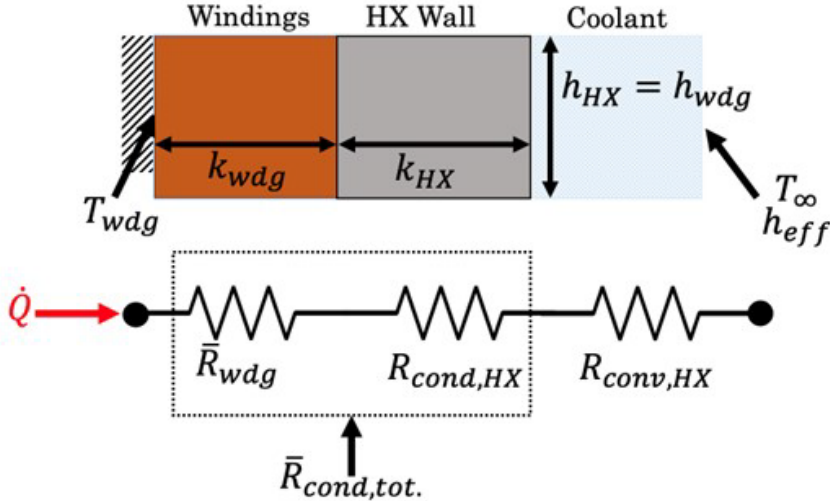


Figure I.1.16.16 Experimental versus CFD/HT heff versus flow rate for both HX designs.

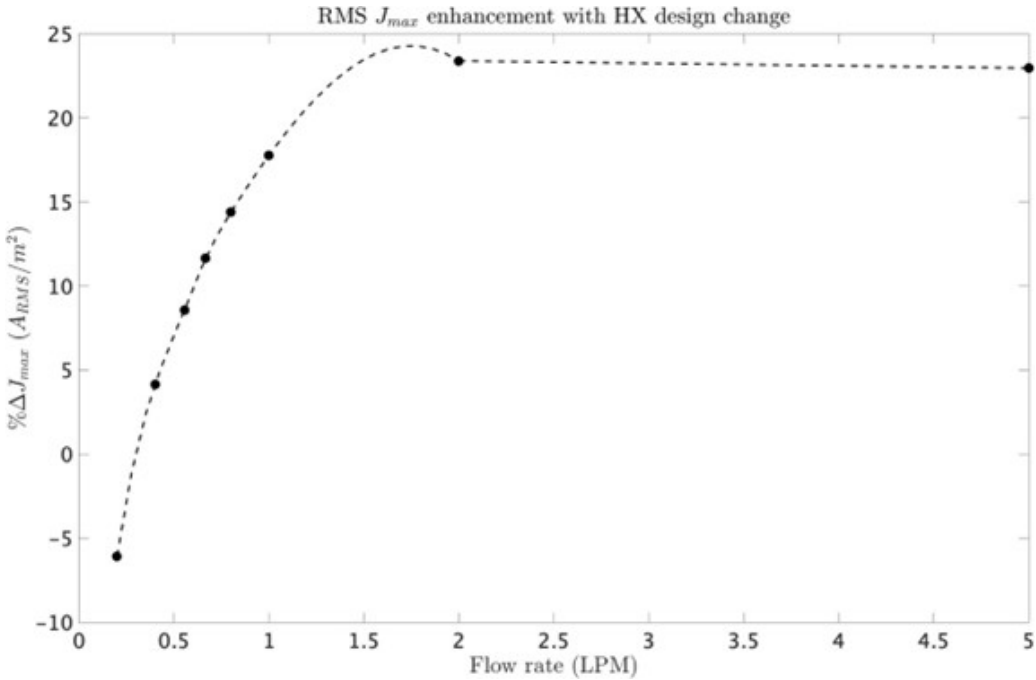


Figure I.1.16.17 Theoretical enhancement in maximum allowable RMS J_{max} with respect to flow rate, resulting from the change in HX design from baseline to proposed.

Subsequently, the universal results indicating enhancement with the proposed design were contextualized at the “peak torque condition” operating point using two parallel models. First, the Ansys Motor-CAD reduced order model was developed by specifying geometry from target parameters in literature and CAD designs. The electromagnetic model was run at the chosen operating point and yielded a loss distribution that was used to drive the thermal model. The thermal model was configured with HX cooling in the slot, and the h_{eff} was input at the HX boundary for the chosen HX design/flow rate to test motor-level cooling impact. The resulting winding and end winding temperature data points for both designs were analyzed across all flow rates in the range. Parallel to this, the loss distribution from Motor-CAD was mass-adjusted and used as input for the accurate half-slot FEA model. The HX cooling was configured here too, and similar winding/end winding data were generated for the FEA model. The reduction in maximum and average temperatures in windings/end windings across flow rates with the HX design change were analyzed for both models (see Figure I.1.16.18).

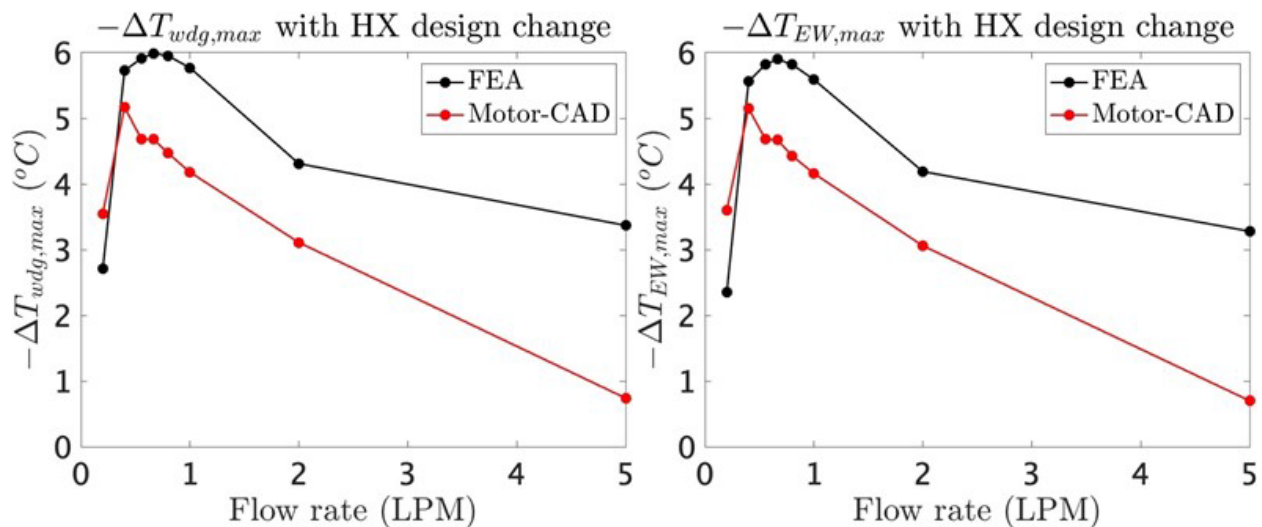


Figure I.1.16.18 Reduction in winding (L) and end winding (R) temperature maximum caused by the HX design change, as evaluated by both the FEA and Motor-CAD models.

Both motor-level models revealed up to 5.2-5.9 °C reduction in maximum winding and end-winding temperatures with the proposed HX design, with optimal thermal enhancement occurring at an intermediate flow rate below 2 lpm in both cases. At higher flow rates, the convective thermal resistances with both designs became negligibly small, and led to a total enhancement that was effectively conduction-based. The trends in the two motor-level models mirrored those for winding-to-coolant thermal resistance and motor current density enhancement, as seen in Figure I.1.16.17.

Use of Metal Foams in Jet Impingement Cooling

The heat transfer performance of two different copper foams having 10 and 100 PPI was assessed by using CFD/HT simulations. Figure I.1.16.19 shows the variation of the heat transfer coefficient with the pumping power. The heat transfer performance data from the previous study [11] are also included for comparison. As can be seen, some potential can be investigated further for 10 PPI metal foams. The higher heat transfer coefficient for 10 PPI metal foams was found for the inlet velocities higher than 0.8 m/s.

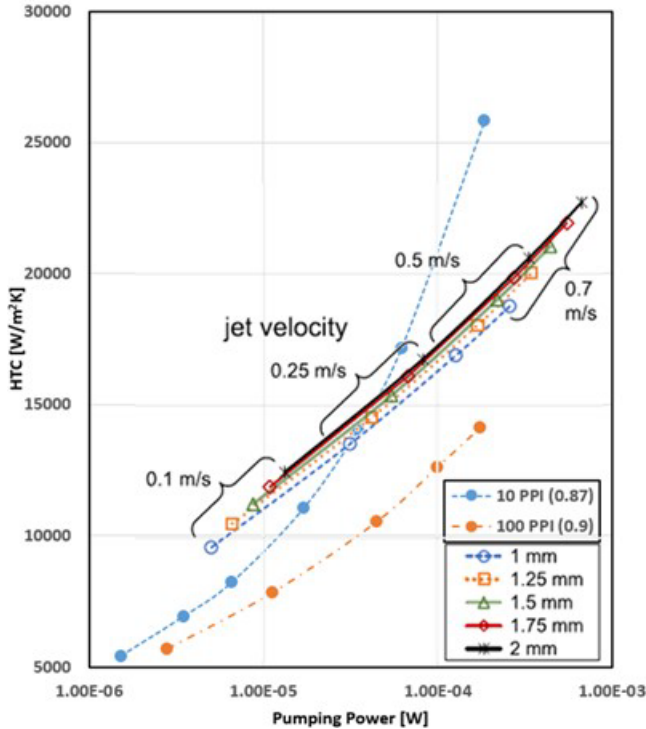


Figure I.1.16.19 Variation of HTC with pumping power compared to a previous study [11].

The flow streamlines, and the temperatures of the solid and the fluid phases are shown in Figure I.1.16.20 for 10 PPI copper foam at 1 m/s jet velocity. There is a considerable temperature difference between the solid and fluid phases of the copper foam. This shows that the interfacial heat transfer area is used effectively for the heat transfer. The average heat spreader surface temperature is assessed as 180.16°C. According to the results, further modeling of the real geometries of metal foams after CT scans can be obtained in order to control the results of porous media modeling and reveal the physics behind the heat transfer enhancement.

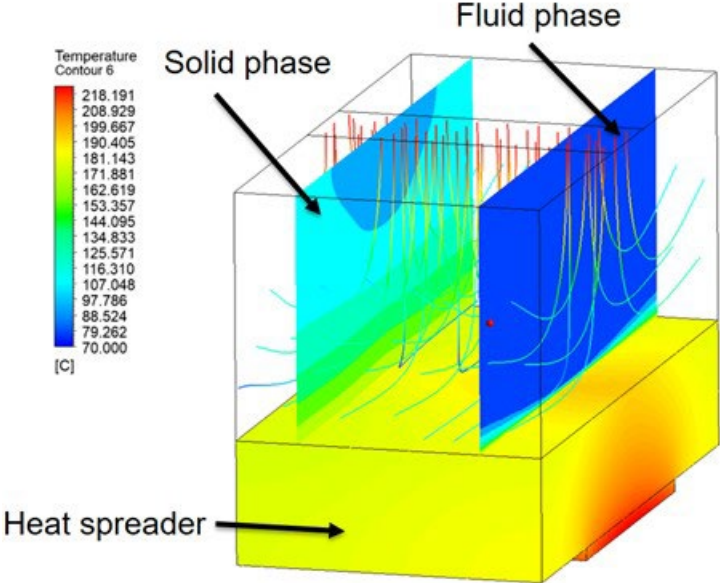


Figure I.1.16.20 Streamlines and temperature contours of heat spreader, solid and fluid phases of copper foam for 1 m/s inlet velocity.

Conclusions

- An exploration of additive manufacturing's potential in advancing power electronics packaging using copper-ink-based conductors is showcased. Additive manufacturing presents a promising alternative to conventional direct bond copper (DBC) manufacturing processes, and offers unparalleled design flexibility, minimized material wastage, and rapid prototyping capabilities. The study details investigations into the practical implementation of this concept through electrical and ampacity assessments. Dielectric measurements and impedance spectroscopy studies affirm the consistent and robust dielectric strength of the aluminum nitride ceramics when integrated with copper-graphene conductors, maintaining a relative permittivity value of 8.5 ± 0.05 . Analyses of conductivity and ampacity highlight the promising potential of the copper-graphene composite. Although electrical conductivity values are of a similar magnitude as bulk Cu, the ampacity of the copper-graphene conductor significantly surpasses traditional counterparts, reaching a peak value of $390 \times 10^6 \text{ A/m}^2$, two orders of magnitude higher than conventional direct bond copper substrates. In summary, this research authenticates the viability of utilizing additive manufacturing to engineer hybrid copper-graphene conductors for advanced power electronics packaging.
- Component-level and system-level thermal analyses for liquid-cooled in-slot heat exchanger designs have been incorporated into a proposed outer rotor motor for EV applications. The validated component-level, analytical resistance network-based and two motor-level models show reasonable agreement to indicate that the proposed HX design has superior thermal performance, and leads to enhanced cooling of windings and end windings. The work demonstrates the virtue of multiscale and multi-pronged analysis approaches, and also reveals the virtues and drawbacks of using rapid reduced-order models instead of full FEA models for motor-level thermal analysis of new, proposed cooling solutions.
- Using metal foams for jet impingement cooling of power electronics has been numerically investigated. The preliminary results showed there is a potential for heat transfer enhancement. However, since porous media modeling has been used to obtain the results, it is intended to model the real geometries for a more detailed analysis.

Key Publications

1. Imediogwu, C., et al., Interdiffusion and formation of intermetallic compounds in high-temperature power electronics substrate joints fabricated by transient liquid phase bonding. *Microelectronics Reliability*, 2022. 137: p. 114788.
2. Imediogwu, C., Pahinkar, D. G., Graham, S., Narumanchi, S., Paret, P. Influence of Copper Concentration on the Thermal Expansion Coefficient and Hardness of Al-Cu Composites. *Manuscript*
3. Imediogwu, C., Khuje, S., Islam, A., Huang, Y., Ren, S., Paret, P., Narumanchi, S., Pahinkar, D.G., Graham, S., Enhanced Electrical Performance and Reliability of Hybrid Copper-Graphene Printable Conductor for Advanced Power Electronics Packaging. *Manuscript*
4. Paranjape, A., Kumar, S., and Joshi, Y., Multiscale Analysis and Validation of End Winding Integrated Heat Exchanger for Motor Thermal Management, *ASME Journal of Electronic Packaging*, *in progress*

References

1. Sheng, A., S. Khuje, J. Yu, D. Petit, T. Parker, C.-G. Zhuang, L. Kester and S. Ren. "Ultrahigh temperature copper-ceramic flexible hybrid electronics." *Nano Letters* 21 (2021): 9279-84. 10.1021/acs.nanolett.1c02942. <https://doi.org/10.1021/acs.nanolett.1c02942>.
2. Accuratus. "Ceramic materials and ceramic components." <http://accuratus.com/>.

3. Printer, V. V.-O. D. "Voltera v-one: 3d printer " <https://www.elektor.com/voltera-v-one-desktop-pcb-printer>.
4. Calmidi, V. and R. Mahajan. "Forced convection in high porosity metal foams." *Journal of Heat Transfer* 122 (2000): 557-65.
5. Marjanovic, M., V. Paunovic, Z. Prijić, A. Prijic, D. Danković and V. V. Mitic. "On the measurement methods for dielectric constant determination in nb/batio3 ceramics." Presented at 2015.
6. Wintle, H. J. and S. Kurylowicz. "Edge corrections for strip and disc capacitors." *IEEE Transactions on Instrumentation and Measurement* IM-34 (1985): 41-47. 10.1109/TIM.1985.4315253.
7. Mu, H. B., Y. H. Guo, C. W. Yao, Z. H. Jia, Z. S. Chang and G. J. Zhang. "Effect of aluminum nitride on discharge mode transition in atmospheric pressure he/o2 dbd." *IEEE Transactions on Plasma Science* 46 (2018): 888-94. 10.1109/TPS.2018.2811381.
8. Thorp, J. S., D. Evans, M. Al-Naief and M. Akhtaruzzaman. "The dielectric properties of aluminium nitride substrates for microelectronics packaging." *Journal of Materials Science* 25 (1990): 4965-71. 10.1007/BF00580114. <https://doi.org/10.1007/BF00580114>.
9. Li, Z., S. Khuje, A. Chivate, Y. Huang, Y. Hu, L. An, Z. Shao, J. Wang, S. Chang and S. Ren. "Printable copper sensor electronics for high temperature." *ACS Applied Electronic Materials* 2 (2020): 1867-73. 10.1021/acsaelm.0c00358. <https://doi.org/10.1021/acsaelm.0c00358>.
10. Lee, J.-W., J. Han, D. S. Lee, S. Bae, S. H. Lee, S.-K. Lee, B. J. Moon, C.-J. Choi, G. Wang and T.-W. Kim. "2d single-crystalline copper nanoplates as a conductive filler for electronic ink applications." *Small* 14 (2018): 1703312. <https://doi.org/10.1002/sml.201703312>. <https://onlinelibrary.wiley.com/doi/abs/10.1002/sml.201703312>.
11. Moreno, G., S. Narumanchi, J. Tomerlin and J. Major. "Single-phase dielectric fluid thermal management for power-dense automotive power electronics." *IEEE Transactions on Power Electronics* 37 (2022): 12474-85.

Acknowledgements

The principal investigators would like to thank Gilbert Moreno, Paul Paret, Kevin Bennion, Emily Cousineau, and Sreekant Narumanchi from NREL for their help and contribution to this project. We would like to acknowledge our collaborators at NREL for conducting C-SAM imaging and providing thin Al coupons, as well as the Georgia Tech Machine shop for their help in cutting AlSiC plates using electrical discharge machining.

I.1.17 Integrated Motor and Drive for Traction Application (University of Wisconsin-Madison)

Bulent Sarlioglu

University of Wisconsin – Madison
1415 Engineering Dr
Madison, WI 53706
E-mail: sarlioglu@wisc.edu

Susan Rogers, DOE Technology Development Manager

U.S. Department of Energy
E-mail: susan.rogers@ee.doe.gov

Start Date: April 1, 2019
Project Funding: \$300,000

End Date: April 1, 2024
DOE share: \$300,000

Non-DOE share: \$0

Project Introduction

The objective of the project is to research, design, develop, and test a high-performance traction motor and a high-efficiency traction inverter and then to combine them into a state-of-the-art integrated motor drive (IMD) that requires only a single housing for use in vehicle applications.

The new IMD system will significantly increase the motor and inverter power density values to meet the aggressive DOE targets while simultaneously taking steps to minimize their cost. The high-power-density, reduced-cost prototype IMD will become a valuable source of technical data that can be used by automakers and their suppliers to improve the performance of future EV traction drive systems.

Objectives

This project performance targets for the power electronics and motor are presented in Table I.1.17.1.

Table I.1.17.1 Power Electronics and Motor Requirements

Power Electronics Requirements	
Parameter	Measure
Cost (\$/kW)	≤ 2.7
Peak Power Density (kW/L)	≥ 100
System Peak Power Rating (kW)	100
Electric Motor Requirements	
Parameter	Measure
Cost (\$/kW)	≤ 3.3
Peak Power Density (kW/L)	≥ 50
System Peak Power Rating (kW)	100

Approach

This project began with an evaluation of several types of electric motors and inverters that are candidates for future land-based vehicle traction applications. The evaluation results led to the selection of the most desirable machine plus inverter topology that is in the process of being developed into a working state-of-the-art prototype integrated motor drive (IMD).

During Budget Period #1, a literature review was carried out that set the stage for trade-off studies to evaluate several alternative motors and inverters that are candidates for adoption in the target integrated motor drive system. The motor configurations, as well as the power inverter topologies, were compared, leading to the selection of the surface permanent magnet (SPM) machine and the current source inverter (CSI) as the best candidates for further development.

During Budget Period #2, a preliminary motor electromagnetic design and power electronics electrical design were carried out for the SPM machine and CSI power converter. A bench-top inverter was designed, fabricated, and tested to verify key IMD concepts and reduce technical risks. In addition, we carried out thermal and mechanical designs of the motor and inverter, including their physical integration into an IMD.

During Budget Period #3, the IMD design was finalized in preparation for prototype IMD construction. Construction of the prototype SPM machine and current source inverter was initiated. A dynamometer test stand was designed and assembled, including instrumentation for testing the motor and power inverter.

During Budget Period #4, the fabrication of the prototype SPM machine and current source inverter was completed. These major system components were integrated into the same IMD enclosure and made operational during the last quarter of this budget period. Initial tests were carried out to demonstrate the functionality of the prototype IMD.

During Budget Period #5, the combined prototype IMD system is in the process of being tested. The IMD performance is being measured to verify the ability of the prototype IMD to meet its performance targets.

Results

Final prototype inverter design for IMD

The CSI-based motor drive including the front-end dc/dc converter is shown in Figure I.1.17.1. The dc/dc converter is responsible for converting the battery voltage source into a regulated current that is delivered to the dc link of the CSI.

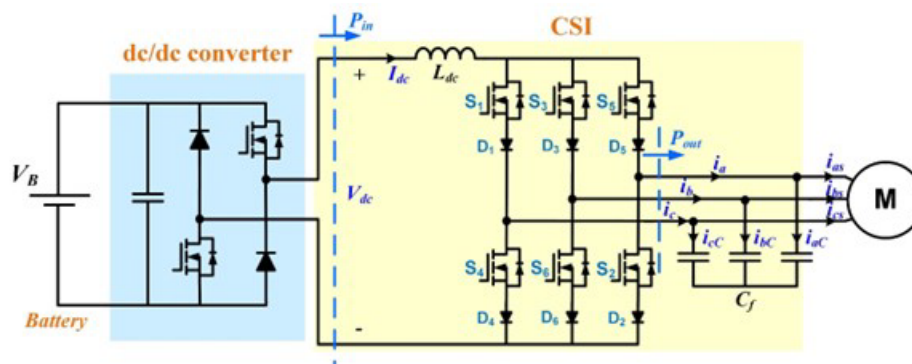


Figure I.1.17.1 Baseline CSI-based motor drive system for traction application

The design of the bench-top prototype CSI with SiC power modules and film capacitors was presented in the last annual progress report. During this year, the final version of the CSI for the prototype IMD was designed and fabricated using ceramic capacitors to further reduce the CSI height and volume. 3-D drawings comparing the CSI power board assembly using film capacitors and ceramic capacitors are shown in Figure I.1.17.2. Ceramic capacitors are much more compact than film capacitors used in the benchtop CSI. The total CSI assembly height was reduced by ~70% from 80 mm to 25 mm. The maximum operating temperature limit of the ceramic capacitors is 150°C compared to 105°C for the film capacitors.

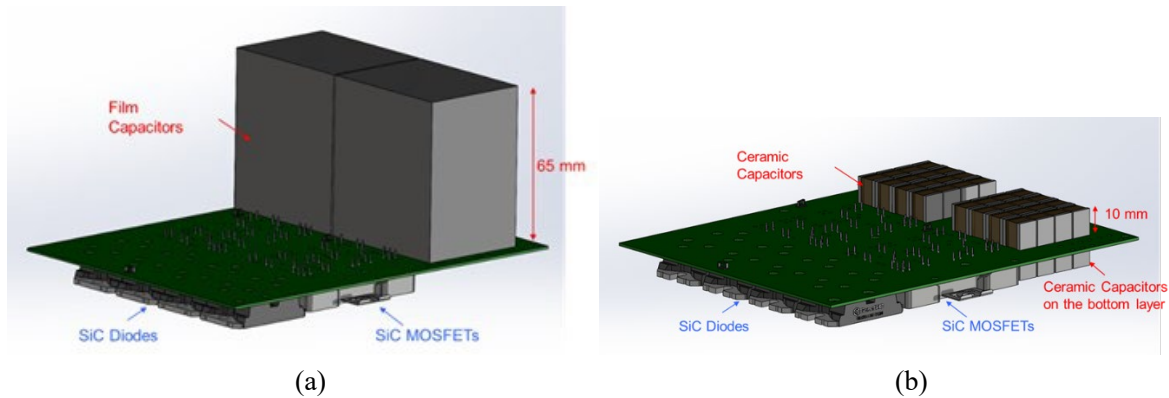


Figure I.1.17.2 (a) Original benchtop CSI design with film capacitors; (b) New prototype CSI design with ceramic capacitors for integration into IMD.

Assembly of the prototype machine

Based on the performance requirements, the machine must deliver 100 kW peak output power with a continuous power rating of 55 kW. The maximum machine speed is 20,000 rpm with a constant-power speed ratio (CPSR) of 3. As a result, the rated torque for continuous power operation is 78.8 Nm, and the peak torque at the 100 kW operating point is 143.2 Nm. One stator and 2 rotors were designed to meet the requirements. One rotor uses a surface permanent magnet (SPM) design, and the second uses a surface inset permanent magnet (SIPM) design.

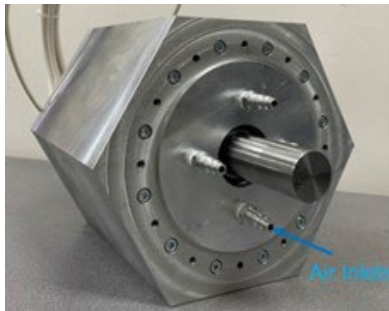


Figure I.1.17.3 Drive-end view of assembled electrical machine showing 4 air inlets.

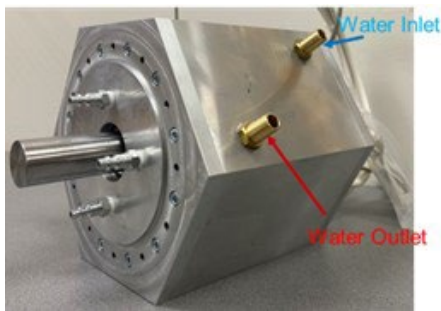


Figure I.1.17.4 Side view of assembled electrical machine with stator jacket water inlet and outlet

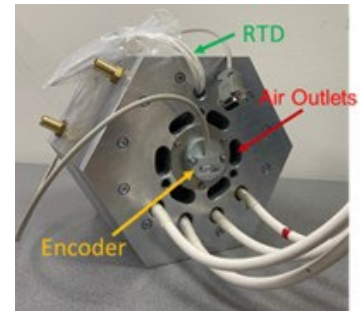


Figure I.1.17.5 Non-drive-end view of assembled electrical machine showing electrical and RTD leads, air outlets, and encoder.

Figure I.1.17.3 shows the drive-end view of the assembled machine. In this figure, four air inlets can be observed that deliver forced air for cooling the rotor. Figure I.1.17.4 shows a side view of the machine that highlights the water inlet and outlet for the housing water jacket. The water flowing through this jacket is used to cool both the machine stator and power electronics. Figure I.1.17.5 shows a view of the machine's non-drive-end, identifying the electrical leads (three-phase terminals and neutral) and air outlet portals. These electrical leads are connected to the inverter output terminals to excite the machine during operation. The encoder can also be observed in this figure, mounted adjacent to the end of the spinning rotor shaft.

Testing of the electrical machine (SIPM rotor)

Back-EMF measurement is one of the key steps to characterize the machine's performance. Figure I.1.17.6 shows the dynamometer test configuration for back-EMF measurement with the electrical machine mounted on the dynamometer testbed. Figure I.1.17.7 shows the measured three-phase line-to-neutral back-EMF waveforms at 4,000 rpm. The waveshape is not perfectly sinusoidal, as expected, due to spatial harmonics introduced by the interactions between the rotor magnets and the stator windings.



Figure I.1.17.6 Dynamometer test configuration for back-EMF measurement

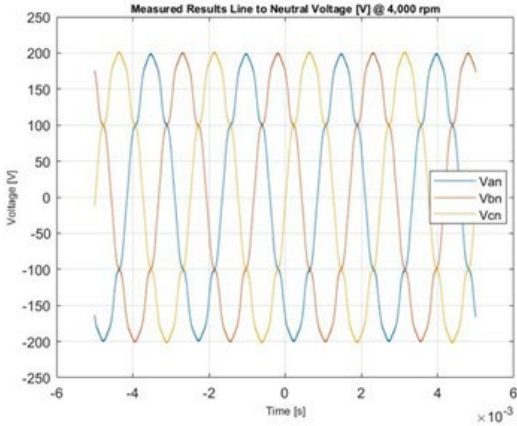
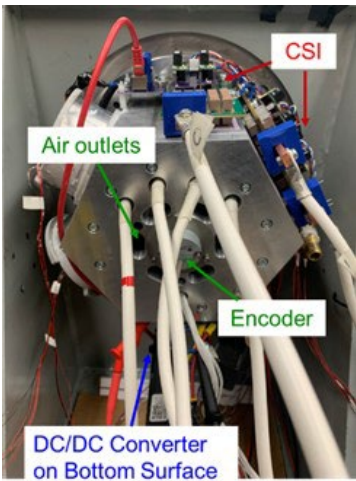


Figure I.1.17.7 Measured line-to-neutral back-EMF voltage waveforms at 4000 rpm

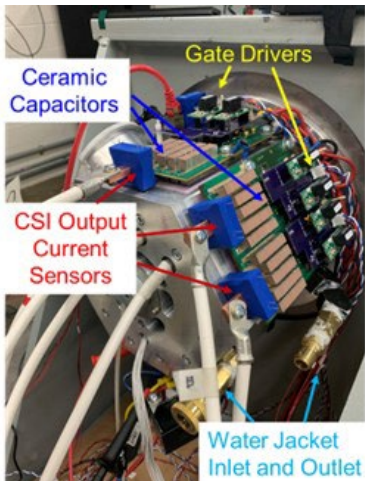
Comparisons between the measured back-EMF and FEA-predicted back-EMF waveforms are shown in Table I.1.17.2. The results show that measurement results are close to the FEA-predicted results, which is very promising. The difference between the predicted and measured peak fundamental voltage component of the back-emf waveforms is less than 3%, demonstrating that the test results match the FEA-predicted results very well.

Table I.1.17.2 Summary of Measured Back-EMF Waveforms (Fund. Component Peak)

Speed [rpm]	Back-EMF Results (Peak Fund. Voltage Component)				FEA Results (Fund.) [Vpk]	Difference
	Van [V pk]	Vbn [V pk]	Vcn [V pk]	Avg. [V pk]		
500	24.51	24.51	24.66	24.56	23.9	2.76%
1,000	48.98	49.09	49.31	49.13	47.81	2.75%
2,000	97.41	97.84	98.24	97.83	95.62	2.31%
3,000	145.58	146.41	146.91	146.3	143.43	2.00%
4,000	194.14	194.84	195.68	194.89	191.25	1.90%



(a) Front view



(b) Right-side view

Figure I.1.17.8 Two views of the fabricated prototype integrated motor drive

IMD fabrication

After assembly of the prototype machine and fabrication of the prototype CSI with ceramic capacitors were completed, all of the power electronic components were mounted on the machine housing to complete the prototype IMD, as shown in Figure I.1.17.8. The physical integration of the prototype machine and power electronics into the prototype IMD assembly has been successfully accomplished.

Control development summary

This year, significant technical progress has been made in developing the control system for the prototype IMD. The initial test to verify the functionality of the prototype IMD was successfully carried out. The CSI's pulse-width modulator was designed and implemented using the digital signal processor (DSP). The CSI's modulator uses space vector pulse-width modulation to synthesize the CSI's desired 3-phase sinusoidal output currents.

The CSI's cascaded closed-loop controller has been designed and implemented, as shown in Figure I.1.17.9.

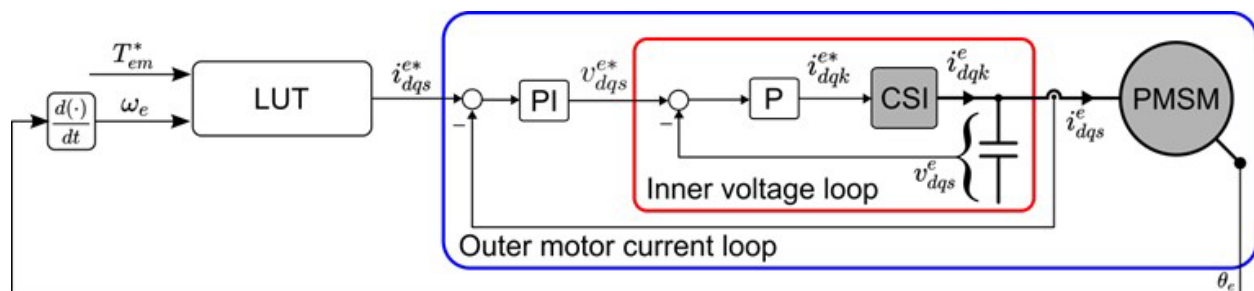


Figure I.1.17.9 Cascaded closed-loop control structure.

The IMD's controller performance has been experimentally validated using the prototype dc/dc converter, CSI, and SIPM motor to deliver high-quality sinusoidal phase current waveforms shown in Figure I.1.17.10.

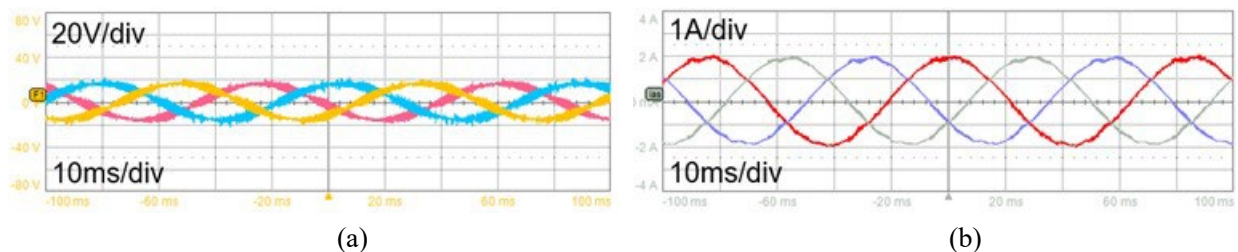


Figure I.1.17.10 Experimental validation of closed-loop control. (a) CSI's line-to-line output voltages; and (b) CSI's motor phase currents.

Integrated sensor boards were designed and fabricated to measure the output voltages and currents which provide the required inputs to the closed-loop control. The schematics of the designed sensor signal conditioning circuits are shown in Figure I.1.17.11. Shielded cables are used to deliver the sensor signals to the DSP in order to prevent electromagnetic interference (EMI) from corrupting these key sensor inputs. The integrated sensor board successfully integrated the voltage and current sensors into a single board, reducing their total volume.

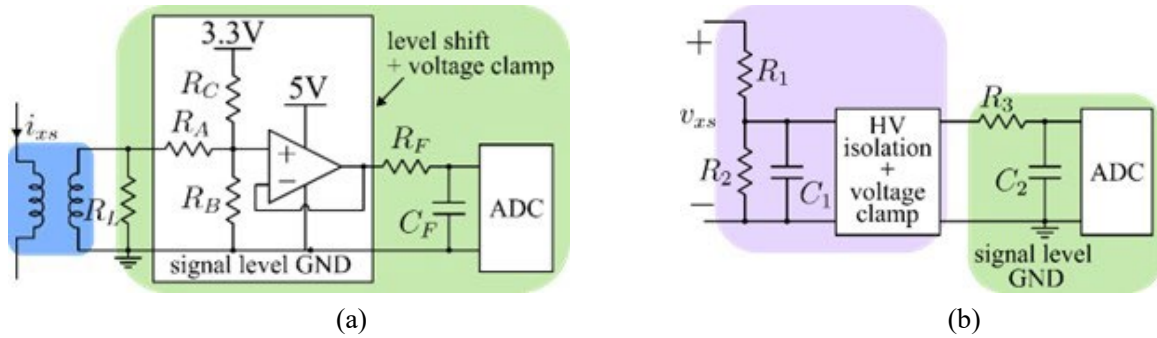


Figure I.1.17.11 Sensor schematics and signal conditioning circuits. (a) current sensor; (b) voltage sensor.

Driving cycle model for electrical vehicle

Driving cycle analysis will be used to predict the performance of the prototype IMD in an electric vehicle (EV) drivetrain in terms of its energy usage requirements. A Chevrolet Spark EV has been selected as the baseline vehicle for analyzing the well-known Urban Dynamometer Drive Schedule (UDDS) drive cycle. Analytical models for the vehicle dynamics have been developed, and all key vehicle forces have been calculated, including acceleration force, rolling resistance force, and aerodynamic drag force. Based on the vehicle configuration, the required machine torque and speed values to meet the UDDS drive cycle have been calculated.

Figure I.1.17.12 shows the required machine torque/speed operating points calculated for the UDDS drive cycle assuming a peak speed of 100 mph with a selected gear ratio of 13.8 between the machine and tire speeds. The IMD’s maximum torque vs. speed envelope curves have been overlaid in Figure I.1.17.12 for both steady-state (55 kW) and transient (100 kW) operations. It can be seen that all of the required torque/speed operating points for the Spark vehicle executing the UDDS drive cycle (blue circles in Figure I.1.17.12) fall within one or both of the torque vs. speed envelopes for the CSI-IMD drive system, and the majority of them fall within the steady-state 55 kW torque-speed envelope.

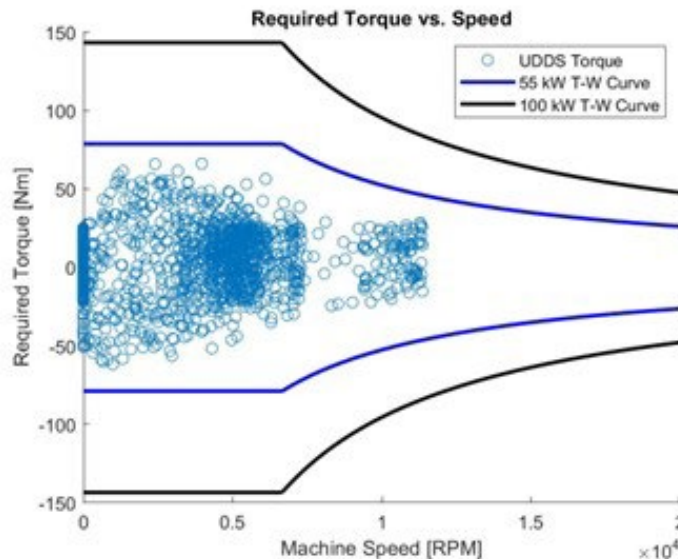


Figure I.1.17.12 Calculated map of torque/speed operating points (blue circles) for Chevrolet Spark during a UDDS drive cycle with overlaid torque/speed envelopes for prototype CSI-IMD unit showing both steady-stage (55 kW) and transient (100 kW) limits. The assumed ratio of motor shaft speed to tire speed is 13.8.

Predicted IMD efficiency evaluation

The predicted IMD efficiency map for 12 different operating points is shown in Figure I.1.17.13. The predicted IMD efficiency values for the two steady-state operating points at the corner speed (6667 rpm) are both greater than 95%, which are appealing values. The predicted IMD efficiency values for the steady-state operating points at speeds of 10,000 rpm or less are all greater than 95%, which is promising for vehicle drive cycle efficiencies, particularly for those that focus on urban driving conditions that are biased towards lower operating speeds.

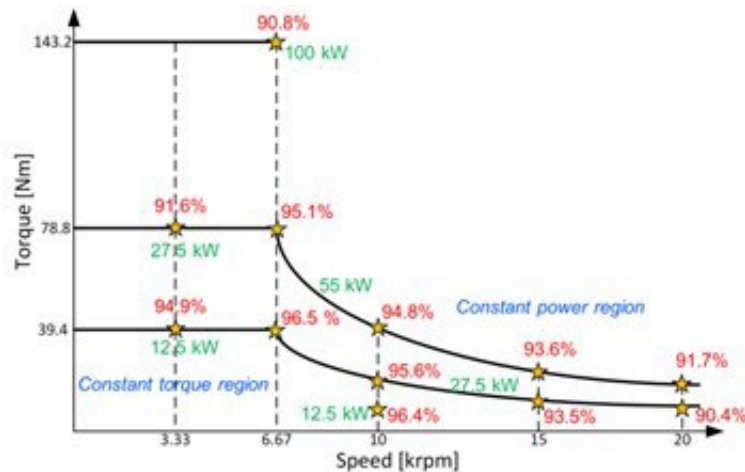


Figure I.1.17.13 Predicted IMD (power electronics + machine) efficiency map for 12 operating points

Thermal analysis

The cooling configuration has undergone only minor modifications since the IMD's original thermal design, consisting of a liquid-cooled stator housing jacket and forced air cooling of the rotor. 20°C distilled water is used in the stator jacket based on the capabilities of the available lab chiller. Thermal FEA has been used to provide a more accurate prediction of the machine's stator thermal performance using this coolant temperature.

The results from the steady-state thermal FEA for the machine operating at 55 kW at both the corner speed and peak speed are presented in Figure I.1.17.14 and Figure I.1.17.15, respectively. This analysis predicts a maximum winding temperature of 124.4°C during the maximum speed and 55 kW operation, attributable to the winding's elevated AC losses. These results indicate that the machine should be safe to operate under steady-state conditions at both 55 kW rated power operating points.

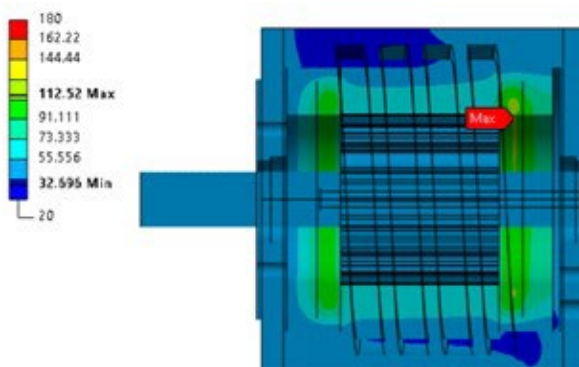


Figure I.1.17.14 Estimated temperature distribution (55 kW at 6,667 rpm)

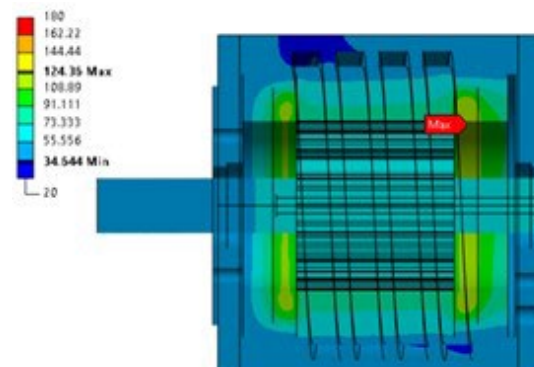


Figure I.1.17.15 Estimated temperature distribution (55 kW at 20,000 rpm)

The availability of 20°C coolant also helps the predicted thermal performance during transient peak power operation, resulting in opportunities for extended periods of operation at peak power. Figure I.1.17.16 presents the thermal FEA results after a 60-second period of peak power (100 kW) operation, starting from steady-state operation at rated power (55 kW). Additionally, Figure I.1.17.17 plots the predicted temperature increases in critical machine components during this 60-second interval at peak power, illustrating the benefits of using the lower temperature coolant on the predicted IMD system thermal performance.

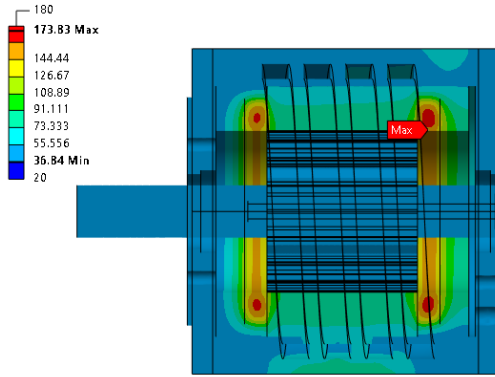


Figure I.1.17.16 Estimated temperature distribution after 60s operation at 100 kW peak power @ 6,667 rpm

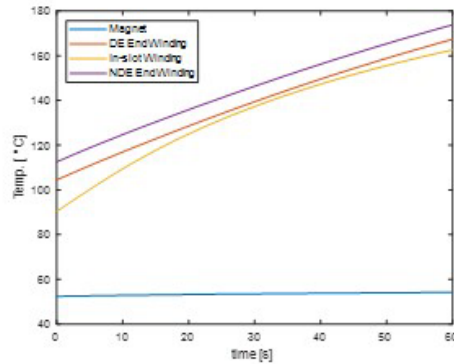


Figure I.1.17.17 Predicted temperature increase of key machine components vs. time during 100 kW peak power application

The predicted maximum winding temperature reaches only 146°C at the end of the required 30s peak power operation and rises to 174°C at the end of the 60s operation at peak power. These results indicate that the machine can safely operate at peak power for twice the required time without thermal overload. It should be noted that the rotor magnets remain at temperatures below 60°C throughout this peak power test, well within their 80°C maximum temperature limit. The predicted maximum temperature of each key machine component is listed in Table I.1.17.3 for four key operating points including the 2 steady-state operating conditions at rated power (55 kW at 6667 and 20,000 rpm) and two peak power transient conditions (30s and 60s).

Table I.1.17.3 Predicted Max. Machine Temperatures From Thermal FEA with 20°C Coolant

Components	55 kW Steady-State Temp. [°C]		100 kW Pk Power Temp [°C]		Rating [°C]
	6,667 rpm	20,000 rpm	30s	60s	
Stator core	86.4	104.2	118.1	139.8	740
Active winding	90.3	114.0	137.3	162.6	180
End winding (DE)	104.5	116.0	139.4	167.3	180
End winding (NDE)	112.5	124.4	146.4	173.8	180
Magnets	52.4	71.5	53.5	54.2	80
Rotor core	52.4	71.4	53.5	54.2	740

Conclusions

Major progress has been accomplished during the past year toward the objective of building and testing the prototype integrated motor drive unit designed to meet aggressive DOE performance targets and power density metrics. More specifically, the fabrication of the prototype PM machine and the current source power converter have been completed. All of the power electronic components have been mounted on the machine housing to build the prototype IMD. Both the motor and power electronics unit have been characterized during initial tests. The closed-loop control for the prototype IMD has also been verified experimentally. Thermal FEA analysis for the final IMD prototype has been carried out, and the results indicate that the machine can

safely operate at peak power for twice the required time without thermal overload when using the 20°C coolant available in our lab.

Full-power testing covering the IMD's complete torque-speed operating envelopes is in progress with targeted completion before the end of BY#5, consistent with the SOPO project plans. Based on both analytical and preliminary test results gathered to date, the prospects for meeting the key project objectives are promising.

Key Publications

1. S. Lee, F. Chen, T. M. Jahns, and B. Sarlioglu, "Alternating Sequence and Zero Vector Modulation with Reduced Switching Losses and Common-Mode Voltage in Current Source Inverters," in *Proc. IEEE Applied Power Electronics Conference and Exposition (APEC)*, Orlando, FL, USA, 2023, pp. 2613-2619
2. S. Lee, F. Chen, T. M. Jahns, and B. Sarlioglu, "Topological equivalence of VSI and CSI commutation cells and its application to switching resonance analysis and damper design," in *IEEE Transactions on Transportation Electrification*, doi: 10.1109/TTE.2023.3287449.
3. S. Lee, F. Chen, T. M. Jahns, and B. Sarlioglu, "Alternative vector modulation for CSI common-mode voltage reduction under voltage-boost operation," in *Proc. IEEE Energy Conversion Congress & Expo (ECCE)*, Oct 29-Nov 2, 2023.
4. F. Chen, S. Lee, T. M. Jahns, and B. Sarlioglu, "Comprehensive efficiency analysis of seven-switch current-source inverter based on voltage-boost function and genetic algorithm," in *Proc. IEEE Energy Conversion Congress & Expo. (ECCE)*, Oct 29-Nov 2, 2023.
5. W. Feng, K. Chen, J. Paddock, T. M. Jahns, and B. Sarlioglu, "Design and comparison of surface inset permanent magnet machine and surface permanent magnet machine without heavy rare earth magnets for traction applications," in *Proc. IEEE Energy Conversion Congress & Expo. (ECCE)*, Oct 29-Nov 2, 2023.
6. K. Chen, W. Feng, F. Chen, S. Lee, J. Paddock, T. M. Jahns, B. Sarlioglu, "Thermal analysis of liquid and air cooling of high-power density integrated motor drives," in *Proc. IEEE Energy Conversion Congress & Expo. (ECCE)*, Oct 29-Nov 2, 2023.

I.1.18 Multi-Objective Design Optimization of 100 kW Non-Rare-Earth or Reduced-Rare Earth Machines (Purdue University)

Scott Sudhoff, Principal Investigator

Purdue University
465 Northwestern Ave
West Lafayette, IN, 47907
E-mail: sudhoff@purdue.edu

Steve Pekarek, Co-Principal Investigator

Purdue University
465 Northwestern Ave
West Lafayette, IN, 47907
E-mail: spekarek@purdue.edu

Susan Rogers, Technology Development Manager

U.S. Department of Energy
E-mail: susan.rogers@ee.doe.gov

Start Date: May 15, 2023
Project Funding: \$300,000

End Date: May 14, 2024
DOE share: \$300,000

Non-DOE share: \$0

Project Introduction

The goal of this project is to reduce the size, weight, cost, and losses associated with rotating electric machinery and its associated power electronics for electric and hybrid vehicle applications. In particular, the goal of this effort is to facilitate electric machinery that will meet the requirements set forth in the U.S. DRIVE Electrical and Electronics Technical Team Roadmap of October 2017. This document calls for an electric machine with a peak power of 100 kW, a continuous rated power of 55 kW, a peak speed of less than 20,000 rpm, a volume of no more than 2 liters, a mass of less than 20 kg, and a useful life of 15 years or 300,000 miles of vehicle service. This will be achieved through a combination of (i) new materials, (ii) new electric machine topologies, (iii) advances in power electronics, and (iv) superior design through the use of formal and rigorous multi-objective optimization-based design built on advanced analysis techniques. This effort is being conducted by a large consortium comprised of national laboratories (Sandia National Laboratories, Oak Ridge National Laboratories, Ames Laboratory, and the National Renewable Energy Laboratory) and universities (Virginia Tech, Georgia Tech, SUNY, Arkansas, Ohio State, IIT, Purdue, University of Wisconsin – Madison, University of California Berkeley, and North Carolina State). Purdue's role focuses on (ii) and (iv).

Objectives

The objective of this effort is to explore the use of new materials and develop new design paradigms to enable unprecedented propulsion motor power densities at a reduced cost. In order to achieve this objective, Purdue's goals will be to investigate new machine topologies, such as the dual rotor homopolar ac machine and inert core machine, and to develop new improved design codes which (i) incorporate high switching frequency performance analysis, (ii) thermal performance, (iii) high-speed rotor structural analysis, and (iv) advanced magnetic analysis techniques into its existing design paradigm based on rigorous multi-objective optimization in order to take best advantage of new materials and machine topologies developed by Purdue and other team members. An additional objective is to build and test a prototype machine whose design is based on the enhanced design paradigm developed under this effort.

Approach

To achieve the objectives described in the previous section, Tasks 5.1.1 and 5.1.2 are the focus of the fifth year of the program. The SOPO for the fifth year of this effort and Tasks 5.1.1 and 5.1.2 are summarized below. It should be noted that there were some delays incurred. In particular, the prototype constructed last year was

found to have some mechanical issues on the rotor and had to be rebuilt. This rebuild has now been completed and the machine is being tested. Although the project is running behind, it is anticipated that it will be back on schedule by the end of the third quarter.

Milestone	Type	Description	Status	Completion Date
Dynamometer Fixturing	Technical	A mounting system will be developed to allow the prototype machine to be used on the dynamometers. Completed for two of three dynamometers. Designs for mounting the third dynamometer is complete but fabrication remains.	In Progress	N/A
Speed Control	Technical	A speed control system for the prototype machine will be developed and implemented. This task is behind schedule. It is hoped that both this milestone and Machine Testing 1 will be completed next quarter.	In Progress	N/A
Machine Testing 1	Technical	The machine will be tested at powers up to 6 kW and speeds up to 12000 rpm on a dyno. Measured and predicted loss will be compared.	In Progress	N/A
Machine Testing 2	Technical	The machine will be tested at powers up to 3 kW and speeds up to 20000 rpm on a dyno. Measured and predicted loss will be compared.	In Progress	N/A

Results

Before discussing the results, it is appropriate to review the performance requirements. These are shown in Figure I.1.18.1 and have not been changed since the previous budget period. Recall that the requirements were based on the ORNL-led machine group within the VTO consortium. The key requirements include a maximum operating speed at 20,000 rpm, a 55-kW continuous power, and a 100-kW peak power. The 3:1 constant power speed range ensures good driving characteristics for passenger vehicles. Note that to characterize these requirements, six operating points are considered. The weighting of these operating points in determining aggregate loss is also indicated in the figure.

In the remainder of this section, results will be presented for the Dual Rotor Homopolar AC Machine (DHAM) and Inert Core Permanent Magnet Machine (ICPM).

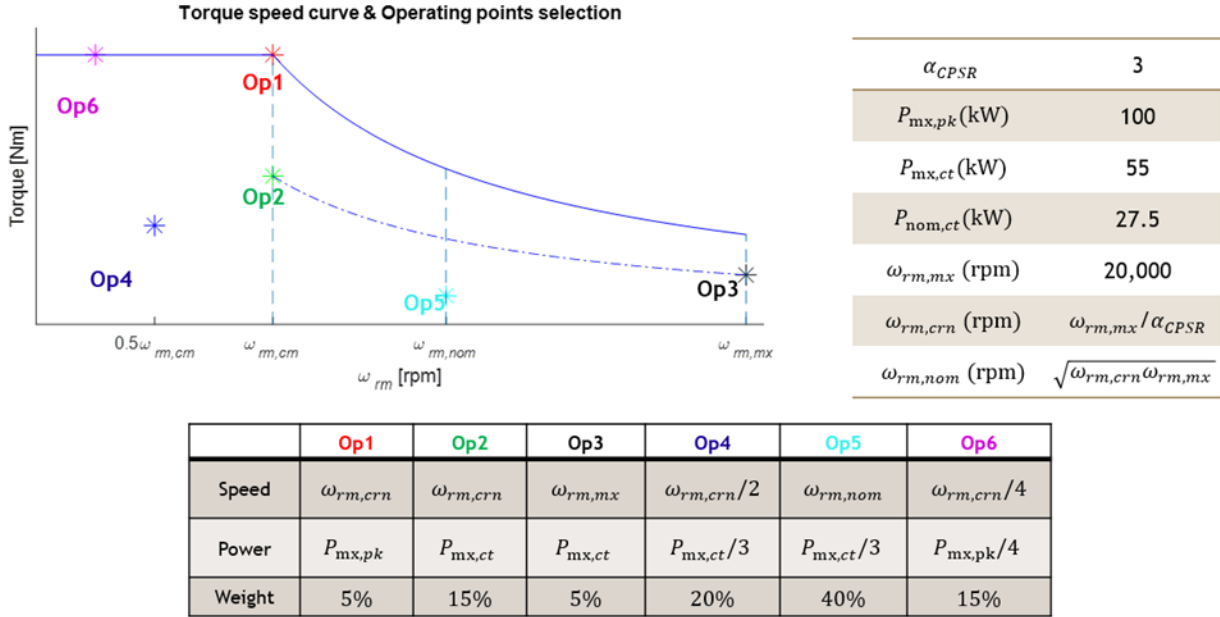


Figure I.1.18.1 Performance requirements.

Dual Rotor Homopolar AC Machine

The Dual Rotor Homopolar AC Machine (DHAM) is a novel rotating electric machine which can operate either as a motor or as a generator. The advantages of the machine include that it is conducive to low mechanical stresses even in high-speed designs, it is conducive to using rare-earth free magnets, it is easy to cool, and, in the permanent magnet version, it can achieve an infinite constant power speed range without impacting the field intensity in the permanent magnet.

During BP4, the DHAM was compared to a standard surface mounted permanent magnet ac machine (PMAC) including a thermal model. Herein, the results for size vs loss are shown in Figure I.1.18.2. The plots include three different optimization runs. The blue curves represent performance obtained with the DHAM using Dysprosium-free magnets, performance obtained using a DHAM with a ferrite magnet is depicted by the red curves, and the yellow curves captures the PMAC using any (including rare-earth) PM material. As can be seen, the inexpensive ferrite DHAM has a Pareto-Optimal front that exceeds that of the rare-earth PMAC. Since the DHAM has an inherent cooling advantage, it can use the Dy-free PMs. Figure I.1.18.2 shows that the Dy-free neodymium-iron-boron PM DHAM dominates the rare-earth based PMAC. The maximum torque density of the DHAM more than doubles that of the PMAC, reaching close to 50 kW/L.

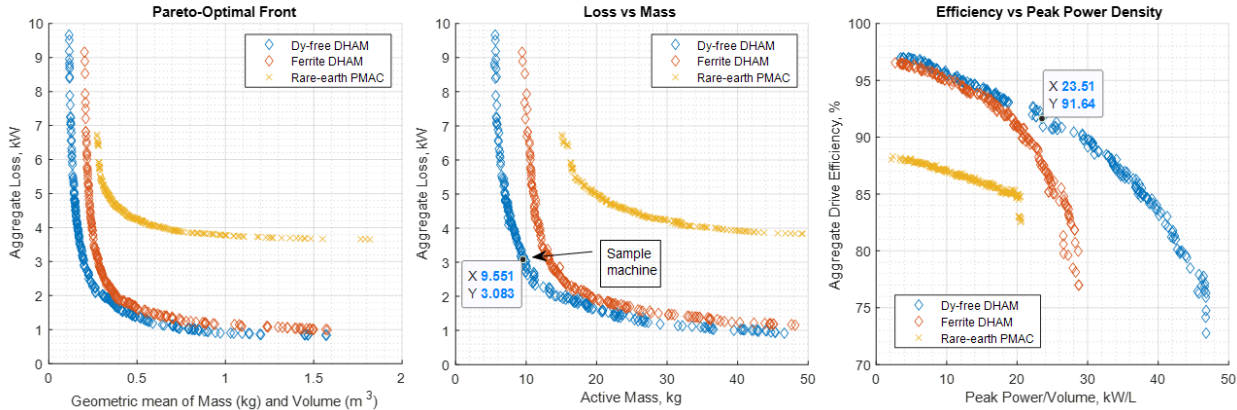


Figure I.1.18.2 DHAM and PMAC comparisons.

A proof-of-concept DHAM prototype was designed in BP4. This prototype machine has a 10-kW continuous power rating, a peak power of 18-kW, and a maximum speed of 20,000 rpm. The prototype was validated using FEA to test its EM capabilities. Figure I.1.18.3 depicts 18-kW. The figure on the left shows the field distribution of the 6-pole, 18-stator-leg prototype design. The blacklines outside the steel region sketches the windings and the overall 3D FEA solution domain. Torque is produced individually in all four air-gap regions of the DHAM. The FEA torque results are plotted in Figure I.1.18.3. Therein, the torque production of each air-gap region is illustrated separately to the total torque. Individual air-gap regions have large torque ripple, as expected. The total torque is ideally constant because the torque ripple of the four airgaps will ideally cancel. However, the upper and lower rotor end air gaps don't produce the exact amount of desired torque. The ideal DHAM model ignores the steel reluctances while FEA accounts for all. Nonetheless, the torque FEA predicted torque is within 1 Nm of the desired torque.

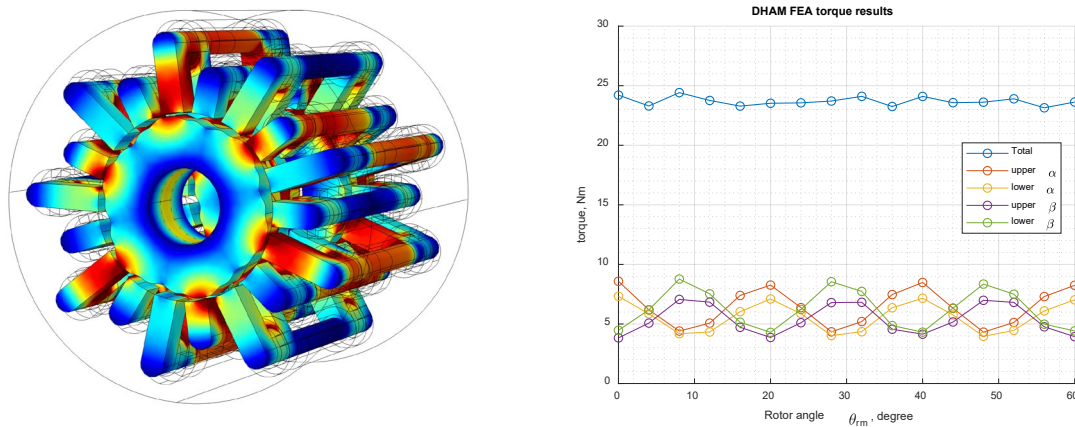


Figure I.1.18.3 Prototype DHAM FEA results.

During the end of BP4 and the beginning of BP5, the DHAM machine prototype was built and set up on a dynamometer, as shown in the upper half of Figure I.1.18.4. Notice that all stator coils of the machine are terminated externally. This allows for direct measurement of each stator coil and provides flexibility in connections, if necessary. The machine is connected to a test inverter, which is shown in the bottom half of the figure. Note that at the current stage, the inverter operates in an open-loop voltage control mode. It supplies the machine with the desired terminal voltage amplitude and phase that are specified by a user.

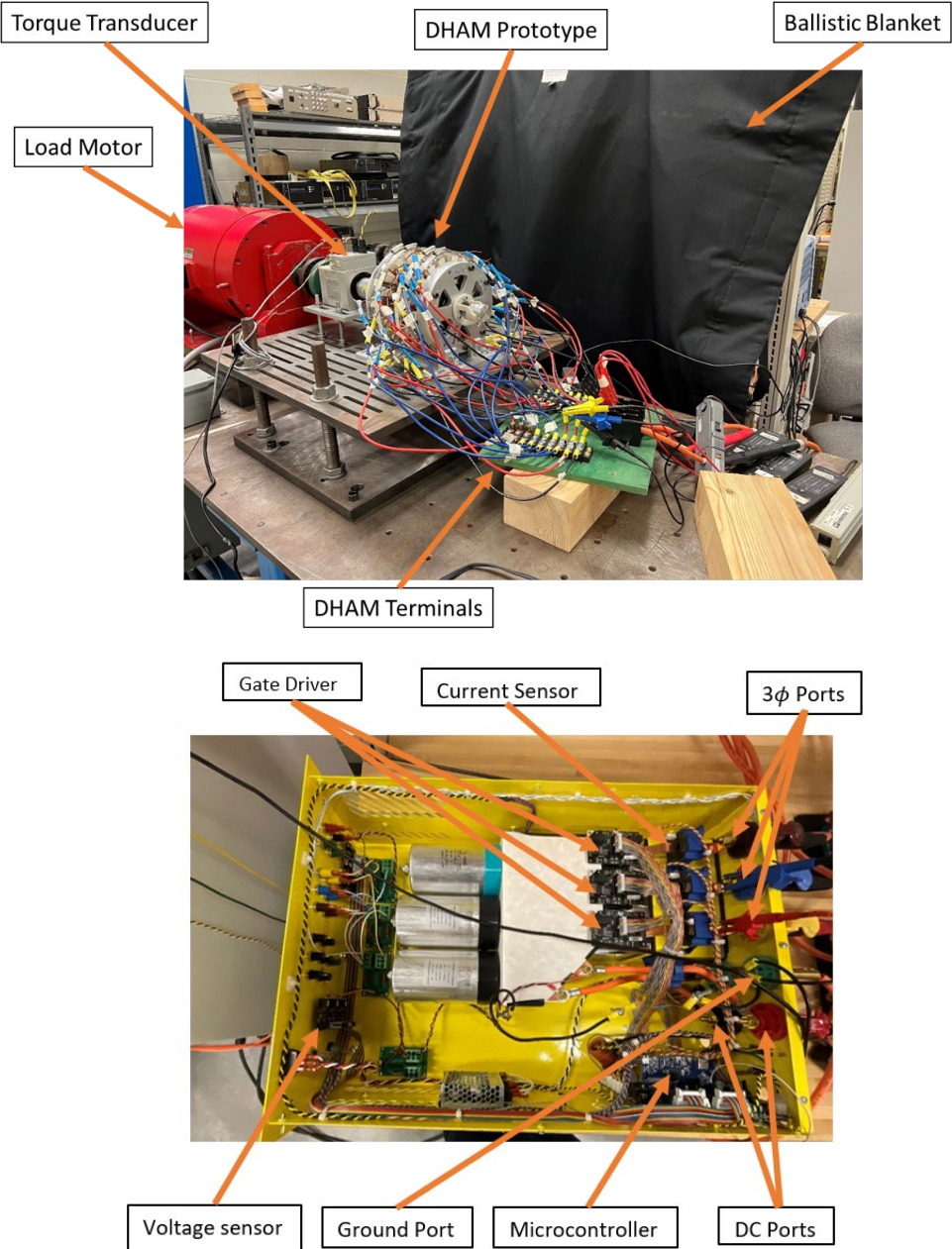


Figure I.1.18.4 Prototype DHAM (upper) and inverter (lower).

Experimentally measured operation of the machine is shown in Figure I.1.18.5. Line-to-neutral voltages, main winding currents, and the a-phase auxiliary winding current of the machine at 3,000 rpm with 20 V rms voltage amplitude (per leg), $\phi_s = \pi/2$, and a dc inverter voltage of 215V are shown, from top to bottom respectively. One important observation is that the main winding currents are sinusoidal despite the inverter being based on an open-loop voltage control. Another important observation is that the auxiliary winding current contains a low order harmonic. It is believed that this harmonic arises from rotor eccentricity.

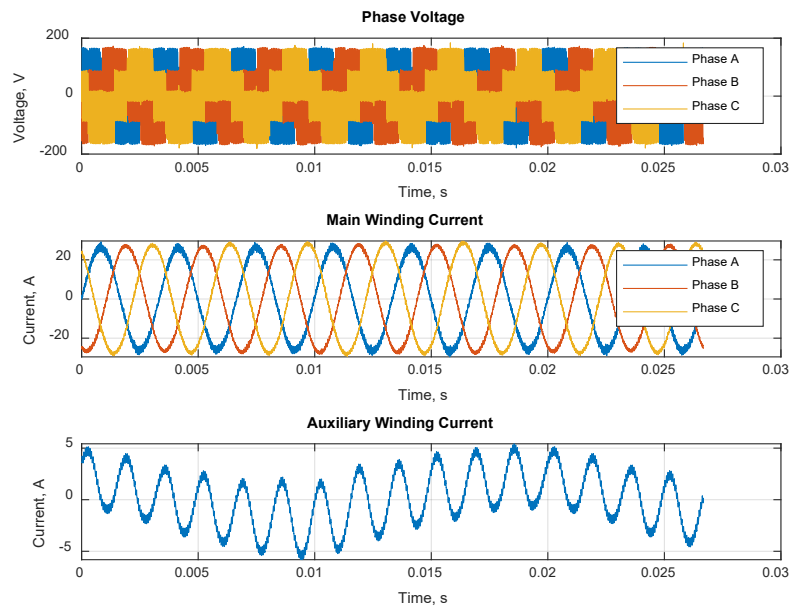


Figure I.1.18.5 Prototype DHAM experimental results.

Operationally, several challenges remain. These include error in achieving the desired airgap reluctances, and more importantly the impact of leakage reluctance. The impact of leg-to-leg leakage reluctance is particularly significant. It is not clear why these effects were not predicted by the FEA, and this remains under investigation. Means of mitigating these effects are also underway. Still, it is anticipated that achieving the third quarter milestone is possible. Also, it should be noted that this is the world's first demonstration of this new class of machine.

In the study shown in Figure I.1.18.5, the machine is operated on a speed-controlled dynamometer. To go to substantially higher speeds (to meet milestone 3), the machine will be transferred to a hysteresis brake dynamometer. This will require a speed control. A simple speed control to this end is shown in Figure I.1.18.6. Therein, ω_{rm}^* is the commanded speed, 'SRL' designates a slew rate limit, PI designates a proportional plus integral control, V_{snom} / ω_{rnom} is the nominal voltage over the nominal speed, V_s is the rms value of the applied voltage (per leg), 'PWM' is a PWM modulated inverter, and V_{as} , V_{bs} , and V_{cs} are the a-, b-, and c-phase line-to-neutral voltages. The simulation of the startup is shown in Figure I.1.18.7. Therein the torque, speed, and phase currents are shown versus time for a speed command of 3000 rpm and a load torque proportional to speed squared such that the load torque is 5 Nm at a speed of 3000 rpm. This control is currently being implemented in hardware and should allow milestone 3 to be achieved.

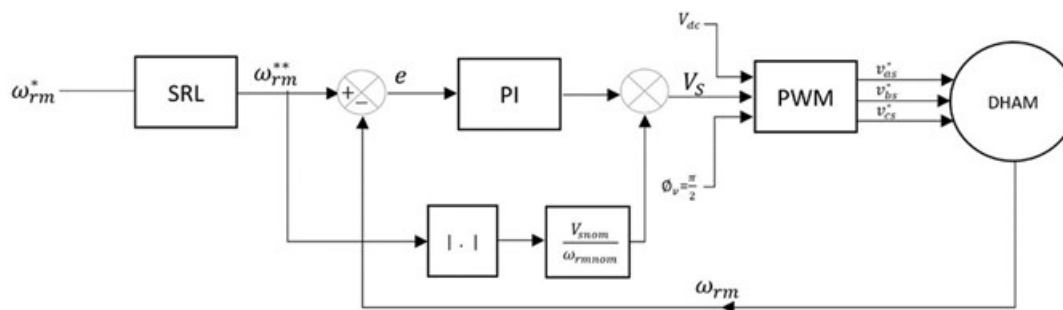


Figure I.1.18.6 DHAM speed control.

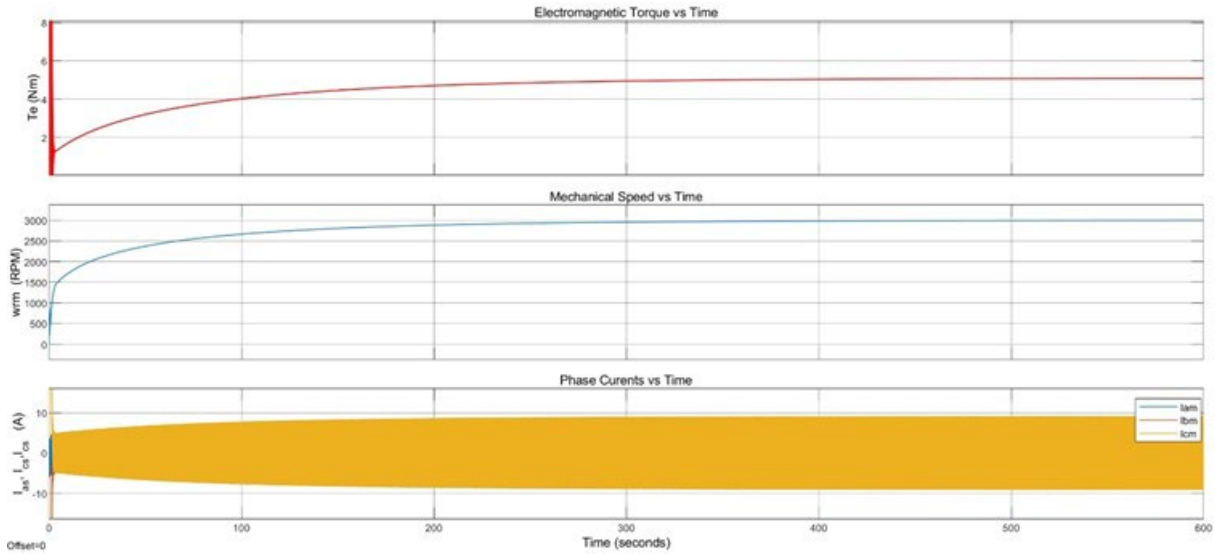


Figure I.1.18.7 Simulation of DHAM startup.

We have also been further developing the inert-core machine and the design codes based upon our method-of-moments modeling technique. A size-competitive ICM topology from BP4 is shown in Figure I.1.1-8. The ICM shown has embedded slot cooling and reached power densities on the order of 54 kW/L for the specified driving cycle. This represented the first time we have reached (exceeded) the power density target with the ICM. One reason we have been able to reach the higher power density is we have utilized a notched thermally conductive cooling pipe within the slot. The goal of the notch is to increase the contact surface between the pipe and the stator conductor. The conductors (Litz wire is necessary) are placed within the notches, as shown in Figure I.1.18.8. A second reason we have been able to reach the target is we have lowered the coolant temperature to 30° C, although we have obtained very close to 50 kW/L with a 60° C coolant (49 kW/L). A third reason for the increased power density is we have eased the current density requirements that have been imposed at OP1 in previous studies. In particular, as this operating point is at a transient condition, we did not incorporate a thermal model for this operating point, but instead utilized a current density limit of 40 A/mm². We have removed this limit within the design studies, which has then resulted in machines with the higher power densities. For the machine shown in Figure I.1.18.8, the current density at OP1 is on the order of 100 A/mm². Subsequent to the design, this operating point was evaluated using a thermal equivalent circuit. The maximum temperature (stator conductor) was found to be 212° C, which we do not view as an issue. This is particularly true as the thermal circuit was a steady-state circuit and so the temperature represents a worst-case scenario.

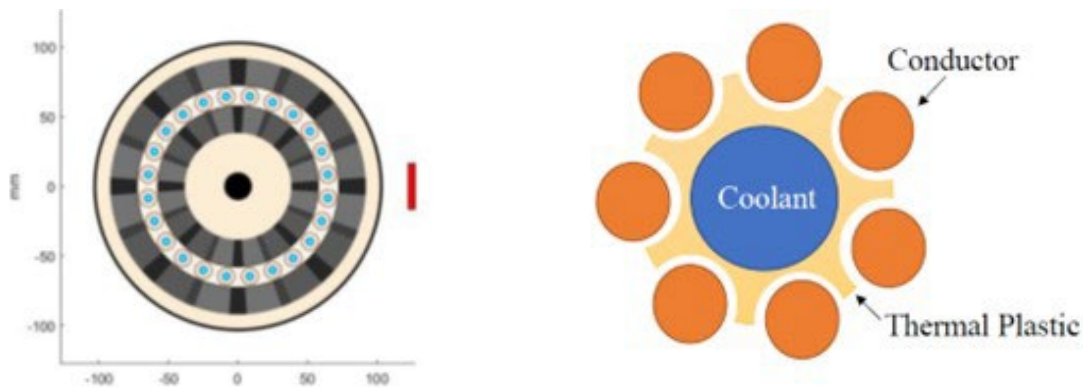


Figure I.1.18.8 Inert-core machine (left) and new notched-pipe cooling topology (right).

It is recognized that the machine requires a dual Halbach array (one on an inner rotor and one on an outer rotor). This is certainly a disadvantage of the geometry. We are also eliminating the outer rotor and its corresponding Halbach array and replacing it with a stationary steel cylinder that will serve as a flux path as well as a means to prevent flux outside of the machine. The design code for this new ICM has been developed and is being validated before use in optimization studies.

Finally, a focus of has been on updates related to the method-of-moment (MoM) toolbox that we developed the foundation for in BP1 and BP2. Specifically, we have found that in machines that operate in heavy saturation, one can utilize a combination of Galerkin and point-matching schemes to keep element counts low, accuracy reasonably high, and overall minimize the computational effort required to simulate the machine. We have applied this to buried-magnet synchronous machines and have been able to reduce computational burden of designing a machine for the target operating points from roughly 30 s to around 5 s. The MoM-based toolboxes have been updated to include the calculation technique.

Conclusions

Although significant challenges remain, the world's first DHAM has been successfully demonstrated in the laboratory. The ICM also has promise, however, there is more work that needs to be done on this machine.

Key Publications

1. Scott Sudhoff, Jiazhou Zhong, Steve Pekarek, "Dual Rotor Homopolar AC Machine," nonprovisional patent application submitted to U.S. patent office in November 2021. Attorney docket number PRF-69245-02.
2. D. Horvath, R. Howard, S. Pekarek, "Calculating Inductance in a 2D Method of Moments Model," Engineering Analysis with Boundary Elements, in review.

Acknowledgements

Although Purdue is collaborating with the entire consortium, the relationship with Sandia National Laboratories has been particularly helpful. Thus, the help and contributions by Jason Neely, Lee Rashkin, Todd Monson, and Vipin Gupta are particularly recognized.

I.1.19 Design, Optimization, and Control of a 100 kW Electric Traction Motor Meeting or Exceeding DOE 2025 Targets (Illinois Institute of Technology)

Ian Brown, Principal Investigator

Illinois Institute of Technology
 3301 S. Dearborn St.
 Chicago, IL 60616
 E-mail: ibrown1@iit.edu

Susan Rogers, DOE Technology Development Manager

U.S. Department of Energy
 E-mail: Susan.Rogers@ee.doe.gov

Start Date: April 1, 2023 End Date: March 30, 2024
 Project Funding: \$342,962 DOE share: \$300,000 Non-DOE share: \$42,962

Project Introduction

The Illinois Institute of Technology (IIT) is a member of the Department of Energy Electric Drives Technologies (EDT) Consortium. IIT’s role in the consortium focuses on developing electric traction motors for electric vehicles with 8x the power density and half the cost of state-of-the art traction motors.

Objectives

The overall objective of the electric motor portion of the Electric Drives Technology consortium is to research, develop, and test electric motors for use in electric vehicles capable of the specifications in Table I.1.19.1. Reduced scale physical prototypes and full-scale design studies are planned at regular intervals to ensure progress towards the targets.

Table I.1.19.1 EDT Consortium Motor Targets

Parameter	Target Value
Peak Power Rating (kW)	100
Power Density (kW/l)	≥ 50
Cost (\$/kW)	≤ 3.3

Approach

To meet the electric traction motor power density and cost targets of Table I.1.1.1, several approaches are being pursued simultaneously throughout the course of this project which address all of the major volumetric power density influences. Many of the approaches are synergistic and complementary with the approaches being taken by partner Electric Drive Technology Consortium member national laboratories and universities.

Specific areas of focus during this budget period include the following:

- Development of mass manufacturable high slot fill winding technologies with enhanced heat transfer potential. In previous budget periods, spaced orthocyclic die compressed windings were developed which minimized the risk of insulation damage. In this budget period, cast windings with end turn surfaces to increase heat transfer during spray cooling were investigated. Work was also continued in this budget period to develop a low-cost continuous wave winding forming and insertion process.
- This budget period, thermal system identification and parameter estimation techniques were developed to extract thermal conductivities, thermal capacitances, and thermal time constants of individual components in the thermal equivalent circuits of electric machines. Once the parameters or time

constants of the thermal equivalent circuits are known, they can be used for electro-thermal control, prognostics, and manufacturing process control.

Results

Cast Coils with End Turn Enhanced Heat Transfer Surfaces for Spray of Jet Cooling

Cast or additively manufactured windings have the potential for very high slot fills, short end turns, flexible and variable cross-sections, and advanced thermal management. Cast coils in particular have the opportunity to be produced in high volume and at low cost leveraging previous automotive casting experiences and processes. There has been relatively little exploration of the flexibility of cast or additively manufactured coils in terms of enhancement of heat removal from windings. This research investigated the incorporation of heat transfer enhancement surfaces or features into the end turns of cast or additively manufactured coils for increasing the heat transfer from spray or jet cooling of the end turns. Potential heat transfer enhancement features that could be incorporated into the end turns include fins, pins, or other more complex topology surfaces. This research investigated the potential for heat transfer enhancement with the addition of pins to the end turns of cast coils.

Three cast copper half coils were manufactured, Figure I.1.19.1. Two of the coils were manufactured with “medium” and “large” pins incorporated into the end turns. The third coil has no pins in the end turns, i.e., traditional construction. To control the heat flux into the coils, square heat distribution blocks were cast to connect the turns. The heat distribution blocks are clamped between heater blocks with cartridge heaters embedded, Figure I.1.19.2(a). Thermocouples are embedded both in the heater blocks and at the base of the turns where they connect with the heat distribution blocks, Figure I.1.19.2(b).

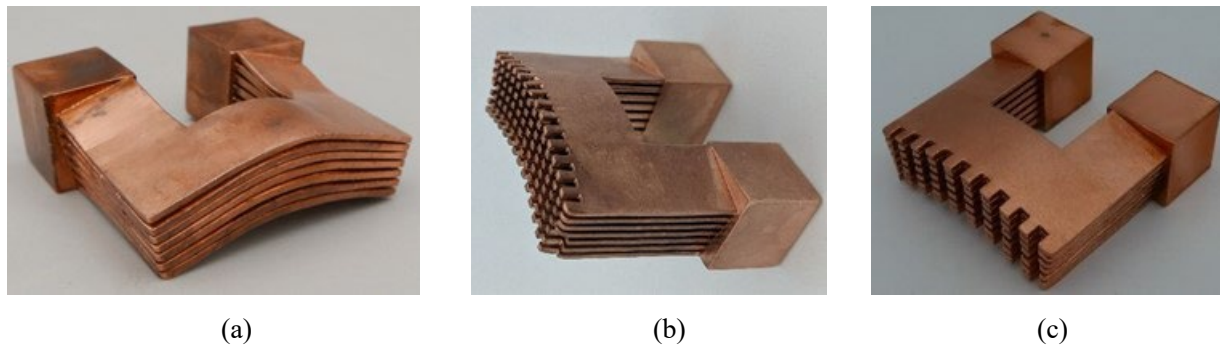


Figure I.1.19.1 Cast copper concentrated windings with seven half turns and square heat distribution blocks connecting the turns. There are three variants of the end turn surfaces, (a) no pins in the end turns (traditional end turns), (b) medium pins in the end turns, and (c) large pins in the end turns

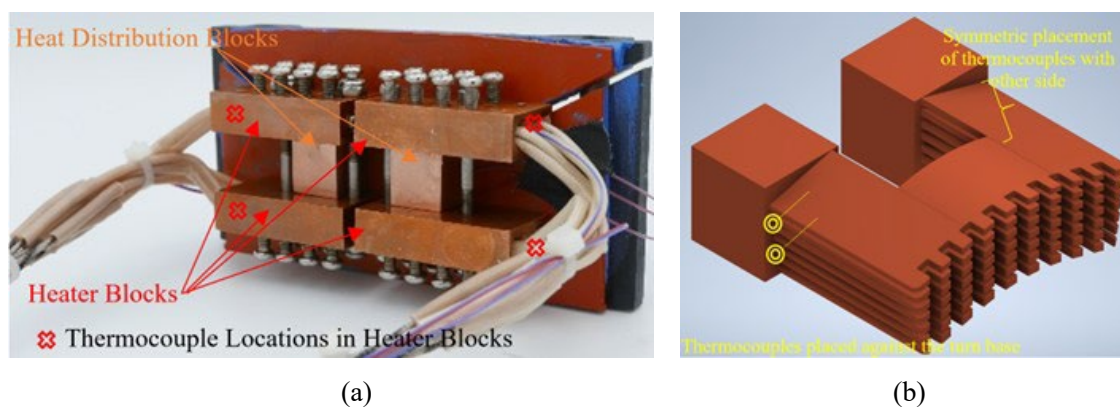


Figure I.1.19.2 Heat flux to the coils provided by (a) cartridge heaters embedded in heater blocks which surround the heat distribution blocks. Thermocouples are embedded in the heater blocks and (b) base of the turns where they interface to the heat distribution blocks.

The temperature rise of the cast copper coils was measured under a variety of automatic transmission fluid (ATF) spray cooling fluid flow rates and heat inputs. The cast copper half coils were mounted in an enclosure, Figure I.1.19.3 where a jet or spray of ATF is direct from a nozzle at the end turns. The cast copper half turn is thermally insulated from the rest of the enclosure with Viton rubber mounts. An example of the flow pattern through the end turn pins is shown in Figure I.1.19.3(c).

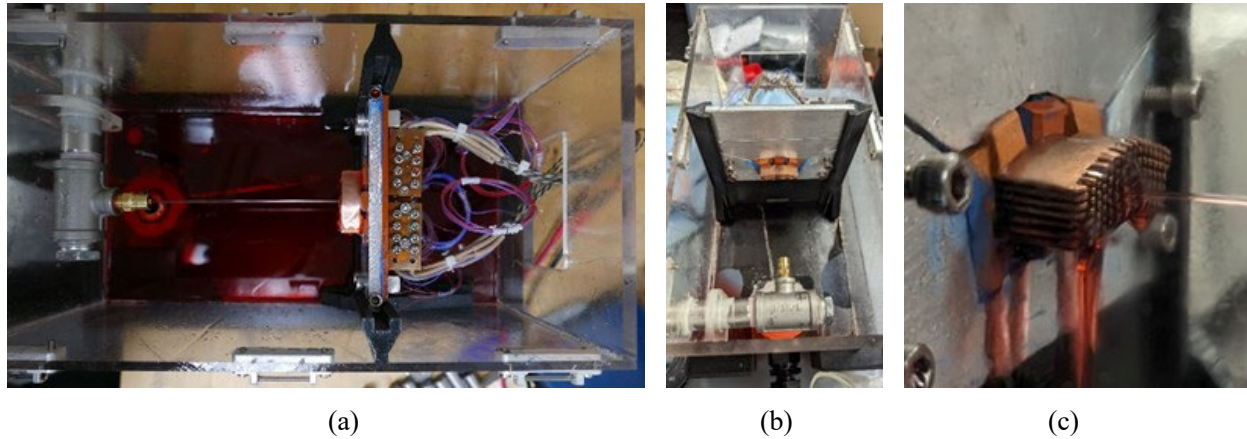


Figure I.1.19.3 Enclosure and spray apparatus for testing temperature rise of cast half coils, (a) overhead view with single concentrated jet of ATF, (b) view of cast half coil without end turn pins mounted in the enclosure, and (c) flow pattern of single concentrated jet of ATF striking cast half coil with large end turn pins.

One way to study the impact of the incorporation of pins in the end turns is to estimate the thermal resistance between temperature measurement locations and the fluid or ambient temperature. Two thermal resistances were estimated in this research, the mean heater block to ambient/fluid and mean turn base to ambient/fluid. The thermal resistances were estimated from the steady state temperature after a step input of heat flux from the cartridge heaters. An example of the temperature step response with and without spray cooling is shown in Figure I.1.19.4(a). The spray cooling provides considerable heat removal even without the pins. Without the spray, the power input to the coil needed to be removed before the steady state was reached to avoid the risk of damage to the test system.

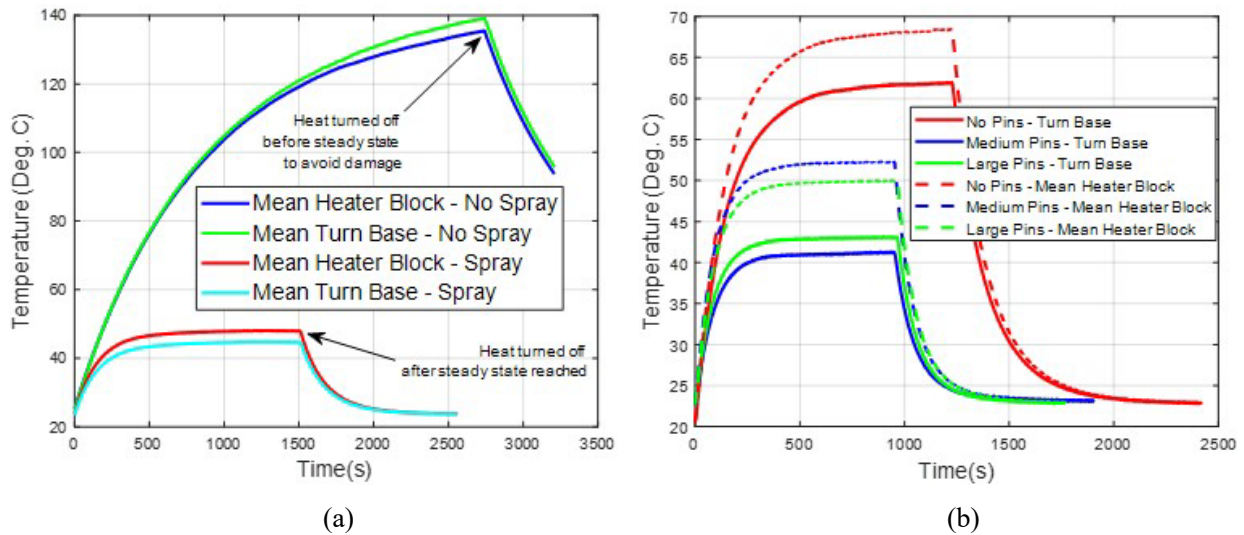


Figure I.1.19.4 Thermal step responses (a) with and without spray cooling for a power input of 20.4 (W) and ATF flow rate of 0.57 (l/m), and (b) three cast copper half coils with and without pins for a power input of 40 (W) and ATF flow rate of ~0.58 (l/m).

Example temperature rises of the three cast copper half coils is shown in Figure I.1.19.4(b) for the same heat input, 40 (W), and flow rate, 0.58 (l/m). The steady state mean heater block temperature and mean turn base temperatures are approximately 21 °C and 17 °C lower in the cast copper half coils with pins. The potential heat transfer improvements due to the incorporation of pins in the end turn surfaces during spray cooling likely depends on a number of factors including the specific sprayed liquid, spray velocity or flow rate, spray temperature, spray distance, spray angle of impingement, temperature of the end turns, and heat flux input. The influence of two of these factors was investigated in this research: the flow rate from the spray nozzle and power/heat flux input from the cartridge heaters.

To systematically explore the influence of these two factors on the equivalent thermal resistances, a central composite design of experiments (DOE) was used. The thermal permeance to fluid power ratio was also estimated. The flow rate range was between 0.345 (l/m) and 0.9 (l/m) and power/heat input from 25.85 (W) to 60 (W). Five levels each of flow rate and heat input were used in the design of experiments. Two 2nd order polynomial response surfaces are fit using the data collected to estimate the thermal resistance and thermal permeance by fluid power ratio for combinations of the flow and heat input other than the sample points.

The estimated thermal resistances and thermal resistance response surfaces of the three cast copper half coils with no pins, medium pins, and large pins are compared in Figure I.1.19.5. The thermal resistance is often more than one and half to two times lower for either set of cast copper half coils with pins in the end turns compared to the half coil with no pins. The thermal resistances with the medium and large end turn pins are very similar.

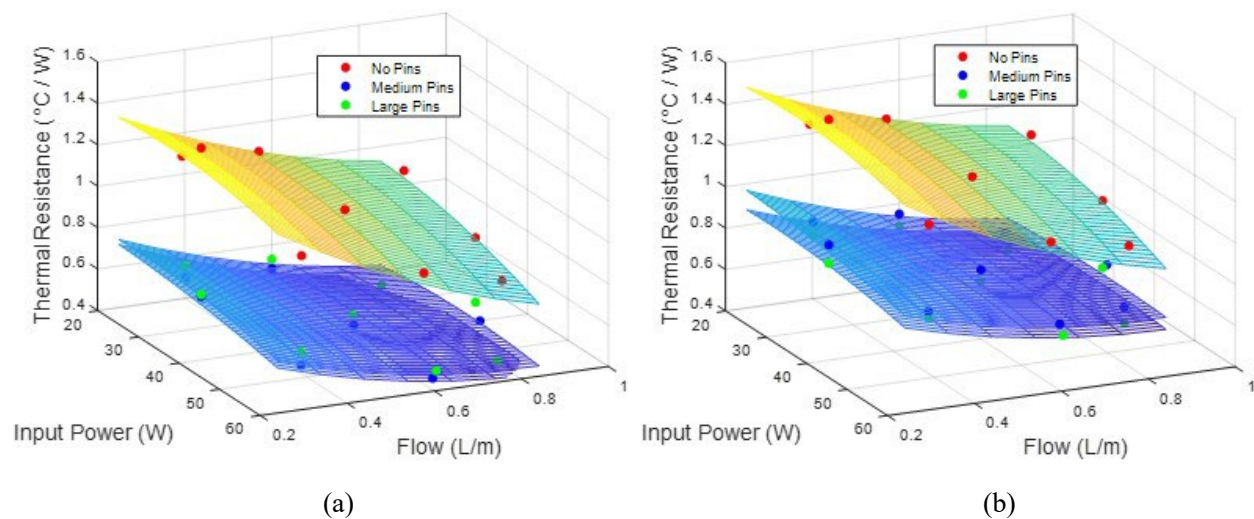


Figure I.1.19.5 Comparison of the estimated thermal resistance to the (a) mean turn bases and (b) mean heater block for the cast copper coils with no pins, medium pins, and large pins. The points are the design of experiments responses and the surfaces the fitted 2nd order polynomial surfaces.

One metric to assess the thermal “efficiency” of a liquid cooling system is the thermal permeance divided by the fluid power. The thermal permeance is the inverse of the thermal resistance. A more liquid cooling system is more “efficient” if the ratio of thermal permeance to fluid power is larger. A comparison of the thermal permeance divided by the spray fluid power is shown in Figure I.1.19.6 for the three cast half coils. For low flow rates, the cast copper half coils with pins can have ~3 times larger permeance to fluid power ratios, i.e., the pins significantly increase the heat removed per Watt of fluid power. The cooling “efficiency” gained by the addition of the pins diminishes at high flow rates.

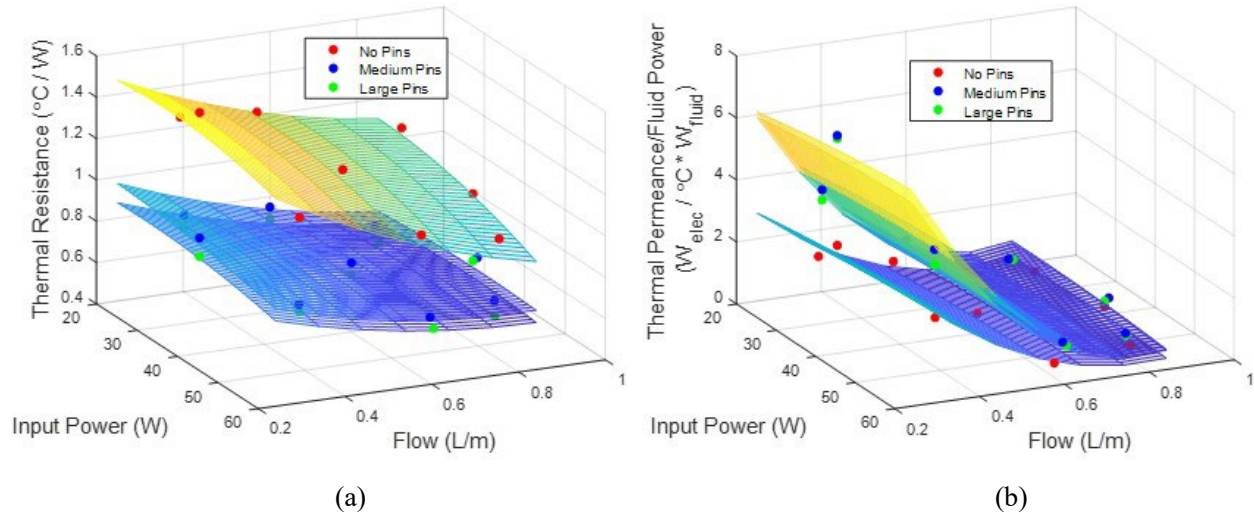


Figure I.1.19.6 Comparison of the estimated thermal permeance to fluid power for the (a) mean turn bases and (b) mean heater block for the cast copper coils with no pins, medium pins, and large pins. The points are the design of experiments responses and the surfaces the fitted 2nd order polynomial surfaces.

The relative temperature rises for the three cast copper half coils corresponding to the center point of the central composite designs for power input and flow rate, i.e. the “nominal conditions”, is shown in Figure I.1.19.4. At the “nominal conditions” the addition of the pins reduces the steady state temperature by ~30%.

Continuous Wave Winding Former and Inserter

This budget period work has continued on the development and refinement of a low-cost continuous wave winding former and inserter, Figure I.1.19.7. Continuous wave winding forming and inserters have been developed by foreign companies but have considerable capital expense and are unlikely to be compatible with very small stator bore high-power density electric motors. The wave winding former and insertion process being developed should have minimal capital costs and work with very small stator bores. Intellectual property protection of the process is under consideration.

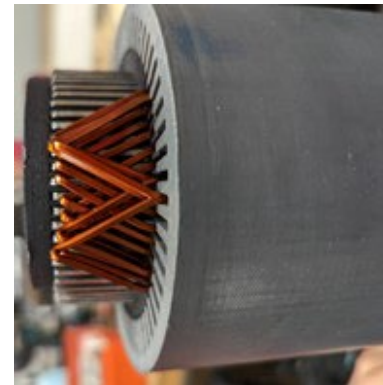


Figure I.1.19.7 Trial insertion of one pole of a continuous wave winding.

Electric Machine Thermal System and Parameter Identification

The torque and power density of electric traction motors is primarily limited by the temperature rise of their windings and in some cases permanent magnets. The thermal dynamics of electric machines may be modeled in a number of ways including computational fluid dynamic models, thermal finite element models, and thermal equivalent circuits. One of the main challenges with all of these modeling techniques is that the thermal properties of electric machines very much depend on material properties with limited data availability and manufacturing methods and tolerances. For example, the thermal resistance of the stator lamination stack

to the housing depends on the roughness of the two surfaces and the pressure of the fit between the two. Another example is the level of the impregnation of varnish into the windings and the positioning of the conductors in the slot.

Electric machine thermal equivalent circuits can range from very complex models with hundreds of elements to very simple first order models with two elements. First order techniques have been previously demonstrated to approximate the overall thermal behavior of the electric machines but not capture their detailed thermal dynamics and thermal time constants. The thermal time constants, however, vary widely due to different material

properties and masses of electric machine components. For example, the winding is made of copper, and has an intermediate mass compared to the overall machine, while the stator laminations are made of iron, and often has much more mass associated with it. The copper winding and laminations are separated by an insulating slot liner, with a very small mass, yielding a thermal model with different time constants due to construction of the machine. In this work, thermal equivalent circuits have been developed with the minimal complexity to capture the major constructional components of electric machines and the important thermal time constants.

An example simple stator thermal equivalent circuit for the radial heat flow in an electric machine is shown in Figure I.1.19.8(a) and the equivalent radial only path in a Cauer model format in Figure I.1.19.8(b). More detailed thermal equivalent which include circumferential and axial heat flow paths are shown in Figure I.1.19.9. This research is focusing on developing techniques to estimate the thermal resistances, thermal capacitances, or thermal time constants by manipulating the power loss in the machine, sampling appropriately, and using a minimum number of sensors. For example, for estimating the stator thermal parameters or time constants only one or two sensors placed on the housing or end turns. The power loss in the machine is manipulated to excite all the thermal dynamics sufficiently.

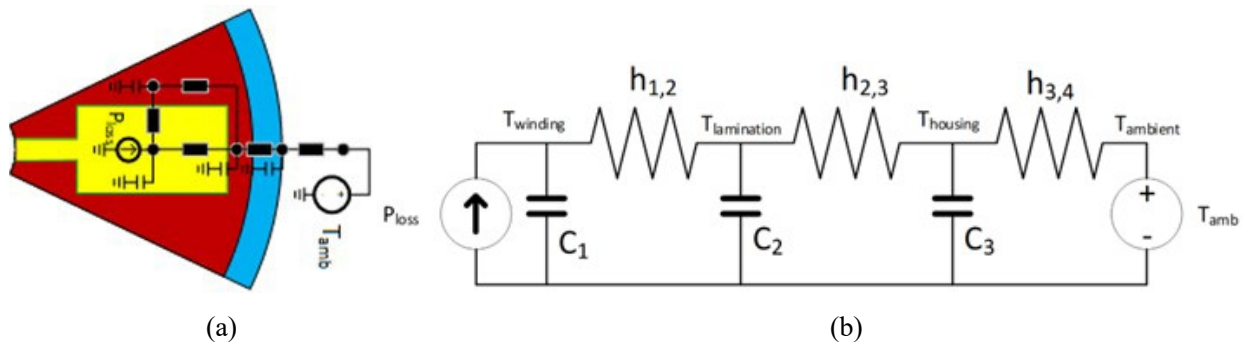


Figure I.1.19.8 Example simple radial heat flux path in the stator of an electric machine, (a) thermal equivalent circuit overlaid on a slot pitch, and (b) equivalent Cauer network model.

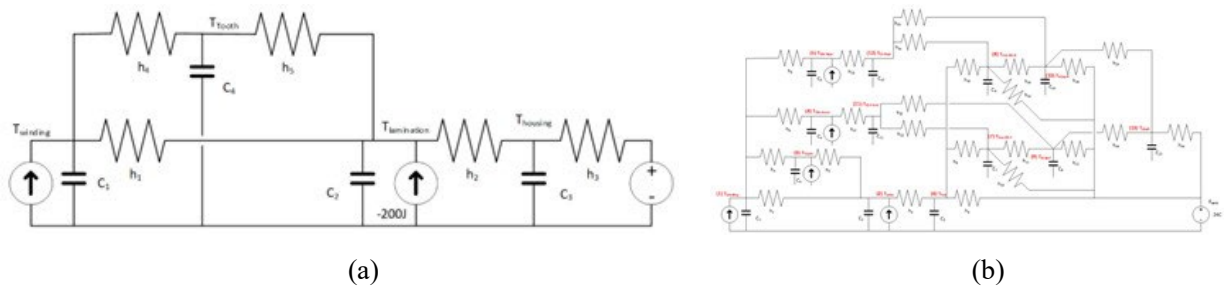


Figure I.1.19.9 Cauer thermal models of electric machine stators capturing, (a) radial and circumferential heat flux paths, and (b) radial, circumferential, and axial heat flux paths.

A number of thermal system identification approaches have been investigated including autoregressive exogenous input (ARX) and grey box optimization techniques. An example of using an ARX technique to estimate the thermal parameters of the radial heat flux path, Figure I.1.19.8, is presented. A discrete time transfer function model (3 pole, 3 zeros) is created which models the thermal dynamics between the winding power loss input and the housing temperature, T_{housing} . The current in the windings is manipulated to follow a Binary Phase Shift Keying pattern which when centered with zero mean has a normal distribution of white noise to excite all the thermal dynamics, Figure I.1.19.10. The output temperature corresponding to the Binary Phase Shift Keying noise input is shown in Figure I.1.19.10. The coefficients of the discrete time transfer function are estimated using a least squares regression. The coefficients which minimize the squared error of the estimated output temperature compared to the measured one are found.

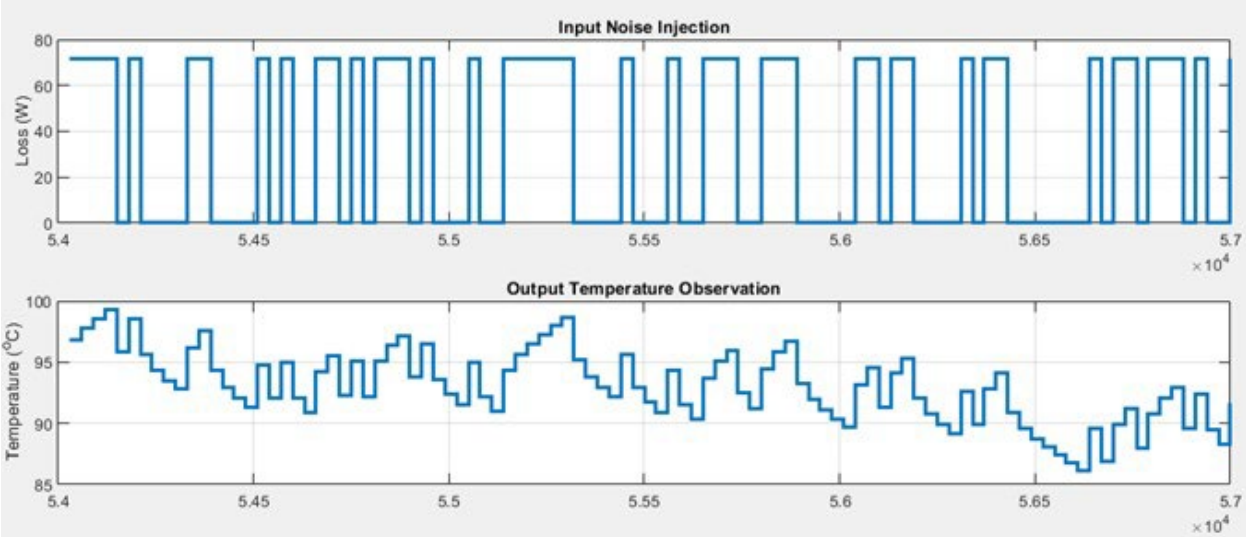


Figure I.1.19.10 Input power loss into the motor winding and output housing temperature used in ARX least squares regression model to estimate coefficients of radial heat flux path transfer function.

The temperature response of the average winding temperature estimated using the discrete time transfer function with estimated coefficients can be compared with a much more detailed thermal model with the reference coefficients, Figure I.1.19.11. For the time being, a more detailed thermal model serves as the reference or experimental system while motorettes for experimental measurements are being constructed. Almost no error is observed between the estimated and reference winding temperature. This comparison had no exogenous noise injected and in the comparison with real experimental data it is likely to be slightly degraded.

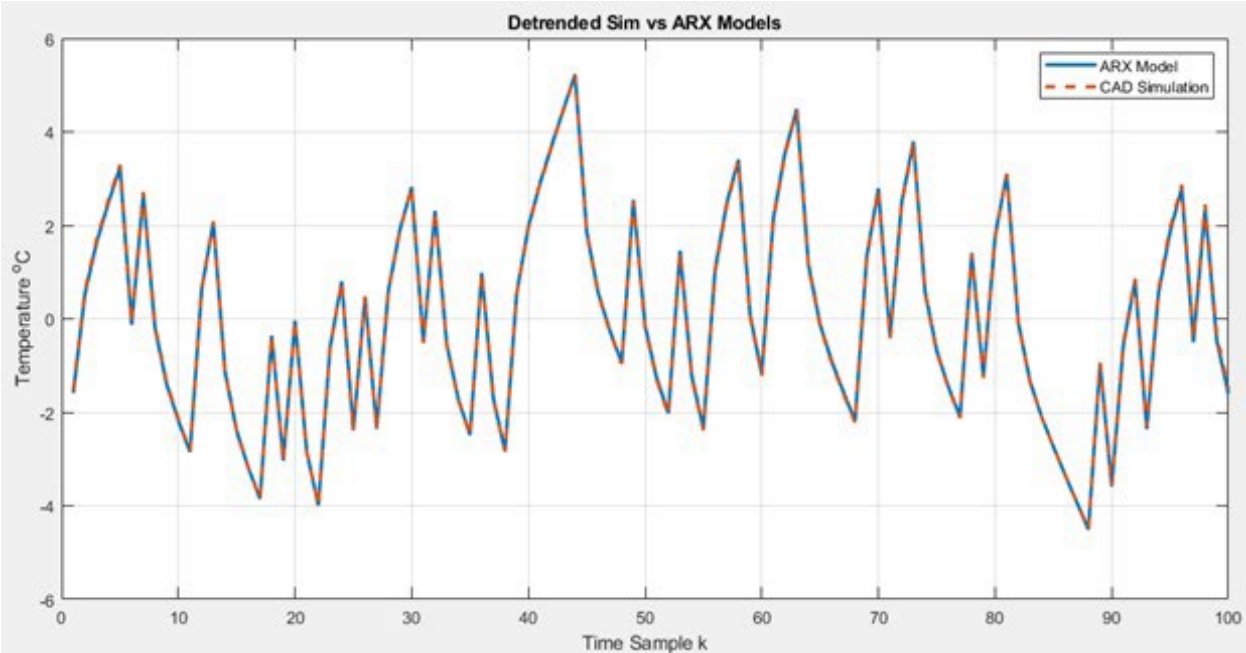


Figure I.1.19.11 Comparison of average winding temperature estimated by reference model and model with ARX identified coefficients.

Conclusions

The flexibility of cast windings allows for the incorporation of innovative features such as pin fin heat exchangers or other features that are not possible with traditional magnet wire. The introduction of pins into the end turn surfaces allows for a considerable reduction in the thermal resistance and temperature rise. The “efficiency” of the heat removal is also considerably increased for low flow rates. Other high slot fill winding technologies are also under development including a continuous wave winding former and inserter to minimize the number of welds needed compared to a hairpin style winding.

Application of system and parameter identification techniques for the estimation of electric machine thermal resistances, thermal capacitances, and thermal time constants has been developed. Having accurate and detailed thermal models for electric machines is important as it allows for electro-thermal control to operate electric machines right to their thermal limit without exceeding it, failure prognostics, and identification of manufacturing variations and quality issues.

Key Publications

1. N. Tang and I. P. Brown, "Exact THD Calculations Applied to Minimize Space Harmonic Content of Winding and Rotor Magnetic Fields," in *IEEE Transactions on Energy Conversion*, vol. 38, no. 3, pp. 1669-1678, Sept. 2023, doi: 10.1109/TEC.2023.3257143.
2. D. Sossong, D. Zdunek, I.P. Brown, “Cast or Additively Manufactured Coils with End Turn Enhanced Heat Transfer Surfaces for Spray or Jet Cooling,” *Proceedings of the 2023 Energy Conversion Congress and Exposition (ECCE) conference*, Oct. 29 – Nov. 2nd, Nashville, TN, 2023.
3. F. Guo, N. Tang and I. P. Brown, "Combined Dimensional and Topology Optimization of Synchronous Machine Rotors Using a Material Density Interpolation Method," in *IEEE Transactions on Industry Applications*, vol. 59, no. 6, pp. 6591-6600, Nov.-Dec. 2023, doi: 10.1109/TIA.2023.3292214.

**I.1.20 Integration Methods for High-Density Integrated Electric Drives
(University of Arkansas)**

H. Alan Mantooth, Principal Investigator

Department of Electrical Engineering
 University of Arkansas
 1475 W. Cato Springs Road, Rm. 211
 Fayetteville, AR 72701
 E-mail: mantooth@uark.edu

Fang Luo, Principal Investigator

Department of Electrical and Computer Engineering,
 Stony Brook University (SUNY at Stony Brook),
 259 Light Engineering Building, Stony Brook, NY 11794-2350
 E-mail: fang.luo@stonybrook.edu

Susan Rogers, DOE Technology Development Manager

U.S. Department of Energy
 E-mail: Susan.Rogers@ee.doe.gov

Start Date: October 1, 2022 End Date: September 30, 2023
 Project Funding: \$300,000 DOE share: \$300,000 Non-DOE share: \$0

Project Introduction

This project focuses on two key aspects of advancing electric drive technologies: integrated circuits and power electronic packaging. As part of the team's electronics portion, this project seeks to provide technologies that enable new power density advances. The first technology effort is integrating gate driving, sensing, and protection functions into the various packaging platforms that will be pursued by the team. Several technologies are possible, but the most advanced is high-temperature SiC / SOI based integrated circuitry that can be co-packaged with the SiC power devices. The team will pursue designs that serve the target electric drive train's specifications, but can survive at the junction temperatures expected to enhance power density while maintaining robustness and resiliency. The second technology effort is in advancing electronic packaging for electric drive train applications. Getting the most out of the advances in wide bandgap power semiconductor devices requires attention to careful packaging to minimize parasitic electrical influences on circuit performance and generated electromagnetic interference. Thermal management of the power devices and the surrounding circuit components must also be carefully managed. This leads to tradeoffs in the layout, arrangement, and interconnection of electronic components to balance these items. This effort will be performed in collaboration with several other organizations to achieve power density improvements for electric drives.

Objectives

The objective of the project is to research, develop, and test a heterogeneously integrated power module platform that will insert into a traction inverter system for power electronics modules capable of the following:

Table I.1.20.1. Power Electronics Requirements

Power Electronics Requirements	
Parameter	Measure
Cost (\$/kW)	≤2.7
Power Density (kW/L)	≥100
System Peak Power Rating (kW)	200

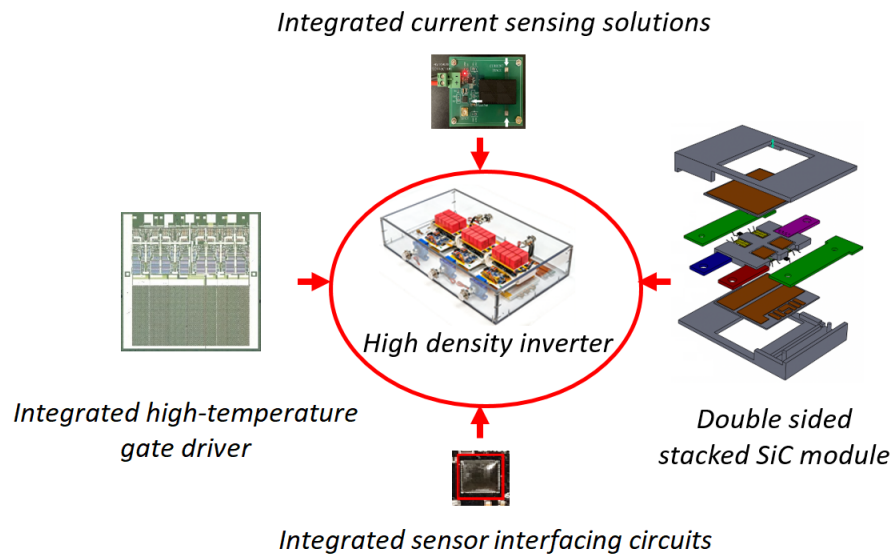


Figure I.1.20.1. Integration methods for high-density inverter

Approach

The combined Arkansas and Stony Brook team broke down its activities across three major areas. The UA packaging research approach is to develop a detailed power module fabrication procedure and fabricate the necessary parts of the power module, such as interposers, housing, and direct bond copper (DBC) substrates. Later parts come as assembly and testing of the integrated components, such as decoupling capacitors, gate drivers and sensor interfacing circuits. The UA IC design group focuses on designing and testing the high-temperature integrated circuits for module integration. For the Stony Brook group, the focus is to develop current measurement methods having features such as small size, high accuracy, lightweight, low cost, and easy integration. In the following section, some key results from FY23 are described.

Results

On the packaging side of the project, an enhancement and design modification are implemented based on the completed Gen1b power module reported last year. Specifically, the stacked half-bridge Gen 2 power module with integrated gate driver boards, decoupling capacitors, and GMR current sensors is designed. Integrating decoupling capacitors and gate drivers within the power module reduces the power loop inductance and gate loop inductance. Integrating the GMR current sensor into the power module measures both AC and DC current. The Gen 2 power module is validated through ANSYS™ and SolidWorks simulations. The proposed power modules' fabrication procedure is planned in detail, and necessary modifications are applied to the substrates, fixtures, and housings. Different fabrication approaches are developed and tested for comparison. Then, the most preferred approaches are selected for fabricating each part of the power module. The integrated gate driver boards and the differential boards are assembled and tested to switch discrete devices in a half-bridge configuration in a double pulse test (DPT) setup at 800 V, 164 A. This verifies the gate driver board's functionality. The fabrication process flow is finalized, and functional power modules (Gen2) are fabricated, as shown in Figure I.1.20.2.

A DPT printed circuit board (PCB) to test the fabricated power module is designed in Cadence's Allegro tool. The LTspice simulation circuit for this DPT setup directs toward the elimination of the external gate resistors to meet the power loss requirements. The external gate resistors can be eliminated because the CPM3-1200-0013A power device has $\sim 6.7 \Omega$ gate resistance integrated within the bare die. Also, the effective pull-up and pull-down output resistances of the gate driver IC used are 4.62Ω and 1.81Ω , respectively. The necessary voltage and current measurements are made using differential probes and Rogowski coils, as shown in Figure I.1.20.3.

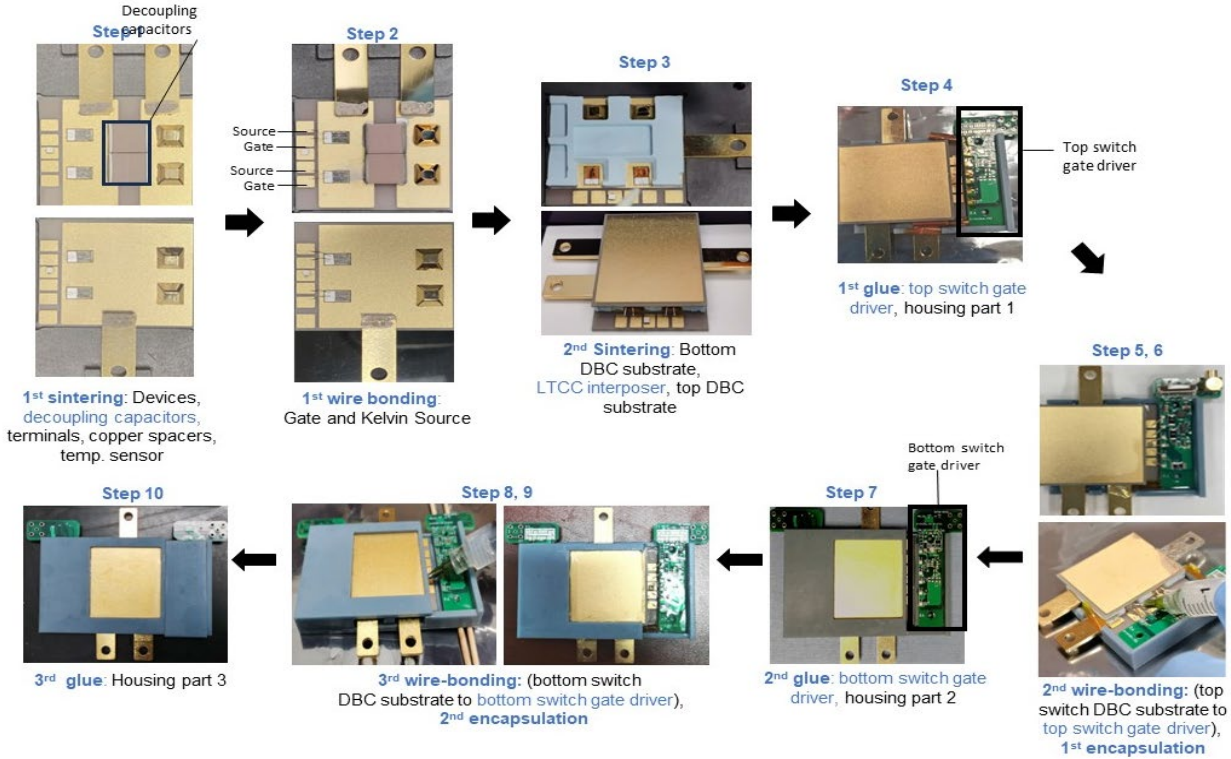


Figure I.1.20.2 Fabrication flow and fabricated Gen 2 power module

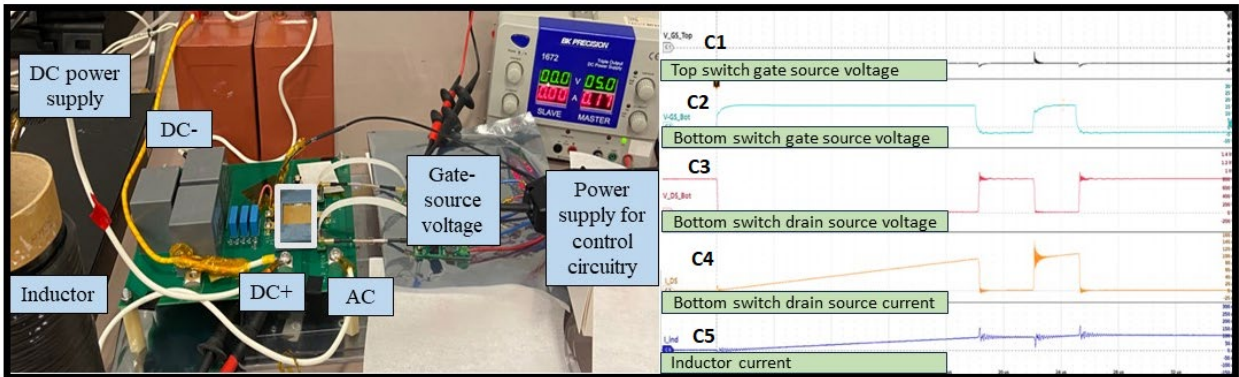


Figure I.1.20.3 DPT setup and resulting waveforms of Gen 2 power module at 800 V, 164 A.

The DPT result at 800 V is also shown in Figure I.1.20.3. Channel C1 shows the -4V output of the top switch gate driver IC to always keep the top switch off during the DPT. Channel C2 shows the gate-source voltage for the bottom switch. Channel C3 shows the drain-source voltage for the bottom switch. Channel C4 shows the current for the bottom switch. Channel C5 shows the inductor current. Table I.1.20.2 gives the simulated power loss capability per device and the experimentally calculated power loss per device, which matches the simulation results closely.

Table I.1.20.2 Power Loss per Device from Simulation and Experiment

Module design	Convection co-efficient (W/m ² K)	Power dissipation capability per die (W) (Simulation)	Power dissipation per die (W) (Experiment)
Two paralleled CPM312000013A	10,000	120	103.3

As a subsequent step, further integration into the Gen 2 power module will be completed to improve the volumetric power density of the overall system. It includes SOI-based gate drivers instead of the commercial Si gate drivers used, which have additional safety features. Also, it includes current sensing in the module and a unique design feature to hold the current sensor in the power module AC terminal. These integrations are implemented in the fabrication process flow. A volumetric system power density increment to 100 kW/L explains how the integrated features have increased the power density to what is a targeted number for this project.

The IC team received the 2nd version of integrated circuits on XFAB's 180 nm silicon-on-insulator (SOI) process in December 2022. Since then, the team has conducted exhaustive testing on those chips and, through multiple iterations, developed the final module-integrable PCB accommodating the gate driver and other auxiliary protection circuits on a single chip driven by a volume-efficient external power supply board.

Figure I.1.20.4 (a) shows the fabricated gate driver bare die. The die area is approximately 5.4 mm by 3.3 mm. It contains the driver core with variable drive strength and protection features such as active Miller clamping, UVLO, input signal filtration, and die temperature monitoring circuits. The PCBs are made out of high-temperature Rogers 4350B material and accommodate the gate driver bare die. Multiple 1 μ F high-temperature ceramic capacitors (bypass capacitors) are connected between VDD and VSS pads to provide a strong localized current supply for the gate driver. Firstly, the die is attached to the PCB using high-temperature, non-conductive epoxy. Connections are then made directly from the die pad to the PCB pads with 25 μ m Al wire bonds, as shown in Figure I.1.20.4 (b). The input and output signals for the gate driver are routed through the PCB traces. Gate-source connections to the power die from this PCB are then established through sustainable wirebonds. The top view of this power module-integrable PCB, along with the power supply board, is shown in Figure I.1.20.5. The purpose of the power supply board is to provide an isolated power supply for the driver. It also contains PWM input signal isolators and isolation buffers with unity gain for an analog input control voltage going into the die that determines drive strength.

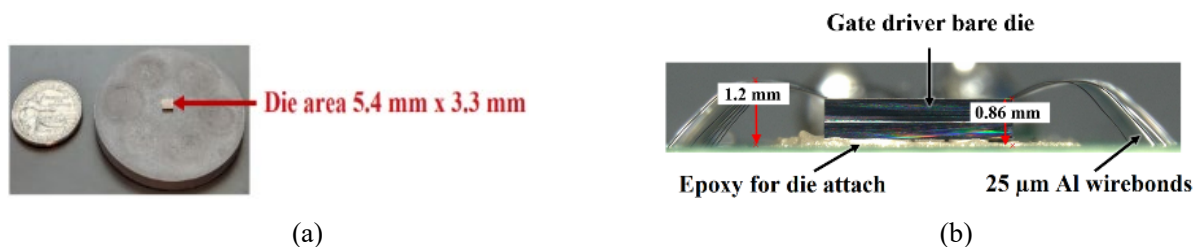


Figure I.1.20.4 (a) Gate driver die size comparison, (b) Close view of the wirebonded die

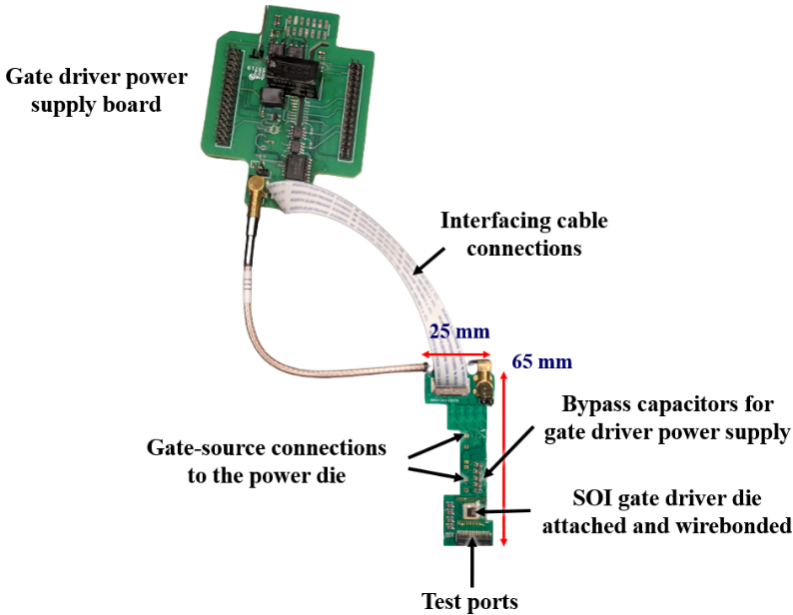


Figure I.1.20.5 Module-integrable gate driver PCB along with the power supply board

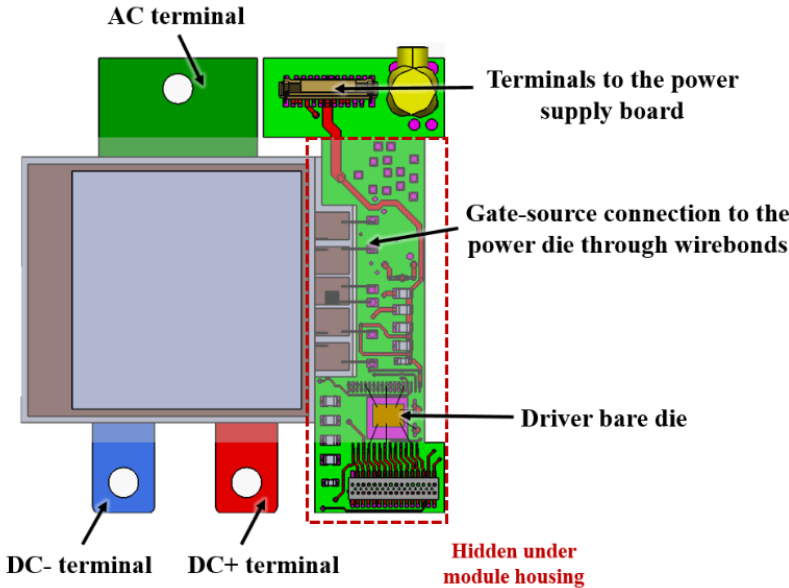


Figure I.1.20.6 Integration method of the gate driver inside the SiC power module.

Figure I.1.20.6 shows the design of the half-bridge SiC power module where this module-integrable driver PCB will be integrated. After making gate-source connections through wirebonds, the PCB can then be safely hidden under the module housing and operated through the power terminal by connecting it to the power supply board. For the sake of simplicity, only the bottom switch substrate of the power module and the corresponding driver PCB are shown. A similar configuration will be assembled for the top switch on the other side (left side). While evaluating, the team felt the need to make some minor adjustments to this module-integrable PCB, like shrinking the edges to fit it inside the housing, altering the terminals to ease the connection mechanism to the power supply board in the inverter assembly, and eliminating some unwanted exposed via holes on the surface. The modified version is in fabrication, and once received, the team will integrate it into the module, following a comprehensive system-level evaluation.

Choosing the appropriate current measurement technique for integration into a power module necessitates a compact size, a high bandwidth, and the ability to measure both AC and DC currents. A viable approach to addressing these requirements is the implementation of the two GMR sensors (TGS) method. In Figure I.1.20.7, an alternative configuration for employing the TGS method is depicted, wherein two sensors are strategically positioned on opposing sides of the current trace, which can be a copper terminal or a PCB-based terminal. The critical aspects involve the meticulous selection of highly accurate current sensors, their precise placement, and the ingenious design of signal conditioning circuitry. This strategic approach helps mitigate the impact of external magnetic fields and temperature variations. The proposed TGS method, with its simplicity, compactness, and feasibility, emerges as a promising solution for current sensing in power modules. For evaluating the performance of this solution, the prototype shown in Figure I.1.20.8 (a) is developed.

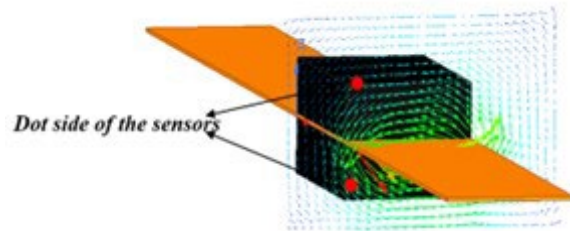
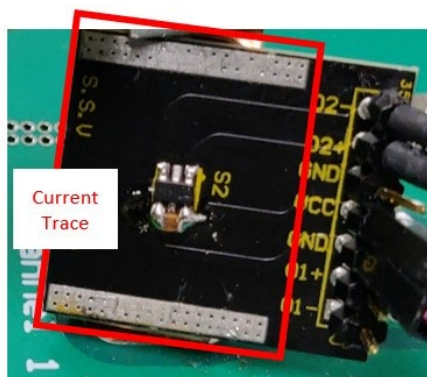
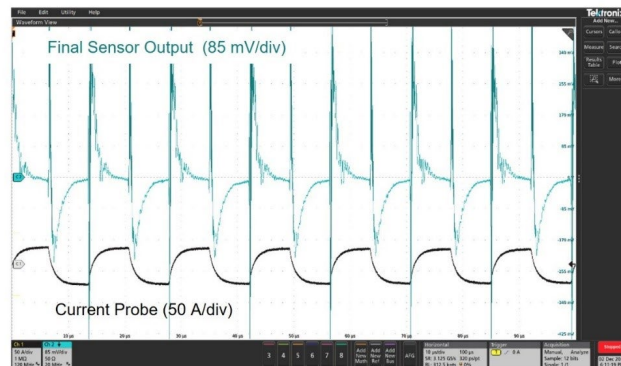


Figure I.1.20.7 TGS solution with the proposed configuration



(a)



(b)

Figure I.1.20.8 (a) Design 1 prototype, (b) Test result

In this design, current sensors on both sides are placed on a current-carrying trace with the configuration shown in Figure I.1.20.7. This PCB is designed to play the role of an AC terminal for the designed power module. Test results for 40 A peak-to-peak 70 kHz current pulses for testing Design 1 are shown in Figure I.1.20.8 (b). While the current measured by the current probe shows some deviations from a perfect square-wave shape due to parasitic inductance, the current sensor output displays a similar waveform with noticeable spikes during transitions. These spikes are caused by coupling between the main current-carrying trace and the sensor output trace. For the purpose of analyzing and evaluating the coupling effect, a PCB terminal with a thinned current trace strategically passing underneath the sensor is designed, as depicted in Figure I.1.20.9 (a), Design 2. This modification aims to reduce the coupling between the main current-carrying trace and the sensor output trace. In Figure I.1.20.9 (b) corresponding test results are presented to assess the influence of the thickness of the current trace on the coupling effect.

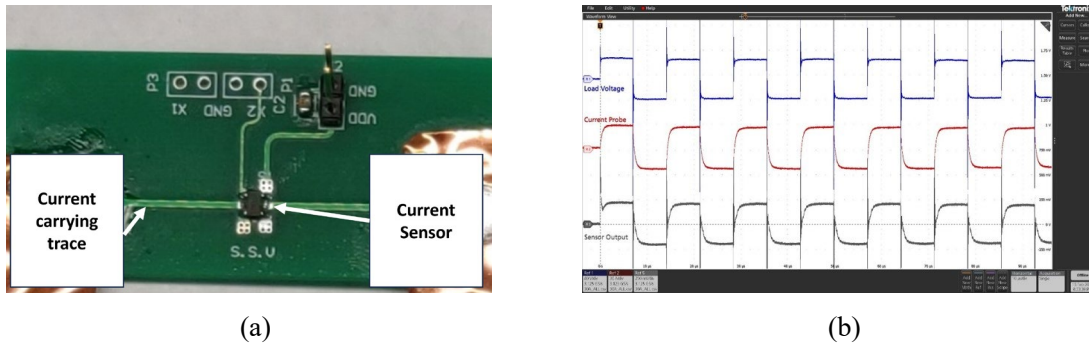


Figure I.1.20.9 (a) Design 2 prototype, (b) Test results for investigating impact of thin current carrying trace underneath sensor on coupling effect, 30A

As can be observed from the test results, thinning reduces the coupling. However, thinning the trace raises concerns about the heating of the trace. To address this concern, a slitted current trace has been designed as shown in Figure I.1.20.10 (a). In this design, the thin trace is carrying a portion of the main current, which will be sensed by the sensors above the trace on the two sides of the board. After validating the performance of the TGS method on a PCB-based terminal, it has been tested on a power module using the designed slitted terminal as the AC terminal of the power module, and the results of the test are shown in Figure I.1.20.10 (b). As can be observed, current measurement with TGS is cleaner than each single sensor's output, which validates the proposed current measurement solution.

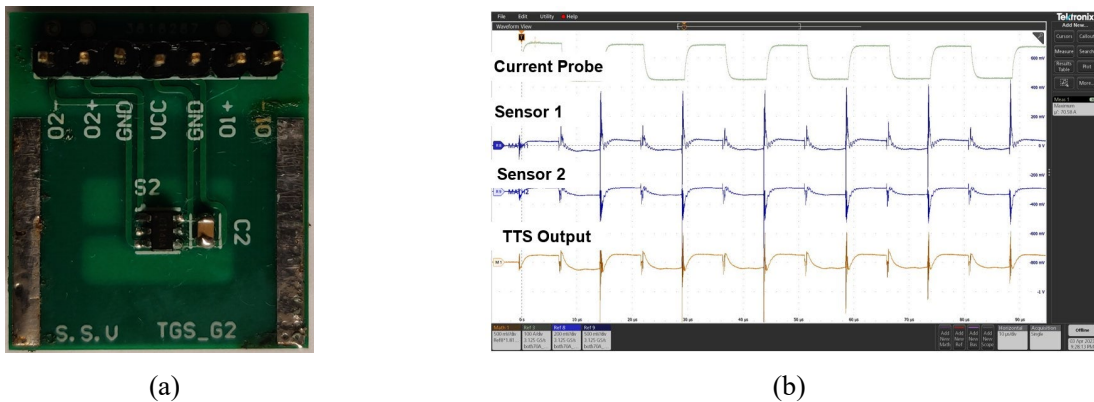
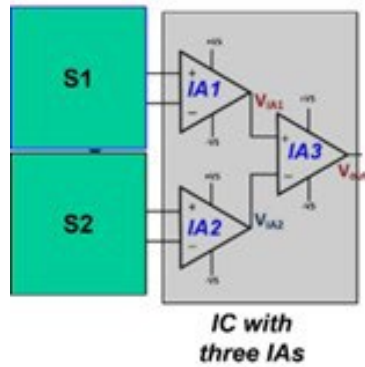


Figure I.1.20.10 (a) Design 3 prototype board for slitted current carrying trace, (b) Test results to validate the TGS method integrated into the power module, 70 A

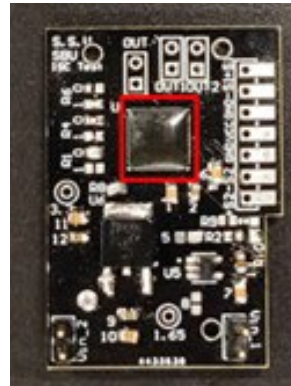
An integrated circuit comprising two stages of instrumentation amplifiers (IA) is developed for signal conditioning of two TMR-based integrated current sensing. The overview of the signal conditioning circuitry is shown in Figure I.1.20.11. $S1$ and $S2$ are sensors, and their output is fed to the first stage of IAs (IA1 and IA2). This is then followed by amplifying the difference between the two amplified sensor outputs through IA3. It is pertinent to mention that the output of the sensors is phase-shifted by 180° . Therefore, the output of the IA3 is two times the output of a single sensor. Figure I.1.20.12 shows the PCB developed using the fabricated integrated IA IC. The IC is supplied with 3.3 V DC with a 1.65 Common Mode (CM) voltage generated using a low-drop voltage reference generator. The board is interfaced with the sensor board, discussed above, and testing is performed for 70 kHz triangular current. Figure I.1.20.13 and Figure I.1.20.14 show the individual outputs of the first stage of IAs (IA1 and IA2). The output is undistorted, and the waveform shape is triangular like the test current. However, the outputs of both IA1 and IA2 have CM voltage spikes at the peak and trough of the current. Figure I.1.20.15 shows the final output of IA3, which is the difference between the outputs of IA1 and IA2. As can be seen, the CM spikes are eliminated as they are subtracted by IA3, justifying the efficacy of the proposed signal conditioning approach in providing a high

Common Mode Rejection Ratio (CMRR). However, the waveform shape is distorted and is not purely triangular. The underlying reason might be that the IA3 is working near the linear region boundary due to an untuned CM reference voltage. The CM voltage supplied to IA3 is 1.65 V, which should be half of the supply voltage of 3.3 V, as designed. Nevertheless, the CM voltage needs to be tuned and is ongoing.



(a)

Figure I.1.20.11 Signal conditioning overview



(b)

Figure I.1.20.12 Signal conditioning PCB

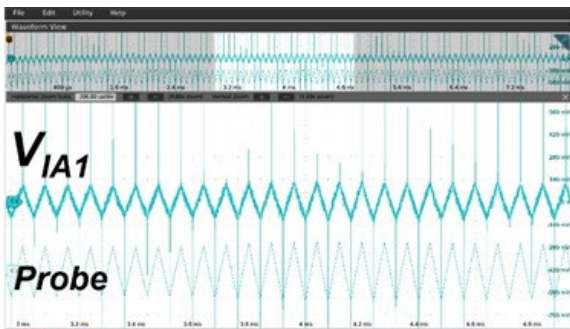


Figure I.1.20.13 Output of IA1.

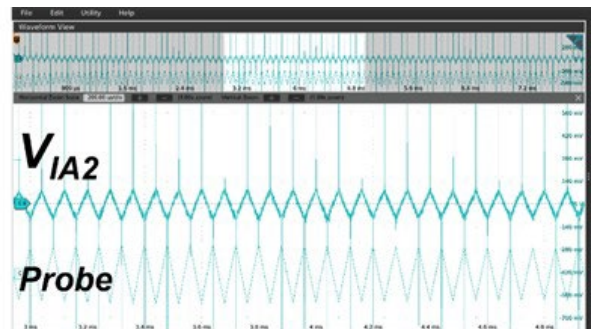


Figure I.1.20.14 Output of IA2

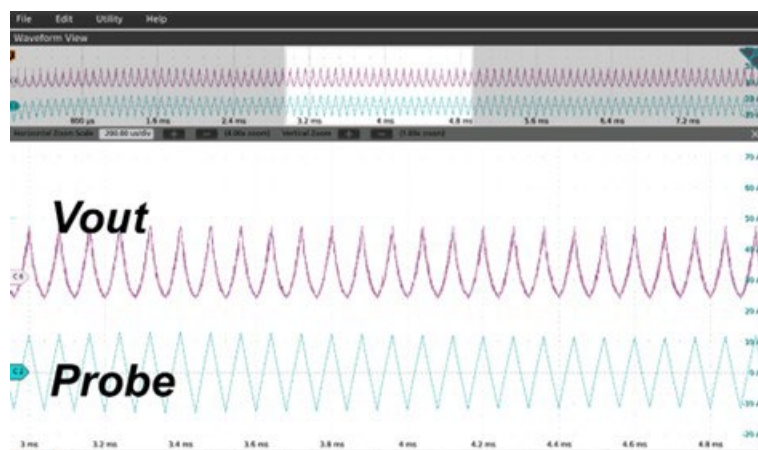


Figure I.1.20.15 Final output (IA3)

Conclusions

UA research is underway, with both packaging and IC design levels in full swing. Biweekly meetings are being held with the broader team, and UA-only meetings are being held in the intermediate weeks such that a project meeting is held each week. The UA team had fabricated and delivered six active Gen1b power modules and differential boards to ORNL for their intended 200 kW inverter build which is currently under evaluation. In the grand scheme, overall project is on track technically. More publications are expected in the coming months as results are obtained from the IC and module developments.

Recent Publications

1. A. Faruque, A. Hassan, R. Paul, and H. A. Mantooh, "Gate Driver Design in 180 Nm SOI CMOS Process for Heterogeneous Integration Inside SiC Power Module," IMAPSource Proceedings 2023 (HiTEC, CICMT, Power): 37–42, <https://doi.org/10.4071/001c.89107>.
2. R. Paul, A. Faruque, S. Chinnaiyan and H. A. Mantooh, "A Heterogeneously Integrated Double-Sided Cooled Power Module for Electric Vehicles," PCIM Europe 2023; International Exhibition and Conference for Power Electronics, Intelligent Motion, Renewable Energy and Energy Management, Nuremberg, Germany, 2023, pp. 1-8, doi: 10.30420/566091199.

I.1.21 Heterogeneous Integration Technologies for High-temperature, High-density, Low-profile Power Modules of Wide Bandgap Devices in Electric Drive Applications (Virginia Tech)

Guo-Quan Lu, Principal Investigator

Virginia Tech
 Department of MSE and ECE – 0111
 Blacksburg, VA, 24060
 E-mail: gqlu@vt.edu

Rolando Burgos, Co-Principal Investigator

Virginia Tech
 Department of ECE, CPES – 0179
 Blacksburg, VA, 24060
 E-mail: rolando@vt.edu

Khai D.T. Ngo, Co-Principal Investigator

Virginia Tech
 Department of ECE, CPES – 0179
 Blacksburg, VA, 24060
 E-mail: kdtm@vt.edu

Susan Rogers, DOE Technology Development Manager

U.S. Department of Energy
 E-mail: Susan.Rogers@ee.doe.gov

Start Date: October 1, 2022

End Date: September 30, 2023

Project Funding: \$300,000

DOE share: \$300,000

Non-DOE share: \$0

Project Introduction

The goal of this project is to develop packaging technologies for making high-temperature, high-density, and low-profile wide-bandgap (WBG) power electronics modules. These modules are aimed at enabling the DOE VTO Electrification Technologies' University Consortium to reach its 2025 targets for the cost, power density, and system peak power rating of automotive electric drive systems.

The objectives of this project are to:

- Develop a low-cost sintered-silver interconnect technology for packaging power modules and gate drivers;
- Develop designs and fabrication processes of double-side cooled power modules with parasitic inductances < 5 nH, heat flux density > 400 W/cm², and working junction temperature > 200 °C; and
- Design and prototype intelligent gate drivers with integrated current sensors and protection for the 200°C module.

A schematic of the hardware to be developed in this project is shown below in Figure I.1.21.1. Planar, double-side cooled phase-leg modules capable of working at 200°C junction temperature will be designed and fabricated. Multiple phase-leg modules will be assembled on cooling plates (with or without double-side cooling) and interfaced to a bus bar and gate-driver boards. The gate driver boards will have integrated current sensors, power supplies, and other components that are capable of working at 65°C ambient.

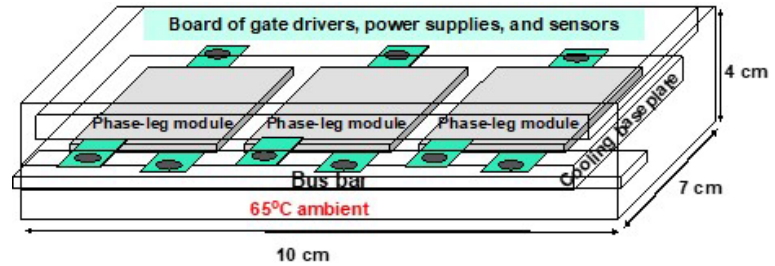


Figure I.1.21.1 Schematic of the hardware to be developed in this project.

For this reporting period, we focused on achieving the following specific objectives:

- Layout modification and fabrication of high-temperature SiC phase-leg modules.
- Continued thermo-mechanical simulations for understanding the effects of encapsulation material properties on the reliability of double-side cooled power modules.
- Temperature-cycling test of fabricated double-modules with different encapsulation materials to validate the thermo-mechanical simulations.
- Continued design, analysis, and test of a package parasitic-based current sensor with compensation schemes to mitigate the impact of the temperature on the output of the current sensor.
- Continued design and test of a Class-E power supply with air-core transformer for a gate driver circuit of the module.
- Integration of the gate-driver power supply and the package parasitic-based current sensor into the gate driver for switching the double-side cooled SiC phase-leg module at 200°C junction temperature.

Approach

This year, the layout and fabrication process of the double-side cooled SiC phase-leg modules were further refined. Six modules of this design were fabricated and delivered for testing in the ORNL inverter assembly, and several back-up modules were also created, along with a module encapsulated with the high-temperature material we identified last year. Simulations on the thermomechanical effects of encapsulant properties on double-side cooled modules were continued. Double-side cooled modules were also fabricated with several different encapsulants for experimental verification of these simulations through thermal cycling tests.

As for the gate driver part, the gate driver integrated with current sensor based on parasitic inductance is designed. The stray inductance in the power loop is used to reconstruct the device current with an ultra-high bandwidth and accuracy. The parasitic resistance of the used trace is compensated with a feedback circuit and an online adaptive algorithm is proposed to eliminate the influence of temperature change on the compensation for the resistance. A gate driver integrated with the proposed current sensor and the isolated power supply for the high-temperature SiC module is designed to verify the performance of the gate driver, sensor, isolated power supply, busbar, and SiC device at the junction temperature of 200 °C.

In the continued effort for the integrated single-phase power module, a two-output power supply with air-core transformer was manufactured and tested. PCB windings are utilized to minimize the converter profile. The design of the air-core inductor and transformer followed similar design steps of the six-output power supply reported in the last reporting period. The inductances were measured to verify the design. The designed power

supply was then tested with resistive load to verify the output voltage and efficiency. Finally, the power supply was tested with the gate driver to justify its performance as a gate power supply.

Results

1. Layout Modification and Fabrication of SiC Phase-Leg Modules

Last year we reported modifications to the layout of the double-side cooled SiC MOSFET phase leg module, resulting in layout design 3.0. This year, further refinements resulted in Layout 3.5, which retains the ten signal pins from the previous version, as shown in Figure I.1.21.2. In the new layout, the source, gate, and drain pins for the top device have been relocated to the top substrate, leaving five pins on each substrate. An improved aluminum solder reflow fixture, shown in Figure I.1.21.3, was designed. This version of the fixture located the three high-voltage leads as well as the signal pins during the reflow process, ensuring good alignment of the terminals to the busbar and gate driver, respectively.

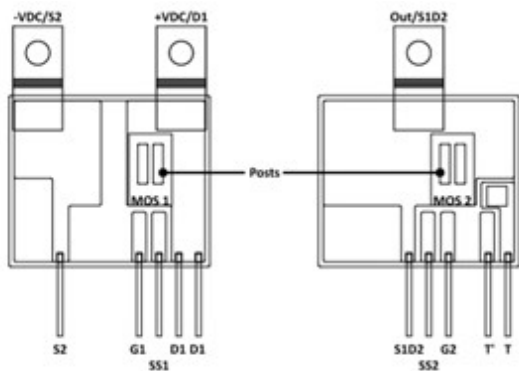


Figure I.1.21.2 Layout 3.5 for the double-side cooled SiC MOSFET phase-leg module.

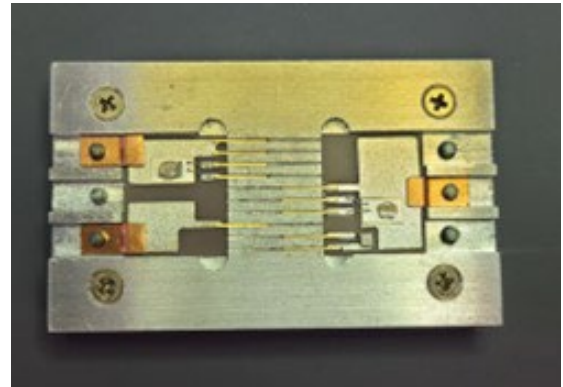


Figure I.1.21.3 An improved aluminum soldering fixture that aligns signal pins and high-voltage leads during solder-reflow.

To achieve the M2.5 milestone which is to demonstrate planar packaging technology of SiC phase-leg module working at a junction temperature of 200 °C, a module shown in Figure I.1.21.4 with Layout 3.0 was made and encapsulated with a high-temperature material, EP-2000 from LORD LCC. More modules of this version are being made as backups to the six modules previously delivered to ORNL for inverter assembly. Some will be tested for high-temperature and reliability study.

Using this layout and fixture, six phase-leg modules were fabricated for the ORNL 100 kW/L traction inverter. These modules were tested on a curve tracer to ensure blocking up to 1.2 kV and an on-resistance of less than 17 mΩ before being soldered to the gate driver motherboard and delivered to ORNL. A further five modules were fabricated as back-ups to these six.

Additionally, one high-temperature module was fabricated, designed to operate at a maximum junction temperature of 200°C, in accordance with the M2.5 milestone. This module, shown in Figure I.1.21.4, used a high-temperature encapsulant, EP-2000 from Lord; it was otherwise identical to the aforementioned modules, which were encapsulated with Lord's ME531.

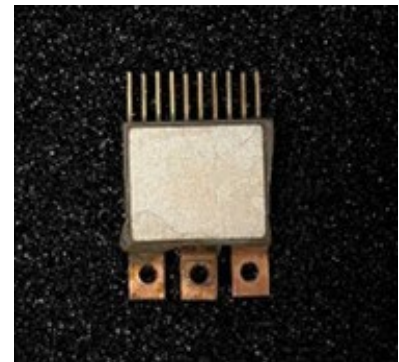


Figure I.1.21.4 EP-2000 encapsulated double-side cooled SiC phase-leg module capable of operating at 200°C junction

2. Simulation and Experimental Study of the Thermo-Mechanical Effects of Different Encapsulation Materials on the Double-Side Cooled Power Module

Last year, we began work on FEA simulations to examine how rigid encapsulant materials affect the thermomechanical reliability of sintered silver bonds within a double-side cooled (DSC) power module. This year, we continued that work with parametric simulations relating the accumulated irreversible deformation of the bonds per thermal cycle to the elastic modulus and coefficient of thermal expansion (CTE) of the encapsulant. A generic DSC module was examined, with sintered silver bonds at three interfaces: between the chip and bottom substrate, between the die and copper spacer, and between the spacer and the top substrate; a cross-section is shown in Figure I.1.21.5. The results, shown in Figure I.1.21.6, indicate that plastic strain is minimized when the encapsulant has a high elastic modulus and a CTE that matches closely with the CTE of the bonded materials.

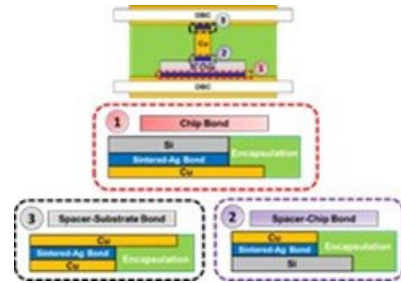


Figure I.1.21.5 Cross-section of the generic DSC module for which FEA simulations were run to analyze the thermo-mechanical reliability of the three sintered-silver interfaces.

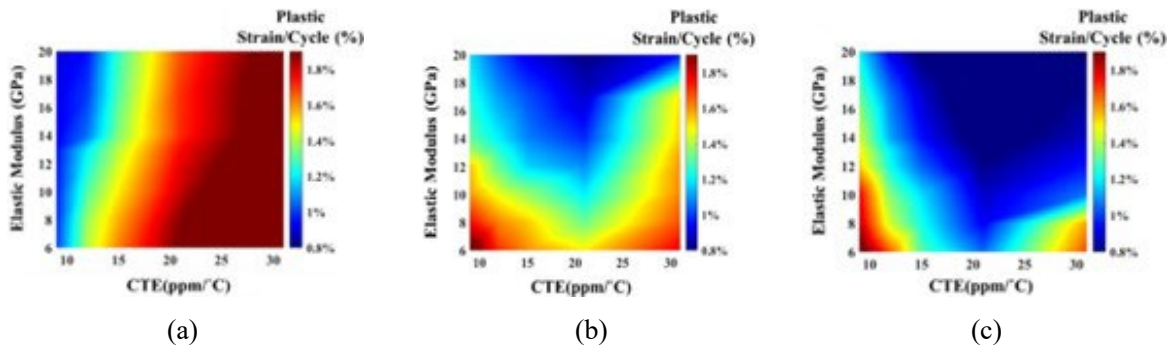


Figure I.1.21.6 Plot of the simulated plastic strain at the sintered-silver (a) chip bond, (b) spacer-chip bond, (c) spacer-substrate bond per temperature cycle versus the encapsulants’ elastic modulus and coefficient of thermal expansion.

Along with these simulations, an experimental study was performed to determine the effects of three commercially available encapsulant materials on the thermomechanical reliability of sintered silver bonds in a generic DSC module. These materials, two rigid epoxies and one soft silicone gel, are shown with their relevant properties in Table I.1.21.1.

Table I.1.21.1 Material properties of the three encapsulants used in the experiment.

Encapsulation Material Name	Encapsulation Type	Elastic Modulus (GPa)	Coefficient of Thermal Expansion, CTE (ppm/ °C)
Nusil R-2188 Silicone elastomer	Soft	0.02	300
LORD ME-531 underfill	Rigid	6.0	21.0
LORD EP-2000 underfill	Rigid	17.1	14.9

Ten modules were fabricated for each encapsulant, then subjected to temperature cycling from -40°C to 125°C. The modules were periodically tested for the on-resistance of their diodes to gauge the effects of the cycling on the bonds. Preliminary results support the conclusions of the simulations, with modules featuring most rigid encapsulant, EP-2000, demonstrating the most longevity. Weibull plots will be included in future reporting to quantify these results.

3. Current Sensor Based on Parasitic Inductance of the Power Device

The device current sensing based on the parasitic inductance of the power device is proposed in this project. The parasitic resistance is a non-ideal factor and leads to an error in the sensor. An integrator circuit with dynamic compensation for the parasitic resistance is proposed and shown in Figure I.1.21.7(a). The FPGA can adjust the compensation for the parasitic resistance with the variation of the parasitic resistance. A timing diagram of the dynamic compensation method is shown in Figure I.1.21.7(b), where the polarity of the sensor output is identified after the power device is turned off and the compensation coefficient k is adjusted according to the polarity of the sensor output. Figure I.1.21.8(a) shows the hardware design of the current sensor based on the parasitic inductance. The GE SiC module GE12047CCA3 is used to work in a Buck DC/DC converter. A PCB trace with parasitic inductance of 2.2 nH is inserted in series with the lower switch of the SiC module. Figure I.1.21.8(b) and Figure I.1.21.8(c) show the waveforms of the current sensor based on parasitic inductance, where the adaptive close-loop compensation is applied. The experimental results show that the proposed current sensor based on parasitic inductance and the adaptive close-loop compensation for the parasitic resistance can be used to reconstruct the device current with a high-bandwidth and accuracy.

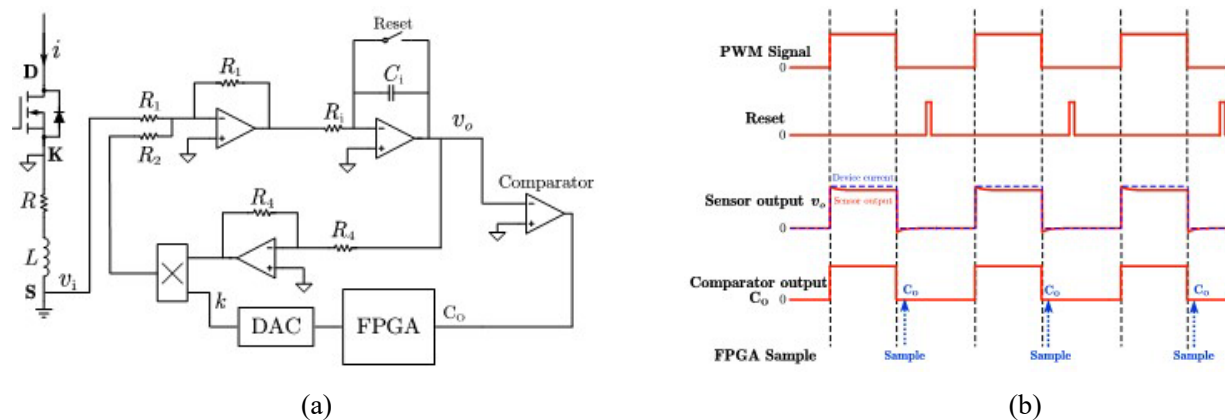


Figure I.1.21.7 The schematic of the integrator circuit with a dynamic compensator for parasitic resistance (a) Circuit diagram (b) Timing diagram.

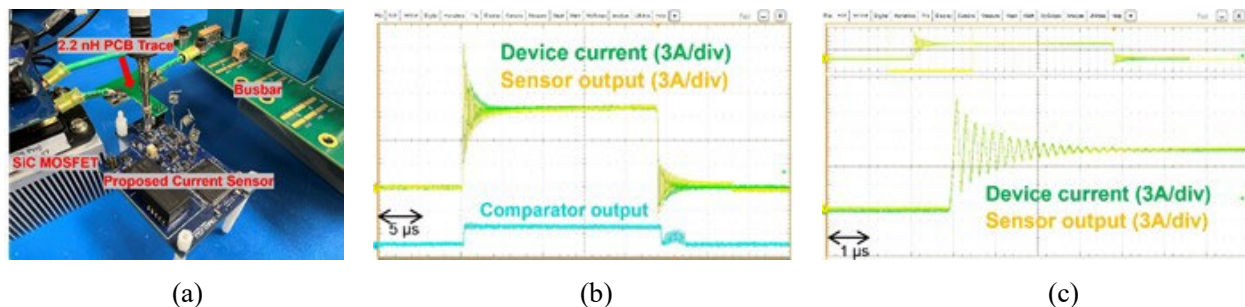


Figure I.1.21.8 The experiments of the current sensor (a) The set-up of the Buck converter (b) The waveforms (c) The waveforms in the turn-on transient.

A high-temperature SiC phase leg integrated with SiC module, Class-E auxiliary power supply, current sensor based on the parasitic inductance, and gate driving circuits are designed and implemented. The junction temperature of SiC device can be pushed to 200 °C. The diagram of the phase leg is shown in Figure I.1.21.9.

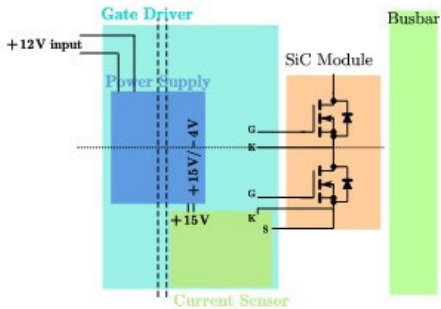


Figure I.1.21.9 The diagram of the phase-leg.

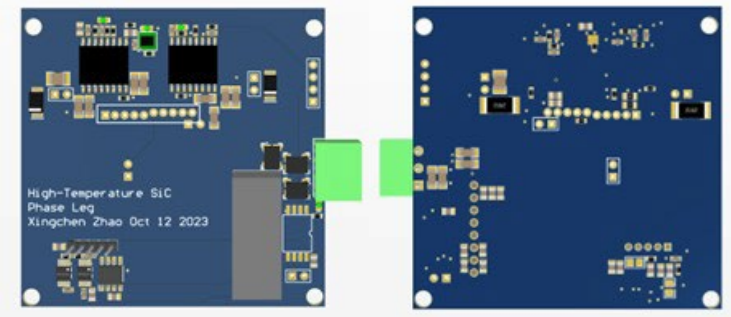


Figure I.1.21.10 The gate driver board.

The gate driver board is shown in Figure I.1.21.10, where the input voltage is 12 V. The high-power side of the gate driver is powered by the Class-E auxiliary power. The current sensor based on the parasitic inductance is applied to the phase leg, which can provide an ultra-fast short-circuit protection and phase current reconstruction. Figure I.1.21.11 shows hardware design of the current sensor based on the parasitic inductance. Figure I.1.21.12 shows the hardware of the high-temperature SiC phase leg integrated with current sensor and auxiliary power supply.

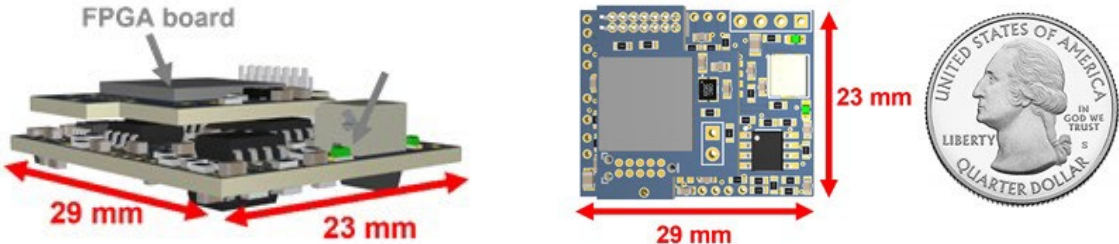


Figure I.1.21.11 The hardware of the current sensor based on parasitic inductance.

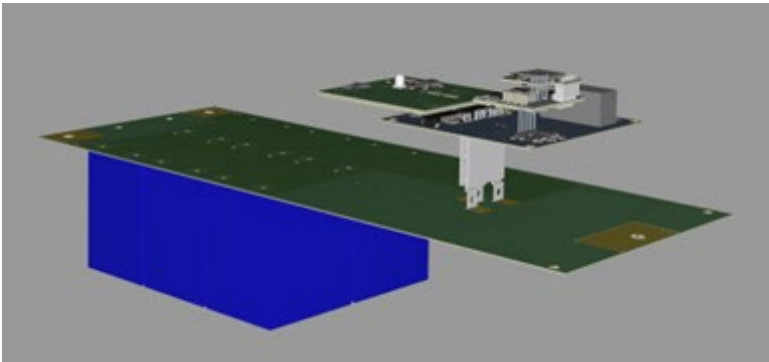


Figure I.1.21.12 The hardware of the high-temperature phase-leg.

4. Design and test of the Six-Output Power Supply with an Air-Core Transformer

4.1. Manufactured Design of the power supply

A two-output Class-E dc-dc converter was fabricated. Figure I.1.21.13 shows the schematics and the hardware. Both the input inductor and two-output transformer are designed with PCB winding and without any magnetic core.

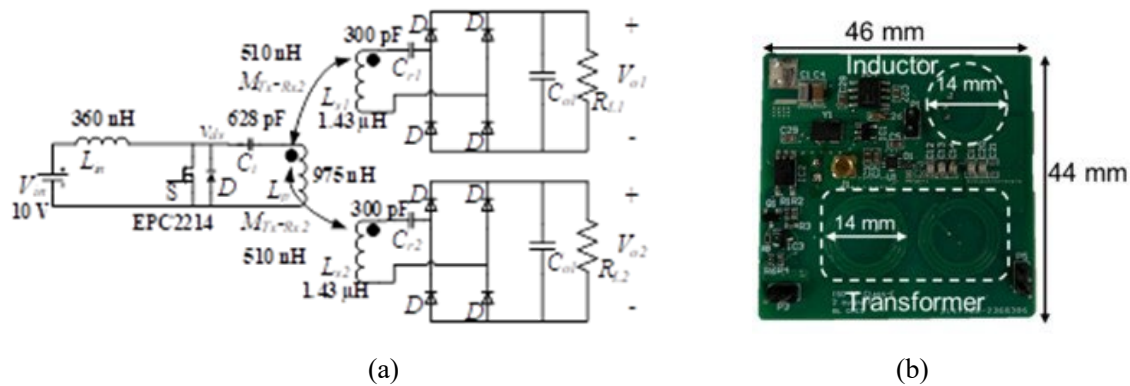


Figure I.1.21.13 The schematics and hardware of the two-output Class-E gate power supply.

Table I.1.21.2 summarizes the measurement results of the inductances compared with the Q3D simulation. It can be seen that the measured inductances match very well with the simulation.

Table I.1.21.2 Inductance measurement results.

Parameters	Description	Simulated	Measured	Error
L_{in}	Input inductance	360 nH	335 nH	7%
L_p	Primary self-inductance	975 nH	1060 nH	9%
L_{S1}	Secondary self-inductance	1.43 μ H	1.47 μ H	3%
M_{P-S1}	Primary-Secondary mutual inductance	510 nH	500 nH	2%

4.2. Performance of the Power Supply with Load Resistor

The power supply was tested with the load resistor shown in Figure I.1.21.13(b). Figure I.1.21.14 shows the waveforms with output voltage regulation at 10 W. The output voltage is 20 V. The load resistance is 80 Ω for each output. On-off control is used with an upper limit of 19.6 V and a lower limit of 19 V. The average output voltages of the two outputs are shown in Table I.1.21.3. From the waveforms, ZVS is observed from the steady-state waveforms.

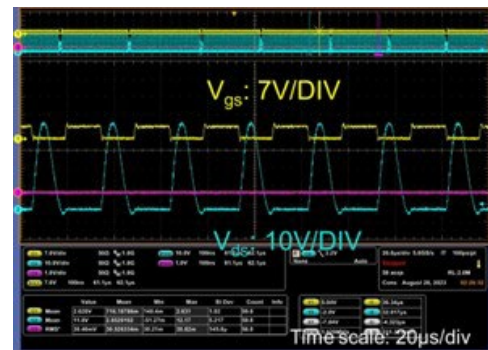


Figure I.1.21.14 Testing waveforms at 10 W output power.

Table I.1.21.3 Summary of the output voltages and efficiency.

Vo1	Vo2	Pin	Po	Efficiency
19.3 V	19.6 V	11.5 W	9.6 W	83%

4.3. Efficiency and Thermal Performance

The Efficiency at different load conditions was measured by changing the output resistance, R_o . Figure I.1.21.15 shows the efficiency curve and the thermal performance at rate power. A peak efficiency of 82% is achieved at rated power. For the thermal performance, the input induct presents the highest temperature at 57°C, a 35°C temperature rise from the ambient temperature, see Figure I.1.21.16.

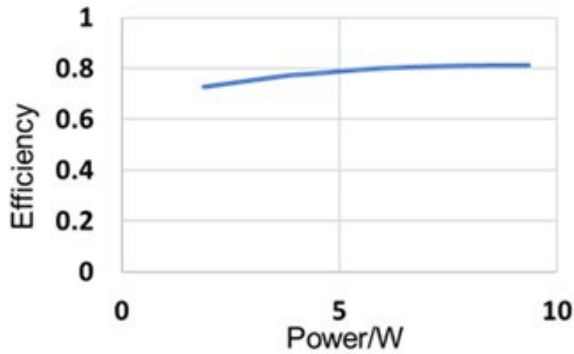


Figure I.1.21.15 Efficiency at different power conditions.

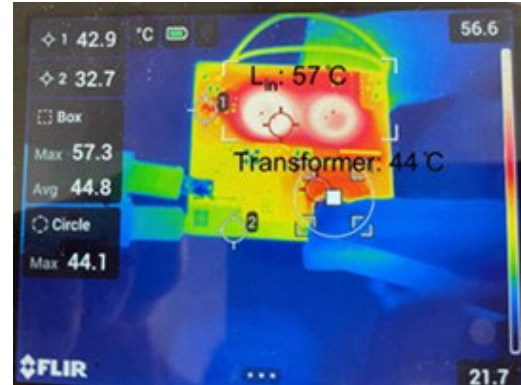


Figure I.1.21.16 Thermal performance at 10 W.

4.4. Performance of the Power Supply with Gate Driver

Tests were run to verify that the power supply provides the right voltage and enough power to drive the power module. The two outputs are paralleled as a single output and connected with the power input of the gate drivers on the daughterboard. The setup is similar to the test reported in the last annual report except that the number of outputs is two. Capacitors were used as the load of the gate driver to represent the gate capacitance of the power module. The PWM signals come from the function generator. The gate output is measured with the oscilloscope. The measured gate waveforms at 40 kHz switching frequency showed that the gate output voltage satisfies the requirement of the power module as +15V/-4V.

Summary

Further refinements were made to the layout and fabrication of phase-leg modules and new modules were fabricated with both low-temperature and high-temperature encapsulation materials. Parametric simulations of the thermomechanical effects of encapsulant properties on double-side cooled modules were conducted as a continuation of the previous year's work. These effects were also studied experimentally on modules encapsulated with various commercially available materials.

A gate driver integrated with current sensor based on parasitic inductance is designed. The current of the SiC device can be reconstructed with a high bandwidth and accuracy by integrating the voltage across a parasitic inductance. The influence of the temperature-sensitive resistance can be cancelled with a proposed compensation circuit and an adaptive algorithm. A gate driver integrated with the proposed current sensor and the isolated power supply for the high-temperature SiC module is designed to verify the performance of the gate driver, sensor, isolated power supply, busbar, and SiC device at the junction temperature of 200 °C.

Air-core inductor and transformer with two secondary windings were designed for a single power supply with two outputs. The measured inductances agree well with the design. The power supply provides identical voltages for all two outputs at the rated power. A peak efficiency at 83% has been achieved at rated power and a 35 °C maximum temperature rise is observed. The testing with the gate driver and power module proved the function of the gate power supply.

Key Publications

1. C. Ding, S. Lu, Z. Zhang, K. Zhang, T. Nguyen, K. D. Ngo, R. Burgos, and G.-Q. Lu, "Double-Side Cooled SiC MOSFET Power Modules with Sintered-Silver Interposers for a 100 kW/L Traction Inverter," *IEEE Transactions on Power Electronics*, 38 (8), pp. 9685 – 9694, 2023.
2. Q. Yuchi, Z. Zhang, S. Lu, C. Ding, F. Boshkovski, B. Li, T. Nguyen, K. Ngo, R. Rolando, G-Q. Lu, G-J. Su, B. Ozpineci, P. Paret, and S. Narumanchi, "Packaging of Double-Side Cooled SiC Power Module for 100 kW/Liter Traction Inverter," presented in the industry session of "Highly Integrated

Power Module for Traction Drives” at 2023 Applied Power Electronics Conference (APEC) in Orlando, FL.

3. G-Q. Lu, “Packaging of Double-Side Cooled SiC Power Modules for Tracton Inverters,” an Invited Presentation for PSMA Power Technology Roadmap Webinar Series, 09/21/2023.
4. F. Boshkovski, C. Nicholas, Z. Zhang, P. Paret, K.D.T. Ngo, and G-Q. Lu, “Effects of Encapsulant Properties on the Thermo-Mechanical Reliability of Double-Side Cooled Power Modules for Traction Inverters”, accepted for poster presentation at ECCE’2023, Nashville, TN.
5. B. Li and K. Ngo, "An Improved Class-E Current Inverter With Two Coupled Inductors for Isolation and Power Scaling Without Affecting Switch Voltage Stress," *IEEE Trans. Ind. Electron.*, online Early Access.

Acknowledgments

We are grateful to Dr. Gui-Jia Su and Dr. Burak Ozpineci of Oak Ridge National Laboratory (ORNL) for their continued support in the test of our modules in their segmented three-phase inverter.

I.2 Electric Drive Technologies Development

I.2.1 Cummins High Power Density Inverter (Cummins Inc.)

Santhosh Krishnamoorthi, Principal Investigator

Power Electronics Technical Specialist

Cummins Inc.

1900 McKinley Ave.,

Columbus, IN 47201

E-mail: santhosh.krishnamoorthi@cummins.com

Susan Rogers, DOE Technology Development Manager

U.S. Department of Energy

E-mail: Susan.Rogers@ee.doe.gov

Start Date: October 1, 2021

End Date: June 30, 2025

Project Funding: \$6,500,000

DOE share: \$5,000,000

Non-DOE share: \$1,500,000

Project Introduction

In medium- and heavy-duty (MD/HD) electric commercial vehicles (ECVs), gross vehicle weight (GVW), lifetime, and total cost of ownership (TCO) are more critical compared to light-duty (LD) vehicles. Increasing the inverter power density enables a smaller electric drive and better management of GVW. Using high-power dense (HPD) and low-cost inverter, the ECV fleet owners can optimize vehicle use by extending the battery range or having more payload reducing the TCO.

ECV inverters must meet higher gradeability, startability, and lifetime requirements compared to LD vehicles. Hence, they must be designed for higher current and handle severe and frequent thermal stresses. Additionally, moving to higher DC voltage rating adversely affects inverter volume, thus, increasing the power density of MD/HD inverters has greater challenges compared to LD inverters. Cummins has developed an inverter rated up to 600 kW, 900 V DC and 750,000 miles for MD/HD ECVs. The power density of the Cummins-designed 300 kW MD inverter is 49 kW/L using discrete components. This project proposes the research, development, testing, and integration of wide band gap (WBG) semiconductors, heat sink, high-energy density capacitors, gate drivers, current sensors, and control board innovatively. The main objective of this project is to develop and demonstrate a 300 kW, 3-liter HPD traction inverter for MD ECVs scalable to HD ECVs meeting the 100 kW/L target. Innovations to increase the power density of the proposed inverter include: 1) use of metal post interconnects in 1.7 kV WBG devices and double-sided cooling, 2) optimization of integrated heat sink designs using genetic algorithm, 3) selection of high-energy dense capacitors and novel packaging to reduce DC link volume, 4) optimized planar- or coil-based filter to mitigate EMI, and 5) component reliability and lifetime studies under various ECV mission profiles. The proposed inverter will be rated for 235 kW continuous, 300 kW peak, 1000 V, and 750,000+ miles meeting or exceeding the Department of Energy (DOE) targets. Cost models for the HPD inverter components will be developed and pathways to achieve 2.7 \$/kW target will be proposed. The HPD inverter will be characterized with an application-target motor in a dyno setup. Novelities of increased DC voltage, current density, lifetime, and modular design targeted towards MD/HD applications can enable compact and reliable class of 1 kV WBG traction inverter technology which can also be beneficial to LD inverters.

Objectives

The objective of the project is to develop a 3 L, 1000 V inverter for MD to HD ECVs with a continuous power rating of 235 kW, peak rating of 300 kW and lifetime of > 750,000 miles. The goal of 100 kW/L power density will be achieved by applying the emerging and novel technologies to the inverter. Figure I.2.1.1 shows the achievable inverter volume reduction through optimal design, careful identification, and selection of

components. The current state-of-the-art ECV inverters are enabled by Silicon (Si) power modules with film capacitors and standalone sensors. In addition, to lower costs and enable manufacturability, conventional topologies viz., 2-level or H-bridge are preferred.

The project will target to improve the Cummins inverter bounding box power density from the current 49 kW/L by 104% to the target of 100 kW/L

Approach

The project will address the following technologies for different stages inside the bounding box:

- Optimal integration of the power module with heat sink, gate driver and sensors to reduce parasitic inductance and losses while enabling higher switching frequencies
- Novel topologies that enable operation at higher DC bus voltages and reduce electromagnetic interference
- Capacitor technologies and packaging concepts that enable a tighter integration of the components to further reduce stray inductance and increase the density of the bounding box volume
- Optimization of heat sink/cold plate design through analytical and experimental approaches including thorough validation of the inverter at component and system level
- Component reliability and lifetime modeling and assessment under ECV mission profile for longer life.

The critical success factors to achieve the high power density goal include:

- A two-level Auxiliary Resonant Circuit Pole (ARCP) topology which enables zero voltage switching (ZVS) reducing losses and improving the EMI performance. Alternatively, a T-type three level topology that will help reduce the noise emission for higher DC bus voltages (1kV+) at higher switching frequencies
- Customized 1.7 kV Silicon Carbide (SiC) metal oxide field effect transistor (MOSFET) integrated module with gate-driver, Rogowski current sensors and double-sided cooling with metal post interconnects which reduces the inductance and the footprint
- Heat sink/cold plate that is optimized for the application through genetic algorithm
- Exploration of printed circuit board (PCB)-mounted film/ceramic capacitors with novel packaging, evaluation of different concepts, and finalization of the selected packaging through experimental analysis.

Finally, cost models for the HPD inverter components will be developed and pathways to achieve 2.7 \$/kW target will be proposed.

Results

1. Power stage - Power Module, Gate-Drive and Bus-Bar board designs and capacitor selection

The goal is to develop a compact power module with integrated current sensing and gate driver circuitry, and double-sided cooling for improved inverter performance and power density. The project team at Virginia Tech completed the design of the power module with SiC devices. The configuration of the design was end-application driven and was chosen based on the selected topology. The power module forms a phase leg with 3 devices in parallel per switching position.

The power modules were started to be fabricated in BP2 starting in July 2023, the team initially tested the SiC devices for characteristics and the obtained positive results and manufactured mechanical power

modules to test the construction of the different layers. Based on the mechanical modules, functional power modules were fabricated and were characterized electrically. The results from the characterization presented the issues with the modules specifically with the on-state resistance ($R_{DS(ON)}$) which was measured to be much higher than the expected value (14 mΩ vs. 6 mΩ). An alternative procedure with newer materials has been started to fabricate the power modules using the clean room facilities at University of Maryland. Additionally, plans to start fabrication with 1-die per switching position to eliminate any challenges that might arise due to known SiC yield issues.

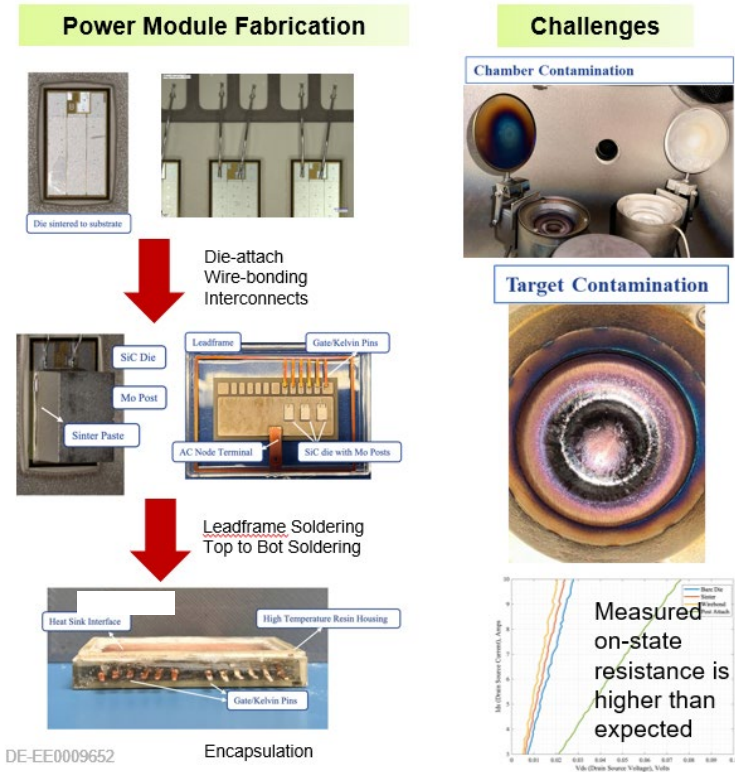


Figure I.2.1.1 (left) Fabrication Steps of Power Module Leading up to Encapsulation & (right) Challenges Faced During the Fabrication Process Due to Contamination in the Processing Facility

The gate-drive board was redesigned towards end of BP1 to incorporate a current transformer-based power supply with a lower coupling capacitance and a smaller footprint. The gate-driver itself was implemented using an existing design from Virginia Tech. The board was fabricated and successfully tested for its full performance of 24V output, <3 pF and >1kV isolation.

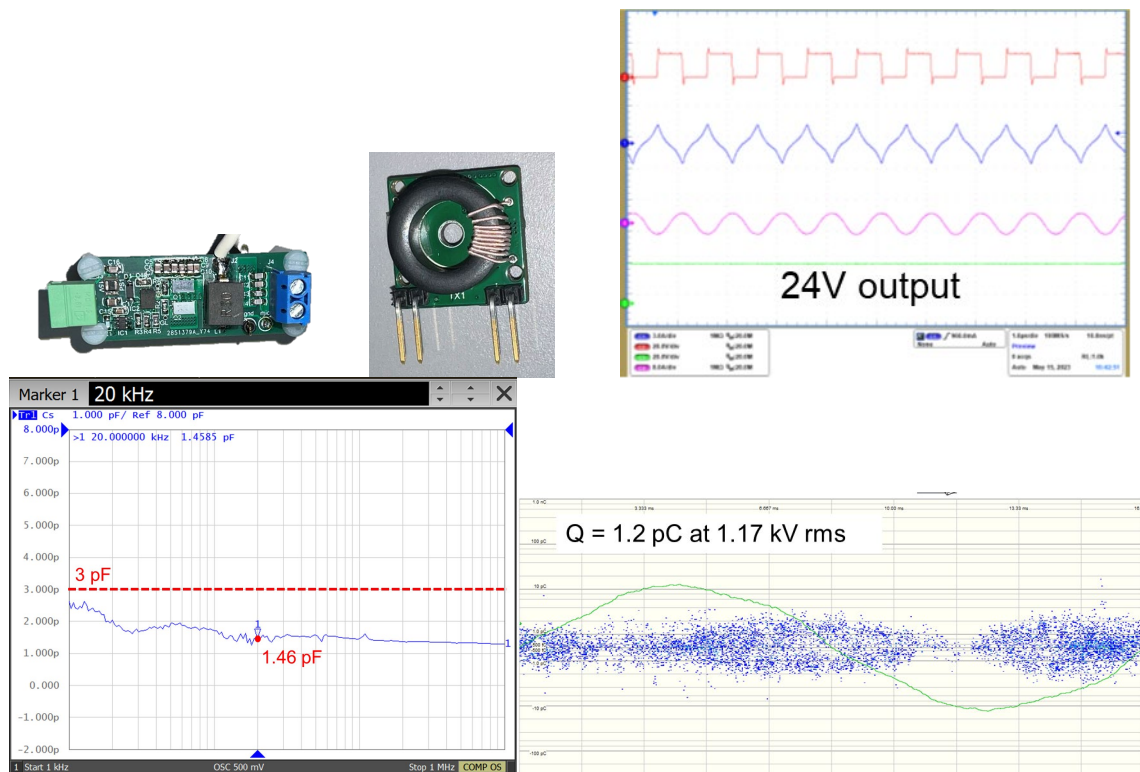


Figure I.2.1.2 (top left) Primary Circuit of the Gate-Drive Power Supply, (top center) Secondary Circuit of the Current Transformer of Gate-Drive Power Supply, (top right) 24V Output From the Gate-Drive Power Supply, (bottom left) Coupling Capacitance Measurement of the Gate-Drive Power Supply Between Primary and Secondary Circuits & (bottom right) Discharge Data to Show Isolation between Primary and Secondary Circuits

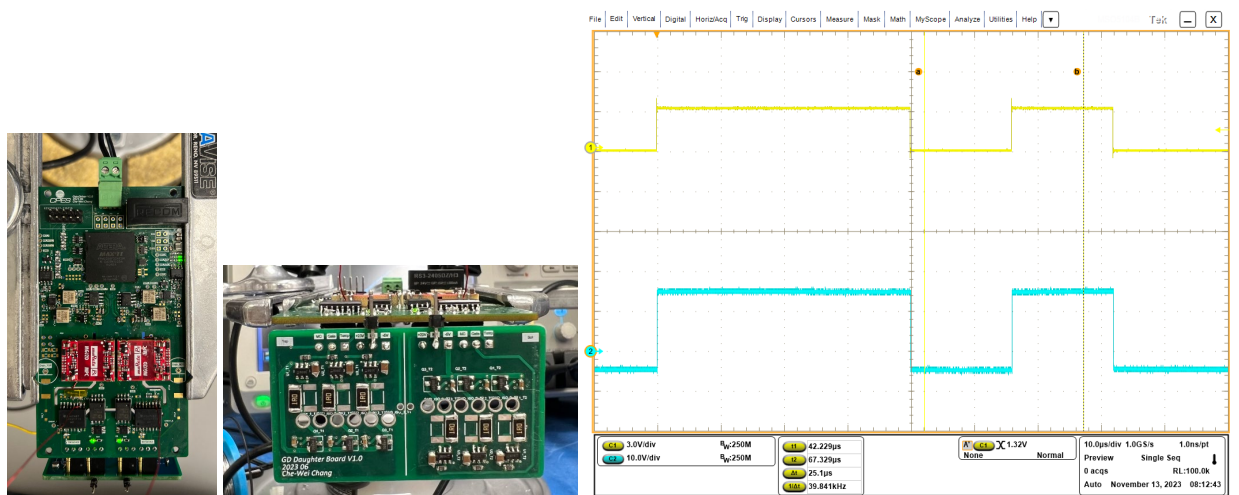


Figure I.2.1.3 (left) Main Gate-Drive board, (center) Daughter Board Interface Between the Gate-Drive Board and the Power Module & (right) Output Gate Pulses Generated During Bench-Testing of the Board

The bus-bar board design was started as a highly integrated design by sandwiching AC bus bars, DC bus bars, current sensors, and interface into the same PCB. Analyses were performed to determine the viability of the design thermally and the team observed that the AC traces dissipate a lot of heat due to the conduction losses and sufficient to raise the temperatures up to 128°C. This affects the components on the board viz., film capacitors which have a max. operating temperature of 105°C. The bus-bar board is hence being modified to reduce the operating temperature and the modifications are expected to reduce the cost as well.

Film capacitors were initially selected as the option for the DC bus link for optimized cost and design but with the updated bus-bar board analysis and packaging exercise, a decision was made to migrate to ceramic capacitors to implement it. Although, ceramic capacitors pose challenges like increased complexity in bus-bar board layout due to increased number of capacitors required (lower operating voltage, 700V and lower effective capacitance, 0.5x due to the nature of the PLZT material). These challenges are currently being addressed through design updates to the bus-bar board by decoupling the AC traces and implementing using solid copper.

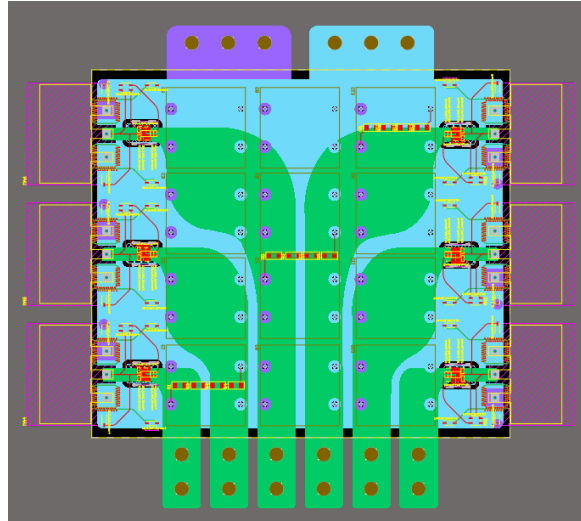


Figure I.2.1.4 Bus-Bar Board Design With AC traces, DC traces, Current Sensors and Power Modules attached

2. Cooling system and Inverter packaging optimization

The goal is to review and compare heat sink technologies and design and optimize the heat sink to integrate with the selected power module to minimize inverter volume and develop a manifold and packaging design to supply and house the heat sinks. The team at ORNL has completed the design of the heat sink meeting the requirements derived from the target applications. The design was customized to the power module developed by Virginia Tech and was optimized using Genetic Algorithm to modify the fin structure created by a FFT function. The function is altered by the algorithm to concentrate more towards the heat sources in the power module to obtain highly efficient heat flow and minimized temperatures across the devices. The current finalized design has two sets of double-sided heat sink structures with the power modules on either side of the bus-bar board. This design was decided to reduce any stress that might be added to the power stage components in other orientations.

The fin structure and the heat sink cavity were further modified according to recommendations from the manufacturer who required minimum tolerances for those parts of the heat sink. A manifold design was also completed by the Cummins team in collaboration with the ORNL team. The manifold design was iterated through several stages in attempts to achieve the best possible pressure drop for the cooling system and to reduce the volume of the inverter as much as possible. The current finalized design supplies the two heat sinks structures individually with two inlets and two outlets. This design helps to optimally route the coolant with appropriate pressure drop and minimize the volume.

With the inverter components getting finalized, the team at Cummins begun designing a package for the inverter that will help house the components and make it ready for testing in BP3. The packaging exercise also provided insights into required improvements in terms of design, placement of components and thermal impacts in bringing together all the elements of the inverter. The packaging design started with a volume of 6 L which helped to identify the parts to be further integrated like control board and gate-drive board and propagated the change from film to ceramic capacitors to further optimize the volume. The height of the stack-up of components was key to optimizing the inverter volume and current final design is expected to be at 2.9L with all optimizations helping us achieve 100 kW/L power density goal.

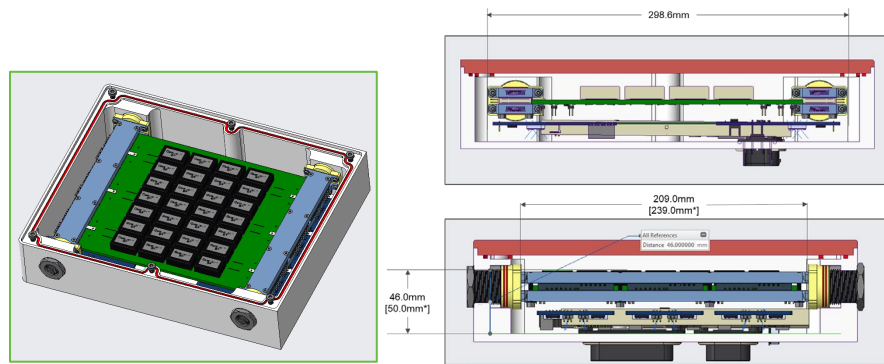


Figure I.2.1.5 (left) Inverter Package Design with Ceramic Capacitors and Bus-Bar Board Attached to the Heat Sink-Power Module Structures on Both Sides with Two-Inlet-Two-Outlet Manifold Design & (right) Dimensions of the Latest Packaging Design Showing a Volume of 2.9 L

3. EMI Mitigation and Filter Design

The goal is to explore EMI mitigation measures, simulate, design, and fabricate EMI filter for WBG system to minimize inverter volume. The project team at ORNL has been working on development of models to determine the noise that will be present in the system because of the high frequency switching and its effects along with the parasitics of the power modules, inverter packaging and a target motor for the application. The parasitics for the system were determined from the power module by Virginia Tech and know parasitic values from existing systems at Cummins. All the parasitic values were hence included in the model developed by ORNL along with a preliminary filter design.

The results from the simulation showed a necessity to implement at least a two-stage filter i.e., a L-C-L filter to meet all the CISPR 25 standards for a powertrain application. The team currently has a preliminary design of the filter and is expected to fabricate it in BP2 and test it with the system for further optimization.

4. Control system design

The goal is to design the control board and develop a software with control algorithms to drive a WBG-based traction inverter. Components will be selected, printed circuit board (PCB) will be laid out, PCB will be developed, and components will be assembled on PCB. The project team at Cummins has completed the schematics of the desired control board with a new ARM processor and has started working on the layout of the board and is expected to complete the process by Jan '24. The layout of the board is complex due to the nature of the components on board and the requirement to keep size appropriate enough to achieve the power density.

The software development for the project has made significant progress with the components like ADC driver, SPI driver etc. being completed and integrated with a new real-time OS for testing and future integration with functional safety enabled systems. The project team is currently porting existing control algorithms to the new OS and will also implement methods to improve the performance of the system like reduction in EMI and losses.

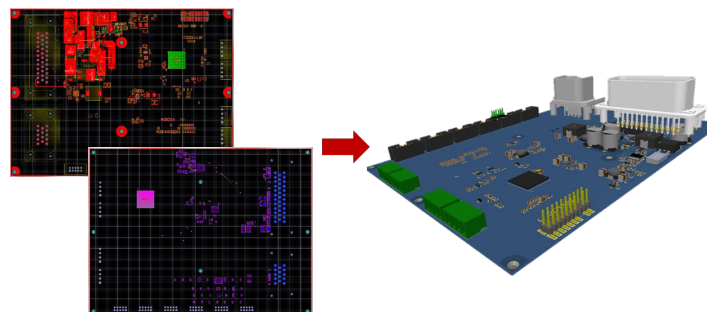


Figure I.2.1.6 Layout Process of Control Board With Top and Bottom Sides Populated and (right) 3D Model of First Steps in the Layout Process

5. High-Fidelity Model Development and Agile Lifetime Modeling

The goal is to develop thermal and thermo-mechanical models of power module packaging and capacitors, analyze system cooling and reliability, and experimentally evaluate new packaging materials. The project team at NREL has completed the model for reliability and lifetime assessment for the customized SiC power module from Virginia Tech. The model was developed using the material properties shared by the power module development team and the drive cycle data was derived from existing applications from Cummins. The models were hence created in Solidworks and simulated through the drive cycles in ANSYS Aemsim tool to determine the temperature cycling that the devices will face. The number of temperature cycles that the SiC devices on the module face determines the lifetime of the power module. Wider temperature cycles have greater impact on the devices and the bonds and more of those cycles will reduce the lifetime further. The model aggregates the count of different temperature cycles to determine the effects on the devices and different layers of the power module. An alternative model that determines the stress on the different elements of the power module was also developed to produce a different perspective of the reliability modeling of power module.

The team also started modeling for the film capacitors along with the bus-bar board to determine the temperature cycling and effects on the reliability of the capacitors in the operating conditions. The capacitor model was developed using the available 3D model from the supplier and the material properties were added together in Solidworks. The bus-bar board and power module-heat sink models were also added from the team at Virginia Tech. The entire model was hence simulated using boundary conditions of an ambient temperature of 85°C. A maximum temperature of up to 110°C was observed on the capacitor windings which is above the max. operating temperature of the selected capacitor parts. This allowed us to choose ceramic capacitors for current solution since they have a higher max. operating temperature. The capacitor modeling is further being improved to determine methods to reduce the temperature. With the completion of models, the capacitors will also be simulated through drive cycles for extended lifetime modeling.

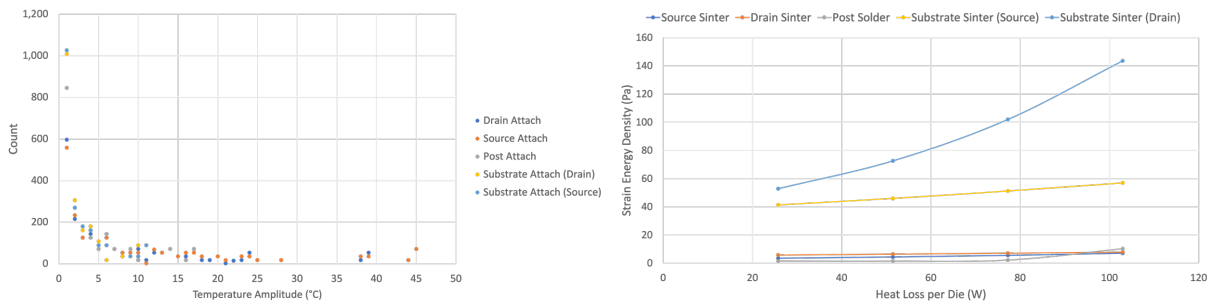


Figure I.2.1.7 (left) Graph Showing Aggregated Temperature Cycles on the Power Module as an Effect of the Drive Cycle & (right) Strain-Energy Density Plots of Different Layers of the Power Module

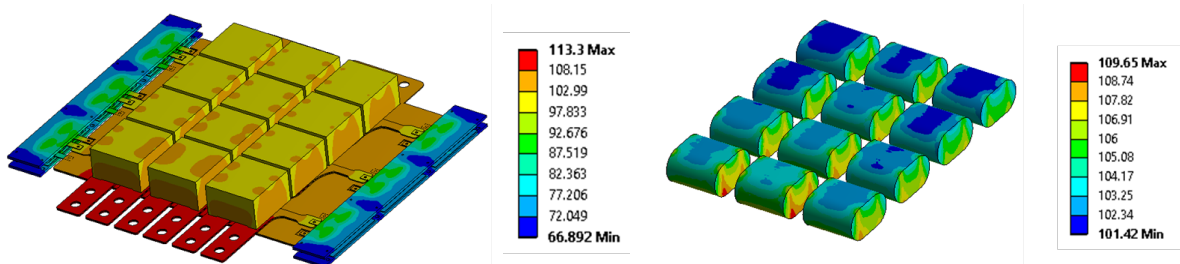


Figure I.2.1.8 (left) Temperature Profile of the Entire Bus-Bar, Capacitors and Power Module – Heat Sink Structure & (right) Temperature Distribution on the Film Capacitors Showing a max. Temperature up to 110°C

Conclusions

In conclusion, in year 2023, the Cummins High Power Density project completed key component designs including 1.7 kV SiC power module, Genetic Algorithm optimized heat sink and 24 V gate-drive (GD) board. Ceramic capacitor selection. Highly integrated bus-bar board design, control board design, EMI filter, software, control Algorithms and OS design were updated. Fabrication of components like power module, GD board were started. Challenges pertaining to the fabrication of power module are currently being addressed using alternative facilities and newly bought replacement materials. The GD board was successfully tested to demonstrate 24V output, <3pF coupling capacitance and >1kV isolation. Inverter packaging and manifold designs were started around the selected components and preliminary concepts have been completed. The current packaging design is expected to set the inverter volume at 2.9L helping to reach the power density of 100 kW/L and manifold design will help feed the heat sink structures with two inlets and two outlets. Reliability and lifetime modeling for power module was completed and has been started for film capacitors with winding temperature analysis completed. The project is expected to complete all the component design and fabrication by end of BP2 and have a complete inverter ready for system testing by BP3 starting Jul '24.

Key Publications

Conference paper at Interpack 2023 by Virginia Tech

1. Roy, Aishworya, Christina DiMarino, and Jesi Miranda-Santos. "Design and Fabrication of an Inverter Module Co-Designed With the Busbar and Gate Driver." In International Electronic Packaging Technical Conference and Exhibition, vol. 87516, p. V001T02A008. American Society of Mechanical Engineers, 2023.

Disclosures on topics

1. Heat sink design with varying fin heights (NREL)
2. Double-sided Heat sink design with opposing coolant flow directions (NREL)
3. Heat sink design with varying no. of find along the width (NREL)
4. Manifold and packaging design with angled inputs for better power density and lower pressure drop (Cummins)

Acknowledgements

Thank you to the teams at

Cummins Inc: Dakshina Murthy-Bellur, Jaroslaw Leonarski, Shankari Ramnath, Zachary Gheaja, Minyu Cai, Joseph Giannini, Sneha Padaki, Gabriel Tenaglia, Jodie Goebel, John Kresse, Brad Palmer, Jaydeep Patel

Virginia Tech (CPES): Christina DiMarino, Rolando Burgos, Dong Dong, Che-Wei Chang, Aishworya Roy, Satyajeet Deshmukh, Zheqing Li, Jesi Miranda-Santos, Yuhao Zhang, Qihao Song

Oakridge National Lab: Shajjad Chowdhury, Himel Barua, Lincoln Xue, Veda Prakash Galigekere

National Renewable Energy Lab: Bidzina Kekelia, Douglas DeVoto, Emily Cousineau, Sreekant Narumanchi

I.2.2 Scalable Ultra Power-Dense Extended Range Super Inverter (BorgWarner, Inc.)

David Bauer, Principal Investigator

BorgWarner Inc.

PowerDrive Systems

E-mail: DaBauer@BorgWarner.com

Susan Rogers, DOE Technology Development Manager

U.S. Department of Energy

E-mail: Susan.Rogers@ee.doe.gov

Start Date: October 1, 2021

End Date: December 31, 2024

Project Funding: \$6,240,000

DOE share: \$5,000,000

Non-DOE share: \$1,240,000

Project Introduction

2025 U.S. Department of Energy (DOE) Vehicle Technologies Office (VTO) goals follow the market trend in setting targets for cost of \$6/kW and power density of 33kW/L for electric traction drive system (ETDS). The system targets include high-voltage power electronics such as one inverter and a single traction-drive electric motor. Compared with 2015, the allocation of the 2025 targets for the inverter requires 54% of cost and an 8x increase in power density. The target also addresses the higher bus/battery voltage (≥ 650 Vdc) and long lifetime expectations ($\geq 300,000$ miles) of many new electric vehicle applications. This requires significant improvement in inverter components and manufacturing technologies. By working together with the DOE, the associated technologies can be commercialized up to 5 years faster than by taking an industry only approach.

Objectives

BorgWarner engineering staff, along with resources and technical support from project partners and vendors, aims to develop and build traction inverter with a new power module design in conjunction with a novel thermal solution and high temperature capacitor technology as well as new control architecture to meet DOE 2025 VTO targets of 100kW/L power density at or below \$2.7/kW cost.

Approach

Technology development within the project will drive innovations and improvements in each of the four major inverter elements to achieve a higher level of performance, integration, and reliability at minimum cost. The project specific innovation areas are:

- Highly integrated and epoxy overmolded power module with double sided cooling, permitting operational junction temperature at or just below 200°C. Subsequently, enabling a higher current carrying capability with similar or less WBG (i.e., SiC) active material area, while maintaining low system losses.
- Next generation cooling module with novel fin structure enabling a scalable and cost-effective solution. Permitting high temperature and performance values based on the new power module requirements.
- Next generation capacitor technology with high temperature ($> 160^\circ\text{C}$) capability and self-healing properties as well as 300% higher energy density. Enabling significant volume reduction in power stack (i.e., power modules, capacitor, and busbar) sub-assembly for inverter packaging.
- New electrical control architecture based on next generation μC and ASICs providing faster feedback loop for sensing, control, and actuation. To achieve performance and efficiency targets as well as realizing future functional safety requirements (i.e., ASIL-D).

The project has three (3) phases, i.e., budget periods:

Research, Technology Down Selection and Component Design from Q4-2021 to Q4-2022 for Budget Period (BP) 1

1. Definition of the component design as well as the supporting technology to achieve 2025 VTO targets in the final prototype hardware.
2. Research materials and processes in the power module, cooling module and capacitor.
3. Definition of the design through the analysis and simulation using newly developed/selected wide bandgap devices, i.e., SiC.
4. Development of the prototype inverter concept design and estimated performance.

Component and Subassembly Verification and System Design from Q1-2023 to Q4-2023 for Budget Period (BP) 2

1. Manufacture and check out of the components while creating the detailed design of the prototype inverter.
2. Validation of component level performance checked against the BP1 design parameter target.
3. Completion of system-level design with the analysis and simulation for the optimization.
4. Implementing component risk mitigation plans.

Prototype Manufacturing and Verification/Validation from Q1-2024 to Q4-2024 for Budget Period (BP) 3

1. Manufacture and test of the final inverter prototype hardware.
2. Validation of the components in life and environmental tests.
3. Demonstration of the final inverter performance and efficiency under the dynamometer condition.
4. Documentation of the component and system development as well as the future work to address any issues identified in the component and system validation.

Results

The focus in FY 2021 has been on the manufacturing and check out of the key components in conjunction with creating the detailed system design of the prototype inverter. Verification and validation activities of component level performance checked against the design parametric targets established in BP1 (2022) including system-level electrical and mechanical simulation and stress analysis to identify component design optimization (revision) and/or risk mitigation.

Power Module Prototype and Checkout

A scalable single switch design serves as the foundation for the power module. The prototype interface methods include screw mount for power lead as well as soldered for auxiliary lead connections. The package architecture includes a unique (patent pending) topology to handle various sized SiC bare dies from separate manufacturers on the same pad layout with up to eight (8) dies in parallel per single switch without alteration of the core structure and the manufacturing process. In addition, a new epoxy molding compound (EMC) material and manufacturing process and machinery has been established for the released power device prototype builds starting in Q1-2024. Released single power switch design is shown below in Figure I.2.2.1.

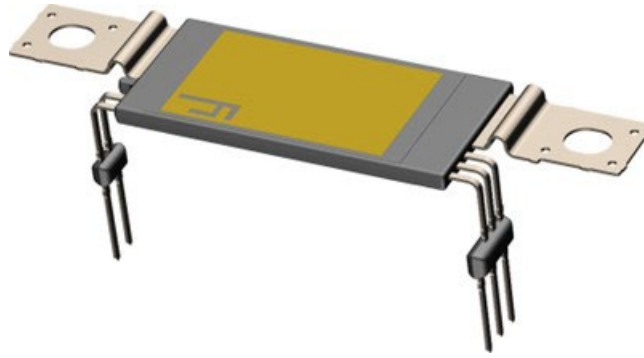


Figure I.2.2.1 Released Single Switch Design

Initial power loss and thermal dependency simulation as well as electrical transient simulation have been verified with current production (Gen3) SiC technology based on vendor datasheets and equivalent circuit models. Electrical behavior (switching) simulation still needs to be completed for the next generation (Gen4) SiC technology. Automotive qualification datasheet and model characterization for the next generation SiC dies to be provided by vendor (Wolfspeed, Inc.) in Q2-2024. The prototype power switches will be manufactured onsite by BorgWarner in early 2024.

Cooling Module Prototype and Checkout

Heatsink materials and process selection has been completed including with using either aluminum (Al) or copper (Cu) and cost balanced metal-joining process of brazing for manufacturing of the assembly. Figure I.2.2.2 shows the planar arrangement of an upper (single) heatsink assembly with the core elements such as base, fins and housing are made from stamped high thermal conductivity Al or Cu alloys, which are brazed together. Figure I.2.2.3 shows the lower and upper copper heatsink prototypes manufactured by BorgWarner.



Figure I.2.2.2 Al and Cu Heatsink Assembly

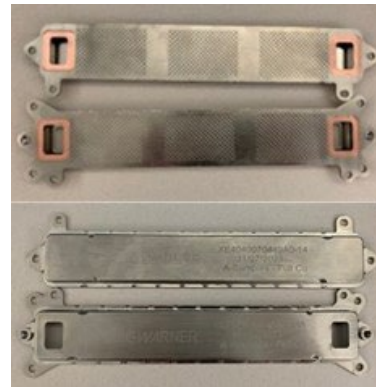


Figure I.2.2.3 Lower and Upper Cu Heatsink Prototype

To improve thermal management and overall reliability, different thermal interface material (TIM) has been verified for the upper and lower joint area between the power device and the two heatsinks. For the upper side, a complaint phase change film material is undergoing verification testing and passed initial thermal cycling. As for the lower side, a hard joining solder preform material is also undergoing verification testing and passed manufacturing process as well as electrical compliance with all six (6) power switches attached. Figure I.2.2.4 shows the TIM allocation for upper and lower side of the cooling module.

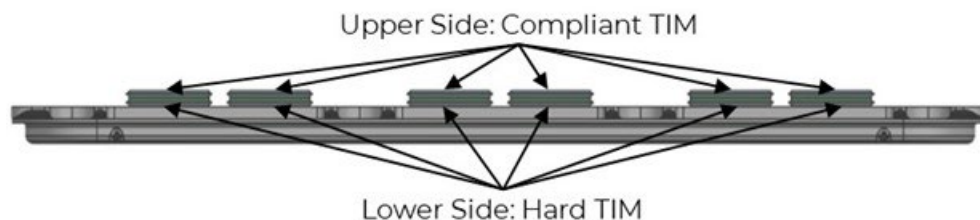


Figure I.2.2.4 Thermal Interface Material (TIM) Area on the Heatsink Assembly

Figure I.2.2.5 displays the design verification / simulation results for thermal distribution for the released heatsink design with next generation (patent pending) cooling channel fin structure, including the allocation of the individual (8 SiC dies per power switch) heat sources within the six (6) power switches.

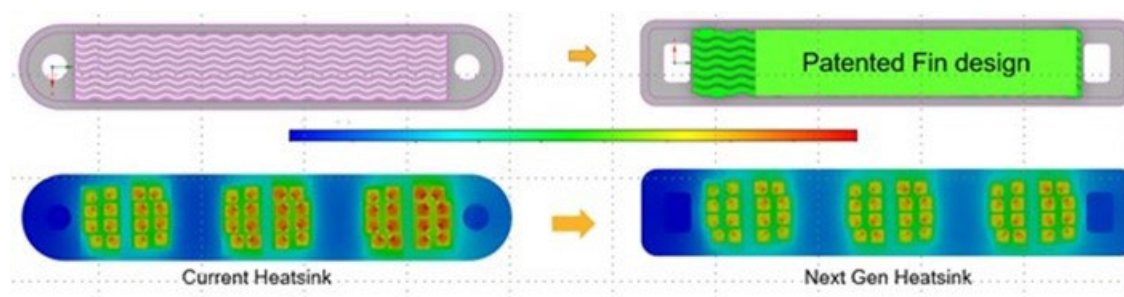


Figure I.2.2.5 Thermal Simulation of Heatsink and Cooling Channel Design

Those verification simulation results provide confidence in achieving the lowest possible pressure drop within the structural area (fins), increasing heat transfer area and mixing, while maintaining a minimum channel gap of greater or equal to 1mm for automotive cleanliness requirements. Ultimately, releasing a novel (patent pending) cooling fin structure, with approx. 40% lower pressure drop, 3.3% lower SiC MOSFET die temperature, and 11 degrees lower temperature deviation among power switches, as displayed in Table I.2.2.1.

Table I.2.2.1 Heatsink verification at 10LPM, 65°C coolant, and WEG 50/50

	Current Heatsink	Next Gen Heatsink
Heatsink ΔP (inlet to outlet) [kPa]	12.2	7.4
Max. SiC die junction temperature difference [%]	100	96.7
Max. ΔT among power switch to switch [°C]	16.3	5.1

Capacitor Prototype and Checkout

Bulk capacitor elements including NanoLam™ blocks and Y-capacitors as well as structural and busbar design was released for prototype builds. Figure I.2.2.6 shows segmentation of a bulk capacitor into elements of six (6) NanoLam™ blocks with approximately 100 μ F capacitance per element.

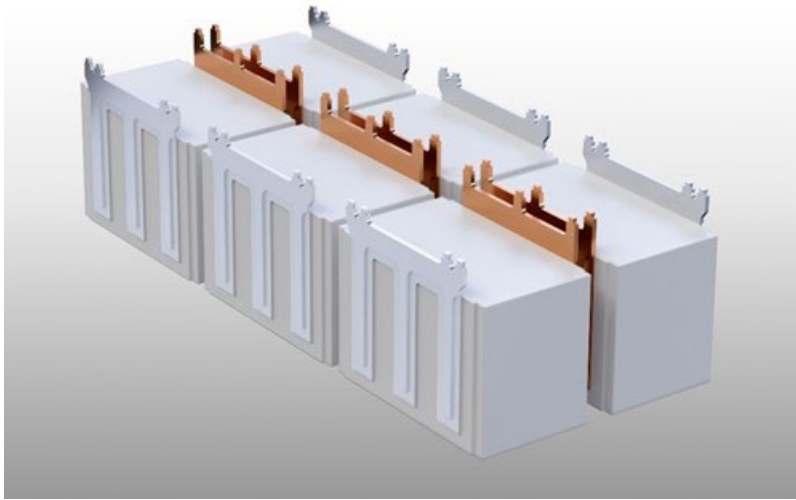


Figure I.2.2.6 Segmented Capacitor with NanoLam™ Blocks

The individual NanoLam™ blocks are laser welded to a planer (laminated) busbar assembly, while the Y-capacitors are also soldered to the same busbar. Thermal and electrical verification and validation activities under way as well as two initial prototypes were delivered for inverter builds. Figure I.2.2.7 shows the initial prototype of the DC bulk capacitor assembly provided by PolyCharge America, Inc.

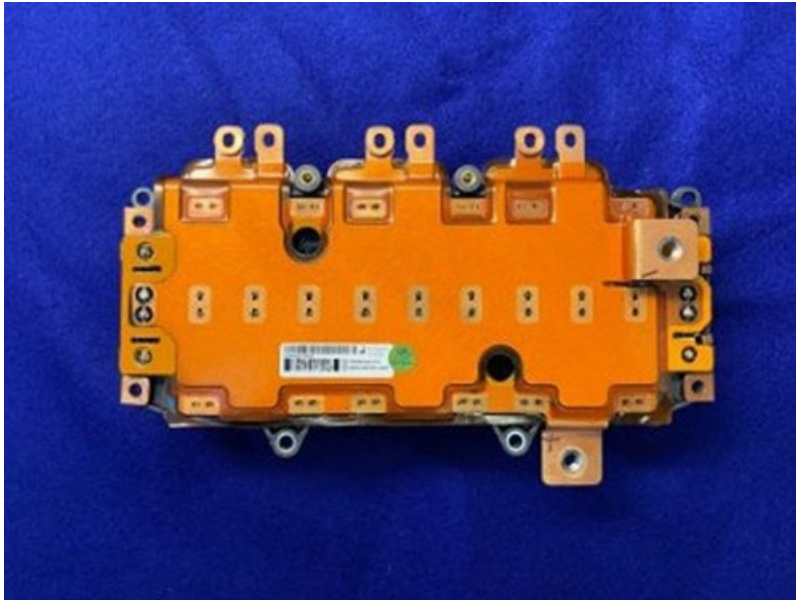


Figure I.2.2.7 DC Bulk Capacitor Prototype (Top view)

During the component checkout, it was observed that the first two capacitors for initial inverter proto builds show higher ESR tolerances as expected. Validation samples are currently under test at PolyCharge facilities.

Controller Prototype and Checkout

Within this project, BorgWarner has now deployed its next generation electrical architecture and integration strategy with the INSSA ASIC (Inverter System Safety ASIC) to drive down cost, component (PCB) size and power consumption all while decreasing the un-safe failure rate specific for traction inverter applications. The improvement in system architecture, which is supported by two INSSA ASICs, is to have fully independent

supplies powering the gate drive circuitry attached to the positive side of the high voltage supply and gate drive circuitry attached to the negative side of the high voltage supply. Each INSSA help supply a fully independent power path that can run off each/either the low voltage vehicle boardnet (LV battery) or a flyback supply from the high voltage boardnet (HV battery and/or motor BEMF) with a patent pending technique [1]. Special care with the system design feature partitioning is done in such a way to ensure that if there was a supply failure, the dual INSSA system would be able to continue to keep the system in a safe state. With this independent supply architecture, any single point fault that would occur results in a system reaction to continue the ability to measure the high voltage supply as well as motor speed and apply correct safe switch enhancements based on those measurements and current fault signature. Furthermore, studies and parametric evaluation of next generation automotive microprocessor from Infineon Technologies has been completed. Software plan and BOM including factory test software (FTS) for inverter hardware checkout and motor control testing activities are underway and to be completed early Q1-2024. Figure I.2.2.8 shows an engineering sample of the main (single) PCB assembly with micro controller, gate driver circuits, including the two INSSA ASICs for the next generation electrical architecture, which are manufactured by BorgWarner in Kokomo, IN.

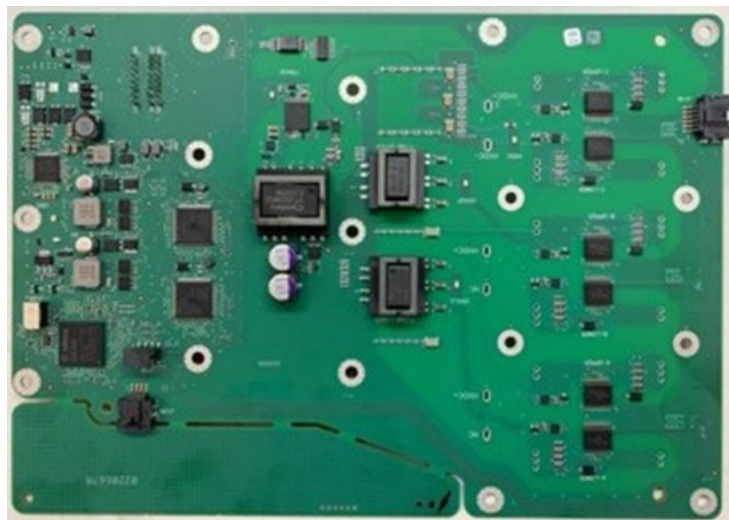


Figure I.2.2.8 Main (Single) w/ Controller, Gate Driver, and INSSA

Additionally, coreless current sensing IC and integration was completed, and design released for prototype builds. HVAC busbar and HVDC prototype assemblies show good correlation between initial verification tests and simulation. Electrical performance within 1% from 50A to 1000A and 1.6% error below 25A after subassembly calibration. Figure I.2.2.9 shows AC phase current sensing subassembly.

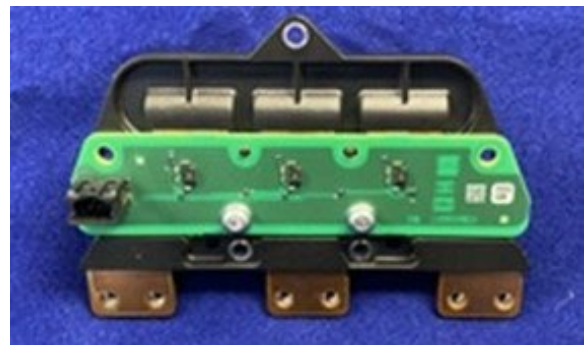


Figure I.2.2.9 AC Current Sensing Subassembly

System Design and Analysis

Figure I.2.2.10 below shows the released system design of the product package and the specific components / subassemblies. Deploying a most simplified (bottom up) assembly process for the core subassemblies, starting with the main housing - step 1, then the bulk capacitor assembly - step 2), the HVAC busbars and HVDC assembly - step 3 & 4, the power module and main circuit board - step 5 & 6, finishing with an optional cover (standalone) or a direct drive unit mounting (integrated) - step 7.

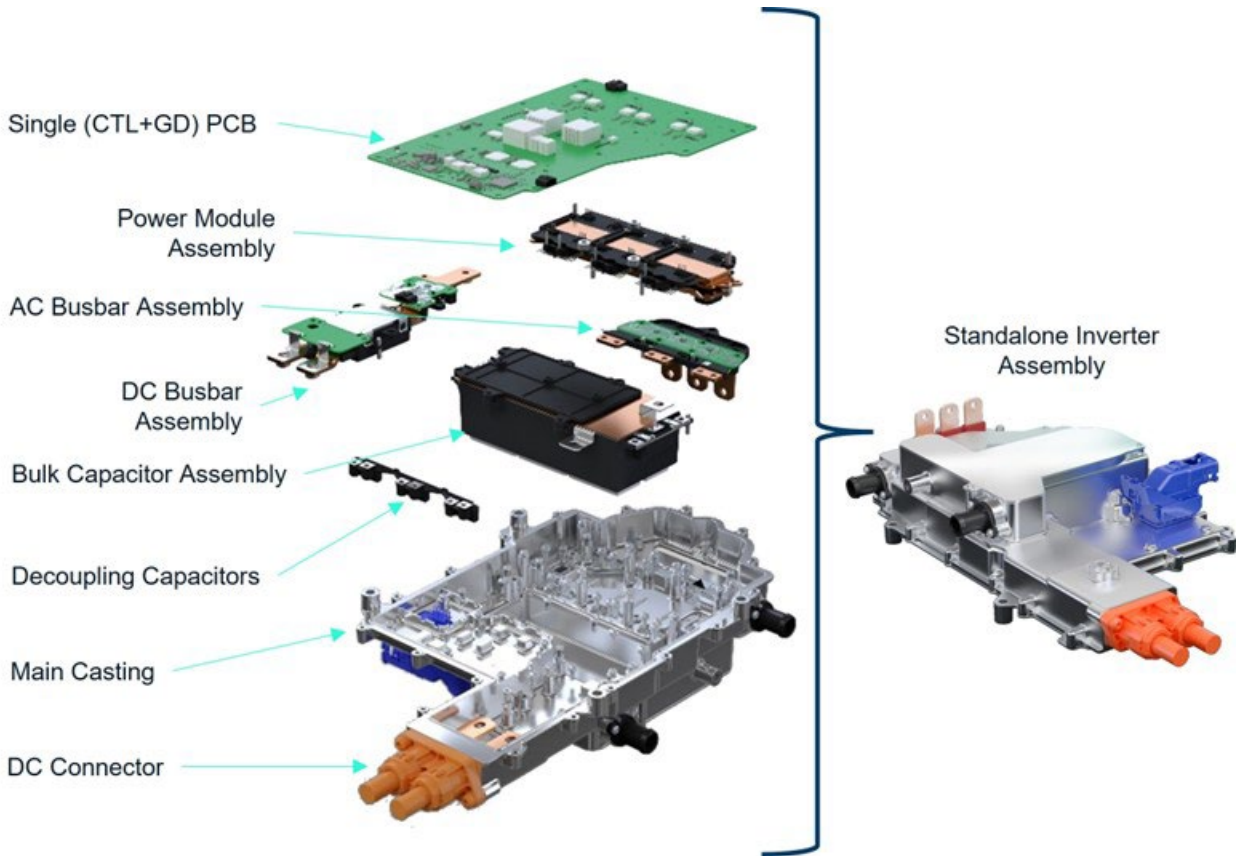


Figure I.2.2.10 Inverter Design and Assembly

While the super inverter power to be scalable between 100 to 300+ kW, the design target for system output power was set to ~350kW using top-down scaling approach. Furthermore, the system is design for higher phase current at ~650Arms to comply with high motor torque requirements within the appropriate vehicle power class (i.e., D segment). Table I.2.2.2 displays power density of three different inverter assemblies.

Table I.2.2.2 Power Density of Inverter Assembly Variants

Inverter ASM	ASM Volume [L]	Output Power [kW]	Power Density [kW/L]
Standalone	4.4	350.6	79.7
Integrated	4.04	350.6	86.8
Active components	3.49	350.6	100.5

Power loss and efficiency simulation activities have been completed with various SiC technologies from three different vendors. Subsequent, two SiC technologies (i.e., Gen3 and Gen4) have been chosen by Wolfspeed, Inc., providing lowest total system power loss demand for thermal management as well as highest efficiency of more than 99% within key operation regions. All while complying with BorgWarner’s production demand and cost targets. Electrical simulation and parametric value extraction has been completed for DC power loop inductance to conduct transient electrical stress simulation. Electrical behavioral (switching) modeling of the power commutation showed no concerns in the corner case operation at 850VDC with respect to oscillations during on > off transition and overshoot amplitude (i.e., overvoltage), which is well below the Wolfspeed Gen3 SiC dies limitation of maximum 1200V. Additionally, transient simulations are to be also completed with Wolfspeed Gen4 SiC dies in early 2024.

Mechanical stress simulation has been completed analyzing frequency response of natural frequencies and normal modes of the full system assembly. Subsequently, there were no major system level concerns within a random vibration analysis with respect to maximum structural displacement. However, there is a minor concern on the single switch power leads to AC phase connection in some vectors as shown in Figure I.2.2.11, which is under investigation.

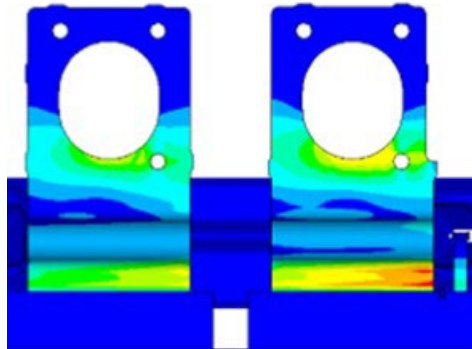


Figure I.2.2.11 Stress Plot of Power Leads

Conclusions

During FY 2023, major progress has been accomplished on procurement, manufacturing and checkout activities of the key system components / subassemblies in collaborations with external partners and vendors. Particularly, the design and initial verification testing of both the cooling module subassembly and the main board controller w/ ASICs are well underway. More specifically, the mechanical design and thermal performance of the next generation heatsink provides a promising approach to further increase power density of an inverter assembly with double-sided cooling power module. Both the controller and gate driver board as well as the current sensing subassemblies successfully completed functional verification on hardware-in-the-loop benches. Capacitor prototypes have been completed and electrical parametric measurement and validation is underway. Power device (single switch) manufacturing process completed and machinery setup underway at BorgWarner facilities in Kokomo, IN. Build of overmolded single switch prototype with next gen (Gen4) SiC technology will start in Q1-2024. High confidence in the design to meet power density and cost target in BP3.

Key Publications

1. Next Generation Inverter Technology for Electric Mobility (paper number 2023-51)
A. Mayer, M.S. Cohen
44th International Vienna Motor Symposium
ISBN: 978-3-9504969-2-5

Reference

1. M. Gose, M. Cohen, T. Nachnani und C. Klaus, Dual Supply Dual Control Architecture.
USA Patent US 20220368268 A1, 14 5 2021

I.2.3 Low-Cost Rare-Earth Free Electric Drivetrain Enabled by Novel Permanent Magnets, Inverter, Integrated Design and Advanced Thermal Management (Marquette University)

Principal Investigator

Ayman EL-Refai
 Marquette University
 1637 W. Wisconsin Ave
 Milwaukee, WI, 53233
 E-mail: ayman.el-refaie@marquette.edu

Susan Rogers, DOE Technology Development Manager

U.S. Department of Energy
 E-mail: Susan.Rogers@ee.doe.gov

Start Date: October 1, 2020

End Date: June 30, 2025

Project Funding: \$6,250,000

DOE share: \$5,000,000

Non-DOE share: \$1,250,000

Project Introduction

This project presents a comprehensive approach to develop low-cost state-of-the art electric drivetrain system enabled by a comprehensive list of novel technologies which will lead to a rare-earth-free system at high DC bus voltage (700-800V) while meeting or exceeding the DOE targets of \$7/kW and 12 kW/L and leapfrogging the state-of-the art. At the end of the project a full system will be designed, built, integrated and fully tested.

Objectives

The project brings together a group of organizations and experts with proven track record of technology developed and continuous research in the area of transportation electrification with special focus on electric and hybrid drivetrains for light-duty vehicle. The project team includes Marquette University (MU), Niron Magnetics Inc., Virginia Tech (VT), National Renewable Energy Lab (NREL), and General Motors (GM). MU will lead the overall effort as well as the development of the rare-earth free traction motor. Niron Magnetics will lead the development of the rare-earth free Iron Nitride (FeN) permanent magnets. VT will lead the development of the low-cost inverter. NREL will lead the development of the thermal management system (TMS) including system integration concepts. GM will lead the system integration and testing as well as oversee the overall effort to ensure that the developed technologies can feed into their future electric drivetrains. The baseline system that will be used in the project is the Chevy Bolt.

Approach

- Budget Period (BP) 1: [Concepts development and trade-off studies]:
 - Develop concepts, performing tradeoff studies of the various concepts and down-selecting concepts.
- Budget Period 2: [Detailed design, sub-component/component testing and risk retirement]:
 - Develop a detailed design, conduct design optimization, and conduct sub-component/component testing.
- Budget Period 3: [System integration and verification testing]:
 - Procure components, conduct system integration, and perform verification testing.

Results

Traction Motor Development

Continued developing optimized designs based on the new set of specs based on higher speed and higher DC bus voltage.

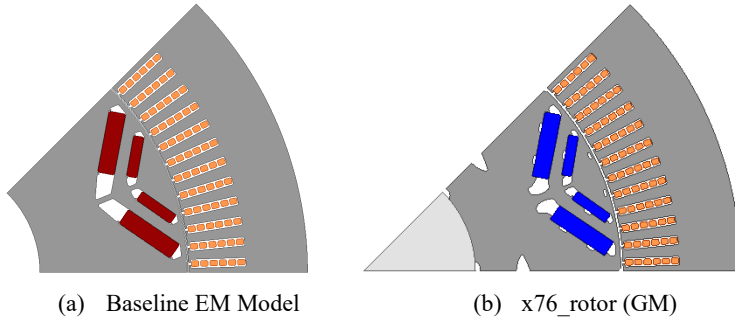


Figure I.2.3.1 Baseline Designs for higher speed and higher DC bus voltage.

Design Specifications (New Baseline)	
Parameters	Values
Slot/Pole Combination	96-Slot/8-pole
Stator Outer Diameter (mm)	220
Rotor Outer Diameter (mm)	150
Rotor Inner Diameter (mm)	65
Air Gap Length (mm)	0.675
Stack Length (mm)	80
Series Turns/phase	48
Number of Parallel Path	2
Lamination Stacking Factor	0.95
Core Material	M-19 Gauge 29
PM Material	GM-PM @70C
Slot Fill Factor	0.49
DC bus Voltage (V)	800
Peak Phase Voltage (V) (taking end-winding drop)	487
RMS Phase Current (A)	220.4
Current Density (A/mm ²)	32.22
Maximum Speed (rpm)	16,000

Performance		
Parameters	Baseline Model	x76_rotor (GM)
Corner speed (rpm)	6700	7000
Torque at Corner speed (Nm)	270	240.5
Torque at 8000 rpm (Nm)	250.5	224.2
Torque at 12000 rpm (Nm)	171.4	145.7
Torque at 16000 rpm (Nm)	125.5	96.6
Torque Ripple at Corner speed (%)	6.4	5.7

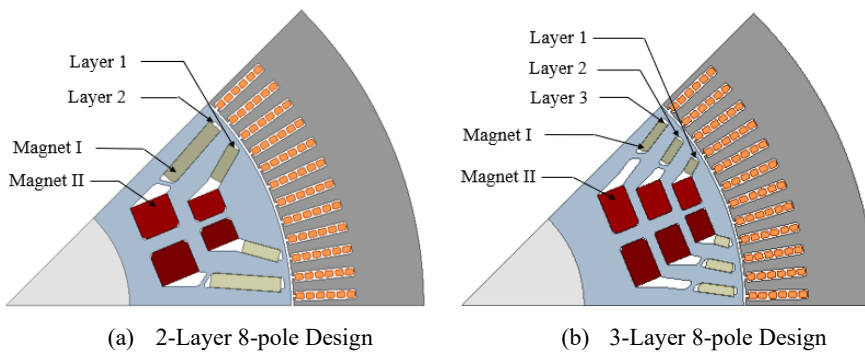


Figure I.2.3.2 2-layer and 3-layer U-shaped PMASynRM designs with side bridges.

Parameters	2-Layer 8-pole	3-Layer 8-pole
Layer 1 Center Post (mm)	1.75	1.5
Layer 2 Center Post (mm)	3.75	3.5
Layer 3 Center Post (mm)	-	3.6
Layer 1 Bridge (mm)	1.1	1.1
Layer 2 Bridge (mm)	1.55	1.55
Layer 3 Bridge (mm)	-	1.6

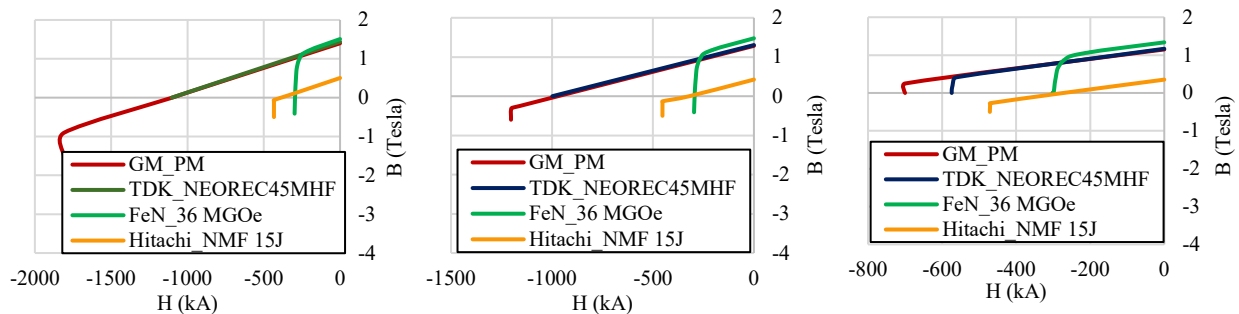


Figure I.2.3.3 B-H curves of various magnet materials at (a) -20oC, (b) 70oC, and (c) 150oC.

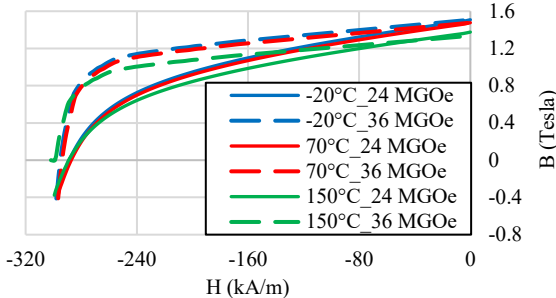


Figure I.2.3.4 36 MGOe vs 24 MGOe B-H curves for FeN magnets.

Magnet Combinations		
	Magnet I	Magnet II
C1	NdFeB (GM_PM)	Iron Nitride (FeN)
C2	Dy-free NdFeB (TDK-NEOREC45MHF)	Iron Nitride (FeN)
C3	Dy-free NdFeB (TDK-NEOREC45MHF)	Ferrite
C4	NdFeB (GM_PM)	Ferrite
C5	Ferrite (Hitachi_NMF-15J)	Iron Nitride (FeN)
C6	Iron Nitride (FeN)	Iron Nitride (FeN)

Optimization Result Summary: 2-Layer 8-pole vs 3-layer 8-pole PMASynRM Designs														
Parameters	Baseline		2-Layer 8-pole				3-Layer 8-pole							
			36 MGOe				24 MGOe		36 MGOe				24 MGOe	
FeN Magnet Grade			C1	C2	C3	C4	C1	C2	C1	C2	C3	C4	C1	C2
Magnet Combination														
Nd Reduction (%)	0	0	58.1	58.4	18.6	16.1	48.8	51.3	59.42	58.68	17.3	15.6	46.6	47.6
Torque at corner speed (Nm)	270	240.5	278.6	273.7	265.1	265.1	270.1	273.2	281.5	276.8	268.1	267.8	275.8	272.5
Torque at 8000 rpm (Nm)	250.5	224.2	249.1	247.1	242.2	242.6	246.2	248.5	254.6	253.5	239.6	239.2	253.1	251.6
Torque at 12000 rpm (Nm)	171.4	145.7	166.3	165.3	161.2	161.8	166.5	167.9	174.8	175.5	157	156.6	173.7	173.4
Torque at 16000 rpm (Nm)	125.5	96.9	120.5	119.5	115.2	116	121.3	122.7	130.1	129.2	109.75	109.2	130	130.5
Torque Ripple at corner speed (%)	6.4	5.7	5.9	9.1	5.7	5.9	7.1	6.8	3.35	3.5	5.2	5.2	3.84	3.51
Corner speed (rpm)	6700	7000	6650	6700	6750	6750	6750	6700	6670	6740	6600	6600	6670	6790
Back EMF Reduction @ -20°C (%)	0	0	1.23	1.9	0.25	0.06	0.3	0.44	2.13	2.08	0.26	0.02	0.21	0.45
Back EMF Reduction @ 150°C (%)	0	0	1.62	3.1	0.35	0.015	0.4	1.8	2.89	2.12	0.53	0.01	0.47	0.55
Rare-earth Magnet Mass (kg)	1.18	1.19	0.493	0.49	0.958	0.987	0.6	0.57	0.48	0.49	0.973	0.993	0.63	0.62
Rare-earth Free Magnet Mass (kg)	0	0	1.12	1.1	0.93	0.93	1.38	1.35	1.25	1.22	0.75	0.75	1.34	1.26

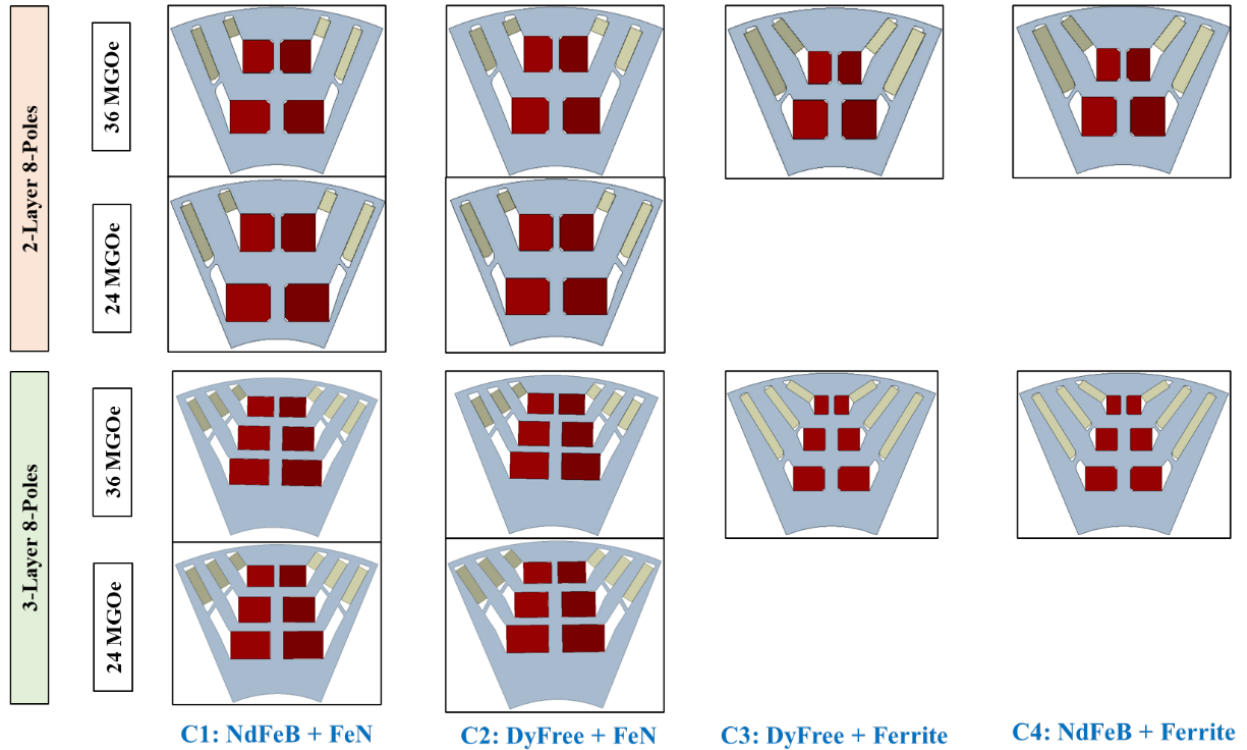


Figure I.2.3.5 Optimized Rotor Designs for 2-Layer and 3-Layer PMASynRMs with C1 – C4 magnet combinations.

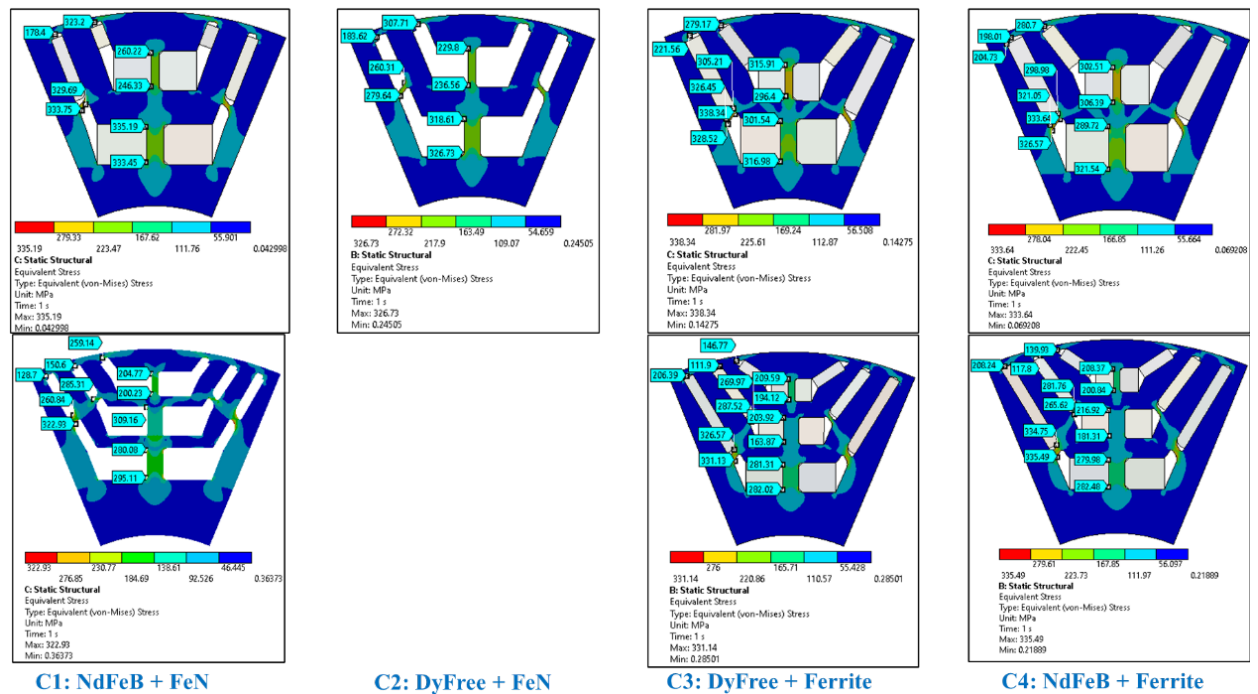


Figure I.2.3.6 Mechanical Stress at 16000 rpm in the Optimized Rotor Designs.

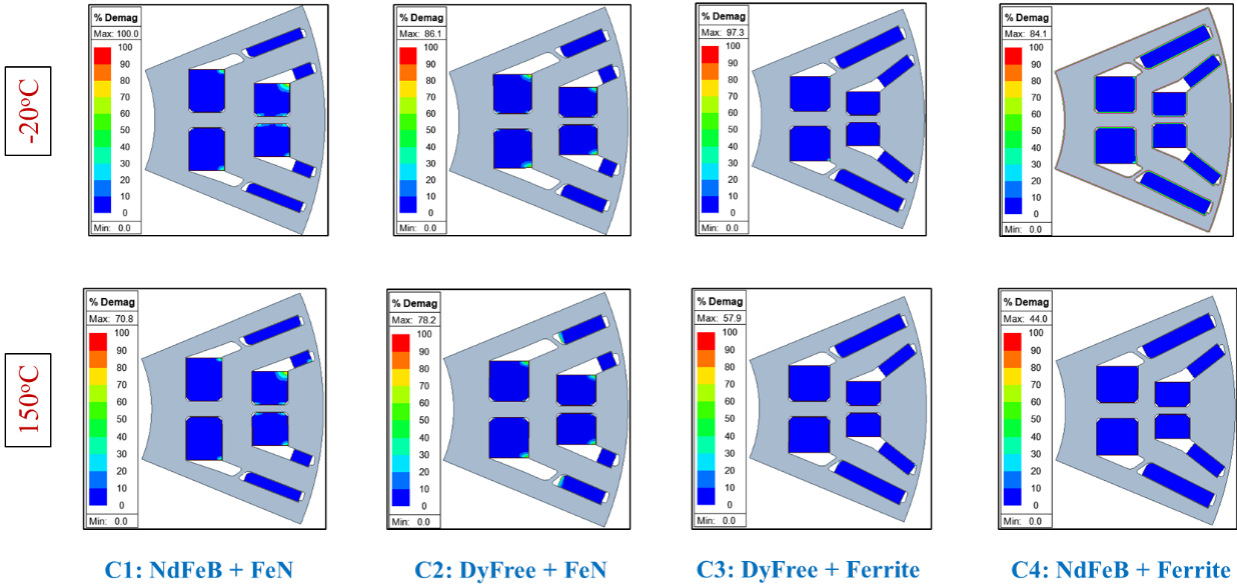


Figure I.2.3.7 Localized demagnetization in the Optimized Rotor Designs of 2-Layer PMASynRMs with C1 – C4 magnet combinations.

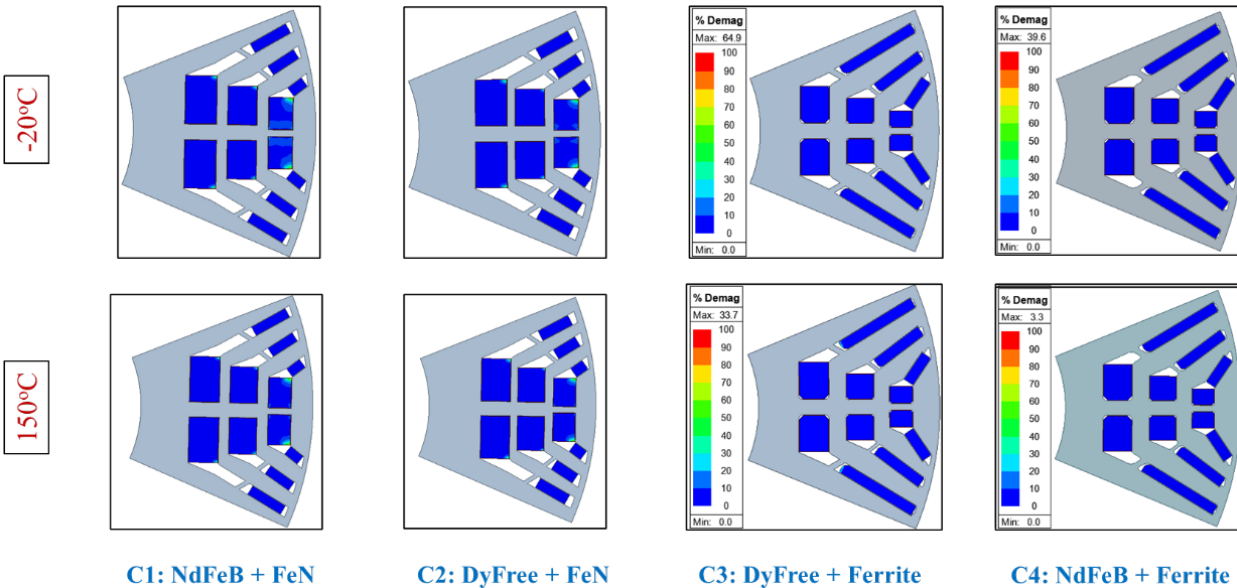


Figure I.2.3.8 Localized demagnetization in the Optimized Rotor Designs of 3-Layer PMASynRMs.

Iron Nitride Magnet Development

Technical work started on January 11th, 2021. The first technical achievement was the selection of a candidate material for the ductile coating needed to enable high shear consolidation of iron nitride nanoparticles. After a literature review, appropriate precursor chemicals were identified for the desired coating. Processing parameters were developed for deposition of the coating on the iron nitride nanoparticles. The iron nitride samples were made by reducing, nitriding, and coating iron oxide nanoparticle starting materials.

The second goal for this project was to achieve a packing density of 95%, a significant step above the theoretical packing density of randomly packed rigid, spherical nanoparticles (63%). This goal has been the

major focus of the work for the team thus far. At this time, a density of 93% was achieved in-house with a density of 94% achieved while working with external collaborators.

The third goal of the project is to achieve a 36 MGOe magnet. To this end, the alignment of the magnets in a magnetic field has been undertaken, but not extensively pursued due to resource constraints. This work did not explore the addition of temperature or lubrication yet.

To discuss the second goal of this project. With the aid of temperature and lubricant, our in-house equipment was able to go from a density of ~83% reported last year to over 93% in the first half of the year (Figure I.2.3.9). External collaborations with promising new technology were also undertaken and achieved a density of ~94%. However, due to scale-up issues with that technology, it was decided to move forward with in-house techniques.

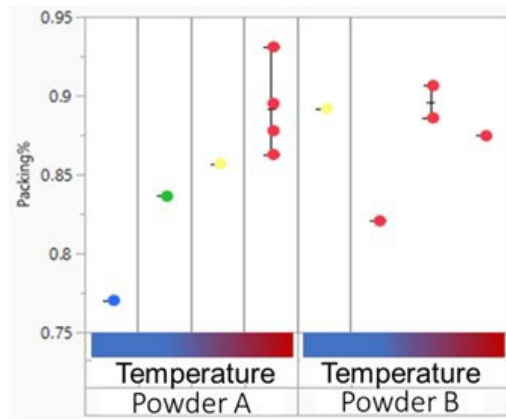


Figure I.2.3.9 Temperature studies: temperature vs. powder packing %.

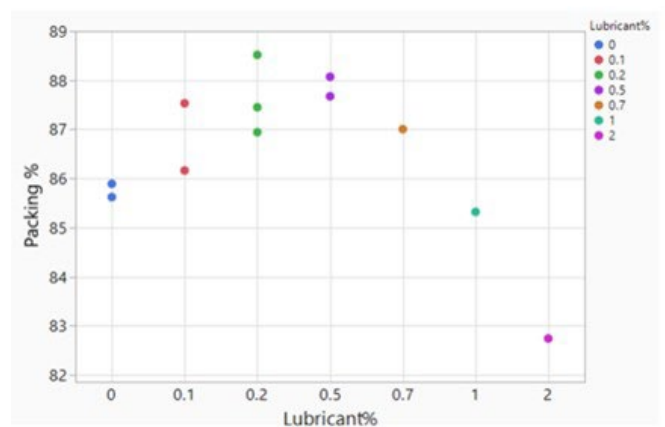


Figure I.2.3.10 Addition of a lubricant compared to packing density (%).

Using initial temperature studies, the lubricant was next optimized under a set temperature. It was clear that lubricant aided in compaction density up to a certain point, but past this concentration it detracted from the density of the magnet (Figure I.2.3.10).

The powder was also aligned and pressed into a magnet to begin exploring the second goal of this project. This work was not done with the aid of temperature or lubrication but done as a baseline to explore the different powder coatings being applied to the iron nitride particles. Figure I.2.3.11 highlights the density differences between pressed magnets from these batches of powder.

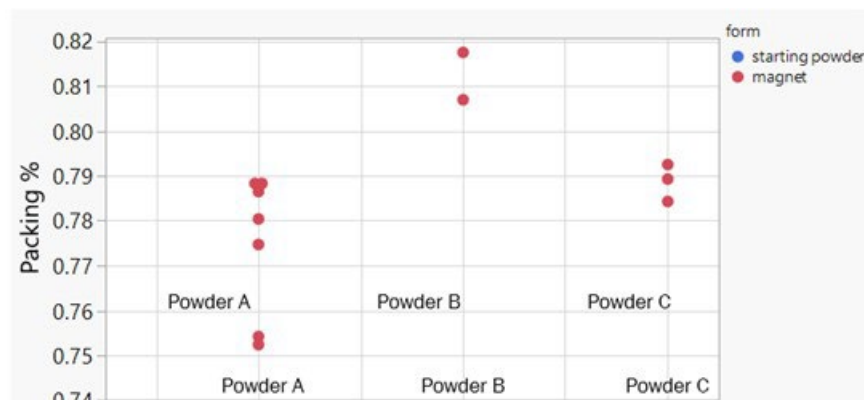


Figure I.2.3.11 Densities of magnets made from different batches of coated powder.

Low-Cost Inverter Development

Below are the key Results from BP1:

1. Electric Drive Topology Investigation concludes that the two-level three-phase voltage source converter topology remains to be the best options among other candidates including multi-level topologies, soft-switching topologies. The cost can be reduced by adopting 1.2 kV MOSFET operating at 800 V dc-link voltage to significantly \$/kW.

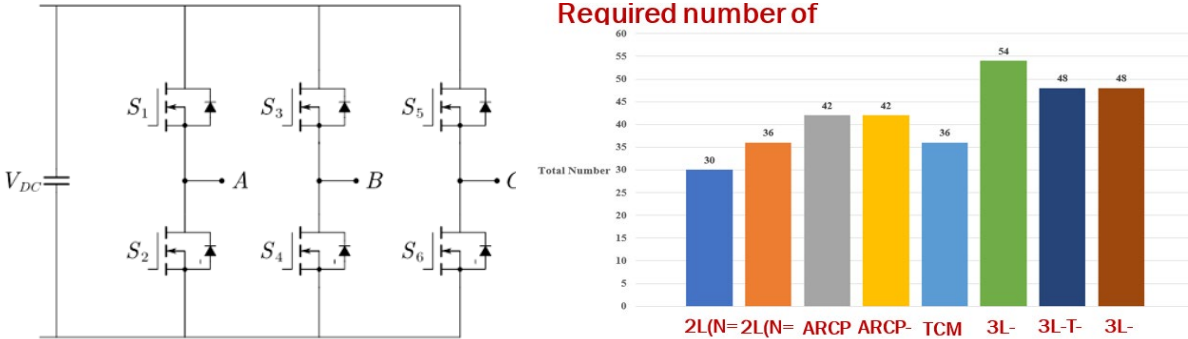


Figure I.2.3.12 Topology Comparison in terms of number of devices needed

2. The team performed detailed investigation and comparison of state-of-the-art 1.2 kV discrete SiC MOSFETs in BP1. The investigation covers both static and dynamic performances. Figure I.2.3.13 and Figure I.2.3.14 shows the summary of the device candidates evaluated and the key results. The recommended device to be adopted in the electric drive design is the Infineon IMZA120R007M1H.

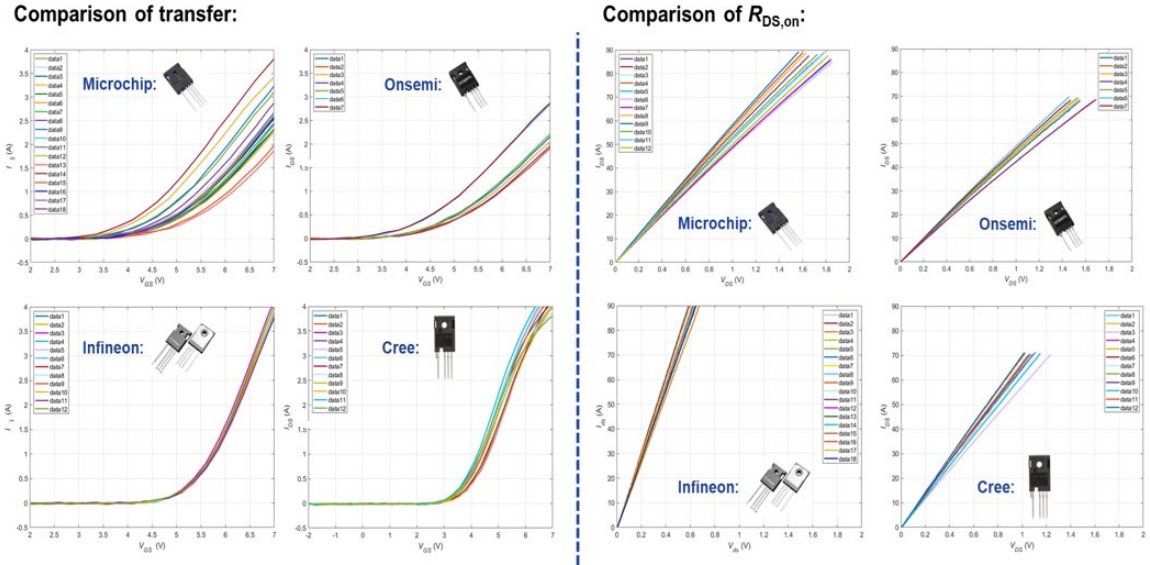



Figure I.2.3.13 Four state-of-the-art 1.2 kV SiC MOSFETs static evaluation and comparison.



	IMZA120R007M1H	C3M0016120K	MSC017SMA120B4	NTH4L020N120SC1
Manufacturer	Infineon	Cree	Microchip	Onsemi
V_{th} Consistency	Best	Good	Worst	Medium
$R_{DS,on}$ Consistency	Best	Medium	Worst	Medium
$V_{overshoot}$ (at both 25 and 100 °C)	Smallest	Medium	Medium	Largest
Switching Energy (at 100 °C)	Largest	Smallest	Medium	Smallest
Measured $R_{DS,on}$ (at 25 °C T_p)	6-7 mΩ	12-14 mΩ	17-24 mΩ	20-22 mΩ
$R_{DS,on}$ on datasheet (at 125 °C T_p)	11 mΩ	19.6 mΩ	22.1 mΩ	28 mΩ
Efficiency (at 20 kHz, N = 4)	99.56 %	99.51 %	99.32 %	99.35 %
Driving voltage	-7/+20 V	-4/+15 V	-10/+23 V	-15/+25 V
Price (from Digikey, Mouser)	\$ 85.1	\$ 91.1	\$ 48	\$ 41

Figure I.2.3.14 Summary of the 1.2 kV discrete SiC MOSFET

3. The paper design and other key components have been designed and selected. One of the key technologies adopted to integrate the electric drive is heavy-copper PCB (HC-PCB) bus-bar solution which can integrate dc-link capacitors, devices, gate-drivers, EM shielding, and sensors together, which reduces the number of miscellaneous components and connectors. Figure I.2.3.15 shows the HC-PCB tested in the BP1.

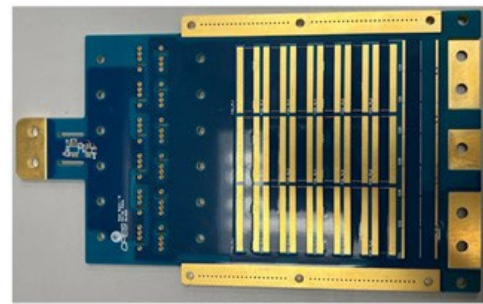
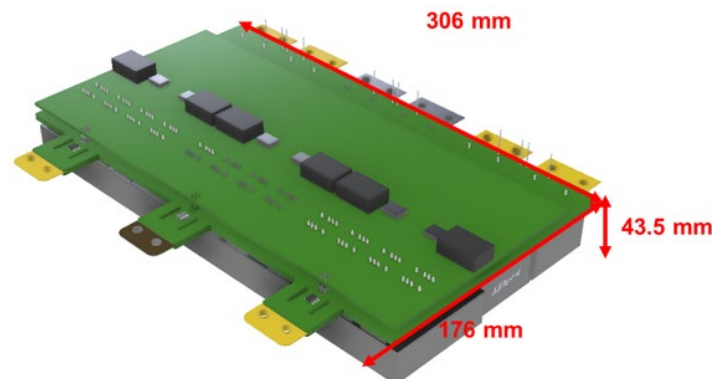


Figure I.2.3.15 HC-PCB Prototype

4. The teams has designed the final 200 kW traction inverter using discrete 1.2 kV SiC MOSFET. Using the proper water-cooling system, the required number of devices per switching position is 4, leading to 36 total number of devices. The expected power density is 85 kW/L.



Power density: 85.37 kW/L (peak power 200 kW)
(Including cold plate, AC sensor, excluding terminals)
Target: 30 kW/L

Figure I.2.3.16 Low-cost 200 kW SiC Traction Inverter design

5. The team also investigated the PCB-embedding technology by using PCB to directly integrate the 1.2 kV SiC MOSFET dies. This allows to further reduce the costs from device packaging, cooling, etc. The team designed and tested two versions of such technologies in the form of a phase-leg with single

die per switch position, as shown in Figure I.2.3.17. The PCB-embedding technology shows superior switching performance, achieving over 70 V/ns with less than 10 V overshoot, as demonstrated in Figure I.2.3.18.

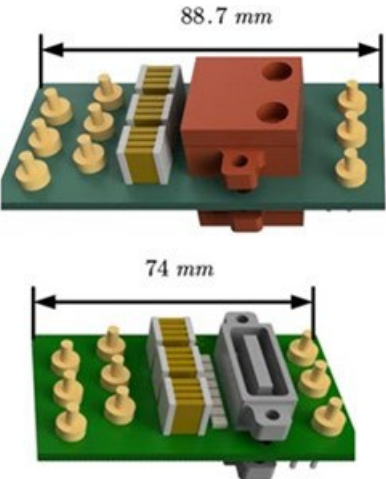


Figure I.2.3.17 1.2 kV SiC MOSFET PCB-embedding phase-legs

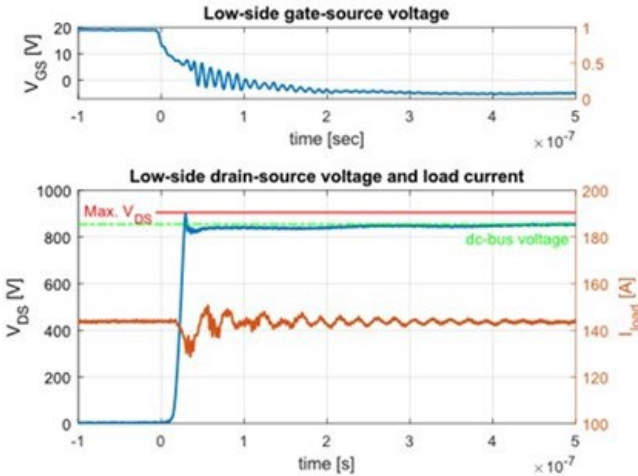
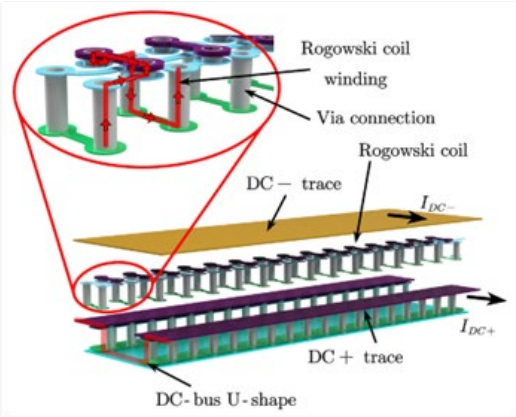


Figure I.2.3.18 Switching speed demonstration of PCB-embedded phase-leg

- 6. The team also designed and demonstrated a novel PCB-based Rogowski current sensor to measure the switching current for protection and control purposes. This sensor can be embedded in the dc-link bus, effectively reducing the EMI challenges in the conventional hall-effect current sensor. Figure I.2.3.19 shows the prototype embedded in the dc-link between the dc-link capacitors and switching devices. Figure I.2.3.20 shows the current measurement performance, which matches with the commercial Rogowski current probe output.

Rogowski coil exploded view:



Top-view X-ray of the planar Rogowski coil:

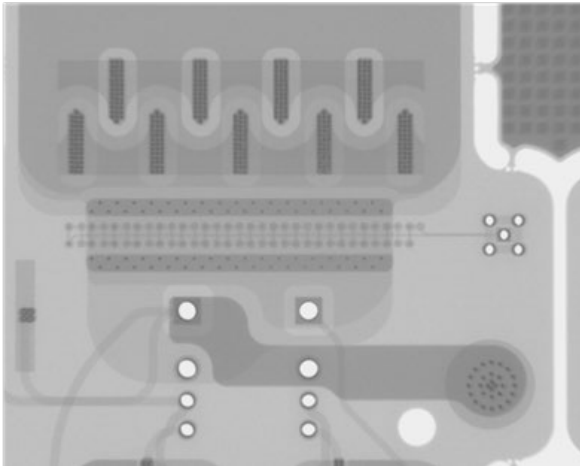


Figure I.2.3.19 PCB-embedded Rogowski current sensor.

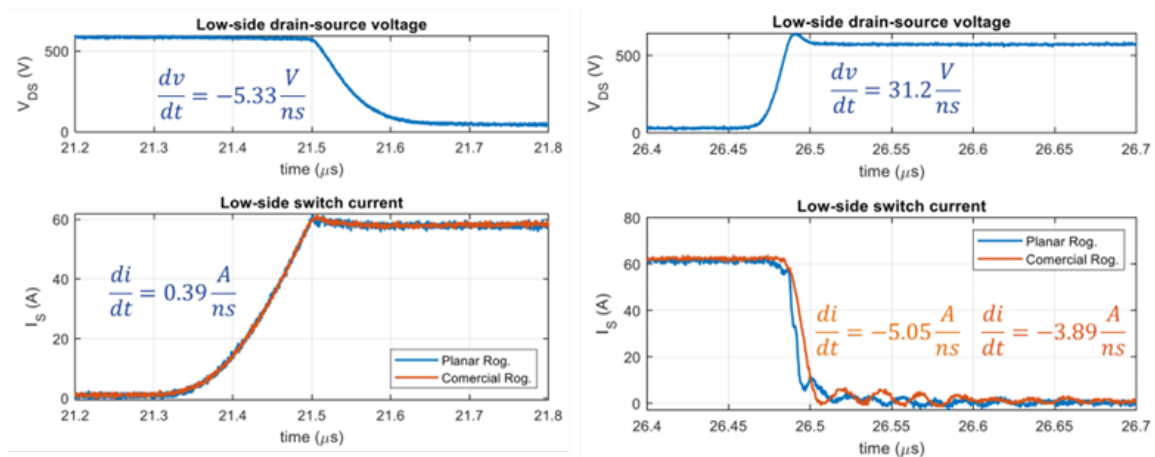


Figure I.2.3.20 PCB-embedded Rogowski current sensor measurement results.

Thermal Management Development

The work at NREL in FY 23 focused on refining the electric motor thermal model and characterizing the thermal performance for several operating conditions. Figure I.2.3.21 shows detailed results for the 9000 RPM operating condition for continuous and peak loading. As shown in the figure, the magnets do not exceed their maximum temperature of 140°C for over 8 minutes, exceeding the 30 s operating time requirement by a wide margin. The stator does not exceed its 180°C at any point during the simulation. For the continuous loading the rotor and stator do not exceed their respective operating temperature in a steady state simulation. Based on these simulations it was determined that oil cooling of the rotor and windings may be unnecessary and a simpler cooling method, such as forced air convection may be utilized and will be investigated in the future.

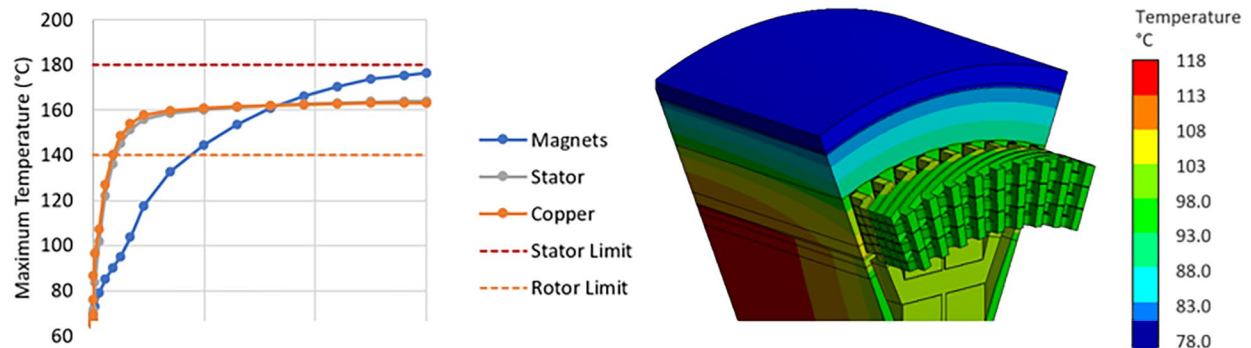


Figure I.2.3.21 Left: Plot of critical temperatures over time for peak loading condition. Right: temperature plot of continuous loading condition at steady-state

The results of power module thermal modeling are provided in Table I.2.3.1 and Figure I.2.3.22.

Table I.2.3.1 Matrix of thermal FEA modeling results for Infineon and Wolfspeed/Cree devices.

Case	Power device manufacturer and model number	Number of parallel devices in switching position	Thermal load per MOSFET device	HTC applied on cold plate surface	Coolant temperature	Maximum device temperature
#			W	W/m ² ·K	°C	°C
1	Infineon IMZA120R007M1H	6	33.7	2500	65	103
2				5000		90
3				7500		86
4		4	55.5	2500	65	122
5				5000		105
6				7500		99
7	Wolfspeed/Cree C3M0016120K	6	33.4	2500	65	102
8				5000		90
9				7500		86
10		4	61.4	2500	65	128
11				5000		110
12				7500		103

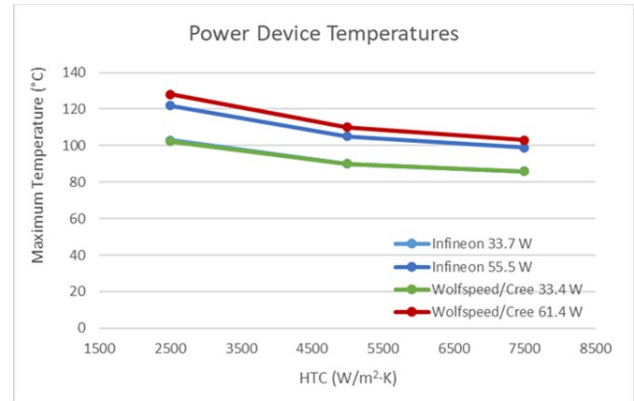


Figure I.2.3.22 SiC discrete power device temperatures at different configurations and cooling intensity.

Based on the initial analysis, the temperatures observed for both 6 and 4 parallel device configurations in each switching position for all cases were below their rated values. Maximum temperature of 128°C for even lowest selected heat transfer coefficient of 2,500 W/m²·K was below desired operating temperature threshold of 150°C. This indicates that with aggressive single-phase cooling power module design with 4 parallel devices in each switching position should be achievable.

Conclusions

Technical achievements by Marquette University (MU) include the following:

- Finished benchmarking of Chevy Boly traction motor
- Finished developed optimized designs that reduce/eliminate rare earth materials based on the Chevy Bolt specifications.
- Continued developing various designs (various magnet combinations, different number of magnet layers, and different number of poles) based on the new set of specs including higher speed and DC bus voltage.

Technical achievements by Niron Magnetics include the following:

- Niron Magnetics, Inc. is developing Iron Nitride, a high performance, completely rare earth free permanent magnet technology. The Goals & Objectives of Niron Magnetics are to develop iron nitride permanent magnets with an energy product of 36 MGOe and produce 2 kg of these magnets for integration into a prototype motor. In the first budget period, a process for producing iron nitride nanoparticles with a nanometer scale ductile coating has been demonstrated. The composition, thickness, and uniformity of the coating have been verified experimentally. Consolidation of the material has led to densities of ~93% density. In the second budget period, alignment of the coated nanoparticles was achieved with various batches of coated powder.

Technical achievements by Virginia Tech (VT) include the following:

- Virginia Tech has performed the major device evaluation and critical sub-component and circuit integration technology prototyping. The main conclusion is that discrete 1.2 kV SiC MOSFET devices, PCB bus integration, surface-mount-sensor are critical components to enable low-cost high-density high-efficient electric drive system. The team continued efforts to assess and minimize any level of imbalance in terms of current sharing among multiple parallel devices.

Technical achievements by NREL include the following:

- During FY23 NREL refined the motor thermal model based on feedback from GM and Marquette, including updates to the rotor geometry and losses, as well as stator losses. Temperature limits were defined and the thermal model was used to characterize the thermal performance of the motor at 4 operating points, including continuous load and peak load for each operating point. Work in FY24 will include continued refinement of the rotor model and investigation into alternative cooling methods for the rotor such as forced air.
- The power module thermal model evaluation provided an initial assessment that single-phase cooling should be sufficient for handling SiC discrete power device losses. NREL is currently working on a more detailed power module thermal analysis which includes PCB-integrated busbar losses. Work in FY24 will focus on evaluation of thermal management strategies for complete power module and power electronics integration in the motor.

Key Publications

1. Ali Al-Qarni and Ayman EL-Refaie, “Design and Optimization of High-Performance Rare-Earth Free Interior Permanent Magnet Motors for Electric Vehicles Enabled by Iron Nitride Magnets” ECCE 2023.
2. Praveen Kumar, Robin Wilson, Towhid Chowdhury and Ayman EL-Refaie, “Multi-Objective Design Optimization and Comparison of 2-layer versus 3-layer Blended Permanent Magnet Assisted Synchronous Reluctance Machine Topologies” ECCE 2023.
3. Robin Wilson, Praveen Kumar and Ayman EL-Refaie, “Minimization of Rare-Earth Permanent Magnets and Demagnetization Risk in PM-Assisted Synchronous Reluctance Motor with Blended Magnets” ECCE 2023.
4. Praveen Kumar, Robin Wilson and Ayman EL-Refaie, "Effect of Varying Number of Poles on Performance of a PM-Assisted Synchronous Reluctance Machine Enabled with Iron Nitride Magnet Combinations," IECON 2023- 49th Annual Conference of the IEEE Industrial Electronics Society, Singapore, Singapore, 2023, pp. 1-6.
5. Praveen Kumar, Robin Wilson, and Ayman EL-Refaie, “Optimization of the Magnetization Direction of Magnets in a PM-Assisted Synchronous Reluctance Machine to Minimize Demagnetization”, IEMDC 2023.
6. Robin Wilson, Praveen Kumar, Ali Al-Qarni, Qingqing Ma and Ayman EL-Refaie, “Robustness of Dynamic FEA-based Demagnetization Calculation in the Multi-Objective Optimization of PM-assisted Synchronous Reluctance Motor with Blended Magnets”, IEMDC 2023
7. Ali Al-Qarni, and Ayman EL-Refaie, “Optimum Rotor Design for Rare-Earth Free High Performance Traction Applications Interior Permanent Magnet Motors”, IEMDC 2023

8. M. Spieler, C. Chang, D. Dong, R. Burgos, M. Alvi and A. EL-Refaie, “A DC-Bus Planar Rogowski Coil Based Current sensor for Half-Bridge Applications,” *IEEE 23rd Workshop on Control and Modeling for Power Electronics (COMPEL), 2023*.
9. C. Chang, M. Spieler, R. Burgos, D. Dong, “Evaluation and Efficiency Comparison of Soft-Switching ARCP SiC-based Traction Inverters in Electric Vehicles,” *IEEE Applied Power Electronics Conference and Exposition (APEC), 2023*.
10. M. Spieler, C. Chang, A. EL-Refaie, M. H. Alvi, D. Dong, R. Burgos, “PCB Technology Comparison Enabling a 900 V SiC MOSFET Half-Bridge for Automotive Traction Inverters,” *24th European Conference on Power Electronics and Applications (EPE), 2022*.

Acknowledgements

The project team would like to acknowledge the help and support from Mr. John Tabacchi, the retired NETL program manager as well as Mr. Benjamin May, the current NETL program manager.

I.2.4 Low Cost High-Performance HRE-Free 3-in-1 Electric Drive Unit (American Axle & Manufacturing)

Mr. David Crecelius, Principal Investigator

American Axle & Manufacturing
One Dauch Drive
Detroit, MI 48211
E-mail: David.Crecelius@aam.com

Susan Rogers, DOE Technology Development Manager

U.S. Department of Energy
E-mail: Susan.Rogers@ee.doe.gov

Start Date: October 1, 2020

End Date: October 31, 2024

Project Funding: \$7,799,531

DOE share: \$5,000,000

Non-DOE share: \$2,799,531

Project Introduction

The project team will expand upon American Axle & Manufacturing's (AAM) baseline technology and develop a high-speed, AC induction electric drive unit (EDU) with total direct-oil-cooling and integrated power electronics. The project will accelerate advancements in EDU technology by allowing AAM to build upon the progress made in developing the underlying baseline technologies. The following seven improvements to AAM's baseline technology are being implemented in this research and development program: 1) Increased speed (30k RPM) AC induction motor, 2) Silver-sintering of discrete silicon carbide (SiC) metal-oxide-semiconductor field-effect transistors (MOSFET) to heat sinks, 3) Electrically insulated rotor bars, 4) Optimized lamination steel, 5) EDU-integrated 650VDC inverter package, 6) Over-molded stator with molded liners, and 7) 650VDC power-dense stator design.

Successful development of the technology will result in a substantial cost reduction for EDU systems in the market. Coupled with falling battery system costs, this will accelerate the market acceptance and related production scaling of battery electric vehicles.

Objectives

The objective of this project is to research, develop, and test a Heavy Rare Earth (HRE)-free 3-In-1 electric drive unit that has class leading power density and cost. The key technologies to be developed will meet or exceed the Department of Energy (DOE) targets of a cost \leq \$7/kilowatt, power density \geq 12 kW/liter, and operating voltage \geq 600 VDC.

Approach

Technology development within the project will build upon and reference against the AAM baseline Gen 5.0 EDU.

The project is being conducted in three (3) phases:

Design Development and Technology Research (Budget Period 1)

- Design, investigate, and develop core technologies
- Investigate stator lamination and over molding development, high speed motor development, and silicon carbide MOSFET packaging development
- Investigate, analyze, and assess costs of the developed technologies
- Select an optimized configuration for prototype build in Budget Period (BP) 2

Prototype Component Fabrication and Unit Build (Budget Period 2)

- Fabricate over molded stators, high speed motors, and MOSFET silver sintered attachments
- Assemble motor-only units and full EDUs for subsequent dyno testing
- Test the motor-only units on the dyno with the test results being compared to the baseline.

Prototype Testing and Commercialization Planning (Budget Period 3)

- Test the full EDU on the dyno, with the results being compared to the baseline technology
- Document the EDU Bill of Materials (BOM) for comparison to benchmarked EDUs and cost targets
- Prepare a manufacturing and commercialization plan to produce the developed technology in high volume.

Results

During Fiscal Year 2023 the project team completed Budget Period 2 tasks as reported below.

Task 2.1 – Fabricate Prototype Components**MOSFET Heat Sinks**

Due to a change required in the ring inverter, the heat sink design was modified. Figure I.2.4.1 shows the updated design of the MOSFET heat sink.

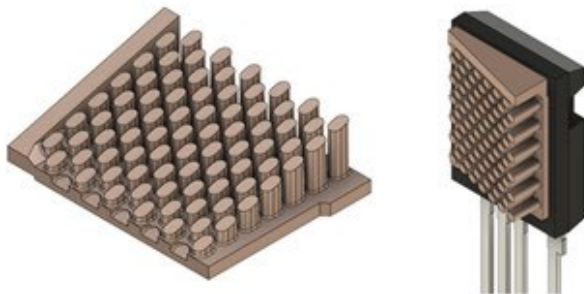


Figure I.2.4.1 Modified MOSFET heat sink design

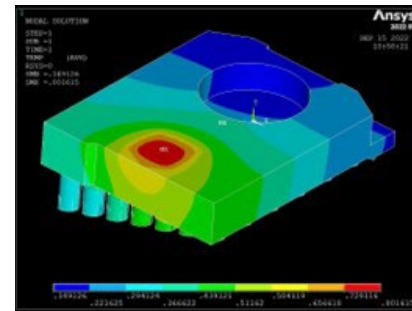


Figure I.2.4.2 Thermal FEA analysis of new heat sink

The new heat sink design was analyzed to confirm that its performance would meet the requirements of heat transfer from the MOSFET back plate to the cooling oil. Figure I.2.4.2 shows results of the thermal finite element analysis (FEA) run on the new heat sink design, resulting in projected performance of 0.8 deg C/W, which is similar to that of the baseline design.

The MOSFET assemblies with a copper sintered heat sink attachment were completed on February 28, 2023, resulting in accomplishment of Milestone 2.2. 55 of these assemblies were received and are now ready for integration into the ring inverter. Figure I.2.4.3 shows the completed assembly.

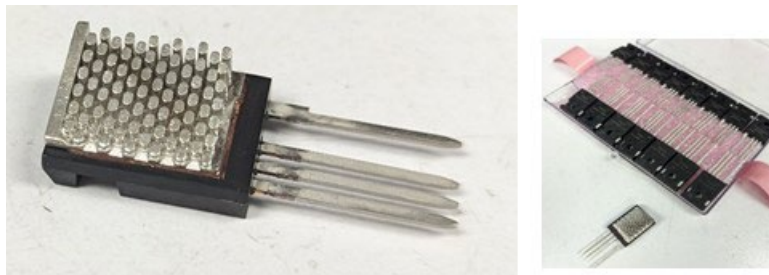


Figure I.2.4.3 Copper sintered MOSFET assemblies

Stator and Rotor Fabrication

The stator core using M15 lamination material was wound and is shown in Figure I.2.4.4. A second core made with Arnon7, a lower loss magnetic steel, was also received. These cores are shown in Figure I.2.4.5.

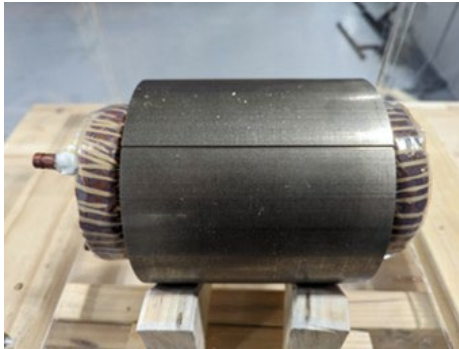


Figure I.2.4.4 Stator core with completed winding

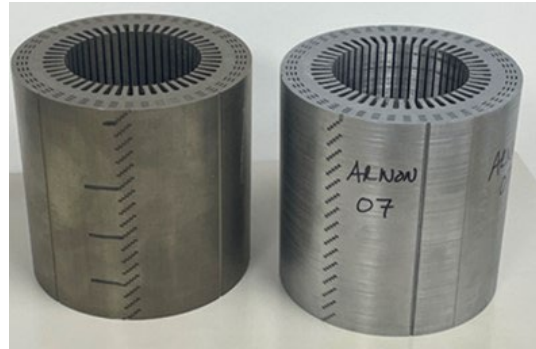


Figure I.2.4.5 Stator cores with M15 material (left) and Arnon7 material (right)

High speed induction rotors were assembled using the non-insulated and insulated copper rotor bars and are shown in Figure I.2.4.6.

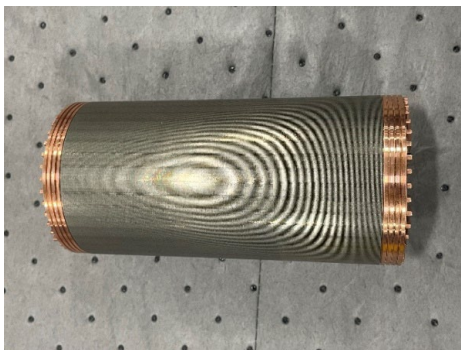


Figure I.2.4.6 Assembled induction rotor with non-insulated copper bars (left) and insulated copper bars (right)

Laser welding was used to connect the copper end rings to the insulated and non-insulated rotor bars.

The rotor shaft with an integrated spline gear, including the oil cooled heat sink inserts and end plug, was assembled. This shaft was then inserted into the rotor assembly. Figure I.2.4.7 shows the rotor shaft assembly and oil cooled heat sink inserts.

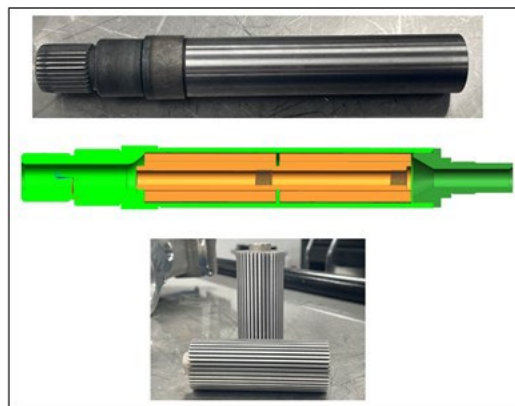


Figure I.2.4.7 Rotor shaft assembly with oil cooled heat sink inserts

The output shaft for the motor only unit was completed. This shaft interfaces with the rotor shaft spline and allows an external mechanical interface to the high-speed dyno.

Over Molded Stator Fabrication

Stator winding was adversely affected due to supply chain issues which caused the over molding project to be delayed at the supplier.

The over molded stator was required to complete the motor only testing. In order to complete milestone 2.4 in BP2, a recovery plan was developed and implemented. An alternative encapsulation method (epoxy vacuum encapsulation), utilizing a LORD EP-3500 epoxy material having similar thermal performance, was developed for the first stators. It included the design and fabrication of silicon molds placed on the end turns of the wound stator and then vacuum potted. Stators were over molded using the alternative encapsulation method. This allowed the motor only testing to be completed.



Figure I.2.4.8 Potted stator assembly using EP-3500 material

Figure I.2.4.8 shows the resultant potted stator assembly with the EP-3500 material. This potted stator was then assembled into the motor housing.

Subsequently, stators using the plastic injection over molding process were received. A Sabic OX11315 material was used for the initial injection over molding process. After the first part was attempted in the injection molding machine, it was clear this material would not properly flow to fill the part due to the high filler content used for increased thermal conductivity. An alternate material was selected based on feedback from the molding supplier. The material selected was a CoolPoly D5110 that allowed for better flow properties at the expense of thermal conductivity. However, the CoolPoly material still achieves a thermal conductivity of 1.0 W/mK. Figure I.2.4.9 shows the over molded stator using the CoolPoly D5110 material. With fabrication and delivery of the injection over molded stator, BP 2 Milestone 2.1 was completed on June 28, 2023.



Figure I.2.4.9 Injection over molded stator assembly using CoolPoly D5110

Other Component Fabrication

A custom rotor position sensor is required for the motor only portion of the prototype testing. This is due to the need to flow the rotor oil in the reverse direction with the oil inlet on the inverter end of the shaft instead of the gear box end. Without a gearbox connected there is no way to flow oil into the rotor shaft at the gearbox end. The position sensor is located on the inverter end of the shaft in the fully integrated EDU. With the need to flow oil into the inverter end of the shaft, however, the position sensor must be moved. The new custom rotor position sensor was received and was mounted external to the EDU on the empty gearbox housing for the motor only configuration.

The machined motor housing was completed. This housing includes the DC link capacitor recess and mounting bosses. Figure I.2.4.10 shows the machined motor housing.

The output (dummy) housing for the motor only unit was completed as a machined assembly and is shown in Figure I.2.4.11. It replaces the gearbox for the motor only unit and includes an oil reservoir and pump attachment point.



Figure I.2.4.10 Machined motor housing

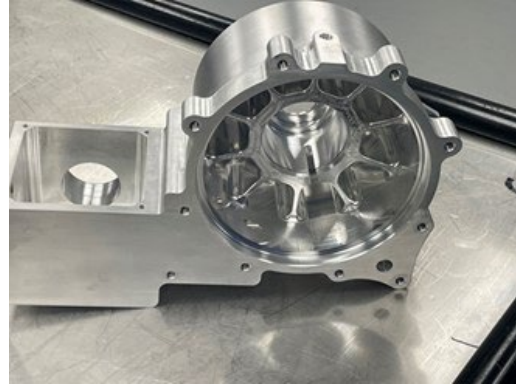


Figure I.2.4.11 Output housing for motor only

The 650V ring inverter needed a design modification to meet the creepage and clearance requirements to operate at this voltage. To gain the space required by the design, the number of MOSFETs was reduced from 5 devices per switch bank to 4. Additionally, since the required phase current of the selected motor design is 350Arms, which is 100Arms lower than the baseline design, the number of MOSFETs could be reduced without affecting the system performance, while contributing to a cost reduction. This necessitated the need for redesigning the MOSFET heat sink. Additionally, the new spacing of the MOSFETs required a change to the inverter gate drive board.

Figure I.2.4.12 shows the completed power stage with 24 MOSFET devices. A new gate drive printed circuit board (PCB) was assembled and then attached to the power stage and is shown in Figure I.2.4.13.

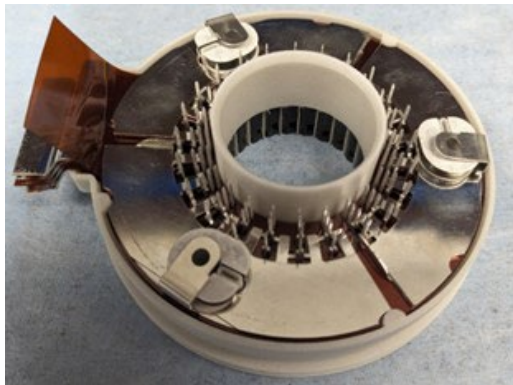


Figure I.2.4.12 Assembled power stage with 24 MOSFETs

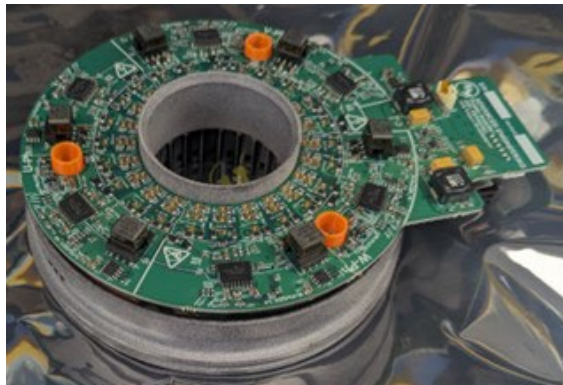


Figure I.2.4.13 Assembled power stage with gate drive PCB

Task 2.2 – Build Prototype Motors & EDUs

Motor Only Assembly

The first assembly of the motor only unit was completed on June 7, 2023, achieving partial completion of Milestone 2.3. Figure I.2.4.14 shows the motor only unit on the high-speed dyno. During the first check-out of the motor only unit it was discovered that oil was entering the air gap and causing excessive drag torque. Further investigation showed that the drain back passages in the housings needed to be modified to correct the problem. Also, it was discovered that the bearing journal in the back cover was tapered and did not allow the bearing to seat properly. Design modifications to the housing and cover were completed to address these issues.

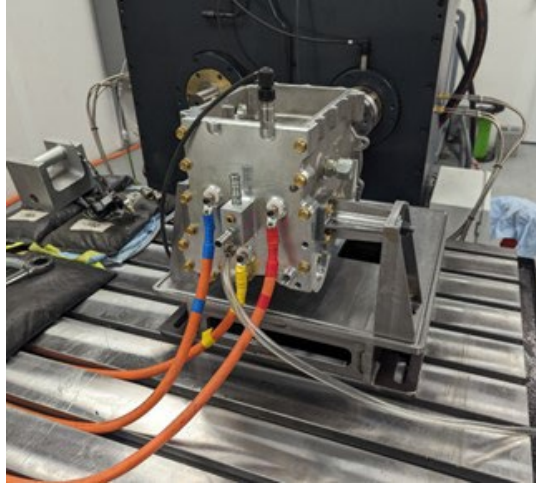


Figure I.2.4.14 Motor only unit on high speed dyno

Full EDU Assembly

Most of the components for the full EDU assembly have been received. The remaining parts needed before integration can begin are the gearbox housing and finished gear set.

Task 2.3 – Test High Speed Induction Motor

High Speed Dyno Install and Commissioning

The high-speed dyno assembly was updated with a new base plate and fixture table. To accommodate the new dyno, a lab expansion was completed which provides more space for the dyno, chillers, data acquisition system, and high voltage battery simulator.

The motor only testing was started by spinning the unit on the high-speed dyno. During the initial no load testing it was discovered that the dyno and motor only assembly showed excessive vibration. Upon further investigation and vibration data collection, it was observed that the dyno output section, including the high-speed torque cell, was not properly designed and balanced. A redesign was completed on the torque cell mounting and interface shaft components. New fixture components were required to be fabricated, which delayed starting the motor only testing. The motor only dyno test setup is shown in Figure I.2.4.15.

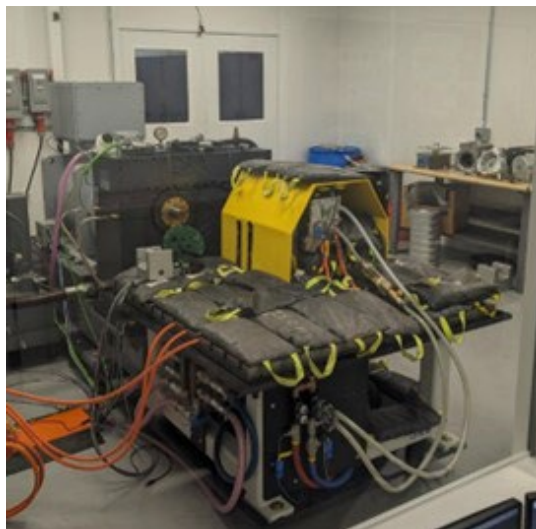


Figure I.2.4.15 Motor only dyno test setup

After the dyno output section was redesigned and balanced the assembly still had excessive vibration. A vibration analysis was completed of the system stiffness; results showed the need to increase the stiffness of the back cover of the motor assembly. The back cover was redesigned with additional ribs, fabricated, and installed in the motor. The motor was then decoupled from the dyno and successfully spun up to 30k RPM with acceptable vibration levels. Upon reconnecting the motor only unit to the torque cell shaft assembly and the high-speed dyno shaft, the system completed a speed sweep to check high speed operation at no load. Excessive vibration levels were again observed as the dyno speed approached 16k RPM. Further investigation was completed on the dyno side of the system. It was discovered that the high-speed output shaft from the dyno had a high runout measurement and was the cause of the high vibration. Therefore, the motor only testing was limited to a maximum speed of 15k RPM for the tests completed during BP2. Testing of the motor up to the designed 30k RPM will be completed in BP 3, when the motor is tested in the full EDU assembly. Peak power of the motor is achieved at its base speed of 10k RPM. Testing completed during BP2 confirmed the power density of the design.

Test Plan and Test Results

A test plan for the motor only unit was developed and executed. The plan includes evaluation of the motor parameters, insulation system, spin losses, and motor performance across the operating envelope. All tests within the test plan were completed and passed. Peak torque of the motor was measured to be 200.6 Nm, peak power was 223.6 kW and peak motor efficiency was measured to be 94.24%. These measured values align well with the MotorCad simulation model and expected performance of the motor.

Task 2.4 – Estimated EDU Costs

The estimation process has been completed by a 3rd party supplier. Data from the 3rd party estimator shows the directional costs to be <\$6.50/kw, meeting the DOE target of <\$7.00/kW.

Conclusions

Through September 2023, the project team completed procurement of all motor only parts and most of the full EDU components and built the motor only assembly. Testing of the motor only unit was completed using the developed test plan; results exceeded those for the baseline design and aligned well with the simulated analysis. The resultant motor only data supports a conclusion that the design achieves all technical objectives of the project: power density > 12kW/L, bus voltage > 600VDC, and estimated cost < \$7/kW.

II Grid and Charging Infrastructure

II.1 Industry Awards

II.1.1 High-Power Inductive Charging System Development and Integration for Mobility

Omer C. Onar, Principal Investigator

Oak Ridge National Laboratory, Vehicle Power Electronics Research Group (VPER) Group
National Transportation Research Center, 2360 Cherahala Boulevard
Knoxville, TN 37932
E-mail: onaroc@ornl.gov

Lee Slezak, DOE Technology Development Manager

U.S. Department of Energy
E-mail: Lee.Slezak@ee.doe.gov

Start Date: October 1, 2019

End Date: September 30, 2024

Project Funding: \$4,707,901

DOE share: \$2,207,901

Non-DOE share: \$2,500,000

Project Introduction

Extreme fast charging (XFC) is considered one of the most important research topics in the field of electromobility with the potential to significantly reduce charging times and range anxiety. With extreme fast charging, i.e., charge rates higher than or equal to 3C, it is possible to reduce EV charging times to 10 minutes for 50% increase in the battery state-of-charge (SOC). However, there are several challenges for establishing XFC systems, such as logistics and infrastructure requirements, design and deployment of the grid interface converters, grid power quality (power factor and harmonic distortions), availability of the power (integration with renewable energy or energy storage systems if needed), isolation requirements, distribution voltage level at the point of grid connection, hardware connectivity, power electronic semiconductor and architecture limitations, thermal management systems, and the vehicle side power delivery architectures. High-power wireless power transfer (WPT) is an attractive option for fast charging because the user is not required to handle any heavy and bulky high-power equipment. WPT is also a key enabling technology for autonomous vehicles. However, power transfer capability of WPT systems is closely linked to the size and mass of the transmitter and receiver pads. The feasibility of high-power WPT systems greatly depend on the ability to improve the power density and specific power of wireless charging systems. The difficulties of high-power wireless charging are exacerbated by the need to meet the same practical constraints associated with vehicle integration as lower power systems. Therefore, more advanced techniques are necessary to improve power density and specific power of wireless charging systems for high-power applications. This project focuses on a WPT system with bipolar phase windings with significantly increased surface and volumetric power density of the couplers.

The primary objective of this project is to address the challenges of XFC charging systems for electric vehicles that increases their utilization factors, improves the total electric miles traveled, and improves their return on investment that results in industry and consumer acceptance. The project also reduces the technology costs through a modular and reconfigurable power electronics architecture and by leveraging the current DOE research activities in power electronics, wide bandgap device-based power electronic converters, vehicle systems, wireless charging systems, and modernization of grid infrastructures in order to meet the project goals. Technology developed in this project is transferable to other vehicle classes such as medium-duty and heavy-duty vehicles.

Objectives

This project is the first research effort that will showcase an inductive XFC charging system with all the outlined functionalities such as using a polyphase electromagnetic coupling coils and a modular, scalable, reconfigurable power electronic converter architecture. The overall goals of the project to address the challenges of XFC charging systems are:

1. Model, simulate, design, develop, test, validate, and integrate a polyphase inductive coupling system that supports a variety of vehicle ground clearances that is designed for 100-kW and 300-kW nominal power levels,
2. Design and develop a polyphase electromagnetic coupling coils with optimal geometry for the highest utilization of the coupler surface area,
3. Achieve end-to-end high charging efficiencies greater than 90%,
4. Integrate wireless charging equipment to test vehicles, and
5. Understand and address vehicle integration issues and demonstrate the proposed 100-kW and 300-kW vehicle integrated wireless charging equipment.

Approach

Starting from the ac grid to the vehicle battery terminals, the system power converters must be well-designed and operated in order to achieve high efficiency. In addition, power flow control to the secondary system should be resolved where the control parameters (dc link voltage, frequency, duty cycle, phase-shift, etc.) are actively controlled to improve efficiency while meeting the vehicle-side target voltage, current, and/or power. In this project, team used iterative design and utilized finite element analysis (FEA) based modeling for the design optimization of the electromagnetic coupling coils. Vehicle battery and grid voltage and power levels are used for the proper system design and cascaded down to the appropriate subsystems and components. Furthermore, research team modeled and simulated the grid interface (front-end) power blocks based on the dc link voltage requirements of the proposed system and the grid infrastructure parameters. Also, the system power conversion stages are designed in an integrated approach for an optimal system design in terms of complexity and compactness. Regarding the system tests, all the power conversion stages are being tested and validated individually before the full system integration (for functionality and performance) which is followed by the entire system tests using grid and battery emulators before vehicle integrations. Although it was not required, team also designed and developed a prototype for proof of concept before designing and developing the high power scaled couplers and converters. The system level circuit diagram of the proposed system is given in Figure II.1.1.1. Also shown in Figure II.1.1.1 is the double-sided LCC resonant tuning configuration implemented both for primary and secondary side with each phase having a dedicated compensation circuitry. In this extreme fast inductive charging system, primary-side power electronics, resonant tuning components, and the primary coupler are interoperable both with the 100-kW receiver and 300-kW receiver systems. In order to achieve high-power at the high-frequency inverter level, the drive system uses open-ended winding dual-inverter design using two inverters sharing the same dc bus. This can also be interpreted as using 3 H-bridge inverters with each inverter feeding one phase of the primary coupler. Using a single three-phase inverter was not possible with ~300-kW output power due to current rating and thermal constraints of the semiconductor power devices. Although a second inverter increases number of components and the complexity, the total power rating and the power density of the drive system is significantly increased as this inverter assembly can provide up to 500-kW at the input. This approach doubles the effective output voltage while maintaining dc-link capacitor size reduction compared to a single 3-phase inverter. Similarly, on the vehicle-side rectifier, an open-ended winding rectifier architecture is used to achieve high-power where each phase of the receiver has its own dedicated H-bridge rectifier. While the 100-kW system operated earlier with about 90.8% efficiency, project team modified and optimized the resonant tuning network of the secondary side to improve the efficiency. The modified tuning capacitor values for the single-

phase equivalent circuit are provided in Figure II.1.1.2. The coupler diameter, surface area, and surface power density parameters are shown in Figure II.1.1.3.

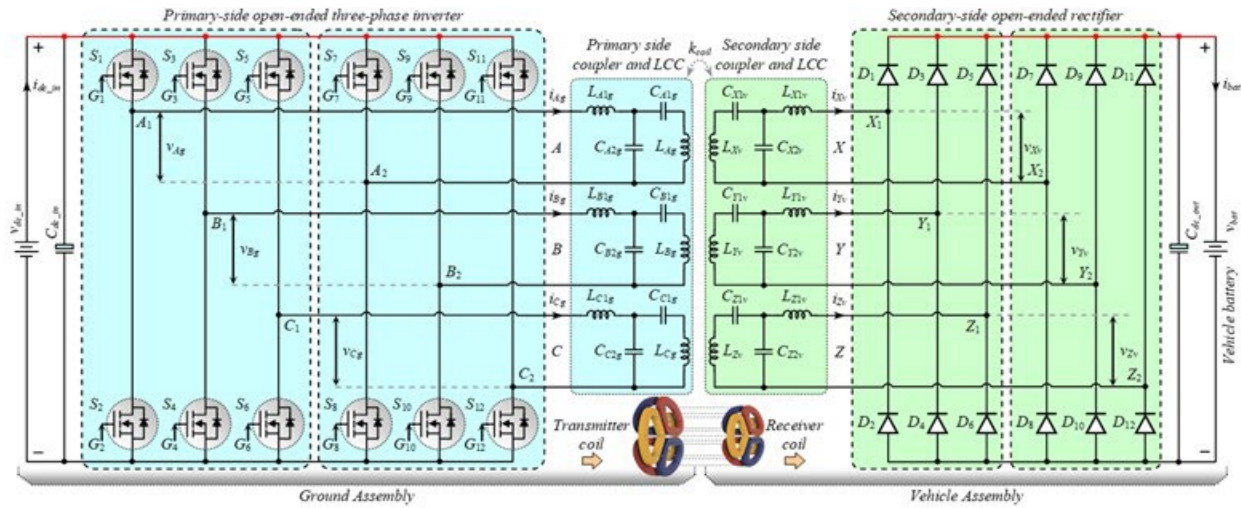


Figure II.1.1.1 System level diagram of the proposed XFC inductive charging system with open-ended winding inverter and rectifier designs and LCC-LCC resonant tuning components.

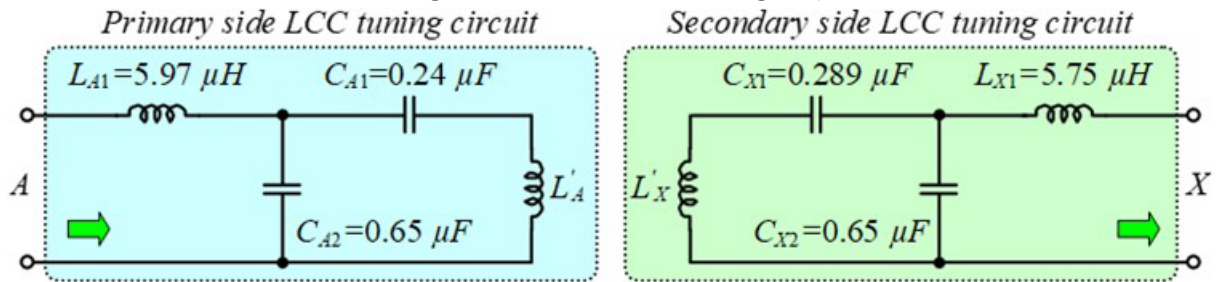


Figure II.1.1.2 The LCC-LCC tuning circuit designed for primary and secondary side in the hardware design.



Figure II.1.1.3 Transmitter and receiver coil diameters, geometric designs, and surface power density.

Results

The 100/300-kW interoperable transmitter coupler and the 100-kW receiver designed and developed for Hyundai Kona characterized in the laboratory for the self and mutual inductances and these results are shown in Table II.1.1.1. This table includes the ground assembly self- and mutual inductances, vehicle-assembly self- and mutual inductances, as well as the ground assembly to vehicle assembly mutual inductances obtained using diagonal series/anti-series method. The experimental test setup is shown in Figure II.1.1.4 where the primary and secondary side hardware is displayed that includes the open-ended winding inverter and rectifier and LCC-LCC resonant tuning components and liquid cooling systems. The setup also includes the coupling coils and multiple instrumentation devices and test equipment including the multi-channel power analyzers and oscilloscopes. Figure II.1.1.5 (a) shows the system efficiency with 1.9 Ohm load resistance while Figure

II.1.1.5 (b) shows the efficiency for a 390V battery load condition to demonstrate the system performance with 100-kW power transfer rate and over 94% efficiency. This figure also shows the input and output voltage, current, and power for these test conditions.

Table II.1.1.1 Primary and Secondary Side Coupler Specifications

	Inductance Parameter	Inductance Value (Simulated)	Inductance Value (Measured)
GA Self- and Mutual Inductances	L_{Ag}	17.56	17.56
	L_{Bg}	17.12	17.12
	L_{Cg}	17.65	17.65
	M_{AB}	-4.65	-4.65
	M_{BC}	-4.65	-4.65
	M_{CA}	-4.60	-4.60
VA Self- and Mutual Inductances	L_{Xg}	14.79	14.79
	L_{Yg}	14.87	14.87
	L_{Zg}	15.02	15.02
	M_{XY}	-4.12	-4.12
	M_{YZ}	-4.22	-4.22
	M_{ZX}	-4.01	-4.01
GA to VA Coupler Mutual-Inductances	M_{Ax}	2.15	2.15
	M_{Ay}	-1.87	-1.87
	M_{Az}	-0.64	-0.64
	M_{Bx}	-0.65	-0.65
	M_{By}	2.44	2.44
	M_{Bz}	-1.79	-1.79
	M_{Cx}	-1.86	-1.86
	M_{Cy}	-0.76	-0.76
	M_{Cz}	2.33	2.33

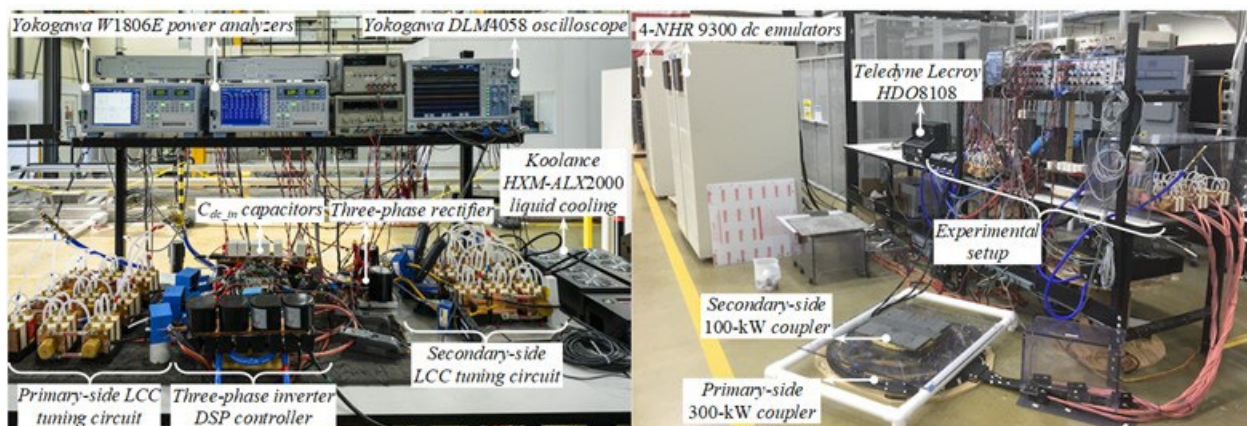


Figure II.1.1.4 Experimental test setup with the hardware and instrumentation.



(a) (b)

Figure II.1.1.5 Power analyzer results for 100-kW power transfer for resistive load (a) and battery load (b) test conditions.

In Figure II.1.1.6, the system efficiency for 10-kW increments is plotted for up to 100-kW power transfer. According to this figure, the efficiency is almost flat and above 94% for over 20 kW load power conditions. Even at 5% of the load, system can maintain over 93% efficiency. This system also maintains the same power transfer rate and efficiency for up to 4 inches of misalignments in any direction.

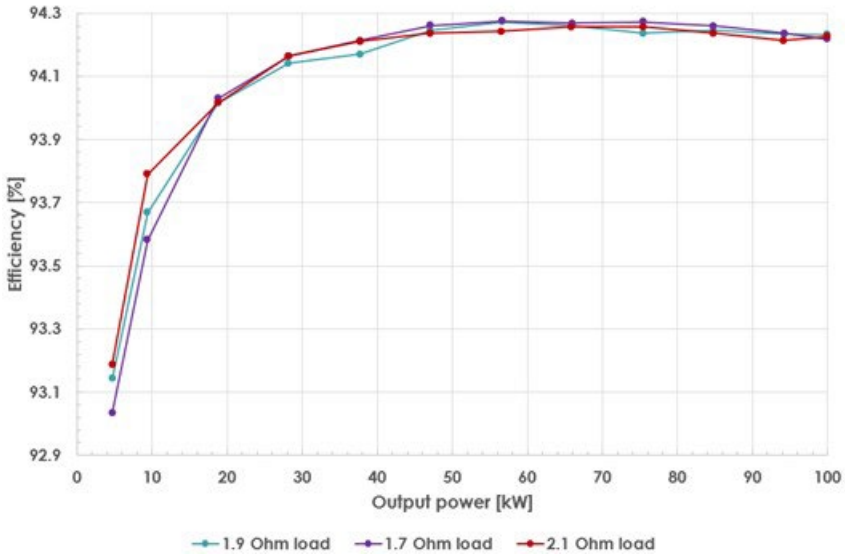


Figure II.1.1.6 Primary-side waveforms and RMS measurements including the inverter input voltage and current and the inverter output Phase-A, B, and C voltage and current measurements.

Conclusions

This project started with modeling, simulations, analysis, and design of the system power conversion stages and control systems and the project team completed the design and simulations of the polyphase inductive charging system with a 300-kW interoperable transmitter and primary-side power electronics that can operate with 100- and 300-kW receiver systems. Within the last couple of budget periods, project team completed all the hardware development, prototyping, and wiring efforts as well as the testing and troubleshooting. This last FY was dedicated to system optimization and efficiency improvements with 100-kW power transfer rate achieved with efficiencies exceeding the project target. The 100-kW power transfer will be demonstrated on a Hyundai Kona EV during next month and the project focus will be on the 270-kW power transfer rate with the

new transmitter and resonant tuning network. The new receiver rated for 300-kW will be slightly larger than the 100-kW receiver and will have a 500 mm diameter that achieves 1.5 MW/m² surface power density.

Key Publications

1. “Overview of High-Power Wireless Charging Systems and Analysis of Polyphase Wireless Charging System Phase Winding and Resonant Tuning Network Connection Configurations,” Accepted for publication, IEEE Transactions on Transportation Electrification, May 2023.
2. “Magnetic Shield Design for Double-D Coil-Based Wireless Charging System,” IEEE Transactions on Power Electronics, vol. 37, np. 12, pp. 15740-15752, December 2022.
3. “A 100-kW Wireless Power Transfer System Development Using Polyphase Electromagnetic Couplers,” in Proc., IEEE Transportation Electrification Conference and Expo (ITEC), pp. 273-278, June 2022, Anaheim, CA.
4. “Modeling and Analysis of a Polyphase Wireless Power Transfer System for EV Charging Applications,” in Proc., IEEE Applied Power Electronics Conference and Exposition (APEC), pp. 1885-1890, March 2022, Houston, TX.
5. “Thermal Design and Optimization of High- Power Wireless Charging System,” in Proc., IEEE Applied Power Electronics Conference and Exposition (APEC), pp. 480-485, March 2022, Houston, TX.
6. “Thermal Analysis of a 50 kW Three-Phase Wireless Charging System,” in Proc., IEEE Transportation Electrification Conference and Expo, pp. 1-6, June 2021, Chicago, IL.
7. “Design and Optimization of Cancellation Coil Topologies for a Ferrite-less Wireless EV Charging Pad,” in Proc., IEEE Transportation Electrification Conference and Expo, pp. 1-7, June 2021, Chicago, IL.
8. “Three-Phase LCC-LCC Compensated 50-kW Wireless Charging System with Non-Zero Interphase Coupling,” in Proc., IEEE Applied Power Electronics Conference and Exposition, pp. 456-462, June 2021, Phoenix, AZ.
9. “Analysis of Magnetic Field Emissions and Shield Requirements for Interoperating High-Power EV Wireless Charging System,” in Proc., IEEE Applied Power Electronics Conference and Exposition, pp. 1586-1592, June 2021, Phoenix, AZ.
10. “A Field Enhancement Integration Design Featuring Misalignment Tolerance for Wireless EV Charging Using LCL Topology,” IEEE Transactions on Power Electronics, vol. 36, no. 4, pp. 3852-3867. April 2021.
11. “Phase Shift Control of a Three-Phase Inverter for Balanced Secondary Currents in Misaligned Three-Phase Inductive Power Transfer Systems,” in Proc., IEEE PELS Workshop on Emerging Technologies: Wireless Power Transfer (WoW), pp. 10-15, November 2020, Seoul, South Korea.
12. “Shield Design for 50 kW Three-Phase Wireless Charging System,” in Proc., IEEE Energy Conversion Congress and Exposition, pp. 842-849, October 2020, Detroit, MI.
13. “Control of Output Power in Primary Side LCC and Secondary Series Tuned Wireless Power Transfer System without Secondary Side Sensors,” in Proc., IEEE Energy Conversion Congress and Exposition, pp. 5532-5536, October 2020, Detroit, MI.

14. "A Tradeoff Analysis of Series/Parallel Three-Phase Converter Topologies for Wireless Extreme Chargers," in Proc., IEEE Transportation Electrification Conference and Expo (ITEC), pp. 1093-1101, June 2020, Chicago, IL.
15. "Review of Safety and Exposure Limits of Electromagnetic Fields (EMF) in Wireless Electric Vehicle Charging (WEVC) Applications," in Proc., IEEE Transportation Electrification Conference and Expo (ITEC), pp. 17-24, June 2020, Chicago, IL.
16. "Comparison of Magnetic Field Emission from Unipolar and Bipolar Coil-Based Wireless Charging Systems," in Proc., IEEE Transportation Electrification Conference and Expo (ITEC), pp. 1201-1207, June 2020, Chicago, IL.
17. "Advances in High-Power Wireless Charging Systems: Overview and Design Considerations," IEEE Transactions on Transportation Electrification, vol. 6, no. 3, pp. 886-919, July 2020.
18. "A 50 kW Three-Phase Wireless Power Transfer System Using Bipolar Windings and Series Resonant Networks for Rotating Magnetic Fields," IEEE Transactions on Power Electronics, vol. 35, no. 5, pp. 4500-4517, May 2020.
19. "A Modular Integration Design of LCL Circuit Featuring Field Enhancement and Misalignment Tolerance for Wireless EV Charging," in Proc., IEEE Applied Power Electronics Conference and Exposition (APEC), pp. 1634-1640, March 2020, New Orleans, LA.
20. "Comparison of Leakage Magnetic Field from Matched and Mismatched Double-D Coil based Wireless Charging System for Electric Vehicles," in Proc., IEEE Energy Conversion Congress and Exposition (ECCE), pp. 5733-5739, Sept.-Oct. 2019, Baltimore, MD.
21. "Variable Duty Control of Three-Phase Voltage Source Inverter for Wireless Power Transfer Systems," in Proc., IEEE Energy Conversion Congress and Exposition (ECCE), pp. 2118-2124, Sept.-Oct. 2019, Baltimore, MD.
22. "Design of an EMF Suppressing Magnetic Shield for a 100-kW DD-coil Wireless Charging System for Electric Vehicles," in Proc., IEEE Applied Power Electronics Conference and Exposition (APEC), pp. 1521-1527, March 2019, Anaheim, CA.

Acknowledgements

Project team would like to thank Jason Conley from National Energy Technology Laboratory for his continued guidance and support on this project.

II.1.2 Wireless Extreme Fast Charging for Electric Trucks (WAVE)

Ryan Calder, Principal Investigator

WAVE, LLC
 4752 West California Ave, Suite B400
 Salt Lake City, UT 84104
 E-mail: rcalder@wavecharging.com

Lee Slezak, DOE Technology Development Manager

U.S. Department of Energy
 E-mail: Lee.Slezak@ee.doe.gov

Start Date: August 1, 2018

End Date: December 31, 2023

Project Funding: \$9, 838, 241

DOE share: \$4, 292, 137

Non-DOE share: \$5, 546, 104

Project Introduction

The purpose of the wireless extreme fast charging (WXFC) truck project is to significantly accelerate the electrification of heavy-duty trucks, starting with shipping ports and expanding to regional delivery operations across the US. Charging time and range anxiety are major barriers to electric vehicle adoption, particularly for truck applications. Therefore, the major goal of this project is to demonstrate high efficiency, WXFC as applied to Class-8 trucks that have a typically higher gap and lower available space than, for example, transit buses.

Objectives

This project aims to develop and integrate a new 500kW WXFC system developed by WAVE into a Class 8 electric drayage truck developed by Cummins so that it can automatically and wirelessly charge at a high charging rate (C-rate) during its dwell times. This prototype charger will be deployed at Venture Logistics facility, which is a truck operator in the mid-west. The project also planned to develop an AC/DC Power Supply that can operate with a direct connection to the Medium Voltage (MV) 3-phase grid developed by Utah State University.

Approach

WAVE has assembled a strong and diverse team to develop, deploy, and operate two all-electric Class-8 drayage trucks with WXFC at Venture Logistics.

The WXFC truck project leverages the active involvement of key partners on six major project tasks, as shown in Figure II.1.2.1 Project tasks include:

- Evaluation of a 250-kW wireless fast charging system in a Class 8 Truck field deployment.
- New development of 500 kW wireless power transmitter and receiver modules
- New battery pack and Class 8 truck powertrain development to support high C-rate charging.
- New development of an MV grid-tied converter to improve safety and simplify grid integration of WXFC stations.
- WXFC grid and vehicle-side system integration
- WXFC system deployment and evaluation at Venture Logistics.

WXFC for electric trucks is a WAVE-led project with assistance from the following partners:

- Cummins – Truck integration and electric drivetrain partner
- Utah State University – Research partner
- Venture Transportation, Inc – Deployment partner

The general project approach for the Wireless charger, and the high c-rate Class 8 drayage truck development is outlined in Figure II.1.2.2

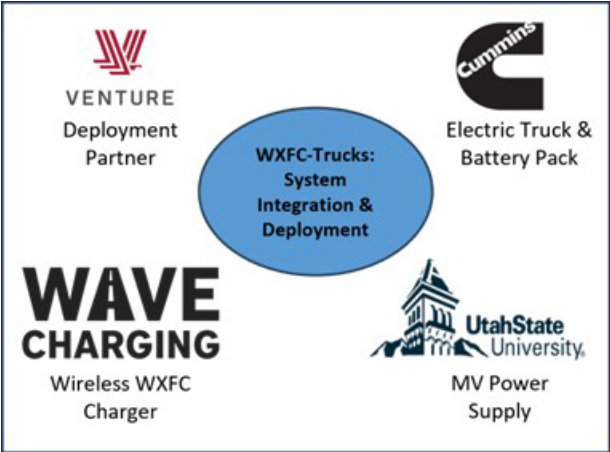


Figure II.1.2.1 WXFC project activities.



Figure II.1.2.2 Project design and implementation approach.

The USU approach to the MV AC/DC supply is:

- 3-phase unfolder with a soft DC bus two-level output
- Develop the 3-phase unfolder to achieve direct MV grid connection with switches commutating at the line frequency.
- Design the series of stacked isolated DC/DC converters to achieve the voltage step-down function from MV naturally with a near-unity conversion ratio to obtain high efficiency.

The WAVE approach to the 500kW wireless charger is:

- Deploy and simulate new magnetics design for the higher power density required at 500 kW.
- Build and categorize a 250-kW prototype pad set based on the new design.
- Leverage deployment experience with the 250kW charger to feed into design updates of the 500kW charger.

The Cummins approach to the extremely fast charging capable electric truck is:

- Investigate appropriate battery chemistry (LTO cells or NMC cells)
- Design custom thermal management for the cell to facilitate charging at 3C.

- Select appropriate battery pack capacity and cell chemistry to integrate with the electric powertrain applicable to Class 8 drayage applications.

Results

The project team has worked together to define the requirements for the MV AC/DC supply, wireless charger, and Class 8 truck to deliver a solution that meets the needs of the deployment partner. A block diagram for the system is shown in Figure II.1.2.3

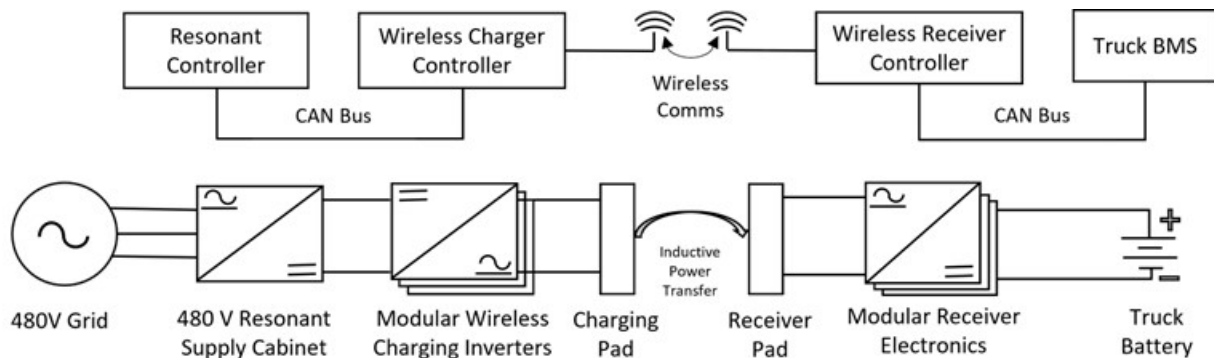


Figure II.1.2.3 System block diagram

Key results and updates from each project partner are outlined below:

- WAVE - 500 kW Wireless Charger Development and Build
 - WAVE along with the project partners has achieved all the milestones in BP2 and successfully transitioned from BP2 to BP3 during the past year.
 - WAVE in the past year focused on the development and validation of the wireless charger for the site demonstration.
 - WAVE has completed the Off-Vehicle Testing of the wireless charger validating the software and controls required to operate the machine safely and achieve the maximum efficiency (Grid to Battery) while delivering the 500 kW across the pads.
 - Truck 2 from Cummins was sent to WAVE in Q1, 2023 for the 2nd charge testing event and assembly of the secondary system to the truck.
 - The 2nd charge testing was successfully completed by WAVE and Cummins teams where the focus was on validating the Safety, Efficiency, Stray Field, and Thermal features with the Truck 2.
 - The power transfer of 500 kW was also reverified with Truck 2 with a push button start automatically which was not possible during the Truck 1 Charge Testing.
 - The key differences between Charge Testing 2 and Charge Testing 1 are:
 - One Control System
 - Fully Automated System
 - Push Button Start
 - Alignment Verification

- Communication with Vehicle BMS
- Automatic Power Regulation
- Finalized the tuning system during this charge testing event which improved the harmonic suppression and the controllability of the system.
- Post testing, WAVE updated the system with the final software and controls updates before shipping the equipment to the site.
- Site Development and Demonstration:
 - WAVE, with support from Cummins selected the deployment partner for the demonstration.
 - WAVE signed contracts with the new deployment partner and the construction company kick-starting the site preparations.
 - The site chosen already has an existing power service that will be utilized to power this project, so a new service will not be required avoiding any constraints related to setting up a new power service.



Figure II.1.2.4 Marked the charger location at the site

- The teams met at the deployment site and completed a feasibility study to select the optimum location that best meets the needs of the project.
- A location at the site has been selected and agreed upon by all the stakeholders in the project which was paint marked at the site. See Figure II.1.2.4 for more details.
- The drawings are being prepared using the final site location details and will be reviewed and submitted to the county.
- The 6 -month demonstration will begin once the construction and commissioning is complete.
- Cummins – Truck Activities:
 - Continued truck validation activities (both trucks) on the test track and public roads.
 - 500 kW wireless charging demonstrated on Truck 2 (at WAVE).

- Identified appropriate project duty cycles with Venture Logistics (Fleet Operator).
- Includes 20-hour double shift operation requiring multiple charge events per day.
- Auto parts deliveries to be made to Subaru Automotive of Indiana.



Figure II.1.2.5 Cummins Truck

- USU - Unfolder and Module Industrialization:

During this year, the planning and assembly for a full integrated cabinet testing were completed. Testing of the MV components testing and the DC-DC modules standalone testing is in progress.

Key Progress:

- 4160 MV feed was integrated into the EVR for testing.
- The MV subsystems and the DC-DC module's standalone testing is in progress.
- Completed the assembly of the MV Unfolder, 8 DC-DC modules, and all MV subsystems.
- Completed the assembly and wiring of the Line-frequency transformer, main feed, and pre-charge circuits.
- Procured and completed the MV wiring required for the full system.
- Fabricated and assembled all boards for control, communication, sensing, and protection.
- Completed the cabinet assembly and wiring of potential transformers, current transducers, sensor boards, LV power supplies, blowers, and the HMI.
- Assembled an external testing setup for module-level validation.



Figure II.1.2.6 All DC-DC Modules



Figure II.1.2.7 DC-DC Module and Unfolder after assembly

- Completed full control testing with the low-power unfolded and three DC-DC Modules to integrate power factor correction, load regulation, and voltage sharing within a single stage.
- Demonstrated close to 50% reduction in THD through modified control algorithms.

Key Challenges:

- MV Testing safety considerations and setups.
- Supply-chain issues and lead times affecting the MV subsystems testing.

Key Testing Efforts:

- Initial MV Components Testing (In Progress).
- DC-DC Modules Standalone Testing (In Progress).
- MV Integrated Cabinet Testing (In Progress): Progress included testing and validation of the LV 480 V special equipment cabinet.

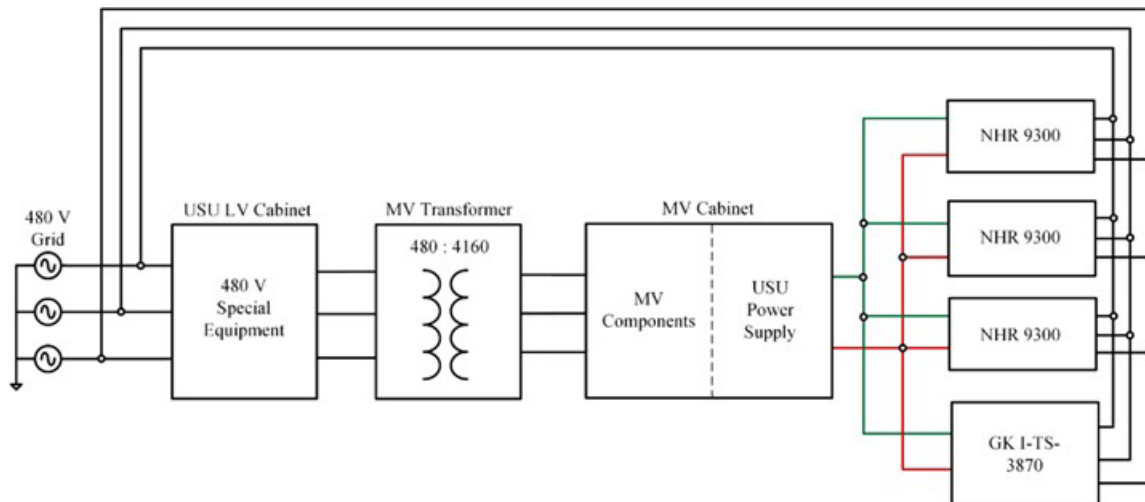


Figure II.1.2.8 Integrated MV Off-vehicle Testing

Challenges

COVID-19 has severely impacted the supply chain of the components needed to build the equipment and other assemblies at WAVE, USU, and Cummins. Significant measures are being taken to address these issues like procuring alternate parts, changing current designs, and adding more resources to reduce delays.

Conclusions

During this budget period, the WAVE team has completed the validation of the charging systems in a lab setting, with Truck 2 at WAVE for 2nd charge testing event with support from the Cummins team. WAVE has also updated the equipment with the software and controls which resulted from the charge testing and then shipped the equipment to the site. Cummins has worked on the validation activities for both the trucks on test tracks and public roads and is ready to be deployed for operations at the demonstration site. USU had finished procuring the rest of the equipment needed for the final validation and was able to finish building the necessary sub-systems for the MV system validation. The new site for the deployment is finalized and the site preparations have been going on to prepare and build the site for the planned demonstration. The trucks along with the charging system will be deployed at the site and will undergo the demonstration in Budget Period 3.

This is one of the crucial milestones that need to be accomplished for the effective deployment of the wireless charging equipment and truck.

Key Publications

1. M. Masquelier, “Wireless Extreme Fast Charging for Electric Trucks.” 2019 DOE VTO Annual Merit Review, Washington, DC, June 2019.
2. M. Masquelier, “Wireless Extreme Fast Charging for Electric Trucks.” 2021 DOE VTO Annual Merit Review, Washington, DC, June 2021.
3. M. Masquelier, “Wireless Extreme Fast Charging for Electric Trucks.” 2022 DOE VTO Annual Merit Review, Washington, DC, June 2022.
4. R. Calder, “Wireless Extreme Fast Charging for Electric Trucks.” 2023 DOE VTO Annual Merit Review, Washington, DC, June 2023, online.

Acknowledgments

The project team would like to thank John J. Conley from the National Energy Technology Laboratory and Lee Slezak from the Department of Energy for their continued support and guidance on this project.

II.1.3 Long-Range, Heavy-Duty Battery-Electric Vehicle with Megawatt Wireless Charging

Ryan Reed, Principal Investigator

Kenworth Truck Company
485 Houser Way N
Renton, WA 98057
E-mail: ryan.reed@paccar.com

Lee Slezak, DOE Technology Development Manager

U.S. Department of Energy
E-mail: Lee.Slezak@EE.DOE.GOV

Start Date: October 1, 2019
Project Funding: \$11,488,452

End Date: November 30, 2024
DOE share: \$4,989,288

Non-DOE share: \$6,499,164

Project Introduction

Most heavy-duty battery-electric trucks in operation today are designed for one shift per day and 100 miles or less operation, such as port drayage, due to the existing technology barriers of battery energy density and charging power capability. However, most truck operators prefer trucks that can achieve longer range without interrupting the daily delivery schedule to cover both intercity and regional hauling routes and to facilitate their dispatch efforts. For fleets where the diesel-powered trucks typically have a range of 350 to 500 miles, introducing trucks with shorter range presents a significant impact on operating cost, productivity, and schedule planning.

This project aims to demonstrate that approximately 400 miles per day across two shifts can be achieved with little impact on a fleet's operations by developing a megawatt wireless charging technology that is capable of fully charging the battery pack during a driver's 30-minute required break. By applying the megawatt wireless charging technology, the daily operating range of the battery-electric truck-tractor can be extended without disrupting the delivery schedule and while keeping the required battery pack mass to a minimum.

Objectives

- Design and build a Class 8 Battery Electric Truck-Tractor with sufficient range to run from Salt Lake City to Logan and Provo at up to 80,000 lbs. Gross Combination Weight.
- Design and build a wireless charging system capable of megawatt power transfer rate.
- Demonstrate the vehicle and charging system in commercial operations of approximately 400 miles per day with a major shipping company.
- Collect and analyze data from commercial use over a period of up to three months, which will provide real-world feedback on how a large, electrified tractor-trailer might be used in freight operations.

Approach

During the project, Kenworth will leverage previously tested electric powertrain technology, and will design and build a Long-Range Battery-Electric Tractor (LRBET) specifically tailored for this application. Technical challenges that will be overcome during this project include mounting this quantity of battery capacity without adversely impacting the tractor's durability or vehicle dynamics, selecting appropriate battery chemistry and pack design to achieve high C-rate charging, providing adequate cooling for the batteries and power electronics during vehicle operations and the extreme fast charging, and developing the controls code to manage the vehicle during vehicle operations and during charging.

Utah State University (USU) will leverage its core expertise in high C-rate battery charging, high power density grid-tied power electronics and wireless charging systems to design the megawatt inductive charging

equipment circuitry and topology. The planned inductive wireless charging system will allow power to be transferred wirelessly between a primary (charging) pad embedded in the ground and a secondary (receiving) pad mounted on the bottom of the vehicle by using high frequency AC magnetic fields. Inductive charging is a mature and proven technology. However, it is seeing wider adoption today due to the availability of high-performance semiconductor devices, capacitors, and cables. The technology can operate in varying environmental conditions, including rain and snow, requires no operator interaction, and maximizes effective use of land with no above ground obstacles or components.

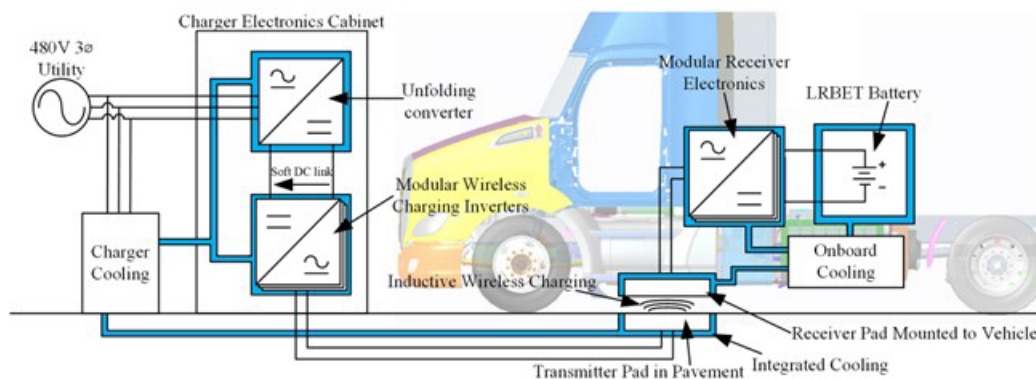


Figure II.1.3.1 System block diagram

WAVE has commercialized wireless charging systems capable of transferring up to 250 kW over an air gap of 10 inches and has obtained UL Field Certification. The maximum power that can be transferred with a wireless charging system is typically limited by the leakage magnetic fields that are generated since international standard bodies such as the International Commission on Non-Ionizing Radiation Protection (ICNIRP) regulate the maximum allowable leakage fields. USU has developed a charging pad configuration that utilizes multiple field shaping strategies as well as newly developed techniques to facilitate charging at power levels of one megawatt while maintaining leakage fields below ICNIRP regulations. USU's system has also considered other aspects of the system such as the power electronics design, thermal management, and tolerances.

Results

A program time extension was submitted and approved with the following adjusted budget period dates:

- BP1: 10/1/2019 – 12/31/2020
- BP2: 1/1/2021 – 3/1/2024
- BP3: 9/30/2023 – 11/30/2024

Directional effort towards Utility and End User Milestone 2.4 - Grid Electrical Power Supply

M2.4 Grid Electrical Power Supply Installed at Each Location and Ready for Connection to Charger.

- Anticipated completion on April 15, 2024

A new site location has been identified directly outside of the Union Pacific Railyard located within the Utah Inland Port (UIPA) of northern Utah. This location was specifically selected due to its high frequency of drayage trucking traffic. The location is shown in Figure II.1.3.2. A lease agreement has been received from UIPA and is currently in the Utah State University legal review process. It is anticipated that the lease agreement will be completed in early November 2023.

A Rocky Mountain Power (RMP) System Impact Study was completed on September 7, 2023. The results were positive and RMP stated that power utility can be brought to the site prior the installation of the 1MW

charger. It is anticipated that UIPA site construction will be complete and the 1MW FALCON charger functional by April 15, 2024.

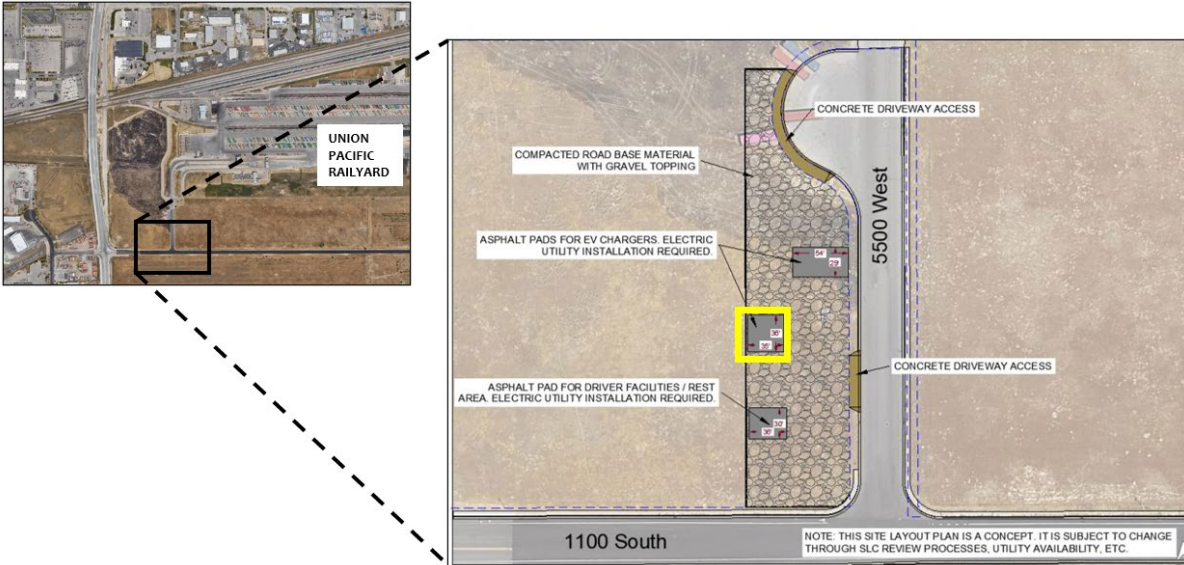


Figure II.1.3.2 Site location of the Union Pacific Railyard located within the Utah Inland Port (UIPA) of northern Utah.

Construction at the Utah State University Electric Vehicle Center (EVR) has begun. The contractor has confirmed that the asphalt surrounding the proposed 1MW charger location will be installed during November 2023. This location can be seen in Figure II.1.3.3. It is anticipated that EVR site construction will be complete and the 1MW FALCON charger functional by March 11, 2024.

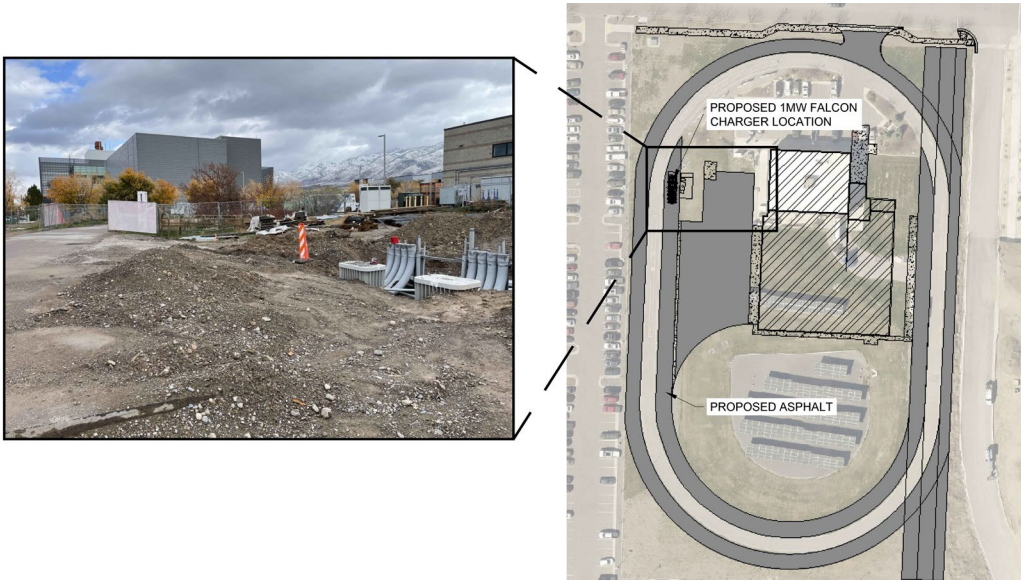


Figure II.1.3.3 Location of Construction at the Utah State University Electric Vehicle Center (EVR) and proposed 1MW charger location.

Procurement of the electrical switch panels presented a critical risk to the project schedule due to long lead times. The procurement time for these would have likely delayed the EVR and UIPA site completion dates back to August 2024. USU understood this risk and was able to utilize its relations with Rocky Mountain

Power to procure switch panels earlier for each site and maintain the site completion dates for the spring of 2024.

Directional effort towards Utah State University and WAVE Milestone 2.5

M2.5 - Demonstrate full-scale MW wireless charger in off-vehicle operation.

- Anticipated completion on March 19, 2024

The 1MW charger system can be organized into four main assemblies. The **Special Equipment Cabinet (SEC), Primary Cabinet, Primary Pad, and Secondary Pad**. The main goals of 2023 have been to finish design documents, conduct design reviews/releases, procure materials, assemble, and test each of these main assemblies.

The **SEC** design has been fully reviewed and released. The only item pending is a UL review for final approval. The long-lead items such as the main capacitors and the surge suppressor have been procured. Once final UL approval is received, the rest of the materials will be procured and assembly may begin.

The **Primary Cabinet** design has been fully reviewed and released. All long-lead items have been ordered and many have already been received. USU is currently testing assemblies of t-types and inductors to ensure functionality. As functionality is proven during October-November 2023, orders will be released for procuring these items for the full 1MW system. All cold plates within the Primary Cabinet have been vetted and orders have been placed for full system procurement. Potting procedures are currently being tested to validate the functionality of the potting material. These tests were finished during the last week of October 2023 and the results were affirmative. As a result, potting material was ordered for the full 1MW system.

The **Primary Pad** design is currently under review and a portion has been released such as the cold plate. The plate was manufactured and arrived at USU on August 18, 2023. Ferrite blocks were measured, aligned, and placed upon the pad to validate the design. USU coordinated with WCI to refine and confirm the feasibility of the potting process and material for the pad. Additional potting tests were carried out to ensure complete adherence and impregnation of the pad by the potting material. The results were positive and the potting material has been procured. The 1kA boards and dam designs were reviewed and released to Alpha Circuits for manufacturing.

The **Secondary Pad** design is currently under review and a portion has been released including the cold plate.

The plate was manufactured and delivered to USU on October 27, 2023. USU coordinated with WCI for the Secondary Pad potting in the same fashion that was carried out and listed above for the Primary Pad. The 1kA boards and dam designs have also been reviewed and released to Alpha Circuits for manufacturing.

The critical path for M2.5 is assembly and potting of the remaining inductors and also procurement of the remaining mosfet cold plates for the Primary Cabinet. USU is working closely with D6 Industries to expedite the manufacturing of the mosfet cold plates. If they are unable to finish the mosfet cold plates by December 14, 2023, then the M2.5 schedule will be affected.

Directional effort towards Kenworth Milestone 3.1

All major components with exception of the wireless charger assembly are received and installed on the chassis. The team continues work with the integration phase of the project. Individual components have completed LV testing and high power HV testing. The components are currently behaving as predicted. Initial road efficiency results were 2.3 kWh/mile for a chassis configuration including a roof fairing and pulling a 43k lb. 53' trailer. The chassis has completed over 5,000 miles to date.

HV Batteries

- The side and back of cab packs are assembled and installed. The supplier battery management system has been updated to allow chassis final arbitration for opening contactors in certain conditions.
- Critical battery responses and prioritized fault messages have been defined. Chassis BMS fault management has been created to delay battery from opening contactors until vehicle is stationary.

Controls

- Optimization of HVAC system: Single condenser fan controls have been implemented to use the single large cooling fan which must also cool the power electronics heat exchanger. Past designs used a separate fan for each of 3 heat exchangers. The fan speed controller has been designed to arbitrate the cooling needs of all 3 systems. AC compressor speeds and pressure set points have been calibrated for optimal performance and component longevity. Battery and cooling tests have been performed to assist with these calibrations.
- Shutdown bug root cause identified and eliminated: A bug in the microsecond watchdog rollover was causing the vehicle to shutdown when the memory location saturated and rolled back to 0. This has been remedied by checking the time between events rather than time since the last epoch.
- Motor/transmission unit: Limited the torque slew rate and increased the torque control message stability. During at the PACCAR Technical Center the torque control message was timed erratically, this was eliminated by increasing the foreground loop rate from 10ms to 2ms. A rate limiter was also added to the drive torque request as an attempt to smooth out low speed torque oscillations.
- Urge to move was implemented allowing the vehicle to creep forward as the brake pedal is released, limiting the need for two foot braking on hills and offering a more consistent driver experience with ICE vehicles equipped with automated/automatic transmissions. Extensive calibrations were performed to give a consistent experience unloaded (~24,000lbs) and loaded (80,000lbs). Initially performance when unloaded was as expected but due to the drag from the trailer resulted in either no movement or jarring oscillations. A dynamic torque ramp was implemented that steps the torque up at zero wheel speed then transitions to a smooth ramp once the wheels are rotating.
- Kenworth assumed fault arbitration during RUN and CHARGE modes from the BMS. The BMS cannot shut the truck down during drive, this was updated for driver safety. The vehicle will detect the fault message from the BMS and transition to limp mode, giving the driver time to safely move the vehicle to the side of the road, retaining power steering, limited propulsion, air compressor function. As soon as the vehicle is placed in neutral, and the park brake applied shutdown will occur. These functions have been tested on the vehicle and confirmed to work as intended.
- ABS/Cruise Control Implementation: Over 70 signals from the Electric power train have been Gatewayed back to the production vehicle control unit and ABS system. Active collaboration with PACCAR embedded team and ABS supplier Bendix is under way. The Falcon project is on track to implement the first functional ABS/Cruise system with this powertrain configuration within PACCAR NA.
- Ongoing drivability updates: With over 5000 miles on the vehicle data and driver feedback has been collected and used to improve the drivability. This includes adjusting Regenerative braking parameters to improve comfort and effectiveness in city driving, urge to move tuning, off throttle negative torque to improve efficiency, and driver feedback of motor power to replace feedback from engine noise.
- Secondary wired DC fast charge box has been upgraded from 110 to 200 kwh for steady state charging. This will allow continued system integration testing.

Milestones

A significant responsibility transition has been implemented from WAVE to USU to clarify scope and responsibility. The latest project schedule suggests the wireless chargers will not be available for full-scale testing until March 2024 and the grid power supply in place until April 2024.

Table II.1.3.1 Project Milestones

MS#	Milestone	Type	Date Planned	Date Achieved
2.4	Grid electrical power supply in place	Technical	10/31/2023	
2.5	Demonstrate full-scale megawatt wireless charger system in off-vehicle operation	Go-No-Go	1/19/2024	
3.1	Vehicle is Assembled and Operable	Technical	9/20/2023	

Major Accomplishments

- Final battery BMS Release software received and implemented
- Vehicle has driven 5,000 miles
- Initiated manufacturing and assembly of the Primary Pad
- Initiated manufacturing and assembly of the Secondary Pad and Cold Plate
- Initiated manufacturing of the Primary Cabinet Shelving and Framing
- Completion of the Rocky Mountain Power System Impact Study
- Selection of a new demonstration site and in process of drafting the property Lease Agreement

Conclusions

At the end of FY2023, the conclusions of this program to date are:

- Fully integrated controls linking the vehicle systems and wireless charging for a road ready vehicle are extensive. Lower-level systems have competing needs which will have final arbitration by the upper-level requirements.
- Vehicle design and procurement is complete with the last remaining hardware the wireless module.
- The majority of the charger system is designed, reviewed, and in the process of procurement, assembly, and testing.
- Charger deployment locations have been identified at the EVR and UIPA.

II.1.4 Improving the Freight Productivity of a Heavy-Duty, Battery Electric Truck by Intelligent Energy Management

Jian Li, Principal Investigator

Volvo Technology of America, LLC
13302 Pennsylvania Ave
Hagerstown, MD 21742
Email: jian.li@volvo.com

William Northrop, Principal Investigator

University of Minnesota
200 Oak Street SE
Minneapolis, MN 55455
Email: wnorthro@umn.edu

Lee Slezak, DOE Technology Development Manager

U.S. Department of Energy
E-mail: Lee.Slezak@ee.doe.gov

Start Date: October 1, 2019 End Date: December 30, 2023
Project Funding (FY22): \$4,869,889 DOE share: \$3,799,536 Non-DOE share: \$1,070,353

Project Introduction

Battery electric Class 8 trucks, including those from Volvo, have made significant advancements in the past five years; however, high battery cost and vehicle weight restricts their ability to match the range and productivity of conventional diesel trucks. Although an electric tractor can be equipped with a larger battery to last for a large portion of a 250-mile daily route, vehicle cost increases non-linearly with increased battery energy and must be sized to last 8 to 10 years to provide a proper return on investment. Therefore, on-route fast charging is necessary to balance economics, functionality, and longevity. The objective of this project is to use vehicle and operations data to increase the vehicle range and lower the operating cost of battery electric Class 8 trucks that drive more than 250 miles per day using physics-based adaptive learning algorithms.

Objectives

The objective of the project is to use vehicle and operations data to increase the vehicle range and lower the operating cost of battery electric class 8 trucks that operate more than 250 miles per day using physics-aware machine learning algorithms. The project team will develop and implement an intelligent-Energy Management System (i-EMS) with vehicle-to-cloud (V2C) connectivity integrated with physics-aware spatial data analytics (PSDA). The i-EMS rule-based methods will use collected vehicle and operations data and calculated parameters as inputs into physics-based algorithms developed in the project to predict and reduce future energy consumption of the vehicle. The resulting i-EMS will increase the vehicle driving range and lower the operating cost of battery electric Class 8 freight movement trucks that drive ≥ 250 miles per day, demonstrating that Class 8 battery electric vehicles (BEVs) are capable of driving over 250 miles while carrying normal payloads and utilizing on-route opportunity charges.

Approach

Our approach is to understand our fleet partners' (HEB Companies and Murphy Logistics) baseline operations to be able to establish project duty cycles. In addition, we will combine physics-based truck model, battery information, utility demand charges and database parameters as inputs to a machine learning algorithm that will predict energy use, operational energy cost, and battery performance. The resulting i-EMS will be implemented on 2 Volvo VNR BEVs, using a low-distraction screen to display charging and routing recommendations to the operators. Charging stations will be installed at depot locations for both HEB Companies in Texas and Murphy Logistics in Minnesota, and an extra on-route charger will be installed in

Minnesota to allow the trucks to complete longer routes while operating from the Murphy Logistics depot. Finally, we will demonstrate the i-EMS in daily operations with HEB Companies in hot weather and Murphy Logistics in cold-weather conditions.

Results

The project has experienced several delays to date; supply chain bottlenecks have contributed to delays in the delivery and installation and commissioning of the on-route chargers, and the repair of the second electric VNR truck. Even with these delays the team has continued to make progress on all tasks. A total 6-month no-cost extension to the end of 2023 has been approved to allow the project team to sufficiently evaluate the i-EMS in hot and cold weather conditions once both electric VNRs are operating regularly with a fully integrated driver vehicle interface.

Task 2: Technology & Algorithm Development

Subtask 2.1 – Create physics-based, battery electric truck model

The testing plans for NME-6 and NME-8 have been revised to mitigate risks associated with transporting NME-8 to Texas. During Q4, NME-8 will remain in Minnesota, and NME-6 will continue testing in Texas.

The current vehicle models for NME-6 and NME-8 use the reported weight measure whenever it is available. However, the UMN team is preparing to test and compare the effectiveness of developed methods for online mass estimation that can operate using connected vehicle data without special instrumentation. These include a deep neural network model, a gaussian belief propagation model (similar to a k-nearest neighbor regressor) [2], and a physics model-based method (comparing expected and observed energy usage). In addition to the state of charge and range estimates, the UMN team will also provide final results on the state of health estimates for NME-6 and NME-8 batteries in different regional climates (e.g., Minnesota vs. Texas).

Subtask 2.2 – Create initial machine learning algorithm

In addition to previously-discussed recurrent neural network (RNN) models used to predict vehicle range and charging requirements, the UMN team has finished the development of a deep neural network (DNN) to predict the energy along road segments to aid the eco-routing algorithm. This is discussed further under Subtask 2.3. The UMN team also plans to develop a reinforcement learning (RL) model to make intelligent real-time decisions regarding rerouting to a charger, given the information from the vehicle and machine learning models about the remaining range, charging required, and energy costs of traveling along the road network. This will complete the i-EMS system by supplementing the eco-routing algorithm with a high-level decision-making agent that can make data-driven recommendations to the driver via the DVI (e.g rerouting the vehicle for charging as needed). Together, these models should save energy, time, and customer costs.

Formal methods of quantifying and classifying battery performance and operational energy cost are closer to being finalized and will decidedly not include the predictive machine learning components discussed in previous reports. Keeping the cost model simple will ensure its output is as explainable as possible. The operational cost model is discussed in detail under Subtask 3.3.

Subtask 2.3 – Develop energy-efficient routing and driving algorithms for use in demonstration

For travel energy consumption estimation, the UMN team proposed a novel Eco-toll estimation Physics-informed Neural Network (Eco-PiNN) framework that integrates the physical laws governing vehicle dynamics with a deep neural network. Experiments on real-world vehicle data shown that Eco-PiNN yields significantly more accurate eco-toll estimation than state-of-the-art methods. The proposed framework is summarized in a paper that has recently been accepted for publication and will be presented at the 2023 SIAM International Conference on Data Mining [4].

The longer route has been identified as the 'Mankato Route + CHARGE'. This route commences at Murphy Logistics Solutions (701 24th Ave SE, Minneapolis, MN 55414) and proceeds sequentially through Murphy - Shakopee Distribution Center (901 Canterbury Rd, Shakopee, MN 55379), Johnson Outdoors (121 Power

Drive, Mankato, MN 56001), and Winegar Inc (1209 S State St S, Waseca, MN 56093), before returning to Murphy Logistics Solutions. The eco-routing results for this test route are displayed in Figure II.1.4.1a. The route's total energy consumption amounts to 74.40-liter equivalents, with a total time of 16,635.55 seconds and a total length of 322,639.957 meters. Conversely, the fastest route, depicted in Figure II.1.4.1b, has a total energy consumption of 103.51-liter equivalents, a total time of 11,616.03 seconds, and a total length of 304,200.362 meters. However, it is worth noting that the eco-routing result includes numerous turns, suggesting that the current edge-based eco-routing algorithm does not account for energy consumption at intersections and turns. To address this limitation, the UMN team is in the process of refining the eco-routing algorithm by developing a physics-informed heuristic for eco-routing that will incorporate the impact of turns and stop-and-go scenarios at intersections.

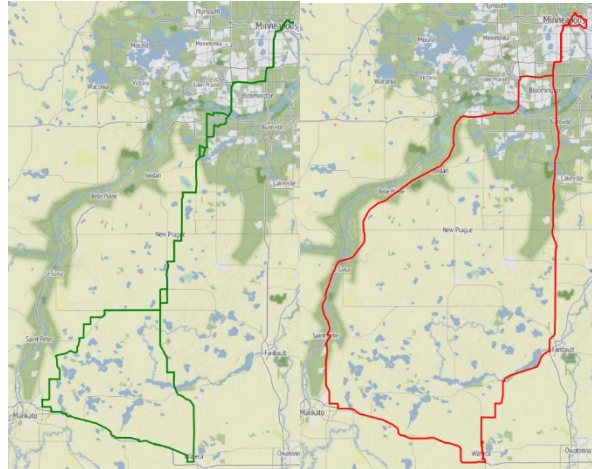


Figure II.1.4.1. Current eco-routing result on the test route (a) and the fastest route (b).

Subtask 2.4 – Define on-route charging locations for demonstration

The established routes at each operator, and other information from Task 1.2 will be analyzed to determine demonstration phase charging locations.

A Gilbarco Veeder-Root RTM75 charger has been installed at Murphy Logistics and is fully operational and online. Additionally, HEB has coordinated with Volvo and Gilbarco Veeder-Root to install a high-powered charger, the Gilbarco Veeder-Root RT175s, to allow for faster charge times that better suit its more ambitious route scheduling. Both chargers are being used regularly. The on-route charger in Minnesota was fully installed and commissioned in Q3 and is ready for the final testing phase. NME-8 will remain in Minnesota through Q4, and (pending maintenance) should make use of this charging station to complete long-route testing.

Go-No-Go Milestone

The UMN team has refined the charger placement analysis for the new charging station, NME-8 can make the round trip with ease by utilizing a small mid-route charge. The model-based Go-No-Go analysis assesses whether NME-8 can make the longer trip to various Murphy customer locations in Mankato, Owatonna, and Albert Lea, using a charger placed at Winegar in Waseca for one or two on-route charges. This general location has the benefit of allowing for more variation in route planning, which provides a valuable testing opportunity for the eco-routing algorithm. Because Murphy has multiple customer locations in the area, multiple different long routes may be made possible by this charger placement. Figure II.1.4.2 shows the results of this analysis. It was also found that NME-8 could complete this trip if the charger were located at the customer locations in Makato, Owatonna, or Albert Lea.

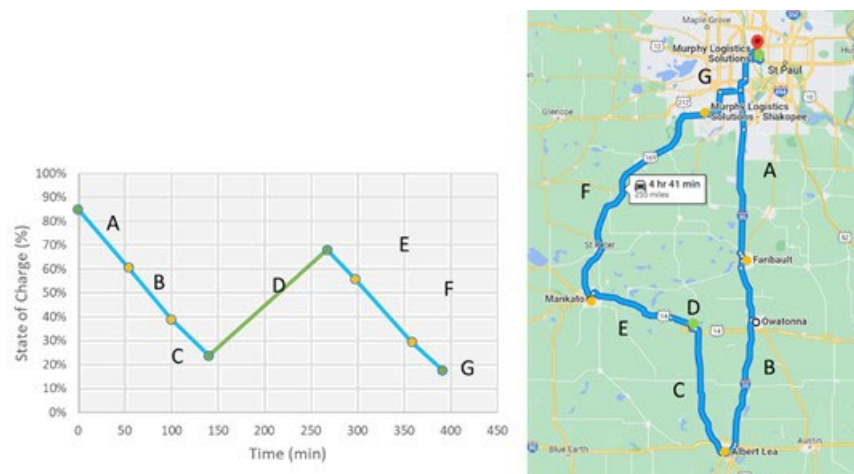


Figure II.1.4.2. Go-No-Go analysis for long-route testing (250+ miles), utilizing a single on-route charge. In this case, the charger was assumed to be placed in Waseca, Minnesota. The total trip time was estimated to be 6.5 hours, including a roughly 2-hour charge to recuperate 44% of the battery SOC (250 kWh out of the total 564 kWh capacity).

The final testing phase will incorporate a modified version of the route shown, in which NME-8 travels to a customer location in Mankato, uses the charger in Waseca (if available by the time long-route testing begins), and returns to the Murphy depot before completing a continuing on to other customer locations in the Twin Cities. The final test route in Texas has not been solidified, but is actively being discussed with HEB.

Subtask 2.5 – Determine optimal on-route charging locations for fleets: Determine optimal locations for on-route charging for the two participating fleet operators.

The UMN team is in the process of applying the method presented in [3] to simulated example routes and to the practical baseline routes driven by Murphy and HEB trucks. This work is planned for completion in Q4 of 2023. While conducting this analysis, a simpler clustering-based method is also being explored, which groups together areas of high charging demand and places chargers at the point closest to each cluster centroid. A separate clustering-based method of charger placement was recently been implemented and tested as part of a separate project [1]. In the coming months, the UMN team hopes to implement and generate final results demonstrating and comparing these charger placement algorithms in both MN and TX.

Subtask 2.6 – Develop Driver Vehicle Interface: A Driver-Vehicle Interface program application (“app”) will be developed to send vehicle information to the team and to receive information from cloud-connected adaptive learning algorithms.

UMN team finished implementing changes to the user interface design of the DVI, and has updated the eco-routing implementation to match the most up-to-date version of the algorithm. However, the range, distance to go, and charging required numbers are still being updated to use information from the Volvo TGW (rather than the UMN on-board logger) and the UMN vehicle model to compute their values. Although it is possible to view the route, and test routes will be pre-loaded for the drivers, the DVI does not provide turn-by-turn instructions to the driver. Therefore, the research team has decided to supplement the DVI with another existing application – OsmAnd. The routes from the eco-routing algorithm will be converted to GPX files, which can be stored as Tracks in OsmAnd. Loading these tracks provides navigation with helpful visual and audio cues. Furthermore, OsmAnd (on Android devices) can provide a cuesheet of printable turn-by-turn instructions, which are easier for the fleet partners to review to ensure the route is safe for trucks to travel on. Eco-routes will be sent to the fleet partners’ devices of choice so that they can display and navigate the route in OsmAnd. The DVI will serve as a separate screen to display an overview of the route alongside the other helpful information about the truck’s expected range and charging requirements. Figure II.1.4.3 shows some of the features of this app, which is available for free on all major mobile device operating systems.

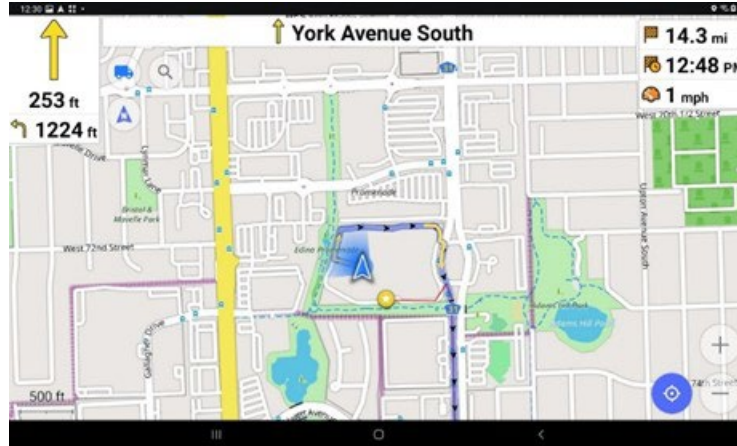


Figure II.1.4.3: OsmAnd will be used on a separate device to help drivers navigate eco-routes, as it provides visual and audio turn-by-turn directions for custom routes. Directions can also be printed for further review by fleet partners.

Task 3.0: Technology Verification and Vehicle Charging Implementation

Subtask 3.3 – Complete an operational cost model: Cost simulations will be developed to determine optimal charge scheduling, duration, and rate during a route.

The cost of electricity is the primary consideration in determining optimal charge scheduling. For simplicity, the cost model will use an (adjustable) average electricity cost per kWh. Charge rates are taken into account, and limited by the chosen charger station model. If charging is done on-route, the optimal charge level (i.e. minimum SOC required to complete the trip) is fully determined by the machine learning range prediction algorithm from Task 2.2. Man-hours, the maximum safe charge rate, and electricity pricing are all major considerations in the final cost model. Smart overnight charge scheduling could also be beneficial for minimizing costs. Additionally, the rate of battery health decline will be considered in the operational cost model. Hotter climates can be detrimental to the long-term health, and therefore useful life, of the vehicle battery.

The cost of placing chargers will be considered separately, as it is unclear what proportion of charging infrastructure investment will need to come from the public versus private sector.

All data generated from testing will be used to simulate different scenarios (e.g., different regional climates) to estimate operating costs over a significant time period for fleets in different regions of the U.S. Prior to determining final cost estimates, the current cost model is written and explained below in theoretical terms.

$$O(T,C,e)=M(T,C)+L(T,C)+F(T,C)+E(T,e)$$

The operating cost O is a mix of fixed costs and variable costs, primarily including materials M (e.g., batteries, chargers, etc.), fees F (i.e. taxes and permits), labor and vehicle maintenance L (i.e., wages), and energy E . These components of the operating cost model are functions of, among other things, the number of trucks T , number of chargers C , and the price of electricity e . The operational cost model will be packaged as a standalone module, with inputs allowing users to adjust things like the price of electricity, the regional climate (and its impact of battery health), and employee wages. The operating costs of the two electric trucks may be compared to those of similar diesel trucks to perform a financial analysis of how long it would take to amortize the higher upfront costs of these new electric vehicles. The increased energy efficiency of the electric trucks and the differences in cost between diesel fuel and electricity is expected to significantly impact the relative value of the electric trucks over time.

Simpler versions of this cost model may be used to validate the effect of other methods, such as eco-routing, on operating costs.

Conclusions

The project team has made significant progress, despite the delay caused by the second electric truck, NME-8, which has been down since May due to the software and hardware issues. Final testing plans are carried on validating the developed models and test the eco-routing algorithm and driver-vehicle interface in operation. NME-6 is being remained in Texas through December of 2023 while NME-8 demonstrates the capability of Class 8 BEVs to travel more than 250 miles a day during normal regional haul delivery operations, even in extreme weather conditions.

Key Publications

1. Yan Li, Mingzhou Yang, Matthew Eagon, Majid Farhadloo, Yiqun Xie, William Northrop, and Shashi Shekhar. 2023. Eco-PiNN: “A Physics-informed Neural Network for Eco-toll Estimation. In Proceedings of the 2023 SIAM International Conference on Data Mining (SDM).” Society for Industrial and Applied Mathematics. <https://doi.org/10.48550/arXiv.2301.05739>
2. Eagon, Matthew, Setayesh Fakhimi, Adam Pernsteiner, and William F. Northrop. “Mass Detection for Heavy-Duty Vehicles Using Gaussian Belief Propagation.” In 2022 IEEE Intelligent Vehicles Symposium (IV), 1655–61. Aachen, Germany: IEEE, 2022. <https://doi.org/10.1109/IV51971.2022.9827370>.
3. Eagon, Matthew, Setayesh Fakhimi, George Lyu, Audrey Yang, Brian Lin, and William F. Northrop. “Model-Based Framework to Optimize Charger Station Deployment for Battery Electric Vehicles.” In 2022 IEEE Intelligent Vehicles Symposium (IV), 1639–48. Aachen, Germany: IEEE, 2022. <https://doi.org/10.1109/IV51971.2022.9827442>.

References

1. Badheka, A., Eagon, M. J., Fakhimi, S., Wiringa, P., Miller, E., Kotz, A., & Northrop, W. (2023). “Development of a heavy-duty electric vehicle integration and implementation (Hevii) tool.” (SAE Technical Paper No. 2023-01–0708). SAE Technical Paper. <https://www.sae.org/publications/technical-papers/content/2023-01-0708/>
2. Eagon, Matthew J., Daniel K. Kindem, Harish Panneer Selvam, and William F. Northrop. “Neural Network-Based Electric Vehicle Range Prediction for Smart Charging Optimization.” *Journal of Dynamic Systems, Measurement, and Control* 144, no. 1 (January 1, 2022): 011110. <https://doi.org/10.1115/1.4053306>.
3. Holden, Jacob, Harrison Van Til, Eric Wood, Lei Zhu, Jeffrey Gonder, and Matthew Shirk. “Trip Energy Estimation Methodology and Model Based on Real-World Driving Data for Green-Routing Applications.” *Transportation Research Record: Journal of the Transportation Research Board* 2672, no. 24 (December 2018): 41–48. <https://doi.org/10.1177/0361198118798286>.
4. Fang, Xiaomin, Jizhou Huang, Fan Wang, Lingke Zeng, Haijin Liang, and Haifeng Wang. “ConSTGAT: Contextual Spatial-Temporal Graph Attention Network for Travel Time Estimation at Baidu Maps.” In Proceedings of the 26th ACM SIGKDD International Conference on Knowledge Discovery & Data Mining, 2697–2705. Virtual Event CA USA: ACM, 2020. <https://doi.org/10.1145/3394486.3403320>.

II.1.5 High Efficiency Powertrain for Heavy Duty Trucks using Silicon Carbide (SiC) Inverter - DE-EE0008806 (Ricardo)]

Steve Peelman, Principal Investigator

Ricardo Inc.
40000 Ricardo Drive
Van Buren, MI 48111-1641
E-mail: steve.peelman@ricardo.com

Lee Slezak, DOE Technology Development Manager

U.S. Department of Energy
E-mail: Lee.Slezak@ee.doe.gov

Start Date: October 1, 2019	End Date: November 30, 2023	
Project Funding: \$7,140,067	DOE share: \$4,605,398	Non-DOE share: \$2,534,669

Project Introduction

The Ricardo led High Efficiency Propulsion (HEP) project will develop a high efficiency and compact 250kW continuous power SiC inverter designed to support the high continuous loads and challenging shock/vibration environment of heavy-duty trucks with an electrified axle specifically designed for high performance and efficiency in battery-electric Class 8 trucks used in medium range (~250 mile) distribution. The project is split into 3 budget periods, with the first two being design and development focused and the final one is a demonstration phase.

The HEP team is comprised of Ricardo as the prime and Transpower (Meritor, now Cummins) and NCSU as the subs with the primary project objective of developing a 250kW SiC continuous power inverter. An electrified axle with integrated 2-speed gearbox developed by Meritor will be utilized and integrated with a variant of the TransPower (now Cummins) efficient EV architecture, which has been successfully utilized in numerous Class 8 truck and tractor models. This combination will provide an extremely compact, lightweight, robust and easy to integrate drive system for electric Class 8 trucks. It is expected that performance of the 250kW continuous power operation on an eAxle integrated into a vehicle with actual in-field use will be verified during the demonstration period.

Objectives

Budget Period 1: Development of Controls and Design of the Inverter (A-Sample)- COMPLETED

Budget Period 2: System Integration and Evaluation of the Proposed Design- CURRENT

Task 2.1 – B-Sample Design

Results of testing from A-sample build will be reviewed and updates to the specification, electrical and mechanical design and testing methodology will be applied as learnings to the B-Sample development effort. An updated system specification will be drafted based on the outcome of the reviews with all team members.

Task 2.2 – Mechanical Design

Thermal and detailed design will be updated along with drawings. FMEA review of mechanical design to ensure improvements include design for manufacturing and assembly (DFM/A), and the lower cost solution.

Task 2.3 – Electronic Design

Updates will be made to the HW requirements spec and design will commence. Schematic design, custom component calculations, specifications and quotation, and PCB design updates will all be performed. FMEA review of electronic design to ensure improvements include design for manufacturing and assembly (DFM/A), and the lower cost solution. Manufacturing data will be generated and checked.

Task 2.4 – Software Update

Software will be updated as required to optimize the design.

Task 2.5 – Prototype Build

Electronics manufacturing will be initiated, and mechanical components procured.

Task 2.6 – Hardware Test

The various electrical and mechanical parts will be assembled and tested first for basic electrical operation, then for functional performance. Additional controls work will be performed to test system functional operation, including early vehicle control interface debugging. Functional testing will be performed until desired specification levels are reached. Simulated load cycles will be performed to test for thermal and mechanical performance.

Task 2.7 – Hardware / Software Integration & Functional Testing

Motor-inverter characterization of hardware/software testing on back-to-back dyno testing continuous operation will be performed.

Task 2.8 – System Integration Testing

Testing of SiC inverter on early drive systems as well as communication testing with the Meritor eAxle and discrete control modules will begin.

Task 2.9 – Hardware Design Documentation Update

Results of testing from B-Sample build will be reviewed and updates to the specification, electrical and mechanical design and testing methodology will be applied as learnings to the final development effort. The data pack will be compiled, and production recommendations provided.

Task 2.10 – Mechanical Design

The mechanical design will be updated, and the 3D design work will be readied for prototype manufacturing quotation and review.

Task 2.11 – Production-Ready Design Validation Performance Testing Complete

Acceptance testing will be completed.

Task 2.13 – eAxle Prototype Fabrication and Testing

Prototypes will be manufactured for in-house testing and for installation into the two demonstration trucks. The axle will be installed into one of the trucks. Powertrain Control Module (PCM) software will be developed to optimize performance of the tandem eAxle system using the new 3-speed gearbox.

Task 2.14 – Drive System Component Development

Assemble the subsystems required to equip the Class 8 demonstration trucks with the upgraded EV architecture featuring the 3-speed eAxle and SiC inverter.

Budget Period 3: Demonstration Vehicle Development- FUTURE***Task 3.1 – Demonstration Vehicle Development***

The subsystems will be integrated and assembled into the two Class 8 demonstration trucks. Two Peterbilt 579 gliders will be acquired and drive system components and all high and low voltage wiring, and integration hardware will be installed.

Task 3.2 – Demonstration

The two demonstration trucks will be entered into operational service to demonstrate the performance of the integrated drive systems in Class 8 trucks under real-world operating conditions. Remote telematics will be used to continuously gather information on the performance of the trucks.

Approach

- Year 1: Design and Prototype Testing with the aim to demonstrate >92.5% SiC inverter efficiency COMPLETED
- Year 2: Inverter B-Sample Development and Drive System Component Development
 - B-Sample SiC inverter design and development go/no-go decision based on inverter design validation efficiency of 98.5% COMPLETED
 - Optimization of gate driver and control board design COMPLETED
 - Update mechanical design COMPLETED
 - Build the inverter and perform functional tests COMPLETED
 - Complete inverter performance testing (ONGOING)
- Year 3: Vehicle Integration and Demonstration of 2 class 8 Trucks
 - Complete vehicle integration
 - Complete vehicle verification testing
 - Place Class 8 trucks (x2) into demonstration service

Results

B-Sample inverter, shown below in Figure II.1.5.1, was tested under static load conditions and achieved the SiC inverter design performance efficiency BP2 goal as shown in Figure II.1.5.2. The inverter then went on to an initial dyno testing, which was used to develop the preliminary inverter motor control and calibration.

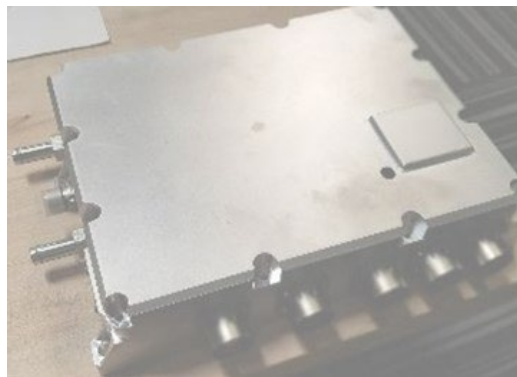


Figure II.1.5.1 Inverter Assembly

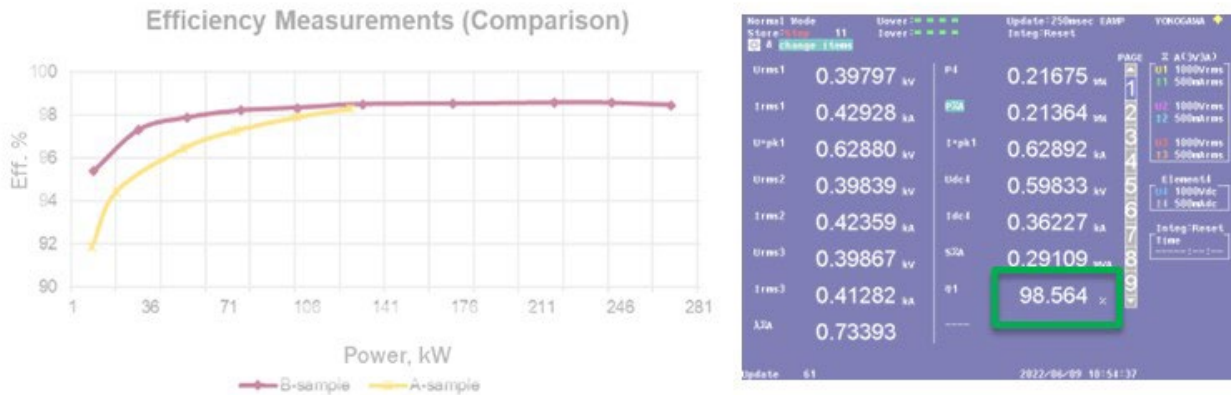


Figure II.1.5.2 Inverter Power Efficiency Test (A vs B-Sample) & Inverter Power Max Efficiency

The following tasks have been completed over last year.

- B-Sample Efficiency target of 98.5% was met, proven through bench testing of the SiC inverter and a “go” decision to continue by the DOE provided
- Optimization of gate driver and control board design
 - Changes to the gate driver circuitry were made based on A-Sample learning
 - A new microprocessor was chosen based on industry direction and to improve the capability to meet future functional safety goals for a production application
 - The software approach was changed to follow industry preferred AUTOSAR compatibility
- A new embedded inverter packaging design was completed to meet the environmental requirements for the demonstration phase on the truck chassis
- The successful A-Sample multi-board circuit board concept was carried over to the B-Sample electronics
- Build the inverter and perform functional tests
 - Inverter components were built and bench tested
 - Software verification was completed through bench testing and on the Hardware in the Loop (HIL) rig
- Complete inverter performance testing
 - Assembled inverters were bench tested for functional use and then tested on the dyne
 - Performance goals were verified with bench level test procedures
 - Dyne testing is still in progress
- Prior to the additional performance tests start, Inverter motor controller was further fine-tuned with the current to torque map, and Ld, Lq versus Id, Iq flux linkage control at motor full speed range. The motor speed controller was developed including field weakening. Test result data show in Figure II.1.5.3, Ld and Lq vs. Id and Figure II.1.5.4 Torque vs. speed map

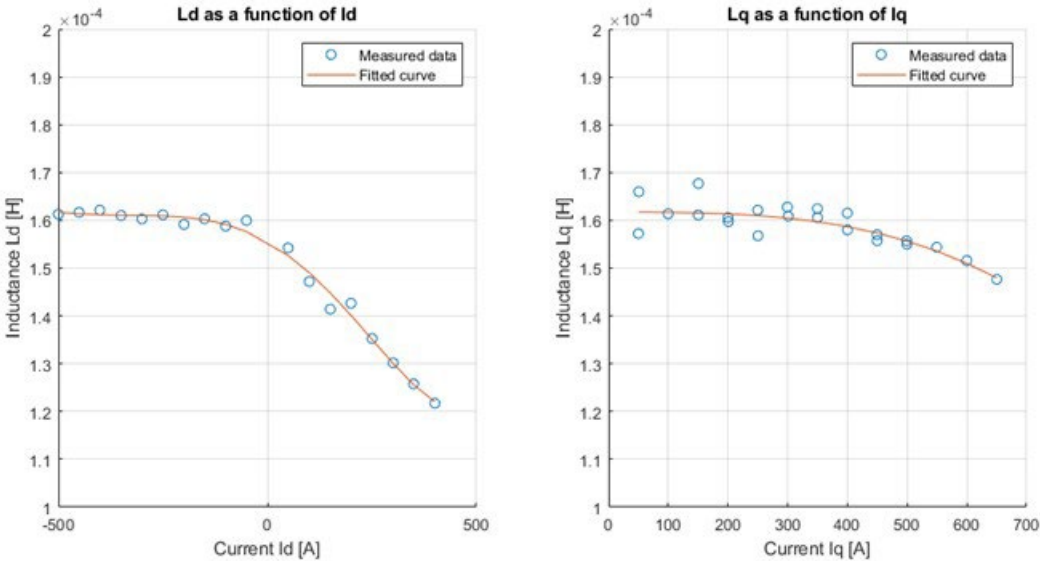


Figure II.1.5.3 Flux Linkage as a Function of Current

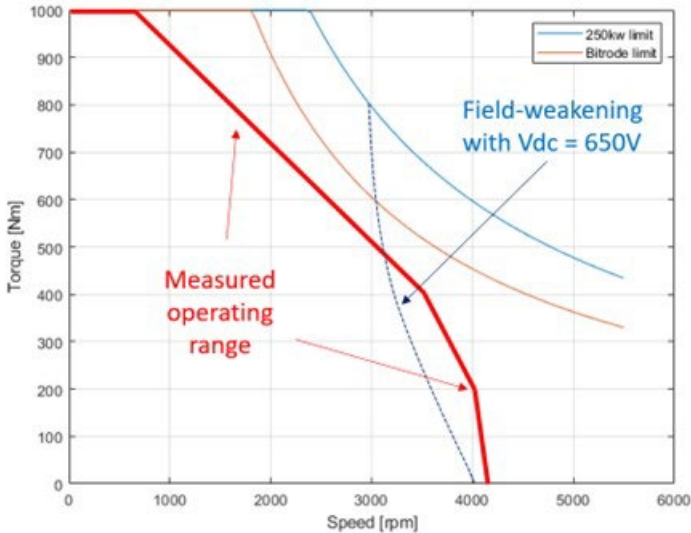


Figure II.1.5.4 Torque vs, speed map

- Two electric class 8 semi-trucks were received by Meritor and baseline acceptance testing and data collection in preparation for retrofit of the inverters has been performed
- Drive System Inverter Component Development testing was successful and the Baseline vehicle with a standard Si inverter accumulated over 5k miles of testing data

Further tests were planned for the additional inverter motor performance testing on dyno with the test cases listed below in Figure II.1.5.5. These inverter motor performance tests are ongoing on dyno.

TEST ID	TEST NAME
2-PERF-01	Inverter/Motor Calibration - Torque Control
2-PERF-02	Inverter/Motor Calibration - Speed Control
2-PERF-03	Inverter Motoring Continuous Torque Envelop Test
2-PERF-04	Inverter Speed vs Torque @ Peak Power - Motoring
2-PERF-05	Inverter Speed vs Torque @ Peak Power – Regen
2-PERF-06	Inverter Transient Tests (Dyno)
2-PERF-06	Motor/Inverter Efficiency Map Tests
2-PERF-07	Inverter Static 4 Corner Tests
2-PERF-08	Inverter Derating Test

Figure II.1.5.5 Inverter Motor Performance Tests on Dyno

Software Development

Inverter control software has been configured for the B-Sample hardware. The control software uses an AUTOSAR compliant design and real time operating system.

A hardware software interface has been designed and a Base Software (BSW) and Complex Device Drivers (CDD) have been developed to support the input-output requirements of the system, including analog and digital inputs for sensors, serial communications (SPI) with gate driver peripherals, and gate drive switching control (PWM).

The AUTOSAR system has been configured to match the CAN communications interface of the trucks, and all required software to support the signals defined in this interface has been developed.

The Application Software (ASW) has been developed to support both torque and speed control modes. A map-based approach for setting current demand has been implemented, including flux weakening control for high-speed operation. A full Space Vector Pulse Width Modulation approach has been implemented to maximize efficiency and DC voltage utilization.

Derating features for temperature, current and voltage are implemented to protect the system at the edges of its operating envelope. Further protection is provided by a fault monitoring system that will place the system into a safe state when derating is insufficient.

The software has been deployed to the control board and tested on a signal-level Hardware in the Loop (HIL) system. This allows testing of the complete control board and software system and allows all aspects of the control software to be tested safely.

Software development is now complete for all required functions. Calibration of most control functions has been completed using a representative motor on a dyne. Fault mode reactions are being refined. High speed operation above the field weakening lower limit is also being refined.

NCSU Status

NCSU completed their project support at the end of October 2022.

Transpower (Meritor) Status

Meritor was acquired by Cummins to form the Accelera business unit. It is understood that the company recently made a decision to consolidate EV product development and integration activities and will no longer maintain the southern California site, established by our original partner TransPower. Further strategic decisions by Accelera have affected the capacity to complete the vehicle demonstration phase which is currently being reevaluated. They were able to accumulate in excess of 5k miles of BEV driving on the two class 8 trucks with baseline data captured.

Conclusions

The B-Sample hardware design has proven capable to meet the application requirements, having passed all the planned testing at the bench and HIL level, with final performance testing on the dyne outstanding.

Final refinement of the control software to handle derating and operating mode faults has been more challenging than expected and final refinement of the algorithms and calibrations for these functions is still in progress. The higher speed field weakening operating range is partially complete due to delays in finishing the fault handling impacting the final calibration of the motor control software.

Final development activities are fine tuning the controller and finishing the inverter performance tests.

The vehicle demonstration phase (Budget Period 3) is undergoing a review with advice from the DOE.

II.1.6 eMosaic: Electrification Mosaic Platform for Grid-Informed Smart Charging Management (ABB Inc.)

James Stoupis, Principal Investigator

ABB Inc.
US Corporate Research Center (USCRC)
1021 Main Campus Dr.
Raleigh, NC 27606
E-mail: james.stoupis@us.abb.com

Lee Slezak, DOE Technology Development Manager

U.S. Department of Energy
E-mail: lee.slezak@ee.doe.gov

Start Date: October 1, 2020

End Date: May 31, 2025

Project Funding: \$7,666,953

DOE share: \$4,933,028

Non-DOE share: \$2,733,925

Project Introduction

Electric vehicle (EV) charging presents a new set of challenges and opportunities to a diverse group of stakeholders. Charging demand should be intelligently managed to reduce its impacts on grid operations but without sacrificing the experience of vehicle owners. Although smart technologies exist already in utility systems, charging networks, and EVs, no viable solution has been vetted to date that provides coordinated integration among them while providing benefits to and meeting the needs of all stakeholders. Most widely available solutions tend to focus on charging site control in isolation, while cloud platforms provide asset monitoring but lack control features. Preferred utilities load management approaches are “set-and-forget” policies and high-level communications and incentives for customers. The “eMosaic” project investigates technologies that enable closer coordination between grid operators and EV owners. New algorithms use prices as an incentive signal to influence EV charging behavior, while an edge+cloud architecture has been built to enable control and data exchange. The purpose of the project is to test and validate these concepts first in a lab setting, then again in a utility field demonstration.

Objectives

The goal of the eMosaic project is to enable and demonstrate the management of diverse EV site types via smart charging management functions, with a special focus on grid support functionality. Several applications have been developed: a reinforcement learning (RL) algorithm that sets real-time EV charging prices in response to grid conditions; a hierarchical, cost-saving optimization algorithm for scheduling the charging of public electric buses; a cloud-based optimization algorithm for aggregating EV charging to participate in grid services, such as demand response and frequency regulation; and a local, rules-based algorithm that controls individual charging sessions as a function of electricity price. A cybersecure communications architecture hosts the applications and enables the exchange of measurements, prices, and control commands between charging sites and back-end resources in the cloud. Supporting the effort to build these features in the lab, a major effort has been to develop real-time hardware-in-the-loop models that co-simulate EV charging and grid operation. The building of the field demonstration is currently ongoing for project partner Rocky Mountain Power’s distribution system in the Salt Lake City, UT area, as well as Utah State University’s facilities. Ultimately, the goal is to test the feasibility of the various applications and technologies on real EV charging equipment and in a real grid operation scenario.

Approach

In the first two (of four) budget periods, laboratory setups were created to test the performance and scalability of the eMosaic platform. In the third budget period, the demonstration phase was started and the installation of new EV chargers is currently underway, in order to enable communications from all connected chargers for project purposes. eMosaic edge gateway devices are currently installed at the ABB US Corporate Research

Center (USCRC) lab in Raleigh, NC and at the Utah State University (USU) Electric Vehicle and Roadway (EVR) lab in Logan, UT. The sites are collectively being used for multiple use cases. The edge devices exchange data with the cloud platform and run the co-simulation of EV charging and grid operation.

After validating the applications and architecture in the labs, the second phase of the project currently underway in the third budget period, focuses on a field demonstration with the project’s utility team, Rocky Mountain Power (RMP). In this phase the project teams are applying the eMosaic solution to charging sites in the RMP territory and integrating applications into RMP’s back-office systems. The field tests will be used to prove the benefit to the utility of a number of concepts: price-based regulation of EV charging, aggregated EV charging control for grid support, cloud-based control of EV charging, etc.

Results

Demonstration Use Case Finalization

Use Case 1: Dynamic Pricing.

ABB and USU have actively worked on demonstration case one in building a mobile application with dynamic price signals suitable for deployment on charging infrastructure in place at USU facilities. The project team has been working to define and finalize the methods in which the use case will be carried out once deployed in the field.

The dynamic pricing engine provides an adaptive hourly EV charging rates based on the health of the distribution grid. An hourly change ensures that the price does not change too often to render the approach ineffective due to constant pricing changes. It also ensures that the change in price is fast enough to be adaptive to grid conditions. A Reinforcement Learning (RL) method is being employed, where an agent learns the grid health by interacting with the grid and interacting directly with the EV system. To train the RL agent, a synthetic environment that captures important dynamics has been developed [1], as shown in Figure II.1.6.1.

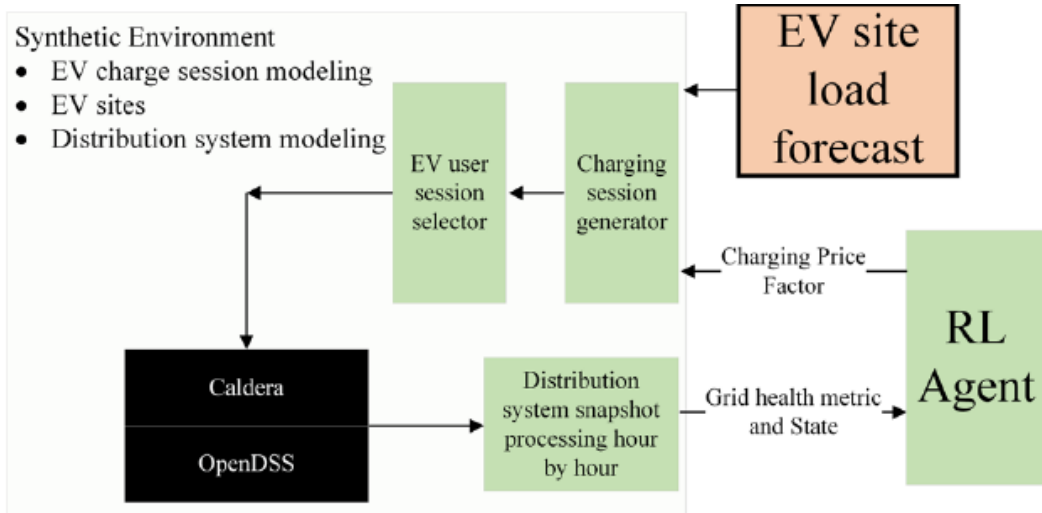


Figure II.1.6.1 Key Components of a Synthetic Environment to Train an RL Agent

Use Case 2: Bus Charge Planning.

USU is also the main contributor to the second demonstration case, Bus Charge Planning. Route data has been received including bus GPS, operating block plans, and charge session details from UTA partners. This information has been used in training the USU route planner and charge optimization algorithm and reviewing results. A key element to the implementation of the plan is the ability to control functionality at the chargers and the ability to track bus status. USU has worked with UTA and ABB this last quarter to troubleshoot limitations to the charging hardware. Ongoing efforts continue to for communication and control of the chargers and to track bus charge and route status. New interfaces have been designed and implemented to facilitate the information flow. Improvements have been made to a receding planning capability to incorporate this data. Plans have also been made for a series of tests to verify the functionality and utility of the developed approach.

Use Cases 3 and 4: OpenADR.

USU has implemented a prototype utility Open Automated Demand Response (OpenADR) 2.0b virtual top node (VTN) server, a virtual end node (VEN) server for USU to act as the OpenADR aggregator, and a VTN to relay communications to ABB's VEN. Project team members met frequently in a series of workshops to perform the detailed OpenADR 2.0b signal mapping for use cases 3 and 4. Detailed discussions were held evaluating the use of the Load_Dispatch OpenADR signal and the various options for signal type that could be used. The team is considering minimum amperage requirements to ensure optimal operation of the EVSEs and EV charging. It was decided to utilize the OpenADR LOAD_DISPATCH Events for load control in use cases 3 and 4.

A cloud-based optimal scheduler has been developed that can receive price signals from grid services markets. The optimizer runs periodically, getting updated charging event and price information to solve for new charging schedules. The cloud hosts three main components for this application: a database of charging reservations, an OpenADR VEN for receiving price events, and the optimization algorithm. The database stores current and upcoming charging event data. Upcoming charging events will be captured from a public-facing charging reservation tool, currently in the final stages of development. As charging events take place, the event database entries are updated with data measured at the charging equipment and sent from the edge. In order to accommodate data from real chargers in the field, the optimizer is being modified to accept this data, providing a comprehensive view of the grid and connected chargers.

The core component of the MPC optimizer is the optimization algorithm itself. The algorithm is based on an ABB product that has a generalized framework for building optimization models. In this case, a model has been created that includes an arbitrary number of EV charging events, with electrical and financial connections to the grid and an energy services market. At regular intervals (e.g. every minute), the application gets updated vehicle data from the database and checks whether there is a new market event. Then it finds the least-cost solution of charging schedules for all the events. For in-progress events, the solution's current-time charging power command is sent to the edge gateway, which applies the command as a budget to the charger. Once the optimizer consumes any OpenADR event, it will assign the budget to connected chargers via Open Charge Point Protocol (OCPP).

Solution Architecture

Members of the ABB, RMP, and USU teams participated in workshops to clearly map out the solution architecture for the project including the telecommunication requirements and integration plans for OpenADR 2.0b and OCPP 1.6. Multiple options were discussed regarding EVSE selection requirements to ensure compliance with the use cases and open protocol criteria. The project team focused on leveraging an OpenADR 2.0b aggregator model to minimize the integration points and to meet typical utility cyber security requirements as well as an OCPP cloud server approach which is typical for the EV industry. Additional updates may be made to the current solution architecture upon completion of the detailed site assessments. The solution architecture is shown in Figure II.1.6.2.

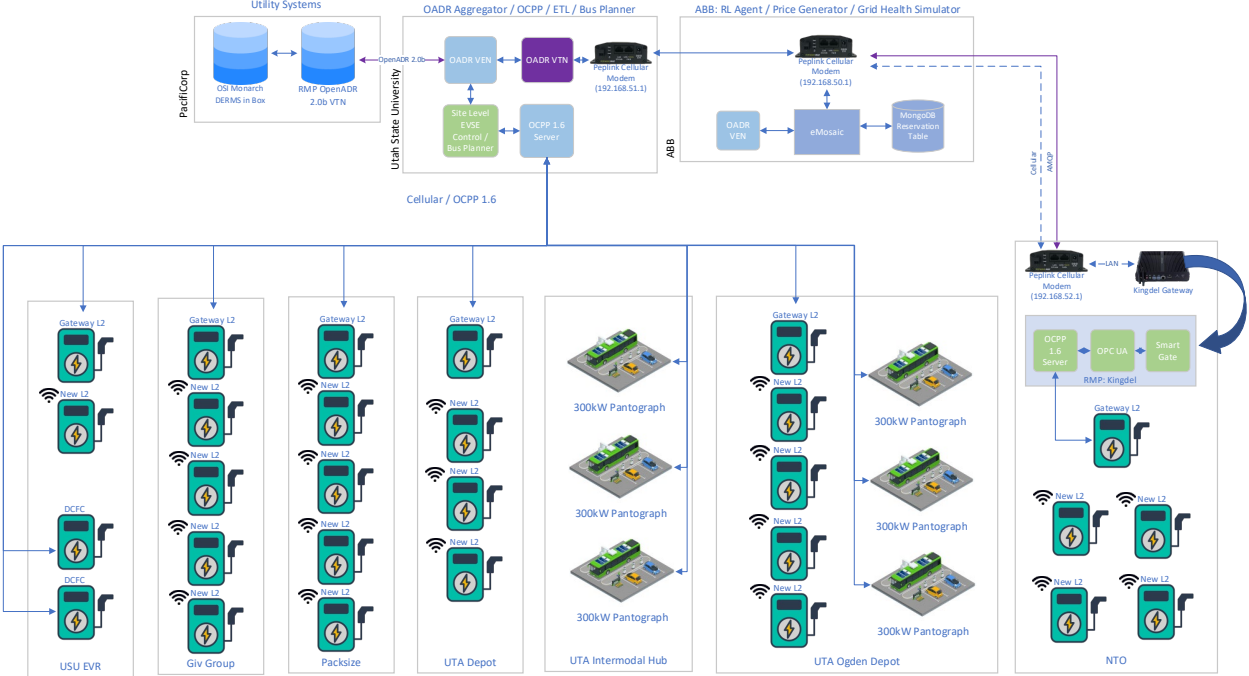


Figure II.1.6.2 High-Level Solution Architecture

Site Assessments

In September 2023, Merge (RMP consultant) completed detailed physical site assessments which included a walk-through for key customer sites. These detailed assessments included an inventory of all of the existing equipment, a review of the associated electrical panels, review of existing electric vehicle supply equipment (EVSE) installation configuration (i.e., power sharing, etc.), and telecommunications available. Through the assessments, the team was in the process of compiling a count of EVSE, confirming the number of ports, evaluating existing infrastructure installation design and power capacity, and evaluating the real estate for additional EVSE equipment. The team now has a clear picture of the needs at each site including upgrade for each site host. The RMP NTO site (North Temple Office) is the RMP Headquarters, while the Packsize and Give Group complexes are sites with all public charging available.

Table II.1.6.1 L2 Charger Deployment Summary Plan

Site	Address	Type	Total Planned L2 Ports	LiteOn 48A Cell	LiteOn 48A WiFi	ABB Terra AC80	Total New Pedestals
RMP NTO	1407 W North Temple St, Salt Lake City, UT 84116	Workplace / Fleet	41	10	29	2	8
Packsize	3760 W Smart Pack Way, Salt Lake City, UT 84104	Workplace	50	5	45	0	14
Giv Citizens West	535 W 300 N, Salt Lake City, UT 84116	Multifamily	25	1	24	0	0
Giv Project Open 1	355 N 500 W, Salt Lake City, UT 84116	Multifamily	42	0	42	0	0
Giv Project Open 2	511 W 400 N, Salt Lake City, UT 84116	Multifamily	4	1	3	0	0
		TOTAL	162	17	143	2	22

Table II.1.6.1 above summarizes the total planned Level 2 chargers that will be available for the project. In most cases, the installation of new L2 chargers will consist of replacing non-networked or proprietary EVSE with open-source OCPP units that can be connected to project OCPP servers. The LiteOn chargers are capable of communicating via WiFi or cellular communications. The chargers with cellular capabilities will be used as gateways to relay data from connected chargers to the OCPP servers. ABB Terra AC chargers will also be used at the RMP NTO (Headquarters) site. It should be noted that while there will be 162 L2 chargers available for the project, the team will integrate a subset of the chargers for the first phase of the demonstration, and add more chargers as feasible for the employed communication system.

Communications and Integration

A next big step in the project is to integrate the various chargers for communication into the aforementioned solution architecture, so that the data can be processed and analyzed for the use cases related to the project. Once the integration occurs, then the connectivity with the OCPP and other servers can be tested and employed for the remainder of the project.

As mentioned in the previous section, the LiteOn 48A chargers have been selected and ordered by RMP for the demonstration sites, as they demonstrate highly flexible configurations, especially for communications. These chargers offer true open source OCPP compatibility across multiple third party servers, the ability to field configure each unit for the existing circuit, WiFi and cellular communication capabilities, and a Local Load Management (LLM) feature that allows the unit to share current if necessary. Figure II.1.6.3 shows an integration that occurred at the ABB labs, where data from an ABB L2 charger was able to communicate data to the Kingdel controller (and eMosaic server) via the LiteOn gateway charger and a cellular connection.

Further connectivity tests are being carried out between a Merge (RMP consultant) site and ABB and USU, in order to test connectivity to OCPP servers.

One last connectivity test that needs to be carried out in the near future is the connection between OpenADR nodes and the L2 chargers (i.e., via the OCPP protocol). RMP will house the main VTN for the OpenADR control commands, and USU will maintain the main pass-through server that contains both VEN and VTN. The USU VTN will connect to all demonstration sites. ABB will implement a VEN on its cloud server to connect to the chargers at the RMP NTO office (Headquarters), so that the data can be routed to the Kingdel edge controller at the ABB site to run the grid services optimizer (GSO) for use case 4 (“slow demand response”).

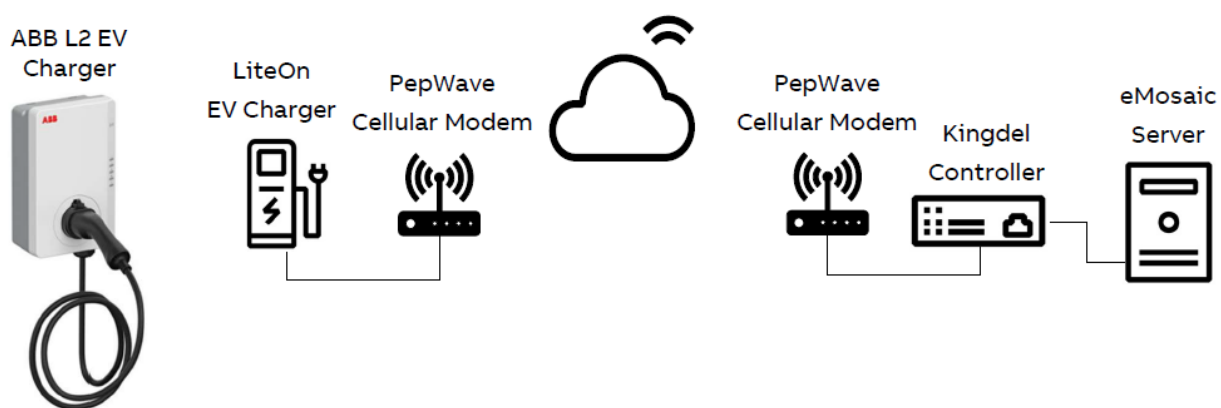


Figure II.1.6.3 LiteOn Gateway Charger Integration Test

Control Systems

RMP is continuing work for implementation of the distributed energy resource management system (DERMS) and OpenADR servers which required meetings with several departments within the information technology department. RMP has gone through initial review of the requirements for configuring distributed energy

resources within the DERMS. Detailed integration and device testing is being conducted with OpenADR with a lab deployment of the OpenADR virtual top node (VTN) at the Utah State University (USU). The USU VEN/VTN will be deployed onto a RMP server once testing is complete and the server is deployed. This will enable RMP to monitor the total active charging power and issue curtailment commands when needed.

Customer Engagement

Host site customers have been getting high-level updates on the project and customer participation agreement drafts have been created and have been going through multiple revisions. These agreements are currently in review with RMP and have been shared with the host site customers along with the EVSE incentive application. The agreement outlines the program details and requirements for participation including definitions, parties' commitments, access to perform equipment upgrades, approval and authorization for participation in EV managed charging events, and data collection requirements, among other things.

Conclusions

As the market for EVs grows, there is a critical need to develop solutions for intelligent EV charging that supports, rather than strains, grid operations. The eMosaic project highlights the complexity of the problem and the array of technologies that need to be assembled into a complete solution: communications architectures, edge and cloud computing platforms, algorithms, standards-based interfaces, etc. At this stage, the eMosaic team has demonstrated a preliminary platform to meet these needs, validating it in a lab setting using various hardware-in-the-loop modeling tools. Based on these efforts, several price-based approaches to managing EV load show promise. With the start of the second half of the project, the team is bringing its solutions to the field, applying them to real EV charging and utility operations, with a goal to evaluate the real-world feasibility, drawbacks, and benefits of the new solutions.

Key Publications

1. D. Mortensen, J. Gunther, G. Droge, "*Cost Minimization for Charging Electric Bus Fleets*", in review at IEEE Open Journal of Intelligent Transportation Systems.
2. D. Mortensen, J. Gunther, G. Droge, J. Whitaker, "*A Bin Packing Approach to Minimize Charging Cost for Electric Bus Fleets*", in review at IEEE Journal of Intelligent Transportation Systems.
3. J. Whitaker, G. Droge, M. Hansen, D. Mortensen, J. Gunther, "*A Network Flow Approach to Battery Electric Bus Scheduling*", in review at IEEE Journal of Intelligent Transportation Systems.
4. H. Suryanarayana and A. Brissette, "*EV charging site day-ahead load prediction in a synthetic environment for RL based grid-informed charging*", 2023 IEEE Transportation Electrification Conference and Expo (ITEC), 2023.

References

1. H. Suryanarayana and A. Brissette, "*EV charging site day-ahead load prediction in a synthetic environment for RL based grid-informed charging*", 2023 IEEE Transportation Electrification Conference (ITEC), 2023.

Acknowledgements

The team is grateful for the efforts and leadership from our partners for their work and planning for the demonstration phase at RMP: James Campbell, Sarah Chatterjee, and David Eckels; and at USU: Regan Zane, Dustin Maughan, Jake Gunther, Greg Droge, Mario Harper, Jackson Morgan, and all their students and staff.

II.1.7 Demonstration of Utility Managed Smart Charging for Multiple Benefit Streams

Stephanie Leach, Principal Investigator

BGE

110 W Fayette St. 15th fl.

Baltimore, MD 21201

E-mail: stephanie.leach@bge.com

Lee Slezak, DOE Technology Development Manager

U.S. Department of Energy

E-mail: lee.slezak@ee.doe.gov

Start Date: October 1, 2020

End Date: December 31, 2024

Project Funding: \$11,400,000

DOE share: \$5,000,000

Non-DOE share: \$6,400,000

Project Introduction

Exelon's mission is to be the leading diversified energy company. Exelon believes that reliable, clean, and affordable energy is essential to a brighter, more sustainable future.

Exelon is already fully engaged with electric grid infrastructure planning processes to enable beneficial transportation electrification. Exelon's distribution utilities operating in Maryland include Baltimore Gas and Electric (BGE), Potomac Electric Power (Pepco), and Delmarva Power & Light Company (DPL) – collectively known as Exelon Maryland Utilities. Maryland is a Zero Emission Vehicle (ZEV) state, and consequently, electric vehicle (EV) penetration is ramping up to meet the state's goal of reach 300,000 EVs on the road by 2025.

As part of their EVsmart® program that was approved in 2019, Exelon Maryland Utilities have begun installing a network of utility-owned and operated public charging stations. This network, which will grow to 850 stations across Maryland by 2025, will complement Exelon Maryland Utilities' other programs that provide charging equipment rebates and time-of-use rates to residential and commercial customers, amongst other program offerings.

Exelon understands the impact large-scale EV adoption will have on the electric transmission and distribution systems if customer charging behavior is not monitored or adjusted to avoid adding enormous charging demand to the system during traditional peak times. If unchecked, EV charging load will increase the ratepayer capital investments required to ensure a stable and reliable electric delivery system. With DOE funds, the Smart Charge Management (SCM) program will show Exelon's commitment to the environment, beneficial electrification, and provide innovative solutions to customers by demonstrating how EV managed charging can provide grid relief that benefits both EV drivers and non-EV drivers alike through cheaper rates and more reliable power. This SCM project will also set the foundation for future EV projects throughout Exelon.

Objectives

The objective of the project is to research, design, and conduct a wide-scale demonstration of a utility Smart Charge Management (SCM) system to develop optimal managed charging structures for grid value as well as evaluate the impact of EV charging on distribution utility operations. The project will also test the utilities' ability to control EV charging load based on grid conditions.

The project will implement large-scale utility managed charging of electric vehicles and is expected to deliver a stack of benefit streams that will accrue to the local distribution utility, the Electric Vehicle Supply Equipment (EVSE) partner, EV owners, and all customers. The project will enable Exelon to demonstrate multi-layer communication and coordination between the local electric distribution utilities (BGE, Pepco, and DPL), an EVSE partner (Shell Recharge Solutions), an EV telematics provider (WeaveGrid), a smart charge

adapter provider (EVmatch), a federal research facility (Argonne National Laboratory), and EV owners participating in the pilot project.

The proposed project will be implemented in two phases:

In Phase One (BP1 2021 – BP2 2022), Exelon will work with the partners to conduct tests and experiments at the Argonne National Laboratory (ANL) to inform and serve as the foundation for the large-scale demonstration. The goals include:

- Demonstrating the integrity of the EVSE, vehicle telematics software and the communication network prior to public deployment through cybersecurity testing and validation at ANL’s Smart Energy Plaza.
- Partnering with Smart Electric Power Alliance (SEPA) to conduct market research and perform industry interviews to develop SCM offerings for customers.
- Simulating the impact of EV charging on the grid in the next 10-15 years in Maryland using ANL’s Agent-based Transportation Energy Analysis Model (ATEAM) tool. This includes analyzing customer charging behaviors in response to EV charging incentives, simulating large-scale co-evolution of EV adoption, and charging deployment in the study area, and potential load impacts to the grid.

In Phase Two (BP3 2023 – BP4 2024), Exelon will carry out the large-scale Smart Charge Management (SCM) demonstration. The goals of the Phase Two demonstration include:

- Understanding EV owners’ charging behavior in response to a portfolio of utility signals and incentive structures across various customer categories to maximize future enrollment in SCM.
- Simulating and evaluating the impact of EV charging on local distribution utility operations and evaluate the utilities’ ability to actively control EV charging load based on grid conditions at the feeder and transformer level.
- Demonstrating the value streams from utility managed smart charging to the EV owner, the EVSE partner, and the local electric distribution utility and its customers.
- Demonstrating the ability for EV charging networks to provide frequency regulation and other electric grid services from EVs.

Approach

In Budget Period (BP) 1, Exelon’s Maryland Utilities partnered with ANL, Shell Recharge Solutions and WeaveGrid to perform cybersecurity testing and validation of the electric vehicle supply equipment (EVSE), smart adapter and vehicle telematics-based software platform’s ability to provide electric grid services. Exelon also partnered with SEPA to conduct market research and perform industry interviews to develop best practices and lessons learned that will guide the managed charging program design.

BP2 (2022) focused on grid impact simulation and customer engagement. ANL developed their Agent-based Transportation Energy Analysis Model (ATEAM) to begin simulating the impact of EV charging on the grid. Exelon also worked with SEPA to design innovative tactics that will maximize customer participation, flexible resource availability, and grid benefits. Exelon marketed the programs to customers and enrolled residential and commercial fleet customers into the managed charging programs. Exelon continued to install a utility-owned charging network and purchased chargers to provide to fleet customers enrolling in the fleet managed charging program.

BP3 (2023) saw the launch of the wide-scale customer demonstration of managed charging across residential, commercial fleet and public charging assets. Exelon conducted the first year of utility-managed charging program under a portfolio of tactics to test customer behavior and grid impact. Exelon evaluated program

impacts and adjusted tactics to deliver more beneficial grid results and better drive customer behavior. Exelon also worked with ANL to collect results from the residential demonstration to update the ATEAM model in preparation for the grid impact analysis.

BP4 (2024) will be the second and final year of the wide-scale customer demonstration of managed charging. Based on the results and learnings from the first year of the demonstration, Exelon will refine the design of the managed charging programs and adjust the program design, where applicable, to optimize the benefits for both customers and the utility. Upon the conclusion of the managed charging demonstration, Exelon and its project partners will perform analysis on customer behaviors, quantify the demonstration benefits, and produce and share a report of the project results.

Results

Task 3.1 – The Recipient will conduct smart charge management demonstration

Working with its residential program vendor, WeaveGrid, Exelon successfully enrolled nearly 3,500 customers into the program by the end of September 2023 (BGE- 2492; Pepco- 918, DPL- 82). Some of these customers have more than one Tesla at their home and opted to enroll both vehicles in the program for a total of 4,382 vehicles actively being managed through the residential program. WeaveGrid's management began in late 2022 with the implementation of the TOU rate demonstration phase. During this phase, customers' EV home charging was optimized based on their electric rate structure, ensuring at all customers enrolled in a time-of-use rate were charged during off-peak hours, incentivizing participants for positive charging habits and providing extra benefits for those customers already enrolled in a TOU rate. These customers not only received the \$10 monthly credit for participated in SCM but benefited from the off-peak charging discount. To align with this off-peak strategy, all customers who had the ability to shift their EV charging to off-peak hours were also included in this bulk group.

The second phase of the demonstration ran from June 21, 2023 through September 21, 2023 and looked at PJM price forecasts, aligning customer charging with the hourly cost of electricity and charging customers when electricity was cheapest and renewable energy was most prevalent in the region (2am-6am) and avoided the most expensive hours (5pm-7pm). The highest electricity values were noted from 5pm-7pm and were avoided through this program. The PJM integration shifted the timing of EV charging load activity, resulting in an estimated 38%-42% avoided costs per vehicle in wholesale purchasing costs according to the forecasted price for BGE. For the BGE participant group, the PJM demonstration was able to increase the number of customers charging from 2am-6am from 9.7% before the demonstration ran to 67.5% during the demonstration. WeaveGrid identified that this shift in managed charging would lead Exelon to potential **annual savings of \$44-91 per vehicle** if the company continued to align with PJM price forecasting.



SCM PJM Scenario Vehicle Group - June 21 to September 21, 2023
 Weekday and weekend hourly home energy consumption and utility signal

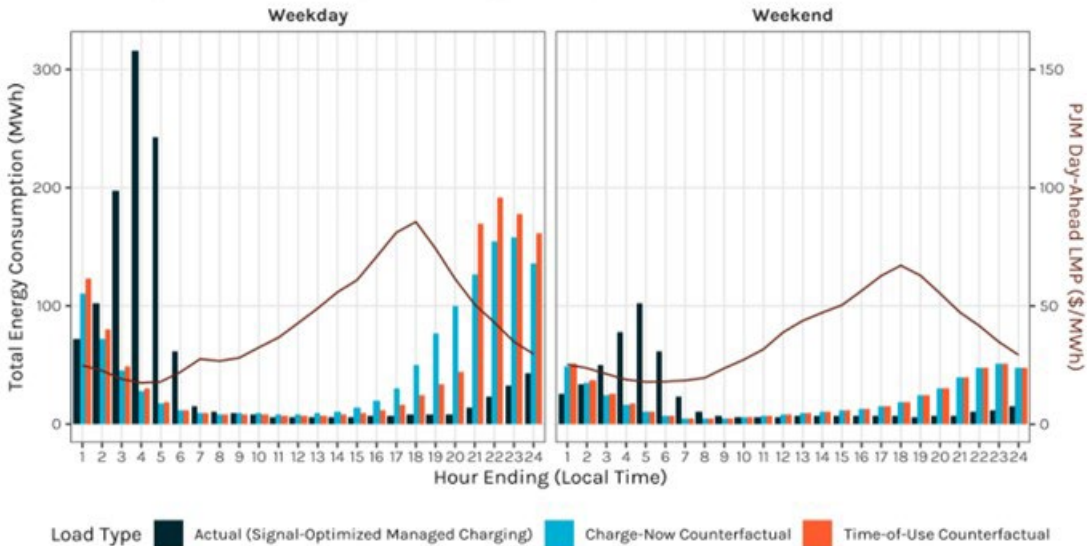


Figure II.1.7.1 (Shift in load from counterfactuals. Source: WeaveGrid PJM Integration Impact Report)

Table II.1.7.1 (Wholesale Cost Savings from PJM Demonstration. Source: WeaveGrid PJM Integration Impact Report)

	BGE	Delmarva	Pepco
Number of Vehicles ²	1,716	71	672
Total Home Charging Energy Delivered (MWh)	1,719	81	540
Energy Delivered per Vehicle (MWh)	1.00	1.14	0.80
Total Wholesale Home Charging Cost (Actual)	\$41,499	\$1,575	\$12,956
Total Wholesale Home Charging Cost (TOU CF)	\$66,422	\$3,095	\$20,421
Total Wholesale Home Charging Cost (Charge-Now CF)	\$71,848	\$3,184	\$20,932

In addition to the residential program, Exelon Maryland Utilities worked with Shell Recharge Solutions to implement both the fleet and public program demonstrations. While the fleet program had a very slow start, the public program saw more success. Exelon held its first demand response (DR) event on its public charging network on April 26. Exelon informed EV drivers of the DR event by posting on their social media (Facebook & Twitter) pages 24 hours in advance along with a message on PlugShare. SRS also setup automatic driver app notifications 8hrs ahead of the DR event to inform drivers. During the event, the SRS mobile app informed drivers about the ongoing DR event, its associated power/rate reductions, and allowed the drivers to opt-in or opt-out of the DR event through the app. After the DR event, SRS extracted reports showing drivers engagement, power and revenue generated during the DR and Control events and share the reports with Exelon. Exelon has since then completed 12 more DR events on its public charging network. Event #11 was implemented at a site-specific location rather than across the entire public charging network to test the ability to reduce EV charging load at a specific charging site rather than across all EV chargers within Exelon’s portfolio. The price and power reductions of all these DR events ranged from 15% all the way to 40%. Events were called on both weekdays and weekends during both the morning and afternoon hours. Events lasted

anywhere from two to four hours. Exelon has not found any trends so far between price, power, and days of the week to explain customer motivations for charging habits. Future site-specific events will be scheduled to continue demonstrating this time of load relief method.

On the fleet program side, the first 4 chargers were commissioned and the participating customer, Department of Public Works in Annapolis, was onboarded to Shell SKY software in August 2023. SRS is currently working with EvoCharge to fix the chargers firmware compatibility with Shell SKY Smart Charging capabilities. SRS identified incompatibilities between EvoCharge's firmware and the SKY platform that make it impossible to set SCM customers up on smart charging. Issues were not resolved in Q3 and firmware testing and validation continues, which has resulted in this first customer not operating on a managed charging schedule by the time this report was written.

Exelon has made progress in designing its frequency regulation demonstration with EVmatch, the new vendor supporting this task. EVmatch's smart charge adapter will connect directly to Exelon's fleet of chargers at BGE's Spring Gardens facility during a single day demonstration in early 2024. Exelon and EVmatch held meetings to design the demonstration, including consulting PJM's capacity market team to ensure the demonstration could be tested against real frequency regulation standards, per PJM requirements. EVmatch has completed all Exelon IT security requirements to move forward with the frequency regulation demonstration and the contract has been signed, allowing the ability to purchase the adapters needed for the demonstration. With the delay in completed IT security requirements, **Exelon has finalized a no-cost time extension to complete the work associated with this task.**

Task 3.2 – The Recipient will re-calibrate and validate ATEAM

ANL met with WeaveGrid and Exelon to learn more about different residential program demonstration strategies which includes TOU rate optimization, PJM price signaling integration, and distribution asset protection. ANL has validated the ATEAM charging load outputs from the initial set of simulation runs and included real-world observations from participants in the residential managed charging program through charging session data shared by WeaveGrid. ANL has completed preliminary EV charging scenarios up to 2035 using rate-based (TOU) managed charging optimization strategies, which was the first phase of the demonstration. They are now working on the demonstration asset protection demonstration, which began October 2023.

Task 3.3 – The Recipient will collect results from ATEAM that will be used in the grid impact analysis from the SCM Demonstration

ANL met with Exelon and WeaveGrid to learn more about the different SCM demonstration phases, including TOU rate optimization, PJM price forecasting, and distribution asset protection. WeaveGrid shared charging session and charging interval data with ANL. ANL used this real-world demonstration information to generate an initial set of results from ATEAM simulation. These results include both the home and public charging load at 15-minute intervals for each census tract in the study area up to 2035. ANL has developed the framework to process the ATEAM results for grid impact analysis.

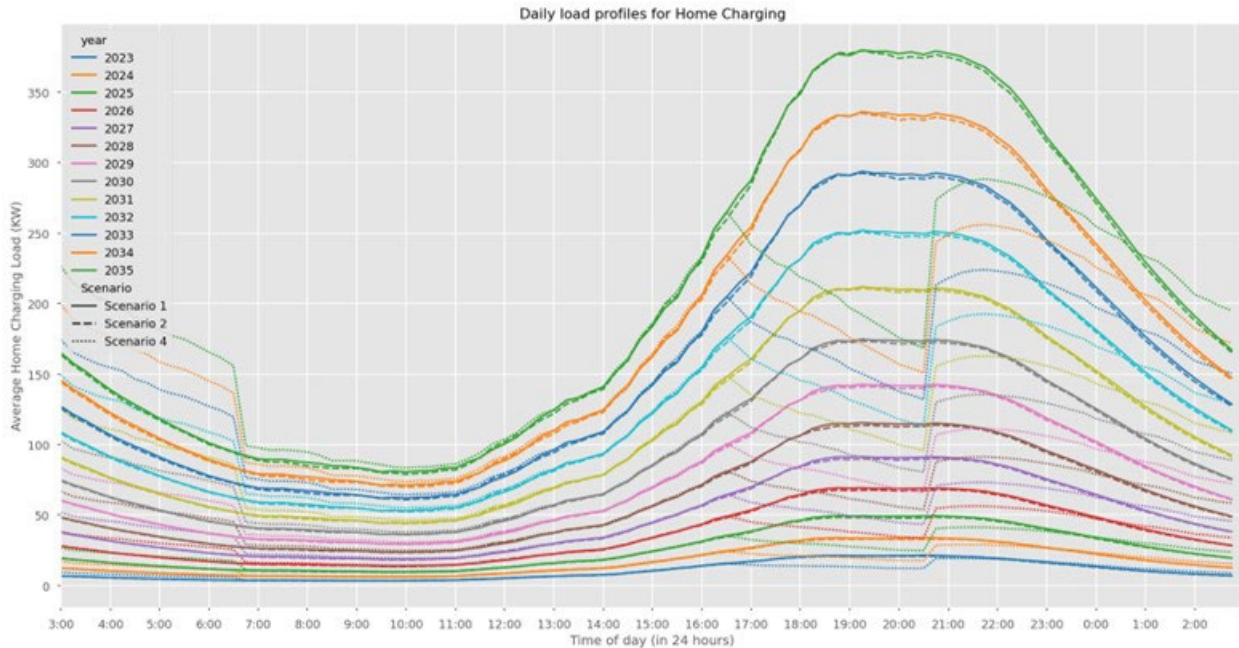


Figure II.1.7.2 (Daily home charging load for 3 of 4 SCM scenarios using real-world TOU demonstration. Source: Argonne National Lab ATEAM model)

Task 3.4 – The Recipient will develop ATEAM-Transmission system-Distribution system co-simulation tool (ATD) to analyze grid impact due to high penetration level of EVs

ANL implemented the ATD co-simulation tool. Data for ATEAM is separately generated and the output is then used, in a time synchronous manner, in ATD where the co-simulation time step is dependent on ATEAM time resolution. ANL ran two of the four managed charging scenarios for the two selected days (Christmas Eve and July 4th), every year from 2022 to 2035 at 15-minutes resolution. Currently, the team has only analyzed feeder level metrics such as histogram of voltage profile and line flows. They will next run additional scenarios and evaluate node level metrics.

Task 3.5 – The Recipient will analyze the economic impact (cost and benefit) analysis on EVSEs and the grid

As of the end of September 2023, ANL has run the scenarios for two selected days, every year from 2022 to 2035 at 15-minute intervals. About 185 million data points across 10 feeders. ANL is in the process of evaluating and understanding the generated results. Additional scenarios will be constructed and run to provide a complete picture. Additional scenarios will be run and node level metrics evaluated. ANL has been working on collecting publicly available data for economic analysis, including LMP for representative days, utility retail price for residential, commercial base load and EV charging for both BGE and PHI feeders. Exelon plans to share their own pricing data with ANL to ensure the economic impact analysis results will be true to Exelon’s Maryland Utilities.

Task 3.6 – The Recipient will perform cyber-physical-threat modeling and impact analysis considering large scale distribution system with EV penetration.

ANL reviewed potential cyber-physical threats emerging from the EV integration in the grid and documented the scale of vulnerabilities intrinsic to the EV cybersecurity landscape, emphasizing concerns like the inherent susceptibility of EV devices and the escalating potential attack surface. ANL classified various cyber threats that EV infrastructure faces, such as device misconfiguration, data interruption, MITM, and DoS attacks. A comprehensive categorization of vulnerabilities was executed, detailing their impacts starting from single-unit breaches to expansive vendor-level intrusions. In ANL’s analysis, vulnerabilities were methodically classified based on their impact levels, ranging from single-unit to widespread vendor-level intrusions. Collaboratively,

ANL conceptualized a simulation framework that integrates both cyber and physical layers of interconnected systems. The team will further refine this framework based on ATEAM's outputs. ANL also highlighted the potential consequences of cyberattacks on EV integrated grids, emphasizing the broad-ranging implications these could have on daily operations and the power network at large. Furthermore, ANL introduced various resiliency metrics aiming to quantify the system's performance in the wake of cyberattacks.

Task 3.7 – Share demonstration progress and results with other utilities and stakeholders

SEPA completed a mid-project report, soliciting feedback from all project partners and producing a professionally designed report and executive brief, available in August 2023. SEPA published a concise, one-page executive brief derived from the interim report, making key findings and recommendations readily accessible to decision-makers and stakeholders. As of October 11, 2023 the report and executive brief have been downloaded over 300 times. SEPA also held its annual RE+ convention on September 12, 2023, which included a 90-minute Managed Charging Workshop featuring Exelon and WeaveGrid project partners.



Figure II.1.7.3 Exelon's Managed Charging Program Phase 1 Review report. Source: SEPA <https://sepapower.org/resource/managed-charging-incentive-design>

Conclusions

Exelon has seen tremendously positive results for its residential program demonstration and has already filed to make it a full-scale program at the conclusion of the DOE pilot. Exelon is eager to see the results of the economic impact analysis and grid impact analysis that ANL is developing and will have completed at the end of BP3. While almost all BP3 Tasks are on track to conclude on time, the tasks associated to the smart charge adapter and frequency regulation are scheduled to conclude in early 2024 and have lead Exelon to ask for a no-cost time extension. The learnings that Exelon will glean from managed charging will help the utilities as they continue to build out their EVsmart programs and other beneficial electrification offerings for customers. This pilot will also provide Exelon with the economic and grid impact research and results it needs to prepare for widescale EV adoption and plan for the any necessary grid infrastructure investments to keep up with electric demand.

Acknowledgements

The author would like to thank members of the project team. From Exelon, Josh Cadoret, Joe Picarelli, Kristy Fleischmann-Groncki, Amanda Janaskie, Vince Wynne. From ANL, Joann Zhou, Nazib Siddique, Zhi Zhou, and Lusha Wang. From SEPA, Garrett Fitzgerald and Carolyn Dougherty. From Shell Recharge Solutions, Adrian Larnaud. From WeaveGrid, Joaquin Obieta, Alex Slaymaker, and Rachel Robinson.

II.1.8 Bidirectional Wireless Power Flow for Medium-Duty Vehicle-to-Grid Connectivity

Steven Sokolsky, Principal Investigator

CALSTART
48 S. Chester Ave
Pasadena, CA 91106
E-mail: ssokolsky@calstart.org

Omer C. Onar, Technical Lead

Oak Ridge National Laboratory, Vehicle Power Electronics Research Group,
National Transportation Research Center, 2360 Cherahala Boulevard
Knoxville, TN 37932
E-mail: onaroc@ornl.gov

Lee Slezak, DOE Technology Development Manager

U.S. Department of Energy
E-mail: Lee.Slezak@ee.doe.gov

Start Date: October 1, 2016	End Date: March 31, 2024	
Project Funding: \$2,631,321	DOE share: \$1,949,007	Non-DOE share: \$712,314

Project Introduction

Wireless power transfer (WPT) is a paradigm shift in electric-vehicle (EV) charging that offers the consumer an autonomous, safe, and convenient option to conductive charging and its attendant need for cables. With WPT, charging process can be fully automated due to the vehicle and grid-side wireless communication systems, and is non-contacting and inherently isolated; therefore, issues with leakage currents, ground faults, and touch potentials do not exist. It also eliminates the need for touching the heavy, bulky, dirty cables and plugs. It eliminates the fear of forgetting to plug-in and running out of charge the following day and eliminates the tripping hazards in public parking lots and in highly populated areas such as shopping malls, warehouse loading areas, recreational areas, parking buildings, etc. Furthermore, the high-frequency (HF) magnetic fields employed in power transfer across a large air gap are focused and shielded, so that fringe fields (i.e., magnetic leakage/stray fields) attenuate rapidly over a transition region to levels well below limits set by international guidelines for the public zone. With the bidirectional wireless power transfer, not only vehicles can be wirelessly charged, but also the vehicles can wirelessly provide power back to the grid or the facility. With bidirectional power flow, vehicles can be enabled to provide microgrid or grid support or ancillary services. Grid support may include peak shaving, renewable energy firming/integration, time of use energy management, power quality improvement, voltage regulation, reactive power compensation, etc. Grid ancillary services to be provided might include spinning and non-spinning reserves, area/frequency regulation, load following, scheduling and dispatch, etc. if a number of vehicles are aggregated to provide such services. In the case of an outage, vehicle batteries can also serve as an emergency backup power for a period of time.

In this project, CALSTART, ORNL, UPS, Workhorse Group, and Cisco Systems proposed to model, research, analyze, design, develop, integrate, and demonstrate a bi-directional wireless power transfer system (BWPT) suitable for Class 5 and Class 6 medium-duty plug-in hybrid delivery trucks. The project team designs, develops, integrates, and tests a bi-directional wireless charging system capable of meeting the 11-inch ground clearance needed for UPS delivery trucks. After integrating to a Workhorse manufactured plug-in hybrid electric vehicle (PHEV), the system performance will be demonstrated at the deployment site. Within the first budget period of the project (May 2017-May 2018), team has completed the modeling, simulations, design, and analysis of the system power conversion stages including the 3-phase active front-end rectifier with power factor correction (also grid interface inverter), primary-side HF inverter (also primary-side rectifier), primary and secondary-side resonant tuning components, primary and secondary-side electromagnetic coupling coils, vehicle-side HF rectifier (also the vehicle-side HF inverter). As of submission time of this report, hardware

both the primary and secondary sides have been completed and the power conversions stages have been successfully tested. All of the subsystems and components have been validated based on their parameters and performance metrics. The full system has recently been deployed with full vehicle integrations and is undergoing final commissioning prior to deployment for and data collection purposes.

Objectives

The overall project objectives can be summarized as follows:

1. Provide an automated, high power, interoperable, high-efficiency wireless charging for a plug-in hybrid electric medium duty delivery truck with a nominal ground clearance of approximately eleven (11) inches.
2. Optimize the add-on vehicle-side wireless charging components through integration and utilization of already existing vehicle-side components while implementing grid-side controls and regulations to reduce the vehicle-side cost, size, volume, and complexity.
3. Utilize bi-directional wireless charging systems when trucks are parked in the yard for staging to provide grid support applications or ancillary or grid support services such as frequency regulation, load leveling/peak shaving/load factor improvement/reactive power support/demand charge management, and spinning/non-spinning reserves.
4. Provide an integrated > 20kW wireless charging system (grid to vehicle) with high efficiency (85%) while meeting the international guidelines on electromagnetic and electric field emissions during charging and include all other appropriate safety features.
5. In vehicle-to-grid mode, achieve 6.6kW wireless power transfer to building or grid loads.

Approach

Starting from the AC grid to the vehicle battery terminals, the system power converters must be well-designed and operated in order to achieve high efficiency. In addition, power flow control to the pick-up system should be resolved where the control parameters (DC link voltage, frequency, duty cycle, phase-shift, etc.) are actively controlled to improve efficiency while meeting the vehicle-side target voltage, current, and/or power. Simultaneously, vehicle-side DC link or battery voltage, current, temperature, and the state-of-charge (SOC) should be carefully monitored and fed-back to the primary side for controls. Moreover, the battery management system (BMS) or other vehicle-side functions (i.e., contactors and liquid cooling system) should be monitored for safety. The bidirectional wireless charging system that will be used in this project is shown in Figure 1. This is the overall system architecture that is determined and agreed upon by the technical team. For this architecture, the baseline performance metrics have been defined, system specifications have been determined, and the hardware including the power stages and passive components have been designed and developed in ORNL PEEM laboratory. As shown in Figure II.1.8.1, system utilizes a three-phase rectifier/inverter system that interfaces the wireless charging system to the grid. During charging, the active-front end rectifier with power factor correction (PFC), delivers power from the grid with high power factor to the HF power inverter's input. The input (grid) current is controlled in order to regulate the inverter input voltage, depending on the amount of power to be transferred to the vehicle-side battery. The HF power inverter generates the HF current for the primary coupling coil. On both primary and secondary, LCC type resonant tuning configuration was utilized for operational symmetry since the bidirectional power flow is needed. Additionally, LCC type resonant tuning circuitry provides load and coupling factor independent constant current on primary coil which simplifies the communication requirements and the control systems. On the vehicle side, there is a receive coil with a rectifier/inverter, and a filter capacitor. During discharging or vehicle battery powering the AC grid/building loads, the vehicle-side converter is operated in an inverter mode and delivers HF current to the vehicle coil. The vehicle-side coil generates a magnetic field that is linked to the ground coil. The ground coil induces a high frequency voltage that is rectified and inverted to 60Hz to power the building loads or to the AC grid.

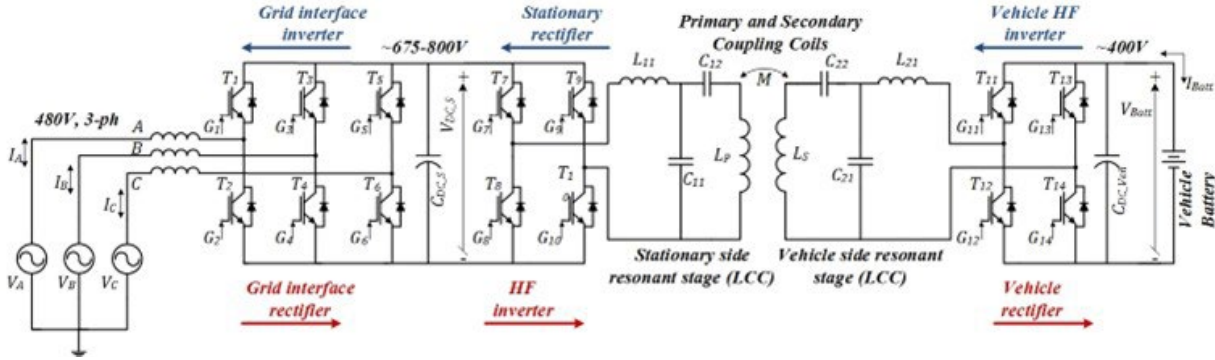


Figure II.1.8.1 System level diagram of the proposed architecture for the bidirectional wireless charging system.

While the hardware development was completed in the previous FYs, this FY the focus was on the hardware improvements targeting a robust and reliable system for long-duration (up to 3 hours) operation. Figure II.1.8.2 shows the final system hardware of the primary and secondary sides.

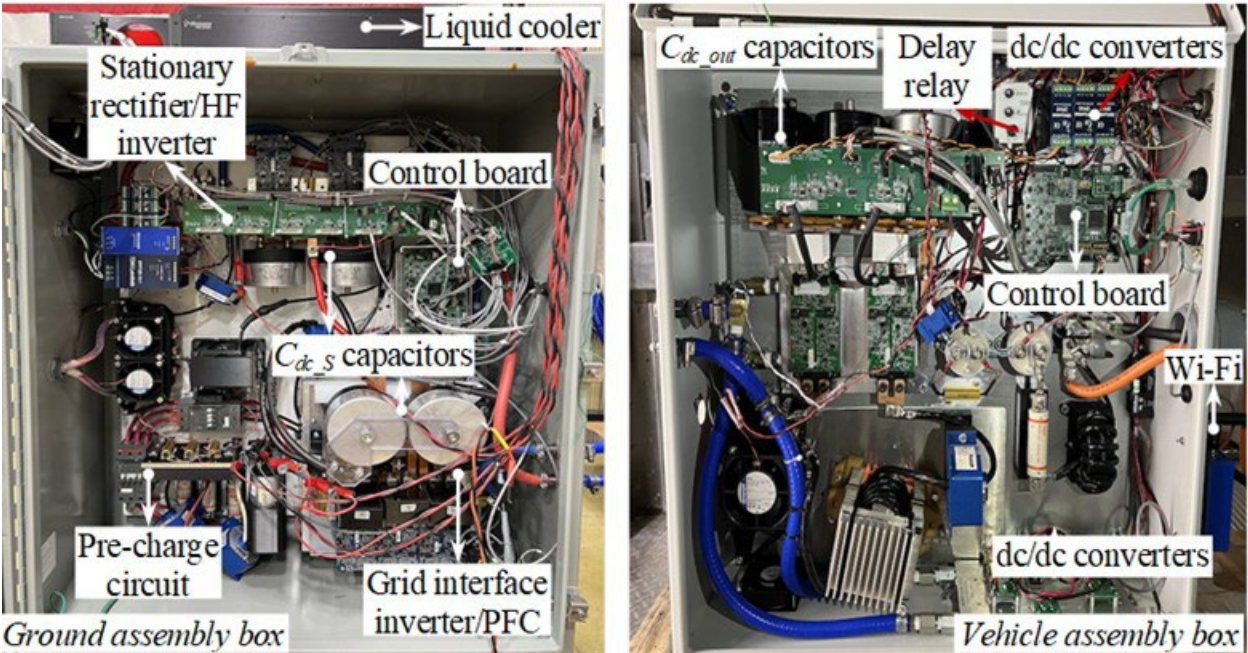


Figure II.1.8.2 Final look of the primary and secondary side hardware enclosures.

A new dual-band wireless communication system has been integrated to the ground and vehicle side systems. On both the primary and secondary sides, LCC resonant tuning components reconfigured to reduce heating to support long-duration operation. These modifications included adding another core stack to the tuning inductors to reduce the core losses and eventually the heat generation. Tuning capacitors were also modified with additional capacitors in parallel to reduce the current and capacitor heating. On vehicle-side unit, earlier the 12V truck battery was used to power all the auxiliary units including the contactors, gate drivers, sensors, digital signal processor (DSP)-based control system, radio communication unit, and the liquid cooling system. In the improved design, project team used a time delay relay and high-voltage (250-425V input voltage range) to 24V dc/dc converter to supply power to the +15V, +/-15V, and 5V converters. A second high-voltage (250-425V input voltage range) to 12V dc/dc converter also utilized in the new system to power the liquid cooling system on vehicle side. With that, the 12V truck battery is used only at the initial start-up for about a minute. And then, the time-delay relay enables the use of these dc/dc converters for a self-sustained operation without using the 12V truck battery for the rest of the charging process. With that, the power transferred to the vehicle

wirelessly is used to power all the auxiliary units. In addition, the vehicle-side unit has been mounted on the side wall of the UPS truck to reduce the size and volume that it occupies. Figure II.1.8.3 shows the UPS truck with the vehicle-side unit mounted on the side wall as well as the transmitter coil on the floor. Project team also added a frame box with bright white reflective color on the transmitter coil to make it more visible to avoid other trucks running over the transmitter coil.



Figure II.1.8.3 UPS truck with bidirectional wireless charging with full operation at the ORNL's GRIDC facility.

Results

After extensive laboratory testing, the UPS truck and the wireless charging hardware were deployed and tested at the Grid Research Integration and Deployment Center (GRID-C) of ORNL as shown in Figure II.1.8.3. While earlier UPS had determined that we would perform an outdoors installation with the primary side being mounted on a wall or pedestal, with the change of the deployment site to Roswell, GA facility, plans have changed to perform an installation underneath the loading dock at indoors at this UPS facility. As a result, the 480V 3-phase supply service with a disconnect switch was installed underneath the loading lock. This approach required mounting the primary side unit under the loading dock and adding about 13.5 feet of extension Litz wire cabling between the ground side unit and the transmitter coil. Moreover, the user control panel, earlier on the primary-side enclosure, needed a separate unit to be installed on a post where the vehicle backs up for easier access to enable the operation of the wireless charging system. This deployment scheme is depicted in Figure II.1.8.4 showing the 13.5' additional distance required from the ground side unit to the transmitter coil.

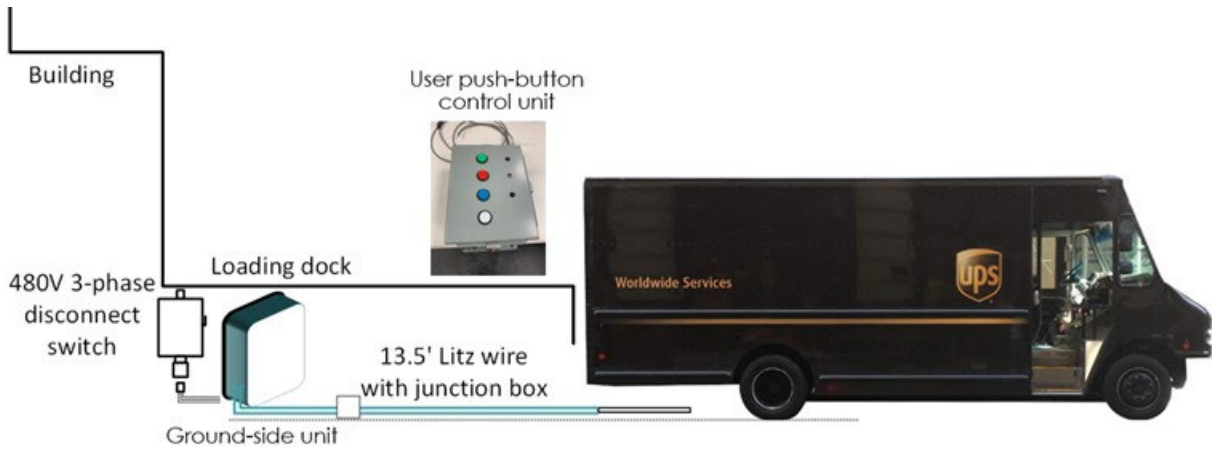


Figure II.1.8.4 UPS truck at the loading dock with the wireless charging equipment installed underneath the dock.

The laboratory testing prior to the deployment included long duration testing for up to three hours since the 20kW wireless charging system takes about a maximum three hours as the truck is equipped with a 60kWh battery pack. The primary and vehicle side coolant temperature profiles for a three-hour charge duration are provided in Figure II.1.8.5 where the initial ambient temperatures were about 22°C and the final temperature for vehicle coolant reached to about 25°C and the final temperature for the primary side unit reached to about 28°C. indicating that the temperature rise for three-hour charge duration was limited to about 6°C maximum for the primary side coolant.



Figure II.1.8.5 Temperature profiles of the primary-side and vehicle-side coolant for a three-hour charge duration.

To further ruggedize the wireless charging system and improve it for real-world grid abnormalities, the control system of the grid interface active front-end rectifier / inverter has been improved with low voltage ride through capability to avoid the equipment damage or any interruptions to the charging service. With that, the system can tolerate voltage sags and swells as well as short-duration brown outs with anti-windup control approaches. With that, the system can survive and recover after brown outs or voltage sags lasting up to 10-12 seconds. In that situation, grid currents to the system can be reduced with the grid voltages and when the grid voltage recovers to the normal operating conditions, the system also recovers, without the grid currents running out of range or getting maximized. An example test scenario results are provided in Figure II.1.8.6 where the grid experiences a brown out for about 11 seconds and recovers. In that case, grid currents are also minimized, and primary-side dc bus voltage falls but quickly recovers upon the grid voltages are restored.

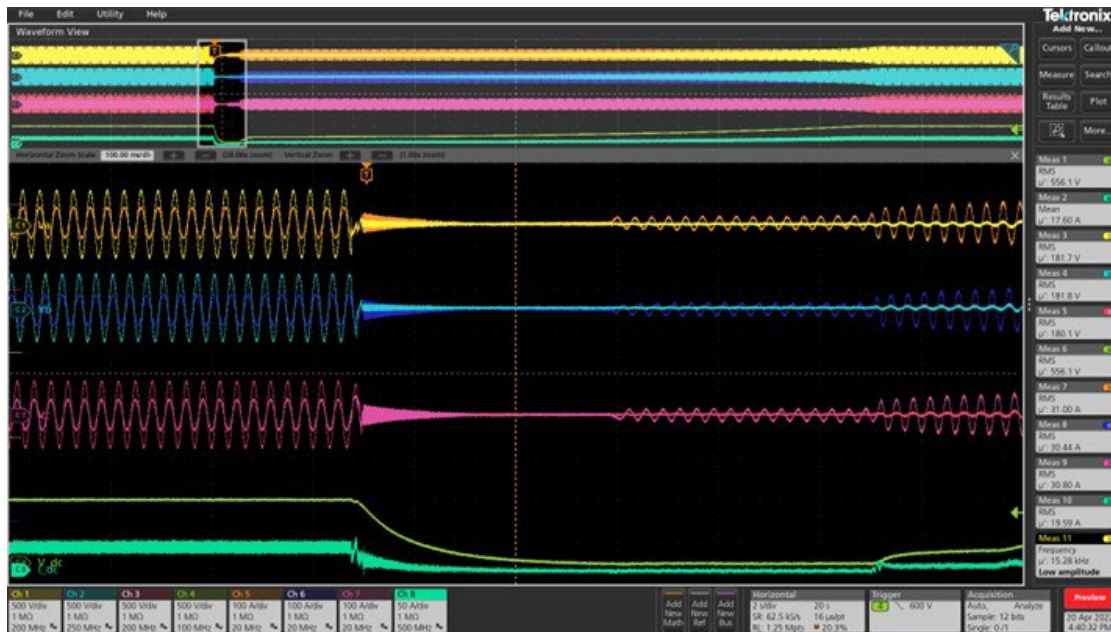


Figure II.1.8.6 The operation of the wireless charging system with low voltage ride through capability.

Conclusions

The third budget period work focuses on overall system improvements, testing the system for long-duration operation, and final systems testing and validation along with the final improvements of system components and control systems. The UPS truck and the wireless charging equipment has been delivered to the UPS deployment site at a UPS facility located in Roswell, Georgia for the real-world demonstration of the wireless charging system equipment including the ground side unit and the vehicle integrated secondary side. Upon the commissioning and brief training, the vehicle will be placed in normal operations at that facility and UPS will use the system for 6 months. Data will be collected during this period to demonstrate the repeatability of the performance and analysis of the use cases. The collected data will enable the project team to analyze the business cases and economics of this system using different use case scenarios.

Key Publications

1. “Secondary Active Rectifier Control Scheme for a Wireless Power Transfer System with Double-Sided LCC Compensation Topology,” in Proc., 44th Annual Conference of the IEEE Industrial Electronics Society (IECON), October 2018, Washington, D.C.
2. “Sensitivity Analysis of an LCC-LCC Compensated 20-kW Bidirectional Wireless Charging System for Medium-Duty Vehicles,” in Proc., IEEE Transportation Electrification Conference and Expo (ITEC), June 2019, Novi, MI.
3. “20-kW Bidirectional Wireless Power Transfer System with Energy Storage System Connectivity,” in Proc., IEEE Applied Power Electronics Conference and Exposition (APEC), pp. 3208-3214, March 2020, New Orleans, LA.
4. “Bidirectional LCC-LCC Compensated 20-kW Wireless Power Transfer System for Medium-Duty Vehicle Applications,” IEEE Transactions on Transportation Electrification, vol. 7, no. 3, pp. 1205-1218, September 2021.

Acknowledgements

Project team would like to thank Lee Slezak of U.S. Department of Energy and Jason Conley of the National Energy Technology Laboratory for their continued guidance and support on this project.

II.1.9 Technology & Design Innovations to Maximize the Reduction Effect on DCFC Unit Cost Economics (Max-REDUCE)

Robert Keefover, Principal Investigator

Chief Engineer
 BorgWarner Morse Systems
 3800 Automation Ave
 Auburn Hills, MI 48350
 E-mail: rkeefover@borgwarner.com

Fernando Salcedo, DOE Technology Development Manager

U.S. Department of Energy
 E-mail: Fernando.Salcedo@ee.doe.gov

Start Date: May 1, 2022 End Date: July 1, 2025
 Project Funding: \$5,180,000 DOE share: \$4,090,000 Non-DOE share: \$1,490,000

Project Introduction

This project directly address DOE’s need to research, develop, fabricate, and test a novel lower-cost EV DCFC. This project will result in a next generation DCFC system that delivers 360kW of power combined with the flexibility to deliver that power based upon specific vehicle requirements at 20% - 30% reduced cost compared with baseline state-of-the-art DCFCs.

Table II.1.9.1 Next Gen Unit Performance vs BorgWarner Baseline

	Baseline unit	Next Gen unit
Architecture	Dual conversion	Single conversion
Operating temp	-30C - +50C	-30C - +50C
AC input voltage	3x400V + 10%-15%	3x400V+10%-15% 3x480V+10%-15%
Max input current	3x188A 130KVA	3x188A 130KVA
Efficiency	94%	97%
Max power out	120kW	350kW+
Max current out	200A	400A+
Voltage out	200V – 850V	200V-1500V
Unit cost at power parity (120kW)	~\$15,000	20%-30%+ reduction
3rd Party State-of-the-Art units		
Unit cost at 150kW	TBD post-teardown	↓
Unit cost at 350kW	TBD post-teardown	↓

Barriers Addressed

- Reduced Cost of Electric Charging Infrastructure
- Enhanced Viability of Fast/Consumer-Friendly Charging
- Enabling Technology Development.

Objectives

The project’s objective are to develop and demonstrate a modular, single stage conversion architecture Direct Current Fast Charger (DCFC) with a unit cost reduction greater than 20% with a minimum 97% efficiency at

maximum output, power density $>4\text{kW/L}$, and improved reliability. A demonstration charger that provides a charge rate of at least 150 kW of DC power for charging multiple fleet vehicles at the same time will be developed.

Approach

To meet the objectives, we will target improvements to baseline technology in five component innovation areas:

- Single stage conversion architecture: Efficient transfer of grid AC power to vehicle battery of greater than 97%, enabled by a power conversion architecture with a lower component count when compared to the standard approach.
 - AC-AC matrix indirectly modifies the 60Hz line frequency to high frequency (50-100kHz) via switching modulation, no need to rectify AC grid power.
 - With high frequency AC a much smaller transformer is needed to isolate the DC vehicle output from the AC power grid.

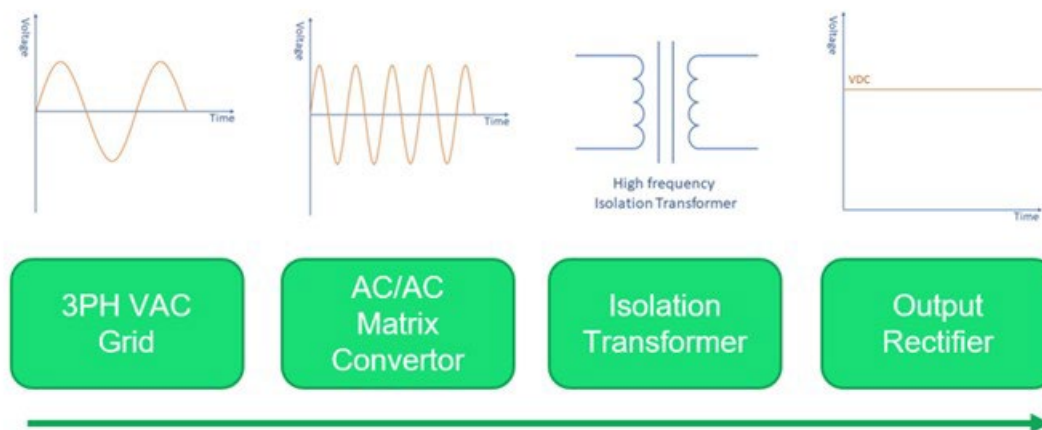


Figure II.1.9.1 Energy transfer topology

- Power conversion module design: Next generation WBG (Wide Band Gap) switches will be used in the power conversion modules that will increase device efficiency; thus leading to less power loss and reduced mechanical sub-components for thermal management (and reduced cost).
- Decoupled power electronics: A single power electronics cabinet serving 6 or more charge points, using smart active power management across the dispensers
- Modular building block approach: 60kW power electronics modules and controlling software (SW) will enable flexible charging point/cord output power ranges from a single electronics cabinet (60kW to 360kW+) for improved power balancing and infrastructure use.



Figure II.1.9.2 Charger and dispensers rendering

Results

Electronics hardware prototype was created and has passed initial testing and being setup for performance power testing at high voltage. Firmware has been developed with controls auto coded algorithm (generated in Matlab-Simulink, and is now in the HW-SW integration phase.

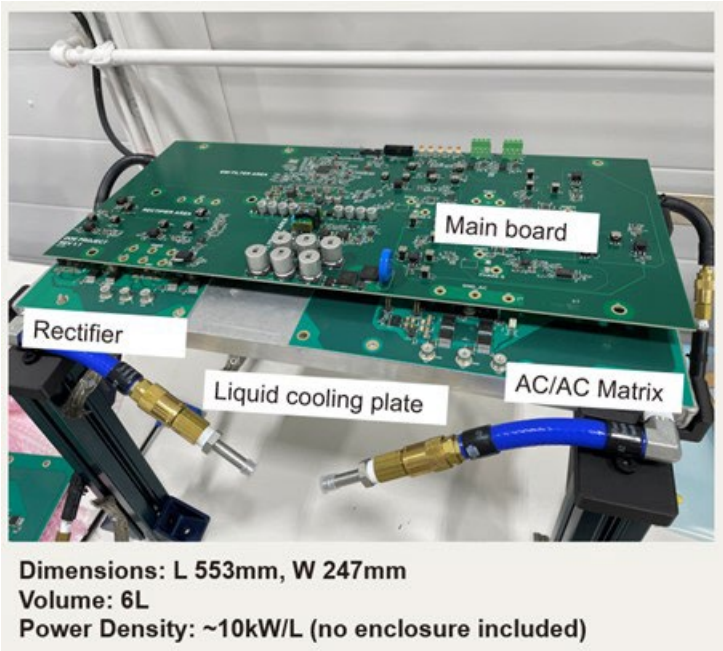


Figure II.1.9.3 60kW A sample power module prototype functional electronics hardware



Figure II.1.9.4 Successful modulation generation on AC-AC convertor



Figure II.1.9.5 Auburn Hills lab implementation

Development lab is now functional and continuing to add development equipment.

Conclusions

The research and development of the MAXREDUCE project so far has shown positive results against the goals for equalized 60kW bidirectional power module.

Remaining Challenges and Barriers

- The single conversion design utilizing the Matrix converter is a power conversion topology with a challenging control loop and a small technical bibliography available.
 - *We are solving this by working with partners to develop a control method and are working to demonstrate this on a 60kW prototype by the end of 2023.*
- The utilization of the integrated power SiC must be carefully assessed from a cost and performance point of view; currently bi-directional configurations are not readily available.

- *BorgWarner is working with industry partners, and internal SiC developments to leverage the best solution.*
- Manufacturability of the tightly integrated charger package and volume optimization of the component layout.
 - *The single stage high frequency design is allowing us to shrink magnetic and passive components greatly and reducing the number of components greatly compared to our existing architectures.*

Table II.1.9.2 60kW power module metrics comparison

	Bi-directional	Uni-directional	New Bi-directional design
Equalized cost (500 units)	(base cost)	22% reduction (approx.)	65% reduction (<i>estimated, achieved by innovation</i>)
Part count	3300 (approx.)	800 (approx.)	1100 (<i>estimated</i>)
Assembly process complexity	high	high	medium
Maximum Efficiency	95%	95%	target >97% (<i>achieved by innovation</i>)
Shipping Weight	high	high	medium
Power Density (W/L)	low	low	high (<i>achieved by innovation</i>)
Electronics commodity complexity	medium	medium	high
Software controls complexity	medium	medium	high

Key Publications

1. DKT22174 Seven-Switch Indirect Matrix Converter Topology with Dual-Gate Bidirectional Switch
Patent application submitted
2. DKT22206 Seven-Switch Indirect Matrix Converter Topology with Unidirectional Switches for AC to DC rectification
Patent application submitted
3. DKT22207 Three-phase to three-phase Direct Matrix Converter Topology for AC to DC power conversion
Patent application submitted
4. DKT23034 Multi-output battery electric vehicle charger with switched mode power supply
Patent application submitted

Acknowledgements

Brian Wightman – Engineering manager; system development
 Luca Di Carlo – Staff engineer; system and electronics development
 Jack Li – Staff engineer; firmware development
 Rakesh Nair – Staff Engineer; Algorithm development
 Jeff Kenyon – Senior engineer; Test execution and development
 Tony Moran – Engineer, firmware development
 Dr. Lee Woongkul – MSU (Michigan State University) Professor
 Mikayla Benson – MSU Grad Student
 Avinash Dornala – MSU Grad student

II.1.10 A Solid-State Technology Enabled Compact, Modular Design to Reduce DC Fast Charging Cost and Footprint (Eaton Corporation)

Dr. Bogdan S. Borowy, Principal Investigator

Eaton Corporation
W126N7250 Flint Drive
Menomonee Falls, WI 53051
E-mail: bogdansborowy@eaton.com

Fernando Salcedo, DOE Technology Development Manager

U.S. Department of Energy
E-mail: Fernando.Salcedo@ee.doe.gov

Start Date: May 1, 2022	End Date: August 31, 2025	
Project Funding: \$2,200,981	DOE share: \$1,760,785	Non-DOE share: \$440,196

Project Introduction

This project proposes an innovative approach to develop and demonstrate dramatic reductions in the cost of DC fast charging equipment. It will reduce weight and size of equipment, real estate, and installation costs for Electric Vehicle Power Supply Equipment. Moreover, it will provide faster charging times than are possible under present charging technology. The current charging technology is prohibitively expensive and charging times are long. The team has identified key areas of research to directly address these issues.

Project Realization & Timeline

In the Budget Period 1 (BP1) of this program, the focus is to develop technical requirements, validation methods, and test plans for each major element or subsystem of the system via modeling and simulations, subscale prototyping to quantify the system's optimization in terms of cost, size, performance, and reliability when employed into a grid as an integrated EV charging infrastructure. These critical elements include high density power conversion stages, High Voltage (HV) insulation, high frequency transformer (HFX), energy storage (inductors, capacitor banks), controls, and thermal cooling. Budget Period 2 (BP2) system development stages will bring the design incrementally into a full power (1.35 MW) / Medium Voltage (13.2 kV) demonstration level realization; the technology will be validated first at the National Renewable Energy Lab. This will be followed by field demonstration and validation at a site with a utility partner.

Major Goals & Objectives

The primary program objectives are listed as follows.

- Develop a compact EV charging infrastructure directly connected to medium voltage distribution networks at 12.5-13.8kV
- Integrate a stationary storage system to the DC to minimize negative impacts on the grid.
- Integrate multiple chargers at the facility with a safe distributed DC architecture.
- Reduce onsite commissioning time with factory commissioning.
- Reduce utility interconnection permit time and installation complexity.
- Develop a site controller that manages the vehicle charging, onsite DER, and utility interconnection requirements.
- Design with an integrated liquid cooling system to ensure long life under aggressive utilization.

- Validate the system charging infrastructure operation in the field with equivalent loads and, eventually electric vehicles.
 - Response to various charging scenarios (ramp rates, profiles)
 - Response to grid events
 - Response to fault conditions

Approach

To reach the listed goals and objectives, an assumed approach at the inception of the program was to divide the overall program into three stages. In the first stage, we address the objectives by identifying the critical technical areas and/or components that are essential for specific objectives such as cost, performance, reliability, etc. In this stage (BP1), the identified critical subsystems (topology selection, control architecture specifications, communications, thermal management approach, system protection and insulation, etc.) or components (active devices selection, high frequency transformer material selection) were subjected to research through computations, modeling and simulations, mathematical and physics-based analysis, and prototyping and testing the prototypes. Next, the individual subsystems and components were iteratively combined into system model to meet the overall system objectives. The results of BP1, therefore, provide a foundation for the development and deployment of the full-scale system – scheduled in BP2. In BP2 each incremental stage of the development is to be first verified against the BP1 results and then adjusted and validated in the laboratory and field real world conditions. Finally, a deployment in a field is scheduled for BP3.

Results

The major tasks and their results are presented in this section.

At a conclusion of BP1, all the objectives for this period listed in Table II.1.10.1 have been met.

Table II.1.10.1. Primary Program Objectives in BP1

Milestone	Type	Description	Progress / Evidence
Models demonstrate the SST and design specifications reduce Power electronics cost	Technical	New topology with 1200V modules to reduce cost by 15% verified compared to 1700V device-based converter	71% savings
HF Transformer Cost reductions verified.	Technical	HF transformer with optimized core results in ≥10% cost reduction compared to Nanocrystalline based system	Ferrite core (\$677 USD) is an 81% reduction in cost compared to Nanocrystal Core (\$3,601).
Charger module prototype design and testing increases efficiency from baseline	Technical	Modular charger efficiency ≥96% compared to AC fed chargers	Efficiency above 98%
Underserved community workshops conducted.	Technical	At least three workshops conducted to target the needs of underserved communities.	Two workshops completed. Two more planned for July 2023.
Site specific requirements for integrated system complete	Go/No Go	Prototype testing and model-based verification of integrated system completed, and the demonstration site specific requirements are ready for identified demo site	(see attached document: "Utility interconnection needs.pdf")

Define System Specifications and Performance Targets

The baseline and target metrics for the design established (Table II.1.10.2). The performance target definition was based on an iterative tradeoff analysis for selected several converters topologies, applicable control architectures, communication schemes vs. footprint sizes, losses and thermal requirements, insulation requirements, and robust operation under abnormal conditions.

Table II.1.10.2. Target Data Matrix

Item #	Description of sub-assembly	Performance Targets	Sub-assembly baseline performance/cost estimate	Relative importance of sub-assembly to the system performance	Target Spec	Unit
1	Cost target for active front end and DAB power electronics	The cost of the power electronics is very dependent on the power modules (voltage ratings, current ratings and number of gate drivers)	The considered devices for the SST design were 1) the 1700V SiC devices and 2) 1200V SiC devices. 1200V SiC modules have become more competitive in pricing but the number of devices needed to build a same voltage rated cascaded SST is larger. The baseline used here is 1700V devices from Wolfspeed. The baseline cost for the power stages (Modules, gate drivers, dc caps) was \$9115 per cell. This cost is for a 1.25MW SST with 11 cells per phase.	The power stage is central to the SST cost and performance; efficiency depends on this stage. Based on tradeoff analysis, the selected topology is based on 1200 V devices from Infineon utilized in 18 level cascaded topology.	Power stage cost should be 85% or less of the 11-cell SST with 1700v device price.	\$/MW
2	Cost target for High Frequency Transformer	The cost for the high frequency transformer is based on a 50kW. Voltage range of input 1200-1500 and output 800-950. Switching	The baseline design that is considered here is the nano-crystalline core used for a 10kHz switching that was developed earlier for a	Since the system will have 54 transformers, and provides key isolation from medium voltage the cost, efficiency, and size of the	The target spec for the transformer is now changed to a Ferrite Core based design to get cost and size benefit	

		frequency 10-30kHz	VTO project. A loading cycle profile will be developed based volumes of EV adoption provided by some studies such as the 1+MW projects with NREL.	transformer are significant.		
3	Replacement of air-cooled power electronics with liquid cooling	The junction temperature variation with ambient and load conditions and the number of such cycles will determine the life of the converter.	The module junction temperature range of operation with air and liquid cooling will be estimated. Then the use case will be used to analyze the cycles per year and used to determine the cooling system size and the junction temperature range.	The Liquid cooled system would reduce the size (footprint) and increase reliability. Reliability will reduce maintenance and replacement costs.	Average junction temperature to be 10 C lower.	Deferred replacement cost (\$/year)
4	Currently the EV chargers use distributed AC for fleets with each charger providing its own rectifier and dc-dc converter. Further, the energy storage has its own dc-dc and inverter to connect to the distributed AC.	In this project the energy storage is connected with another DC-DC to the common dc bus of the SST. The benefits of this connection of energy storage verses a storage with its own inverter are considered here. The cost advantage and requirements to meet the cost targets are provided here.	A baseline of a 400kW 200kWH battery storage connected to the ac distribution is used to estimate the cost and effectiveness of the control. When estimating the effect of the control on how well the grid impact is reduced by the energy storage connected to a common dc bus compared to an ac distribution is evaluated.	Cost of a MV connected 400kW Energy storage will involve a step-down transformer and installation of one. Typical cost is \$40,000.	Cost of additional DC-DC converter for energy storage should be less than \$20k	\$/MW

5	The integrated package proposed in this project is considered and compared with the distributed ac solution to compare the footprint in a typical fleet charging application.	Publicly available information will be used to evaluate the footprint per 1MVA current AC solution as the baseline footprint. (Data from NREL 1+ MW project)	MV Gear 60Hz Xfrmer LV Mains and Distribution sw. board Chargers Dispensers 150kW chargers 6 Cost: \$1013,000 with cost of land but inclusive of installation. Footprint: Based on ANL install: 400 sqft	Cost and footprint are important metrics for adoption of EV	Cost target \$1M Footprint target 300 sqft	
6	The utility connection for the system changes with utility and the location. By standardized solutions that can be offered the installation/permitting process cost can be reduced.	Cost of utility connection per 1MVA	Base model requires: Design 2-year wait period 6 Month purchase delay	Design is based on selection from options – no lead time No purchase delays	Target selection time of 2 months	Months
7	The proposed system integrates the chargers with the MV power converter. This will be compared with the distributed AC system with individual ac/dc rectifiers in the chargers with isolated dc-dc converters.	Cost of installation of non-integrated solution	Baseline from NREL is \$18000 per 150kW charger in addition to the MV/LV system installation	Dispensers need to be installed with minimal trenching and concrete:	Target cost of installation per dispenser: \$3000	\$/Dispenser

Scalable Architecture Definition

A medium voltage solid state transformer (MV-SST) is constructed using a multilevel cascaded H bridge (CHB). Each level consists of an active single-phase AC-DC rectifier. The output of this active front end (AFE) is fed into a DC-DC converter, which is configured as a bidirectional DC-DC converter. There is a high frequency transformer which isolates, and level translates the input square wave voltage. Isolation is provided to meet local and national electric codes. The bidirectional DC-DC converter is configured as a dual active bridge (DAB) and is associated with higher efficiency and lower EMI. A typical multilevel Cascaded H-Bridge is shown in Figure II.1.10.1. Figure II.1.10.2 gives a broader perspective of the complete developed system.

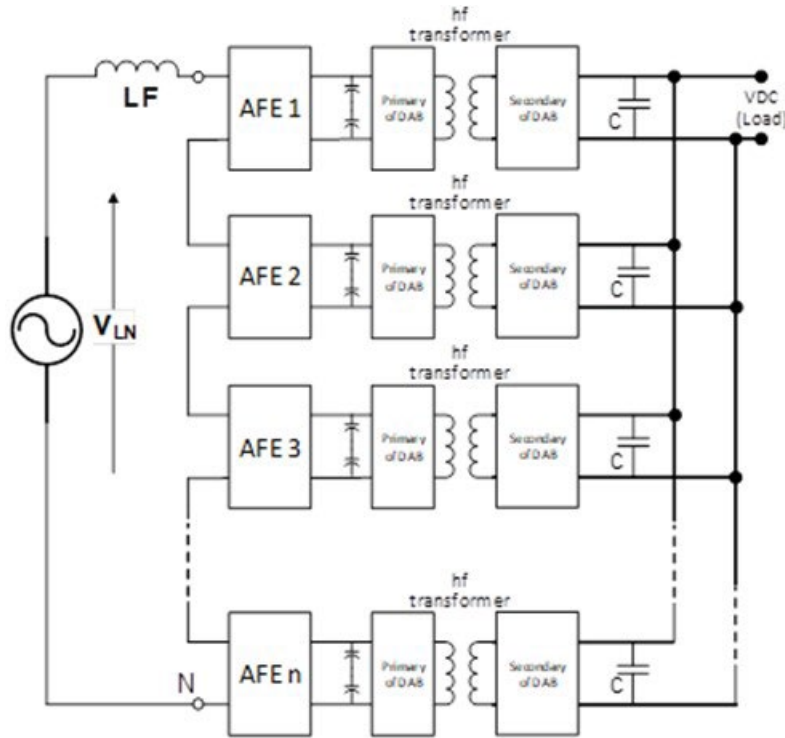


Figure II.1.10.1 Single Phase Rendering a Multilevel Cascaded H-Bridge Based Solid State Transformer Topology

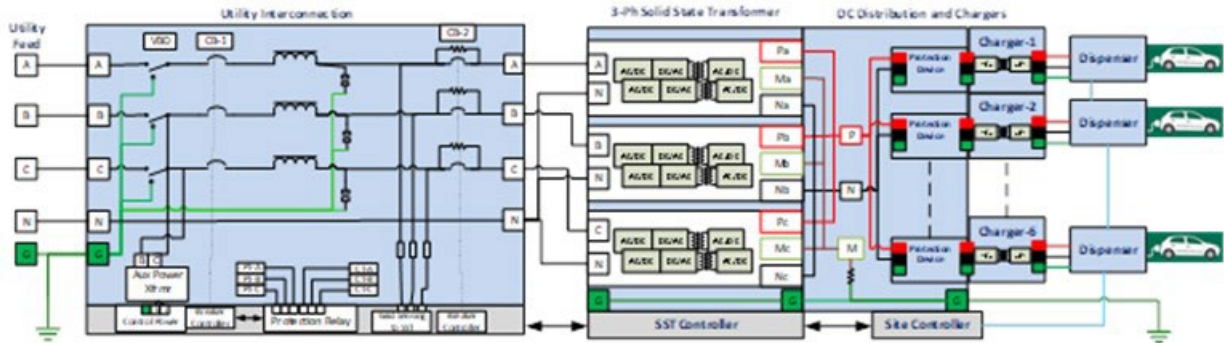


Figure II.1.10.2 Overall MV-SST System Architecture based on Cascaded H-Bridge Topology

The embedded control architecture reflects the defined system architecture as described above. It comprises three main controllers: a system controller, a high voltage side local controller and a low voltage side local controller. The system controller serves as the central hub for managing the overall system, with its primary functions including an EtherCAT master controller for communication, processing grid voltages/currents, containing the PLL, the DQ transformation and an HMI for user interaction. The EtherCAT communication protocol propagates the data collected from the system controller to the high voltage side local controller.

Simulation Model Development

Controllers and the system including power electronics converters and high frequency transformers were modeled and simulated on a Matlab/Simulink platform. The control algorithms and detailed controllers structure along with intermodular communications are based on results of the modeling. In addition, the model was utilized to estimate conduction and switching losses in the critical elements (active switching devices and high frequency transformers). The controls part of the developed simulation model is directly used in a rapid prototyping and Model Based Control development on a TI2000F28377D microprocessor from Texas Instruments.

Magnetics Design and Testing

Based on extensive team experience, most advanced literature review on MV SST topology, and IEEE/IEC standards, the DAB transformer design and parameters have been studied and identified. A special focus was directed to address the insulation requirements and passing all the insulation standards and partial discharge requirements. Moreover, the team has carried out a detailed comparison in-terms of mass/temperature rise/flux density utilization/ and minimum-through insulation distance at 10/15/20kHz between ferrite and nanocrystalline materials. The major findings and results are summarized in four sections as below: system level, electromagnetic, thermal, and most importantly insulation.

Based on Finite Element Analyses, three figures of merit were constructed to select optimal magnetic core material for the HF Transformer. These figures of merit are: 1) Total Mass vs. Coil Space, 2) Transformer Temperature Rise vs. Coil Space, and 3) Transformer Flux Density vs. Coil Space as shown in Figure II.1.10.3.

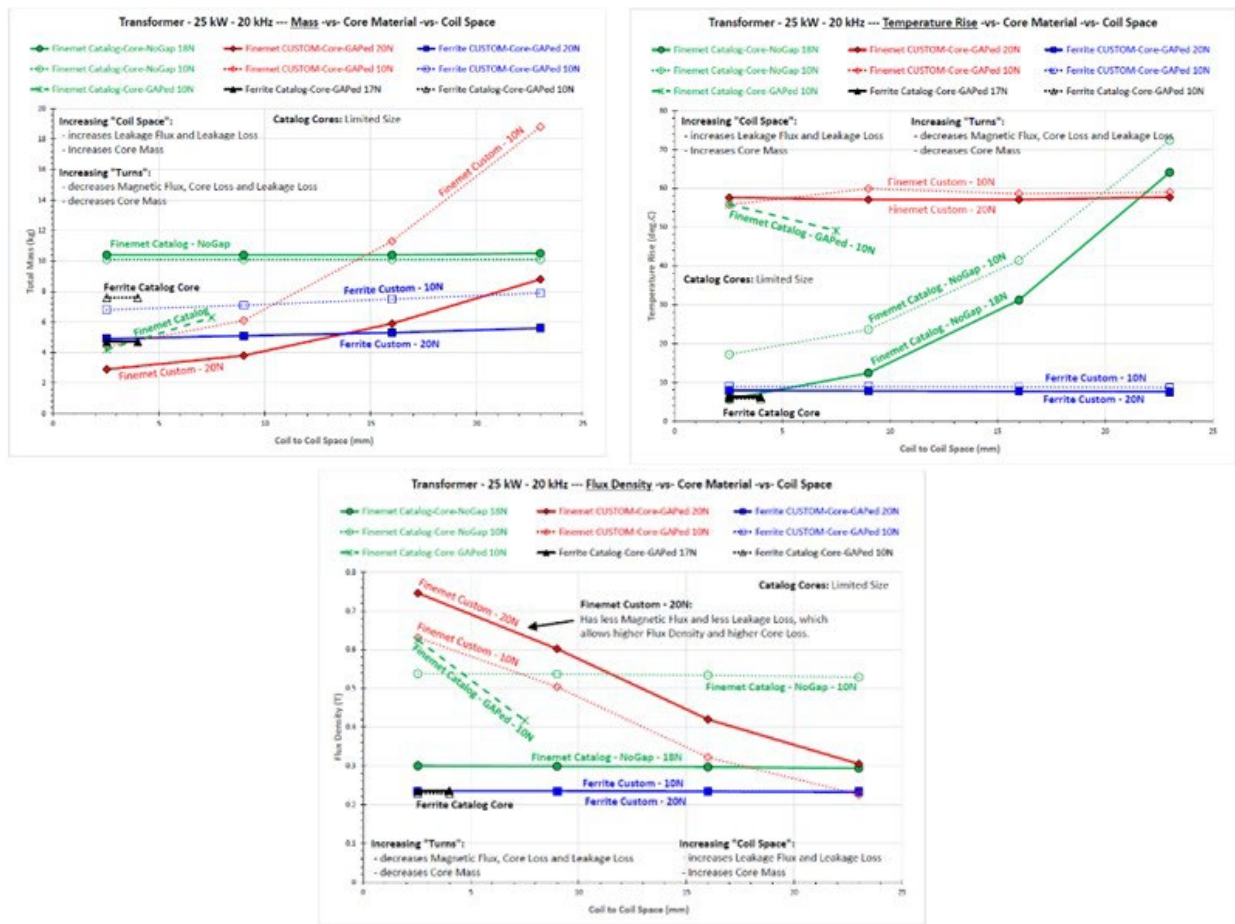


Figure II.1.10.3 Figures of Merit: Top Left: Total Mass vs. Coil Space; Top Right: Temperature Rise vs. Coil Space; Bottom: Flux Density vs. Coil Space

A first batch of the high frequency transformer has been fabricated and tested for insulation strength and partial discharge – all design requirements with necessary margins have been validated.

Thermal Design

The assumed modular system topology combined with low cost requirements and ease of field deployment necessitates built-in integrity of thermal management within each module. This approach adds another important integrity aspect: the modules can be completely electrically isolated from each other without a need of utilization of de-ionized water, what in the given MV application is particularly important from reliability

and maintenance angle. Packaging concepts were developed with liquid cooling thermal management is shown in Figure II.1.10.4. Each cascaded module is cooled with individual, electrically insulated, thermo-syphon; the power electronics devices are mounted on the evaporators and the condensers will be transferring heat to ambient. Both air cooling and liquid cooling concepts were studied for the heat transfer to ambient and the later was eventually selected as optimal. LV sections of all cascaded blocks are liquid cooled- as no electrical insulation is needed for these sections.

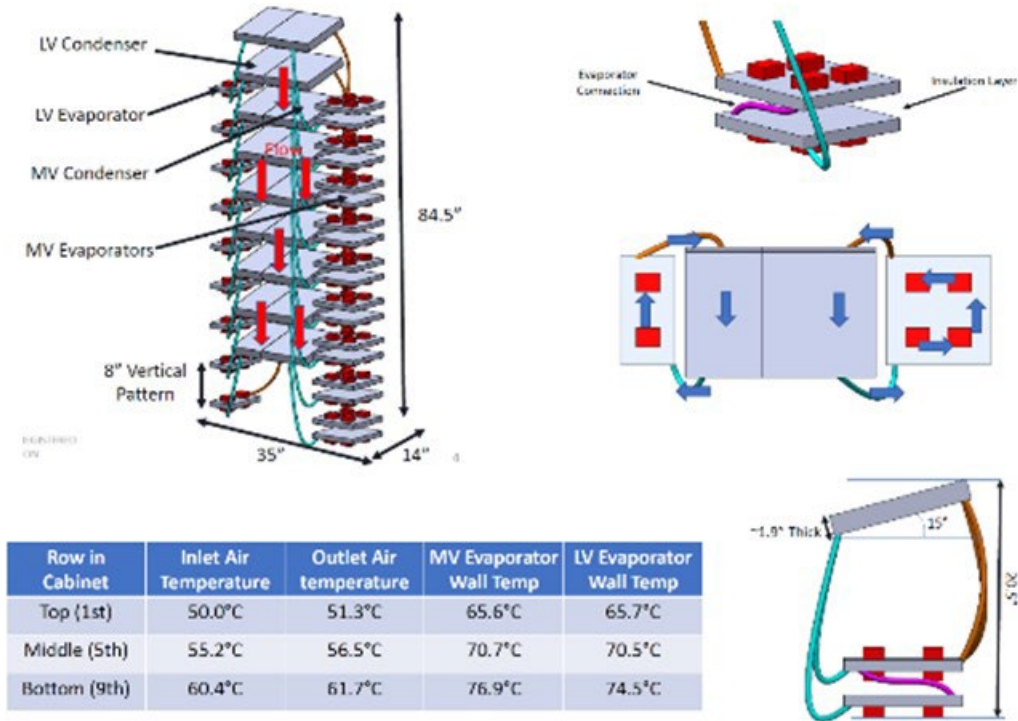


Figure II.1.10.4 Thermal Management Design with Thermo-Syphon (MV section)

Conclusions

For the reported period, significant progress was made; all BP1 milestones have been reached, the preliminary design of the critical elements of the system have been completed, the control architecture has been defined. Currently, the system entered BP2; the individual cells are tested in the laboratory, a full system including mechanical packaging and thermal management entered final design stage, the fabrication of HF transformers is an ongoing process, the embedded controllers are being designed and fabricated for the final version, and electrical tests passed low voltage tests phase.

II.1.11 Development and Demonstration of Zero-Emission Technologies for Commercial Fleets - SuperTruck 3 (PACCAR)

Maarten Meijer, Ph.D., Principal Investigator

PACCAR Inc.
12479 Farm to Market Road
Mount Vernon, WA, 98273
E-mail: Maarten.Meijer@paccar.com

Siddiq Khan, DOE Technology Development Manager

U.S. Department of Energy
E-mail: Siddiq.Khan@ee.doe.gov

Start Date: May 1, 2022	End Date: April 30, 2027	
Project Funding: \$68,382,193	DOE share: \$32,971,041	Non-DOE share: \$35,411,152

Project Introduction

The medium- and heavy-duty truck sector, due to a high level of daily use supporting critical goods movement, currently accounts for 23% of GHG gas emissions from transportation and is the largest contributor to mobile NOx emissions in the US. The SuperTruck 3 program supports decarbonization of U.S. commercial transportation, with PACCAR specifically focusing on the development of the next generation of Kenworth and Peterbilt battery electric and fuel cell vehicles, along with charging infrastructure solutions.

PACCAR alongside its project partners Schneider Electric, Knight Swift, The Ohio State University, University of North Texas, Accelera, Argonne National Lab and LG Energy Solution with leadership in energy management and infrastructure, commercial transportation, research institutions, electrified drivetrain, modeling and analysis and battery development, respectively, will contribute expertise in the respective fields to achieve overall SuperTruck 3 program goals.

Within the SuperTruck 3 program, PACCAR will make robust progress towards the DOE's 2030 technical goals. The technology developed will significantly reduce the barriers to widespread deployment by reducing total cost of ownership, improving applicability and productivity, and decreasing infrastructure timelines. Benefits of the resulting mass deployment include improved air quality, U.S. employment through manufacturing of clean technologies, and reduced societal cost of eliminating carbon from the transportation network.

Objectives

The objective of the project is to develop and demonstrate next generation Medium and Heavy-Duty (MD/HD) Battery Electric Vehicles (BEVs) capable of 75% or more reduction of the well-to-wheel greenhouse gas (GHG) emissions when compared to 2021 model year Class 6-8 diesel tractor trucks using a freight system efficiency analysis approach.

Additionally, to support customer adoption of ZEV powertrain solutions, the total cost of ownership (TCO) reduction goal which includes vehicle, infrastructure and overall operational costs encountered by our fleet deployment partner Knight-Swift, will be reduced by 30% when compared to the initial field deployment of first-generation PACCAR BEV and chargers under the program.

Lastly, next to GHG and TCO evaluations, Argonne National Lab will complete a community impact analysis for environmental equity and justice as a result of the ZEV and infrastructure field deployment activities and overall development activities performed under the PACCAR SuperTruck 3 program.

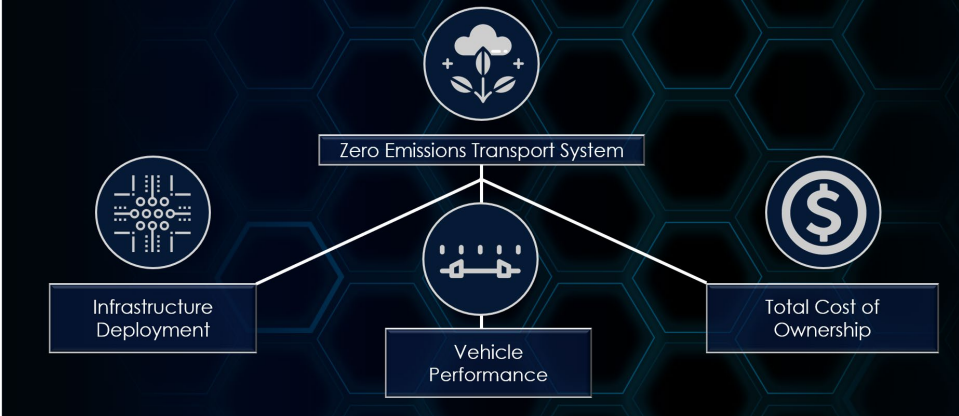


Figure II.1.11.1 Overview of PACCAR SuperTruck3 Goals to Support the Transition to a Zero Emissions Transport System.

Approach

To achieve the program goals, this project comprises both technological development scope and field deployments throughout the project to allow real-world data to be fed-back into the technical development process. The proposed technical improvements can be grouped into three research areas: (1) Next generation zero-emissions vehicle development; (2) Infrastructure, including development of high-power charging, and a micro-grid; (3) Freight system efficiency optimization using ADAS and connectivity enhancement. A high-level program overview is shown in Figure II.1.11.2.

Contributors:
 PACCAR, alongside partners with leadership in energy management, infrastructure, commercial transportation, research institutions, electrified drivetrain, modeling and analysis, and battery development will contribute expertise in their respective fields to achieve SuperTruck 3 goals.

Lead Applicant

Project Goals:
 75% CO₂ Reduction Relative to Baseline Diesel Fleet
 30% Total Cost of Ownership Reduction Compared to BEV Ph2 Vehicles

Kenworth OEM Manufacturers

Peterbilt OEM Manufacturers

KNIGHT TRANSPORTATION Fleet Partner and Featured Operator

SWIFT LA Port & Inland Operating Areas

PACCAR TECHNICAL CENTER Project Management
Fleet Connectivity

PACCAR ZERO EMISSIONS POWERTRAIN Powertrain Development

PACCAR INNOVATION CENTER ADAS

Schneider Electric Energy Management & Microgrid Development

-chargepoint+ Infrastructure and Megawatt Charging

THE OHIO STATE UNIVERSITY ADAS & Simulation

UNT ADAS

accelera MERITOR Ultra-Efficient eAxle

Argonne NATIONAL LABORATORY Modeling, Analytics

LG Energy Solution Increased Energy Density Battery

Technology Development and Deployment:
 New Components, Systems, Processes, Controls, Communications, and infrastructure will be deployed to demonstrate 75% CO₂ Reduction and 30% Total Cost of Ownership Reduction, key goals and requirements supporting decarbonization and mass market adoption of zero emissions transportation products.

Budget Period 1+

- Grid + Solar + BESS
- Installation of 20 Charging Stations
- Integrated Inverter/Axle + SIC MOSFETS

Budget Period 2+

- L2 Advanced Driver Assistance Systems
- Brake Blending, Adaptive Cruise + Stop & Go
- Route Planning, Driver Coax h
- Ecosystem Simulation
- Profile Optimization V2X Connectivity
- Heat Pump + Thermal Management

Budget Period 5

- Next Gen Battery Technology MW Charging
- Increased Efficiency Axle/Batteries
- Integrated Power Electronics
- EV Cab + Chassis Evaluation

Gen 1: TCO Baseline, incremental CO₂ Reduction

Gen 2: 75% Fleet CO₂ Reduction, Path to 30% Total Cost of Ownership Reduction

Gen 3: Technology Demonstration, 30% TCO Red.

Figure II.1.11.2 PACCAR SuperTruck 3 Program Overview

Under the program, PACCAR is developing various generations of BEV’s in parallel to accelerate the product development cycles and time to market. The proposed technical improvements will be embedded in these BEVs and validated in testing campaigns by Knight-Swift and at various PACCAR R&D facilities. The different BEV generations included in this program are:

- Gen1: Small volume production vehicles that are currently available to consumers.
- Gen2: Vehicles currently under development, and close to field testing validation. In addition, proposed additional powertrain improvements will be implemented and tested on upfitted Gen2 vehicles (referred to as Gen2+).

- Gen3: Next generation large volume production series, with start of production scheduled after the SuperTruck 3 program. This generation of BEVs will have enhanced load, range, and fast charging capabilities that will significantly extend current BEV applications towards Diesel class-8 load and range performance.

The deployment of vehicles gets supported by infrastructure deployment required to fuel BEVs. A stepped approach will be followed in order to support the increase in required chargers as a result of the number of vehicles deployed (capacity) and the increasing charging rates to reduce down time (power). A micro-grid which includes a solar power canopy array, and a battery energy storage system is part of the development work to provide flexibility from the grid and to optimize charging at a fleet level. Since the Gen3 BEVs will be capable to support fast-charging, a >1MW fast charger infrastructure proof-of-concept demonstration will be part of the program deliverables.

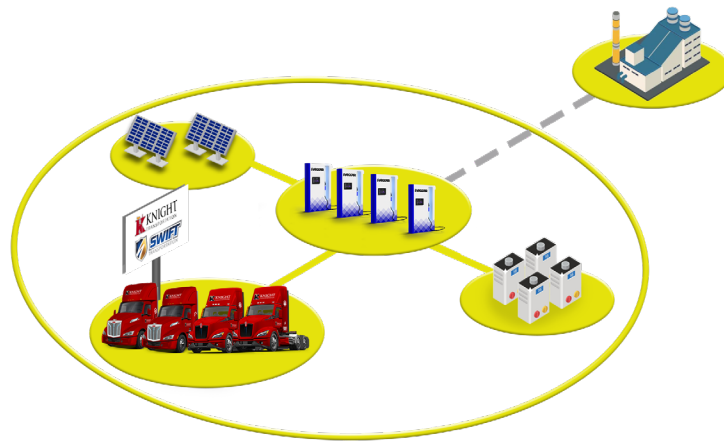


Figure II.1.11.3 Micro-grid including chargers, solar panels, and battery energy storage system.

Vehicle technology development planned for this program consists of new components such as next generation high energy density NMCA battery technology (LGES), next generation e-axes with integrated power-electronics and a 3-speed gearbox (Accelera), increased efficiency auxiliaries and power electronics all operating at an elevated nominal vehicle voltage level of ~1000V. In addition, significant gains are needed relative to current BEV product on aerodynamics, tires, and weight reduction to meet the program goal of demonstrating a vehicle capable of long-haul applications approaching 400–500 mile range with a payload exceeding 90th percentile of loaded class-8 diesel trucks.

In order to support ZEV cost reduction goals, a future increase in production volumes of specific electric vehicle components is required (i.e. economy of scale). This goal is directly supported through commonization and modularity of components between BEVs and FCEVs. PACCAR will perform an analysis study on the next generation FCEV system, component specifications and requirements, which will be incorporated into an overall next generation FCEV definition. With a FCEV concept definition in place, the impact on a system-level freight efficiency can be evaluated taking hydrogen infrastructure developments and deployment outlook scenarios into account.

For all technology development domains, the project has adopted a structured system engineering approach for the development and integration of vehicle technologies as well as the Technology Readiness Level (TRL) process to assess technology maturity in a structured and traceable manner.

Results

The major activities accomplished during the first year of the SuperTruck 3 program were focused on the deployment of the Gen1 BEV trucks with an initial charging infrastructure at our fleet partner Knight Swift.

This consisted of 4 HD BEV trucks and 2 180kW DC Fast Charger stations installed at the Jurupa Valley Terminal location. Both vehicles and chargers have been equipped with high-resolution (1 Hz) data-loggers to record detailed operation of BEV and infrastructure for baseline GHG and TCO performance analysis which is currently ongoing. The image below, Figure II.1.11.4, shows the first truck and charger put in service at the fleet partner facility.



Figure II.1.11.4 First Gen1 BEV (Peterbilt 579EV) Deployed at Knight Swift

Another key objective accomplished during this period has been the definition of Gen 2+ and Gen 3 BEV vehicle platforms. Gen 2+ scope definition supports increased range and increased charging rate without negatively impacting the total vehicle weight by improving vehicle packaging & layout (e.g. a midship to e-axle architecture upfit), advanced thermal management controls, and BEV Specific Fleet V2C Connectivity. The Gen2+ proposed definition for improving high-power charging includes modifying the High Voltage Junction Box (HVJB) to meet the requirement of 500A continuous charging. In addition to specific technology updates to the vehicle, additional PoC system connectivity enhancements, such as eco-score, has the potential to improve energy efficiency by providing driver coaching. As a result, the deployment of these Gen2+ vehicles will already result in a significant expansion of vehicle applications, total cost of ownership reduction, and reduction of fleet level GHG emissions.

The Gen 3 vehicle scope definition is focused on achieving a significant longer range in combination with mega-charging level capabilities. The vehicle scope has been derived from detailed analysis/simulations of using the required application coverage to define specific targets projected on potential technical improvements. The integration of the aforementioned next-generation BEV components (e.g. batteries and e-axles) into a Gen3 specific chassis design, leads to improved packaging and weight distribution. For the battery-packs, the design direction for cell chemistry and module are determined & finalized, while analysis has been progressing for cell & pack performance characteristics necessary for vehicle-pack integration. The Gen3 has a unique high voltage architecture in which the charging components have been fully integrated into the newly developed HVJB. This HVJB includes an integral Megawatt Charging System (MCS) charge inlet, Charge Control Unit (CCU) as well as pre-charge circuits, charge fuses and contactors. E-Steering development for the Gen 3 vehicles includes supporting front suspension design as well as improvements in reliability, steering performance, packaging, and total cost of ownership. Based on these attributes, a decision matrix evaluated power steering solutions including rack and pinion, recirculating ball, linear drive, and bell crank. The final decision pointed to a rack and pinion with independent front suspension as the best configuration for Gen 3 vehicles. The design of the Gen 3 e-HVAC Heat Pump is centered around reduction of

total cost of ownership by increasing range during hot and cold ambient conditions. To further increase efficiency, additional heat transfer opportunities are being investigated between the cabin, battery, and rest of the vehicle. To evaluate the effectiveness of these waste heat recovery opportunities, ongoing simulations are aligned with thermal use cases based on frequency. Current simulation results show energy consumption benefits of operating a heat pump in relatively cold conditions but limited performance in extreme cold temperatures.



Figure II.1.11.5 Gen3 BEV Development Scope

Further vehicle efficiency improvements are realized by developing BEV specific Level-2 ADAS features for the Gen3 vehicles. The level-2 ADAS and Fleet-Connectivity requirements have been completed within this first year of the program. The Level-2 ADAS features in scope for development include Active Lane Keeping (ALK), Adaptive Cruise Control (ACC) and Predictive Cruise Control (PCC). Under the Connectivity features to be developed within this program, the team will support Truck Specification Software, Eco-Score and Advanced Range, and Vehicle-2-Vehicle (V2V). The in-scope connectivity features to support a connected fleet energy optimization approach are summarized in Figure II.1.11.6.

In addition, the team has supported the definition of high-power charging infrastructure. The current scope includes >1 MW level charging to support our Gen 3 vehicles and would conform to the new MCS standard.

On the infrastructure side, significant progress has been made on high-power charging development. In scope is a megawatt capable charging system at the PACCAR Technical Center in Mount Vernon, WA. The system will be capable of charging our Gen 3 BEV trucks at up to 1.6 megawatts at 1600 amps or four other vehicles at up to 400 kW at 500 amps each.

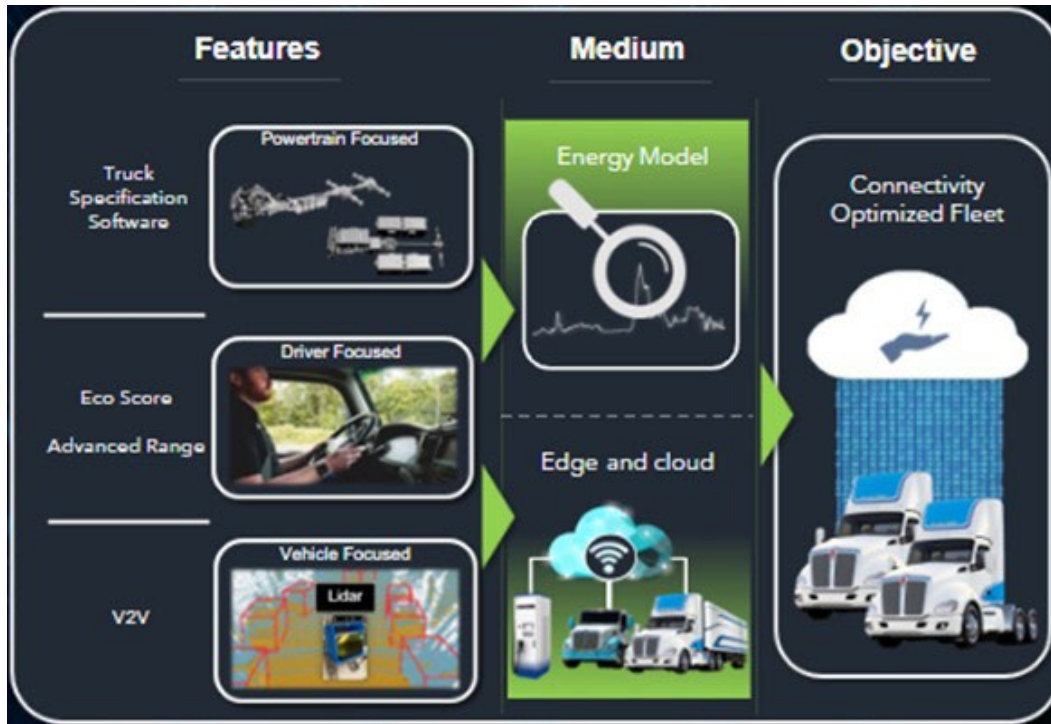


Figure II.1.11.6 Connectivity Feature Development Overview

Conclusions

This report reflects the great amount of work that has been accomplished by the different teams that contribute to the progress of PACCAR SuperTruck 3 Program. The focus has been channeled to ensure deployment of the first Gen1 Battery Electric Vehicles (BEVs) with our partner Knight Swift, as well as to support the analysis on technology improvements by working to finalize all vehicle performance targets, initial design concepts and freight system improvements.

Moving forward, the PACCAR SuperTruck 3 program will continue to develop and validate the next generation vehicle platforms, analyze the data derived from deployed vehicles and chargers, and continue development and deployment of the micro-grid and mega-watt charging infrastructure.

Key Publications

1. DOE Quarterly Progress Report Q3 – January 30th, 2023
2. DOE Quarterly Progress Report Q4 – April 15th, 2023
3. 2023 Annual Merit Review Presentation – June 15th, 2023
4. DOE Quarterly Progress Report Q5 – July 30th, 2023
5. DOE Quarterly Progress Report Q6 – October 30th, 2023

Acknowledgements

Ralph Nine, National Energy Technology Laboratory Project Manager.

II.1.12 Volvo SuperTruck 3: A Zero Emission Freight Future (Volvo Group)

Eric Bond, Principal Investigator

Volvo Group North America
7900 National Service Rd.
Greensboro, NC 27409
E-mail: eric.bond@volvo.com

Siddiq Khan, DOE Technology Development Manager

U.S. Department of Energy
E-mail: Siddiq.Khan@ee.doe.gov

Start Date: August 1, 2022

End Date: July 31, 2026

Project Funding: \$36,233,360

DOE share: \$18,070,333

Non-DOE share: \$18,163,027

Project Introduction

Volvo's SuperTruck 3 (ST3) will utilize valuable learnings from the preceding SuperTruck projects to influence and optimize future zero emission vehicle solutions. SuperTruck 1 (ST1) and SuperTruck 2 (ST2) focused on freight efficiency improvements on a conventional internal combustion engine platform. Such technologies include aerodynamic improvements, friction reduction, thermal management, and light-weighting. With the transition to a battery electric vehicle for ST3, new challenges will need to be taken into consideration. As load capacity, range / performance, and costs remain top priority, it is critical to evaluate the benefits and tradeoffs when selecting the right combination of technologies to develop and industrialize for specific applications.

Objectives

Overall Objectives

- Develop and demonstrate a Class 8 battery electric vehicle (BEV)
 - Capable of 400 miles with a representative payload
 - Correlated to defined freight corridor and urban area freight models
- Demonstration of Megawatt Charging System (MCS)
- Assess Greenhouse Gas (GHG) emission reduction potential (target >75%) and Total Cost of Ownership (TCO) impact.

Fiscal Year 2023 Objectives

- Define logistics use cases
- Document complete vehicle requirements
- Complete planning of vehicle charge site
- Simulate preliminary design relative to design targets.

Approach

The project consists of four work packages and four sequential phases as illustrated below:

Work Packages:

Project Management & Diversity, Equity, and Inclusion (DE&I)

Freight Modeling & Simulations
Vehicle Development
Charging Demonstration

Phases:

- Simulation & Analysis
- Design
- Vehicle Integration
- Vehicle Demonstration

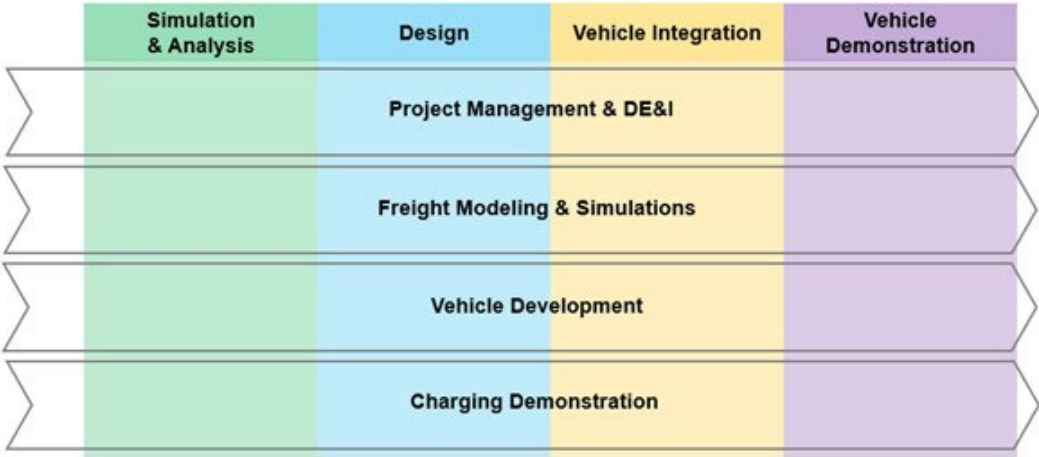


Figure II.1.12.1 Updated Project Schedule & Phasing (Volvo)

The first phase of this project focused primarily on simulation and analysis and establishing baselines. Data has been collected and used to define the current specifications, requirements, and application/usage of Class 8 trucks operating in either regional or long-haul operations. This information was used to support the development of a virtual environment which serves as a basis for freight modeling and simulations. Advanced concepts are being simulated and analyzed as considerations towards the ST3 demonstrator concept decisions.

Based on the requirements established during the initial phase, the project has moved into the second phase. Concept decisions will be taken for the ST3 demonstrator, and the systems and components will be designed during this phase. Megawatt Charging System (MCS) plans will also be established. Advanced concepts will continue to develop alternative solutions to be applied to the simulations as the freight corridor scenarios are defined for augmented demonstration.

In the third phase, procurement for the ST3 demonstrator will begin with the ambition to have all systems fully integrated, and the truck built and commissioned, by the end of this phase. A virtual model of the ST3 demonstrator, as well as additional advanced concept solutions, will be integrated into the freight corridor augmented demonstration environment and analyzed against the baseline. A sensitivity analysis will be conducted, and scenarios will be created for a virtual environment to represent urban areas. The megawatt charging system will be procured and installed.

During the fourth and final phase, the ST3 demonstrator vehicle will complete testing, verification, and validation. Results from the augmented demonstrations will be summarized for the urban area and freight corridor, including correlation of the demonstrator vehicle data in the virtual environment. Additionally, virtual demonstration and assessment of the advanced concepts / complete transport solutions will be concluded, and a customer forum will be conducted to share results of the project.

Results

Activities associated to the Freight Modeling and Simulations work package focused on quantifying baseline conditions by determining the usage profiles of the selected highway and urban area samples which are representative of the overall North America truck population. To accomplish this task, existing telematics data was collected to determine variables such as daily distance, energy requirements, and distance between stops to establish the general usage profiles of the population. Understanding of the vehicle usage profiles will enable the simulations to be used as proxies for the real-world vehicle usage.

The Interstate 81 (I-81) highway corridor was defined as the highway simulation use case and supported by Volvo Group operations and logistics data:

- Route 1 (~150 mile each way): Hagerstown to Lehigh Valley Operations
- Route 2 (~420 mile each way): New River Valley to Lehigh Valley Operations
- Route 3 (~275 mile each way): Hagerstown to New River Valley.

The methodology was established for sampling vehicle telematics for trucks traveling within the selected I-81 highway corridor. To support this task, the cloud environment (sandbox) to collect data was prepared, and care was taken to follow privacy and cybersecurity guidelines. This sandbox provides a scalable solution for data collection and processing, and it provides the ability to process data in volume.

Using an algorithm that was developed for telematics data collection, an initial baseline dataset was created for the I-81 corridor. This includes high-resolution data from over 1,500 unique vehicles operating on this corridor between January and May 2023.

Towards the end of FY2023, work began with Oak Ridge National Laboratory and Rensselaer Polytechnic Institute. The data collected by Volvo was delivered to the University and National Lab partners, and the team continued to gather data and information for the study area (I-81 corridor and metropolitan Chattanooga), including the network, number of lanes, slopes and grades, traffic control details, weather and environmental conditions, and traffic demands, which are needed for developing realistic traffic microsimulation.

A preliminary zoning system for modeling freight activities was determined. The developed zones include one high resolution (mostly county-level) zone in the study area; and two external zones mostly based on freight analysis framework (FAF) zones with exceptions of large port cities (kept with higher resolution) and zones west of the Mississippi River (aggregated into one large zone to reduce computational burden). A highway network was also created.

The team began gathering and generating inputs, e.g., freight trip attraction (FTA) and freight trip production (FTP), employment density, and population density, for conducting Behavioral Microsimulation (BMS).

Additionally, activities have initiated with the American Transportation Research Institute (ATRI) to identify the detailed data that will be needed to support the project.

The Vehicle Development work package started by quantifying the basic performance requirements to satisfy the defined use cases, goals, and objectives of the project. Preliminary calculations using simplified highway cycles provided guidance for the initial concept development, and the vehicle configuration and technologies needed to meet these requirements were identified. Energy storage and consumption will be the keys to success, and achieving project objectives will require technology development in the areas of aerodynamics, rolling resistance, driveline efficiency, light weighting, thermal management, battery technology, and energy management.

Results from initial simulation activities were used as input to the demonstrator truck design, mainly related to the propulsion system and battery capacity. These simulations were done using various road profiles and

vehicle speeds and will be used to support concept decisions regarding major systems, including energy storage system, electric propulsion axles, rear suspension, and cooling system.

Simulation activities during FY2023 also included an overview for the fuel cell simulations, gathering topography results for US highway routes, and performing energy calculations for the two primary Volvo performance routes.

Vehicle configuration and weight distribution was one of the first major concept decisions required to progress with the vehicle development. Once deciding on a 6x4 axle configuration to support 82,000lbs gross combination weight (GCW) with 14k/34k/34k axle loading, the Volvo team collaborated with the tire development partner, Michelin, to select the most appropriate tire size and construction for the demonstrator. Utilizing the same 19.5" diameter wheels and tires as ST2 would provide weight and aerodynamic benefits, but that tire size is not capable of the loading required in ST3. The 22.5" diameter wheel and tire concept was analyzed and determined to provide additional load carrying capacity for the steer axle and allowed the largest improvements in tire rolling resistance without penalties in tire longevity, acceleration, and braking performance, as well as road damage. Furthermore, the 315/70R22.5 tire size allowed an increase in the steer axle loads from 12,000 to 14,000 lbs. while respecting loads per inch limits of at least 565 pounds per inch. ST3 will utilize an existing tire for the steer axle, while a new, ultra-low rolling resistance, wide base tire will be developed for the drive and trailer axles. Tire concept development and tire wear prediction simulation will continue into the next phase of the project.

Energy storage system (ESS) development for the demonstrator vehicle was a major focus throughout FY2023. The ESS requirements were established, and an investigation into the ESS solution is ongoing. Research areas are cell type and chemistry, ESS configuration, and ESS mounting. The ESS remains the most challenging system in the project. Activities with a backup solution continue, following the delays with our main ESS design concept. The vehicle charge site planning was complete by the end of FY2023 and has been submitted for approval.

Simulation and development of the integrated thermal management systems, also impacted by the ESS concept decisions, are under review to support future decisions.

Electric drive axles (eAxles) are also under investigation. eAxle requirements were defined, which will help determine the optimum solutions for motor types and transmission.

Extensive simulation has been performed to support the chassis concept development. Several different concepts for the integrated front end modules have been evaluated, and the team is working to improve the middle section of the chassis based on a complete vehicle stress analysis. The frame concept will continue to be refined during the design phase of the project, including stresses, damage ratio compared to the baseline, and crash worthiness.

Green steel exploration activities for the frame material were also performed. Research results showed two potential alternatives that may result in a reduction of the Global Warming Potential (GWP). These alternatives are being considered to develop new structural concepts for siderails and crossmembers.

The external surface of the demonstrator vehicle concept proposal continues to be matured. Proposal includes carrying-over the ST2 chassis fairings and cab and creating new split lines in the front end to reduce hood size and hinge weight while providing adequate, visual access to the front brake chambers and pneumatic plumbing.

New front chassis fairings were developed to match the updated front end and have been adapted to the ST2 cab. New ground effects were developed for the rear chassis fairings and trailer skirts. These new pieces are required due to the increase in ride height for ST3 versus ST2.

The aerodynamics of the new concept were analyzed using computational fluid dynamics (CFD). When comparing to ST2, most of the increase in aerodynamic drag is due to the increased ground clearance resulting from the switch from 19.5" to 22.5" wheels. To optimize axle load, the gap between the cab and trailer has also increased by approximately 7", which also increases drag. Aerodynamics were improved with modifications to the hood centerline profile and wheel closeouts to improve the coefficient of drag (CdA) to be within 5% of the ST2 CdA. Once the cooling package is defined and the need for a grille opening is established, however, additional cooling drag penalty is expected.

Conclusions

The Volvo SuperTruck 3 project achieved all of the FY2023 objectives. Logistic use cases were defined, vehicle requirements were documented, charge site plans were complete, and the demonstrator concept was simulated relative to the use cases to achieve the design targets. Simulation and analysis activities continue as the project progresses into the design phase.

Acknowledgements

Ralph Nine (National Energy Technology Laboratory Program Manager) and all partners of the SuperTruck 3 team: Michelin Tire, Oak Ridge National Laboratory, and Rensselaer Polytechnic Institute.

II.1.13 Intelligent, Grid-Friendly, Modular Extreme Fast Charging System with Solid-State DC Protection (North Carolina State University)

Srdjan Lukic, Principal Investigator

North Carolina State University
1791 Varsity Drive
Raleigh, NC 27695
E-mail: smlukic@ncsu.edu

Fernando Salcedo, DOE Technology Development Manager

U.S. Department of Energy
E-mail: Fernando.Salcedo@ee.doe.gov

Start Date: October 1, 2018

End Date: September 30, 2023

Project Funding: \$667,626

DOE share: \$2,675,952

Non-DOE share: \$3,323,774

Project Introduction

The development of electric vehicle (EV) charging infrastructure is crucial for the widespread adoption of electric transportation. However, implementing such infrastructure is a complex task that requires consideration of factors such as space limitations, adherence to industry standards, grid capacity, and other technical and policy issues. This project seeks to create a framework for the efficient design of compact medium voltage (MV) extreme fast charging (XFC) stations for EVs. The station design involves the use of a solid-state transformer (SST) that connects to the MV distribution network, delivering power to a shared DC bus. This innovative approach eliminates the need for a step-down transformer to provide low-voltage service by connecting directly to the MV distribution network. This elimination of the low-frequency transformer not only reduces the system footprint and losses but also eliminates inrush currents during grid black-start. Additionally, placing power electronics directly on the distribution system allows for high-bandwidth filtering and power factor correction. The inclusion of a shared DC bus enables multiple charging dispensers and DC storage/generation units to connect, forming a DC microgrid. This setup facilitates power sharing with minimal conversion stages. The project showcases a DC distribution network protected by intelligent solid-state (SS) DC circuit breakers (DCCB) capable of isolating the smallest section of the faulted circuit much faster than existing mechanical solutions.

Objectives

The objective is to design and deploy a 1MVA XFC station that connects directly to the power distribution system, operating at 13.2kV. This XFC station comprises a solid-state transformer (SST) that supplies power to a shared DC bus. Multiple EV charging dispensers and DC storage/generation units connect to this bus (refer to Figure II.1.13.1). The shared DC bus naturally allows power sharing between all generators/loads, with minimum number of conversion stages. The resulting DC distribution network is protected using novel intelligent SS DCCB capable of isolating the smallest section of the faulted circuit much faster than existing mechanical solutions. Each vehicle interfaces with the DC bus through an EV charging dispenser, which is an isolated DC/DC converter. The integrated energy management platform enables the utility to take control actions, including curtailing power to the station and managing power ramp rates.

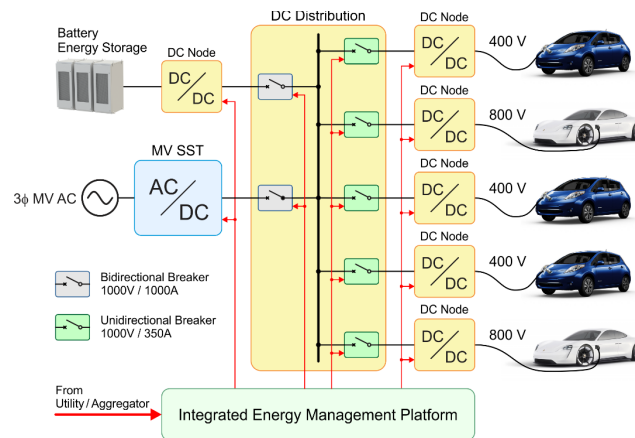


Figure II.1.13.1 Key components of the proposed XFC Station: MV SST, DC distribution network, and dispenser (DC node) that contains the dc/dc converter and vehicle interface.

Approach

The scope of this project is to design, prototype, and test the proposed MV XFC station and then deploy it in the field. The key focus was on the design and demonstration of two novel components that make up the proposed system: the SST and the SS DCCB. For each system, the team developed innovations that reduce system cost and improve system efficiency and reliability. The team then finalized, packaged, and tested the SST, dispensers, SS DCCB, DC distribution network protection scheme, and integrated energy management system; and tested the integrated system in the laboratory environment prior to system deployment. The integrated IMVA XFC was shipped to the demonstration site and commissioned.

Results

The focus in FY2023 has been on the system integration and final at NC State University (NCSU) prior to system deployment to a New York Power Authority (NYPA) facility in Marcy, NY. In addition, the team completed the final deployment site preparation, prior to system shipping and commissioning. What follows is a brief description of the system design, followed by the integration and demonstration efforts that occurred in FY 2023.

Solid-state transformer (SST) design

The SST topology is made of 18 identical modules, each consisting of an active front end (AFE) stage and the dual active bridge (DAB) DC/DC converter stage. Each phase of the SST is packaged into a single cabinet, with six AFE+DAB modules connected in series-input-parallel-output configuration, with the six series-connected modules blocking the 8kV line-neutral input voltage. Figure II.1.13.2 shows the SST under test in the NCSU lab, with the three phases of the SST visible. Figure II.1.13.3(a) shows the design of one of the 18 AFE+DAB modules that makes up the SST. The AFE uses a full bridge topology, with each full-bridge switch using a series connection of three SiC MOSFET devices. The high voltage stage of the DAB uses an identical design as the AFE, while the DAB low voltage stage uses 1.2kV SiC modules in a full bridge configuration. The DAB isolation transformer is immersed in oil to ensure that no partial discharge occurs at the system operating voltages. The module efficiency was tested and reported in Figure II.1.13.3(b).



Figure II.1.13.2 Prototype of one phase of the SST assembled in the lab with the front panels in place.

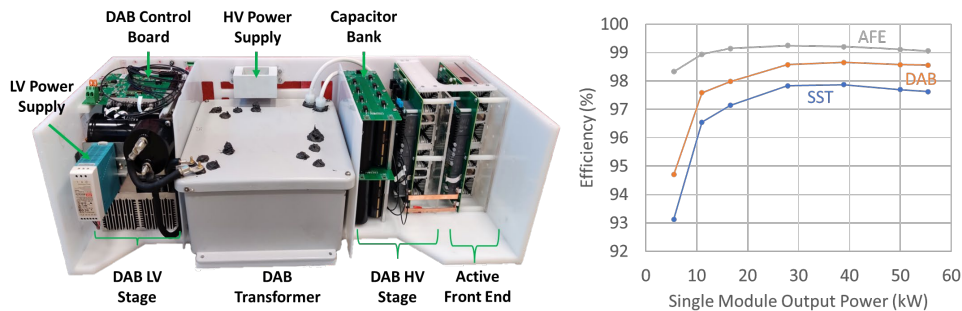


Figure II.1.13.3 (Left) AFE+DAB module implementation. (Right) Module efficiency measurements, showing the efficiency of the AFE stage, the DAB stage and the overall efficiency.

Development of solid-state circuit breakers

To ensure selective and rapid isolation of any fault in the proposed XFC station operating as a DC microgrid, the team members from ABB developed a solid-state DC switchgear and the associated protection coordination schemes. The DC switchgear features two types of SS DCCB’s: two 1500A class SS DCCB bi-directional circuit breakers, used to interface to the SST and battery energy storage systems, and four 500A class SS DCCB unidirectional breakers, used as branch circuit breakers for the protection of EV charger dispensers (refer to Figure II.1.13.1 for the system overview). The two variants of the SS DCCB were designed, built, tested, and installed in a customized switchgear cabinet. The switchgear, shown in Figure II.1.13.4, has forced ventilation for cooling and a compact bus structure for power distribution.

System Integration

Key components of the proposed XFC Station, shown in Figure II.1.13.1 were all shipped to the NCSU laboratory and tested as an integrated system. As part of this effort, the team created a graphical user interface to manage all the components collectively, and this interface underwent testing prior to disassembling the system for shipment. The system including the SS DCCB, the SST and MV switchgear were placed inside a shipping container and delivered to NYPA for field testing. The shipping container provided for easy placement and removal of the equipment at the site and ensured safety and no tampering at site when the unit is not in use. Figure II.1.13.5 shows the integrated system in the shipping container.



Figure II.1.13.4 ABB switchgear after testing at ABB and prior to shipping to NCSU.

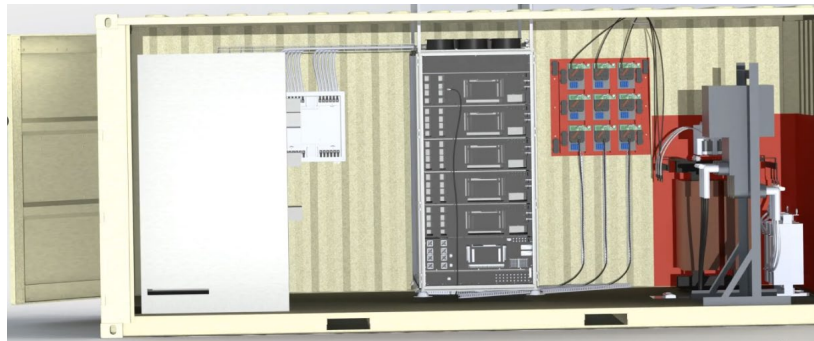


Figure II.1.13.5 CAD drawing of interconnected system within the shipping container.

Site preparation for deployment

At the NYPA demonstration site, trenching, conduit and cable for the entrance and exit between the shipping container and the 15 kV transformer, were completed. Bonding, and grounding procedures were all followed, in accordance with NYPA requirements. The site layout is shown in Figure II.1.13.6. The installation includes a (1) dedicated disconnect switch to the 13.2kV utility feed; (2) A shipping container that houses the MV filters, breakers, the SST, and the SS DCCB inside a shipping container; (3) an auxiliary 208V power feed; and (4) charging ports. Two Trenwa trenches are used to route MV cable between the grid connection and the four-way switchgear and between the switchgear and the SST; and another trench distributes DC power from the SS DCCB to each individual charging port.

System Deployment

The system was transported in a 20-foot shipping container, serving as both its protective enclosure during transit and an additional layer of security at the deployment site. This arrangement ensured that all equipment, including the solid-state breaker and medium-voltage components, remained enclosed within the shipping container, shielded from user exposure. Upon reaching the site, the team connected the medium-voltage and low-voltage lines, previously installed by NYPA team. Initial tests were conducted on the solid-state transformer, revealing a failure in several high-frequency transformers within the system. Consequently, it was deemed necessary to halt any additional testing for safety reasons.

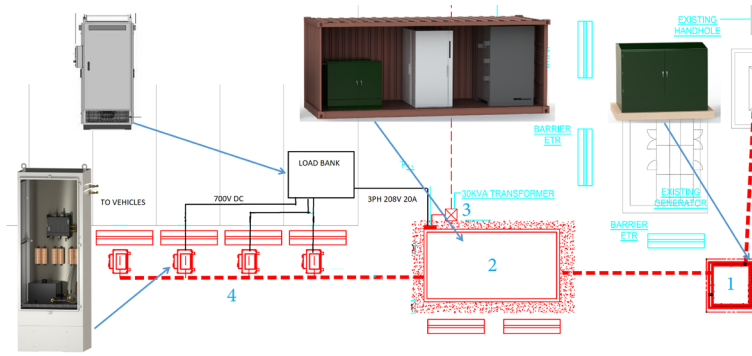


Figure II.1.13.6 One line diagram of the planned installation. The installation includes a (1) dedicated disconnect switch to the 13.2kV utility feed; (2) A shipping container that houses the MV filters, breakers, the SST and the SS DCCB inside a shipping container; (3) an auxiliary 208V power feed; and (4) four charging ports.



Figure II.1.13.7 Charger deployment at NYPA site. (Left) View of system installation with three DC/DC nodes, shipping container and Trenwa trench housing the DC cables. (Right) View inside the container showing DC connection.

Conclusions

In FY2023, the primary focus has centered on the system integration and final testing of the integrated XFC system at NCSU in preparation for its deployment to a facility operated by the NYPA in Marcy, NY. The integrated XFC charging station underwent thorough testing within the laboratory setting. Prior to the system's deployment, NYPA completed essential site preparations at the Marcy, NY location. The shipment and subsequent installation of the system in the field followed these preparations. Upon arrival at the designated site, the team proceeded to connect the medium-voltage and low-voltage lines. Initial tests on the solid-state transformer uncovered failures in several high-frequency transformers within the system, leading to the decision to suspend further testing for safety reasons.

Key Publications

1. M A Awal, O. Montes, F.Teng, D. Wang, M. R. H. Bipu, W Yu, S Lukic, I Husain, "Medium Voltage Solid State Transformer for Extreme Fast Charging Applications" to be presented at *2023 IEEE Applied Power Electronics Conference and Exposition (APEC)*, Orlando, FL, USA, March 2023
2. M. R. H. Bipu, D. Dadzie, S Lukic, I Husain, "Open Circuit Switch Fault Management Method of a Multi-Phase Synchronous Buck Converter for EV charging application" to be presented at *2023 IEEE Applied Power Electronics Conference and Exposition (APEC)*, Orlando, FL, USA, March 2023
3. H. Tu, H. Feng, S. Srdic and S. Lukic, "Extreme Fast Charging of Electric Vehicles: A Technology Overview," in *IEEE Transactions on Transportation Electrification*, vol. 5, no. 4, pp. 861-878, Dec. 2019.

4. Dakai Wang and Wensong Yu, "Series Connection of SiC MOSFETs with Hybrid Active and Passive Clamping for Solid State Transformer Applications," presented at *2019 IEEE 7th Workshop on Wide Bandgap Power Devices and Applications (WiPDA)*, Raleigh, NC, October 2019.
5. M.A. Awal, I Husain, Md R. H. Bipu, O. Montes, F. Teng, H. Feng, M. Khan, S. Lukic "Modular Medium Voltage AC to Low Voltage DC Converter for Extreme Fast Charging Applications", *arXiv preprint*, submitted June 2020, arXiv:2007.04369
6. M.A. Awal, Md. Bipu, O. Montes, H. Feng, I. Husain, W. Yu and S. M. Lukic, "Capacitor Voltage Balancing for Neutral Point Clamped Dual Active Bridge Converters", in *IEEE Transactions on Power Electronics*, vol. 35, no. 10, pp. 11267-11276, Oct. 2020.
7. L. Qi, P. Cairoli, Z. Pan, C. Tschida, Z. Wang, V. R. Ramanan, L. Raciti, A. Antoniazzi, "Solid-State Circuit Breaker Protection for DC Shipboard Power Systems: Breaker Design, Protection Scheme, Validation Testing" in *IEEE Transactions on Industry Applications*, Vol. 56, No. 2, March-April 2020
8. S. Chen, M. Bipu, D. Wang and W. Yu, "Analysis and Solution of the Unbalanced Device Voltage Issue for SiC MOSFET Based Diode Neutral Point Clamped Converter," presented at *2020 IEEE Applied Power Electronics Conference and Exposition (APEC)*, New Orleans, LA, USA, March 2020
9. P. Cairoli, R. Rodrigues, U. Raheja, Y. Zhang, L. Raciti, A. Antoniazzi, "High Current Solid-State Circuit Breaker for safe, high efficiency DC systems in marine applications", *2020 IEEE Transportation Electrification Conference and Expo (ITEC)*, 24-26 June 2020, Chicago, IL
10. R. Rodrigues, U. Raheja, P. Cairoli, L. Raciti and A. Antoniazzi, "Accelerated aging test of Solid-State DC Circuit Breaker based on 2.5 kV Reverse Blocking IGCT," *2020 IEEE Energy Conversion Congress and Exposition (ECCE)*, Detroit, MI, USA, 2020, pp. 6024-6029.
11. Y. Zhang, U. Raheja, R. Rodrigues, P. Cairoli, L. Raciti and A. Antoniazzi, "Experimental Validation of Parallel Connection of RB-IGCTs for High Efficiency Solid State Circuit Breaker," *2020 IEEE Energy Conversion Congress and Exposition (ECCE)*, Detroit, MI, USA, 2020, pp. 6036-6042.
12. R. Rodrigues, U. Raheja, Y. Zhang, P. Cairoli and A. Antoniazzi "Power loop busbars design and experimental validation of 1 kV, 5 kA Solid-State Circuit Breaker using parallel connected RB-IGCTs" *2020 IEEE IAS annual meeting*, October 2020
13. R. Rodrigues, Y. Du, A. Antoniazzi, P. Cairoli, "A Review of Solid-State Circuit Breakers", *IEEE Transactions on Power Electronics*, Vol. 36, No. 1, January 2021
14. R. Rodrigues, U. Raheja, Y. Zhang, P. Cairoli and A. Antoniazzi, "Power Loop Busbars Design and Experimental Validation of 1 kV, 5 kA Solid-State Circuit Breaker Using Parallel Connected RB-IGCTs," in *IEEE Transactions on Industry Applications*, vol. 57, no. 3, pp. 1920-1927, May-June 2021, doi: 10.1109/TIA.2021.3062591.
15. X. Song, Y. Du, P. Cairoli, "Survey and Experimental Evaluation of Voltage Clamping Components for Solid State Circuit Breakers", *IEEE Applied Power Electronics Conference and Exposition (APEC)*, Phoenix, AZ, 14-17 June 2021
16. R. Rodrigues, Y. Zhang, U. Raheja, P. Cairoli, L. Raciti, A. Antoniazzi, "Robust 5 kA, 1 kV Solid-State DC Circuit Breaker for Next Generation Marine Power Systems", *IEEE Electric Ship Technologies Symposium 2021*, August 3-6, 2021

17. Feng, Hao, Fei Teng, Oscar Andres Montes, M. A. Awal, Md Rashed Hassan Bipu, Iqbal Husain, and Srdjan Lukic. "Passive Capacitor Voltage Balancing of SiC-based Three-level Dual-Active-Bridge Converter Using Hybrid NPC-Flying Capacitor Structure." in *IEEE Transactions on Power Electronics*, vol. 37, no. 4, pp. 4183-4194, April 2022.
18. M. R. H. Bipu, O. Montes, S. Lukic and I. Husain, "Hierarchical Failure Mode Effect Analysis for the Protection Design of a MV AC-DC Solid State Transformer based EV Extreme Fast Charging Station," 2023 IEEE Energy Conversion Congress and Exposition (ECCE), Nashville, TN, USA, 2023.

II.1.14 Enabling Extreme Fast Charging with Energy Storage (Missouri S&T)

Jonathan Kimball, Principal Investigator

Missouri University of Science and Technology
301 W. 16th St.
Rolla, MO 65409
E-mail: kimballjw@mst.edu

Sam Gillard, DOE Technology Development Manager

U.S. Department of Energy
E-mail: samuel.gillard@ee.doe.gov

Fernando Salcedo, DOE Technology Development Manager

U.S. Department of Energy
E-mail: fernando.salcedo@ee.doe.gov

Start Date: October 1, 2018	End Date: September 30, 2023	
Project Funding: \$5,831,080	DOE share: \$2,915,377	Non-DOE share: \$2,915,703

Project Introduction

This project aims to advance electric vehicle (EV) adoption by enabling widespread deployment of charging stations that can re-charge an EV in a time similar to refueling a conventional vehicle. The proposed work will create and demonstrate an extreme fast charging (XFC) station that operates at a combined scale exceeding 1 MW while mitigating grid impact with smart charging algorithms and local energy storage. An active front-end (AFE) will connect directly to a distribution feeder and provide reactive power support and harmonic compensation.

The station will incorporate high-frequency transformers instead of conventional low-frequency transformers for isolation, thereby reducing size. A stationary battery will be used to buffer power transients due to charge initiation and termination. The complete station will be coordinated by a high-level controller that uses information gleaned from distribution network analysis to ensure grid compatibility.

There are three basic challenges: power conversion at 1 MW from a medium-voltage (12.47 kV) source; grid compatibility between this large, dynamic load and a wide range of possible distribution networks; and battery charging at high rates (beyond 5C) with minimal degradation. Battery charging algorithm development must account for the internal construction of the cells, modules, and pack, and also requires innovation in the pack design.

Objectives

The high-level objective of this project is to demonstrate a complete XFC station, capable of charging three vehicles at 350 kW each, with local energy storage to mitigate active power transients and station control to ensure grid compatibility. The station will connect to a 15-kV-class network (e.g., 12.47 kV three-phase). The objective for the budget period that began in FY 2021 and continued through FY 2022 is to develop a full-scale version of the station.

Due to pandemic-related material delays, the project team pivoted to an approach that demonstrates all of the various features of the target XFC station within the time available. A full-scale power converter is being built to demonstrate charging at 350 kW, 1000 V. A sub-scale power converter is being built that has the proper topology (the requisite number of levels, etc.) for connection to a 12.47 kV system. The algorithms, for both battery charging and grid interface, are being prepared for implementation on the full-scale converter in a simplified manner, suitable for the compressed timescale of the testing, while being simulated and tested in the lab. During FY 2023, the full-scale converter was demonstrated with multiple battery packs.

Approach

The overall XFC station architecture is illustrated in Figure II.1.14.1. The station comprises a multi-level AFE, a multi-phase dc-dc converter with isolation, multiple non-isolated dc-dc converters to provide charging ports, and a bidirectional dc-dc converter that connects to a fixed battery (energy storage system, or ESS).

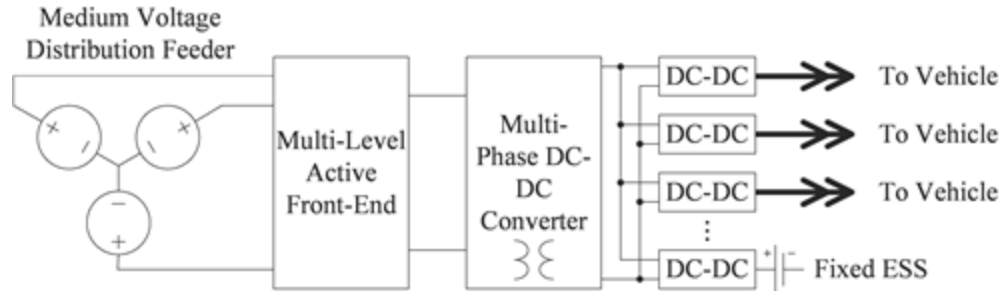


Figure II.1.14.1. Block-diagram schematic of the XFC station.

The project has three main thrusts: grid interaction optimization; power conversion; and battery charging algorithms. In FY 2023, the three thrusts came together in a demonstration. A full-scale power converter was demonstrated. The station successfully charged two battery packs simultaneously, managed power flow with one battery pack used as an energy storage system, and injected VARs to regulate voltage. In addition, the cell-level charging algorithms have been tested on modules and the grid-interface algorithms have been tested extensively in simulation.

Results

Multi-period Coordinated Planning of BESS-assisted Extreme Fast Charging Infrastructure in Coupled Transportation and Power Networks

Previously, a multi-level energy management framework was developed to manage active and reactive power flow on a wide range of timescales. The present effort assumes the use of such a framework and extends the time horizon into the planning regime. The proposed approach presents a strategic traffic flow-based spatio-temporal coordinated planning model for siting and sizing of battery-energy-storage-system-assisted (BESS-assisted) extreme fast charging stations (CSs) in a highway transportation network (TN) and photovoltaic (PV) systems in a power distribution network (PDN), as shown in Figure II.1.14.2.

A variety of scenarios were examined, including a diversity of investment budgets, pre-existing charging stations, charger types, and EV range capabilities. As an example, Figure II.1.14.3 illustrates the impact of EV range on the number of charging stations and ports, BESS size, PV system size, and total project cost, as well as the remaining unmet EV demand. The proposed planning tool may be used for a wide range of planning applications.

Power Conversion System

Full-Power Station

The full-power station is built upon the Bitrode FTF platform. Whereas a typical FTF has one or two battery ports, the XFC station has four ports: three for vehicles, one for a stationary BESS. In addition, VAR control has been added. The modified FTF architecture is illustrated in Figure II.1.14.4. The boxes in yellow are new additions developed as part of this project.

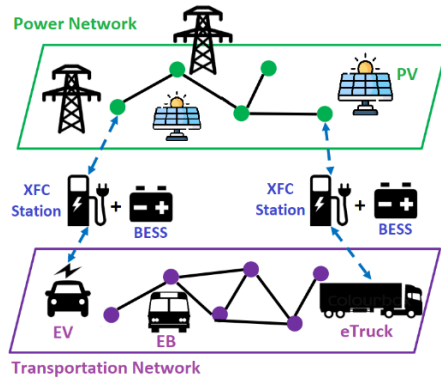


Figure II.1.14.2. Coupled power and transportation networks.

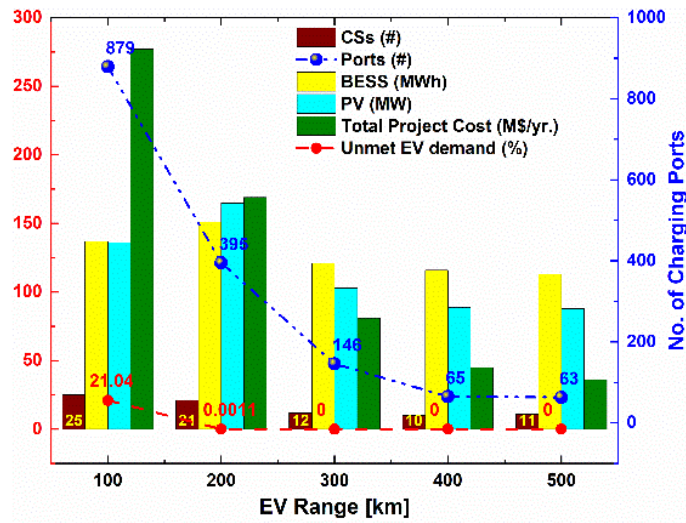


Figure II.1.14.3. Coordinated planning results with different EV driving ranges.

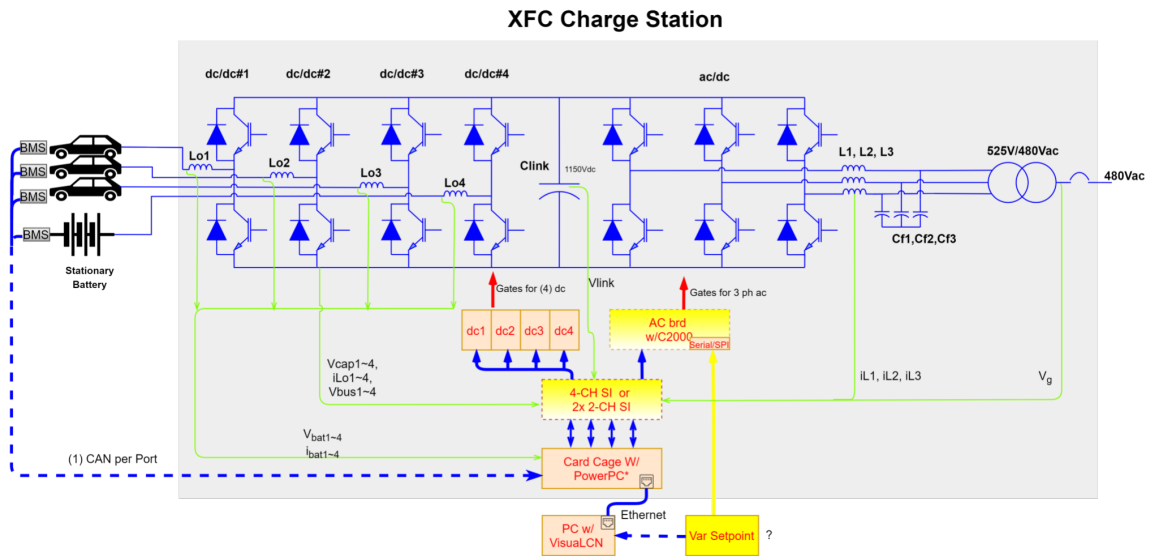


Figure II.1.14.4. Modified Four-Port FTF Architecture with VAR Injection.

The complete charge station was demonstrated during August 2023. Results are described below. As part of the integration of the station, a number of interfaces were constructed, as illustrated in Figure II.1.14.5. Each battery pack has an Arduino that translates its data onto a shared CAN bus. A Raspberry Pi is used to coordinate the charging of all of the batteries, as well as VAR setpoints and implementation of the high-level controller.

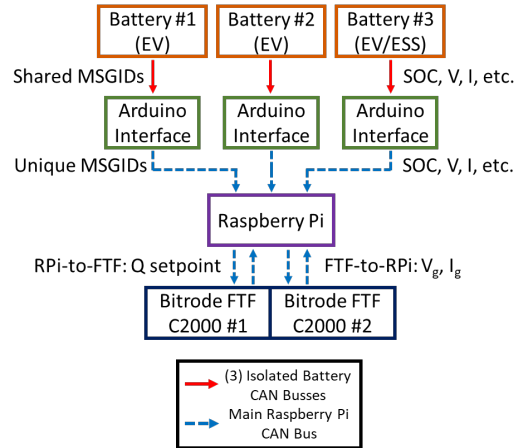


Figure II.1.14.5. XFC CAN Communication Layer.

Low-Power Station

Because of pandemic-related material delays, full-power testing on a medium-voltage feeder is not feasible. Therefore, the converter topology and control will be demonstrated at low-power and low-voltage. Initially, a six-module converter is being constructed and tested, comprising two modules per phase as illustrated in Figure II.1.14.7. Each module, shown in Figure II.1.14.6, includes three H-bridges: one for grid interface, one for the high-voltage side of a high-frequency transformer, and one for the low-voltage side of the transformer. Each module also incorporates a controller that receives high-level commands from a central controller.

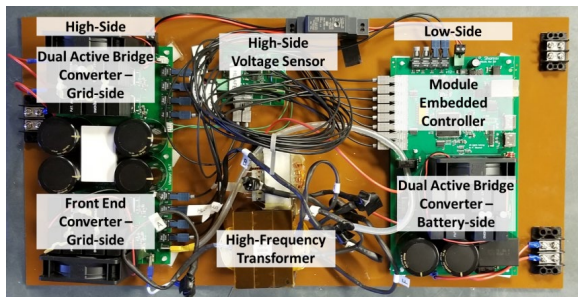


Figure II.1.14.6. Single low-voltage prototype module.

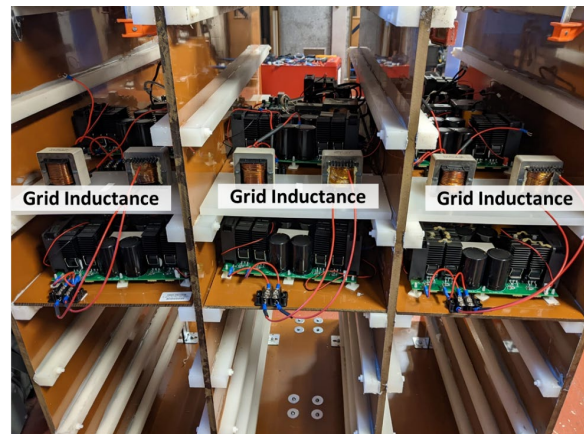


Figure II.1.14.7. Low-voltage prototype cabinet showing the six modules integrated and ready for testing.

Battery Charge Algorithm

The XFC project objective is to reduce the charging time of electrical vehicles while minimizing the degradation. This goal was achieved by the development of the CQtCV algorithm (that is, constant lithium plating current followed by constant voltage) which has been proven to reduce charging time and degradation compared to the conventional CCCV (constant terminal current followed by constant voltage) algorithm. Previously cycled cells were opened to demonstrate the reduction of visible surface degradation. Figure II.1.14.8 illustrates the difference between anode degradation with CQtCV and CCCV charging. The CQtCV significantly reduced visible degradation to the surface of the anode as the anode remained pristine. In contrast, the anode cycled with CCCV shows large cracks and possible fragmentation, this results in a loss of active material and thus capacity. Near the outer edges of the anode surface, Li-plating can be seen.

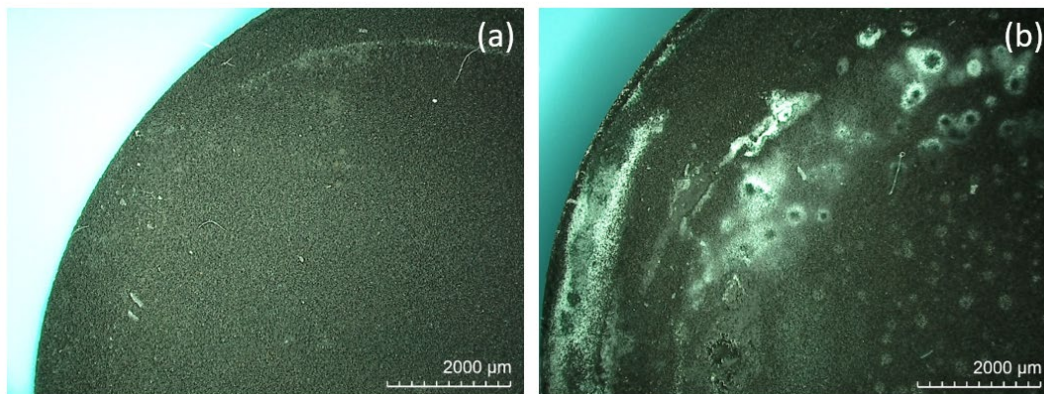


Figure II.1.14.8. Anode of cells cycled with CQtCV (a) and CCCV (b) after 130 cycles using Hirox KH-8700 microscope.

Demonstration

On August 22, 2023, two DOE representatives visited the Bitrode facility in St. Louis, MO, to witness the demonstration of the combined station. The integrated system, shown in Figure II.1.14.9, comprised the charge station (with two grid connections at 500 kW each and four charge ports at 350 kW each), two battery packs designed and constructed by LG Energy Solution, a Raspberry Pi and three Arduinos as illustrated in Figure II.1.14.5, and multiple terminals to monitor the system. Full details will be provided in the project final report. Tests performed included:

- Charging one pack, 16% to 80%, at 350 kW max.
- Charging one pack while discharging the other, to demonstrate ESS behavior.
- Charging both packs with staggered start and stop.
- VAR injection to change the grid voltage.

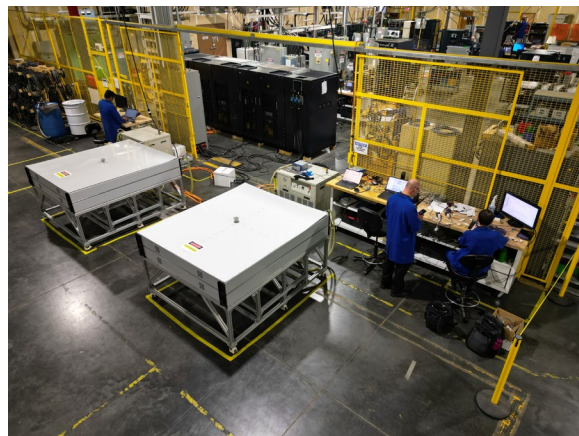


Figure II.1.14.9. XFC Project Testbed at Bitrode Corporation. Battery packs are in the foreground (white). Charge station is centered in the background (dark blue).

All tests were successful. As an example, Figure II.1.14.10 and Figure II.1.14.11 illustrate the second scenario where “Battery 2” is being charged and “Battery 3” is being used as an ESS to reduce the load on the grid. One major issue uncovered in this integrated test was the impact of thermal management. Even with a high-performance thermal management system designed into the battery packs, repeated XFC events proved to be impossible due to excessive heating of the battery modules. This is an issue that will be addressed in future work.

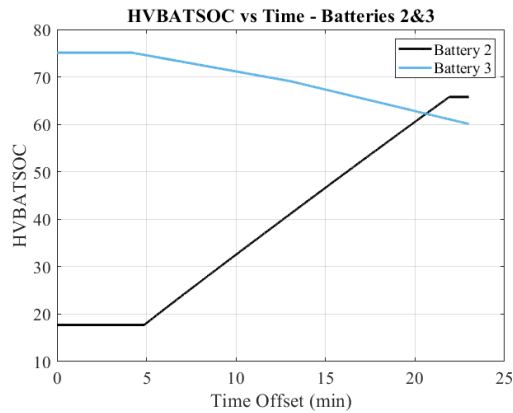


Figure II.1.14.10. Battery Charge + ESS Discharge Results: State-of-Charge

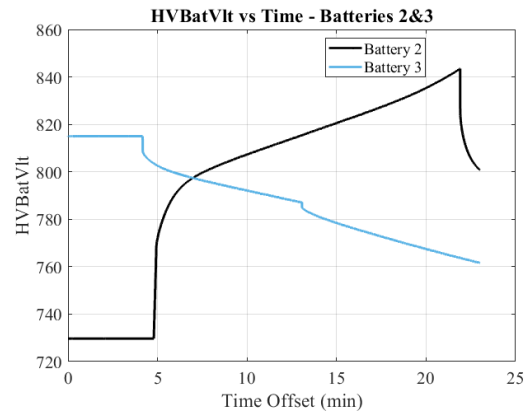


Figure II.1.14.11. Battery Charge + ESS Discharge Results: Pack Voltages

Conclusions

This project has successfully concluded. Within the restrictions imposed by the shift in approach, all capabilities were demonstrated, including high-power charging, the use of a stationary energy storage system, VAR injection for voltage regulation, innovative battery charging algorithms, and a multi-layer grid interface algorithm.

Key Publications

1. A. Sharma and J. W. Kimball, “Hybrid model to evaluate the frequency-dependent leakage inductance of partially-filled transformers,” *Power Electronic Devices and Components*, vol. 5, p. 100038, Jun. 2023, doi: [10.1016/j.pedc.2023.100038](https://doi.org/10.1016/j.pedc.2023.100038).
2. A. Sharma and J. W. Kimball, “Transformer Leakage Inductance Design Methodology,” in *2023 IEEE Applied Power Electronics Conference and Exposition (APEC)*, Mar. 2023, pp. 1572–1578. doi: [10.1109/APEC43580.2023.10131409](https://doi.org/10.1109/APEC43580.2023.10131409).
3. Waqas ur Rehman, Jonathan W. Kimball, and Rui Bo, “Multi-layered Energy Management Framework for Extreme Fast Charging Stations Considering Demand Charges, Battery Degradation, and Forecast Uncertainties,” in *IEEE Transactions on Transportation Electrification*, 2023, DOI: 10.1109/TTE.2023.3275110.
4. Waqas ur Rehman, Rui Bo, Hossein Mehdipourpicha, Jonathan W. Kimball, “Sizing battery energy storage and PV system in an extreme fast charging station considering uncertainties and battery degradation”, *Applied Energy*, Vol. 313, p. 118745, 2022, 10.1016/j.apenergy.2022.118745.
5. O. Oboreh-Snapps *et al.*, "Virtual Synchronous Generator Control Using Twin Delayed Deep Deterministic Policy Gradient Method," in *IEEE Transactions on Energy Conversion*, doi: 10.1109/TEC.2023.3309955.

Acknowledgements

At Missouri S&T, other faculty on the project are Rui Bo, Mehdi Ferdowsi, Jonghyun Park, and Pourya Shamsi. (Robert Landers was previously a co-PI as well.) Subawardees are Ameren (Jason Wibbenmeyer, Technology Transfer Manager); Bitrode Corporation (Elaine Raterman, Engineering Director); and LG Energy Solution (Mohamed Alamgir, Director of Research).

II.2 EVs at Scale - VGI and SCM

II.2.1 EVs@Scale Flexible charging to Unify the grid and transportation Sectors for EVs at scale (FUSE)

Jesse Bennett, Principal Investigator

National Renewable Energy Laboratory
5013 Denver West Parkway
Golden, CO 80401
E-mail: Jesse.Bennett@nrel.gov

Jason Harper, Principal Investigator

Argonne National Laboratory
9700 South Cass Avenue
Lemont, IL 60439
E-mail: jharper@anl.gov

Manoj Kumar, Principal Investigator

Idaho National Laboratory
775 MK Simpson Boulevard
Idaho Falls, ID 83415
E-mail: ManojKumar.CebolSundarrajan@inl.gov

Andrea Mammoli, Principal Investigator

Sandia National Laboratories
7011 East Avenue
Livermore, CA 94550
E-mail: amammo@sandia.gov

Lee Slezak, DOE Technology Development Manager

U.S. Department of Energy
E-mail: lee.slezak@ee.doe.gov

Start Date: January 1, 2022

End Date: December 31, 2026

Project Funding (FY22): \$3,150,000

DOE share (FY22): \$3,150,000 Non-DOE share: \$0

Project Introduction

Electric vehicle (EV) adoption will greatly expand beyond light-duty (LD) vehicles capable of charging at single-family residences to now include LD, medium-duty (MD), and heavy-duty (HD) applications, with more powerful charging at additional public stations and private depots. The increasing power demand will challenge the electric grid in various ways, requiring mitigation through vehicle grid integration (VGI) and smart charge management (SCM) solutions designed to integrate with all vocations. There is also geographic and seasonal diversity in the electrical demand and generation across the United States. As EV adoption expands, the best VGI or SCM solutions to integrate EV charging will depend on several factors such as vehicle type and travel patterns, available charging infrastructure, and local grid characteristics, which may need to be selected on a case-by-case basis. To facilitate the electrification of these transportation sectors and ensure a maintained reliable and resilient electric grid, the following barriers must be addressed:

- Existing SCM strategies are effective for low adoption of LD EVs; however, a shift in charging locations, patterns, and charging power for EVs@Scale will impact efficacy

- MD and HD adoption will expand rapidly though grid planning for this new load, and SCM strategies that account for vocational needs and differences do not currently exist
- SCM and VGI benefits for consumers and utilities have not been demonstrated with EVs@Scale across the range of conditions (geographies and seasons) found in the US.
- There is a lack of enabling technologies for smart charging in a utility environment.

The EVs@Scale Laboratory Consortium has identified the SCM/VGI pillar to investigate barriers and develop solutions to mitigate these barriers. The Flexible charging to Unify the grid and transportation Sectors for EVs at scale (FUSE) Project Team is developing an adaptive ecosystem of SCM strategies and VGI tools that will be relevant to a wide geographic area and numerous vocations of electric vehicles across all class sizes. These solutions will both be analyzed in a simulation environment and developed in the lab with newly developed prototypes and market available solutions. These Solutions will be developed through a grid and transportation approach, assessing the potential transportation energy needs of these vehicles and their charging power demands throughout the grid. This two-pronged approach will resolve practical implementation challenges for communication, control, and hardware deployment and work directly with utility partners and travel data providers to analyze the effectiveness of these SCM and VGI solutions for EVs@Scale.

Analysis of these solutions will focus on transportation in the state of Virginia and charging demands throughout the utility partner service territory. Building on past efforts [1], [2], this project will develop travel patterns for local MD vehicle travel, HD travel throughout the state including the port of Newport News, and LD vehicles with and without access to home charging in both urban and suburban settings. Applying realistic SCM strategies will require a detailed understanding of EV, charger, and grid communication standards to ensure proper assessment of grid impacts and SCM efficacy. Early-stage R&D for the development of enabling technologies will expand on the analysis efforts to demonstrate the capabilities of these technologies in a lab environment and generate adequate real-world data on the performance of these new technologies. These analysis and demonstration efforts will assess the effectiveness of SCM and VGI solutions at mitigating the grid impacts of EVs@Scale, while testing the performance of these technologies in a lab environment to ensure these capabilities provide grid support for utilities while ensuring vehicles receive the energy they need.

Objectives

Enabling Technology Development & Demonstration

The testing of SCM and VGI often requires the development of new technologies to enable deployment of these solutions. This task will develop and demonstrate enabling technologies for the smart charging ecosystem, including a smart interoperable EVSE, EV driver reservation system, and smart charge scheduling. The effort will leverage previous developments including CIP.io, the SpEC module, charge reservation system, and schedule optimization. The system will be integrated, tested, and demonstrated at the Energy Plaza, then transferred to an industry for a pilot program.

Demonstrating SCM solutions in environments with diverse EVSEs, EVs, utility programs, and technologies presents a significant challenge. This challenge must be addressed to promote widespread EV adoption and mitigate potential impacts on the power grid. Understanding and identifying the boundaries and limitations, whether from the equipment side or the utility perspective, is crucial for developing effective and applicable SCM solutions. This task also has three objectives:

- Identify OCPP charge control capabilities and limitations of EVSEs from various vendors, including aspects like accuracy, precision, resolution, and response time
- Test the response of EVSEs and EVs under various grid conditions, including voltage drops, sags, harmonics, and outage
- Demonstrate custom SCM solutions developed under FUSE.

SCM Controls and VGI Solutions

These enabling technologies will leverage the SCM and VGI developed and tested throughout the FUSE project. Different SCM control strategies are being developed to leverage the temporal flexibility of most vehicle charge sessions to shift charging and support a wide range of grid services across different portions of the grid. This project is also developing VGI solutions that leverage the spatial flexibility of vehicles charging mid-route, to mitigate grid impacts and avoid both transportation and electrical congestion. Research is being conducted to expand the current set of SCM controls and VGI solutions in several areas:

- Granular pricing structures to mitigate transmission congestion.
- Novel methods for shifting dwell-period charging to maximize the use of peak solar generation.
- Price controls to shift mid-route charging spatially and temporally, which can more optimally balance the utilization within and across XFC stations and reduce spikes and demand charges.

Grid Impacts

The SCM and VGI controls that are developed in FUSE must be assessed for their effectiveness on real-world feeder models to determine their potential value. Through a partnership with Dominion Energy, the FUSE team received grid feeder models for analysis of grid impacts and mitigation through SCM and VGI. These distribution feeder models are converted from Synergi format to OpenDSS format for the total of 29 feeders around the Newport News region of Virginia, to be followed by 31 feeders from the Richmond Virginia area.

The development of these OpenDSS feeder models enables detailed analysis on grid capacity and power flow to assess the grid impacts on distribution equipment as a result of EV loads. Nodal EV hosting capacity assessments are conducted to estimate the available capacity of the feeder nodes in order to accommodate EV charging without causing any grid issues. The hosting capacity assessments then lead to concentrated charging analysis, which encompasses three components:

- Determine appropriate locations for concentrated EVSE
- Estimate the charging need at the EVSE locations
- Determine methods to assess how charging profiles could be modified alongside user behavior as a function of external parameters such as price or congestion.

Travel and Charging Loads

In order to both assess the potential effectiveness of SCM and VGI, as well as determine the optimal deployment opportunities for these solutions, it is critical to understand the underlying transportation load and resultant charging demands. This task will synthesize travel schedules and charging demand datasets, including LD vehicles (produced in 2022 and further refined in 2023) and MD/HD vehicles (primary focus of 2023). Each segment of the electric vehicle population is sized to represent projected 2040 EV adoption levels in the Virginia analysis regions. There is substantial variation in adoption levels, travel patterns, and energy consumption rates across vehicle types and vocations, and this task will determine separately for each category the most appropriate datasets and travel models to produce synthetic travel and charging demand datasets. The datasets produced describe uncontrolled (“business as usual”) charging load profiles under different conditions and also estimate the room for charging flexibility. The datasets will be used to enable implementation of SCM strategies on vehicle charge sessions to mitigate the grid impacts of charging EVs@Scale.

Approach

Enabling Technology Development & Demonstration

Argonne National Laboratory is pioneering innovative approaches to the development and demonstration of Smart Charging Management (SCM) systems for electric vehicles (EVs). This initiative addresses the growing demand for intelligent EV charging solutions and integrates advanced technology into the smart grid

ecosystem. In pursuit of this goal, Argonne is actively exploring three key strategies: EVrest, EV Charge Scheduling, and the OptiQ Smart AC L2 EVSE. These approaches offer solutions to improve EV reservation systems, enhance charge management, and combine analog-based charging with high-level communication, all contributing to the advancement of EV charging technology.

The EVrest mobile app, utilizing the Open Charge Point Protocol (OCPP), enhances EVSE station management and resolves issues related to unreserved port usage. This app capitalizes on networked OCPP stations, providing valuable data for advanced VGI/SCM research. Recognizing the importance of smart charge management amid the transition to electric vehicles in the US, efforts are underway to develop an ISO 15118-based EV charge scheduling system. This system caters to the needs of all stakeholders, including EV drivers, contributing to grid load stabilization. Additionally, the OptiQ Smart AC L2 EVSE introduces an integration of analog-based AC charging, ISO 15118 high-level communication (HLC) AC charging, and single-wire CAN HLC AC charging. This innovation enables the integration of a significant portion of the US light-duty EV fleet into the smart grid.

OCPP Charge Control Characterization

For the OCPP charge control characterization at NREL, a Hyundai Ioniq 5 was charged using a Wallbox Pulsar Plus 48 A over the OCPP protocol (Figure II.2.1.1). The charging current limit set-point was changed at different intervals across different increments to statistically characterize the accuracy, precision, resolution, and response of the charge control over OCPP.

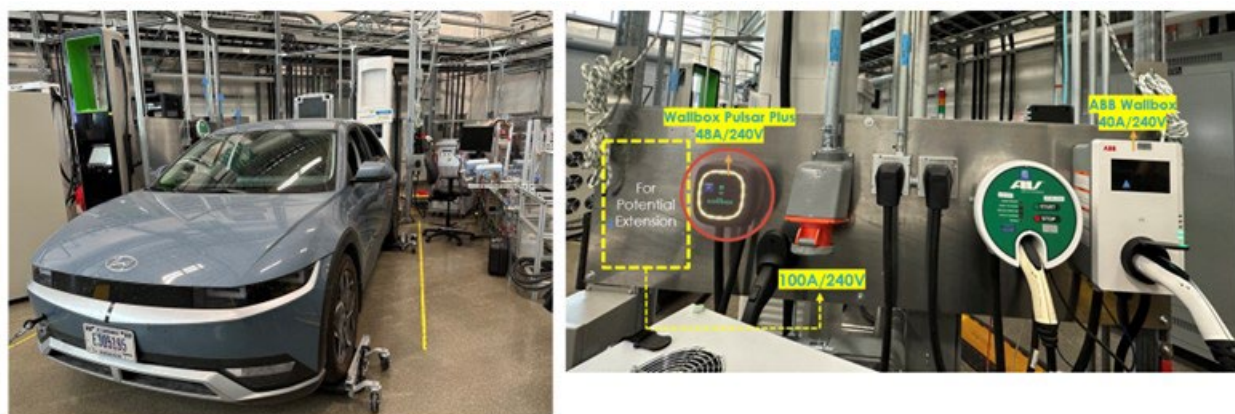


Figure II.2.1.1 Charging hardware testbed at NREL.

SCM Controls and VGI Solutions

In order to support high EV adoption, it is important to develop varying controls to address the wide range of potential grid impacts. This includes the development of adaptive pricing schemes, active SCM controls, and high-power charging deployment strategies for mid-route charging.

Varying the price of electricity is one way for utility companies to communicate desirable times for charging, as well as times when charging should be avoided. PJM's locational marginal pricing (LMP) offers a granular rate structure that varies by the hour and changes every day, based on local grid conditions and forecasts. Utility companies may also try to maximize the use of low-cost and low-emission generation sources such as solar PV and wind, which vary throughout the day. The FUSE team has developed multiple SCM controls that are intended to leverage a vehicle charge session's temporal flexibility to take advantage of these rates and generation sources, as well as provide a range of other grid services.

These SCM controls leverage temporal flexibility during long dwell sessions, but some dwell periods are relatively short, resulting in much less flexibility for SCM. Mid-route charging may not have the opportunity to shift within a dwell period but could determine the best location throughout a route to support high-power

charging. This spatial flexibility provides an opportunity for VGI solutions to determine high-capacity locations for concentrated charging and enable reservations for the best mid-route charging sessions.

Grid Impacts

Distribution model development and validation

The first step in assessing grid impacts is to convert feeder models to OpenDSS using NREL’s tool DiTTO, which reads the input Synergi files in an automated process and creates OpenDSS scripts representing power flow models for the feeders. After conversion, the team compared nodal voltage power flow results from both software. Metrics of the max and mean difference are shown to be within an acceptable range (e.g., within 3%) for 19 feeders (the remaining feeders are being thoroughly reviewed to ensure the models are within a reasonable range). An example of the voltage comparison between OpenDSS and Synergi (node-by-node in the feeder) is shown in Figure II.2.1.3 for a feeder in the Newport News area. The close alignment shows the conversion process is accurate for this sample feeder and the converted model provides an effective baseline. Figure II.2.1.2 shows a boxplot of the voltage differences for the 19 feeders - the mean difference for most of these feeders is very small and maximum variation is within 3%. After the models have been validated, they are then prepared for use in hosting capacity analysis, as well as a co-simulation to assess uncontrolled and controlled charging impacts.

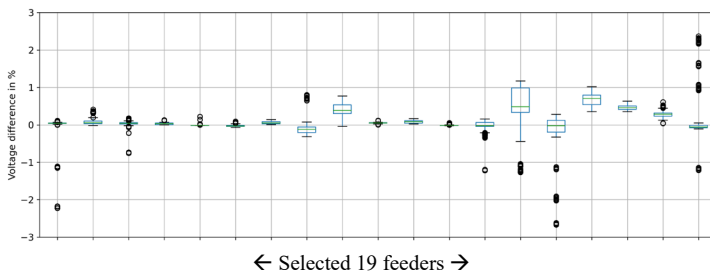


Figure II.2.1.2 Boxplots of voltage difference for 19 feeders

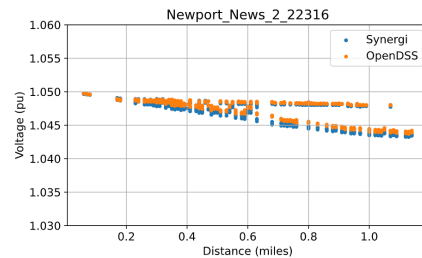


Figure II.2.1.3 Distribution feeder voltage comparison - sample voltage distance plots

Travel and Charging Loads:

LD vehicle charging datasets, initially produced in 2022 using Wejo travel data, were further refined in 2023 to capture seasonal variation in energy consumption, to more accurately assign vehicles to specific parcels, and to provide additional information regarding trip trajectories and precise charging coordinates. The first stage of MD/HD charge load modeling focused on three vocations that have long overnight dwells at consistent depot locations: school buses, transit buses, and local freight (class 2b-6 delivery vehicles). These vocations’ long dwells are amenable to SCM and to early electrification (evidenced by existing production model EVs). Three data collection and analysis workstreams were completed in parallel:

- For local freight, after a review of public and proprietary datasets, a license to Geotab’s Altitude API was acquired and used to estimate vehicle duty cycles and dwell patterns. Land use data was used to assign granular depot locations. 20,200 Class 2b-6 vehicles were included. NREL’s TEMPO model was used to derive 2040 MD/HD electrification rates (53% for Classes 2-3 and 44% for Classes 4-6).
- For school buses, the team compiled school schedules for Richmond County and, while other counties, leveraged NREL FleetDNA duty cycles. This resulted in a dataset of 2,655 school buses across 307 schools. 100% electrification by 2040 was assumed for the region’s school bus fleets.
- For transit buses, we gathered schedules from the General Transit Feed Specification and located depots using the National Transit Database. The regions’ three major transit agencies were modeled, with 456 vehicles in total. 100% electrification by 2040 was assumed for regional transit buses.

For each vocation, week-long vehicle travel itineraries were synthesized. Across multiple assumptions for energy consumption rates (winter versus summer) and charging rate, these itineraries produced “business as usual” charging load profiles and more detailed datasets describing each charging session’s flexibility.

Results

Enabling Technology Development & Demonstration:

EVrest: EV Driver Reservation System

Argonne researchers have made significant progress in the development and testing of both the Android and iOS versions of the EVrest app during this fiscal year. EVrest now offers support for single and dual port OCPP 1.6J AC and DC EVSE. Researchers diligently identified and resolved any discovered bugs, and they enhanced the user interface (UI) and user experience (UX) to ensure a successful launch. Furthermore, they collaborated with the Argonne Sustainability group to effectively plan and communicate the launch of EVrest for use by Argonne employees. As part of the testing phase, a select group of employees participated as pre-beta testers.

EV Charge Scheduling

Argonne researchers created a charge scheduler bridge that enables non-ISO 15118 vehicles to participate in the EV Charge Scheduling System (EVCSS) by deploying EV agents to negotiate charge schedules on their behalf. These agents emulate ISO 15118 messages, allowing seamless integration and testing of the scheduler's performance with both simulated and real EV/EVSE pairs. A proof-of-concept was developed and demonstrated [3].

OptiQ: Smart AC L2 EVSE

Two proof-of-concept OptiQ EVSE units were deployed at Argonne National Laboratory for most of FY23. These units served over 220 charging sessions and dispensed more than 2 MWh of energy. One of the two OptiQ EVSE units was integrated into the EVrest platform and used by a select group of employees to test both the EVSE and the EVrest platform. Further development of the OptiQ firmware and the design of a commercial alpha prototype were successfully completed. Figure II.2.1.4 displays a photograph of the commercial Mk II prototype OptiQ EVSE.



Figure II.2.1.4 Commercial Mk II Prototype OptiQ EVSE.

OCPP Charge Control Characterization

In the described hardware testbed setup (Figure II.2.1.1), the charging current exhibits a bias of approximately 1A for a 1A step increment, with a deviation of 0.35A (Figure II.2.1.5). The mean response time of the vehicle to set-point changes is 2.88 seconds, with a maximum time of 5 seconds, accounting for network latency and equipment delays. This time can slightly increase for larger set-point changes. Based on our test results, a controller time-step of 10 seconds, allowing for an expected error of 0.5 kW at 240V, can be considered a safe margin for this specific setup. The effective current resolution was also measured to be 1A.

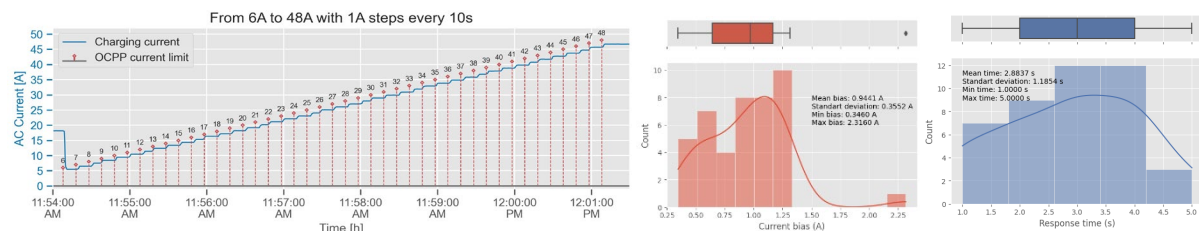


Figure II.2.1.5 Changing current set-point limits through OCPP (left). Histogram of charging current error and response time (right).

Travel and Charging Loads:

Results for the three long-dwell MD/HD vehicle vocations are shown in Figure II.2.1.6. Relative to other vocations, transit bus charging is more spread out over the course of the day, but more spatially concentrated; local delivery has a single evening peak while school buses (depending on charging scenario) have two distinct daily peaks, one after each trip.

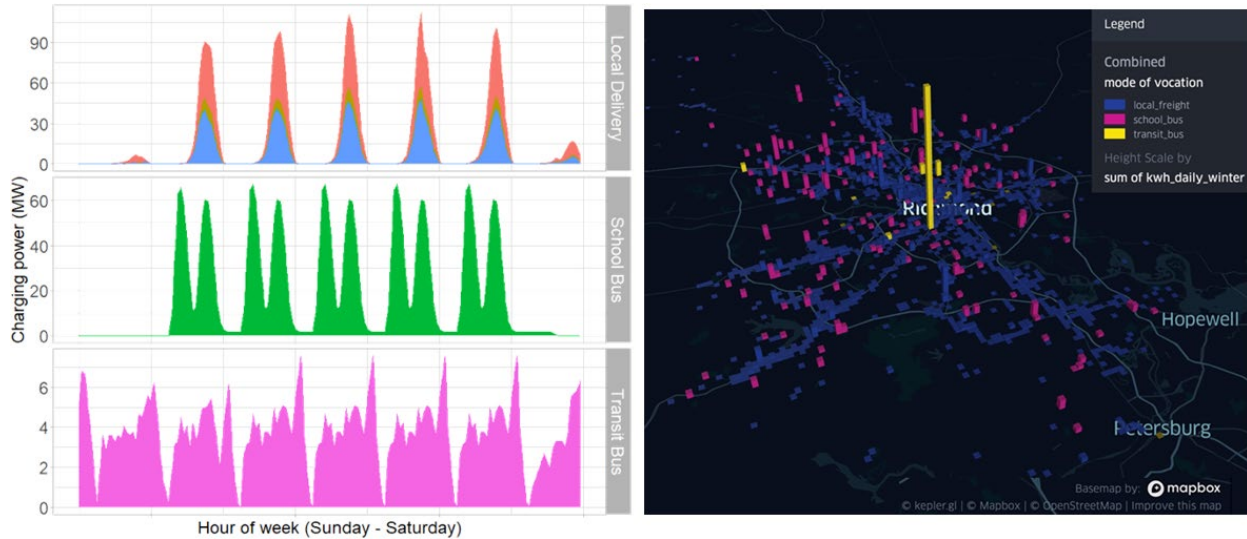


Figure II.2.1.6 Long-dwell MD/HD vehicle charging loads over one week (left) and across a subregion of the analysis area (right)

The average daily winter charging needs for local freight exceeds 335 MWh and is more geographically distributed than buses. However, 15% of these vehicles could not be served exclusively with overnight depot charging due to long daily trips. Additional work is planned to model the necessary mid-day charging strategies for these vehicles (en-route or at depots).

The average daily winter charging needs for school buses exceeds 400 MWh (less in summer). Charge patterns show substantial room for SCM, both in terms of shifting load between midday and overnight and in shifting load within the night (especially in scenarios where some charging needs are met during midday dwells).

The average daily winter charging needs for transit buses exceeds 235 MWh and is highly concentrated at a small number of bus depots. Overnight dwells are often shorter than for school buses or local freight. Results suggest SCM may reduce peak load and spread charging more evenly between depots and each route’s terminal endpoints.

SCM Controls and VGI Solutions:

When considering dynamic utility rates, the team has examined different LMP pricing structures and simulated vehicle charge responses to those structures as applied to the IEEE 13 bus test feeder and subject to simulated vehicle schedule constraints. These simulations show that for medium and heavy-duty (MD/HD) vehicles, fleet operators or charging station operators are more incentivized than independent operators to leverage pricing variation and temporal charging flexibility at a much higher granularity to reduce operational costs. This approach also has the potential to better align charging with the real-time power balance and thus decrease transmission congestion. However, the direct exposure of customers to highly varied market-cleared price signals presents new challenges for fleet operators and charging management operators. This new Day-Ahead pricing control will be further tested with real world charging schedules and utility feeders as supported by the HELICS co-simulation platform.

Controls and infrastructure are needed to maximize daytime charging and align with the solar peak, especially in regions with significant solar generation. In cases such as in El Paso, TX where the winter solar generation is more than the non-EV demand, it is critical for EVs to maximize charging during the solar peak to avoid curtailment. SCM strategies previously studied were limited in their effectiveness at shifting demand to take full advantage of peak solar generation. Two existing SCM strategies from previous projects - Time-of-Use (TOU) Random and Centralized Aggregator - were updated with newer objective functions to maximize charging from peak solar generation. Two regions were studied: the El Paso Electric (EPE) region and the ISO New England Vermont region, in both summer and winter conditions, and with both home- and work-dominant scenarios. The updated SCM controls had the greatest success shifting charging for the work-dominant scenario to the solar-peak due to most work-charging occurring during the day. Additional research will expand these SCM controls to account for other kinds of variable energy generation, including wind-generation and solar with cloud-cover projections.

SCM strategies for mid-route XFC charging must be approached differently than long-dwell SCM strategies because there is no temporal flexibility to shift charging throughout the brief dwell period. A new VGI solution was studied that introduced a mechanism for drivers to schedule-ahead a charge at a particular charger station, allowing the driver to compare multiple stations and to select the station that best suited their needs based on factors including price and out-of-way distance. Using the Caldera CDM software, a population of 300,000 EVs were modeled in the Richmond, Virginia area with predetermined itineraries spanning three weeks. The energy needs of these vehicles were met via a combination of L2 home, work, and destination chargers, and a set of 70 pre-set XFC stations, each with six 350 kW chargers. The effect of price variation on charging choices was investigated, allowing for charge events to shift both temporally and spatially. A baseline simulation was run where all drivers charged at XFC stations in an unscheduled first-come-first-serve manner, without knowing beforehand whether plugs were available. The results from the first-come-first-serve simulation showed the most convenient stations being over-utilized, while other nearby stations were left under-utilized. Results from the schedule-ahead simulation showed that setting the prices at over-utilized stations higher compared to under-utilized stations shifts charging events from over- to under-utilized stations. A temporal shift away from rush-hour timeslots was also observed. The overall peak demand on the grid was also reduced. Additional work will provide more insight into which pricing schemes are the most feasible and effective.

Grid Impacts:

EV Hosting Capacity Analysis

The EV hosting capacity assessment tool was developed to identify the thermal loading limit and voltage violations as criteria to determine local capacity limits. Lines and transformers with loading greater than 100% of rated capacity for any duration are considered overloaded, while nominal voltage levels

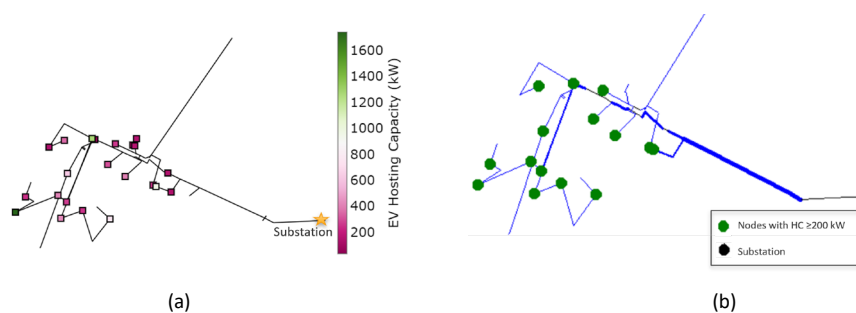


Figure II.2.1.7 Feeder network topology; (a) EV hosting capacity heat map, (b) High power charging capable nodes. marked.

beyond the standard 5% deviation [0.95 to 1.05 per unit (p.u.)] are considered to be violations beyond capacity. Figure II.2.1.7(a) shows an EV hosting capacity heat map for a feeder in a relatively densely populated area. The maximum EV hosting capacity of the typical node in this feeder is about 1.7 MW, while nodes in other

feeders have comparatively lower hosting capacities. EV hosting capacity at this feeder is typically limited by transformer thermal limitations. Figure II.2.1.7(b) highlights the nodes with EV hosting capacity greater than 200 kW, which is optimal for XFC stations. Different EV hosting capacity results are observed in different feeders due to local conditions.

Concentrated Charging

Locations for concentrated charging were selected by first super imposing a 250 m x 250 m grid on Census block group geometries of areas surrounding Richmond and Newport News. Various data points from The Census, Open Street Map, Wejo, Virginia Department of Transportation, and Homeland Infrastructure Foundation-Level Data were associated with each grid section. The data points were selected to identify locations that had parking lot availability, were near electrical substations and high traffic volume roads, as well as being in census block groups that contained multi-unit housing and large amounts of renters and car owning renters. For each grid section, geographically close data points were weighted and summed resulting in a ranked list of locations that best met selection criteria. From that ranked list, the best locations for locating EVSE could be chosen based on need, for example to serve renter populations for night-time charging or to serve drivers who need to charge en-route.

The ability to reconstruct trips based on selected origin or destination is the first step to understand charging loads resulting from travel between selected areas. To enable this, Wejo trips are binned into 217 5 km x 5 km squares covering the area of interest. Statistics describing trip probability are then calculated for each of the 47,089 origin-destination pairs. An arbitrary number of start and destination addresses can then be sampled from the probability distribution, and the exact route can then be determined using a routing optimization algorithm such as Figure II.2.1.8. Finally, the energy required for each trip can be determined using physics-based principles of varying complexity.

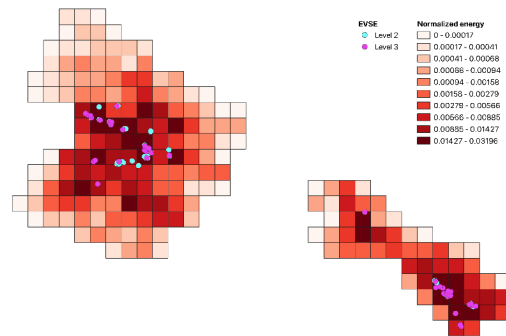


Figure II.2.1.8 density of charging need based on EV charging at the end of each trip

Conclusions

Although the electrification will significantly expand the electrical demand throughout the electric grid, this project identifies many opportunities to better understand the variety of transportation and charging loads that will result from this transition. Assessing these loads provides opportunities to both forecast and understand the potential grid impacts, as well as develop SCM and VGI solutions to mitigate these impacts with minimal effect on vehicle operations. There is a wide range of technologies that must be developed to support these solutions, but many are in development and undergoing performance testing.

The next steps for this project are to further investigate the potential value these technologies offer utilities and drivers, as well as demonstrating their performance in a utility environment to prove their viability as a real-world solution. This includes further assessments of mid-route charging requirements for LD MD and HD EVs. Following these assessments, the necessary SCM and VGI solutions to leverage spatial and temporal flexibility will be completed and prepared for both OpenDSS simulations and field demonstrations. The HELICS co-simulation environment will be leveraged, alongside the verified feeder models, to assess uncontrolled, and controlled charging impacts and determine the effectiveness of each control. Finally, these technologies will be deployed in a utility environment through additional industry partnerships and field demonstrations.

Key Publications

1. Cebol Sundarrajan, Manoj Kumar, Bennett, Jesse, Scoffield, Don, Chaudhari, Kalpesh, Meintz, Andrew, Pennington, Timothy, and Zhang, Bo. 2023. "Performance and Implementation

Requirements for Residential EV Smart Charge Management Strategies". United States.
<https://doi.org/10.1109/ITEC55900.2023.10186998>.

References

1. Meintz, A. and J. Bennett. 2020. "Smart Electric Vehicle Charging for a Reliable and Resilient Grid (NREL)." In Electrification:2019 Annual Progress Report, U.S. Department of Energy Office of Energy Efficiency and Renewable Energy Vehicle Technologies Office, 386–402.
<https://www.energy.gov/eere/vehicles/downloads/electrification-fy2019-annual-progress-report>.
2. Bennett, J.etal. 2021."Charging Infrastructure Technologies:Smart Electric Vehicle Charging for a Reliable and Resilient Grid (RECHARGE)." Presented at the U.S. Department of Energy Vehicle Technologies Office Annual Merit Review, June 23, 2021.
3. Harper, Jason D., Ghosh, Shibani, Zhang, Mingzhi, Sundarajan, Manoj Kumar Cebol, Lohse, Joachim, and Edie, Christie-Anne. 2023. "Electric Vehicles at Scale (EVs@Scale) Laboratory Consortium Deep-Dive Technical Meeting: May 18, 2023". United States.
<https://www.osti.gov/servlets/purl/1988039>.

II.3 EVs at Scale - High Power Charging

II.3.1 High-Power Electric Vehicle Charging Hub Integration Platform (eCHIP)

John Kisacikoglu, Principal Investigator

National Renewable Energy Laboratory (NREL)
 15013 Denver West Parkway
 Golden, CO 80401
 E-mail: John.Kisacikoglu@nrel.gov

Jason Harper, Principal Investigator

Argonne National Laboratory (ANL)
 9700 South Cass Avenue
 Lemont, IL 60439
 E-mail: jharper@anl.gov

Prasad Kandula, Principal Investigator

Oak Ridge National Laboratory (ORNL)
 2360 Cherahala Blvd., Knoxville, TN 37932
 E-mail: kandular@ornl.gov

Lee Slezak, DOE Technology Development Manager

U.S. Department of Energy
 E-mail: lee.slezak@ee.doe.gov

Start Date: January 1, 2022 End Date: December 31, 2026
 Project Funding: \$2,500,000 DOE share: \$2,500,000 Non-DOE share: \$0

Project Introduction

Large-scale adoption of electric vehicles (EVs) will introduce new challenges for high-power charging (HPC), grid load management, and charging facility operations. This type of charging infrastructure is vital to charge the next generation of light-, medium-, and heavy-duty EVs fast enough to make them viable for all use cases. Megawatt-scale HPC stations today vary greatly in facility power usage and communication architecture construction. Three of the most common builds that are available for large HPC site design are shown in Figure II.3.1.1. The unit cost of the site varies based on the selected architecture, site electrical supply, number of ports, and port charging capacity, aside from the control policy implemented. The ability to connect on a common DC bus via a central inverter/rectifier (Figure II.3.1.1(b) and (c)) reduces the unit cost, especially when the size of the site design increases [1]. Alternatively, having multiple inverters per each port (as with today’s commercial off-the-shelf products-Figure II.3.1.1(a)) would increase the size and number of components. Systems with a common AC bus come with disadvantages, including a higher number of power conversion stages, which lead to increased costs and reduced efficiency. Overall, the common DC bus approach provides heterogeneous port power ratings and upgrades during the lifetime of the station—supporting operation flexibility with minimal investment.

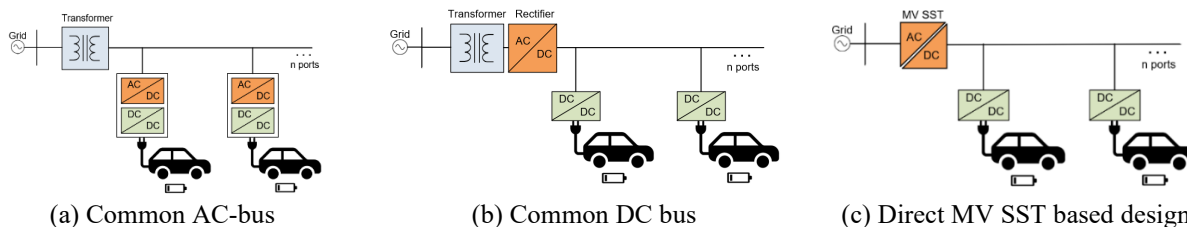


Figure II.3.1.1 Charging site architectures available today.

Today, the SAE J3271 megawatt charging system (MCS) describes the requirements for these types of high-power charging equipment, such as standards for charging connectors, chargers, DC distribution systems, DC protection, and grid interconnection. However, development and adoption of these high-power charging systems are still inadequate. There is a need to design and validate efficient, low-cost, interoperable hardware for high-power DC-hub charging, communication, and control architectures, which are crucial for accelerating adoption of EVs and their infrastructure.

This project aims to develop and demonstrate the DC charging hub approach. The project objective is to design a high-power, interoperable charging experimental platform to research, develop, and demonstrate integration approaches and technological solutions. The proposed work includes (1) interconnection and management of a grid-tied inverter; (2) development of a DC distribution system that is responsible for system energy management, interoperability, and DC protection; (3) modular DC-DC conversion for vehicle charging; (4) EV charging interface and DC-DC integration; and (5) smart charge control and vehicle-to-edge (vehicle-to-building [V2B], vehicle-to-everything [V2X]) capability.

Objectives

The proposed plug-and-play solution allows a charging site to organically grow with additional chargers and distributed energy resources (DERs) through predefined compatibility with standards that will ensure interoperability and reduce upfront engineering expense. A common backbone that flexibly supports these use cases across all vocations will demonstrate integration approaches and solutions that overcome barriers for efficiency, cost, and power density. This project will establish existing state-of-the-art efficiency, equipment cost, and power density metrics and show an improvement through the proposed DC-connected site approach.

Overall goals of the project are listed below:

- Broadly identify limitations and gaps in DC distribution and protection systems that would allow for modular high-power charging systems
- Develop and demonstrate solutions for efficient, low-cost, and high-power-density DC-DC for kW- and MW-scale charging
- Determine interoperable hardware, communication, and control architectures for high-power charging facilities that support seamless grid integration and resilient operation

Approach

We have designated four technical topic areas under which this project will develop: i) System power electronics architecture and development, ii) DC distribution bus design and protection, iii) Grid integration, and iv) Site energy management. Regarding hub architecture, the system will include multiple isolated DC-DC converters connected to the common DC charging hub. One of these DC-DC converters will be developed in-house, while the rest of the converters will be acquired commercial off-the-shelf. The system will have a central grid connected inverter, which handles grid integration. A site energy management system (SEMS) will control the operation of the individual system components.

DC-DC Universal Power Electronics Regulator (UPER)

The objective is to develop the isolated DC/DC converter, hereby referred to as universal power electronics regulator (UPER), interfacing the DC distribution bus and the vehicle. In the previous year, specifications and requirements for such a charger were identified [2]. A comparison of various topologies to implement the proposed bi-directional charger was performed and dual active bridge (DAB) was selected [2]. A detailed design of the 1000 V, 175 kW charger has been completed. The design has the following main features:

- Dual active bridge for bi-directional capability
- 1700 V SiC MOSFETS

- 20 kHz switching frequency
- Innovative modulation technique for achieving zero voltage switching (ZVS) over wide voltage (250-900 V) and wide current (0-200 A) operation
- ZVS operation to enable high efficiency (> 99%) even under light load conditions
- Compact, 175 kW, 20 kHz 1000 V isolation transformer with dimensions of 8”x7”x7”
- Small input/output capacitances (< 200 μ F)
- Air cooling for ease of maintenance
- Integrated vehicle communications and isolation monitoring

It was identified that achieving a wide voltage range (250 V-950 V) using DAB based charger is a key technical challenge. The proposed DAB based charger achieves zero voltage switching (ZVS) over wide current and voltage range by implementing passive and active techniques. The passive technique involves adding a tap on the secondary of the medium frequency transformer as shown in Figure II.3.1.2a. The tap is used to provide correct voltage to either a 400 V class vehicle or an 800 V class vehicle. The proposed active method is a novel zero state modulation (ZSM) technique that will be implemented at lower currents and non-unity voltage ratios as shown in Figure II.3.1.2b. ZSM method allows ZVS operation at lower currents and for non-unity voltage ratios. In the high current range, the standard single phase modulation technique (SPM) will be implemented as this will result in ZVS, high efficiency, and low RMS current operation.

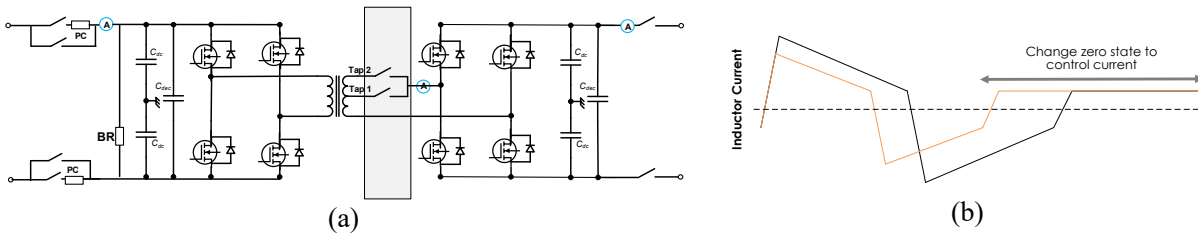


Figure II.3.1.2 (a) Proposed taps to select between 400 V class and 800 V class vehicles. (b) Proposed zero state modulation (ZSM) technique to improve optimal DAB control range.

Integration of UPER, Spec Module, and Site Energy Management

Three key components for implementing bi-directional charging in the eCHIP project are (1) hardware and firmware development of supply equipment communications controller (SECC), (2) developing communication protocol between the SECC and DC-DC UPER, and (3) designing and developing the software architecture as well as main applications for the SEMS platform.

Hardware and Firmware development

Leveraging ANL's previous work and experience with the SECC development, the approach for this project was to integrate the ANL SpEC module with the ORNL UPER to create a bi-directional DC coupled charger. ANL researchers utilized both the Gen I (Figure II.3.1.3 on the left) and Gen II (Figure II.3.1.3 on the right) SpEC modules in the development and demonstration phase of the project. Leveraging the DIN 70121 stack, researchers are working to update the firmware to implement the ISO 15118-20 standard to accomplish bi-directional DC charging. Custom firmware will be written to interface with the UPER and the SEMS platform.



Figure II.3.1.3 SpEC module Gen I (left) and Gen II (right).

Communication Interface Development

To demonstrate bi-directional DC charging with the UPER, researchers collaboratively defined the interface requirements and protocols. ORNL and ANL researchers worked closely together to learn the intricacies of the UPER power electronics as well as the DIN/ISO charging standard requirements. Clearly defining communication protocol and logic helped the labs create emulators of the SECC or UPER controllers. Development of emulators aided researchers in integration testing and reduce the risk of future integration issues when onsite testing between ORNL and ANL occurs.

Site Energy Management System (SEMS) Platform

One of the critical barriers to implementing a high-power charging facility is that interoperable hardware, communication, and control architectures do not exist to support seamless grid integration and resilient operation. Researchers are tasked with defining requirements as well as development and deployment of a SEMS platform. The SEMS scheme will flexibly handle the high-level control of the system, including DER management, vehicle charge scheduling, site load forecasting, and device onboarding. A modular open-source approach will allow scalable control across many use cases. This task will reduce barriers to integration by improving connectivity, defining communication and control approaches, and enabling a simplified integration approach with the distribution system utility.

Development of Power Hardware-in-the-loop Experimental Testbed

This work proposes the development of a power hardware-in-the-loop (P-HIL) testbed to support model validation, testing, and demonstration. The testbed will demonstrate high-power charging through a DC network. Multiple DC-DC chargers, distributed energy resources (DERs) and energy storage systems will be integrated into a common DC power distribution network at NREL EV Research Infrastructure (EVRI) Laboratory. The target P-HIL testbed is depicted in Figure II.3.1.4. The figure shows two commercial-off-the-shelf (COTS) chargers, one COTS bidirectional inverter, ORNL-developed UPER, energy storage system, and distributed energy resources and will be rated at 1 MW of power. In this setup, the SEMS controller accepts feedback from the system nodes (i.e., chargers, DERs, grid-tied inverter, etc.) and direct their operation to safely manage power and energy in the hub and react to grid fluctuations, dynamic charging demand, system faults, and other events. A use-case will be described in the Results section of this report.

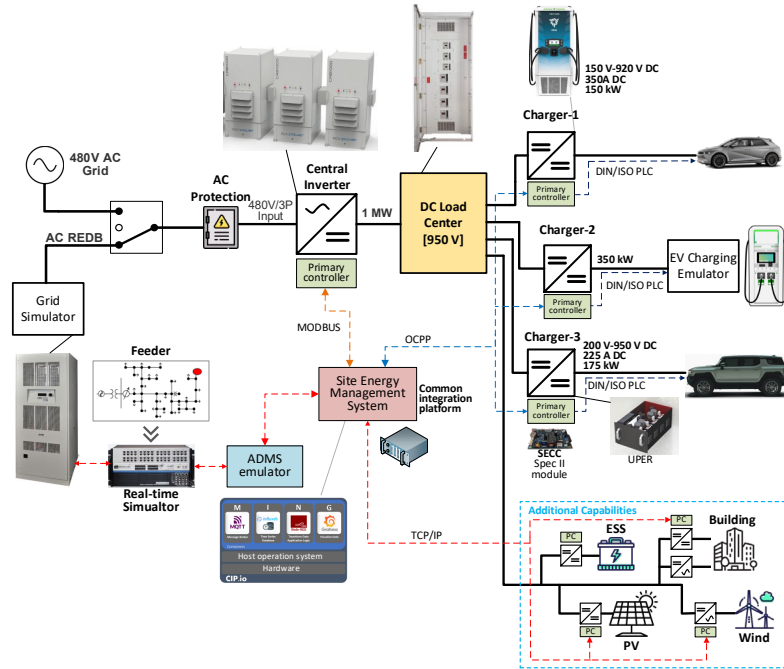


Figure II.3.1.4 MW-Level DC charging hub demonstration.

To reach the P-HIL setup described above, an intermediary testbed is constructed as depicted in Figure I-5 as a mid-way to the final testbed setup. The current P-HIL testbed accommodates the charging demonstration of an EV and a battery energy storage system emulator. A grid-connected Anderson power conversion unit, capable of sourcing/sinking 660 kW, connects to the DC Bus as a place-holder for the 1 MW bidirectional inverter, shown in Figure II.3.1.4. The SEMS ensures stable operation of the DC hub by communicating appropriate set-points or limits to each hub component. The SEMS implementation is closely tied to the communication system architecture. Data is communicated through the MQTT Broker (as shown in Figure II.3.1.5b) to the OCPP server and protocol adapters. Different measurements and feedback data points are also communicated back to the site level controller. An example site-level controller will be shown in the Results section.

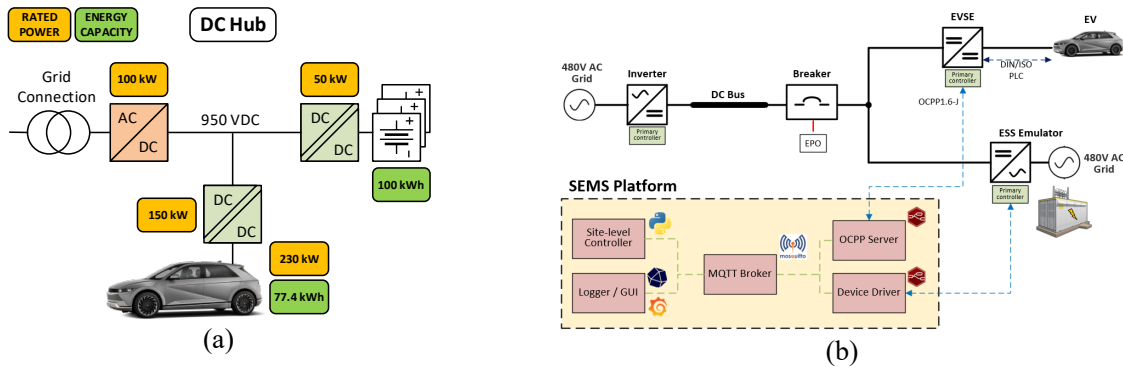


Figure II.3.1.5: DC charging hub demonstration tested at 150 kW: (a) Overview of the setup, (b) SEMS platform implementation on hardware.

Results

UPER Design and Testing Results

The fully assembled 175 kW, 1000 V class charger is shown in Figure II.3.1.6a. The charger was tested at 950 V and 150 A, which is approximately corresponds to 150 kW. The important waveforms from the DAB converter operation are shown in Figure II.3.1.6b.

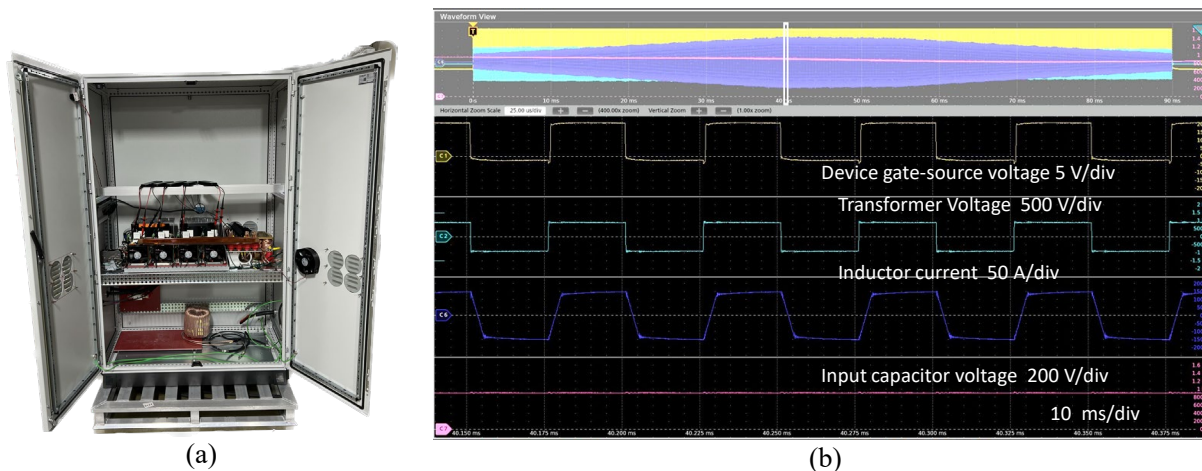


Figure II.3.1.6 UPER: (a) 1000 V, 175 kW, 20 kHz DC/DC charger, (b) Charger test results at 950 V and 150 A.

ANL developed SPEC module was selected to act as an interface between the ORNL UPER and the external components, which are the EV and the SEMS platform. The interface between UPER and SPEC is implemented over CAN, and the protocol is developed in a collaborative way. To test the developed SPEC-UPER interface, the UPER was tested in the setup developed at ORNL shown in Figure II.3.1.7a. The two sources act as DC bus and vehicle emulator. The SPEC is represented by an equivalent DBC file while the actual testing and integration of UPER-SPEC integration will be done in FY24. The test results attained are shown in Figure II.3.1.7b. In this test, the commands are sent by the SPEC equivalent DBC file. All the relevant modes such as cable check, pre-charge, voltage, and current regulation, and shutdown are tested successfully.

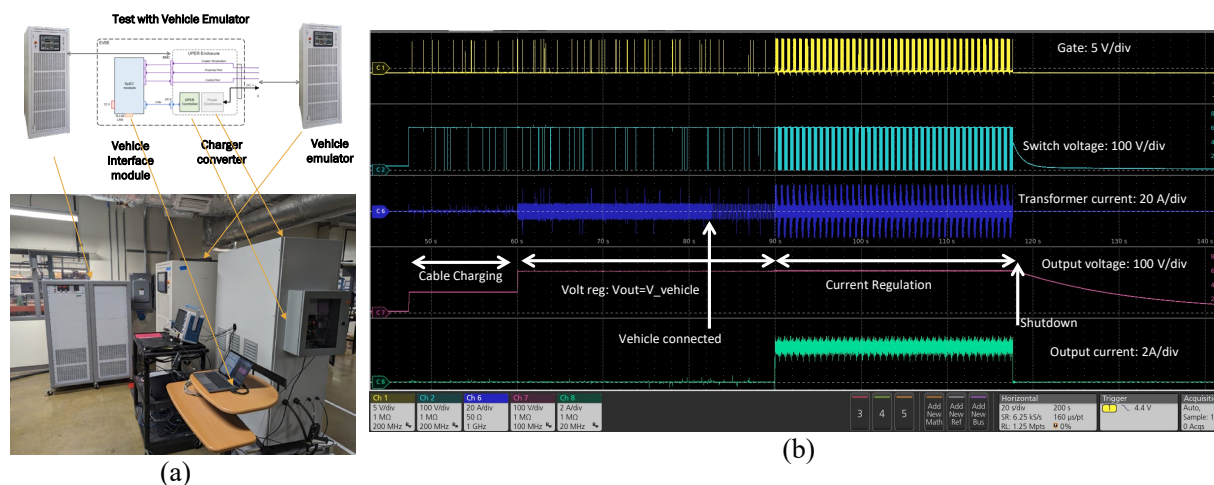


Figure II.3.1.7 (a) UPER-Spec Integration setup, (b) UPER-SPEC interface testing Results at 600 V and 10 A.

Integration of UPER, Spec Module, and Site Energy Management

In support of the eCHIP project, several significant developments and improvements were made. First, the SpEC II module underwent an extensive update, with a revision 3 of the boards designed to enhance the performance. This involved addressing bugs and introducing new features that not only improved the overall functionality but also added more robust debugging capabilities, both on the PCB and in the software. Additionally, a standalone UPER emulator was developed to seamlessly interface with the SpEC I and SpEC II modules. While the controller board for UPER at ORNL was still under development at the time, the emulator allowed for the swift development of the necessary firmware on the SpEC module for interfacing with the UPER controller board. Notably, this setup was successfully demonstrated by performing a full charge session on a Ford F-150 Lightning using the UPER emulator, which also interfaced seamlessly with the ABC-170 DC power supply.

In the pursuit of developing and showcasing DC vehicle-to-grid (V2G) capabilities, several significant achievements were attained. We achieved a major milestone by creating an ISO 15118-2 bidirectional power transfer (BPT) stack for the SpEC II communication controller, a crucial step towards enabling V2G capabilities on SpEC-based DC chargers. Simultaneously, we designed a custom MQTT protocol for the SpEC-based DC charger, allowing previously unavailable information exchange beyond the OCPP 1.6J standard. This protocol opens doors for advanced smart charging management (SCM) and vehicle grid integration (VGI) strategies within the eCHIP framework. Furthermore, the protocol was utilized to develop a real-time visualization dashboard for monitoring and controlling SpEC-based DC chargers.

ANL also formed a partnership with Lion Electric, culminating in a compelling demonstration at the Fall 2023 EVs@Scale Semi-Annual meeting hosted at Argonne National Laboratory [3]. Leveraging the Aerovironment ABC-170 as the power source and pairing it with the SpEC II module, we successfully conducted a V2G session with the Lion Bus, demonstrating rapid switching between charging and discharging in real-time using the dashboard. This demonstration underscores the practical application and promise of these cutting-edge developments in EV charging and vehicle grid integration. The setup for the demonstration is shown in Figure II.3.1.8.



Figure II.3.1.8 Demonstrating a V2G session with the Lion Electric Bus at ANL.

Site Energy Management System

ANL and NREL researchers collaborated to identify energy management challenges and requirements for a high-power charging facility. They have initiated the development of a Site Energy Management System (SEMS) platform to integrate DC coupled bidirectional chargers using Open Charge Point Protocol (OCPP) and MQTT for charge session monitoring and control. Additionally, the researchers have prepared a detailed document outlining design guidelines and specifications for a DC charging hub [4].

Development of Power Hardware-in-the-loop Experimental Testbed at NREL

The developed DC charging setup was shown in Figure II.3.1.5. We run a use case utilizing this setup. This use case demonstrates the grid integration capability of the DC hub platform. During a demand response event, the SEMS controller adjusts the inverter power rating to meet the specified load reduction. Rest of the DC hub will adjust according to the developed rule-based SEMS controller. As an example of this use-case, the following implementation is presented. Utilities commonly use the openADR protocol to implement automated demand response, whereas IEEE 2030.5 may also be used. Automated demand response may be realized as part of a broader ADMS or DERMS system. Test case emulates an openADR “fast DR” event using an openADR 2.0b profile. A “LOAD_DISPATCH” signal of signal type “multiplier”, to specify a 50% load reduction. Many other signals types and use cases are possible under the openADR protocol, e.g. other means of load control, energy storage charge / discharge control, communication of electricity pricing. Below explains how rule-based SEMS controller operates:

- Charge EVs as soon as possible;
- Inverter will supply power to EV first;
- If inverter supply is not enough, ESS will provide remaining power;
- If both inverter and ESS are not sufficient to meet load, then EV charging power will be reduced; and
- If there is generation on DC hub, it will be offered to ESS first, then inverter will feed it back to the grid if necessary.

Figure II.3.1.9 shows the experimental results of the operation. In region A, there is no EV connected to the charger. The ESS is charged from the grid connection via central inverter. An EV connects and charges in regions B through E. In region B, the EV charging power is slightly less than the inverter capacity, and the ESS continues charging with the remaining available inverter power. In region C, the EV charges around 150 kW, so ESS is idle. The demand response event occurs in region D. The available inverter capacity is reduced by the SEMS by 50% from 150 kW to 75 kW. The ESS discharges at rated capacity to support EV charging at around 125 kW. In region E, the inverter capacity returns to 150 kW following the demand response event. The EV can again charge up to 150 kW. As EV reaches top of charge curve, charging power reduces and the ESS again charges with the remaining available inverter power. In region F, the EV is disconnected having reached 80% SOC. The ESS continues recharging from the inverter at 50 kW.

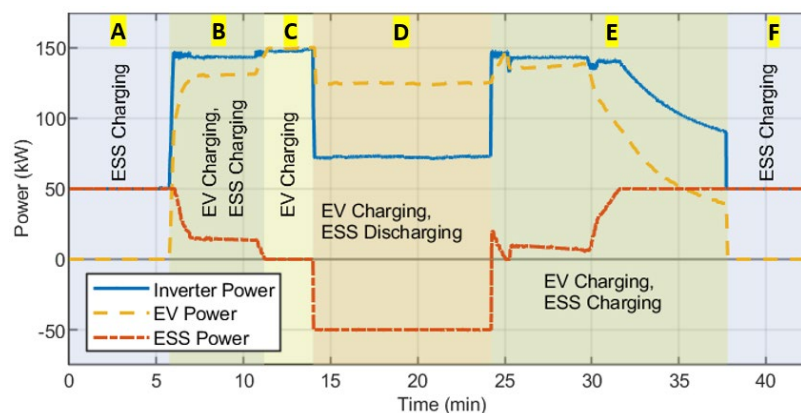


Figure II.3.1.9. Experimental results for DC charging hub operation with rule-based SEMS.

Conclusions

This project aims to develop a high-power, DC distribution-based, interoperable, grid-integrated charging hub platform that can scale to MW+ charging hardware development and testing. The second year of the project focused on developing hardware and control solutions for the DC charging hub. The design and integration of 175 kW UPER DC/DC charger and SPEC module has progressed and is on track to be finalized in FY24. Researchers worked collaboratively together to develop a SEMS platform and tested it using the developed hardware DC-hub testbed. The testing platform included inverter, EV, and ESS, and performed a rule-based SEMS control. Future work will include integrating emulated PV system, building site load, and UPER/SPEC DC/DC charger to the developed hardware testbed. The research team will focus on investigating real-world use-cases and implementing those utilizing the hardware testbed.

Key Publications

1. A. Meintz, L. Slezak, M. J. Kisacikoglu, P. Kandula, T. Bohn, E. Ucer, J. D. Harper, M. Mohanpurkar, "Electric Vehicles at Scale (EVs@Scale) Laboratory Consortium Deep-Dive Technical Meetings: High Power Charging (HPC) Summary Report," NREL/PR-5400-84093. [Online]. Available: <https://www.nrel.gov/docs/fy22osti/84093.pdf>
2. A. Meintz, L. Slezak, S. Thurston, B. Carlson, A. Thurlbeck, M. J. Kisacikoglu, P. Kandula, E. Ucer, A. S. Ali, "Electric Vehicles at Scale (EVs@Scale) Laboratory Consortium Deep-Dive Technical Meetings: High Power Charging (HPC) Summary Report," NREL/PR-5400-86407. [Online]. [Online]. Available: <https://www.nrel.gov/docs/fy23osti/86407.pdf>
3. M. J. Kisacikoglu, J. Harper, P. Kandula, E. Ucer, A. Ali, A. Thurlbeck, R. Mahmud, S. Khan and E. Watt, "High-power DC-Coupled Charging Hub: Design Guidelines and Specifications," NREL, Golden, to be published.
4. M. S. U. Khan, E. Watt, Emin Ucer, Rasel Mahmud, A. Thurlbeck, M. J. Kisacikoglu, A. Meintz, "Development of a DC distribution testbed for high-power EV charging," IEEE Energy Conversion Congr. Expo. (ECCE), 2023.
5. E. Ucer, A. Thurlbeck, E. Watt, M. S. U. Khan, M. J. Kisacikoglu, A. Meintz, "Controller hardware-in-the-loop modeling and operation of a high-power DC charging hub," IEEE Energy Conversion Congr. Expo. (ECCE), 2023.

References

1. H. Tu, H. Feng, S. Srdic and S. Lukic, "Extreme fast charging of electric vehicles: a technology review," IEEE Tran. Transport. Electrific., vol. 5, no. 4, pp. 861-878, 2019.
2. Vehicle Technologies Office, "Electrification 2022 Annual Progress Report," 2022.
3. "EVs@Scale Lab Consortium Semi-Annual Stakeholder Meeting," Argonne National Laboratory, 27-28 Sept 2023. [Online]. Available: <https://www.anl.gov/taps/evsatscale>. [Accessed 30 Nov 2023].
4. J. Kisacikoglu, J. Harper, P. Kandula, E. Ucer, A. Ali, A. Thurlbeck, R. Mahmud, S. Khan and E. Watt, "High-power DC-Coupled Charging Hub: Design Guidelines and Specifications," NREL, Golden, to be published.

II.3.2 Assessment and Validation of Next Generation Electric Vehicles High Power Charging Profiles

Sam Thurston, Principal Investigator

Argonne National Laboratory
9700 S. Cass Ave.
Lemont, IL 60439
E-mail: sthurston@anl.gov

Keith Davidson, Principal Investigator

National Renewable Energy Laboratory
15013 Denver West Parkway
Golden, CO 80401
E-mail: Keith.Davidson@nrel.gov

Barney Carlson, Principal Investigator

Idaho National Laboratory
2525 N. Fremont Ave
Idaho Falls, ID
E-mail: richard.carlson@inl.gov

Omer Onar, Principal Investigator

Oak Ridge National Laboratory
1 Bethel Valley Road
Oak Ridge, TN 37830
E-mail: onaroc@ornl.gov

Lee Slezak, DOE Technology Development Manager

U.S. Department of Energy
E-mail: lee.slezak@ee.doe.gov

Start Date: October 1, 2020
Project Funding: \$9,190,000

End Date: September 30, 2024
DOE share: \$9,190,000

Non-DOE share: \$0

Project Introduction

In both commercial and consumer electric vehicle (EV) segments there are concerted efforts by EV and Electric Vehicle Supply Equipment (EVSE) Original Equipment Manufacturers (OEMs) to increase charge energy delivered while simultaneously decreasing charging time. To accomplish these goals, innovations must be made to increase the peak charging power of EVs. As the first High Power Charging (HPC) systems, 200kW+, are emerging, it is apparent that HPC profiles can vary greatly by EV. To intelligently integrate HPC systems within the grid and among co-located loads and sources it is critical to quantify and characterize the charging profiles that these systems will present. This project leverages laboratory team capabilities, OEM stakeholder relationships, current HPC fleet deployments, and XCEL project outputs to quantify and characterize current and next generation HPC EV profiles and EVSE characteristics. The assessment performed in this project includes both conductive and inductive charging topologies from a variation of vehicle classes including light, medium, and heavy duty. The output from this project will provide critical inputs to several ongoing efforts including modeling of electrified transportation systems, battery design, standardization best practices, and grid energy management systems.

Objectives

Develop Test Procedures – Collaboratively develop the test requirements, procedures, and measurement parameters for both conductive and wireless charging evaluation. These procedures to be used for laboratory

HPC profile capture and EVSE characterization. This objective also develops guidelines for data capture for fleet and in-field evaluations.

Capture HPC Profiles – Develop rich profile sets from each of the EV project assets. Assets constitute consumer and commercial EVs that include both conductive and inductive charging and span light, medium, and heavy duty EVs. The profiles are to be gathered through a combination of in-lab evaluations, field evaluations, and data gathering of in-use HPC EV fleets. Whenever possible, HPC profile sets include a nominal charging profile with subset profiles that are gathered during off-nominal conditions that include varied ambient temperatures, grid events, and/or managed charge control.

Characterize HPC EVSE – To fully quantify the charging load as seen by the grid, EVSE performance characterization of power transfer, efficiency, power quality, and harmonics injection, to be conducted for laboratory XFCs across the rated operating ranges and with next generation HPC profiles. These characterization measurements focus on quantifying the efficiency, power quality, harmonics, thermal management operation, etc. Characterization across the full operating range of XFC will eliminate the need for assumptions and extrapolation from the limited XFC operational data currently available.

Integrate, Analyze, and Report Data – Evaluation outputs and data collection to be shared publicly and among project partners. Throughout the project data analysis will be required to ensure all shared data is of requisite quality. Late-stage analysis will be conducted to report outcomes and findings of the resulting data. Results and data will be directly provided to modeling teams upon request.

Approach

Procedure Development - Collaborative development of the test requirements, procedures, and measurement parameters for both conductive and wireless charging evaluation. This includes the definition of ‘nominal’ conditions as well as developing the factors for in-depth laboratory investigations. Prior to procedure execution, the project team will solidify the minimum measurement requirements and calculated parameters that will be generated from evaluations as a primary output from this project. Project collaborators and industry partners will be queried for input and feedback on the measurements, calculated parameters, procedures, and process of the characterization.

HPC Profile Capture, Characterization of HPC EVSE, And Fleet HPC Utilization – The project team must align resources and leverage relationships to line up a wide breadth of HPC EV and EVSE assets; all capable of HPC (200kW+). These assets include partner laboratory resources, OEM partner share, OEM and laboratory field evaluations, in-use and planned fleet EV/EVSE, and use of XCEL research profiles. The project team has budgeted time and effort to continue outreach to emerging potential partners as the electric vehicle and infrastructure landscape changes.

Evaluation Methodology – Determine baseline HPC EV and EVSE equipment characteristics/charge profiles. Baseline datasets will be gathered during the procedure-defined nominal boundary conditions. Similar equipment characterization must follow utilizing factors identified in the procedure such as EV/battery conditions, ambient temperature, grid conditions, and charge management controls to observe how HPC profiles and equipment characteristics are affected by factors or factor combinations. These secondary evaluations will be referred to as off-nominal tests. The combination of these characterizations will allow evaluation of HPC EV and EVSE metrics that include; overall charging load profile, EV and EVSE thermal management loads, EV and EVSE charging efficiency, ramp rates, peak power, power quality, and external factor effects.

Dissemination and Reporting - Datasets and project outputs will be available for use by other research groups, grid planners, OEMs, and various other industry stakeholders. For the project results to be useful the datasets need to be clear, comprehensive, and consistent. The project team has planned a budget to include regular data quality checks to ensure data from multiple sources are aggregated in identical formats using common labels.

These practices will ensure that use of the datasets has low thresholds and can produce effective research and planning.

Results

Argonne National Laboratory Results

The ANL Team led recurring meetings, maintaining coordination between the participating four labs within Next-Gen Profiles. ANL lead task definitions, milestone planning, and final report outlining, working to ensure sufficient data would be gathered and presented in a meaningful way. Maintaining industry relationships, ANL worked through vehicle loan agreements and secured asset collaboration from 3 unique OEMs.

EV Profile Capture

ANL added (4) new LD EV assets to the Next-Gen portfolio, conducting (63) EV charging profiles using BTC XFC equipment on site, and (10) charge profiles off-site through Tesla's Supercharger network, utilizing both NACS and Magic Dock CCS connectors. These EV profiles explore nominal and off-nominal conditions for DCFC, examining performance impacts caused by start SOCs, battery temperature, vehicle pre-conditioning, OCPP curtailment, EVSE limitations and boost converter topologies. Time-series data from these sessions collected at 10Hz from the EV and EVSE were formatted/synchronized and added to the NGP repository to be used for analysis and reporting. This data will specifically feed directly into the *Next-Gen Profiles: EV Profile Capture* report scheduled for release at the end of CY2024. Initial analysis of can be seen in Figure II.3.2.1, where the top performing EV charge profiles are compared/contrasted with a focus on time spent above power thresholds in a 10-100% session.

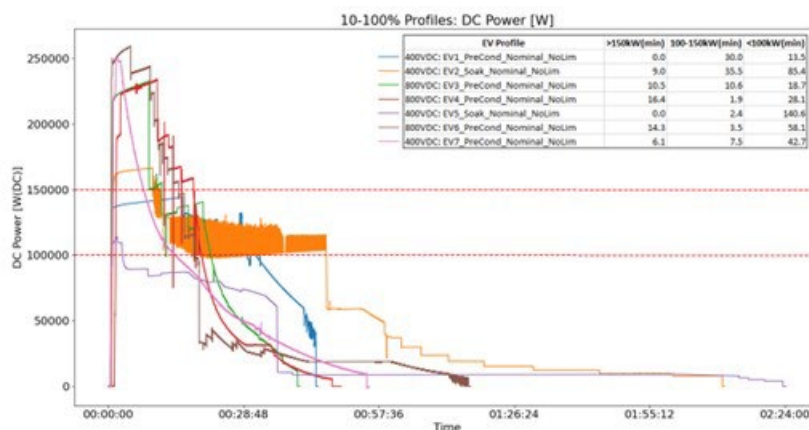


Figure II.3.2.1 Seven NGP EVs, Nominal Temperature 10-100% DCFC Power Analysis

Fleet Utilization

ANL team created an EV and EVSE fleet metric analysis python-based repository, with the ability to format, identify, and calculate standardized metrics of interest with regards to the individual fleet's utilization, power, energy, and temporal usage in particular charging and routing usage metrics for EV fleets and charging metrics for EVSE fleets. A standardized list of metrics was used in conducting statistical analysis of the individual fleets of interest. Low-level analysis of metric data was conducted (i.e., simple, and cumulative, moving averages) to quantify and locate trends within the data that will be meaningful for future and current fleet operators, grid planners, and technology developers. Identification of temporal incremental utilization within the fleets metric data allowed for understanding of fleet charging and routing metric usage rates in daily and weekly timescales, leading to identifications of habits and a description of the fleets EV and EVSE necessities.

Idaho National Laboratory Results

In support of the multi-national lab collaborative efforts in this project, INL completed the characterization of one 350kW Extreme Fast Charger (XFC) during nominal and off-nominal operating conditions. This testing

was conducted in a laboratory environment using high-accuracy power analyzers, a data acquisition system, a grid emulator capable of 500kVA and a high-power EV emulator that consists of a 400kW DC load bank and a CCS communications module for the necessary vehicle-side communication to enable a charge session.

Off-nominal AC grid input characterization of one XFC was completed for voltage deviation, frequency deviation, and harmonics injection. The testing was conducted at four power transfer levels. Overall, for the off-nominal AC grid input test cases, the XFC power transfer continued as requested, except when AC input voltage drops below 418VAC (13% voltage sag), resulting in the interruption of the charge session power transfer until the AC input voltage recovers to greater than 418VAC. Additionally, the DC output current ripple during all test cases was very low except for the highest power transfer test conditions. High DC current ripple and large AC phase-to-phase current unbalance was measured during the 5% AC harmonics test condition while power transfer was 350kW. One of the three listed off-nominal test cases can be seen in Table II.3.2.1 for AC Voltage Deviation, showing a voltage sag/swell from 426VAC/518VAC providing a very stable DC current, low DC ripple, and uninterrupted power transfer.

Table II.3.2.1 Impact of AC Input Voltage Deviation on DC Output Current

Input AC Voltage Deviation Tests	Maximum DC output current	Minimum DC output current	Maximum DC output current ripple %
350kW at 850VDC	410.3A	410.2A	0.65%
150A at 850VDC	150.1A	149.6A	0.65%
500A at 400VDC	500.0A	499.5A	0.11%
150A at 400VDC	149.7A	149.8A	0.28%

National Renewable Energy Laboratory Results

The NREL team participated in regularly recurring project review meetings and provided input and feedback as needed on matters related to data collection, analysis, presentation, and reporting. Fiscal year 2023 has been a year of achievements with respect to improving hardware testing capabilities, continued collection of EV, EVSE & Fleet charge data, simulation environment developments, asset acquisition, and reporting.

Lab-based Hardware Capabilities & Testing

The team collaborated with internal lab partners to upgrade and commission auxiliary equipment necessary to perform high voltage / high power EVSE charging envelope characterization tests. Power conversion equipment has received hardware upgrades that increase impedance of the charging circuit to ground and are awaiting internal certification before initial energization and subsequent operation. Also, Charge Control Box (CCB) vehicle simulators were upgraded to enable full 500A simulation capabilities, allowing for full power, temperature-controlled EV emulation. With upgraded charging equipment, NREL completed (2) low voltage / lower power EVSE charging envelope characterization tests while maintaining DC EVSEs in an operable condition to support NGP charge testing.

NREL Developed the capability to utilize vehicle sensors to query and record charging telemetry utilizing the vehicle OBDII port and instrumented EVSEs to collect parameters required by NGP Test Plans and Procedures document. Collected (37) EV charging profiles under diverse initial conditions across (4) light duty vehicles. In addition to on-site EV profile capture, NREL acquired a 2023 Kia EV6 to capture vehicle charge data when paired with Tesla Magic Dock Supercharger station & to collect boost converter charging performance. EV6 telemetry was setup/configured and subsequent Magic Dock / supercharger performance testing was conducted in and around Buffalo, NY.

Wireless fleet charging data was gathered from Link Transit / Momentum Dynamics charging system to be added into our fleet data repository, later to be included in the *Next-Gen Profiles: Fleet Utilization* report.

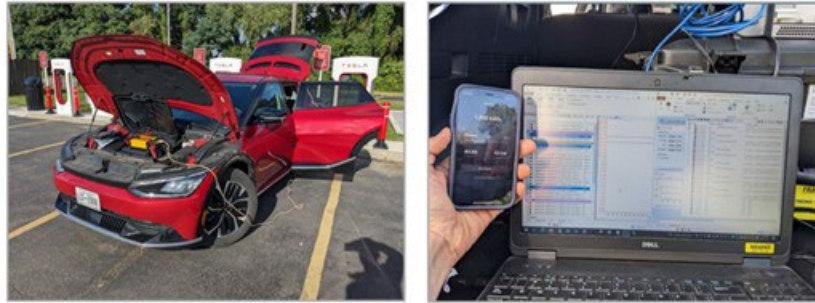


Figure II.3.2.2 EV Profile Capture Boost Converter Physical Setup

Oak Ridge National Laboratory Results

Oak Ridge National Laboratory (ORNL) has worked on standardized test procedures for wireless power transfer (WPT) based EV charging systems (wireless EVSEs) for nominal and off-nominal test conditions. The EVSE Characterization Recommended Test Procedures for WPT Systems document has been completed and used as the guide to complete the 100-kW rated WPT EVSE characterizations including the meta data and results parameters. The efficiency data was collected with 10kW increments for up to 100-kW both with resistive load and battery load conditions including the full range of the load resistance and full range of the battery voltage, i.e., 300 to 400V. While the nominal conditions represent nominal z-gap and perfectly aligned transmitter and receiver coils with zero yaw, roll and pitch angles, off-nominal conditions include change in nominal z-gap and misaligned conditions for $\Delta x = \pm 7.5\text{cm}$ while $\Delta y = 0$ and $\Delta y = \pm 10\text{cm}$ while $\Delta x = 0$ and combination worst case misalignment of $\Delta x = \pm 7.5\text{cm}$ and $\Delta y = \pm 10\text{cm}$. The other off-nominal conditions as per SAE J2954 include yaw angle of $\Delta\Phi = \pm 3^\circ$, roll angle of $\Delta\phi = \pm 2^\circ$, and pitch angle of $\Delta\theta = \pm 2^\circ$.

Efficiency characterization of the 100-kW WPT system is given in Figure II.3.2.3 under different power levels with 10 kW increments for four different battery voltage levels. As shown in this figure, while the light load efficiency is relatively lower, above 30 kW power transfer level, efficiency is almost constant.

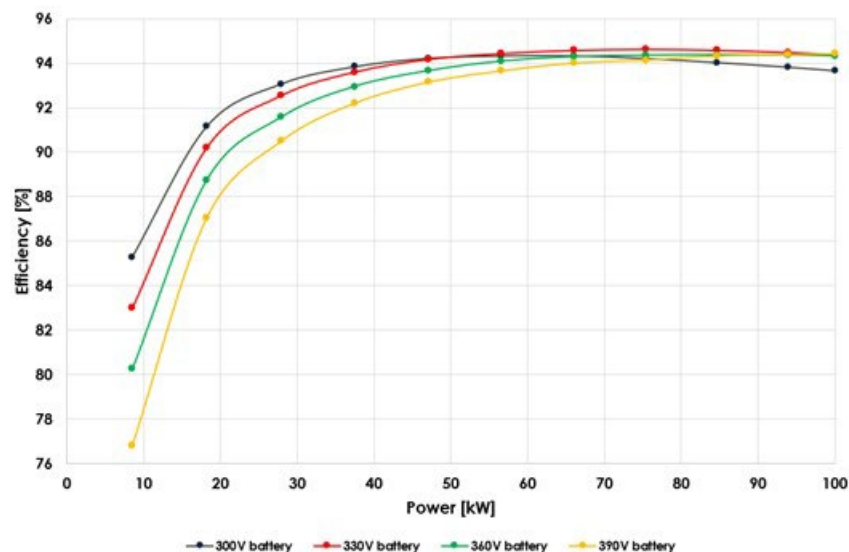


Figure II.3.2.3 Efficiency characterization of the 100-kW WPT system under four different battery voltages at different power levels.

For the off-nominal test conditions, the receiver coil was moved to create the misalignment for x, y, or in x and y combined directions to evaluate the system performance under these conditions. The definition of these off-nominal conditions is illustrated in Figure II.3.2.4 where the x misalignment is towards the direction of travel

(longitudinal), y misalignment is lateral, yaw angles indicate angular misalignment, roll angle indicates lateral angular misalignment, and pitch angle indicates longitudinal angular misalignment.

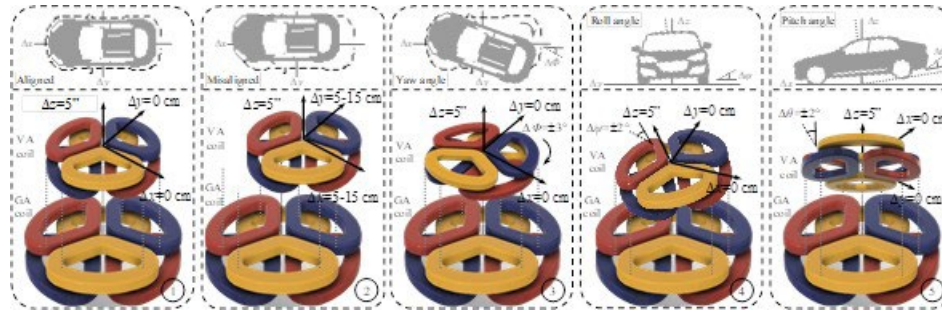


Figure II.3.2.4 Off-nominal condition definitions with respect to coil positions.

System performance under all off-nominal conditions, including the x, y, and x-y misalignments and angular misalignments including yaw, roll, and pitch have been accurately cataloged, and will be presented in greater detail within the WPT section of *Next-Gen Profiles: EVSE Characterization CY2023* report.

Conclusions

The multi-laboratory effort continues to strive towards achieving a high level of quality EV, EVSE, and Fleet characterization data. FY2023 had a directed focus on the continuation of data collection, additional assets, and report planning for the scheduled release of four documents at CY2023's end. The NGP team worked to gather (113) EV profiles, (30+) EVSE characterizations across conductive & WPT systems, and (6) long-term fleet utilization data. The team has been quick to respond to new testing requests, such as the addition of boost converter testing, and continues to keep open minds about expanding the scope of Next-Gen Profiles as the EV market develops.

Lab participants continue to pursue OEM partnerships and asset acquisition to add greater depth to the NGP portfolio. In FY2024 the team looks to release public reports on our findings, gather feedback, revise our procedures document to include additional tasks, continue to characterize EVs, EVSEs, Fleets, and work towards another round of findings presenting through CY2024 reporting.

Key Publications

1. Carlson, B. 2023. "State-of-the-Art HPC Equipment Performance Characterization" Presented at the EVs@Scale High Power Charging Pillar Deep Dive, May 02, 2023
2. Thurston, S. 2023. "High Power Charging Profiles (HPC) for New generation EVs" Presented at the EVs@Scale High Power Charging Pillar Deep Dive, May 02, 2023
3. Thurston, S. 2023. "Next Generation Profiles: Project Overview & Progress" Presented at the EVs@Scale Semi-Annual Consortium Meeting, Sept 27, 2023

Acknowledgements

This work is sponsored by the Vehicle Technologies Office in the Office of Energy Efficiency and Renewable Energy Office, U.S. Department of Energy

II.4 EVs at Scale - Advanced Charging Grid Integration Technologies

II.4.1 Feasibility of Dynamic Wireless Power Transfer Corridors for Heavy-Duty Battery Electric Commercial Freight Vehicles (Oak Ridge National Laboratory)

Veda Galigekere, Principal Investigator

Oak Ridge National Laboratory
2360 Cherahala Boulevard
Knoxville, TN, 37932
Email: galigekerevn@ornl.gov

Lee Slezak, DOE Technology Development Manager

U.S. Department of Energy
Email: lee.slezak@ee.doe.gov

Start Date:

End Date:

Project Funding: \$0

DOE share: \$0

Non-DOE share: \$0

Project Introduction

A high-power dynamic wireless charging–based electrified roadway enables energy to be provided to the electric vehicle (EV) while it is in motion by means of transmitting coils embedded in the roadway. This has the potential to alleviate range anxiety by extending the mission and concurrently reducing the required onboard energy storage. Architecting an economically viable dynamic wireless charging roadway requires the identification of a solution that includes the appropriate roadway power transfer level, roadway coverage, road traffic loading and utilization, vehicle energy requirements based on vehicle class, and battery chemistry. Dynamic wireless charging also offers potential benefits to the grid by distributing the charging load over time and location, thereby mitigating peak load on the grid.

Objectives

The overall objective of this project is to identify the appropriate use cases and vehicle classes for which high-power dynamic wireless charging can offer significant value and to evaluate and compare quantitatively the key metrics, including the total cost of operation (TCO) for a battery electric vehicle (BEV) with dynamic wireless power transfer (DWPT) and without DWPT. Oak Ridge National Laboratory (ORNL) has developed an advanced commercial vehicle CV road and freight network, energy systems architecture optimization, and system-of-systems analytics using the OR-AGENT (Optimal Regional Architecture Generation for Electrified National Transport) modeling framework [1]. A similar framework is developed and utilized to architect a dynamic wireless charging solution and compare the system-level metrics.

The specific objectives are as follows:

- Identify the use cases in commercial vehicle and freight transportation for which high-power dynamic wireless charging can have significant value. This is to be done with inputs from stakeholders across the board including vehicle original equipment manufacturers, utilities, freight operators, and research and development organizations.
- Conduct a techno-economic use-case analysis to compare BEVs with and without DWPT for the use cases identified previously.

- Conduct a techno-economic use-case analysis to compare the TCO of a BEV with DWPT against a BEV without DWPT, fuel cell electric vehicle (FCEV), and diesel vehicle in the scenario of drayage application.

Approach

The approach to achieve the objectives was as follows:

1. Based on extensive engagement with a broad set of stakeholders including vehicle manufacturers, Tier-1 automotive suppliers, electric utilities, fleet operators, and government agencies, the use cases suitable for dynamic wireless charging were identified as the following:
 - a. Line haul
 - b. Regional haul
 - c. Drayage
 - d. Last-mile delivery

The assumptions or the attributes of the identified use cases are shown in Figure II.4.1.1.

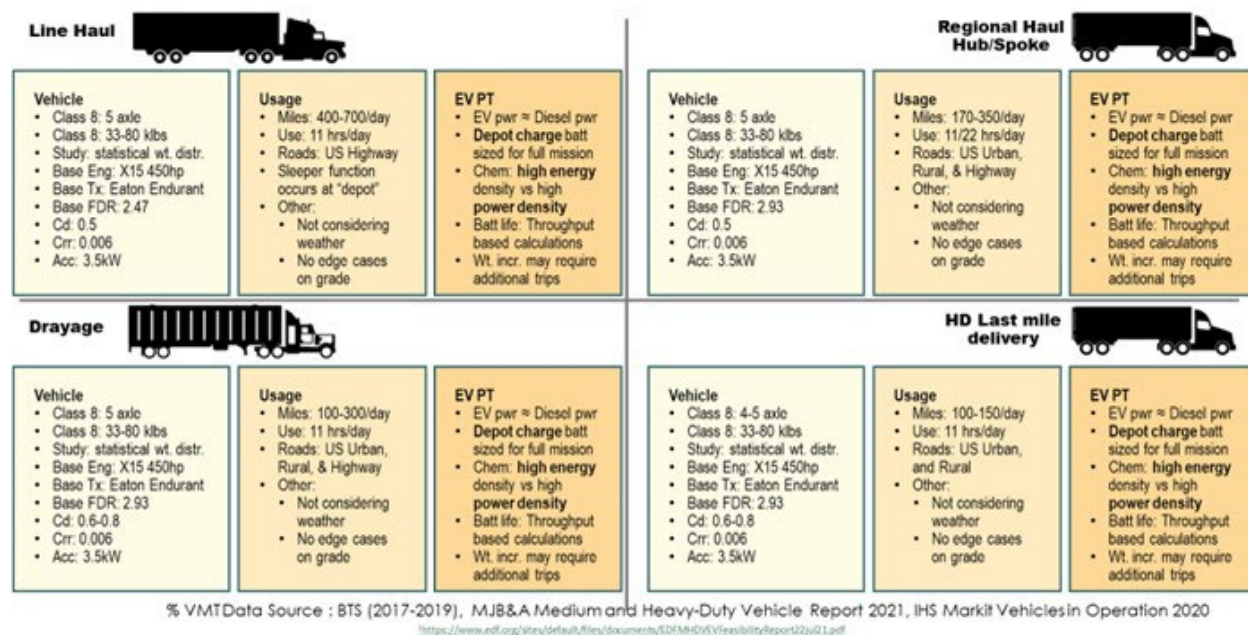


Figure II.4.1.1 Use cases selected for exploration in techno-economic analysis.

2. Representative vehicle routes were identified based on the applicable roadway based on application (e.g., the interstate was sampled for long haul, and urban haul was sampled for last-mile delivery). The road profiles included distance and grade.
3. ORNL has developed an advanced CV road freight network, energy systems architecture, and system-of-systems analytics termed the OR-AGENT (Optimal Regional Architecture Generation for Electrified National Transport) modeling framework [1], and the workflow is shown in Figure II.4.1.2. Within this framework, we conducted a parametric study that utilized integrated subsystem data and models encompassing various aspects of electrified vehicle powertrain architecture and dynamics, freight logistics (including vehicle origin-destination data, schedules, and weights), traffic patterns, roadway conditions, weather factors, and energy flow pathways (including grid capabilities, energy storage, dispensing facilities, and distributed energy resources). This unique methodology for interconnected

systems analysis combines insights from vehicles, operational logistics, and energy pathways. It yields a region-specific, seasonally adapted, and constrained-optimal solution for the architecture of vehicles and infrastructure. This optimization process is guided by techno-economic metrics aligned with the needs of stakeholders in the system, such as fleet operators, electrified equipment suppliers, energy service providers, utilities, and planning agencies. By employing a defined cost function that reflects the interests of these stakeholders, this approach equips local government bodies, industry end users, energy suppliers, and equipment providers with a versatile planning tool. This tool facilitates the strategic deployment of electrified freight transportation systems, accommodating regional variations and constraints arising from diverse stakeholder motivations within this ecosystem. The representative vehicle routes with over 30 parameters as shown in Figure II.4.1.3 covered over 47,000 configurations. The framework enabled the comparison of the following:

- a. BEVs with DWPT against BEVs only for line-haul, regional, haul, drayage, and short-haul applications
- b. The TCOs over a 5-year period for diesel vehicles, FCEVs, BEVs, and BEVs with DWPT

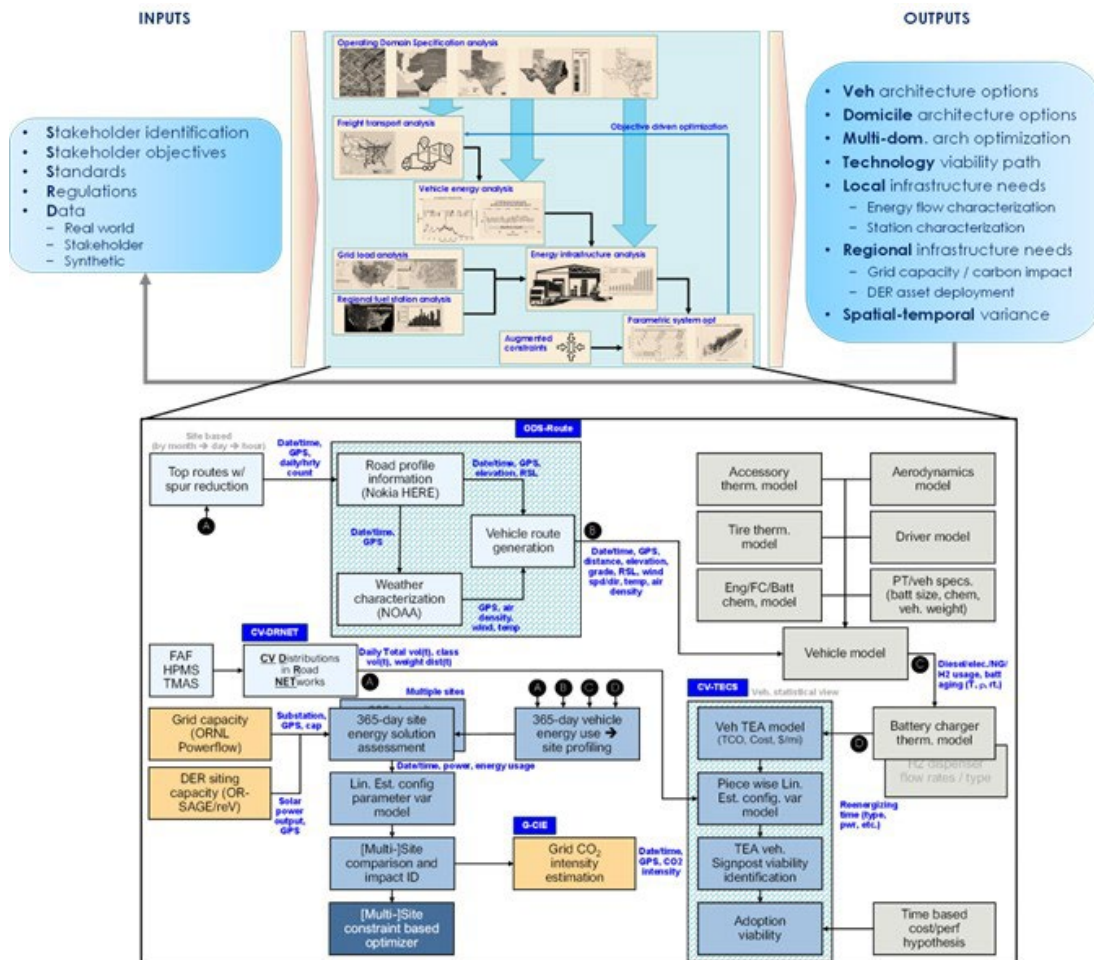


Figure II.4.1.2 Overall workflow based on OR-AGENT.



Figure II.4.1.3 Parameters considered for the techno-economic analysis.

- The outcomes of the use-case analysis and techno-economic analysis were summarized based on quantitative comparison.

Results

The outcomes of the comparison of line haul, regional haul, drayage, and short haul for BEVs only and BEVs with DWPT are shown in Figure II.4.1.4. From Figure II.4.1.4., it can be inferred that drayage is ideally suited for dynamic charging application. It can also be inferred that all use cases benefit from the reduction of the required battery pack to meet the designated mission profiles and from possible increases in battery life as well. Table II.4.1.1 shows the comparison of TCOs for diesel vehicles, FCEVs, BEVs, and BEVs with DWPT by considering BEVs as the baseline. The parameters varied for BEVs with DWPT were the battery price and battery range. Notably, BEVs with DWPT offered improved TCOs for all the cases considered.

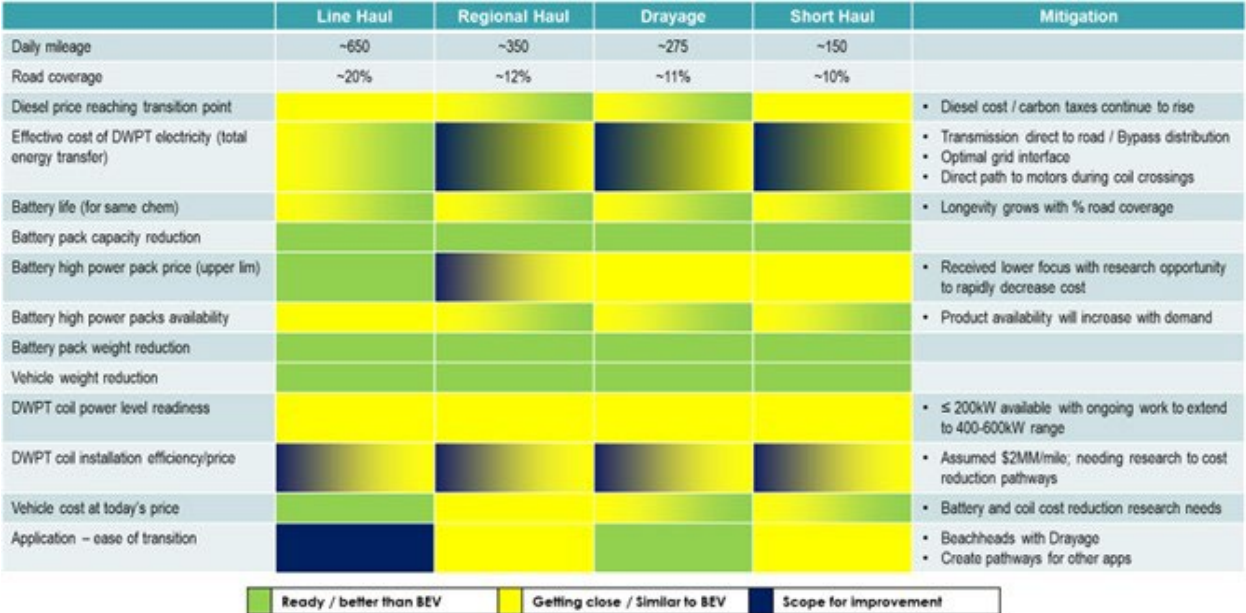


Figure II.4.1.4 Outcome of use-case analysis study.

Table II.4.1.1 TCOs for diesel vehicles, FCEVs, BEVs, and BEVs with DWPT for drayage application

	Diesel	FCEV		BEV	BEV with DPWT options			
Diesel fuel (\$/gal)	4.5							
H2 fuel (\$/kg)		3	5					
Fuel cell (\$/kW)		250	250					
Battery size (kWh)		100	100	600	200	200	100	100
Battery chem		NMC ^a	NMC	NMC	LTO ^b	LTO	LTO	LTO
Battery price (\$/kWh)		250	250	250	600	500	1,000	750
Battery range (mi.)				~235	~80	~80	~40	~40
Depot elec (\$/kWh)				0.07	0.07	0.07	0.07	0.07
DWPT elec (\$/kWh)				N/A	0.03	0.05	0.05	0.07
TCO 5 years	\$306K	\$296K	\$382K	\$285K	\$277K	\$273K	\$265K	\$256K
TCO Δ %	+7.4%	+3.9%	+34%	0%	-2.8%	-4.2%	-7.0%	-10.2%

^a NMC = nickel manganese cobalt

^b LTO = lithium titanate

Conclusions

The noteworthy conclusions are as follows:

- Based on extensive engagement, line haul, drayage, regional, and last-mile delivery were selected as the use cases for which using BEVs with DWPT would potentially have significant benefit.
- All four applications (line haul, drayage, regional, and last-mile delivery) showed benefit from BEVs with DWPT compared with depot-charging BEVs.
 - For all four applications, the required onboard battery capacity, and thus vehicle weight, was reduced compared with DWPT with depot charging.
 - The results strongly suggested that BEVs with DWPT reduce vehicle cost for all four applications.
- The study indicated a value proposition in achieving the cost of DWPT installation to be less than \$2 million/mi. Significant research and development are necessary to realize this target.
- BEVs with DWPT reduced TCO up to 10.2% compared with DWPT with depot charging.
- The study indicated that the drayage application has the highest readiness level for a DWPT pilot demonstration.

References

1. Sujan, V., A. Siekmann, S. Tennille, and E. Tsybina. 2023. *Designing Dynamic Wireless Power Transfer Corridors for Heavy Duty Battery Electric Commercial Freight Vehicles*. SAE Technical Paper 2023-01-0703. <https://doi.org/10.4271/2023-01-0703.References>.

Acknowledgements

The project team would like to thank Lee Slezak from DOE for his continued guidance and support on this project.

II.4.2 Behind-the-Meter Storage (NREL, INL, ORNL, SNL, ANL)

Anthony Burrell, Principal Investigator

National Renewable Energy Laboratory
15013 Denver West Parkway
Golden, CO, 80401
E-mail: anthony.burrell@nrel.gov

Brian Cunningham, DOE Technology Development Manager

U.S. Department of Energy
E-mail: Brian.Cunningham@ee.doe.gov

Start Date: October 1, 2018 End Date: September 30, 2023
Project Funding (FY21): \$2,400,000 DOE share: \$2,400,000 Non-DOE share: \$0

Project Introduction

Enabling Technologies for an Advanced Rack Design

Behind the meter storage (BTMS) systems are envisioned to improve grid stability and levelized cost of electricity (LCOE) for fast charging of light-, medium-, and heavy-duty EVs as they are expected to penetrate the market requiring various levels of charging infrastructure (350 kW to 1+MW). With rapid growth in research and design of efficient and high-performance chemistries for novel battery cells such as those made from lithium ion, battery systems could prove to be the solution that can minimize stability challenges posed by high penetration of EVs in the market. However, we need to address the hazards associated with lithium-ion batteries used in stationary applications for BTMS to become a reality.

Objectives

Enabling Technologies for an Advanced Rack Design

The main objective is to develop a strategy to enable a fail-safe rack design over a three-year period. “Fail-safe” is defined as preventing cell to cell propagation in a best-case scenario and preventing rack to rack propagation in a worst-case scenario.

Approach

Enabling Technologies for an Advanced Rack Design

In 2017, Bloomberg estimated that 94MWh of grid storage were affected by lithium-ion battery fires in South Korea. After a thorough review, the Korean Ministry of Trade, Industry and Energy (MOTIE) determined that the four primary causes of the fires were:

1. **Insufficient battery protection systems against electric shock** - systems were not able to properly protect against electrical hazards due to ground faults or short circuits. Existing fusing for the energy storage system (ESS) was not able to interrupt large electrical surges which led to catastrophic failure of the contactors. The short circuit current allowed the failures to cascade to the bus bar which resulted in fires inside the ESS.
2. **Inadequate management of operating environment** - Of the 23 fire incidents that occurred, 18 were installed in harsh conditions - the mountains or coastal areas. It was concluded that these environments resulted in conditions including large temperature swings, high humidity and elevated levels of dust and particulates which ultimately led to failure modes resulting in fires.
3. **Faulty Installations** - Human error during installations led to system faults resulting in ESS fires.
4. **ESS System Integration** - The integrated protection and management systems were found to be insufficient with the ESS installation. The committee indicated that there were gaps in the energy

management system (EMS), integration of the battery management system (BMS), and power management system (PMS) leading to the potential for fires.

More recently, South Korea experienced five ESS fires in 2019 and MOTIE determined that the fires originated due to internal defects within the batteries in combination with high charging rates at high states of charge. The committee attributed the defects to foreign matter in the cathode and lithium plating on the separator and anode after performing a physical analysis of the batteries. Due to similar concerns associated with lithium-ion ESS, the BTMS program is assuming that existing and future quality control measures at battery manufacturing facilities will not eliminate all single cell thermal runaway events and that improvements are needed to the EMS, BMS, and PMS systems. Thus, BTMS formed a team, Enabling Technologies for Advanced Rack Design, that has developed a four-pronged approach to mitigate the hazards associated with BTMS systems:

- **Advanced Cell, Module, and Rack Thermal Design:** Battery thermal management techniques will be investigated to regulate battery systems under normal temperature ranges to minimize temperature differences and achieve optimum performance and life. These thermal management strategies will further be optimized to mitigate/prevent thermal runaway propagation that might occur in a battery system.
- **Advanced Battery Management Systems (BMS):** Develop advanced BMS systems capable of cell balancing, state of health estimation, regulating temperature gradients between cells, and monitoring the health of individual cells and the pack.
- **Advanced Sensors and Controls:** Advances in battery management sensing and controls will be investigated in the interest of maximizing life, performance, and safety of large battery systems.
- **System Safety:** Reduce, isolate or eliminate the combustible products/potential within the cell and system design.

As expected, there are several standards and certification guidelines available and the Team will be using them to inform the “fail-safe” design. The following specifications in Table II.4.2.1 will help guide the development of technologies engineered under this task. Even though this is not a comprehensive list, the specifications outlined below are commonly used within the grid storage industry.

Table II.4.2.1 Design standards certifications to be used for the rack design. Source: NREL

Safety	Description
UL 9540	Safety for energy storage systems and equipment.
UL 1973	Batteries for use in light electric rail applications and stationary applications. ¹
NFPA 70E	Standard for electrical safety in the workplace.
UL 1642	Standard for lithium batteries. ²
IEC 61508	Functional safety of electrical/electronic/programmable electronic safety-related systems. ³

¹ Applicable to battery modules and racks only.

² Applicable to battery cells only.

³ Evaluation of battery management system only, in support of UL 1973, UL 9540, and IEC 62619 certification.

The technologies contributing to a safe rack design involve a very complicated design space. To limit the number of design considerations, we will only be considering three cathode/anode combinations: lithium manganese oxide (LMO)/lithium titanate oxide (LTO), lithium iron phosphate (LFP)/lithium titanate oxide, and lithium iron phosphate/graphite. The chemistries were chosen due to their lack of critical materials and excellent safety record. It is understood that the specific and volumetric energy densities of these battery systems is lower than those used for transportation and consumer electronics, but we are assuming that weight

and space restrictions will not be as severe for behind-the-meter-storage applications. Furthermore, our focus will be to develop a system primarily focused on the volumetric energy density as this is considered a more critical/important parameter. Figure II.4.2.1 shows graphically how the specific and volumetric energy densities will be affected from the cell to rack level – our target will be developing a rack system with 36% of the cell’s specific energy density and 30% of the cell’s volumetric energy density.

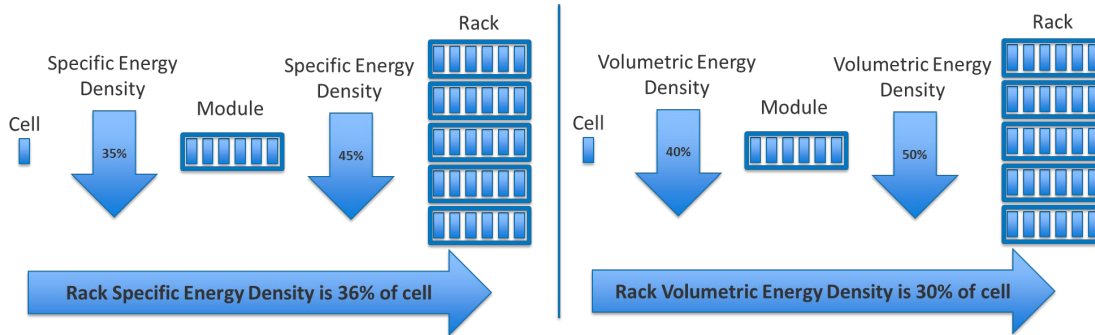


Figure II.4.2.1 Decrease in specific and volumetric energy density of ESS from the cell to the rack. Source: NREL

Another important aspect of the study will be to limit the battery discharge capacities to 10 Ah, 50 Ah, and 100 Ah. Even though some existing grid storage systems are using cells greater than 250 Ah, cell-to-cell propagation is difficult to limit or prevent in larger cells if a cell enters thermal runaway. As such, part of the study will investigate the positives/negatives of various series and parallel connected systems to achieve the appropriate fail-safe design and overall energy metrics for the system. Finally, temperature is critical to the lifetime and safety of the system. Initial, design specifications will be to limit the temperature of the batteries to between 20°C and 45°C and limit the temperature spread across the cells in the rack to 3°C. Table II.4.2.2 summarizes the important design parameters for our study. However, it should be noted each of the four efforts under this task will have additional design variables such as overvoltage, undervoltage, overcurrent, balancing requirements, etc... and these will be covered in the subsequent sections of this report.

Table II.4.2.2 Important design parameters for the advanced rack design. Source:NREL

Design Parameter	Units	
Rack Specific Energy Density	Wh/kg	> 36% of Cell Specific Energy Density
Rack Volumetric Energy Density	Wh/liter	> 30% of Cell Volumetric Energy Density
Rack Power Density	W/kg	> 40% of Cell Power Density
Rack Design Cost – (Cells, Modules, Racks, and BMS)	\$/kWh	210
Power Conversion Cost (Inverter, Electrical BOS)	\$/kW	240
Maximum Temperature ¹	°C	45
Minimum Temperature ¹	°C	20
Temperature Delta across Rack	°C	3

¹ TBD by cell development team.

As previously indicated, we envision this effort to occur over the next three years. A generic timeline of the activities is given below.

- Year 1: Simulation and Design – the first year’s effort will focus on modeling and designing the
- Year 2: Bench scale prototypes/verification
- Year 3: System integration and characterization

Results

Enabling Technologies for an Advanced Rack Design

Advanced Battery Management System (BMS)

Battery management systems (BMS) are essential for the safe operation and longevity of a battery pack. In FY22, we developed an active balancing method-based BMS for different cell chemistry structures to be used in behind-the-meter storage (BTMS) applications. The proposed structure utilizes modular isolated dual active bridge (DAB) DC/DC converters to actively balance the battery pack through a low voltage (LV) bus. No communication is required among the modular DAB converters. Instead, a supervisory controller monitors all the cell voltage, current, and state of charge (SOC) values. Detailed modeling and the control approach of the modular DAB converters are accomplished in FY22. Moreover, the control strategy of the supervisory control is also analyzed. The proposed method and structure can be extended to any combination of the number of cells to design the battery pack. Simulation results are provided for a system consisting of three cells in parallel to form a cell block and 14 cell blocks in series to form the battery module. Experimental results are provided for three modular DAB converters operating with a LiFeMnPO₄ prismatic cell with 3.2V, 20Ah rating.

BMS Design Progress: In FY21, modular isolated DAB converters are selected to be used for cell balancing and connecting the strings to the high voltage DC bus because of advantages such as bidirectionality and galvanic isolation. Supervisory control monitors the SOCs of individual cell groups and generate reference currents for these cell groups to actively balance their SOCs by transferring charge through a low voltage (LV) bus. The inner or primary control of the cell groups is designed to follow the reference current and simultaneously maintain the LV bus voltage. In FY22, simulation and initial experimental results are provided to validate the proposed method.

Overview of the modular battery pack design including the associated BMS is shown in Figure II.4.2.2. In this modular battery pack, each module is constructed by connecting several cells in parallel first and in series afterwards. The configuration has a low power DAB converter connected across each cell group in series through an LV bus. These converters enable power to transfer between the series-connected cell blocks to minimize SOC imbalance. Multiple modules are connected in series to increase the power and energy rating, and the string is finally connected to a high voltage (HV) DC bus through another DAB. Since the modular strings are decoupled from the HV bus, this allows for strings of different battery chemistries to be integrated within the pack. Figure II.4.2.3 shows the communication structure for the BMS system composed of three modular DAB converters.

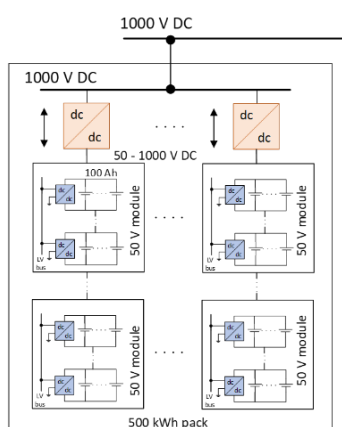


Figure II.4.2.2 Modular DC-coupled battery pack for BTMS. Source: NREL

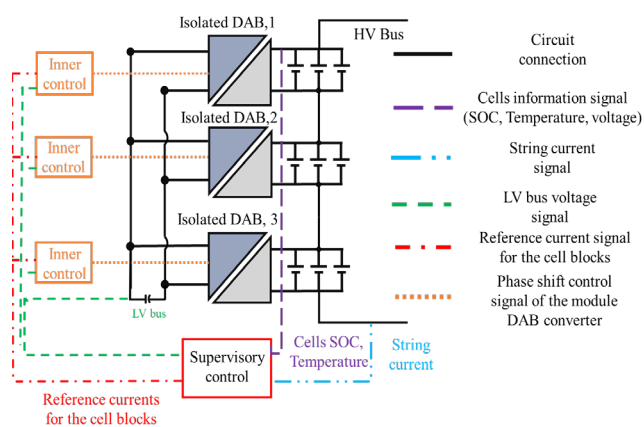


Figure II.4.2.3 Overview of the BMS for a modular battery. Source: NREL

The experimental setup of the three modular 50W DAB converters integrated on a single 3.2V, 20 Ah, LiFeMnPO₄ prismatic cell along with the supervisory control is shown in Figure II.4.2.4. The output of the

DAB converters is connected to the LV DC bus through a capacitor. The supervisory control is implemented in the dSPACE MicroAutobox. To validate the performance of the single DAB converter, it is operated at a 50W discharge mode. Two different experimental test procedures are followed to validate the performance of the proposed topology and control approaches. First, fixed reference currents are given as input for the DAB converters without implementing supervisory control approach. While providing the reference currents, one of the converters is kept in discharging mode while the other two are in charging mode. As shown in Figure II.4.2.5, during the transient period, the LV bus voltage is regulated as 12V while following the reference currents for the DAB converters. As the voltage loop control gains are higher, it prioritizes the LV bus voltage regulation while still maintaining the reference current. This validates the performance of the proposed controller. Then, a supervisory controller is included in the system to validate the overall performance of the system. The trajectory of the SOCs for different cell blocks is shown in Figure II.4.2.6, where the SOCs are slowly converging towards a steady-state value which is the average value of the SOCs, and they are becoming balanced. The reference currents for the cell blocks, along with the LV bus voltage regulation, are shown in Figure II.4.2.7, where the balancing currents slowly become zero after the SOCs are balanced. While the SOCs are getting balanced, and the balancing currents are becoming zero, the LV bus voltage is maintained at 12V, which further validates the performance of the proposed structure and the control methodology through experimental results.

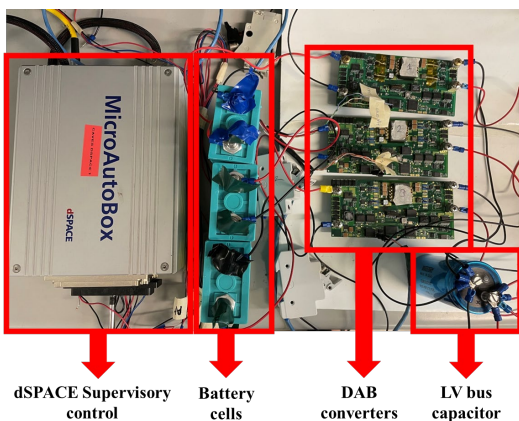


Figure II.4.2.4 Experimental setup for the three modular DAB converters. Source: NREL

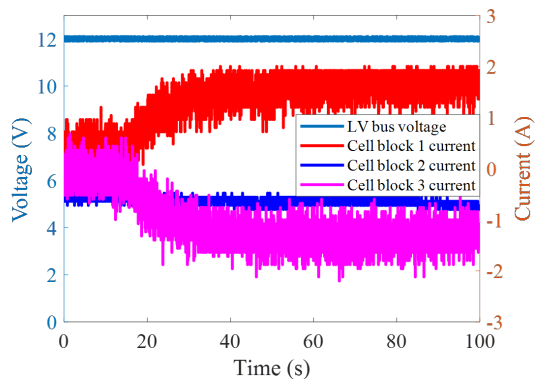


Figure II.4.2.5 DAB converters following a reference current to verify the controller. Source: NREL

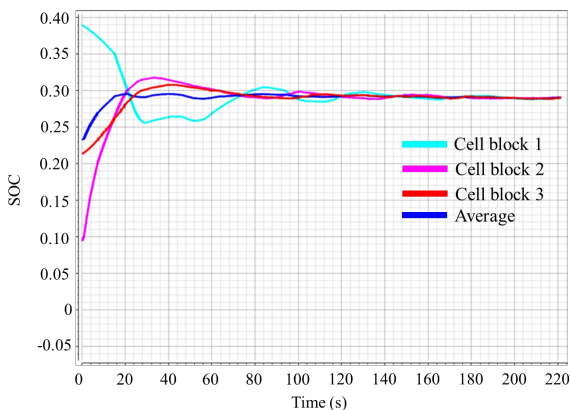


Figure II.4.2.6 Experimental results for SOC equalization. Source: NREL

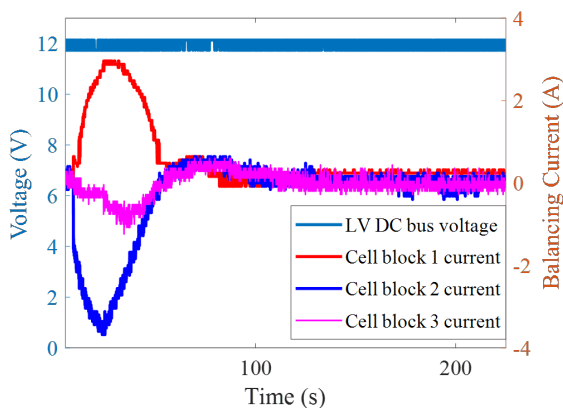


Figure II.4.2.7 DAB converter current and voltage satisfying SOC equalization. Source: NREL

Advanced Cell, Module, and Rack Thermal Design

Advanced thermal design aims to maintain desired temperature for battery rack operating at target temperature ranges, and to prevent cell-to-cell thermal runaway propagation. In FY 22, additional thermal runaway propagation modes and mitigation solutions were investigated with 3D thermal model, including heat conduction by busbars and mass ejection. Based on modeling analysis and experimental study, silicone-based fire-retardant foams were incorporated in the 60 Ah module used for nail penetration testing at Sandia National Laboratory (SNL). Additionally, Energy dissipation of neighboring cells/modules to prevent thermal runaway propagation was proposed. A multi-objective optimization tool is being developed, which is based on a trade-off analysis between passive thermal insulation and dissipation considering both nominal operating and fail-safe conditions.

Thermal Design Progress: Cells at less than 50% SOC produce significantly less amount of thermal runaway heat. As such, thermal runaway propagation can be stopped if energy within the neighboring cells can be rapidly dissipated to lower their SOC. The key is the energy dissipation time should be less than thermal runaway propagation intervals. LFP and LTO cells can be discharged at high C-rates. For example, 50% DOD can be achieved at 6C in five minutes. Recent thermal runaway experiments show propagation interval is about two minutes for NMC/Gr prismatic cells. Abuse testing in FY23 will verify whether propagation between LFP/LTO prismatic cells take longer time. Preliminary analysis shows this approach may work better to prevent module-to-module thermal runaway propagation. This approach is an active approach and compatible with modular battery racking systems.

In FY21, cell-to-cell thermal runaway propagation caused by prismatic cell surface thermal contact was studied. In FY22, thermal runaway heat dissipation from the failed cell to neighboring cells through busbar heat transfer was investigated using a 3D thermal model. The model estimates busbar heat transfer does not likely lead to thermal runaway propagation between LFP cells if cells are only thermally connected with busbars. Compared to heat transfer through busbar, surface thermal contact was predicted to be a higher risk. Heat transfer through busbar and tab took a significantly longer time to reach a quasi-steady state between the failing cell and its neighboring cells. There was no thermal shock produced in neighboring cells. The dissipated heat was gradually absorbed by neighboring cells' active material without large temperature gradients.

Additionally, an ejection model was developed to address potential propagation due to thermal runaway mass ejection. Self-heating rate (SHR) is employed to quantify ejection hazards. SHR can be used to distinguish thermal runaway hazards for different cell chemistries, SoCs, and abuse trigger conditions. Ejecta temperature is identical to instant average temperature of the thermal runaway cell. As shown in Figure II.4.2.8, the 3D model capture temperature distributions within the failure cell, neighboring cells, and the impinged cell. Neighboring cells contacting the failed cell may have a higher risk due to direct heat conduction. The model was used to compare the difference between slow and fast thermal runaway. In the simulations, the amount of thermal runaway heat releases by the failed cell was constant but SHRs were varied from 1°C/min to 1000°C/min. The model predicted higher SHR led to hotter ejecta, increasing risk of thermal runaway propagation caused by cell ejection. For LFP cells, temperatures of the impinged cell were below the onset temperature of rapid thermal runaway (i.e., 150°C).

To balance thermal designs for cell nominal operations and thermal runaway mitigation, multi-objective optimization is required. The multi-objective optimization being developed is illustrated in Figure II.4.2.9. In FY21 and FY22, single-objective optimizations for nominal condition and fail-safe design have been completed. Multi-objective optimization is based on a trade-off analysis between passive thermal insulation and dissipation considering both nominal and abusive conditions.

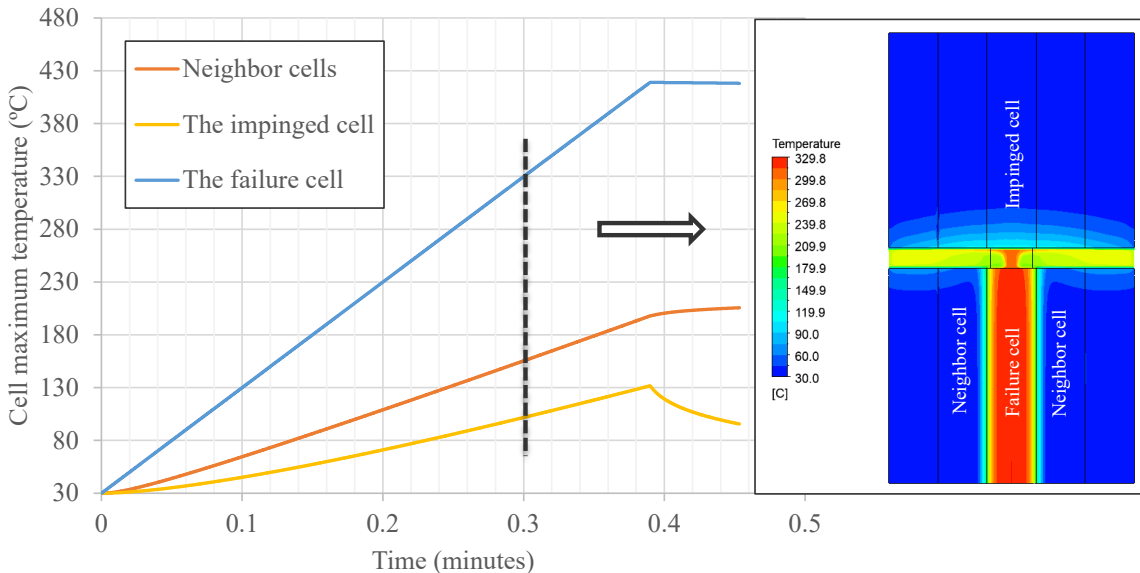


Figure II.4.2.8 Temperature contour and profiles of the maximum temperature in the failure cell, the impinged cell and neighbor cells predicted by the ejection model when SHR is 1000 °C/min.

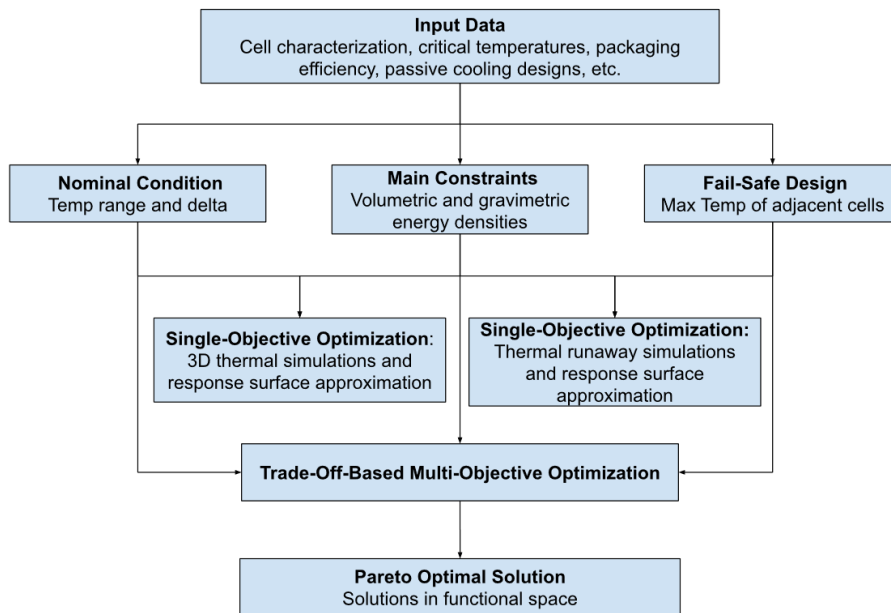


Figure II.4.2.9 Flowchart of the multi-objective thermal design and optimization.

System Safety Progress

The BTMS program is currently performing a scoping exercise where a fail-safe rack design will be realized in three years. The program is assuming the risk that a single cell thermal runaway event is unavoidable and to limit cell to cell propagation the heat generated from a cell runaway event must be managed. The results discussed herein will outline the abuse testing performed on a representation of a multicell BTMS module.

To prevent cell to cell propagation in a module the management of the heat generated from a cell thermal runaway must be managed. Different strategies on how to effectively do this have been reported on previously. The series of tests were intended to probe how to best mitigate the thermal runaway heat source as well as the cell discharge heat source in a parallel rack design. In these tests graphite lithium iron phosphate (LFP) cells were chosen because they were determined to be the most exothermic of the low energy density chemistries as determined by accelerating rate calorimetry. As shown in Figure II.4.2.10, three test cases were assembled to probe various thermal management strategies under a 1S3P configuration of 20Ahr LFP cells.



Figure II.4.2.10 Three different thermal control strategies were used for three 20 Ahr lithium iron phosphate cells connected in parallel.

The Control case contained no thermal mitigations and was used to demonstrate a worst case scenario. The Insulation test case contained a sheet of 2.85” x 6.10” pad of Rogers Corporation PCL-350 3mm foam between each cell. The intent of this foam was to isolate the heat generated from a runaway event from propagating to adjacent cells. The final test case incorporated insulation along with fuses between the individual cells. This test case contained the foam sheets described above as well as AA72AB0 thermal fuse that will open the circuit at 72°C and/or 60A (rated for 35A continuous). The intent of this test case was to not only isolate the heat generated from a runaway event, but additionally eliminate the other parallel cells from contributing to the heat generation via discharge. Each test case is designed to determine impact of each heat source and the contributions of each heat source was evaluated via thermocouples and thermal imaging.

Before testing could commence a discussion was held to determine the most appropriate thermal runaway initiation method. Two options were considered utilizing a heating element or nail penetration. While both methods were viable, nail penetration was chosen as it is more representative of an internal short circuit defect. The center cell of the module was penetrated with a nail to represent worst case for heat propagation and due to the cell construction, the penetration location on the cell was adjusted to the inner quarter on the long side. A short time lapse of an abuse case is shown in Figure II.4.2.11.



Figure II.4.2.11 Nail penetration of the insulation only module.

The eight images show the video and the corresponding thermal image at the same point in time. From left to right the image steps through initiation of thermal runaway (~2 min), approximately half way through the runaway event (~8 min), the highest temperature reached during the event (~12 min), and the final thermal equilibrium when the event had finished (~60 min). The data shown above was further augmented with thermocouples. Each cell had a total of 10 thermocouples to probe the heat flux across the cell. Results from the thermocouples from each test is depicted in Figure II.4.2.12.

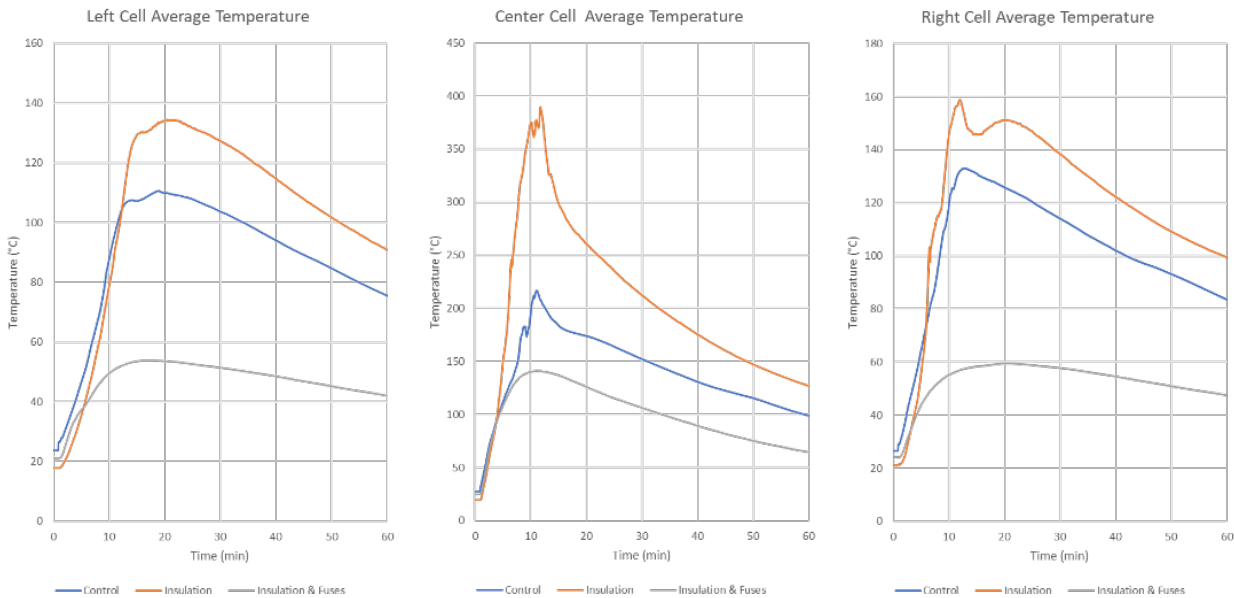


Figure II.4.2.12 Average temperature of each cell (left, center, right) for the three thermal strategies during nail penetration.

Results show that in the three tests the insulation test case demonstrated the highest temperatures, while the insulation and fuses produced the lowest temperatures. These results suggest that insulation may not be an appropriate strategy for a parallel design. This is because the heat from both the runaway and the cell discharge are sequestered in the center cell and the heat eventually transfers to the adjacent cell. While the adjacent cells did not vent, their temperatures exceeded +140°C. This further suggest that a heat conduction strategy may prove more effective in this use case. However, when the insulation is paired with fusible links the isolation strategy is very effective as the cell discharge heat source has been eliminated. While the center cell reached ~140°C the adjacent cells did not go above 60°C, well within their operational temperature. It is currently unknown what the temperature of the cells would be when only fusible links are used will be a future test case. Results from the rack test show that with the proper controls in place cell to cell propagation can be prevented in a rack design. By understanding the sources of heat present in thermal runaway and rack design and placing proper controls in the design a fail-safe design can be achieved.

Conclusions

In FY22, we developed passive thermal management strategies that prevented cell-to-cell propagation within a 1S3P module. In FY23, the thermal management strategies will be optimized and applied to a 5 kWh module.

Acknowledgements

We wish to acknowledge Samm Gillard, Brian Cunningham, and DOE for sponsoring these efforts. We would also like to acknowledge the co-authors of this report – Matthew Keyser (NREL), John Kisacikoglu (NREL), Chuanbo Yang (NREL), and Brian Perdue (SNL).

II.5 EVs@Scale - Cyber-Physical Security

II.5.1 Cybersecurity Projects with Unified National Lab Collaboration (CyberPUNC)

Barney Carlson, Principal Investigator

Idaho National Laboratory
2525 N. Fremont Ave
Idaho Falls, ID
E-mail: richard.carlson@inl.gov

Craig Rodine, Principal Investigator

Sandia National Laboratories
P.O. Box 5800 MS1033
Albuquerque, NM 87185-1033
E-mail: crrodine@sandia.gov

Tony Markel, Principal Investigator

National Renewable Energy Laboratory
15013 Denver West Parkway
Golden, CO 80401
E-mail: tony.markel@nrel.gov

Thomas E. Carroll, Principal Investigator

Pacific Northwest National Laboratory
PO Box 999, MS-IN J4-45
Richland, WA 99352
E-mail: thomas.carroll@pnnl.gov

Omer Onar, Principal Investigator

Oak Ridge National Laboratory
1 Bethel Valley Road
Oak Ridge, TN 37830
E-mail: onaroc@ornl.gov

Roland Varriale, Principal Investigator

Argonne National Laboratory
9700 S. Cass Ave.
Lemont, IL 60439
E-mail: rvarriale@anl.gov

Lee Slezak, DOE Technology Development Manager

U.S. Department of Energy
E-mail: lee.slezak@ee.doe.gov

Start Date: October 1, 2022
Project Funding: \$2,110,000

End Date: September 30, 2023
DOE share: \$2,110,000

Non-DOE share: \$0

Project Introduction

Prior VTO-funded research discovered significant security gaps in high-power electric vehicle (EV) charging infrastructure, that if exploited, could cause significant harm to the grid and EV users. New research and outreach are needed to develop novel countermeasures, help industry deploy best practices, and train the nation's cyber workforce. With the increasing growth of electrified transportation and the charging

infrastructure required to support its energy needs, cybersecurity of this infrastructure is critical to gain and maintain consumer confidence through safe and reliable operation. Trust in the electric power system and transportation sectors must be built on secured communications between grid operators, electric vehicle supply equipment (EVSE) owners/operators, EVSE vendors, EVSEs, and EVs. If the collective power of these internet connected EVSE networks are manipulated in a coordinated attack, it will have a substantial impact on critical infrastructure and can potentially lead to cascading failure. This may disproportionately affect members of disadvantaged communities, where grid infrastructure is traditionally underbuilt and more susceptible to failure. Research and industry engagement are emphasized to ensure secure, safe, and reliable EV charging infrastructure operation that supports grid reliability and builds consumer confidence.

Objectives

The objective of the cybersecurity pillar of the Electric Vehicles at Scale Laboratory Consortium (EVs@Scale Lab Consortium) is to address and provide solutions to four key challenges and barriers to realizing secure and resilient high-power EV charging infrastructure:

1. *Industry implementation and utilization of latest security methods is not consistent* in legacy and new-product design, security configurations and operations. Examples observed range from the use of trivial passwords, outdated vulnerable software, adherence to insecure standards and protocols, and misinterpretation of secure standards. A means to assess and certify the EV charging infrastructure's security performance is needed to inform potential purchasing decisions and drive improvements.
2. *Lack of methods to identify, protect, detect, respond, and recover from cyber events* results in less secure communications, operations, and power transfer across the EV charging ecosystem. Novel countermeasures and safeguards are needed for integration with the charging infrastructure during component and system development to ensure reliable and secure EV charging.
3. *Unknown vulnerabilities in new, emerging features and standards* for advanced charging infrastructure may compromise security. Due to increased features and complexity of controls across multiple components, vulnerabilities may be inadvertently introduced. Examples include Plug & Charge EV-to-EVSE communications, advanced energy management controls communications, wireless charging controls communications, and vehicle-to-grid (V2G) bi-directional power flow.
4. *Existing training for the EV charging infrastructure cybersecurity workforce*, which lacks sophistication and is limited to a narrow audience, is insufficient to combat the growing threats to electrified transportation and charging infrastructure. Through direct education and outreach, national lab staff can significantly enrich EV charging infrastructure cybersecurity training for a diverse workforce.

Approach

Six national labs are collaborating to address and provide solutions to the four key challenges and barriers identified in the objective of this EVs@Scale Lab Consortium pillar. The cybersecurity pillar is co-led by Idaho National Lab and Sandia National Laboratories in collaboration with NREL, Pacific Northwest, Oak Ridge, and Argonne National Laboratories.

Engagement with industry is leveraged to more effectively address several of the key challenges and barriers previously identified. Additionally, laboratory hardware and unique capabilities are leveraged to aid and accelerate these efforts to provide accurate, and insightful results and solutions to provide benefit to the EV Charging Infrastructure industry for improving cybersecurity and cyber-physical security attributes.

Results

EV Charging Infrastructure Cyber-physical Security Technical Support for the 2023 CyberAuto Challenge

The CyberAuto Challenge is an annual event for college students to learn about cutting-edge cybersecurity and cyber-physical security with state-of-the-art plug-in vehicles and EV charging infrastructure. Several

equipment manufacturers sponsor the event by providing state-of-the-art vehicles and EV charging infrastructure, enabling a rich learning experience as well as in-depth networking and recruiting opportunities of the next-generation cybersecurity work force. At the 2023 CyberAuto Challenge, INL staff provided cybersecurity expertise and technical support as well as instructed the EV charging infrastructure tutorial sessions. The support provided by INL contributed to a successful event in 2023 with approximately 60 students in attendance. During the 24hr. event, several students worked with EV charging infrastructure hardware and software. INL staff advised students on assessment and exploit attempts focused on the EV charging infrastructure at the event. Numerous exploits were attempted by the students, and a few were successful.

The CyberAuto Challenge is an excellent learning opportunity for the next generation of the cybersecurity work force as well as a great opportunity for the industry collaborators to utilize the independent assessment and exploit attempts of their equipment hardware and software that is provided to the event. To ensure business-sensitive information is not released from this event, all participants, organizations, visitors, and collaborators sign a non-disclosure agreement at the beginning of the event. All materials, findings, and notes that are created during the event are destroyed at the end of the event or secured by the owner of the system to which the information pertains.

Emulated EV Ecosystem with PKI Security Developed

This effort builds upon prior year engagements with industry to conduct tests within a laboratory environment with physical systems using PKI technology. The prior testing was focused on functionality of small-scale individual vehicle to charger and charge network operator scenarios. The research team has taken on the task of scaling this architecture to enable 100s of devices interacting across a wide range of scenarios. The team is using the NREL Cyber Range to construct this complex network of interacting devices. Within the Cyber Range, virtual machines are created to represent unique devices to be networked together and monitored for cyber threats and security enhancements. The platform will eventually enable testing of the resilience of the EVSE PKI architecture to cyber threats.

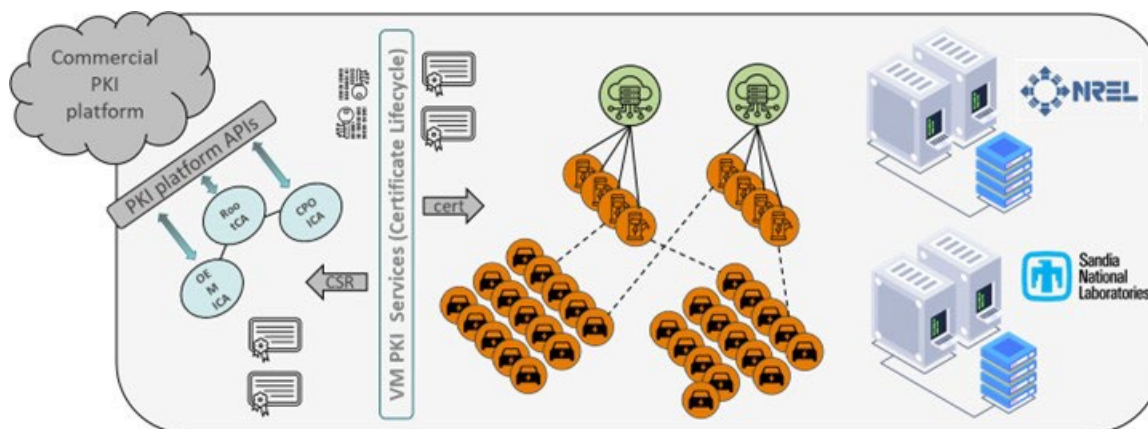


Figure II.5.1.1 EVSE PKI Virtual Testing Platform Enables Scaled Testing of Security and Resilience (credit: Craig Rodine, SNL)

This effort directly supports the first key challenge of assisting industry to test and deploy the latest standards-based security mechanisms applied to EV charging systems. PKI provides for the creation and distribution of public and private key pairs to authenticate end devices; encrypt the communications between entities; and automatically authenticate driver identity and authorize service. The technology provides end-to-end trust (integrity) and CIA (confidentiality, integrity, availability) for charging operations.

NREL and SNL researchers completed a review of the PKI architecture documents and prior work on threat assessment and are developing a detailed report capturing the potential risks and mitigations that need to be

better understood using the simulation environment. Details of the simulation environment and functions are also being captured in the report. The completion of the documentation is expected in the coming project year.

In the coming tasks, the team will need to confirm functionality at larger scales (1000s of devices) and align capabilities with the progress and needs of industry. Using the platform to test PKI network functions that ensure security and resilient operations will provide guidance to industry on operational and recovery decisions.

Cybersecurity Mitigation and Solutions Development

A cybersecurity mitigation solution named Cerberus was developed for high-power DC charging infrastructure to detect, respond, and recover from a wide range of cyber exploits and anomalous events. This mitigation solution not only ensures continued resilient functionality, it also greatly reduces potential safety risks, negative grid impacts, and hardware damage to the charging infrastructure. Cerberus was styled after an industrial Safety Instrumented System (SIS) that is typically used for large automated industrial systems where safety and resiliency are critical. Cerberus incorporates similar features as an SIS including monitoring all internal and external communications as well as physical measurement of critical systems properties to ensure safe and resilient operation. Cerberus is comprised of two types of modules as shown in Figure II.5.1.2. A 'core' module is integrated into each charger (EVSE) at a charge station site and a single 'aggregator' module is integrated at each charge site to coordinate the numerous core modules. Each core module can detect and prioritize anomalous event into categories "Warnings", "Alerts", or "Errors". From this information, the core module and the aggregator module can respond appropriately to prevent or minimize the impact severity of the event. Additionally, the Cerberus system can execute recovery action to ensure continued resilient charging functionality.

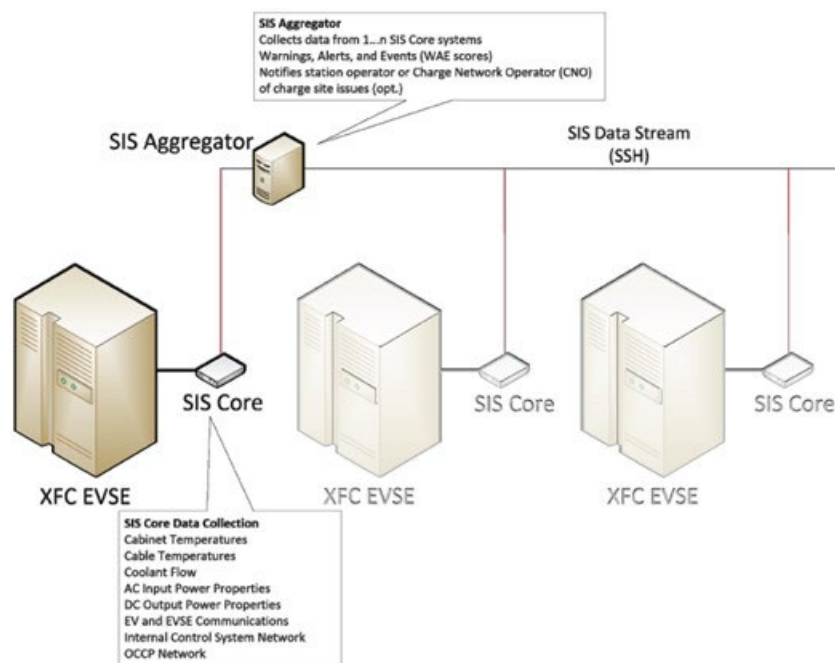


Figure II.5.1.2 Cerberus Cybersecurity Solution for High-Power EV Charging Infrastructure

Cerberus detection, response, and recovery was demonstrated at the 2023 U.S. DOE CESER EV SALaD demonstration of cybersecurity best practices in partnership with PNNL and SNL. Cerberus was also recently named an R&D100 award winner. Cerberus significantly advances the secure and resiliency of high-power DC charging infrastructure by preventing or greatly reducing the potential impact severity anomalous events, therefore improving customer/user confidence and reducing potential negative grid impacts.

“AcCCS” – CCS Communication Device for DC Charger Vulnerability Assessments

AcCCS is a communications device that was developed in the EVs@Scale Consortium *CyberPUNC* project to investigate CCS vulnerabilities in DC chargers. AcCCS uses commercial off-the-shelf components to enable a CCS communication TCP/IP session between the EV and EVSE. Using AcCCS, the internal network configuration of a high-power DC charger was investigated for vulnerabilities. It was determined that vulnerabilities exist which enable an external user to access the charger’s internal communications network through the CCS communication board, via the control pilot wire on the CCS-1 charge cable. Additionally, since other devices or systems are connected to the high-power DC charger internal communications network (such as the OCPP server), access to these other devices or systems may also be possible from the CCS charge cable control pilot wire. Figure II.5.1.3 provides an overview communications network schematic that is representative of a modern XFC. The software developed by INL to use the AcCCS hardware components is intended to be open-source software (OSS).

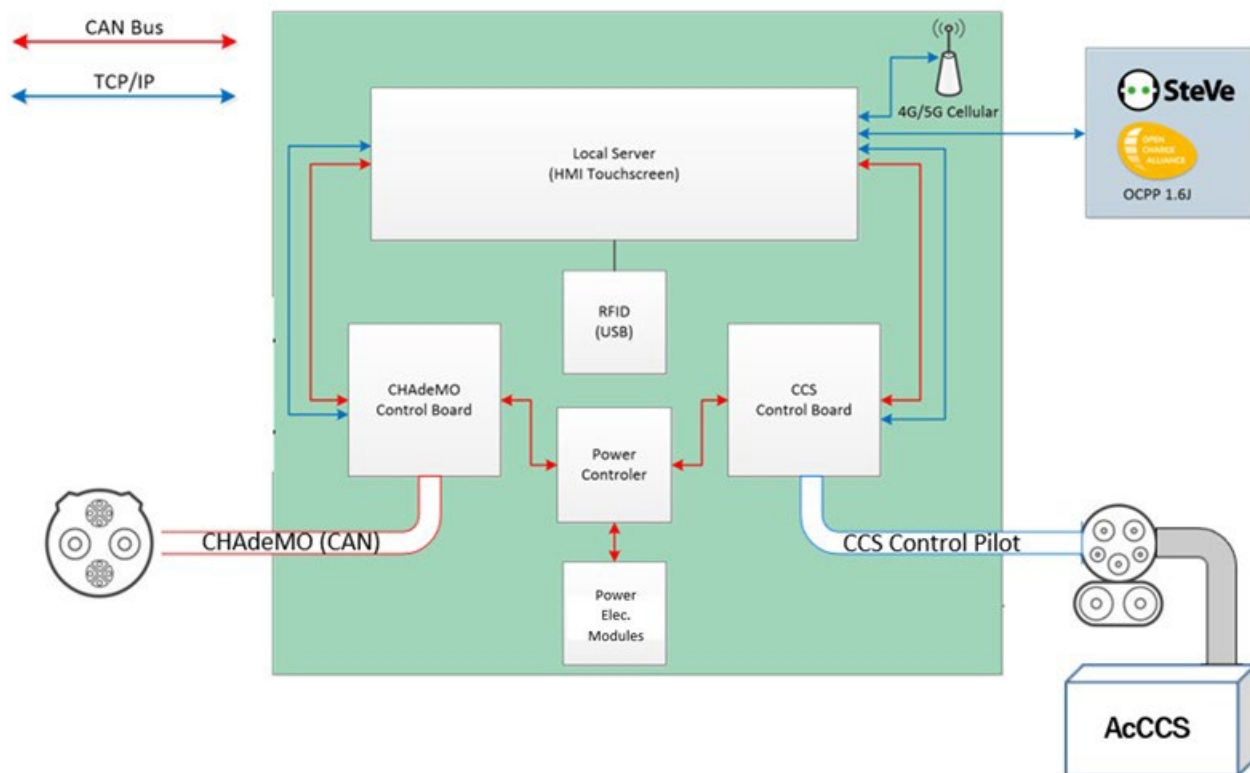


Figure II.5.1.3 Representative Schematic of a DC Charger’s Communications Networks

EVSE Upstream Analysis and Design (UPSTaND)

The UPSTream Analysis aNd Design project aims to identify infrastructure that could cause undue risk to Electric Vehicle Supply Equipment (EVSE) adoption and deployments based on security misconfigurations, insecure components or software usage, and unnecessary information leakage within Electric Vehicle Charging Infrastructure (EVCI). Supporting infrastructure and backend connections provide enticing targets for attackers since they contain aggregated data, can control multiple EVSEs, and may provide entry points, or opportunity for denial-of-service attacks, if not properly secured.

This project’s initial reconnaissance included identifying Central Servers, Charging Station Management Systems, and other EVCI based on open-source intelligence and analysis. EVCI IP addresses were identified based on relevant metadata, certificate information, and running services. The versions of services and other metadata, which are cataloged by services such as Shodan or Censys, were recorded and compared against

vulnerable versions of software noted by common vulnerability enumerations (CVEs) and common weakness enumerations (CWEs) to identify potential risks of exploitation. This allows for a holistic understanding of the EV ecosystem by allowing analysis of EVSE to EVCI interactions, and chained attacks, to judge likelihood and impact of consequences more accurately.

Furthermore, by observing both secure and insecure deployments of different infrastructure we can glean information about common deployments and uncloak some of the security measures, including security through obscurity, performed by the more secure deployments. This led to characterizations of the different systems and the start of recording observed best practices.

Conclusions

As part of the EVs@Scale Consortium, the multi-lab CyberPUNC team within the EVs@Scale Cyber-physical security pillar have support electrified transportation security and resiliency through vulnerability assessments, development of mitigation solutions, and support of cybersecurity workforce training.

Acknowledgements

This work is sponsored by the Vehicle Technologies Office in the Office of Energy Efficiency and Renewable Energy Office, U.S. Department of Energy

II.5.2 Electric Vehicle Integrated Safety, Intelligence, Operations (eVision)

Madhu Chinthavali, Principal Investigator

Oak Ridge National Laboratory
1 Bethel Valley Road
Oak Ridge, TN 37830
E-mail: chinthavalim@ornl.gov

Thomas Carroll, Principal Investigator

Pacific Northwest National Laboratory
902 Battelle Boulevard
Richland, WA 98354
E-mail: Thomas.Carroll@pnl.gov

Timothy Pennington, Principal Investigator

Idaho National Laboratory
1955 N. Fremont Avenue
Idaho Falls, ID 83415
E-mail: timothy.pennington@inl.gov

Lee Slezak, DOE Technology Development Manager

U.S. Department of Energy
E-mail: lee.slezak@ee.doe.gov

Start Date:
Project Funding: \$0

End Date:
DOE share: \$0

Non-DOE share: \$0

Project Introduction

This work looks to examine methods for resiliency improvement of the EV charging station. This work is targeting EV charging networks that belong to a fleet of chargers that could support commercial building interconnections for clients and employees, charging of fleet vehicles at shipping facilities via a depot, and long-haul charging stops for large vehicles. System resilience has been defined in terms of the electric grid support as the “ability to withstand and recover from deliberate attacks, accidents, or naturally occurring threats or incidents [1].” In this work, the focus is on EV charging resilience or sustaining EV charging operation and/or recovering under a set of different anomalies.

In this work, EV charging resiliency has been categorized by three different target areas: 1) the EV charger and supporting communications and controls, 2) the station management controller (or site controller) with considerations on energy management response and coordination of resources, and 3) a detection system monitoring for potential threats and attacks. These areas of resiliency improvement are presented in Figure II.5.2.1. Within each domain, key technology areas are in development.

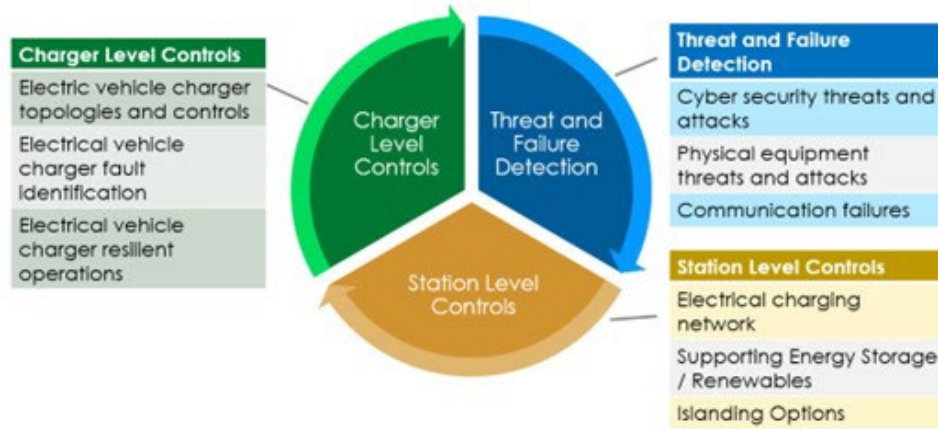


Figure II.5.2.1 Areas for resiliency improvement.

Objectives

In this work, the objective is to validate the electric vehicle (EV) charging anomaly detection methods and control strategies developed. These solutions must both mitigate impacts on charging infrastructure and the interconnected grid. The challenge is that EV charging stations can support different electrical topologies and EV types including heavy-duty (HD), medium-duty (MD), and light-duty (LD).

Approach

Three national labs are collaborating to address and provide solutions to the three target areas identified: Oak Ridge National Laboratory is investigating the charger level controls and detection methods using controller hardware in the loop testbeds, Idaho National Laboratory is developing anomaly detection methods and control approaches considering a vendor high power charger, and Pacific Northwest National Laboratory is developing communication, optimization and control solutions using simulation and controller development strategies.

Results

Typhoon-HIL Testbed for Vetting Use Cases in CHIL Constructed

The developed framework for evaluating failure modes and resiliency controls in an automated platform for a charging station is presented in Figure II.5.2.2. This system is composed of four primary architecture layers [2]: 1) real-time simulation environment, 2) digital signal processors (DSPs) or converter controllers (CC), 3) resource integration controllers (RIC), and 4) resource management controller (RMC).

The RMC is a desktop computer operating with Ubuntu and python software packages that support optimization, data collection (historian), communications (message queuing telemetry transport protocol (MQTT)), and intelligent decision-making. The RMC, behaving as a station controller, is used to coordinate the various EV charging systems modeled in the simulation platform.

The RICs are Raspberry Pi computers operating with Raspbian and using python software packages that support an agent-based system [2]. The RICs are used to coordinate integration between resource systems (EVs) and PES. The RICs use agents to interface and perform the integration with complex interactions reduced to requests such as ‘start-up’ and ‘shutdown’. An interface agent is used to communicate to the RMC using MQTT.

The CCs are Texas Instruments DSPs that utilizes a developed interface board to engage the analog and digital input/output ports of the Typhoon HIL Platform. The CCs perform three core functions: 1) converter state machine, 2) communication with the systems software layer, and 3) closed loop controls. A user datagram protocol (UDP) is used to communicate to the RIC.

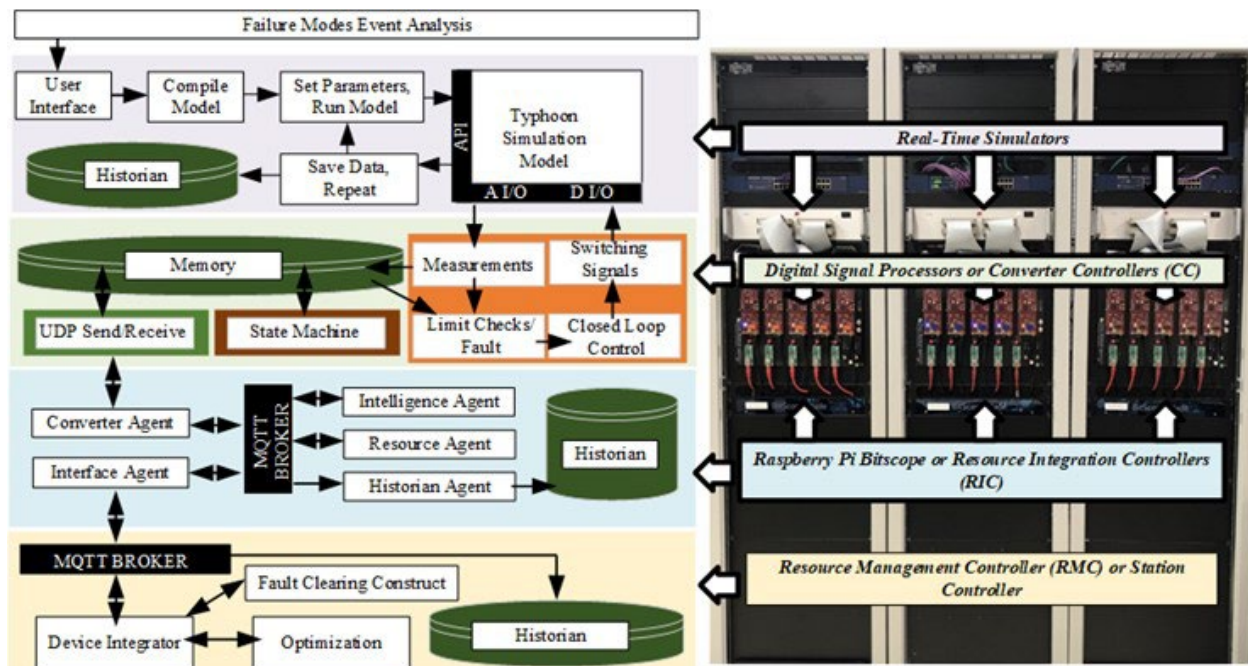


Figure II.5.2.2 Typhoon HIL controller hardware-in-the-loop with integrated automation and testing system.

The real-time simulation platform is composed of Typhoon-HIL real-time simulators. The physical electrical network, power electronic systems, and resources (EVs) are all modeled within the Typhoon-HIL simulation environment. Analog and digital input and output channels on the Typhoon-HIL platform are used to couple the CCs to the simulation environment for controls.

The Typhoon-HIL real-time simulation environment supports a Python interpreter (for directly coding and compiling python scripts) and an application programming interface (API) (for interacting with the simulation platform [3].) Using the Typhoon-HIL Python environment, a tool with a graphical user interface (UI) has been developed. This tool provides a user the ability to select a preconstructed Typhoon model to be configured into the tool. From this configuration, the user is able to extract the parameters of interest and identify the measurements or importance for simulation runs. The user also has options on the number of simulation iterations, the time length of each individual simulation, and the timestep of data to be captured. Upon the user selections, the tool provides an automatic compile and run option. Data from the simulation environment is automatically stored locally in .mat files according to user selection.

Since the Typhoon-HIL python application and CC, RIC, and RMC hardware controllers are all hosted on different platforms, a coordination strategy has been developed to provide a means to reset the hardware controllers in coordination with the simulation. When the Typhoon HIL platform is not actively performing computation for a simulation, the analog and digital channels are all inactive (essentially reading zero). This minimum reading is perceived as an abnormally low measurement (or an electrical fault) to the CCs. Each CC enacts a safe state by deactivating any control and opening contactors. The fault status is communicated to the station controller through the RICs. On observance of the condition (all systems are faulted), the station controller attempts to clear the fault by sending a 'reset' command to all the individual RICs. This is repeated until each RIC communicates a 'Standby' status indicating normal operation. Following this state, the RMC performs an optimization and dispatch routine to actively start-up and optimize the use of each DC fast charger.

Key to achieving the strategy is timing. To guarantee that the CCs can detect the simulation reset, a 15-second delay has been introduced between simulation iterations (or the analog and digital channels remain low for 15 seconds). Furthermore, the needed time for the various DC fast charging elements to perform fault-clearing,

recommissioning, and start-up must also be established. This represents the base time required for the simulation to reach a steady state in preparation for an event. The event is a set action (such as the activation of a device or modification of a parameter such as voltage) that is used to drive a controlled response.

A post analysis is performed by collecting the data captured in the RMC historian and Typhoon-HIL platforms. The Typhoon-HIL data files provide the direct measurements of the system as observed in the simulation while the RMC historian provides the data observed by the CCs. These derived conditions are plotted against the parameters for analysis and establishing potential boundary conditions or baselines. These can be used to develop mathematical experimental limits associated with operations.

Grid Fault Ride-Through Detection and Control Development using Automation Platform

As a proof of principle of the platform and evaluation procedure, two automated CHIL simulation runs have been conducted: 1) a simulation run with no resilient control embedded and 2) a simulation with control described in [4] enacted. In both runs, the event is a three-phase voltage sag introduced at the grid connection. The voltage sag is varied from 0% to 100% in 5% steps. This represents a total 42 different operational runs.

The base time was set to be 150s (2.5 minutes) to provide sufficient time for system start-up and normal operations. The voltage sag event is programmed to hold for 0.2 seconds with a post normal operation time of a little more than an additional minute. Figure II.5.2.3 illustrates the CHIL Typhoon results plotted from the data collected during each iteration (up to 50% voltage sag). As shown, without the resilient control enabled, the charger can ride-through up to a 15 % voltage sag condition (as a result of sufficient energy contained within the DC bus capacitor and the 0.2 fault duration). Under $\geq 20\%$ voltage sag conditions, the DC bus voltage drops to $\leq 1.76kV$, and the charger triggers the DC bus under-voltage fault protection (charging stop). For evaluation of the benefits of the resilient control for each different voltage sag condition, the difference in energy not delivered to the EV (END) is calculated. Thus, energy not delivered to the EV during charging in the case of a fault compared to baseline is 400kJ. Since the resilient control is enacted most of the 400kJ is recovered (some is lost due to the need to temporarily support the DC bus (5-69kJ as shown)).

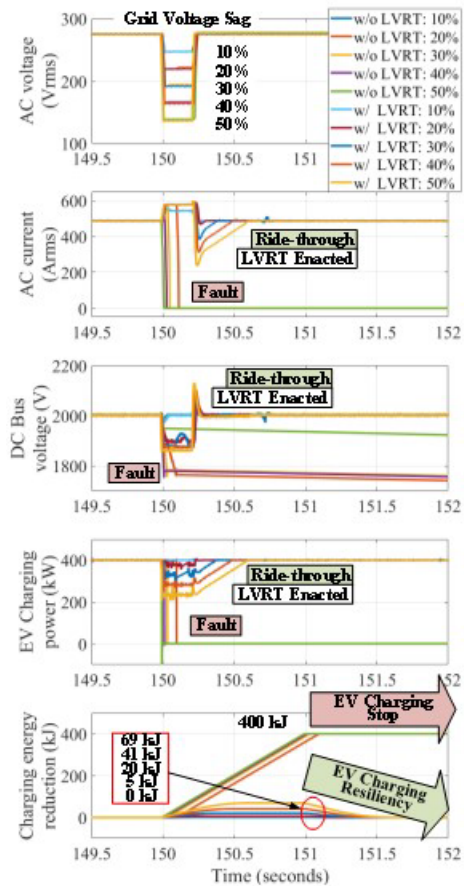


Figure II.5.2.3 Automated test platform results plotted from fault use case.

Device Fault Ride-Through Detection and Control Development

A detection, control, and coordination strategy has been developed for the DC/DC stage of a high-power charger with the topology of interleaved DC/DC converter. This strategy is discussed in detail by architecture layer within the following subsections.

Converter Controller (Control Routine): The converter controller digests measurement data such as voltages and currents every control routine cycle. The control routine, which is also called as an interrupt service routine (ISR) in the DSP, uses these measurements and runs fault detection & protection, closed-loop controls, PWM duty cycle ratio update, and PWM signal enable/disable every PWM switching cycle period. In the case of an open circuit fault (OCF), the condition is detected by the DC/DC converter controller through the inductor current measurement. A sudden drop in the current indicates a sudden break in the circuit. A corresponding warning flag is set and used as a trigger signal to start the device fault ride through (DFRT) control function

added in between the $i_{EV,ref}$ ramp function and $i_{Lx,ref}$. Following a device fault OCF detection, the converter controller has been coded to deactivate control to affected H-bridge legs thereby protecting the converter and providing a means to continue to operate. The individual inductor current control references and PWM phase-shift angles are also adjusted. The converter controller calculates a per-unitized converter derating ratio based on the number of HBs tripped which is used to update converter rating information.

Converter Controller (Communication Routine): The converter controller utilizes a slower communication service routine (10 ms) to process data exchange with the RIC. A user datagram protocol (UDP) is used to communicate information between RIC and converter controller with the communication routine acting as a translator of the messages. When a DFRT is enacted, the converter controller has been coded to send a device fault ride through (DFRT) warning message to the res while also providing an updated converter rating.

Resource Integration Controller (1-second Routine): The agent architecture (composed of 4 core agents: converter, resource, intelligence, and interface [3]) within the RIC supports system communications and decision making for systems integration. The converter agent sends and receives UDP messages to the converter controller, translates the messages, and pushes the messages onto a locally hosted MQTT network. The resource agent communicates to the EV and is responsible for generating a EV charging forecast based on available data. Upon the occurrence of a fault, the converter agent would traditionally enter a faulted state and message all of the other agents to enact shut-down procedures. In the case of a DFRT, the converter agent instead has been programmed to continue in the normal operational state, to update the converter rating information and to flag a warning message that is propagated to the intelligence, resource, and interface agents. Based on the updated rating, the resource agent has been configured to adjust the projected EV forecast and broadcast this information on the MQTT network. The intelligent agent compares the EV charging request (forecast), and the station request and selects the lowest value to be sent as a setpoint to the converter agent for distribution to the converter controller. The interface agent updates the station controller through another MQTT message via the MQTT broker hosted on the station controller.

Station Controller (5-minutes Routine): The station controller has been developed in previous work to receive the configuration, measurements, and status data from the integrated RICs and performs an optimization and dispatch periodically (every 5 minutes) [5], [6]. During a DFRT event, the station controller now receives a warning message and updates configuration and status information regarding the EV charger. This information is used to notify the user via an indicator in the graphical user interface (GUI) that the converter is operating under a DFRT event. The updated EV forecast is automatically used in the next optimization cycle to reallocate additional charging capacity to other chargers as needed. In the next section, the controller hardware Figure II.5.2.4. illustrates the changes of converter ratings, EV charging setpoints, and measurements according to the system limitations and the station controller optimization. The station controller data shown in Figure II.5.2.4. is updated every second and stored in the station controller historian. Upon the detection of the device fault at A1, the converter controller updated the derated converter ratings (400 kW \rightarrow 267kW and 267 A \rightarrow 178 A) along with the warning messages (DFRT Enacted). The converter controller also limited the EV charging current to 176 A which is the maximum available from the two HB legs. The framework responds accordingly in two locations: the RIC and the station controller. In the RIC at A2, the EV charging forecast was recalculated to account for the derated converter power rating (267 kW). The recalculated forecast is reviewed and compared to the setpoint request from the station controller. The RIC reduced the converter control target to 267kW, and the converter controller regulated the EV charging current as 167 A (corresponding to 264 kW charging power.) At A3, the RIC sent the derated converter ratings and updated EV forecast to the station controller. At A4, the periodic optimization cycle is completed, and the optimization routine (problem formulation and solver call) is performed. The optimal setpoint of 267kW is sent from the station controller to the RIC and down to the converter controller. As shown, the station controller along with the different hierarchal layers all worked on directing the EV charger to the same limit.

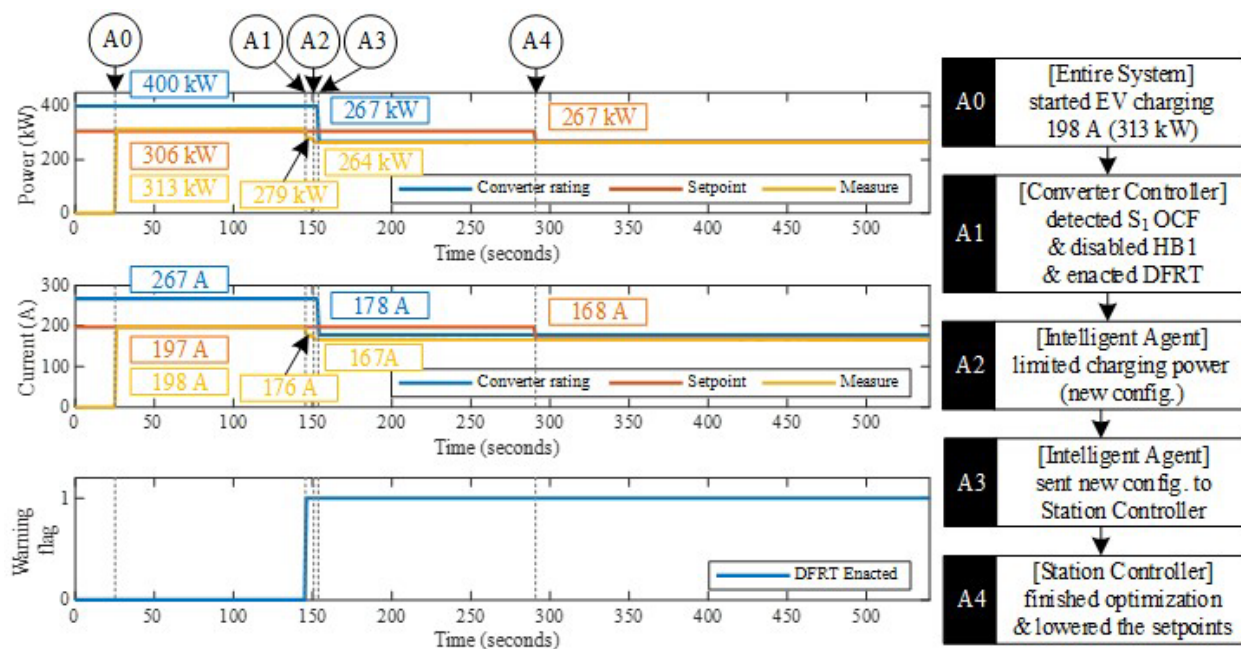


Figure II.5.2.4 CHIL RT simulation results (stored in the station controller historian): DFRT strategy conducted in the multi-layer control framework. Changes of converter ratings, EV charging setpoints, and measurements according to the system limitations and the station controller optimization.

Improvements to Resilience Depot Charging Operations

Extending the FY22 work, the team also examined depot and fleet control impacts to grid- and cyber-based events on the system, with the goal to demonstrate how different, individual contributions to the resilience of the system improve the overall charging efficiency. The architecture was expanded to include an extra charging connection – overall charging power was maintained (power electronics), but each bank now had four connections instead of three. Short-term transients are mitigated through the updated power electronics front-end designed by ORNL. Anomalous conditions in the charging events are detected and reported by INL’s Safety Instrumented System (SIS). The depot power and charge management system from PNNL utilizes the SIS and longer duration outage information to coordinate on-site distributed resources (energy storage) and charging dispatch.

To demonstrate the charging resilience of these combination of technologies and/or approaches, the team simulated a variety of scenarios, with four outlined in the results of Figure II.5.2.5 and Table II.5.2.1. The “Baseline” scenario represents full, unrestricted charging (the ideal case). Building off the scenario of FY22 (distributed energy storage and a single energy storage unit fails), the remaining scenarios involve the system subjected to a power limit at the point of interconnection (POI), such as one imposed by a demand charge limit or a public-safety-power-shutoff (PSPS) event. On top of that event,

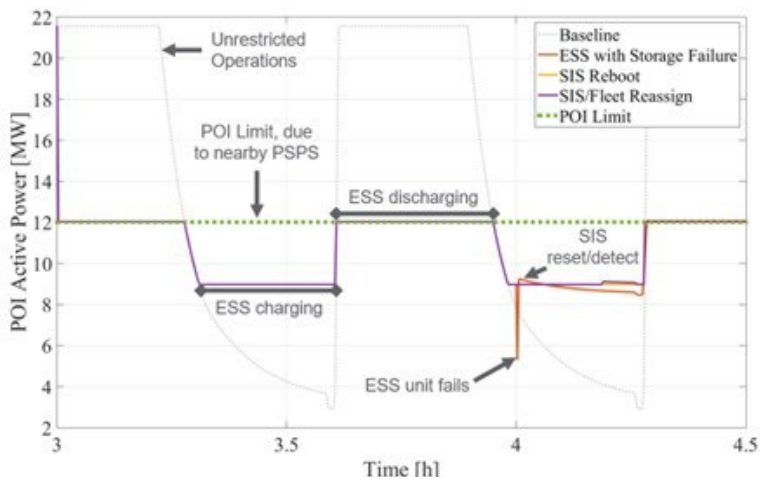


Figure II.5.2.5 MD/HD Charging Depot Point of Interconnection (POI) Power for Different System Events

three further scenarios are examined: the loss of an energy storage unit, an SIS-detected fault and reboot, and an SIS-detected fault and redispach.

Table II.5.2.1 Energy and Completed Sessions for Different Scenarios

Scenario	Energy Transferred (MWh)	Charging Sessions Completed (count)
Baseline No POI Restriction	32.34	198
ESS Failure POI Restriction	31.41	180
Pedestal Failure SIS Reboot	32.32	180
Pedestal Failure SIS Detect/Fleet Redispach	32.32	179

Figure II.5.2.5 highlights a small 1.5-hour sequence of these scenarios. The gray line shows charging during an unconstrained system, and the green-dashed line represents the POI limit from the PSPS. The other curves are harder to distinguish, but all the different events occur shortly after $t=4.0$ hours of the simulation. The ESS failure provides the most significant transient, but the chargers easily ride through this transient and all scenarios adjust charging or redispach the vehicles to maintain maximum throughput.

Table II.5.2.1 shows a quantification of the different scenarios. It's important to note that the table represents a full day charging scenarios, whereas Figure II.5.2.5 only shows 1.5 hours of operations. For the PSPS-related scenarios (all except the baseline), the energy storage eventually is depleted and charging gets curtailed, resulting in fewer sessions (hence the 198 to 180 session change). However, outside of the energy storage depletion, the impacts to EV charging sessions were minimal, with even a fleet redispach to cover a faulty charging pedestal only resulting in one fewer vehicle charged during the session.

Demonstration of EVSE Charging Emulator

To explore more details in the charging session sequences, PNNL has developed an EVSE charging emulator. The emulator provides a hardware-in-the-loop capability for both exploring sequencing of various charging commands and responses, as well as incorporating it via the HELICS cosimulation platform into the depot-level simulations mentioned in the prior section. The developed emulator is comprised of off-the-shelf components and provides a cost-effective alternative to purchasing and deploying full-scale, full-power EVSE charging stations. This research deployment is especially useful for communication and EVSE/EV interaction studies, where the power level transferred to it is not an immediate concern (and may trigger additional safety mechanisms).

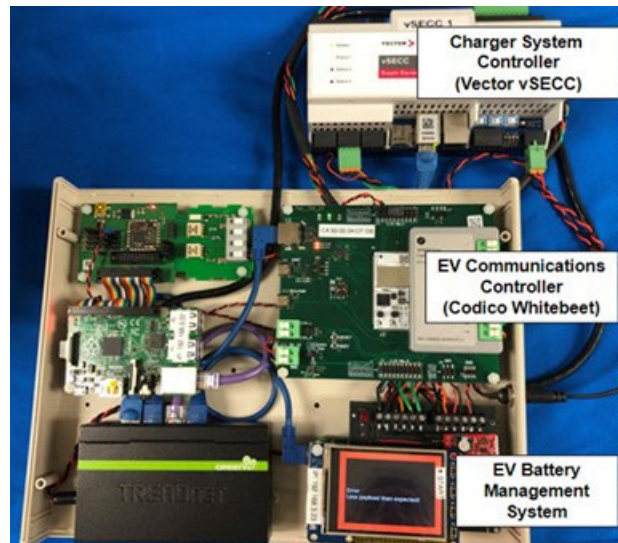


Figure II.5.2.6 EVSE Charging Emulator Components and Layout

Figure II.5.2.6 shows the initial hardware implementation and layout of the charging emulator, with the various off-the-shelf components and their system representation. The emulator was used to successfully sequence charging sessions from the charging controller, including passing Open Charge Point Protocol (OCPP) messages between the EVSE and “battery”

system. This includes standard charging request, as well as reduced or curtailed charging scenarios (utilized for the PSPS events mentioned above).

Key Publications

1. M. Starke, M. Chinthavali, N. Kim, T. Carroll, F. Tuffner, B. Varghese, C. Reiger, K. Rohde, and T. Pennington, "Improving Resiliency for Electric Vehicle Charging," in Proceedings of the *2023 IEEE Power & Energy Society General Meeting (PES-GM)*, 2023, pp. 1-5.
2. M. Starke, N. Kim, B. Dean, S. Campbell and M. Chinthavali, "Automated Controller Hardware-In-The-Loop Testbed for EV Charger Resilience Analysis," *2023 IEEE Transportation Electrification Conference & Expo (ITEC)*, Detroit, MI, USA, 2023, pp. 1-6.
3. B. Varghese, F. Tuffner, M. Starke, T. Carroll, T. Pennington, and C. Reiger, "Cyber-Physical Resilience for Electric Freight Vehicle Charging Depots" in Proceedings of *2023 Resilience Week*, 2023, pp. 1-7.

Conclusions

As part of the EVs@Scale Consortium, the multi-lab EVision team within the EVs@Scale Cyber-physical security pillar have developed techniques to support improved resiliency for EV charging using simulation, controller hardware in the loop, and hardware systems in various testbeds.

References

1. s. Afzal, H. Mokhlis, H. Illias, N. N. Mansor, and H. Shareef, State-of-the-art review on power system resilience and assessment techniques, *IET Generation, Transmission & Distribution Journal*, Vol. 14, No. 25, pp. 6107-6121, 2020.
2. M. Starke et al., "Agent-based distributed energy resources for supporting intelligence at the grid edge," in *IEEE Journal of Emerging and Selected Topics in Industrial Electronics*, vol. 3, no. 1, pp. 69-78, Jan. 2022.
3. Typhoon HIL, Solutions - Distribution Automation, online: <https://www.typhoon-hil.com/solutions/distribution-automation/>.
4. M. Starke, S. Bal, M. Chinthavali and N. Kim, "A control strategy for improving resiliency of an DC fast charging EV system," *2022 IEEE Transportation Electrification Conference & Expo (ITEC)*, 2022, pp. 947-952.
5. R. S. K. Moorthy, M. Starke, B. Dean, A. Adib, S. Campbell and M. Chinthavali, "Megawatt Scale Charging System Architecture," *2022 IEEE Energy Conversion Congress and Exposition (ECCE)*, 2022, pp. 1-8.
6. M. Starke et al., "A MW scale charging architecture for supporting extreme fast charging of heavy-duty electric vehicles," *2022 IEEE Transportation Electrification Conference & Expo (ITEC)*, 2022, pp. 485-490

II.5.3 Zero Trust Approach to Electric Vehicle Charging Infrastructure Security (PNNL)

Thomas E. Carroll, Principal Investigator

Pacific Northwest National Laboratory
 PO Box 999, MS-IN J4-45
 Richland, WA 99352
 E-mail: Thomas.Carroll@pnnl.gov

Lee Slezak, DOE Technology Development Manager

U.S. Department of Energy
 E-mail: lee.slezak@ee.doe.gov

Start Date: October 1, 2022

End Date: September 30, 2023

Project Funding: \$960,375

DOE share: \$\$960,375

Non-DOE share: \$0

Project Introduction

The Bipartisan Infrastructure Law (BIL) provides \$7.5 billion of new funding to support and incentivize the buildout of EV infrastructure (EVI) [8]. The substantial funding, which expires FY26, is anticipated to spur the buildout of a vast network of chargers that will tackle a primary concern of EV ownership: insufficient infrastructure. Given the scale of the buildout, there is strong desire and expectation that that EVI is secure and can resiliently operate when faced with cyber threats over its lifetime. Economy-wide transportation system electrification will create strong and substantial interdependence between the historically disparate electric supply and transportation systems. The coupling will extend the reach of and heighten the risks posed by cyber-attacks, going beyond just charging service disruption and potentially causing wide-ranging consequences to vehicles, electric supply, and transportation systems.

Enhanced cybersecurity practices are paramount to securing long-lived EVI. This project investigates two security thrusts—zero trust and post-quantum cryptography—to bolster the security of the charging infrastructure. With respect to each thrust, the project investigates relevance and application, identifies and addresses deficiencies, and develops guidance with respect to EVI security. While the approaches are discussed independently, they are complementary and can be used simultaneously to further improve the security of the infrastructure.

Zero trust is a cybersecurity model—a set of design principles—that eliminates implicit trust by implementing a deny-by-default security posture. The primary benefit of zero trust is its ability to limit the scope of compromise and, consequently, minimize costs, downtime, and damage associated with an attack. In practice, devices and users must explicitly verify every request before network access to a resource is granted.

Public key cryptography (PKC) is the foundation for security in EV charging and zero trust. A sufficiently large quantum computer can break the mathematical underpinnings of traditional PKC in a fraction of the time it takes a traditional computer, thus jeopardizing digital trust, secure communications, and data protections. Adoption of post quantum cryptography (PQC), cryptosystems designed to be secure against traditional and quantum computing, is needed to secure against this risk.

Objectives

The project has two objectives. The first objective is to demonstrate that zero trust architectures and strategies can defend EVI from cyber compromise and curtail the likelihood of high-consequence events [2]. Specifically, the objective is to design, develop, demonstrate, and evaluate zero trust approaches that bolster EV charging infrastructure security. Evaluation will be accomplished by studying at least three different architectures, each architecture with a distinct character and approach to the zero trust principles. Zero trust prototypes are deployed and evaluated to assess the effectiveness of the approach and identify deficiencies. Both physical and network access by malicious entities are considered. Moreover, considerations are given to

zero trust technologies that can be incrementally deployed. The primary outcome will be a validated blueprint describing zero trust architectures and strategies applicable to EVI. The second objective is to assess the impact of PQC and develop guidance for an orderly transition to PQC from traditional public key cryptography.

Approach

Zero Trust

The approach comprises five tasks:

“Build system model” – PNNL models the EVI system relationships, information exchanges, interfaces, and trust boundaries. Ancillary functions such as management and credit card payments will be mapped, along with relationships to cloud computing and third-party services. Finally, authorities and trust boundaries are designated.

“Analyze Use Cases and Define Security Controls” – The objective is to identify requirements, objectives, and security controls that influence the design and implementation of zero trust are identified. The system models are studied to discover pathways causing high-consequence events. Additional examples of vulnerabilities are culled from publicly available resources. The pathways are generalized to develop use cases. The use cases, applied to the system model, are analyzed to define the security objectives and security controls. Further analysis of use cases and security controls are used to derive evaluation criteria.

“Design Architecture” – Guided by [4], a zero trust solution is selected and the security controls are mapped to it.

“Prototype Architecture”—A zero trust architecture is prototyped in a testbed. To further enhance the authenticity and fidelity of the testbed, a fast charger simulator, comprising of off-the-shelf components, is used to exercise the prototype. A simulator, as opposed to a physical charging system, provides several benefits including size (can sit on a bench top) and speed (provides automated charging sessions, minimizing the time necessary to study the effects over multiple charging sessions).

“Evaluation”—An evaluation of the prototype is conducted based on criteria developed in “Analyze Use Cases and Define Security Controls.” Further analysis is conducted to identify deficiencies in the controls or limits of the scopes of the security objectives. The testbed results are analyzed, improving the fidelity of the security objectives evaluation analysis feeds, at which point the process repeats. The project will generalize over the prototypes to identify character, features, and functions that will inform the validated blueprint.

Evaluation will be accomplished by evaluating at least three different solutions, each scenario with a distinct character and approach. Zero trust prototypes are deployed and evaluated to assess the effectiveness of the approach and identify deficiencies.

5. *Post quantum cryptography*

The approach is defined in four tasks:

“Inventory Public Key Cryptography in EV Charging”—EVI system models and EV charging models are examined to discover applications of public key cryptography. These applications are generalized to identify what will be evaluated in the next task.

“Test & Measure” – Microcontrollers representative of controllers found in EVI are selected and application benchmarks are developed. The benchmarks are used to assess performance of the PQC cryptosystems and recognize performance and resource constraints.

“Identify Challenges” – Based on prior tasks results and other issues found in a literature review, challenges to adoption are identified.

“Develop Migration Guidelines” – Based on identified challenges, PNNL develops orderly transition guidelines to inform the EV ecosystem about PQC adoption.

Results

6. Zero trust

“Build system model” – The system model was updated to incorporate additional services that are typically found in EVI. Specifically, the model was revised to document open payment and MQTT components and communications. MQTT is an opensource messaging standard used to integrate distributed subsystems. Open payment allows the use of standard credit card.

“Analyze Use Cases to Define Security Objectives” – The system model was analyzed to discover pathways leading to high-consequence events and other undesirable outcomes. Analysis of the pathways identified commonalities, resulting in the construction of four use cases. Use cases were specifically designed to cover critical pathways. The first use case is based on a disruption triggered by malformed messages [3]. The second use case was motivated by an attack from early 2023, where SaiFlow demonstrated EV charging infrastructure risks associated with the inadequate authentication and connection handling by OCPP 1.6 [5]. The third use case involves using the trusted communication from the charger to gain unauthorized network access, in part motivated by the Log4J vulnerability and improperly configured TeamViewer instances, and considers the scenario where an attacker induces a charger to communicate with other elements [1]. The types of communications involved in these types of vulnerabilities (both local and external) are sought to be identified and analyzed so that the relevant policies can be defined in the zero trust testbed with the purpose of mitigating the vulnerable charger communication paths. Use case 4 considers abusing authorized access. Each use case contains several test cases, and each test case demonstrates the impact before and after zero trust implementation.

The following security controls guided the implementation of zero trust: authentication and authorization, end-to-end encryption, private DNS, and micro-segmentation. All identities must be enrolled in the zero-trust fabric to access any network resources and go through a continuous process of authentication and authorization. Only authorized services can be accessed, and broader communications to potential alternate data sources are unallowed, even if the fabric authenticates the identity. End-to-end encryption ensures that the data traversing these networks are encrypted and protected by security controls of the fabric. Private DNS secures a vital engine of wide area networks by allowing only those specified communicating entities in the fabric to resolve with one another without outside interference. Isolated Network Namespaces and Network Micro-Segmentation limit communications even at a physically local site and with external entities to prevent lateral movement in the wider EV charging network and beyond. Each use case contains one or more security controls.

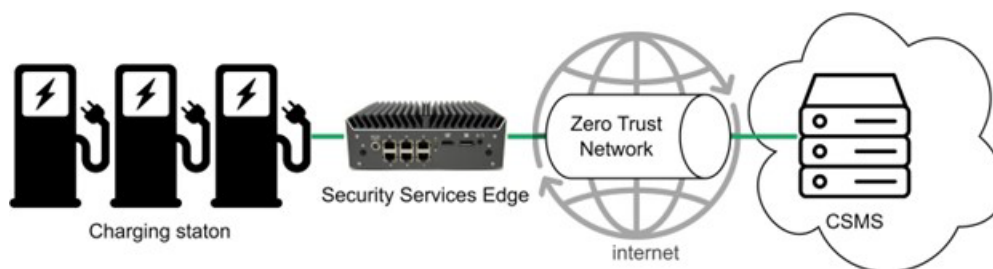


Figure II.5.3.1 The security services edge networks the chargers

“Design Architecture” – Analyzing the landscape of available zero trust architectures and frameworks, it was observed that the mapping of controls to a solution is dependent on the solution’s architecture. The project members decided on three solutions. The solutions were selected based on the compatibility with EVI and

differences in how they approach zero trust. The mapping of controls to the first two solutions was completed; The mapping of controls to the third solution continues. An essential component of the architecture is a security services edge. As illustrated in Figure II.5.3.1, the security services edge interfaces unmodified chargers to the zero trust solution. While the security services edge is conceived as a distinct system, the project has an outyear goal of redistributing the functionality to the cloud and imparting the remaining functionality into low-resource cellular gateways.

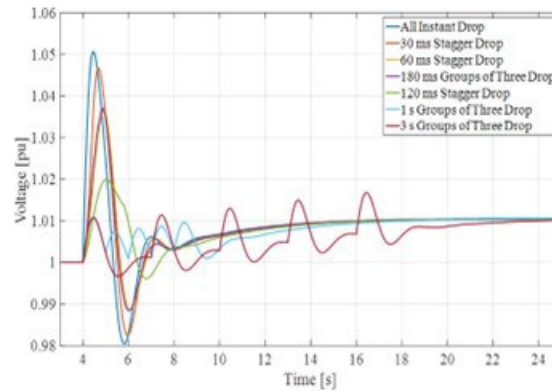


Figure II.5.3.2 Request rate limiting and shaping reduce electric supply impacts

The full set of controls for the fourth use case could not be mapped onto the solutions. The key aspect of the use case is targeting weakness found on authorized pathways. Consider an inattentive operator who is an authorized system user who carelessly performs their role and terminates several charging sessions. Based on the scenario of with fifteen chargers on a weak feeder, instantly terminating multiple charging sessions induces a grid overvoltage/undervoltage on the distribution. As shown in Figure II.5.3.2, the voltage raises above 1.05pu for 279ms, which exceeds the ranges of ANSI C84.1, a North American utility voltage tolerance standard. In a prolonged or regular coordinated disruption, equipment damage may result, such as insulation breakdown. Further simulation demonstrated the benefit of introducing metering/staggering, where the OCPP `RemoteStopTransaction` requests are admitted every 60ms, on average. The result of the policy, shown as the red line in Figure II.5.3.2, is positive as the voltage remains below 1.04pu. Other strategies and their implications were considered, including the stochastic “drops” of `RemoteStopTransaction` requests or metering the requests to the chargers.

A security function specific to OCPP was conceived to address the deficiency and a proof-of-concept was added to the security services edge. Sitting in on the communications between charger and management system, the function parses and validates OCPP messages. Besides syntax and structure, the ruleset the OCPP messages must pass are configurable and can express business objectives, such as when to permit the software updates.

“Prototype Architecture” – PNNL engineered and deployed zero trust solutions to a testbed. The testbed extends over the PNNL campus, integrates with the Amazon Web Service cloud computing, and has DCFC fast charging simulators. Two solutions were prototyped, work on the third solution continues. In all cases, the security services edge role is mapped to a hardware device that exists near the chargers.

“Evaluate Prototype” – PNNL evaluated the prototypes using the use case and test criteria designed in the first task. Each test case in each scenario was able to be addressed with the prototyped environment. Regarding the first use case involving malformed messages, it can be demonstrated that with proper message parsing and validation, incompatible requests can be intercepted and handled such that the system does not fail closed and availability of the systems is maintained. With regards to the second use case of adversarial external connections stemming from the internet and targeting the charger, we demonstrate with a zero trust fabric deployed, only the enrolled identities within the fabric (including the charger itself) may communicate with the

charger, keeping all unauthorized outside traffic from even reaching the network in which the charger resides. Additional examples are then demonstrated for the zero trust fabric capabilities in the third use case by enabling different policies that further segment the communications between co-located chargers on the same network, chargers on different networks, and charger to internet communications. Using private DNS capabilities, chargers can connect to needed services that reside on the open web but are then prohibited from those entities that do not match in a delegated domain. Finally, the mitigation of the use case of an adversary with physical access to the charger is demonstrated with a combination of different technology integrations including the use of zero trust policies to limit what a charger can communicate with, cloud security capabilities such as security groups and cloud network firewalls, and novel authentication means.

7. *Post quantum cryptography*

“Inventory Public Key Cryptography in EV Charging” – PNNL released the report PNNL-34843, which identified and discussed public key cryptosystems and applications in the EV charging infrastructure and also identified potential consequences of leaving EV charging systems vulnerable to quantum computing.

“Test & Measure” – Examination of FIPS 204 PQC cryptosystem [6] discovered that the keys and signatures were significantly larger, 20.50-40.5x and 37.81-71.8x, when compared to the ISO 15118-indicated cryptosystems, P-256 and P-521. Based on a selection of microcontrollers typical of EVI (i.e., ARM Cortex-A8, ARM Cortex-A9, and ARM Cortex-A53), the performance was characterized using benchmarks developed to assess the impact of PQC. Timing, memory, and storage metrics were recorded. ML-DSA-44, ML-DSA-65, ML-DSA-87, and the hybrid system P-256 & ML-DSA-44 completed more than 7.5 TLS handshakes/second when ran on the ARM Cortex A53, compared to P-256 completing 10.796, and P-521 completing 3.669 handshakes/second. ML-DSA-44 and hybrid were the most comparable algorithms to P-256 when comparing time to sign. P-256 completed 5,764.7 signatures/second on the Cortex A53, ML-DSA-44 completed 1,053.9, hybrid completed 880.9, and P-521 completed 59.9 signatures/second. ML-DSA-44 outperformed P-256 when verifying a signature on the A53, completing 3,206.6 verifications/second, P-256 completing 1,937.1, ML-DSA-65 completing 1,936.5, and P-521 completing 78.6 verifications/second. From these tests, the team concluded that on all three of the chips tested, PQC cryptosystems were comparable to P-256 when creating and verifying signatures and when completing the TLS handshake, and outperformed P-521 in all cases. These findings lead the team to believe supporting larger keys and signatures will likely be one of the most critical technical hurdles the industry needs to overcome during the transition to post-quantum resistant algorithms.

“Identify Challenges” and “Develop Migration Guidelines” are scheduled to start in FY24.

Conclusions

As part of EVs@Scale, the project supports electrified transportation security and resiliency. Zero trust and post quantum cryptography continue to demonstrate promise in enhancing EVI security and improving its resiliency.

Key Publications

1. Carroll, Thomas E., Lindsey M Redington, Addy M Moran-Schmoker, and Andrew J Murray. 2023. “Inventory of Public Key Cryptography in US Electric Vehicle Charging.” PNNL-34843. Pacific Northwest National Laboratory.

References

1. Amariei, Florin. 2023. “New Electrify America Charger Gets Hacked, Displays Tesla’s Supercharging Network.” Autoevolution. January 29, 2023. <https://www.autoevolution.com/news/new-electrify-america-charger-gets-hacked-displays-tesla-s-supercharging-network-209367.html>.

2. Carlson, Barney, Kenneth Rohde, Matthew Crepeau, Sean Salinas, Anudeep Medam, and Stacey Cook. 2023. “Consequence-Driven Cybersecurity for High-Power Electric Vehicle Charging Infrastructure.” Technical Paper 2023-01–0047. SAE.
3. hacsjalano. 2023. “Grizzl-E Smart Firmware V05.621 #442.” Open Source. GitHub. March 15, 2023. <https://github.com/lbbrhzn/ocpp/issues/442>.
4. Kerman, Alper, Murugiah Souppaya, Parisa Grayeli, and Susan Symington. 2022. “Implementing a Zero Trust Architecture, Volume A: Executive Summary.” NIST Special Publication (SP) 1800-35A. National Institute of Standards and Technology.
5. Lakshmanan, Ravie. 2023. “Is Your EV Charging Station Safe? New Security Vulnerabilities Uncovered.” The Hackernews. February 3, 2023. <https://thehackernews.com/2023/02/is-your-ev-charging-station-safe-new.html>.
6. National Institute of Standards and Technology. 2023. “Module-Lattice-Based Digital Signature Standard.” NIST Federal Information Processing Standards Publication (FIPS) 204. National Institute of Standards and Technology. <https://doi.org/10.6028/NIST.FIPS.204.ipd>.
7. Rose, Scott, Oliver Borchert, Stu Mitchell, and Sean Connelly. 2020. “Zero Trust Architecture.” NIST Special Publication (SP) 800–207. National Institute of Standards and Technology. <https://doi.org/10.6028/NIST.SP.800-207>.
8. The White House. 2023. “FACT SHEET: Biden-Harris Administration Announces New Standards and Major Progress for a Made-in-America National Network of Electric Vehicle Chargers.” The White House. February 15, 2023. <https://www.whitehouse.gov/briefing-room/statements-releases/2023/02/15/fact-sheet-biden-harris-administration-announces-new-standards-and-major-progress-for-a-made-in-america-national-network-of-electric-vehicle-chargers/>.

Acknowledgements

This work is sponsored by the Vehicle Technologies Office in the Office of Energy Efficiency and Renewable Energy Office, U.S. Department of Energy.

II.6 EVs at Scale - Codes and Standards

II.6.1 Support development and validation testing of SAE J1634 (ANL)

Michael Duoba, Principal Investigator

Argonne National Laboratory
9700 South Cass Ave., Bldg. 362
Lemont, IL 60439
E-mail: mduoba@anl.gov

Lee Slezak, DOE Technology Development Manager

U.S. Department of Energy
E-mail: lee.slezak@ee.doe.gov

Start Date: April 1, 2023
Project Funding: \$300,000

End Date: April 1, 2024
DOE share: \$300,000

Non-DOE share: \$0

Project Introduction

The gains electrified vehicles are expected to make (and thus the entire reason DOE is focused on electric vehicles at scale) are based upon metrics that can only come from standardized testing. Vehicle efficiency and emissions testing standards have evolved since the 1970s and consist of carefully crafted dynamometer test procedures aimed at capturing the energy economy and emissions of conventional vehicles. However, electric vehicle (EV) efficiency is so much higher than conventional vehicles, variances and physical phenomena that were largely ignored because they were “lost in the noise” have become significant concerns in EV testing. As we gain more experience in EV testing, a consensus has grown that more control over these variances is required and more precise procedures need to be drafted if EV test procedures are to provide acceptable test reproducibility.

The consequences can be catastrophic if errors or systemic bias in EV test results arise from oversights in the design of test procedures. If EV test procedures miss reality by providing overly optimistic results, consumers and DOE will be disappointed, wasting their substantial investments. If results are biased in the other direction (overly pessimistic), opportunities are lost. This project to update and further develop EV test procedures provides a risk management function to ensure efficiency, range, and performance results are a true representation of the technology upon which DOE builds its advanced vehicle technology research portfolio. DOE’s national labs are the perfect 3rd party entity to investigate (while working with regulatory bodies and OEMs) the development of improved test protocols and making honest assessments of standard practice test procedures. ANL staff have been creating and validating electrified vehicle chassis dynamometer testing standards for 30 years.

Objectives

The rapid growth of EV sales has led to the migration of EV development and testing activities from niche industry programs into mainstream mass production. Consequently, the goal of this work is to mitigate concerns regarding the consistency and reproducibility of EV testing results. EV test procedures need to be refined so the results are robust, and the methods easily-followed. Amidst this, there's a competing challenge: the need to minimize the exhaustive time and resource burdens of testing EVs. This program aims to further develop efficient testing methods without compromising the accuracy of the outcomes.

Approach

ANL has a long history of using advanced test facility assets to develop new test procedures for emerging vehicle technology. The effort is highly leveraged by participating in SAE Standards committees focused on vehicle testing and electrified vehicle standards. ANL has chaired committees or provided key roles in the development of virtually all SAE electrified vehicle standards since the late 1990s.

The adoption of standardized vehicle test procedures is typically facilitated by SAE International (among other standards organizations). Whereas EPA and CARB have the authority to certify vehicles as they see fit, much of what is found in the CFR and California regulations refer specifically to SAE standards documents. The main focus of this work is in support of the continued development of *SAE J1634 Battery Electric Vehicle Energy Consumption and Range Test Procedure*. However, there are a host of other SAE vehicle testing standards documents that require some refinement or modifications to accommodate the unique characteristics of EVs.

The approach involves a systematic procedure that starts by compiling known issues and potential concerns for investigation, followed by testing to determine whether there is a need to adjust test procedures. The specific steps are as follows:

1. Leveraging SAE and other standards organizations, work with experienced, global-leading subject matter experts to capture known EV testing uncertainty issues and to seek new issues that could also be potential problems.
2. Develop test plans designed to help resolve the captured issues.
3. Using ANL's state-of-the-art 4WD dynamometer cell in thermal chamber, run tests on EV test vehicles
4. Collaborate with other testing laboratories to share and pool data to solidify conclusions regarding EV test procedures.
5. Develop and validate modifications or new techniques to eliminate repeatability and reproducibility issues.
6. Help modify and ballot updated SAE standards documents

Results

Multi-Cycle Test (MCT) vs Short Multi-Cycle Test (SMCT)

Testing an EV requires significantly more laboratory resources than conventional vehicle testing. Whereas a conventional vehicle test that covers both the urban and highway EPA cycles requires 1.2 hours of dyno test time, a long-range EV can take as long as 4-6 hours. As such, the pressure to reduce the testing burden is a major thrust area in the SAE standards committees. Updates of SAE J1634 have focused on new procedures that have significantly reordered the test cycles to facilitate a reduction in testing time.

Two types of SAE J1634 test sequences are shown in Figure II.6.1.1, the Multi-Cycle Test (MCT) and the Short Multi-Cycle Test plus Steady-State (SMCT+). The important differences are the placement of the steady-state portions and the cycle order. The objectives of both tests are to collect cycle efficiency results and to completely discharge the pack to collect the Usable Battery Energy. The steady-state portion of the SMCT+ is put at the end, to accommodate the option of removing the vehicle from the dynamometer and completing the discharge with an off-board electrical discharge device, thus reducing dynamometer time by as much as ½ for long-range EVs. Currently, no commercial discharge device facilitating this time-savings procedure exists, so we use the on-dynamometer steady-state discharge option for testing.



Figure II.6.1.1 Test sequence diagrams for the MCT (from older version of J1634) and the SMCT+ (from latest version of J1634)

At ANL, tests were run on several test EVs using both SAE J1634 procedures to investigate the variances – we encountered biases and new issues to consider. The cycle energy consumption results for both procedures are shown in Figure II.6.1.2.

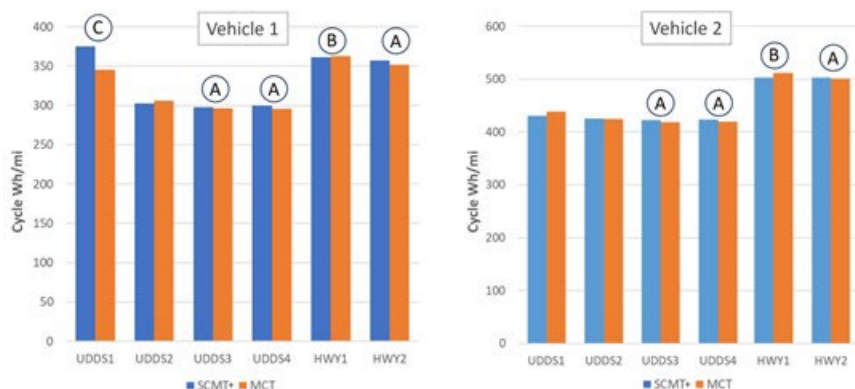


Figure II.6.1.2 Looking for bias in two different test procedures (J1634 MCT and SMCT+) with results from two EVs

The first trend to discuss is denoted by (A) in the bar charts in Figure II.6.1.2. The trend seen here has been noticed in other testing at ANL and the OEMs, the Wh/mi of later cycles in the MCT indicates slightly more efficient operation. The variables that differ in the two procedures that could account for the bias are: a different thermal state and a different SOC. The bias is seen for all the later MCT cycles (after the steady-state). This is most likely due to SOC because the thermal state of both UDDS4 cycles were roughly similar, but the SOC is markedly different. Members of the SAE committees have also noted the effect of lower Wh/mi for tests running at lower SOC. There is speculation on the part of some electrical engineers that this is related to the lower bus voltage and how it changes the dynamics of the inverter, motor, and switching frequency. We plan to do more tests to isolate the varying results due to the thermal state compared to SOC.

The trend denoted by (B) in Figure II.6.1.2 shows the MCT Wh/mi to be higher than the SMCT+. In this case, it is likely due to differences in the thermal state instead of SOC because SOC is relatively high in both tests, but the HWY1 in SMCT+ occurs after two UDDS tests instead of one. In conventional vehicle testing, results are assumed to be stabilized before the first ½ of the first UDDS cycle is complete. There is ample evidence that this is not the case for EVs. Because EV heat rejection in the powertrain is so low and the tires are

designed for high efficiency, warmup trends are slower and take much longer for results to stabilize. This is a persistent concern for repeatable Wh/mi test results with varying test sequences.

It shall be noted that the effects observed in (A) and (B) are noticeable but relatively small. Quantifying these differences with more testing will help regulatory agency staff make informed decisions about allowing different test options or if test options must be standardized to prevent varying results.

The trend denoted in (C) revealed an unexpected issue of concern. The first UDDS cycle in both procedures should have the same results as the procedure conditions are the same. What caused this particular discrepancy? Looking closer at the extensive signals we collect during testing explains the source of the difference. In Figure II.6.1.3, the battery power while driving is shown at the beginning of UDDS1 for both procedures. The increase in Wh/mi for the SMCT+ test is due to regenerative braking (“regen”) delayed for a much longer period. Most EVs reduce or eliminate regenerative braking at high SOC levels. For both sequences, the initial SOC was the same. However, the battery’s initial temperature was slightly different. Looking further into test conditions, the problem was the day before, the prep conditions were slightly different (a difference completely ignored in conventional vehicle testing). The MCT ran the vehicle until the battery was all the way empty whereas the SMCT+ did not go quite as low. Running the battery at a very low SOC generates internal heating of the battery due to increases in battery resistance. These slight differences in temperature carried over to the next test day. This brings up an interesting issue. Driving an EV to empty is not a normal situation in typical driving. However, for repeatability, every aspect before the test must be identical and repeatable in order to repeat test results.

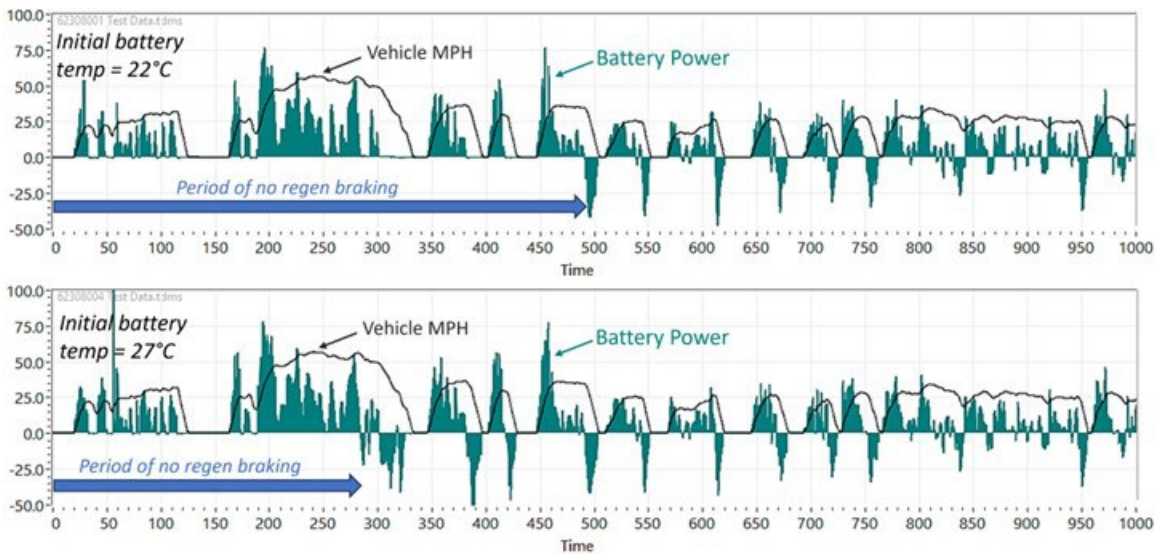


Figure II.6.1.3 Comparing regen operation in two different tests of the same EV. Slight changes in initial battery temperatures yielded substantially different operation and cycle consumption results.

Changes in Usable Battery Energy (UBE) with Temperature

The results for the EPA-adjusted MPGe and range label are derived from data collected through one of two testing options. One option is to run the “EPA 5-cycle” tests which include additional test cycles run at -7° C and at 35° C. The SAE standards committee wants more data on the usable battery energy at these test temperatures to determine how much extra testing is required to collect the information needed to satisfy the 5-cycle procedure. J1634 test sequences were run at 4 different temperatures, three of which are part of the “5-cycle” test procedure. In Figure II.6.1.4, the usable battery energy (UBE) for each test is shown (normalized to standard ambient tests). This information is helpful to show that the results from the “hot” test are not significantly different compared to the ambient test, however, there is a significant change in UBE as

temperatures get colder. To properly characterize EV range at low temperatures, both the consumption and UBE are needed to get accurate results.

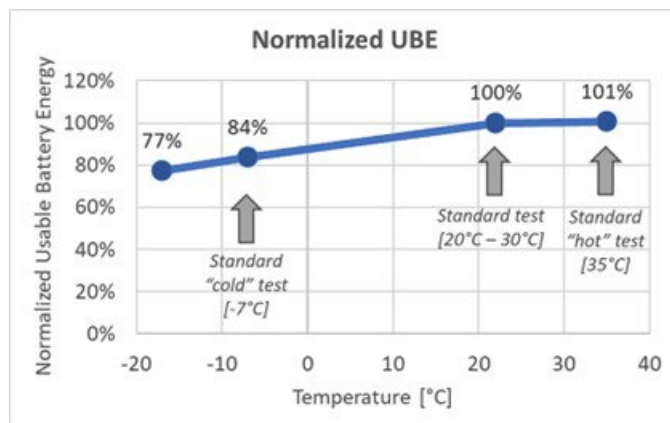


Figure II.6.1.4 Comparing the effect of changes in usable battery energy (UBE) across varying test temperatures.

It is worth noting here that standard “hot” test results are run at 35°C (95°F), but media attention has been highlighted an observed precipitous drop in range that occurs at 100 °F and above (which in some states can be a frequent summer occurrence). This effect is related to the fact maximum allowable temperatures for Li-Ion batteries is around 100°F and the only way to reject heat at these temperatures is to engage the A/C compressor which imparts significant parasitic loads during driving. As part of this project, discussions are ongoing with the testing community to address this additional concern.

Future Testing

This annual report represents a funding period of 6-months. The results herein represent a start to addressing a whole list of concerns the SAE EV testing standards committee has been collecting for a number of years. This project maintains a living document of EV testing issues that are reviewed at each SAE monthly meeting. Future testing is planned to continue addressing the list that includes the following themes: temperature impacts, test procedure variations, instrumentation errors, robot driver variations, cooling and cooling fan impacts, and road load uncertainty, among others.

Key Publications

1. SAE J1711-202302: “Recommended Practice for Measuring the Exhaust Emissions and Fuel Economy of Hybrid-Electric Vehicles, Including Plug-in Hybrid Vehicles”
2. SAE J2908-202301: “Vehicle Power and Rated System Power Test for Electrified Powertrains”

References

1. SAE J1634_202104, “Battery Electric Vehicle Energy Consumption and Range Test Procedure,” https://www.sae.org/standards/content/j1634_202104/

Acknowledgments

We extend our sincere gratitude to the staff and technicians at Argonne and members of the SAE vehicle test standards community. Their unwavering support and decades of rewarding collaboration have been instrumental to this program. This achievement is the culmination of a team effort, bringing together dedicated individuals from diverse backgrounds.

II.6.2 Wireless Charging Standard- (J2954/1-2-3) and Closeout of SWIFT Charge Consortium Support (Argonne National Laboratory, Idaho National Lab, Oakridge National Lab)

Theodore Bohn, Principal Investigator

Argonne National Laboratory
9700 S. Cass Avenue
Lemont, IL 60439
E-mail: tbohn@anl.gov

Lee Slezak, DOE Technology Development Manager

U.S. Department of Energy
E-mail: Lee.Slezak@ee.doe.gov

Start Date: January 1, 2023	End Date: Dec. 30, 2023	
{ANL} Project Funding: \$50,000	DOE share: \$50,000	Non-DOE share: \$0
{INL} Project Funding: \$50,000	DOE share: \$50,000	Non-DOE share: \$0
{ORNL} Project Funding: \$90,000	DOE share: \$90,000	Non-DOE share: \$0

Project Introduction

Problem Statement

The EVs at Scale lab call program is divided into 5 pillars, including Codes & Standards as one of the pillars. Wireless power transfer is one of the focus areas within codes & standards support. ANL, INL and ORNL representatives actively participate in standards defining organizations meetings and give input to support review as well as refinement of standards documents.

There are insufficient resources from stakeholder participants in standards defining organizations (SDOs) since most are not-for-profit and rely on donated time and effort of subject matter experts. DOE support via national lab participants fills some of the gaps to define, create and refine EV charging related standards.

The International Electrotechnical Commission (IEC) headquartered in Geneva, Switzerland, is the organization that prepares and publishes international Standards for all electrical, electronic and related technologies. The IEC 61980-1:2020 Electric vehicle wireless power transfer (WPT) systems - Part 1: General requirements standard was last updated in 2020. <https://webstore.iec.ch/publication/31657>

The SAE J2954 wireless power transfer standard was launched in 2010 and has made slow but steady progress over the past 13 years with three levels of power/vehicle class covered today.

- SAE J2954/1 Wireless Power Transfer for Light-Duty Plug-in/Electric Vehicles and Alignment Methodology https://www.sae.org/standards/content/j2954_202208/
- SAE J2954/2 Wireless Power Transfer for Heavy-Duty Electric Vehicles https://www.sae.org/standards/content/j2954/2_202212/
- SAE J2954/3 Dynamic Wireless Power Transfer for both Light and Heavy Duty Vehicles <https://www.sae.org/standards/content/j2954/3>

The SWIFTCHARGE consortium was formed in 2020 with membership details and draft scope held confidential to only consortium members. Avoiding any details in this annual progress report (APR) relating to patent claim disputes, the SWIFTCHARGE consortium was formed to provide a forum for wireless power transfer (WPT) innovation that was not constrained by technical decision consequences in SAE J2954-IEC61980. Figure II.6.2.1 describes an early vision of the mission of the SWIFTCHARGE consortium.

Momentum Dynamics representatives reached out to DOE-VTO to fund National Laboratory staff to support review and refinement of the draft SWIFTCHARGE specification that would eventually mature to an SDO level document for adoption or inclusion of a TBD standards organization document.



Figure II.6.2.1 Vision of SWIFTCHARGE consortium on industry led wireless power transfer methodology not constrained by decisions set in SAE J2954/IEC61980, facilitating technical innovation with fewer boundaries.

The description inserted in the FY22 lab call on wireless power transfer is;

High Power Scalable/Interoperable Wireless Charging (including SWIFTCharge)

The present J2954/1 wireless charging standard only spans to 11kW and J2954/2 is a work in progress high power standard, not interoperable with low power infrastructure. SWIFTCharge is new industry based consortium (analogous to USB/Bluetooth roots) creating a requirements document that can be adopted by an SDO, accelerating the process to a validated solution. As an SAE J2954 alternative, it is interoperable as well as scalable from residential size single emitter (GA) to high power public and commercial (up to 1MW) systems.

This APR covers ANL, INL and ORNL support for SWIFTCHARGE meetings and specification development.

An overlap of the umbrella codes and standards tasks include NIST Handbook 44-3.40 (HB44) for commercial dispensing of electricity as a fuel, including conductive and wireless power transfer methods. Previous APRs covered past HB44 tasks related to evolving test and certification procedures for WPT systems, primarily tied to SAE J2954-IEC61980 but included in SWIFTCHARGE specifications as well.

Objectives

Primary goals

Address challenges and barriers for high-power WPT EV charging standards by identifying and filling gaps in charging equipment including regulatory hurdles, interoperability, and safety topics. The collective ANL-INL-ORNL goals to support SAE J2954 and SWIFTCHARGE are the same, the goals to

- Facilitate creation and improvement of codes and standards enabling ‘EVs at scale’ charging
- Engage with industry stakeholders to create a consensus based EV standards
- Create interoperability guidelines and criteria to evaluate standards compliance/implementation
- Support methods to collect validation test data with industry partners for standards refinement

Achieving this goal is facilitated via active participation in monthly SDO meetings to review and develop standards documents.

Approach

The task numbers in this section are references to the DOE Annual Operating Plan (AOP), specifically for ANL tasks in this area of the annual report. Tasks for INL and ORNL are listed in subsequent sections of the annual report. The barriers and solutions for each of the tasks are similar since the standards process is iterative and at times unending with 5 year document reviews and updates to all active standards as part of the renewal process.

Task 1.1b Supporting SAE J29254-2 and SWIFT Charge standard development activities to cover recent technological developments in power electronics and electromagnetics.

Barriers

- SAE J2954 has been published for wireless charging of light duty vehicles; a similar standard does not exist for heavy duty vehicle wireless charging, necessitating SAE J2954-2 that reflects 2023 technologies.
- A standard does not exist for dynamic wireless charge
- SWIFT Charge wireless vehicle charging consortium was formed by member companies that are anonymous while the recommended practice documents are drafted, with an end goal of adoption by a standards defining organization after field validation and testing. National lab participants bring independent perspectives to objectively assess the goals and methods of the SWIFT Charge consortium. This consortium seeks to overcome fundamental limitations of the SAE J2954 methods of coupling fields, EMC limitations and higher power density while meeting EMF limits. The consortium is not unlike the phone/consumer device Wireless Power Consortium; <https://www.wirelesspowerconsortium.com/>.

Solution

ANL staff have participated in monthly SAE J2954 meetings and testing since the standard work area was launched in 2010. Supporting SAE J2954-2 for heavy duty applications as an extension of past activities. J2954-3 was launched in April 2023 (<https://www.sae.org/standards/content/j2954/3>) has expanded to include dynamic power transfer for electrified roadways and leverages state/federally funded demonstration projects. These projects include ASPIRE, based at the Utah State University facility, including 4 NSF funded universities. <https://aspire.usu.edu/presentations/enabling-technologies-for-dynamic-wpt-vehicle-automation/> The SAE J2954 committee has several subcommittees that also meet each month, focused on EMC compliance/assessment, alignment-interoperability, and testing activities.

The SWIFT Charge consortium was led by Momentum Dynamics of Malvern PA that changed ownership and is now InductEV (<https://inductev.com/>). The authors of the SWIFT Charge technical specifications committee met monthly to review document drafts and gather input from national lab participants (ANL, INL, ORNL). Funding for task 1.1 is limited to participation in monthly meetings and document review/feedback/input.

Results

The results here are specific to lab activities for the tasks covered in this part of the Annual Report. Since the task for ANL, INL and ORNL are to support the J2954 and SWIFTCHARGE consortium the activities and results are the same for each national lab.

Task 1.1b Supporting SAE J29254-2 and SWIFT Charge standard development activities to cover recent technological developments in power electronics and electromagnetics.

The work-in-progress SAE J2954/2 for heavy duty electric vehicles was published in December 2022, covering power levels from 22kW to 500kW, and up to 1MW with parallel receivers matching ground assembly coils. The SAE J2954/3 'Dynamic Wireless Power Transfer for both Light and Heavy Duty Vehicles' standard was launched in April 2023 with monthly progress toward publication possibly in 2025.,

In the past 5-10 years the WPT industry has gone through a steady consolidation of manufacturers that have failed to bring products to market and/or have expended all available working capital. There are no known WPT systems offered by a vehicle OEM, with WiTricity, Hevo, Lumen Group, Wave and InductEV demonstrating stationary charging systems only on retrofit light, medium, heavy duty electric vehicles. Figure II.6.2.2 shows the SWIFTCHARGE consortium view of the range of vehicles, power levels and shared distributed network of chargers. A DC-as-a-Service (DCaaS) power distribution scheme was included in the draft specification, incorporating elements of IEEE P2030.13 with DC coupled energy storage and local generation to feed multiple WPT charge points from a share DC source.

As a result of consolidation and shift in WPT member company priorities on engineering resources the SWIFTCHARGE consortium is dissolved with no immediate plans to continue development.

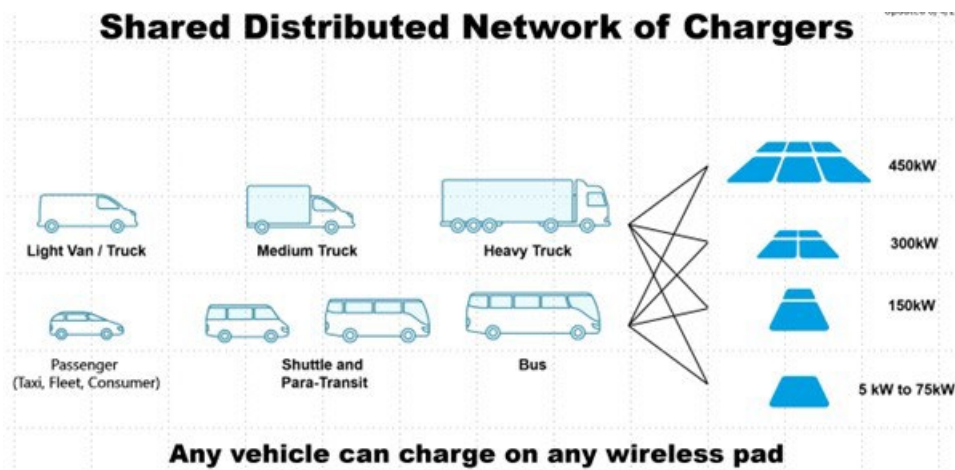


Figure II.6.2.2 Vision of SWIFTCharge range of interoperable arrays of ground assemblies in a distributed network

Conclusions

With the change of control of Momentum Dynamics in 2022, and its subsequent loss of leadership and expertise, the one proven successful commercial wireless charging company marked the end of serious innovation and the eventual demise of the wireless charging industry.

Wireless power transfer standards for commercial heavy duty vehicles were advanced to publication as part of SAE J2954/2 and the SAE J2954/3 dynamic WPT standard work-in-progress was launched.

The SWIFTCHARGE consortium has been disbanded as a result of consolidation in the WPT industry.

II.6.3 Wireless Power Transfer, DER Standards Tasks (Idaho National Laboratory)

Timothy Pennington, Sr. Research Engineer

Idaho National Laboratory
1955 Fremont Ave.
Idaho Falls, ID 83415
E-mail: Andrew.Meintz@nrel.gov

Lee Slezak, DOE Technology Development Manager

U.S. Department of Energy
E-mail: Lee.Slezak@ee.doe.gov

Start Date: January 1, 2023	End Date: Dec. 30, 2023	(5 year project-Dec 2027)
Project Funding (FY22): \$50,000	DOE share: \$50,000	Non-DOE share:

Project Introduction

Problem Statement – The EVs at Scale lab call program is divided into 5 pillars plus consortium management. This section covers INL Codes & Standards tasks.

Objectives

Primary goals – The INL portion of codes and standards pillar tasks focus wireless power transfer standard. The goal is to create and improve codes and standards enabling ‘EVs at scale’ charging.

Approach

INL leveraged previous SAE standards testing and procedure development to support the WPT standards

Tasks 1.5 and 1.6 Support SWIFTCharge Alliance and SAE J2954-2 wireless power transfer standard development and lab evaluation efforts in performance, interoperability, EM safety and communications.

Barriers

- Same barriers as Task 1.1, different lab activity.

Solution

INL staff have participated in SAE J2954 monthly meetings and will continue to give input to the J2954-2 work group. The same with SWIFT Charge on the similar mission consortium.

II.6.4 Wireless Power Transfer, Medium Voltage Power Converter Standards Tasks (Oak Ridge National Laboratory)

Omer Onar, Principal Investigator

Oak Ridge National Laboratory
National Transportation Research Center
PO Box: 2008 MS-6472
Oak Ridge, TN 37831
E-mail: Onaroc@ornl.gov

Lee Slezak, DOE Technology Development Manager

U.S. Department of Energy
E-mail: Lee.Slezak@ee.doe.gov

Start Date: January 1, 2023	End Date: Dec. 30, 2023	(5 year project-Dec 2027)
Project Funding (FY22): \$90,000	DOE share: \$90,000	Non-DOE share:

Project Introduction

Problem Statement – Same as previous. This section covers ORNL Codes & Standards tasks.

Objectives

Primary goals – The ORNL portion of codes and standards pillar tasks focus mostly on wireless power transfer topics, with liaison activities coordinating researchers on medium voltage power converters. The goal is to create and improve codes and standards enabling ‘EVs at scale’ charging.

Approach

ORNL leveraged previous and current DOE funded wireless power transfer activities to support WPT standards. The same with medium voltage power converter activities under a previous lab call.

Tasks 1.1a and 1.2 Support J2954, SWIFT Charge for WPT

Barriers

- Same barriers listed for task 1.1 above.

Solution

ORNL staff have participated in past J2954 WPT work group meetings and SWIFT Charge consortium meetings and continued that activity in FY2022. The same for IEEE Power Electronics Society Technical committee #9 past and future meetings.

Solution

ORNL conducted interoperability assessment of the higher surface power density (ORNL designed) polyphase WPT coupler compared to DD and circular couplers using a polyphase transmitter and DD-circular receivers and DD-circular transmitters with a polyphase receiver. Data used to support J2954 standards.

Key Publications/Presentations

1. Critical review and input to upcoming SAE World Congress paper #24AE-0058 – Validation and Comparison of Vehicle to Ground Assembly Alignment Methodologies for SAE J2954 Standard, Wireless Power Transfer.

Acknowledgements

This project is sponsored by the Vehicle Technologies Office in the Office of Energy Efficiency and Renewable Energy Office, U.S. Department of Energy. The work was conducted by researchers in the Advanced Mobility and Grid Integration Technology Section of the Energy Systems Division of Argonne National Laboratory along with industry collaboration partners.

(This page intentionally left blank)

U.S. DEPARTMENT OF
ENERGY

Office of
**ENERGY EFFICIENCY &
RENEWABLE ENERGY**

For more information, visit:
energy.gov/eere/vehicles

DOE/EE-2879 • August 2024